Synthesis, Characterization and Biophysical Assessment of Quantum Dots and Application in Electrophysiology

A thesis submitted in partial fulfillment of the requirements for award of the degree of Doctor of Philosophy

Ms Runjun Sarma

Registration No. TZ121470

Nanoscience and Soft Matter Laboratory
Department of Physics
School of Sciences, Tezpur University
Napaam, Tezpur-784028
Assam, India

July, 2014

Dedicated to

My beloved parents

Late Krishna Mohan Sarma & Mrs Runima Sarma

Abstract

Semiconductor nanocrystals, or quantum dots (QDs) are now regarded as alternative, yet effective luminescent probes/labels for numerous biological applications. This is due to their unique size dependent optical features such as, broad absorption and narrow emission response and resistance to photobleaching [1]. The chalcogenide systems (e.g., CdSe), in particular, are considered as efficient candidates owing to their large band gap tunability over a wide range of electromagnetic spectrum, apart from bright emission features. Though questionable for large scale use, the toxicity level of cadmium ions is likely to reduce in the nanometer region, when it forms CdTe or CdSe than available in elemental form [2]. Consequently, there exists plentiful scope for safe use of nanoscale CdSe and similar particles in biophysical and biomedical research.

On the other hand, magnetic impurity doped semiconductor nanocrystals have gained remarkable attention owing to their immense value in magneto-optics, nonlinear optics, nano-photonics and nano-biotechnology [3,4]. These QDs exhibit special properties, including localization of magnetic ions and size-dependent *sp-d* exchange interactions. In contrast, manganese selenide (MnSe) QDs, have attractive magneto-optic responses owing to the availability of large number of unpaired electrons in Mn^{2+} high-spin state along with size dependent optical gaps [5]. Although, hexagonal phase of MnSe is quite unstable and extremely rare as compared to cubic MnSe, yet they are of significant worth because of their structural compatibility with other II-VI semiconductor systems [6]. Moreover, the cooperative effect of fluorescence response and magnetic ordering could offer a new window for tuning bright-fluorescence imaging in response to an externally applied magnetic field. A number of critical issues need to be addressed prior to nanobio-interface applications. To name a few, water solubility, bio-functionality, cytotoxicity etc. [1] and consequently, optical stability of synthesized QDs is extremely important in biological environments/cell culture media. Furthermore, cellular functioning in living organisms are generally governed by ion transport mechanism [7]. However, functional nanopore creation across a lipid bilayer leading to passage of ions in live cells, has not been fully understood. The artificial bilayer membrane can be used as a model system to

evaluate the nature of transient nanopores created by insertion of QDs when the bilayer is subjected to an external field.

This thesis is comprised of eight chapters. The motivation and historical background is discussed in *Chapter* 1. In *Chapter* 2, different synthesis protocol, methodology and elaboration of basic characterizations of synthesized CdSe and MnSe QDs are highlighted. Furthermore, characteristic structural and optical features of the synthesized $Cd_{1-x}Mn_xSe$ QDs with varying stoichiometry parameter x is discussed. The water soluble CdSe QDs are prepared by using polyvinyl alcohol (PVA) as the host matrix which not only act as an efficient surface passivating agent, but also responsible for enhancing radiative emission response. In addition, CdSe and MnSe QDs are fabricated using thioglycolic acid (TGA) and sodium dodecyl sulphate (SDS) as coating agents. The coating layer provides both water solubility as well as bioconjugation capability of the QDs. A detailed discussion on dependence of optical responses of the QDs on different reaction environment is presented in *Chapter* 3. The growth of QDs is largely dependent on the reaction environment where the reactant concentration, reaction time and surfactant concentration play an key role. More importantly, the optical behavior of the QDs in different cell culture media, in absence and in presence of a dispersing agent (e.g., bovine serum albumin, BSA protein), has been emphasized. An attempt to assess the optical properties of the QDs in natural environment, like lemon water and rose water media is also worked out. The optical behavior of the synthesized QDs is found to be strongly modulated due to varying reaction parameters. The CdSe-PVA QDs prepared from a precursor of larger Cd^{2+}/Se^{2-} ratio (3:1) as compared to lower ratios (1:1, 2:1), and with a reaction time of 60 min. is characterized by a sharp absorption feature and symmetric luminescence response. Similarly, as revealed from X-ray diffraction patterns, the MnSe-TGA QDs are optimized to crystallize into a hexagonal WZ phase, when grown with a higher TGA concentration (10%) and a lower precursor ratio (Mn^{2+}/Se^{2-}: 2:1). The QDs possess a sharp, blue shifted excitonic absorption with respect to the bulk WZ phase MnSe and along with symmetric band edge emission behavior. With BSA as a dispersing agent, the above mentioned QDs display an improved optical stability in *Dulbecco's Modified Eagle Media*® (DMEM) and *Minimum Essential Media*® (MEM) media as compared to the *Roswell Park Memorial Institute*® (RPMI-1640) media depending on their constituents.

These media finds their use for growing and preserving live cells.The study of variation of magnetic properties of MnSe QDs coated with different surfactants is elaborated in *Chapter* 4. The magnetic property of the QDs are found to be surface dependent [6] and the magnetic property changes with capping agent type. Both TGA and SDS coated MnSe QDs have exhibited a mixed para and antiferromagetic phase, at low temperature (27 K) but only paramgnetic phase at room temperature (300 K). Moreover, the Neel temperature is found to be affected by the TGA concentration employed for synthesizing MnSe-TGA QDs. *Chapter* 5 demonstrates QD-BSA protein bioconjugation, fluorescence imaging, and confocal microscopy of the synthesized QDs. The bioconjugation capabilities are evaluated by using BSA as model protein. The biophysical aspects of the QDs are discussed in terms of time resolved phenomena, fluorescence resonance energy transfer mechanism, cytotoxicity and bioimaging competence. The cytotoxicity behavior and fluorescence imaging capability of the CdSe and MnSe QDs are studied by using human lymphocyte cells collected voluntarily. The results show that the cell viability of the lymphocytes has a direct influence on the concentration of MnSe QDs, with a safe limit upto 0.5 μM. High biocompatibility and fluorescent behavior of the QDs are witnessed in the cellular environment.

Chapter 6 highlights the possible electrophysiology application of highly fluorescent CdSe QDs. The water soluble CdSe QDs were used as ion channel forming agents across a soy-extracted lecithin formed lipid bilayer following a planar chip technique. To record current fluctuation across the bilayer, different experimental steps are considered, such as suppression of electromagnetic noise, micropore formation, lecithin extraction, formation of a stable lipid bilayer and finally, ion channel recording. The voltage-dependent current fluctuation, across the lecithin bilayer (supported on a ~100 μm thick, ~100 μm aperture cellulose acetate substrate) is attributed to the insertion of water-soluble CdSe QDs into impermeable bilayer and spontaneous aggregation resulting in the nanopore formation [8]. Apart from a closed state, the first observable conductance levels are found as ~6.3 and 11 nS, which correspond to a biasing voltage of -10 and -20 mV; respectively. Higher observable conductance levels, at corresponding voltages, are found as ~14.3 and 21.1 nS. Based on two simplified models, the formation of non-spherical pores (d_{nspore}) can be predicted as a better approximation over spherical nanopores (d_{spore})

for witnessing a definite conductance level. It is observed that, for a definite conductance state $d_{spore} \leq 4d_{nspore}$. In addition, the number of QDs required to form a nanopore of diameter d_{nspore}, is smaller than that of d_{spore}. The current events are observed to be partly stochastic, possibly due to thermal effects on the aggregated QDs that form nanopores. The dwell time of the states are predicted in the range of 384–411 μs. Assuming simple diffusion, a description on ion channels can also be found in the light of a theoretical frame work to be discussed in *Chapter* 7. Starting with *Saffman-Delbruck* approximation [9], both non-aggregate and aggregate form of QDs are considered where a definite conductance state is defined by a select numbers of QD aggregation.

Finally, conclusive remarks and future directions is discussed in *chapter 8* followed by appendix and addenda sections.

References

[1] Jamieson, T., et al. Biological applications of quantum dots, *Biomaterials* **28**(31), 4717--4732, 2007.

[2] Zayed, J. & Philippe, S. Acute oral and inhalation toxicities in rats with cadmium telluride, *Int. J. Toxicol.* **28**(4), 259--265, 2009.

[3] Zhu, Y.-H. & Xia, J.-B. Giant Zeeman splitting in manganese-doped ZnSe quantum spheres: Eight-band effective-mass calculations, *Phys. Rev. B* **74**(24), 245321, 2006.

[4] Archer, P. I., et al. Direct observation of *sp-d* exchange interactions in colloidal Mn^{2+} and Co^{2+} doped CdSe quantum dots, *Nano Lett.* **7**(4), 1037--1043, 2007.

[5] Furdyna, J. K. Diluted magnetic semiconductors, *J. Appl. Phys.* **64**(4), R29--R64, 1988.

[6] Yang, X., et al. Morphology-controlled synthesis of anisotropic wurtzite MnSe nanocrystals: optical and magnetic properties, *CrystEngComm* **14**(20), 6916--6920, 2012.

[7] Hodgkin, A. L. & Huxley, A. F. A quantitative description of membrane current and its application to conduction and excitation in nerve, *J.Physiol.* **117**(4), 500--544, 1952.

[8] Sarma, R. & Mohanta, D. Recording ion channels across soy-extracted lecithin bilayer generated by water-soluble quantum dots, *Philos. Mag.* **94(4),** 345--357, 2014.

[9] Saffman, P. & Delbrück, M. Brownian motion in biological membranes, *Proc. Natl. Acad. Sci.* **72**(8), 3111--3113, 1975.

DECLARATION

I hereby declare that the thesis entitled "**Synthesis, Characterization and Biophysical Assessment of Quantum Dots and Application in Electrophysiology**" being submitted to the Department of Physics, Tezpur University, Napaam, Tezpur, Assam, India, in fulfillment of the requirement for the award of the Doctor of Philosophy, has previously not been submitted anywhere for the award of any degree, diploma, fellowship or any other similar title or recognition

Runjun Sarma

Date: 4/3/15

Place: Tezpur University

Runjun Sarma

CERTIFICATE

This is to certify that the thesis entitled "**Synthesis, Characterization and Biophysical Assessment of Quantum Dots and Application in Electrophysiology**" submitted to the School of Sciences, Tezpur University in partial fulfillment for the award of the degree of Doctor of Philosophy in Physics is a record of research work carried out by **Ms Runjun Sarma** under my supervision and guidance.

All help and support received by her from various sources have been duly acknowledged.

No part of this thesis has been submitted elsewhere for award of any other degree(s).

(D. Mohanta)

Date: 04-03-2015
Place: Tezpur

Associate Professor
School of Sciences
Department of Physics
Tezpur University
Tezpur, Assam

ACKNOWLEDGEMENTS

In my quest towards enlightenment from the fountain of learning during all these years, I have been blessed by the Almighty God with some of the most wonderful people whose presence at different phases of my doctoral studies have enriched my learning experience and have helped me evolve as a better human being.

I express my profound sense of gratitude and veneration to my supervisor Dr. Dambarudhar Mohanta for guiding me all the way during my PhD tenure. His constant inspiration and encouragement have been a great motivation for me behind all the work I have conducted. He has always boosted me to put in extra efforts and I am indebted to them what I am today. I am also thankful to him for providing me opportunities to handle some short-term projects which enabled me to fortify my skills.

I extend my sincere and hearty gratitude to Prof. A. Choudhury for his personal involvement, constant encouragement, stimulating discussions from time to time carry out my research work. I am extremely grateful to Dr. A. Ramteke for his helping hand and suggestions in different research aspects related to biophysics.

I express my deep sense of gratitude to all the faculty members of Department of Physics, Tezpur University who have given valuable suggestions in my PhD work. I would like to extend sincere thanks to Dr. H.L Das, Gauhati University for constant inspiration in carrying out research work. I am also thankful to Dr. P. Puzari, Department of Chemical Science, Tezpur University, for suggestions and supports in different aspects in my duration in Ph.D.

I am extremely grateful to Anowar Hussain, Department of Molecular biology and Biotechnology, Tezpur University who have been supportive in providing me fluorescent microscopy study facilities to improve the quality of this research work. I would like to thank Mr. Dipankar Kalita, Department of Food Engineering and Technology, Tezpur University for extending helping hand in the work of extraction of lecithin.

I would like to give special thank to Dr. Biswajit Choudhury, Department of Physics, Tezpur University and Dr. Sidananda Sarma, Department of Physics, IIT-G for their all possible supports in my research works.

I am extremely grateful to Department of Science Technology, New Delhi (project no. SR/FTP/PS07/2008) and Tezpur University for providing financial assistance to carry out my research work smoothly.

I gratefully acknowledge Dr. A. Saha of UGC-DAE-CSR, Kolkata for extending Raman spectroscopy facility. I would like to thank stuff of TEM facility of SAIF, North-East Hill University, Shillong. It would have never been possible to me to enjoy the facts of nanoscale materials without the cooperation of Mr. Joston Nongkynrih in each TEM analysis. As for TEM measurements, the help and support received from Dr. Jungwon Park at SEAS, Harvard University is also gratefully acknowledged. I am also very much thankful to WEITZ Group, Department of Physics, School of Engineering and Applied

Sciences, Harvard University for confocal microscopy experiment. This was possible while my supervisor was visiting Harvard University through Indo-US research program of IUSSTF, New Delhi. I owe thanks to A Srinivasan of Department of Physics, IIT-G for all magnetic characterizations, and CIF, IIT-G for extending TR-PL measurements of all my nanoparticles.

I would like to thank my lab mates Manjit, Rizwin, Samiran, Manashi ba, Swati Nibedita,who gave their valuable effort in countless way in times of need and requirement in last 3 years. I thank all of them for always cheering me up. Working with them was a nice experience.

This work would not be possible without the support and encouragement from my friends, seniors and juniors. My thanks go to Madhulekha, Bondita, Anisha, Saurav, Nomita, Nayanmoni, Pratibha, Ankita, Pallavi, Priyanka, Deepak, Kakoli, Kashmiri, Kaushik, Pawan and Susmita.

I owe thanks to technical and laboratory staffs, of Tezpur University, for their timely helps to complete my PhD research work.

I am deeply indebted to my mother and my sisters for their constant inspirations invaluable support, patience and encouragement during the entire duration of my doctoral studies. I am very much grateful to Mr. Manash Jyoti Kashyap, IIT-D for his constant inspirations and helps till the end of my thesis works.

Finally and above all, I would like to thank the Almighty God. It would not have been possible for me to reach at this stage of academic pursuit without his grace.

Runjun Sarma

TABLE OF CONTENTS

List of Figures

Chapter 1

Chapter 2

Chapter 5

Chapter 7

List of Tables

List of Symbols

$g(E)$	:	Density of states
E	:	Total energy of a particle
h	:	Planck's constant
$\hbar$	:	Planck's constant divide by 2π
ε	:	Dielectric constant of semiconductor
m_0	:	Rest mass of electron
μ_{eh}	:	Electron- hole reduced mass
m_e^*	:	Electron effective mass
m_h^*	:	Hole effective mass
a_B	:	Bulk Bohr exciton radius
λ_B	:	de Broglie wavelength
R	:	Size of the nanocrystal
L	:	Dimension of impenetrable barrier
φ	:	Probability of finding the particle
E^*_{Ry}	:	Rydberg energy
R_y	:	Rydberg constant
d	:	Average size of QDs
N	:	Number of QDs
2θ	:	Bragg's angle
d_i	:	Interplanar spacing
h,k,l	:	Miller indices
a, c	:	Lattice parameters
D_{cry}	:	Crystallite size of QDs
ε_s	:	Strain magnitude
β_{hkl}	:	Full width half maxima
λ_{onset}	:	Onset of absorption
E_g	:	Band gap energy
$\Delta\lambda$	:	Blue shifted wavelength
ΔE_g	:	Blue shifted energy
λ_{ex}	:	Excitation wavelength
λ_{BE}	:	Band edge emission wavelength
λ_{DE}	:	Defect related emission wavelength
I_{BE}	:	Band edge emission intensity
I_{DE}	:	Defect related emission intensity

Φ_Q	:	Quantum yields of QDs
n	:	Refractive Index of solvent
I_Q	:	Integrated Emission Intensity of QDs
I_{ref}	:	Integrated Emission Intensity of reference
A_Q	:	Absorbance of QDs
A_{ref}	:	Absorbance of reference
ϵ_a	:	High frequency dielectric constant of QDs
ϵ_d	:	Static dielectric constant of QDs
ϵ_s	:	Dielectric constant of water
ω_{LO}	:	Longitudinal optical phonon frequency
ω_{TO}	:	Transverse optical phonon frequecny
ω_{LA}	:	Longitudinal acoustic phonon frequency
ω_{TA}	:	Transverse acoustic phonon mode frequency
ω_{SO}	:	Surface optic phonon
Δ_{Stokes}	:	Stokes shift
S	:	Huang –Rhys parameter
$\Delta\nu$	:	Raman shift
T_N	:	Neel temperature
H_c	:	Coercivity
M_r	:	Remanence
M	:	Magnetization
T	:	Temperature
H	:	Magnetic field
T_{bf}	:	Bifurcation temperature
τ	:	Lifetime of QDs
τ_{av}	:	Average lifetime
$J(\lambda)$	:	Overlapping integral
$F_D(\lambda)$	:	Integrated fluorescence intensity of donor
ε_A	:	Molar extinction coefficient of the acceptor
F_{DA}	:	Integrated fluorescence intensity of the donor in the presence of the acceptor
R_0	:	Förster radius
k	:	Dipole orientation factor
E_F	:	Energy transfer efficiency in FRET
r	:	Donor acceptor separation distance
$S_D^2(f)$	:	Power spectral density of dielectric noise
$I_D(f_c)$	:	rms dielectric noise

D_f	:	Dissipation factor of the material(s)
C_D	:	Capacitance of the dielectric(s)
f_c	:	Cut-off frequency
C_{se}	:	Substrate capacitance
ε_r	:	Dielectric constant of the substrate material
ε_0	:	Permittivity in free space
t_s	:	Thickness of the substrate material
C_{el}	:	Capacitance of the immersed electrode
C_m	:	Membrane capacitance
C_s	:	Specific capacitance of substrate material
d_p	:	Diameter of the pore
ρ	:	Density of substrate material
K	:	Thermal Conductivity of substrate material
T_m	:	Melting point
Y	:	Young's modulus
I	:	Measured current across the bilayer
dV/dt	:	Ramp voltage
d_t	:	Thickness of the lipid bilayer
ε_m	:	Dielectric constant of the membrane
d_{pore}	:	Diameter of nanopore formed by aggregation of QDs
d_{dot}	:	Diameter of an individual QD participating in the formation of nanopore
G_s	:	Conductance level due to spherical nanopore creation
d_{spore}	:	Diameter of spherical shaped nanopore
σ	:	Conductivity of the electrolytic buffer
G_s	:	Conductance level due to nonspherical nanopore creation
d_{nspore}	:	Diameter of nonspherical shaped nanopore
l	:	Length of the pore in lipid bilayer
N_Q	:	Number of QDs involved in the creation of an aggregated structure
D_0	:	Diffusion coefficient of the QDs in electrolytic solution
t	:	Diffusion time
MSD	:	Mean square displacement of the QDs in electrolytic solution
τ_r	:	Relaxation time of the QD in electrolytic solution
D_{cl}	:	Concentration dependent diffusion coefficient of the QDs in electrolytic solution
k_d	:	Interdot interaction parameter in the solution
C	:	Concentration of QD in the solution
λ_l	:	Dipole interaction parameter among QDs

U	:	Attractive interaction energy between the two dipoles (QDs)
L_t	:	*Separation distance between two QDs in electrolytic solution*
MSD_C	:	Concentration dependent MSD of the QD in electrolytic solution
τ_C	:	Concentration dependent relaxation time of the QD in electrolytic solution
ε_h	:	Reduced size in hydrodynamic model
l_h	:	Hydrodynamic length
η_m	:	Surface viscosity of membrane
h	:	Lipid bilayer thickness
μ	:	Bulk viscosity of membrane
η	:	Viscosity of the membrane surrounding fluid
γ	:	Euler's constant
ε_L	:	Dielectric constant of lipid bilayer
D_L	:	Diffusion coefficient of the QD in lipid bilayer in pre-aggregated state
MSD_L	:	Mean square displacement of the QD in lipid bilayer in pre-aggregated state
τ_L	:	Relaxation time of the QD in lipid bilayer in pre-aggregated state
D_{LA}	:	Diffusion coefficient of the QD in lipid bilayer in pre-aggregated state
MSD_{LA}	:	Mean square displacement of the QD in lipid bilayer in aggregated state
τ_{LA}	:	Relaxation time of the QD in lipid bilayer in aggregated state
ε_{sp}	:	Reduced size of QDs in lipid bilayer
ε_{LA}	:	Reduced size of aggregated structure formed by QDs in lipid bilayer
D_{c2}	:	Concentration dependent diffusion coefficient of the QDs in lipid bilayer
MSD_{LC}	:	Concentration dependent *MSD* of QDs in electrolytic solution
τ_{LC}	:	Concentration dependent relaxation time of the QDs in lipid bilayer
MSD_{LAF}	:	Mean square displacement of fully inserted aggregated structure created by QDs
MSD_{LAP}	:	Mean square displacement of partially inserted aggregated structure created by QD
τ_{LAF}	:	Relaxation time of fully inserted aggregated structure created by QD
τ_{LAP}	:	Relaxation time of partially inserted aggregated structure created by QD
G_F	:	Conductance of fully inserted aggregated structure created by QD
G_P	:	Conductance of partially inserted aggregated structure created by QD

CHAPTER- 1: Introduction and Literature Review

CHAPTER 1

Introduction and Literature Review

"*There's Plenty of Room at the Bottom*" -Richard Feynman

"*Nanotechnology, is the field of future that will replace microelectronics and many fields with tremendous application potential in the areas of medicine, electronics and material science*"- A.P.J. Abdul Kalam

Nanotechnology represents an exciting new area of scientific discovery, the manipulation of matter at the atomic or molecular level. Whereas, nano-biotechnology, has been an exciting interdisciplinary field of research which can helps tackle diseased/infected cells, through techniques such as, targeted drug delivery, repair tissue with bioactive nanomaterials apart from dealing with the environmental issues related to remediation, food packaging and storing. Nanomaterial is a state of matter in the transition region between bulk solid and molecular structure with a dimension of the order of 1-100 nm [1]. Quantum dots (QD) are semiconductor nanocrystals (typical size 1-10 nm) that form a spatially confined system with prominent quantum confinement [2,3]. They are regarded as efficient luminescent probes and labels for numerous biological applications including diagnostics [4], therapeutics [5], surgical devices/implants [6], novel drug delivery systems [7-9] etc. This is because of their size dependent tunable colour yet highly photostable optical, optoelectronic and physico-chemical properties [10].

1.1 Quantum structures and quantum confinement

Any nanoscale object with pronounced quantum mechanical property can be considered as a quantum structure. The type of structure depends on the nature of spatial confinement along different directions.

1.1.1 Quantum confinement

In solids, the free movement of the carriers (electrons, holes) can be restricted by forcing them to move in a confined region. This leads to the formation of discrete energy levels in which the carriers are localized. Depending on the confinement direction, the structure of confined solid state systems can be categorized in the following classes:

(a) **3D Bulk material:** In the bulk material, the charge carriers do not experience quantum confinement in any direction. They are free to move in any direction.

(b) **2D Quantum wells**: In this configuration, the charge carriers experience strong quantum confinement in their movement in one dimension. But, in the other two dimensions, they behave as free particles.

(c) **1D Quantum wires**: In this structure, charge carriers experience strong quantum confinement in two dimensions, but are free to move along the third dimension.

(d) **0D Quantum dot:** Here, electrons experience strong quantum confinement in all the three dimensions. This is considered a special case, as all the dimensions are smaller or at least comparable to bulk Bohr radius of the system. However, a zero dimensional system has no physical meaning and is therefore called as "quasi-zero dimensional QDs".

The confinement of electron wave function in reduced dimensions modifies the electron energy spectrum [11,12]. The quantum confinement effect on the electronic properties of a low dimension system can be represented by the density of states (DOS). The DOS of a particular system describes the density of available energy states per unit of energy [13]. In 3D bulk system the DOS ($g(E)$) of volume a^3 is described by

$$g(E)\,dE = \frac{a^3}{2\pi^2}\left(\frac{2m}{\hbar^2}\right)^{\frac{3}{2}}\sqrt{E}\,\mathrm{d}E \tag{1.1}$$

For a bulk system where the DOS is proportional to the square root of energy, the electrons' energy states continuous which appear in the form of a band. Reducing the dimensionality of the system only along a particular direction to the 2D structure, gives rise to DOS of the 2D quantum-well structure expressed as [12]:

$$g(E)\,dE = (a^2 m/\pi\hbar^2)\,\mathrm{d}E \tag{1.2}$$

Interestingly, while exhibiting a step-like character, the DOS do not depend on the energy. Each step in the DOS is described as,

$$g(E) = (m/\pi\hbar^2) \tag{1.3}$$

The equal height staircases correspond to the quantized electronic states in the direction of confinement.

In the 1D structure (quantum wires) where the electrons can move only in 1-direction the DOS is similar to an array of spikes [12] i.e.,

$$g(E)\,dE = \frac{1}{\hbar\pi}\sqrt{\frac{m}{2E}}\,dE \tag{1.4}$$

A 0 D structure has no physical significance. One can use quasi-zero dimensional structure in 0 D quantum dot (QD) structure [12], no free motion of electrons is possible as they are confined in three spatial dimensions. In this case, DOS is expressed by a delta function (δ) i.e.

$$g(E)\,dE = 2\delta\,(E-E_c) \tag{1.5}$$

i.e. density of states has a functional dependence of energy and all available states exist only at discrete energy levels. This explains the atomic like behavior of QDs which exhibits unique optoelectronic properties. As QDs exhibit discrete state, similar to atoms and/or molecules, very often they are termed as "artificial atom" or "man made atom". In fact, the QDs represent an intermediate state of matter with energy gap in between the bulk and molecular systems. The discrete energy levels and enhanced energy gap of the QDs, as compared to their 3D bulk counterpart make them useful over a wide range of applications from switching to sensing elements, from labeling to contrast agents etc.

The schematic diagram of (DOS) of the above mentioned confined structures are presented in Fig.1.1

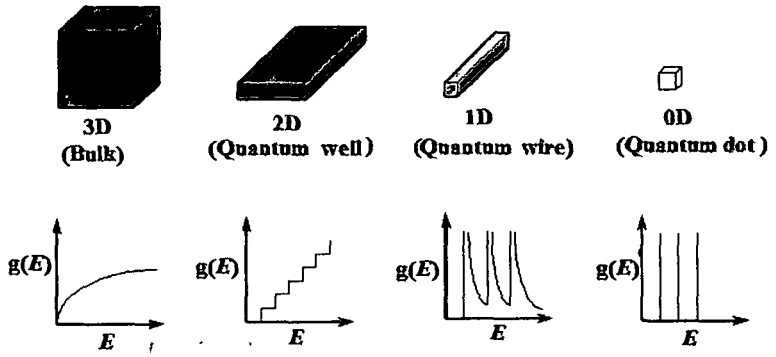

Figure 1.1: Density of states of vs. energy response of different quantum structures

1.1.2 Bohr excitons

In a semiconductor, absorption of a photon promotes an electron from the valence band to the conduction band, leaving a positive charge ('hole') behind in the valence band. The weakly bound electron–hole (e-h) pair formed as a result of Coulomb interaction potential is defined as an exciton [14]. Consequently, the exciton is characterized by exciton radius, analogous to Bohr radius of hydrogen like atoms. The bulk Bohr exciton radius (a_B) can be defined as [15]

$$a_B = \frac{\hbar^2 \varepsilon^2}{\mu_{eh} e^2} \tag{1.6}$$

Here, $\mu_{eh} = 1/m_e^* + 1/m_h^*$ is the electron- hole reduced mass. The exciton Bohr radius is dependent on the static dielectric constant (ε) of the semiconductor as well as on the electron (m_e^*) and hole (m_h^*) effective masses. The exciton Bohr radius can be different for different semiconductor systems. The excitonic Bohr radius is useful in determining the quantum confinement effect in QDs. Quantum confinement effect arises when the size of the nanocrystal (R) is comparable to the length of the Fermi wavelength (λ_F) in metals and exciton Bohr radius (a_B) in semiconductors. In the strong confinement regime ($R \leq a_B$), energy due to the quantum confinement effect of the carriers dominates the Coulomb interaction energy. In this regime, electrons and holes are viewed as individual particles in their respective single particle ground states. In the weak confinement regime ($R \geq a_B$), however, the exciton is envisioned as a single quasiparticle moving around the QDs with small Coulomb binding energy [16,17].

1.1.3 Particle in a box

In quantum mechanics, particle in a box model describes the characteristics of a particle restricted by an impenetrable barrier of dimension L in a region, $0 \leq X \geq L$. The probability of finding the particle outside this region is zero. i.e.,

$$\varphi(0) = \varphi(L) = 0 \tag{1.7}$$

here φ is the wave function of the particle. Thus, for the free particle the Schrodinger equation can be expressed as [18].

$$(d^2\varphi/dx^2)+2mE\varphi(x)/\hbar^2=0 \quad (1.8)$$

Here, E is the total energy of the particle.

By solving the Schrodinger wave equation for the boundary conditions (i) $\varphi(0)=0$ and (ii) $\varphi(L)=0$, the total energy of the particles can be obtained as [18],

$$E_n=n^2\pi^2\hbar^2/2mL^2 \quad (1.9)$$

Here, n is the quantum number and $\hbar$ is the reduced Planck's constant ($=h/2\pi$). This 'particle in a box' model could account for size dependent optical property of 3 dimensionally confined solids. An electron, moving freely in all directions can have a wave function (similar to the matter wave in quantum mechanics) defined at all points in space. Confining its position between barriers of infinite height would cause the electron to have a zero space probability outside of this 'box'. A result of this restriction is that the ground state kinetic energy of the particle must increase to satisfy the Heisenberg uncertainty principle. In addition, as the size of the box decreases, the ground state energy would increase. Similar to the 'particle in a box', a QD can be considered as a spherical box which contains two particles, an electron and a hole. The kinetic energies of these two carriers increase as the size of the QD decreases. As a result, both the excitation and emission spectra shift to shorter wavelengths (higher energies) with decreasing particle size [4]. The first explanation for the size-dependence of electronic properties in nanocrystals was given by Efros and Efros [19]. It is accounted for the effective masses of the electron (m_e^*), and the hole (m_h^*) and is popularly known as the Effective Mass Approximation (EMA) model. The assumptions considered for EMA model are as follows [17, 20-22]:

(a) The crystal structure of QDs is same as that of the bulk system,

(b) The QDs are spherical in shape,

(c) Confining potentials of the carriers (e and h) are infinite outside the QDs.

Using EMA model, Kayanuma *et. al.* predicted the following expression for the confinement energy in the strong confinement regime [20]

$$E=\hbar^2/2(1/m_e^*+1/m_h^*)\pi^2/R^2-1.786e^2/\varepsilon R-0.248E^*_{Ry} \quad (1.10)$$

Here $E^*_{Ry} = 13605.8(1/\varepsilon^2)(m_0/m_e+m_0/m_h)^{-1}$ is the effective Rydberg energy in meV.

The first term in eqn. (1.10) corresponds to the sum of the single particle ground state energies, the second term to the coulomb attraction, and the third term to the spatial correlation between the particles. However, defining the strong confinement regime by the absence of substantial electron-hole correlations, Kaynuma predicted that in a realistic situation, the wave function will penetrate into the barrier and in the zero radius limit the exciton energy will approach the bulk value in the barrier material. Later, considering finite barrier case, Kaynuma has incorporated an improvement to the EMA model [23].

1.2 Colloidal semiconductor quantum dots

Colloidal QDs are composed of an inorganic core surrounded by an organic outer layer of surfactant molecules (ligands). While preventing undersigned aggregation, the small size of the QDs (<10 nm) experience significant quantum confinements of charge carriers along 3D directions. While possessing extremely large surface to volume ratio ($s/v \sim 3/R$), the QDs are highly reactive resulting in a state of very unstable equilibrium [24]. The QD surface passivation can be obtained by growing a thin layer of shell over the QD core. This could lead to a higher photochemical stability, improved luminescence along with higher quantum yields at room temperature.

Depending on the band alignment of the bulk material, core/shell QDs have been classified into three categories: type-I, reverse type-I and type-II. In the type-I structure (i.e., CdSe/CdS, CdSe/ZnS, InAs/CdSe etc.), the band-gap of the shell material is larger than that of the core and both electrons and holes are confined in the core. In the reverse type-II configuration (i.e., CdS/HgS, CdS/CdSe, ZnSe/CdSe etc.), the band-gap of the shell material is smaller than that of the core, and, dependent on the thickness of the shell. In this configuration, the holes and electrons are partially or completely confined in the shell. In the latter type i.e., in type-II (ZnTe/CdSe, CdTe/CdSe, CdS/ZnSe etc.), the valence and conduction band edge of the core are lower and higher than the band edges of the shell [25].

1.3 Top-down and bottom-up approaches

In the field of nanotechnology, one of the most important challenges is controlled synthesis. The potential applications are largely dependent on the quality and integrity of

the materials. A number of techniques have been employed both using cost effective and sophisticated instruments to fabricate nanostructures and nanomaterials of diverse morphologies [26]. Common ways of processing nanomaterials are 'top-down' or 'bottom-up' routes. A top-down approach comprises breaking down of the bulk material into pieces of nanoscale dimension [27]. In contrast, a bottom-up approach refers to the building up of a system from several smaller subunits such as, atoms, molecules or clusters [28]. Both the methods have their own advantages and limitations and play important roles in modern industry and technology approaches. The biggest problem with top-down approach is the development of undesired imperfections at the surface structures. In the conventional top-down technique, for instance, lithography can cause significant crystallographic damage to the processed patterns. This results additional defects during the etching steps [27]. The bottom-up approach is considered to be a

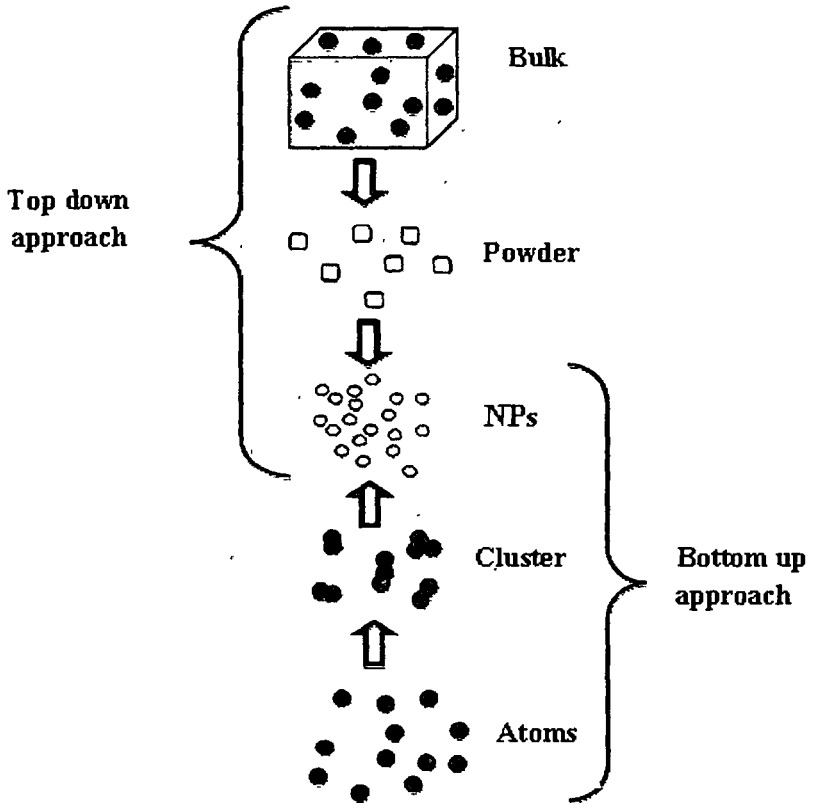

Figure 1.2: Schematic diagram of top-down and bottom-up approach

better technique over top-down one owing to likelihood of less defects, homogeneous chemical composition etc. This is because of reduction of Gibbs free energy that provides thermal equilibrium in the nanostructured system. On the other hand, top-down approach produces internal stress, in addition to surface defects and contaminations [26,27].

1.4 Biocompatible quantum dots

As an important application, QDs and their assembly could be integrated with the biological sciences. The main prerequisites of the QDs for making them useful in biological applications are water solubility, environmental stability, bioconjugation capability, biocompatibility etc. Biocompatibility and biological targeting can be achieved through surface modification and funtionalization with antibodies, peptides and other or small molecules of biophysical relevance.

1.4.1 Fabrication and functionalization of biocompatible QDs: capping and coupling of QDs

The synthesis of stable QDs demands an organic ligand on the surface of the nanocrystals including core/shell types [29]. These organic capping ligands are always nonpolar and are not soluble in aqueous solution. [5]. Several strategies have been adopted to avoid the problem of solubility and stability which are summarized as follows:

1.4.1 (a) Capping of QDs

By using different stabilizing agents, water soluble QDs can be synthesized directly in aqueous media. The ligands used during synthesis procedure is ultimate biocompatible surface capping anchor which do not require an exchange step. The ligand molecule carry functional groups that are reactive towards the nanocrystal surface at one end, and hydrophilic group on the other end, which ensure water solubility. In this regard, synthesis of thiol-capped CdTe QDs in aqueous solution is an appreciable effort as first reported by Rajh and coworkers [30]. Thiol containing ligands such as glutathione (GSH) [31], cystine [32] are able to provide improved biocompatibility as compared to many other water-soluble ligands such as phosphate, amines [31] and carboxylates [33].

1.4.1 (b) Surface silanization of QDs

Surface silanization is a way of coating QDs by growing a hydrophilic silica shell around the nanocrystal to make it hydrophilic [34]. A silica layer can be coated around the QDs through either direct ligand exchange [35] or indirect encapsulation (microemulsion, micellization of siloxane surfactants) [36,37]. In the direct ligand exchange method, original hydrophobic surfactant (trioctylphosphine oxide, TOPO), covering the QD is mixed with mercaptopropyltrimethoxysilane (MPTS) in alkaline methanol. The mercapto-group (SH^-) binds to the QD surface thereby displacing the TOPO layer followed by the release of three methoxy groups in the solvent upon heating [31,38]. Furthermore, the methoxysilane groups react with each other to form siloxane bonds to promote a silica shell around the nanocrystal. The silica shell can be modified with different functional groups such as, thiols, amines, or carboxyl groups to ensure covalent attachment to the bio-molecules. Moreover, the surface charges of the silica coated QDs can be changed by different surface anchoring groups. By adding phosphate group with methoxysilane the QD surface become negatively charged. Due to this the QDs repel each other through electrostatic interaction.

Indirect encapsulation of QDs with microemulsion process is observed to be more convenient in compared to direct ligand exchange method [37]. The microemulsion process can be explained with two hypothetical mechanisms: first, phase transfer without ligand exchange and second, phase transfer with ligand exchange. In the first mechanism, surfactants (tensids) form an inverse bilayer around the TOPO capped QDs in presence of ammonium ion. Tetraethylorthosilicate (TEOS) precursors are transferred through one tensid layer and form silica shell around the nanocrystal after hydrolysis. In the second mechanism, the TOPO ligand is replaced by TEOS and QDs are transferred to the aqueous phase followed by the polymerization of TEOS from the QD surface [37] Silanized semiconductor nanocrystals are extremely stable in electrolytic solution due to high degree of cross-linking between the silane molecules. They remain stable even if some thiol groups are lost. Moreover, non toxic coating silica are easy to functionalize which have the capability to protect the surface of the nanoparticles from oxidation, but the silanization process is somewhat laborious and the resulting shell becomes inhomogeneous.

Another method of coating the QD to make it hydrophilic is the use of amphiphilic ligands. The native non-polar molecules of the amphiphiles work as binding intermediates. While the hydrophilic region ensures water solubility, amphiphilic polymer can be efficiently used to transfer hydrophobic nanoparticles into water [38]. Other surfactant molecules such as phospholipids [39], α-cyclodextrin [40] etc. can be employed as amphiphilic ligands.

Amphiphilic ligand coating phenomena is regarded as a better method over silica-shell coating or, capping by ligand exchange technique owing to several advantages including (a) absence of direct interaction with the surface atoms of the QDs, thus preserves the original quantum efficiency, (b) formation of a thin, homogeneous shell by cross linking polymeric shell covering the QDs without replacing the hydrophobic shell with the hydrophilic layer and (c) commercial availability and viable cost of these amphiphilic polymers compared to other molecules such as, peptides and phospholipids.

1.4.1 (c) Coupling of QDs for bio-functionalization

While considering pharmaceutical and biological applications the covalent coupling of nanomaterials to biomolecules is a critical intermediate step [41]. The linking of QDs with the biological environment depends on the surface chemistry of the QDs as well as on the reactive group present in the biomolecules. The nanobio conjugation efficacy of the QDs can be enhanced through different coupling reagents. It was shown that, carbodiimide coupling would covalently link carboxylic acid groups present on the surface of the QDs with the amines present in enzymes *via a* "zero length" amide bond in presence of sulfo-NHS [41]. The sulfo-NHS can stabilize the intermediate by preventing it attacked by water molecules [41]. Similarly, maleimide coupling was used to conjugate primary amines to thiols [42]. The most commonly used maleimide-derived coupling reagent is sulfosuccinimidyl-4(maleimidomethyl)cyclohexane-1-carboxylate (Sulfo-SMCC). The maleimide coupling has been employed to conjugate biomolecules such as DNA, herceptin, proteins [43,44] and the concerned NPs.

Another one most interesting approach to functionalize the QDs is with peptides. Peptide-coated QDs can work as natural protector of the cell from the toxic inorganic materials of the QDs. Moreover, their native functional groups such as $-NH_2$ and –COOH can be manipulated by standard chemistries to react with the target of interest [45].

1.5 Advantages of QDs over organic dyes

It is well known that, QD have many advantages over conventional fluorophores, such as, organic dyes, fluorescent proteins, lanthanide chelates etc. Firstly, the absorption and fluorescence spectra of the QDs are remarkably different from those of the organic fluorophores. The QDs exhibit continuous and broad absorption spectra along with narrow and symmetric emission spectra. Whereas, the fluorophores have narrow absorption spectra whose spectral positions depends on the particular fluorophores. Moreover, the fluorophores exhibit broad, asymmetric emission spectra. Any wavelength of excitation shorter than the emission wavelength, can be chosen to exploit size dependent absorption and emission response of the QDs [46]. The flexibility of choosing any wavelength shorter than the emission wavelength in case of QDs, helps reduce the autofluorescence in biological samples. The QDs exhibit lower autofluorescence response as compared to the traditional dyes [31].

Secondly, an improved detection sensitivity can be obtained with the QDs by changing the size of the QDs. This makes QDs well suited for multiplex imaging [47]. In contrast, the broad emission spectra of different dyes, overlap to a great extent and thus limiting the use of different fluorescent probes to mark different biological samples which need to be resolved simultaneously [47].

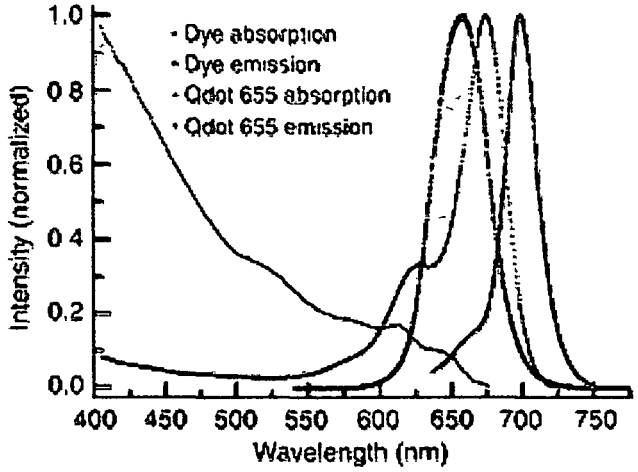

Figure 1.3: Normalized absorption and emission spectra of the Qdot 655 NCs and organic dyes measured in solution [48]

Thirdly, because of extended fluorescent lifetimes of the QDs (typically, tens to hundreds of nanoseconds (ns)) as compared to the organic dyes (~5 ns), they are considered as ideal probes for adequate temporal bias of the signal from cellular autofluorescence time-gated measurements. This enhances the selectivity and sensitivity [49]. Additionally, QDs are extremely photostable as well as possess a larger quantum yield (ratio of light emitted to the light absorbed) compared to the organic dyes. Moreover, because of their extreme photostability, the QDs can undergo repeated cycles of excitation and fluorescence for hours with an intense illumination and photobleaching threshold. In contrast, the bleaching of the fluorescent dyes could be carried out within duration short (a minute) [50]. Although some fluorescent dyes posses very high quantum yield in the visible region, their quantum yield decreases significantly in the near infra red (NIR) wavelength range after bio-conjugation. In contrast, fluorescence quantum yields of properly surface passivated QDs are generally high; both in visible light range as well as for the NIR wavelength region, even after bio-conjugation. The drawbacks like reduced quantum yields and limited photostability restricts the use of fluorescent dyes in biological applications including, but not limited to cell tracking, cell imaging etc. which require long term monitoring of the probes.

1.6 Relevant semiconductor systems

In recent decades, a great deal of research work on binary compound semiconductor systems, i.e. CdX (X= S, Se, Te) and ZnX (X= O, S, Se, Te) have been carried out worldwide. Of particular interest, cadmium selenide (CdSe), is regarded as an efficient optoelectronic candidate due to an advantage of large band gap tunability and bright radiation emission response. Earlier, it was predicted that, CdSe QDs are about ~20 times brighter and 100 times more stable than single rhodamine 6G dye molecules [51]. Table 1.1 depicts some physical properties of CdX and ZnX semiconductor QDs system.

Table 1.1: Physical properties of several semiconductor systems

Physical Properties of CdX				**Physical Properties of ZnX**		
Properties	**CdSe**	**CdS**	**CdTe**	**ZnSe**	**ZnS**	**ZnTe**
Melting Temperature (K)	1541	2020	1314	1790	1458	1511.5
Refractive Index	2.5	2.38	2.64	2.5	2.36	2.72
Specific gravity	5.81	4.82	5.85	5.42	4	6.34
Band gap (eV)	1.74	2.42	1.56	2.82	3.68	2.3
Dielectric constant	8.6	8.9	10.2	9.1	8.9	7.4
Density (g/cm^3)	5.8	4.82	5.85	5.26	4.11	5.65
Effective mass of electron (m_e^*)	m_e^*~0.13m_0[#]	m_e^*~0.21m_0	m_e^*~0.11m_0	m_e^*~0.17m_0	m_e^*~0.21m_0	m_e^*~0.2 m_0
Effective mass of hole (m_h^*)	m_h^*~0.45m_0	m_h^*~0.80m_0	m_h^*~0.40m_0	m_h^*~1.44m_0	m_h^*~0.6 m_0	m_h^*~0.2 m_0
Crystal phase, Lattice parameters (nm)	Wurtzite, a=0.43, c=0.70	Wurtzite, a=0.41, c=0.67	Zinc blende, a=0.43, c=10.3	Zinc blende, a=0.39, c=0.65	Zinc blende, a=0.38, c=0.62	Zinc blende, a=0.42 c=0.69
Phonon energy (meV)	30	37	21	0.31	44	26
Bohr radius (a_B) (Å)	56	30	68	38	25	62

[#]m_0 is the rest mass of electron (9.1×10^{-31} Kg)

1.7 Magnetic semiconductors

Diluted magnetic semiconductors (DMS) also referred as semimagnetic semiconductors are semiconducting alloys whose lattice is formed, in part of substitutional magnetic atoms. The most extensively studied and most thoroughly understood materials of this type are the $A^{II}_{1-x}Mn_xB^{VI}$ alloys in which a fraction of the group is replaced at random by Mn [52-54]. DMS of $A^{II}_{1-x}Mn_xB^{VI}$ type are of interest for several important reasons: Their ternary nature allows the possibility of "tuning" the lattice constant and band parameters by varying the composition of the material. The random distribution of magnetic ions over the cation sublattice leads to important magnetic effects. The substitutional Mn-atoms in the $A^{II}B^{VI}$ lattice are also characterized by highly efficient

electroluminescence behavior, which makes dilute $A^{II}_{1-x}Mn_xB^{VI}$ alloys important in the context of optical flat panel display applications [55]. Furthermore, the presence of localized magnetic ions in these semiconductor alloys leads to an exchange interaction between the *sp* band electrons and the *d* electrons associated with Mn^{2+}, resulting in an extremely large Zeeman splitting of electronic (band and impurity) levels.

Manganese selenide (MnSe) is a classic example in the family of chalcogenides and binary- semiconductor systems and is the end member (x =1) of the magnetic semiconductor $Zn_{1-x}Mn_xSe$ system. Essentially, MnSe comes in two polymorphic forms: α-MnSe with a cubic modification that gives rock salt structure (RS) [56], and β-MnSe with hexagonal modification of zinc blende (ZB) and wurtzite structures (WZ) [57,58]. The octahedrally coordinated RS structure of MnSe offers a stable cubic phase, while the system is metastable in the hexagonal configuration [58,59]. Although ZB and WZ types of MnSe are quite unstable and extremely rare, yet they are of significant interest because of their structural compatibility with other II-VI semiconductor systems which are not only fluorescent but also highly photostable [60]. It is expected that, the cooperative effect of fluorescence response and magnetic ordering could offer a new window for tuning bright-fluorescence imaging in response to an externally applied magnetic field. Table 1.2 provides some physical properties of MnSe and MnS systems.

Table 1.2: Physical properties of MnX systems

Physical Properties of MnX		
Properties	**MnSe**	**MnS**
Melting Temperature (K)	1733	1883
Refractive Index	2.6	1.39
Specific gravity	5.55	3.99
Band gap (eV)	3.5 (Wurtzite structure), 2.5 (Rock salt structure)	2.1
Dielectric constant	10	-
Density (g/cm^3)	5.59	4
Lattice parameter (nm)	a=0.41, c=0.67	a=0.52
Stable phase	Rock salt	Rock salt
Phonon energy (meV)	34	-

To date, amongst highly fluorescent semiconductor systems, Cd-based ones (e.g., CdSe, CdTe, CdS, and CdSe/ZnS core shell QDs) have received a great deal of attention in biophysical research, particularly in tagging, labeling, and imaging agent. Though questionable for large scale use, the toxicity level of cadmium ions is likely to reduce in the nanometer scale, when it forms CdTe or CdSe clusters than available in elemental form [61]. As a matter of fact, there exists plentiful scopes for safe use of nanoscale CdSe and similar particles in biophysical and biomedical research. Nevertheless, biocompatible nature of these QDs in cellular environment and under UV illumination remained questionable owing to the releasing of heavy metal ions of Cd^{2+}. Replacing Cd by Mn (for instance, choosing MnS and MnSe instead of CdS and CdSe), would help reducing the toxicity level by avoiding the photobleaching of Mn^{2+} [62-65]. Knowing that, Mn^{2+} precursor is a hard Lewis acid [63, 66] while Cd^{2+} precursor is a relatively softer one, the former is less reactive to the surrounding, thereby experiencing much lowered photobleaching as compared to its counterpart [63].

1.8 Overview on biological application of QDs

Superior optoelectronic properties of the QDs may provide new but versatile approaches for use in biomedical fields. The QDs have potential biomedical applications ranging from intracellular tagging of biological molecules to applications such as tracking devices for neuronal receptors and as interfaces between nerve cells. Fig.1.4. depicts the generic view on the application of QDs in various biological fields.

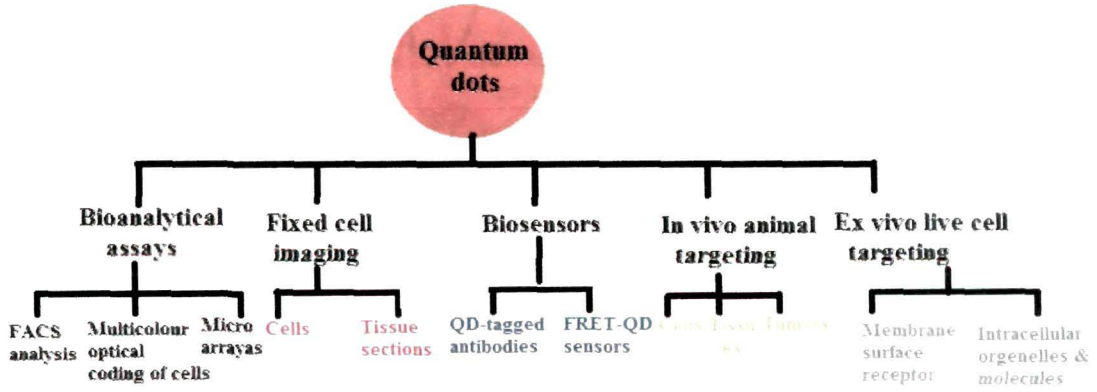

Figure 1.4: Use of QDs in various biomedical and bioengineering fields

1.8.1 Fluorescence resonance energy transfer (FRET) QDs sensors

The potential uses of inorganic fluorescent QDs in biolabeling and sensing could be expanded through their ability to function as resonant energy-transfer donors [67]. Fluorescence resonance energy transfer (FRET) involves the transfer of fluorescence energy from a donor particle to an acceptor particle when the distance between the donor and the acceptor is smaller than or comparable to a critical radius, known as the Förster radius. This results in the reduction of the donor emission response and an increase in the

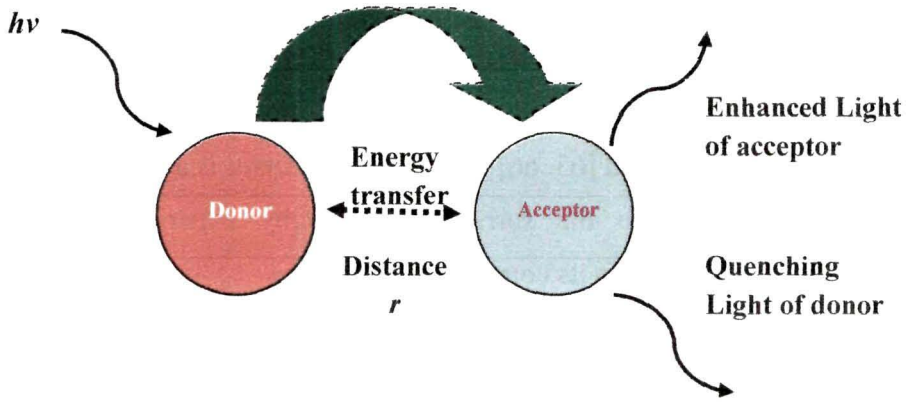

Figure 1.5: Schematic diagram on FRET mechanism

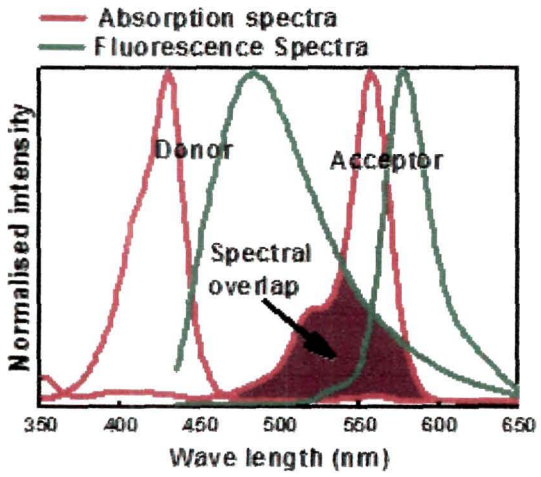

Figure 1.6: Absorption and fluorescence spectra of an ideal donor-acceptor pair. Brown colored region is the spectral overlap between the fluorescence spectrum of donor and absorption spectrum of acceptor

acceptor emission intensity. The energy transfer efficiency increases with increasing spectral overlap between the donor emission and acceptor absorption. Typically, the FRET is significant over donor–acceptor distances ranging from 10 to 100 Å [68]. It is also worth mentioning here that the arrangement of energy-transfer donors and acceptors is critical in the development of FRET sensors. Earlier, it was shown that by using a unique QD surface chemistry, QD–protein conjugates can act as efficient bio sensors [69]. Moreover, subsequent studies have shown that QD-FRET can detect activity of caspase-1, thrombin chymotrypsin and trypsin etc. [70,71]. It was reported that a QD-FRET assay of collagenase is able to distinguish normal and cancerous breast cells [72].

1.8.2. In *vitro cell* labeling: fixed cells and tissue imaging

Analysis of fixed tissue samples is a standard technique that is important in cancer diagnostics and morphology studies [73]. The brightness and photostability of QDs are advantageous for this type of analysis because they are much brighter than any background autofluorescence from the tissues and cell counterpart. In addition, the background autofluorescence can be photobleached with prolonged exposure to light excitation, while QDs remain unaffected. Their principal application is very similar to that of organic fluorophores. After attaching a ligand, such as an antibody, to the label, the conjugate binds with high specificity to its target receptor, which in turn can visualized by the fluorescence of the label. If only a few cells are to be labeled, fluorescence-marked ligands can be injected into the live cells with micropipettes. Again, in order to stain many cells in parallel, cells are made fixed and their membrane is permeabilized with appropriate reagents (e.g. by triton). Antigen detection in fixed cellular monolayers by QDs was first demonstrated by A. Paul Alivisatos and his group in 1998 [74]. They could detect nuclear antigens and F-actin filaments simultaneously in fixed mouse fibroblasts, by green silica-coated CdSe/ZnS QDs and red QDs; respectively. Moreover, QD conjugates for detection of cancer biomarkers in cancer cells was reported by several groups [75-77]. In addition, other QD bio-conjugates include CdS passivation by DNA [78], CdSe/L-cysteine QD conjugate [79], silica coated CdTe QDs/ immunoglobulin G (IgG) [72] and magnetic nanocrystal [80] conjugates. In last decades, QDs have demonstrated immense potential for *in vitro* tissue engineering and

diagnostics; though several critical issues need to be addressed for long term adaptation [81].

1.8.3 In *vivo cell* labeling

Live cells are composed of various components such as plasma membrane, cytoplasm, nucleus, mitochondria etc. The ability to track and tag fluorescently in cellular and sub-cellular compartments in living cells is a powerful concept in cell biology and nanotechnology [82]. Live cell imaging by QDs is a more difficult task compared to fixed cells and tissues as extra care is necessary to keep cells alive along with the key challenge of delivering probes into the cytoplasm and organelles such as, nucleus and mitochondria. Sahi and groups demonstrates the tracking of fast molecular diffusion of dye labeled lipids, diffusing in the plasma membrane of living cells [83]. A.M Derfus and coworkers first reported the way of successful uptake of QDs by cells for intracellular tagging [84]. They used both biochemical (translocation peptides, cationic liposomes, dendrimers) and physical (electroration and microinjection) methods to the delivery of PEG coated QDs into HeLa cells. With the help of fluorescent microscopy and flow cytometry they confirmed that, delivery of QDs/liposome complexes and electroporations can be efficient schemes to deliver QDs to the cytoplasm of a large population of a cell. Wu *et al.* have demonstrated that, QDs can be used to label molecular targets at the sub-cellular level [85]. They could use polymer shell encapsulated QDs with bio-functionalization to streptavidin and IgG to stain actin and microtubule fibers in the cytoplasm and to detect nuclear antigens inside the nucleus target in both fixed and live cells. In addition, the first study of live cell labeling by QDs was demonstrated by Chan and Nie *et. al.* in 1998 [86]. They observed that, the cancer cells could spontaneously endocytose mercaptoacetic acid coated CdSe/ZnS QDs conjugated with the transferrin protein. The QDs maintain their bright fluorescence to label of intracellular regions apart from staining plasma membrane. Targeting of QDs to specific cytoplasmic or nuclear locations in order to observe sub-cellular events become more difficult task due to the plasma membrane barrier as well as the snaring in the endocytic pathway.

1.8.4 Ion channels and nanopore creation

Recognizing the importance of the lipid bilayer membrane in cell biology and molecular biology, the use of size controlled QDs, in these 2-D bilayer membrane structures, has realized significant interest among the scientific community working in the area of as far as nanobio-interface applications. It may be noted that, nanopores and nanoporous artificial membranes were proven to be useful in the fields of bioengineering and environmental studies, to name a few, scope for DNA translocation [87], fuel cell studies [88], coulter counter device [89], and ultra-high water purification systems [90]. However, functional nanopore creation leading to passage of ions in live cells, has not been fully understood. In fact, the activity and longevity of cells are largely governed by the control uptake/release of ions and other molecular species through transient nanopores available in the bilayer membrane. To be specific, active and passive ion channels could determine the physiological state of the cells by way of linking intracellular compartments with the extracellular matrix. Moreover, the unhealthy and disease-affected cells, both in animal and plant kingdoms, do not support normal ion transport process thereby causing abnormal intracellular activity. Ion channels (pore forming peptides) may be classified by the nature of their gating; voltage gated, magneto gated, light gated and ligand gated. There are naturally forming antimicrobial channel forming peptides such as, alamethicin, magainin, gramicidin etc [91-94]. Their amino acid composition, amphipathicity, cationic charge, conformation and structure, hydrophobicity, and size are the characteristics which affect the antimicrobial activity with high specificity thus allowing them to attach and insert into the membrane bilayers resulting in the formation of ion conducting pathways (pores) [95]. The pore formation is demonstrated through 'barrel-stave', 'carpet' or 'toroidal-pore' mechanisms [96].

The study of ion migration through the nanopore across the lipid can be studied by both patch-clamp and planar lipid bilayer experiments. However, solid supported bilayer experiments are found to have more advantages over traditional patch-clamp techniques. [77]. The artificial bilayer membrane can be used as a model system to explore transient nanopore creation, in presence of external stimuli such as voltage, magnetic field and light. The first evidence of voltage-gated channel has been obtained for the alamethicin peptide channel, as reported by Mueller *et al* [97]. Alamethicins are characterized by

conductance states of 19–4400 pS when inserted into an artificial phospholipids bilayer [98]. Moreover, it was reported that the presence of magnetic field in the range of ~1 mT-1 T can create ion channels in artificial liposomes [99]. The magnetic field has a strong influence on the diamagnetic nature of the phospholipid molecules thereby causing appreciable changes in the membrane properties [100]. The nanopore creation and ion channel forming in artificial lipid bilayer with the result of oligomeric aggregation of QDs has already been demonstrated [101]. It was illustrated that, CdSe QDs can initiate current bursts in lipid bilayer membranes upon application of a bias voltage. The current bursts observed resemble those produced by the peptaibol class of antibiotics, such as, alamethicin and trichorzins [102]. It was believed that that, the QDs with dipole moments, create a torque in presence of an external electric field which results in their insertion into the lipid membrane, in aggregate form.

1.9 Objectives of the present study

The motivation of our thesis work involves synthesis, characterization and biophysical assessment of biocompatible CdSe and WZ-MnSe QDs. The study of optical stability of CdSe and MnSe QDs, in different biological media is discussed in great detail considering different reaction parameters. Moreover, the study of bioconjugation capability of synthesized QDs is carried out through steady state photoluminescence spectroscopy, time resolved photoluminescence spectroscopy and FRET mechanism. The bioimaging aspects of CdSe and MnSe QDs are evaluated exploring fluorescence and confocal microscopies. As an important application of CdSe QDs, in electrophysiology, the water soluble QDs are inserted in to lecithin bilayer derived from soyabean extract. Lets not mislead the ion channel studied by us as the ion channel created by proteins. The channels of our study are created by transient aggregation of QDs in the lipid bilayer in presence of electric field. To minimize confusion we can term it as quasi ion channels.

We also highlight the Browning dynamics of spherical QDs, in lipid bilayer, in pre aggregated and aggregated (ion channel forming stage) forms using simple theoretical model.

References

[1] Leutwyler, W. K., et al. Semiconductor clusters, nanocrystals, and quantum dots, *Science* **271**(5251), 933--937, 1996.

[2] Brus, L. Electronic wave functions in semiconductor clusters: experiment and theory, *J. Phys. Chem.* **90**(12), 2555--2560, 1986.

[3] Brus, L. E. Electron-electron and electron-hole interactions in small semiconductor crystallites: The size dependence of the lowest excited electronic state, *J. Chem. Phys.* **80**(9), 4403--4409, 1984.

[4] Menon, J. U., et al. Nanomaterials for photo-based diagnostic and therapeutic applications, *Theranostics* **3**(3), 152--166, 2013.

[5] Xue, X., et al. Emerging functional nanomaterials for therapeutics, *J. Mater. Chem.* **21**(35), 13107--13127, 2011.

[6] Sivolella, S., et al. Silver nanoparticles in alveolar bone surgery devices, *J. Nano. Mater.* **2012**(2012), 15, 2012.

[7] Zarrabi, A., et al. Design and synthesis of novel polyglycerol hybrid nanomaterials for potential applications in drug delivery systems, *Macromol. Biosci.* **11**(3), 383--390, 2011.

[8] Gupta, A., et al. Nanotechnology and its applications in drug delivery: A Review. Webmed Central Medical education 3(1), WMC002867. 2012

[9] Parveen, S., et al. Nanoparticles: a boon to drug delivery, therapeutics, diagnostics and imaging, *Nanomed. Nanotech. Biol. Med.* **8**(2), 147--166, 2012.

[10] Alexson, D., et al. Semiconductor nanostructures in biological applications, *J. Phys. Condens. Matt.* **17**(26), R637--R656, 2005.

[11] Sako, T., et al. The energy level structure of low-dimensional multi-electron quantum dots, *Adv. Quantum Chem.* **58**, 177--201, 2009.

[12] Bimberg, D., et al. *Quantum dot heterostructures*, Wiley-Blackwell, London, United Kingdom, 1999.

[13] Kittel, C. *Introduction to Solid State Physics,* Wiley & Sons, Inc., New York: John 1986.

[14] Scholes, G. D. & Rumbles, G. Excitons in nanoscale systems, *Nature mater.* **5**(9), 683--696, 2006.

[15] Krahne, R., et al. *Physical properties of nanorods,* Springer, Berlin Heidelberg, 2013.

[16] Martinez-Duart, J. M., *Nanotechnology for Microelectronics and Optoelectronics*, Elsevier Science, Great Britain, 2006.

[17] Einevoll, G. T. Confinement of excitons in quantum dots, *Phys. Rev. B* **45**(7), 3410--3417, 1992.

[18] Schiff, L. I., *Quantum Mechanics*, McGraw-Hill, New York, 1965.

[19] Efros, A. L. Interband absorption of light in a semiconductor sphere, *Sov. Phys. Semicond.* **16**(7), 772--775, 1982.

[20] Kayanuma, Y. Quantum-size effects of interacting electrons and holes in semiconductor microcrystals with spherical shape, *Phys. Rev. B* **38**(14), 9797, 1988.

[21] Brus, L. A simple model for the ionization potential, electron affinity, and aqueous redox potentials of small semiconductor crystallites, *J. Chem.Phys.* **79**(11), 5566--5571, 1983.

[22] Brus, L. E. Electron–electron and electron-hole interactions in small semiconductor crystallites: The size dependence of the lowest excited electronic state, *J. Chem.Phys.* **80**(9), 4403--4409, 1984.

[23] Kayanuma, Y. & Momiji, H. Incomplete confinement of electrons and holes in microcrystals, *Phys. Rev. B: Condens. Matt.* **41**(14), 10261--10263, 1990.

[24] Pierce, D. T. & Zhao, J. X., *Trace analysis with nanomaterials*, John Wiley & Sons, USA, 2010.

[25] Reiss, P., et al. Core/shell semiconductor nanocrystals, *Small* **5**(2), 154--168, 2009.

[26] Bhushan, B., *Springer handbook of nanotechnology*, Springer, USA, 2010.

[27] Koch, C., *Nanostructured materials: processing, properties and applications*, William Andrew, New York, 2002.

[28] Tobias, K., et al. Nanoparticle printing with single-particle resolution, *Nature Nanotech.* **2**(9), 570--576, 2007.

[29] Rosenthal, S. J., et al. Biocompatible quantum dots for biological applications, *Chem. Biol.* **18**(1), 10--24, 2011..

[30] Rajh, T., et al. Synthesis and characterization of surface-modified colloidal cadmium telluride quantum dots, *J. Phys. Chem.* **97**(46), 11999--12003, 1993.

[31] Zhang, Y. & Clapp, A. Overview of stabilizing ligands for biocompatible quantum dot nanocrystals, *Sensors* **11**(12), 11036--11055, 2011.

[32] Zhao, W., et al. L-cysteine-capped CdTe quantum dots as a fluorescence probe for determination of cardiolipin, *Anal. Sci.* **26**(8), 879--884, 2010.

[33] Liu, Y., et al. Highly luminescent, stable, and water-soluble CdSe/CdS core-shell dendron nanocrystals with carboxylate anchoring groups, *Langmuir* **22**(14), 6341--6345, 2006.

[34] Michalet, X., et al. Quantum Dots for Live Cells, in Vivo Imaging, and Diagnostics, *Science* **307**(5709), 538-544, 2005

[35] Gerion, D., et al. Synthesis and properties of biocompatible water-soluble silica-coated CdSe/ZnS semiconductor quantum dots, *J. Phys. Chem. B* **105**(37), 8861--8871, 2001.

[36] Stöber, W., et al. Controlled growth of monodisperse silica spheres in the micron size range, *J. Colloid Interface Sci.* **26**(1), 62--69, 1968.

[37] Darbandi, M., et al. Single quantum dots in silica spheres by microemulsion synthesis, *Chem.Mater.* **17**(23), 5720--5725, 2005.

[38] Parak, W. J.; et al. Labelling of cells with quantum dots, *Nanotechnology* **16**(2), R9-R25, 2005.

[39] Smith, A. M., et al. A systematic examination of surface coatings on the optical and chemical properties of semiconductor quantum dots, *Phys. Chem. Chem. Phys.* **8**(33), 3895--3903, 2006.

[40] Lala, N., et al. Phase transfer of aqueous gold colloidal particles capped with inclusion complexes of cyclodextrin and alkanethiol molecules into chloroform, *Langmuir* **17**(12), 3766--3768, 2001.

[41] Song, F. & Chan, W. C. Principles of conjugating quantum dots to proteins via carbodiimide chemistry, *Nanotechnology* **22**(49), 494006, 2011.

[42] Thanh, N. T. & Green, L. A. Functionalisation of nanoparticles for biomedical applications, *Nano Today* **5**(3), 213--230, 2010.

[43] Wolcott, A., et al. Silica-coated CdTe quantum dots functionalized with thiols for bioconjugation to IgG proteins, *J. Phys. Chem. B* **110**(11), 5779--5789, 2006.

[44] Liu, B. R., et al. Cell-penetrating peptide-functionized quantum dots for intracellular delivery, *J. Nanosci.Nanotech.* **10**(12), 7897, 2010.

[45] Pinaud, F., et al. Bioactivation and cell targeting of semiconductor CdSe/ZnS nanocrystals with phytochelatin-related peptides, *J Am Chem Soc.* **126**, 6115–6123, 2004.

[46] Bruchez, M., Semiconductor Nanocrystals as Fluorescent Biological Labels, Science **281**(5385), 2013-2016, 1998.

[47] Jamieson, T., et al. Biological applications of quantum dots, *Biomaterials* **28**(31), 4717--4732, 2007.

[48] Xiao, J., et al. Carrier multiplication in semiconductor nanocrystals detected by energy transfer to organic dye molecules, *Nature Commun.* **3**, 1170, 2012.

[49] Alivisatos, A. P., et al. Quantum dots as cellular probes, *Annu. Rev. Biomed. Eng.* **7**, 55--76, 2005.

[50] Cheng, X., et al. Colloidal silicon quantum dots: from preparation to the modification of self-assembled monolayers (SAMs) for bio-applications, *Chem. Soc. Rev.* **43**(8), 2680--2700 2014.

[51] Chan, W. C., et al. Luminescent quantum dots for multiplexed biological detection and imaging, *Curr. Opin. Biotech.* **13**(1), 40--46, 2002.

[52] Sines, I. T., et al. Colloidal synthesis of non-equilibrium wurtzite-type MnSe, *Angew. Chem. Int. Ed.* **49**(27), 4638--4640, 2010.

[53] Wu, M., et al. Hydrothermal preparation of α-MnSe and $MnSe_2$ nanorods, *J. Cryst. Growth* **262**(1–4), 567--571, 2004.

[54] Furdyna, J. K. Diluted magnetic semiconductors, *J. Appl. Phys.* **64**(4), R29--R64, 1988.

[55] Chakraborti, D., *Novel diluted magnetic semiconductor materials based on zinc oxide,* ProQuest, United States, 2008.

[56] Decker, D. L. & Wild, R. Optical properties of a-MnSe, *Phys. Rev. B* **4**(10), 3425, 1971.

[57] Bouroushian, M., *Electrochemistry of metal chalcogenides*, Springer, Greece, 2010

[58] Murray, R. M., et al. The preparation and paramagnetic susceptibility of β-MnSe, *Can. J. Chem.* **50**(24), 4059--4061, 1972.

[59] Schlesinger, M. The Mn-Se (manganese-selenium) system, *J. Phase Equilib.* **19**(6), 588--590, 1998.

[60] Yang, X., et al. Morphology-controlled synthesis of anisotropic wurtzite MnSe nanocrystals: optical and magnetic properties, *CrystEngComm* **14**(20), 6916--6920, 2012.

[61] Zayed, J. & Philippe, S. Acute oral and inhalation toxicities in rats with cadmium telluride, *Int. J. Toxicol.* **28**(4), 259--265, 2009.

[62] Pradhan, N., et al. Efficient, stable, small, and water-soluble doped ZnSe nanocrystal emitters as non-cadmium biomedical labels, *Nano Lett.* 7(2), 312--317, 2007.

[63] Pradhan, N., et al. An alternative of CdSe nanocrystal emitters: pure and tunable impurity emissions in ZnSe nanocrystals, *J. Am. Chem. Soc.* **127**(50), 17586--17587, 2005.

[64] Wang, C., et al. Aqueous synthesis of mercaptopropionic acid capped Mn^{2+} doped ZnSe quantum dots, *J. Mater. Chem.* **19**(38), 7016--7022, 2009.

[65] Zhu, D., et al. Green synthesis and potential application of low-toxic Mn: ZnSe/ZnS core/shell luminescent nanocrystals, *Chem. Commun.* **46**(29), 5226--5228, 2010.

[66] Pearson, R. Hard & Soft Acids and Bases, *J. Am. Chem. Soc.* **85**(22), 3533--3539, 1963.

[67] Willard, D. M. & Van Orden, A. Quantum dots: Resonant energy-transfer sensor, *Nature Mater.* **2**(9), 575--576, 2003.

[68] Loura, L. M., et al. Quantification of protein–lipid selectivity using FRET, *Eur. Biophys. J.* **39**(4), 565--578, 2010.

[69] Medintz, I. L., et al. Self-assembled nanoscale biosensors based on quantum dot FRET donors, *Nature Mater.* **2**(9), 630--638, 2003.

[70] Medintz, I. L., et al. Proteolytic activity monitored by fluorescence resonance energy transfer through quantum-dot–peptide conjugates, *Nature Mater.* **5**(7), 581--589, 2006.

[71] Shi, L., et al. Luminescent quantum dots fluorescence resonance energy transfer-based probes for enzymatic activity and enzyme inhibitors, *Analyt. Chem.* **79**(1), 208--214, 2007.

[72] Shi, L., et al. Synthesis and application of quantum dots FRET-based protease sensors, *J. Am. Chem. Soc.* **128**(32), 10378--10379, 2006.

[73] Walling, M. A., et al. Quantum dots for live cell and in vivo imaging, *Int. J. Mol. Sci.* **10**(2), 441--491, 2009.

[74] Bruchez, M., et al. Semiconductor nanocrystals as fluorescent biological labels, *Science* **281**(5385), 2013--2016, 1998.

[75] Gao, X., et al. In vivo cancer targeting and imaging with semiconductor quantum dots, *Nature Biotech.* **22**(8), 969--976, 2004.

[76] Yezhelyev, M. V., et al. In situ molecular profiling of breast cancer biomarkers with multicolor quantum dots, *Adv. Mater.* **19**(20), 3146--3151, 2007.

[77] Hanash, S. M., et al. Mining the plasma proteome for cancer biomarkers, *Nature* **452**(7187), 571--579, 2008.

[78] Ma, N., et al. DNA-passivated CdS nanocrystals: luminescence, bioimaging, and toxicity profiles, *Langmuir* **23**(26), 12783--12787, 2007.

[79] Wang, Q., et al. Conjugation and fluorescence quenching between bovine serum albumin and L-cysteine capped CdSe/CdS quantum dots, *Protein Peptide Lett.* **18**(4), 410--414, 2011.

[80] Huh, Y.-M., et al. In vivo magnetic resonance detection of cancer by using multifunctional magnetic nanocrystals, *J. Am. Chem. Soc.* **127**(35), 12387--12391, 2005.

[81] Xing, Y. & Rao, J. Quantum dot bioconjugates for in vitro diagnostics & in vivo imaging, *Cancer Biomark. A* **4**(6), 307--319, 2008.

[82] Medintz, I. L., et al. Quantum dot bioconjugates for imaging, labelling and sensing, *Nature Mater.* **4**(6), 435--446, 2005.

[83] Sahl, S. J., et al. Fast molecular tracking maps nanoscale dynamics of plasma membrane lipids, *PNAS* **107**(15), 6829--6834, 2010.

[84] Derfus, A. M., et al. Intracellular delivery of quantum dots for live cell labeling and organelle tracking, *Adv. Mater.* **16**(12), 961--966, 2004.

[85] Wu, X., et al. Immunofluorescent labeling of cancer marker Her2 and other cellular targets with semiconductor quantum dots, *Nature Biotech.* **21**(1), 41--46, 2002.

[86] Chan, W. C. & Nie, S. Quantum dot bioconjugates for ultrasensitive nonisotopic detection, *Science* **281**(5385), 2016--2018, 1998.

[87] Panwar, A. S. & Muthukumar, M. Enzyme-modulated DNA translocation through a nanopore, *J. Am. Chem. Soc.*. **131**(51), 18563--18570, 2009.

[88] Tominaka, S. & Osaka, T. Nanoporous PdCo catalyst for microfuel cells: Electrodeposition and dealloying, *Adv. Phys. Chem.* **2011,** 1--9, 2011.

[89] Ito, T., et al. Simultaneous determination of the size and surface charge of individual nanoparticles using a carbon nanotube-based Coulter counter, *Anal. Chem.* **75**(10), 2399--2406, 2003.

[90] Menzl, G., et al. Phase transition and interpore correlations of water in nanopore membranes, *Phys. Rev. Lett.* **109**(2), 020602, 2012.

[91] Ludtke, S. J., et al. Membrane pores induced by magainin, *Biochemistry* **35**(43), 13723-13728, 1996.

[92] He, K., et al. Mechanism of alamethicin insertion into lipid bilayers, *Biophys. J.* **71**(5), 2669--2679, 1996.

[93] Prenner, E. J., et al. The interaction of the antimicrobial peptide gramicidin with lipid bilayer model and biological membranes, *Biochim. Biophys. Acta - Biomembranes* **1462**(1), 201--221, 1999.

[94] Yeaman, M. R. & Yount, N. Y. Mechanisms of antimicrobial peptide action and resistance, *Pharmacol. Rev.* **55**(1), 27--55, 2003.

[95] Boheim, G., et al. Alamethicin pore formation: voltage-dependent flip-flop of α-helix dipoles, *Biophys. Struct. Mech.* **9**(3), 181--191, 1983.

[96] Mueller, P. & Rudin, D. O. Action potentials induced in biomolecular lipid membranes, *Nature* **217**(5130), 713 -- 719, 1968.

[97] Hanke, W. & Boheim, G. The lowest conductance state of the alamethicin pore, *Biochim. Biophys. Acta - Biomembranes* **596**(3), 456--462, 1980.

[98] Hughes, S., et al. The influence of static magnetic fields on mechanosensitive ion channel activity in artificial liposomes, *Eur. Biophys. J.* **34**(5), 461--468, 2005.

[99] Naito, A., et al. Dynorphin induced magnetic ordering in lipid bilayers as studied by 31P NMR spectroscopy, *Biochim. Biophys. Acta* **1558**(1), 34--44, 2002.

[100] Ramachandran, S., et al. Current bursts in lipid bilayers initiated by colloidal quantum dots, *Appl. Phys. Lett.* **86**(8), 083901--083901-083903, 2005.

[101] Klein, S. A., et al. Formation of nanopores in suspended lipid bilayers using quantum dots, *J. Phys.: Conf Series.* **109**, 012022, 2008.

[102] Duval, D., et al. Ionophoric activity of the antibiotic peptaibol trichorzin PA VI: a 23Na- and 35Cl-NMR study, *Biochim. Biophys. Acta (BBA)* **1372**(2), 370--378, 1998.

CHAPTER- 2: Synthesis Protocol: Materials, Methods and Basic Characterizations

CHAPTER 2

Synthesis Protocol: Materials, Methods and Basic characterizations

Apart from conventional organic flourophores, semiconductor nanocrystals, or QDs are presently regarded as efficient luminescent probes/labels for numerous biological applications. This is because, the QDs display unique optical and optoelectronic properties, such as, size-dependent tunable colour, narrow emission line-width, broad absorption spectrum, resistance to photobleaching along with multiplex capabilities [1-3]. Despite the potential use of QDs as fluorescent probes in a biological environment several concerns need to be fixed prior to long term applications. The critical issues, to name a few are environmental stability, size selectivity, bio-specificity and bio-functionality etc [2]. In order to achieve QDs with narrow size distribution and long term stability, previously the QDs have been synthesized in different hydrophobic media e.g., using organic solvents like, *tri-octylphosphine* and *tri-n-octylphosphine oxide* (TOP/TOPO) at high temperatures [4]. The solvents were used both for bare and core-shell type of QDs. These QDs are soluble only in nonpolar hydrophobic solvents e.g., chloroform. They are mostly toxic and hazardous to biological systems. To overcome these difficulties, several attempts have been made for synthesizing water soluble QDs [5-7]. Unfortunately, these processes were found to be not only complicated but also expensive and time consuming. In this regard, growth of QDs in polymers (e.g. polyvinyl alcohol (PVA), polyvinyl pyrrolidone (PVP) can ensure an alternative but highly efficient approach due to commercial availability, water solubility and bio-compatibility of the host polymers [8]. Moreover, these polymeric hosts are not only capable of improving surface passivation of the QDs, but also likely to enhance the excitonic emission feature while lowering environmental degeneration. These polymers have been widely used for encapsulating semiconductor nanocrystals (NCs) [9,10]. Conversely, magnetic nanoparticles (NPs) encapsulated by the polymer host are not stable under ambient environments and are easily bleached by the acidic solution, resulting in loss of their magnetization. Furthermore, polymer-coated magnetic NPs have the relatively low intrinsic stability of the coating at higher temperature [11]. The polymer coating is thus least preferred to protect very reactive magnetic NPs.

Secondly, for use in biological application, surface modification of the QDs is a necessity to establish water solubility as well as bio-conjugation capability. This can be

achieved through using effective linkers (such as, silica, thiols, or phospholipid micelles and surfactants) following a suitable method *viz.*, ligand exchange, silica encapsulation, polymer encapsulation etc [6, 12]. Reactions with the water soluble QDs are generally considered depending on the available chemical groups attached to the biomolecules. QDs coated with a surfactant (e.g. sodium dodecyl sulphate, SDS) and an amphiphillic ligand (e.g. thyglycolic acid, TGA) helps in dispersal of NCs in aqueous media.

In this chapter, different fabrication strategies along with synthesis protocols of water soluble, surface functionalized CdSe and MnSe QDs are discussed. The water soluble CdSe QDs are synthesized by using the polyvinyl alcohol (PVA) host matrix. The water soluble, MnSe QDs are prepared by using TGA as a coating agent. The surface functionalizations of both types of QDs are provided by using TGA and SDS as functional entities. Transmission electron microscopy (TEM) and X-ray diffraction (XRD) are employed to reveal structural and morphological details. Moreover, the optical properties are exploited by UV-Visible (UV-Vis) and photoluminescence (PL) spectroscopies. The IR-active vibrational characteristics are revealed by fourier transform infrared (FT-IR) spectroscopy, whereas phononic features are evaluated by Raman spectroscopy studies*.

2.1 Physical and chemical properties of materials used

We discuss below physicochemical properties of materials used in different steps of various synthesis procedures.

2.1.1 Polyvinyl alcohol matrix (PVA)

The representation of PVA is shown in Fig. 2.1. Basically, polyvinyl alcohol represents polymers formed by the polymerization of vinyl alcohol. They are classified under water soluble polymer category and possess several interesting physical properties. The solubility of PVA depends on the degree of polymerization and in the degree of hydrolysis. It dissolves slowly in cold water and goes fairly fast at high temperatures.

---

* *Appendix-1*

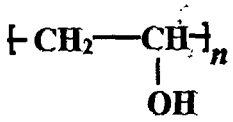

Figure 2.1: Molecular structure of PVA

PVA is an environmental-friendly polymer due to water solubility, high transparency and low cytotoxicity. This allows potential applications of PVA in a number of fields including biophysical and biomedical research. Additionally, in tissue engineering, PVA-based scaffolds have been widely studied in order to replace the currently available artificial grafts [13]. The appearance and feel of PVA hydrogel are similar to those of native arterial tissue and this makes it very adequate for vascular implanting [14,15]. Due to its tissue-like elasticity and mechanical strength, PVA is considered as a promising candidate suitable for tissue culturing and mimicking. Physical properties of PVA are highlighted in Table 2.1.

Table 2.1: Physical properties of PVA

Physical form, colour	Solid, white
Glass transition temperature (K)	343
Degree of polymerization (minimum)	2000
Melting Temperature (K)	413
Refractive Index	1.55
Specific Gravity	1.3
Density (g/cm^3)	1.19
Thermal Conductivity ($Wm^{-1}K^{-1}$)	2
Specific Heat ($J(gm)^{-1})K^{-1}$)	1.5

2.1.2 Thioglycolic acid (TGA)

Thioglycolic acid (TGA) is an organic compound containing both thiol and carboxylic acid (Fig. 2.2). TGA is primarily used in cosmetics, beauty and other miscellaneous applications such as, pharmaceutical, agrochemical, leather processing, fire extinguishing foams etc. TGA continues to draw attention in cosmetic products, particularly, for depilatories and hair straightening. TGA can also be used as a water- soluble chain

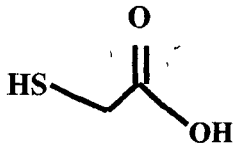

Figure 2.2: Structural representation of TGA molecule

transfer agent for certain acrylic polymers [16]. Although, TGA in excess quantities is toxic, it facilitates photostablity, bright fluorescent response of the QDs. This is why there has been a rapid growth in the development of TGA coated QDs for biological applications [17,18]. Some physical properties of TGA are enlisted in Table 2.2.

Table 2.2 Physical properties of TGA

Physical form, colour	Liquid , colourless
Melting Temperature (K)	257
Refractive Index	1.55
Specific Gravity	1.32
Viscosity (cP)	6.55
Electrical Conductivity (Ω^{-1} cm^{-1})	2×10^{-6}
Dielectric constant	2.25
Density (gcm^{-3})	1.32

2.1.3 Sodium dodecyl sulfate (SDS)

Sodium dodecyl sulfate (SDS or, NaDS) is an organic compound with the formula $CH_3(CH_2)_{11}OSO_3Na$. It is an anionic surfactant routinely used in many cleaning and hygiene products. The salt is an organo-sulfate consisting of a 12-carbon tail attached to a sulfate group (Fig. 2.3), making the material amphiphilic. Amphiphiles is a property that describes both hydrophilic and hydrophobic nature coexisting in the same molecule. Due to the amphiphilic nature of SDS, it can easily be made water soluble while linking to desired QDs.

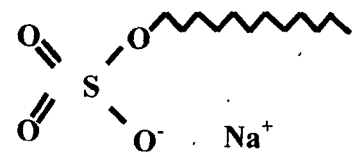

Figure 2.3: Structural representation of SDS molecule

2.2 Experimental details

2.2.1 Water soluble CdSe QDs in PVA matrix

PVA matrix: First, 10 g of polyvinyl alcohol (Mol. wt. ~80,000) was dissolved in 100 mL distilled water followed by stirring at 80° C temperature for 3 h until the solution becomes transparent.

Preparation of QDs: 0.62 g of cadmium nitrate-tetra hydrate [$Cd(NO_3)_2.4H_2O$] was dissolved in 100 mL of distilled water followed by stirring at 60°C temperature for 20 min. 20 mL of 10% PVA was added to Cd^{2+} solution during stirring. The pH of the solution was adjusted to 11 by adding 5N aqueous sodium hydroxide (NaOH) in a drop-wise manner. Then, 0.11 g of selenium di-oxide (SeO_2) was added to the reaction mixture and subsequently, 0.1 g sodium borohydride ($NaBH_4$). The purpose of using a reductant like $NaBH_4$ was to reduce SeO_2. Finally, the mixture was subjected to stirring for 1 h at 100°C temperature. The precursor extract was then subjected to centrifugation (~5,000 rpm) followed by filtration using a Whatman® filter. The precipitate (residue) was washed with distilled water several times.

2.2.2 Synthesis of TGA and SDS functionalized CdSe QDs

At first, 0.93 g of cadmium nitrate-tetra hydrate [$Cd(NO_3)_2.4H_2O$] was dissolved in 100 mL of water followed by stirring at 40°C temperature for 20 min. 0.046 gL^{-1} (0.16 gL^{-1}) of TGA (SDS) was added to Cd^{2+} solution during stirring. The pH of the solution was adjusted to 11 by adding aqueous sodium hydroxide (NaOH) in a drop-wise manner. Next, 0.22 g of SeO_2 was added to the reaction mixture which is followed by addition of 0.2 g of solid $NaBH_4$. The mixture was then subjected to stirring for 1 h at 80°C temperature. Finally, the precursor extract was subjected to centrifugation (~5,000 rpm) followed by filtration using a Whatman® filter. The precipitate (residue) was washed with distilled water repeatedly for several times. The following chemical reactions are

Dissociation: $Cd(NO_3)_2 \longrightarrow Cd^{2+} + 2NO_3^-$ (2.1)

Initial reduction: $SeO_2 \longrightarrow Se^0$ (2.2)

Subsequent reduction: $Se^0 \xrightarrow{80\,^\circ C} Se^{2-}$ (2.3)

Complete redox reaction: $Cd^{2+}(aq.) + Se^{2-}(aq.) \longrightarrow CdSe\ (QDs)$ (2.4)

favoured in the formation of CdSe QDs.

Note that, CdSe QDs prepared by method described in section 2.2.1 will be used in electrophysiology experiment. However, no PVA will be used as dispesing media.

2.2.3 Synthesis of water soluble/ functionalized MnSe QDs

Both water solubility and functionalization property of the MnSe QDs have been obtained by TGA and SDS as coating materials. The protocols used for synthesizing and functionalizing the MnSe QDs are discussed below.

In a typical synthesis procedure, 0.62 g of manganese chloride-tetra hydrate [$MnCl_2.4H_2O$] and 0.11 g SeO_2 were dissolved in 22 mL distilled water followed by the addition of $NaBH_4$ of 0.1 g. The pH of the solution was adjusted to ~11 by adding a few drops of NaOH followed by stirring at 60°C temperature for 5 min. In separate cases, TGA and SDS (of concentration 10%) were added to the above mixture, independently. Finally, the solution was transferred to a 50 mL capacity teflon-lined stainless steel autoclave. The autoclave was sealed properly and subjected to heat treatment at 180° C for 6 h. On completion of the reaction, the autoclave was allowed to cool down to room temperature naturally. The precursor extract was then subjected to centrifugation (~5,000 rpm) followed by filtration using a Whatman® filter. The precipitate (residue) was washed thoroughly with distilled water several times.

The relevent chemical reactions can be explained below

Dissociation: $MnCl_2 \longrightarrow Mn^{2+}+2Cl^-$ (2.5)

Initial reduction: $SeO_2 \longrightarrow Se^0$ (2.6)

Subsequent reduction: $Se^0 \xrightarrow{180\,^\circ C} Se^{2-}$ (2.7)

Complete redox reaction: $Mn^{2+}(aq.) + Se^{2+}(aq.) \longrightarrow$ MnSe QDs (2.8)

2.2.4 Production of $Cd_{1-x}Mn_xSe$ QDs with TGA coating agent

The step-by-step synthesis protocols, for obtaining alloyed QDs with varying x, are as detailed below. The QDs corresponding to stoichiometric parameter x=0 (CdSe) and x=1(MnSe) have already been discussed in #2.2.2 and #2.2.3.

The ternary QD systems of $Cd_{1-x}Mn_xSe$, with x=0.3, 0.6, 0.8 were prepared following the previously mentioned procedure described in subsection #2.2.3 but with little alteration. Here, Cd^{2+} precursor of a given concentration was simultaneously

considered with a specified Mn^{2+} precursor. While Se^{2-} precursor concentration was fixed, the Cd^{2+} to Mn^{2+} molar concentration was varied for $x = 0.3, 0.6, 0.8$.

2.3 Characterization of synthesized QDs

Below we discuss basic characterization aspects of the as synthesized CdSe and MnSe QDs.

2.3.1 Morphological analysis through high resolution transmission electron microscopy (HRTEM)

2.3.1 (a) TEM study of water soluble CdSe QDs

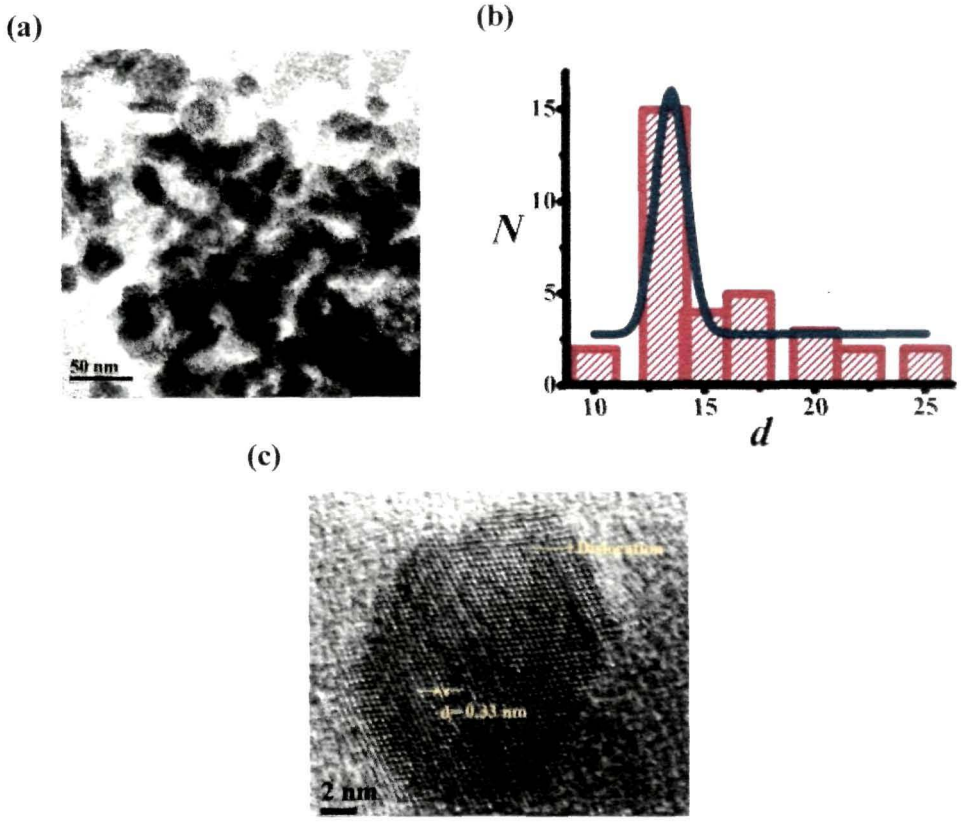

Figure 2.4: HRTEM images of CdSe QDs at a) low magnification (b) histogram depicts particle-size distribution. An enlarged, view of an isolated QD is shown in (c) with crystal lattice fringe

The TEM micrographs of the as-synthesized CdSe QDs dispersed in PVA are shown in Fig. 2.4 (a). The average size (d) of the QDs is found to be ~13.2 nm as predicted from the particle size histogram (Fig. 2.4(b)). The micrograph 2.4 (c) depicts an isolated nearly spherical QD. A clear lattice fringe pattern has ensured good crystallinity of the specimen (Fig. 2.4 (c)). The perfect periodicity of the lattice atoms is mostly witnessed in the core, while missing atoms (vacancies) and planes are found close at the surface-edge. The characteristic interplanar spacing (d_I) is estimated to be ~0.33 nm which is close to the value predicted in an earlier work [19]. As can be found at the upper right side portion of the figure, the orientation of the atomic planes has altered with respect to the main part. We attribute this to the existence of several edge dislocations in the QD-system [20]. Essentially, the edge-dislocations occur as a result of undeveloped lattice planes and due to spontaneous termination of growth at the QDs surface/ boundary.

2.3.1 (b) TEM study of water soluble TGA and SDS coated CdSe QDs

The TEM images of the as-synthesized, TGA and SDS coated CdSe QDs are shown in Fig. 2.5(a) and 2.6(a), respectively. All the QD systems are found to be fairly spherical, with size variations reflected in the particle size histogram (Fig. 2.5(b) and (Fig. 2.6(b)). The average size (d) of the CdSe-TGA and CdSe-SDS systems are found to be ~14.3 nm and ~10.9 nm; respectively. Furthermore, the lattice fringes due to single crystalline planes are clearly observed in the magnified views of the samples (Fig. 2.5(c) and Fig. 2.6(c)).

A typical fast Fourier transform (FFT) image of the Fig. 2.5(c) of CdSe-TGA QDs, is shown in Fig. 2.5(d). It predicts the hexagonal structure of the QDs, bright spots indicating growth of lattice planes along (101) and (102) directions. From FFT diffraction spots, interplanar spacing (d_I) was estimated to be ~0.35 nm, ~0.22 nm for TGA coated QDs along the lattice planes (101) and (102); respectively. The inverse FFT pattern ((Fig. 2.5(e)) gives well- resolved lattice planes of the QDs.

On the other hand, clear diffraction spots of only (102) plane can be observed from FFT image of Fig. 2.6(c)) for CdSe-SDS QDs. Correspondingly, the diffraction spots indicates interplanar spacing (d_I) of ~0.37 nm.

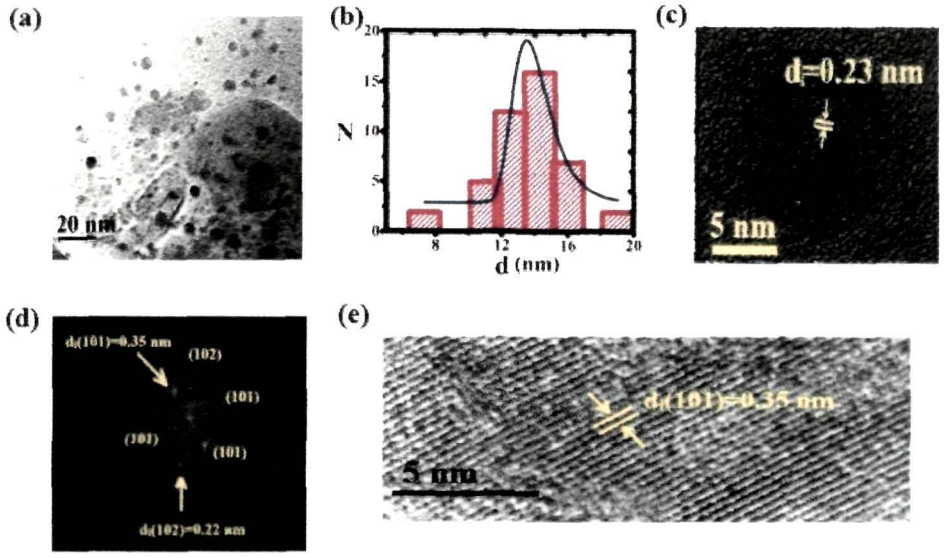

Figure 2.5: (a) HRTEM image of CdSe-TGA QDs at a) low magnification. The histogram (b) depicts particle-size distribution, (c) depicts an isolated QD with crystal planes. FFT image of (c) is shown in (d) along with spots indicating Miller indices, (e) shows the inverse FFT pattern with well- resolved lattice planes

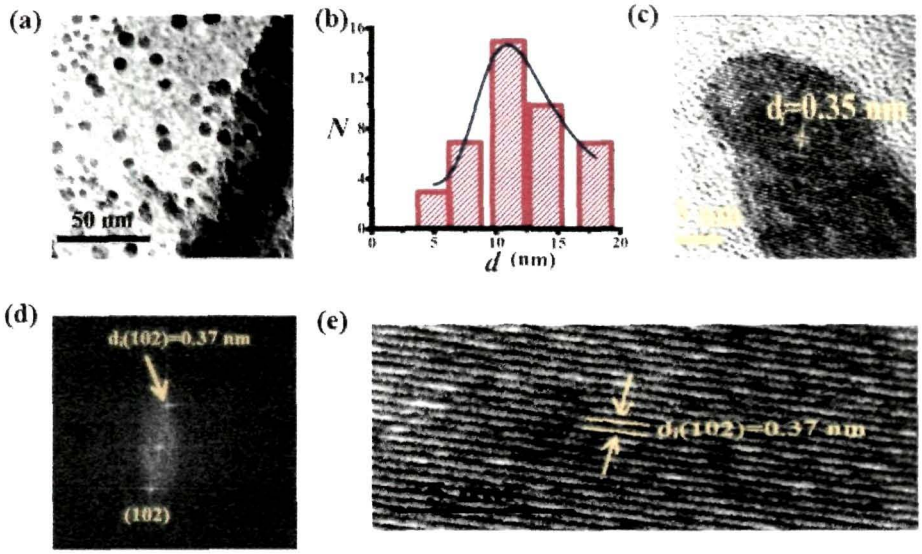

Figure 2.6: HRTEM image of CdSe-SDS QDs at a) low magnification. The histogram (b) depicts particle-size distribution, (c) depicts an isolated QD with crystal planes. FFT image of (c) is shown in (d) along with spots indicating Miller indices, (e) shows the inverse FFT pattern with well- resolved lattice planes

2.3.1 (c) TEM study of water soluble, TGA and SDS coated MnSe QDs

Electron microscopy imaging was also performed on MnSe- TGA and MnSe-SDS QDs to assess QD size, shape and size distribution. TEM micrograph of MnSe-TGA QD system is shown in Fig. 2.7(a). Isolated, nearly spherical QDs of size (d) ~7 nm can be predicted from the size distribution plot highlighted in Fig. 2.7 (b). The magnified view of an isolated QD is shown in Fig. 2.7(c). A thin TGA layer (yellow arrow) along with a fairly distinguishable lattice fringe pattern can be witnessed in the same figure (Fig. 2.7(c)). The interplanar spacing is estimated to be ~0.25 nm which is consistent to an earlier report on WZ type MnSe QD system [21]. An excessive coating of TGA, spreading over the terminal lattice planes of the QD surface, makes fringe pattern slightly blurred at the edge boundary. Nevertheless, it was possible to identify a few point defects (vacancies) and edge-dislocations in the corresponding image which were indicated by red and pink arrows; respectively. The FFT pattern gives a clear indication of lattice plane along (100) direction that has an interplaner spacing of ~0.26 nm.

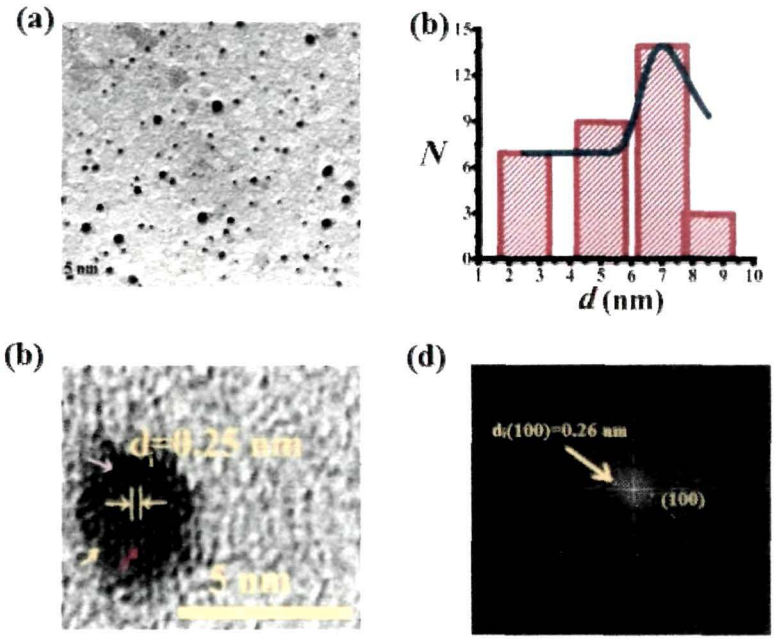

Figure 2.7: HRTEM images of MnSe-TGA QDs at a) low magnification (b) histogram depicts particle-size distribution. An enlarged, view of an isolated QD is shown in (c) with crystal lattice fringe, (d) depicts the FFT spots indicating Miller indices.

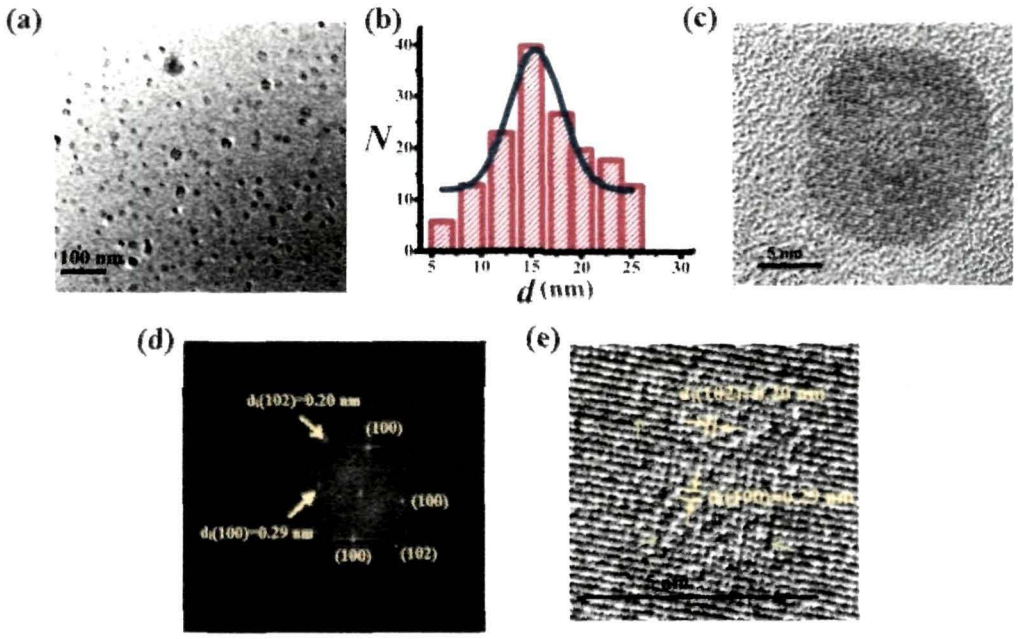

Figure 2.8: HRTEM images of MnSe-SDS QDs at a) low magnification. The histogram (b) depicts particle-size distribution, (c) depicts an isolated QD with crystal planes. FFT image of (c) is shown in (d) along with spots indicating Miller indices, (e) shows the inverse FFT pattern with well- resolved lattice planes

The TEM micrograph of water soluble, MnSe-SDS QDs is depicted in Fig. 2.8(a). The average size (d) of the QDs is found to be ~15 nm with visualization of lattice planes in an isolated QD (Fig. 2.8 (b), (c)). Shown in Fig. 2.8(d), is the FFT pattern of Fig. 2.8(c) which predicts a hexagonal crystal structure of the QDs with preferred orientations along (102) and (100) crystallographic planes. The respective d_i are estimated to be ~0.20 and 0.29 nm. The inverse FFT pattern, as shown in Fig. 2.8(e) depicts well resolved lattice fringe patterns with identifiable lattice imperfections including voids and dislocations (green arrows).

2.3.2. Crystallographic analysis through X-ray diffraction studies[†]

2.3.2 (a) X-ray diffraction studies of CdSe-TGA and CdSe-SDS QDs

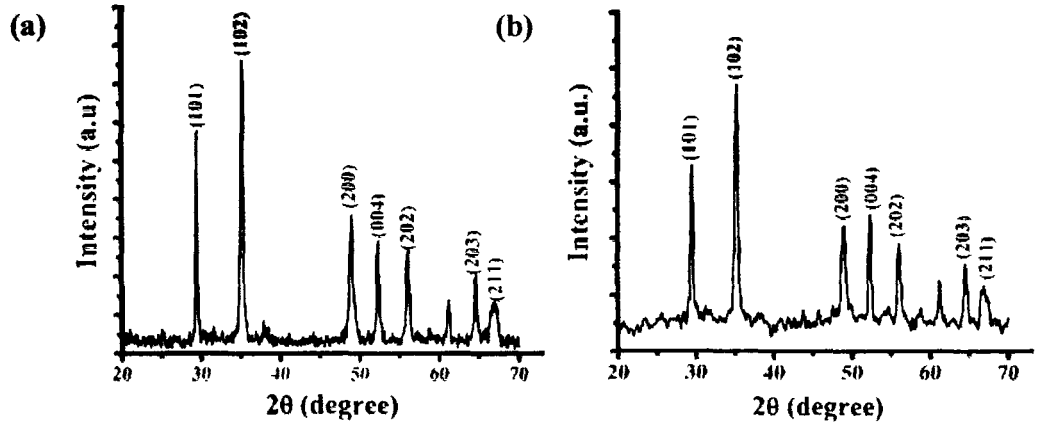

Figure 2.9: Powder XRD pattern of (a) CdSe-TGA (b) CdSe-SDS system

The XRD pattern of CdSe-TGA and CdSe-SDS QDs are shown in Fig. 2.9(a) and (b). The diffraction peaks located at 29.5°, 35.1°, 48.9°, 52.2°, 56.0°, 64.5°, 67° and corresponding to (101), (102), (200), (004), (202), (203) and (211) crystallographic planes depict hexagonal WZ phase of CdSe systems (JCPDS-770046) [22]. As predicted from the Williamson–Hall (W-H) plot[‡], the average crystallite size (D_{cry}) and micro-strain (ε_s) of CdSe-TGA QDs are found to be ~0.003 nm (±0.004) and -0.0016 (±0.002), respectively. Whereas, for CdSe-SDS system, the respective values are observed to be ~10.7 (±0.006) and 0.0036 (±0.003) nm[§].

The lattice parameters (a=b and c) are estimated by using the following relation applicable to a hexagonal system, with an interplanar spacing d_{hkl} (Miller indices h, k, l):

$$\frac{1}{d_{hkl}^2} = \frac{4}{3}\left(\frac{h^2+hk+k^2}{a^2}\right) + \frac{l^2}{c^2} \qquad (2.9)$$

[†] *Appendix-2*

[‡] *Appendix-2*, Figure:1(a)

[§] *Appendix-2*, Figure:1(b)

$$\frac{c}{a} = \left(\frac{8}{3}\right)^{\frac{1}{2}} \tag{2.10}$$

The lattice parameters are calculated to be a = 4.5 Å, c = 7.2 Å, for CdSe-TGA and a = 4.34 Å, c = 7.2 Å, for CdSe- SDS QDs and are in consistency with an earlier report [22].

2.3.2 (b) X-ray diffraction studies of MnSe-TGA and MnSe-SDS QDs

The X-ray diffractograms of the MnSe-TGA QDs system is shown in Fig. 2.10(a). The diffraction peaks located at 25.8°, 26 .8°, 28.6°, 36.1°, 43.9°, 47.8°, 50.2° , 52.05° , 53° and 58.7° and corresponding to (100), (002), (101), (102), (110), (103), (200), (112), (201) and (202) crystallographic planes of MnSe-TGA QDs represents hexagonal WZ structure of MnSe and consistent to other works [21, 23]. Moreover, $MnSe_2$ phase is also observed in the form of impurity at a diffraction angle of ~23.8° and 31.4° [23]. An average crystallite size (D_{cry}) of ~7 nm and a negative micro-strain of the order ~10^{-3} are predicted from the W-H plot**. A small negative slope of the order of ~10^{-3} indicates the presence of more relaxed crystallites [24]. The lattice constants are evaluated with TGA QDs system as a = 3.9 Å, c = 6.34 Å, using eqn. (2.9) and (2.10), and in consistency with others work [23]. The preferred orientation of the crystallites is along the (100) plane.

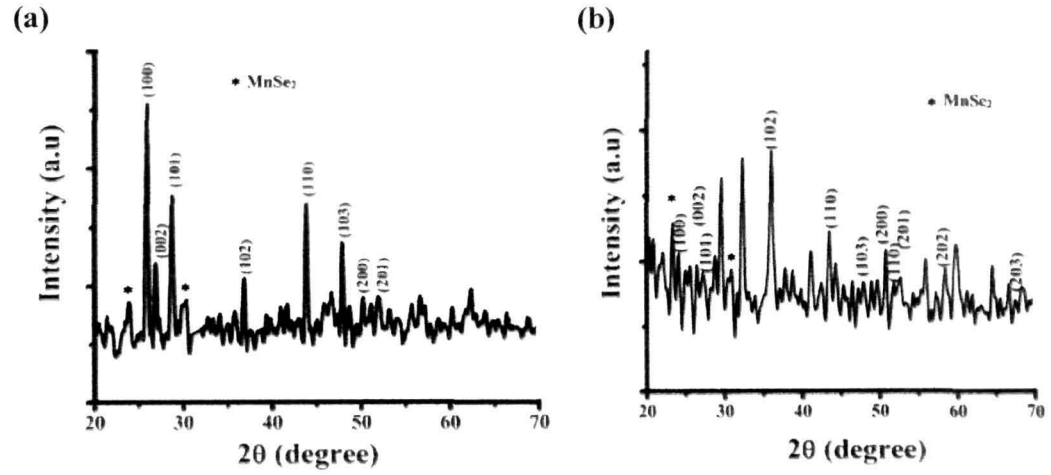

Figure 2.10: Powder XRD pattern of (a) MnSe-TGA (b) MnSe-SDS system

** *Appendix-2*, Figure:1(c)

The structural phase of the as- synthesized MnSe QDs with SDS surfactant coating, also exhibit WZ phase (Fig. 2.10(b)). The diffraction peaks located at 24.1°, 26.3°, 27.4°, 36°, 43.4°, 47.9°, 50.7° , 51.7° , 52.6°, 58.4 ° and 67.1 correspond to (100), (002), (101), (102), (110), (103), (200), (112), (201), (202) and (203) crystallographic planes of hexagonal WZ MnSe crystal structure (Fig. 2.10(b)). The, $MnSe_2$ phase is detected in the form of impurity at a diffraction angle of ~23.1° and 31.9° [23]. The diffraction peak at 29.5° is assumed to SDS [25]. The average crystallite size (D_{cry}) of MnSe-SDS system is ~15.1 nm and a micro-strain value of the order of $\sim 10^{-4}$ can be estimated from the W-H plot[††]. The lattice parameters are: a = 3.8 Å and c = 6.12 Å. The observed noise in the diffraction pattern of MnSe SDS QDs is can be due to the presence of excess long chain molecules like, SDS. Table 2.3 depicts different parameters of the QDs obtained from TEM and XRD analyses. Since the average size of the QDs obtained from TEM analyses, are equivalent to the crystallite size, it indicates the presence of fairly single crystallites in the QD systems under study.

Table 2.3 Parameters obtained from TEM and XRD analysis

QDs System	Crystallographic orientation	d (nm)	D_{cry} (nm)	ε_s	d_{hkl} (nm)	$a=b$* (Å)	c* (Å)
CdSe-TGA	Hexagonal	3.7	3.7±0.004	0.003±0.002 (-ve)	0.21 (d_{102}), 0.35 (d_{101})	4.5	7.3
CdSe-SDS	Hexagonal	10.9	10.7±0.006	0.0036±0.006 (+ve)	0.37(d_{101})	4.34	7.2
MnSe-TGA	Hexagonal (WZ)	7	7	10^{-3} ±7.5*10^{-4} (-ve)	0.25(d_{100})	3.9	6.34
MnSe-SDS	Hexagonal (WZ)	15	15.1	10^{-4} (+ve)	0.23	3.8	6.12

[††] *Appendix-2*, Figure:1(d)

2.3.3 Optical properties of CdSe and MnSe QDs

Optical properties of the synthesized QDs are evaluated by UV-Vis and PL spectroscopy as discussed below. Throughout the thesis, we have presented normalized absorption/emission spectra with values in the range of 0 and 1. This helped us in comparing the strength of absorption/emission spectra for a given set of samples.

2.3.3 (a) UV-Vis analysis of CdSe QDs

The optical absorption spectra of PVA dispersed CdSe QDs is shown in Fig. 2.11(a). The respective optical absorption response of TGA and SDS coated CdSe QDs are shown in Fig. 2.11(b) and (c). As can be observed, in all the QD samples, the onset of absorption is blue shifted wrt the bulk CdSe value (λ_{onset} ~716 nm). This implies effective quantum confinement of the charge carriers in the synthesized QD product. The UV-Vis optical absorption spectrum of the PVA dispersed QDs is characterized by a strong 1*s*-1*s* excitonic absorption positioned at ~302 nm (E_g = 4.09 eV) and thus featuring a blue shifting of ~2.35 eV (Fig. 2.11 (a)). The ground state excitonic wavelength value corresponds the already reported value (~310 nm) where mercapto-acetic acid was used as a coating agent [26].

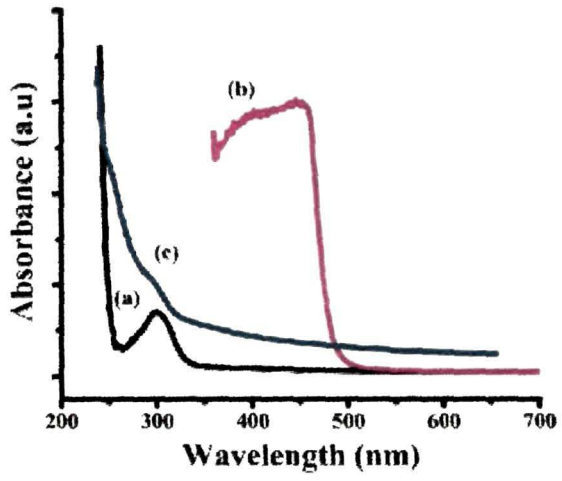

Figure 2.11: Optical absorption spectra of (a) PVA dispersed (b) TGA and (c) SDS coated CdSe QDs

However, away from fundamental absorption, CdSe-TGA QDs system is characterized by a broadened absorption response in the range of ~370 - 460 nm (Fig. 2.11 (b)). This is likely to be due to the superposition of several weakly confined excitonic levels. On the other hand, the excitonic wavelength of SDS coated CdSe QDs (Fig. 2.11 (c)) is found to be located at ~305 nm highlighting a significant blue shifting wrt the bulk value. Consequently, the band gap is blue shifted by an amount of (~2.33 eV) from the energy gap of the bulk CdSe (1.74 eV).

Looking the absorption peaks (Table 2.4), we speculate that CdSe QDs coated with TGA can have larger dimension as compared to PVA dispersed and SDS coated one. The larger particle size of TGA functionalized CdSe QDs over others has also been confirmed from the TEM studies. Table 2.4 shows parameter related to UV-Vis spectra of different CdSe QDs system.

Table 2.4: Parameters related to UV-Vis spectra of CdSe QD systems

QDs System	**Excitonic wavelength, λ (nm)**	**Band gap energy E_g (eV)**	**Blue shifted energy, ΔE_g (eV)**
CdSe-PVA	302	4.09	2.35
CdSe-SDS	305	4.06	2.33
CdSe-TGA	370(460)	3.37(2.71)	1.63(0.97)

2.3.3 (b) UV-Vis analysis of MnSe QDs

Figure 2.12 depicts optical absorption spectra of MnSe QDs functionalized with different capping agents. Referring to MnSe-TGA QDs, an observable excitonic absorption feature is located at ~303 nm (E_g ~4.09 eV, Table 2.5). This implies effective quantum confinement of the charge carriers in the QDs characterized by a blue-shift (~0.5 eV) from the bulk value (E_g~3.5 eV, Table 2.5) of the WZ MnSe system [23, 27-29]. But the estimated value of E_g is significantly larger (by ~1.6 times) than the case for rock-salt (RS) type MnSe (~2.5 eV) nanoscale system [23]. In contrast, excitonic absorption is red

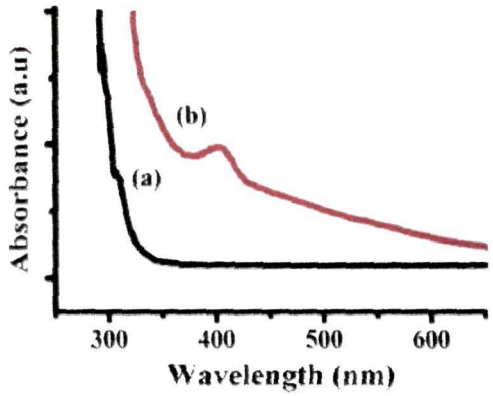

Figure 2.12: Optical absorption spectra of (a) MnSe-TGA (b) MnSe-SDS QDs

shifted to ~330 nm (E_g = 3.75 eV) for SDS coated MnSe QDs as compared to the TGA coated one. However, the former exhibited a blue shifting of ΔE_g = 0.25 eV from the bulk value of concerned WZ MnSe system indicating thereby adequate carrier confinement. The different of excitonic absorption feature in different types of MnSe systems can be attributed to size effect (Table 2.5). Our prediction is also supported by the earlier discussion on TEM analysis (Fig. 2.7 and 2.8). Different optical parameters with regard to MnSe QD systems are shown in Table 2.5.

Note that, with respect to bulk, MnSe system experienced a smaller blue shift in comparison with the CdSe system. This may be due to the highly localized nature of the 3*d* electronic bands of Mn atoms [29]. Correspondingly, the quantum confinement induced by cordially bonded organic layers is likely to result in a much smaller change in these bands [29].

Table 2.5: Parameters related to UV-Vis spectra of MnSe QD systems

QDs System	**Excitonic wavelength, λ (nm)**	**Band gap energy E_g (eV)**	**Blue shifted energy, ΔE_g (eV)**
MnSe-TGA	303	4.09	0.5
MnSe-SDS	330	3.75	0.25

2.3.3 (c) PL spectra of CdSe QDs

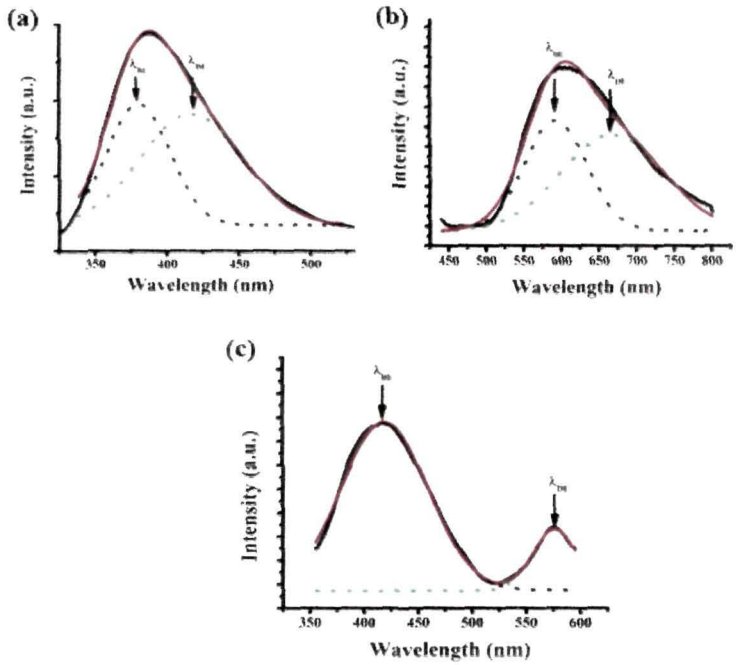

Figure 2.13: PL spectra of (a) PVA dispersed (b) TGA and (c) SDS coated CdSe QDs. The excitation wavelength was λ_{ex}~300 nm

The PL spectra of CdSe QDs prepared with different coating agent are depicted in Fig. 2.13. After deconvolution, each of the emission spectra is found to be comprised of two distinct peaks: one is relatively narrow and symmetric, that represents radiative recombination mediated near band edge emission (λ_{BE}) (NBE), while the other one, is adequately broad (with a larger full width) and represent, defect related emission (λ_{DE}). The first peak located at ~380 nm of CdSe-PVA is attributed to the direct recombination of carriers and second peak observed across the wavelength at ~420 nm is assigned to the radiative emission via surface defect centers (Fig. 2.13(a)). The centers are created by entrapped electrons inside a selenium vacancy with holes in the valence band.

As for, TGA (Fig. 2.13 (b)) and SDS coated QDs (Fig. 2.13 (c)) the respective λ_{BE} peaks are found to be located at ~590 nm and ~418 nm. The respective λ_{DE} positions are ~657 nm and ~575 nm. The defect related emission appeared at ~657 nm in case of CdSe-TGA QDs, can be assigned to emission through deep trap levels. Possibly, the origin of these defect levels is mediated via V_{Cd}-V_{Se} divacancy centers available in the

nanocrystalline specimens. One di-vacancy is related to the orientation along *c*-axis, whereas the other one is believed to be oriented along the basal Cd–Se bond directions. On the other hand, the peak at ~575 nm of CdSe-SDS QDs corresponds to the shallow, virtual levels of the QDs. The ratio of band edge-to-defect emission intensities (I_{BE}/I_{DE}) are ~1.06, 1.14 and 1.7 for CdSe-PVA, CdSe-TGA and CdSe-SDS QDs; respectively (Table 2.6). This apparently signifies larger surface passivation of the CdSe QDs by SDS molecule than other coating/dispersing agent. Different parameters wrt PL response of CdSe QD systems are highlighted in Table 2.6.

Table 2.6: Parameters related to PL spectra of different CdSe QDs

QDs system	λ_{BE} **(nm)**	λ_{DE} **(nm)**	I_{BE}/I_{DE}
CdSe-PVA	380	420	1.06
CdSe-TGA	590	657	1.14
CdSe-SDS	418	575	1.7

2.3.3 (d) PL spectra of MnSe QDs

The PL spectra of the MnSe QDs coated with TGA and SDS are shown in Fig. 2.14 (a) and (b); respectively. Upon deconvolution, the λ_{BE} of MnSe-TGA and MnSe-SDS QDs are found to be located at ~373 nm. It may be noted that ZB type MnSe system has a cherectistics λ_{BE} is at ~364 nm [30]. Whereas, the λ_{DE} peaks are observed at ~436 nm and ~413 nm for the respective QDs. The defect related emission peaks may have arisen from the defects in the metastable WZ nanocrystal core [31]. In

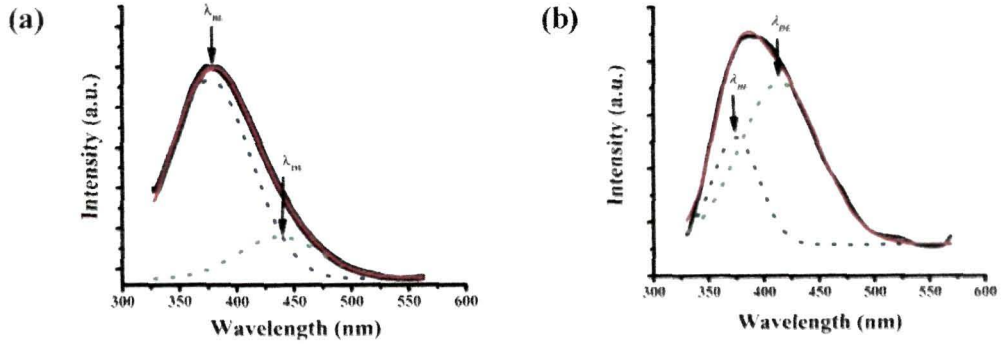

Figure 2.14: PL spectra of (a) MnSe-TGA (b) MnSe-SDS QDs. The excitation wavelength was λ_{ex}~300 nm

MnSe-TGA QDs, the ratio of band edge to defect emission intensity is ~3.08. For MnSe QDs functionalized with SDS capping agent, the intensity of the defect related emission is dominant over band edge emission by a factor of ~1.3. This suggests significant surface passivation of MnSe QDs by coating agent TGA. Table 2.7 depicts different PL parameters assigned to MnSe systems.

Table 2.7: Parameters related to PL spectra of different MnSe QDs

QDs system	λ_{BE} (nm)	λ_{DE} (nm)	I_{BE}/I_{DE}
MnSe-TGA	373	436	3.08
MnSe-SDS	373	413	0.76

2.3.3 (e) Quantum yield determination of synthesized QDs

Typically, the fluorescence quantum yield (*QY*) gives the efficiency of a process undergoing fluorescence events. It is defined as the ratio of the number of photons emitted to the number of photons absorbed. In general,

$$QY = No.\ of photons\ emitted\ /\ No.\ of photons\ absorbed$$

The quantum yield (Φ_Q) of the QDs can be predicted more accurately using from the following relation [32]:

$$\Phi_Q = Q_{ref}\,(n/n_{ref})^2\,(I_Q/I_{ref})\,(A_{ref}/A_Q) \qquad (2.11)$$

The Q_{ref} represents the quantum yield of a reference specimen; I (QDs) and I_{ref} (reference) are the integrated emission intensities; A_Q (QDs) and A_{ref} (reference) are the absorption intensities; n (sample) and n_{ref} (reference) are the refractive indices of the solvents. By taking Rhodamine 6G® as reference, the *QY* of the CdSe and MnSe QDs coated with different coating agents can be estimated (Table 2.8). The *QY* of TGA coated QD is invariably larger than the SDS coated counterpart, for both the CdSe and MnSe systems. The CdSe-TGA QDs characterize a *QY* value as large as 89%, which is nearly ~1.34 and ~1.64 times larger than the PVA dispersed and SDS coated QDs. In contrast,

Table 2.8: A comparative view of Quantum yields of different QDs with Rhodamine 6G as reference

Sample	Integrated Emission Intensity (I) (a.u.)	Absorbance at 523 nm (A) (a.u.)	Refractive Index of Solvent (η_s)	QY (Φ_Q)
Rhodamine 6G	46598.23	0.099	1.33	96% [33]
CdSe-PVA	19075.92	0.059	1.33	66%
CdSe-TGA	23060.00	0.052	1.33	89%
CdSe-SDS	67466.4	0.252	1.33	54%
MnSe-TGA	34636.53	0.093	1.33	75%
MnSe-SDS	76030.00	0.633	1.33	24%

the MnSe-TGA QDs exhibit ~3.12 fold larger value of QY as compared to the SDS coated MnSe QDs system.

2.3.4 FTIR spectroscopy

This is a sophisticated technique that is capable providing information wrt structural, bending and bonding vibrations of a molecule.

2.3.4 (a) FTIR spectra of different CdSe QDs

Figure 2.15(a) depicts the FTIR spectra of PVA dispersed CdSe QDs. The peak at ~3436 cm^{-1} arises from the hydroxyl (O-H) stretching mode of H_2O molecules. The peak at ~2928 cm^{-1} has arisen due to –CH stretching vibration. Whereas, the peaks located at ~1746 cm^{-1}, 1453 cm^{-1} and 1168 cm^{-1} are attributed to carbonyl (– C=O) stretching, -CH bending, –C-O stretching of PVA molecule; respectively [34]. The peak observed at ~716 cm^{-1} is assigned to Cd-Se bending mode [35]. On the other hand, an FTIR spectrum of CdSe-TGA QDs is shown. Fig. 2.15(b). The peak at ~3418 cm^{-1} arises from the hydroxyl O-H stretching mode of the H_2O molecule. The appearance of the bands at ~678 cm^{-1}, and at 1646 cm^{-1} are attributed to C–S stretching and asymmetric $\nu_{as}(COO^-)$ vibration of the TGA capped QDs. Moreover, as mentioned in earlier case, the peak observed at ~748 cm^{-1} can be assigned to the Cd-Se bending [35].

The FTIR spectra of SDS capped CdSe QDs is shown in Fig. 2.15(c). It can be

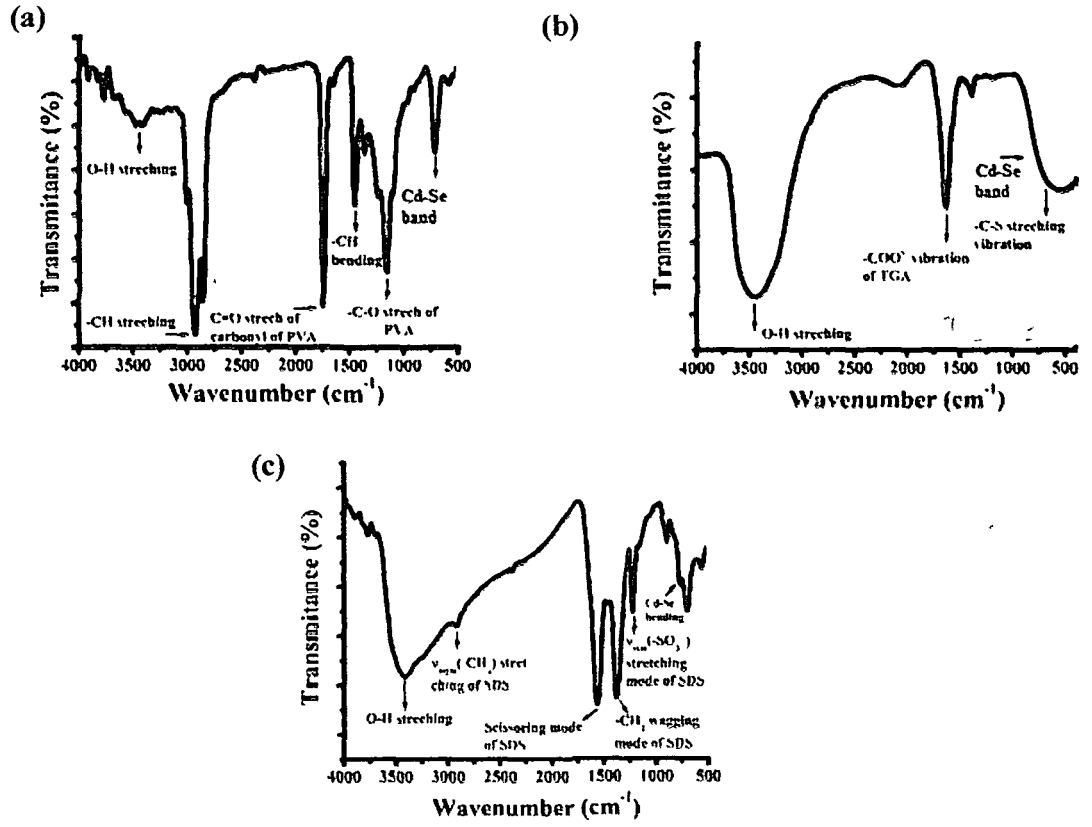

Figure 2.15: FTIR spectra of CdSe QDs (a) dispersed in PVA and coated with (b) TGA (c) SDS agents

observed that, with SDS capping, though the O-H stretching mode is positioned at 3434 cm^{-1}, the peak due to the asymmetric $-CH_2$ stretching ($\nu_{asym}(-CH_2)$) of the SDS surfactant is witnessed at ~2916 cm^{-1} [36]. However, the peak at 1579 cm^{-1} is assigned to the scissoring mode of the SDS surfactant; which is shifted to a higher wavenumber (~1579 cm^{-1}) wrt 1559 cm^{-1} of pure SDS molecule [37]. Note that, in SDS, the spectral region located in 1300–1400 cm^{-1} is characteristic of the $-CH_2$-wagging modes [37]. This region exhibits peaks which are related to gauche conformations. Thus, the peak observed at ~1381 cm^{-1} of the CdSe-SDS QDs can be assigned to the CH_2 wagging modes. Whereas, the peak corresponding to ν_{sym} ($-SO_3^-$) stretching mode of the SO_3^{2-} group is located at ~1272 cm^{-1} [37]. The observed shifting of $\nu_{sym}(-SO_3-)$ mode from a value of 1084 cm^{-1} of pure SDS to a value of ~1272 cm^{-1} for CdSe-SDS QDs system, is likely to describe an enhancement of interactions of the headgroups with availability of plentiful Na^+

counterions [37,38]. The peak observed at ~783 cm^{-1} is assigned to an effaceable bending of Cd-Se itself.

2.3.4 (b) FTIR spectra of different MnSe QDs

The FTIR spectra of MnSe QDs are depicted in Fig. 2.16 (a, b). Four prominent, IR-sensitive, vibrational peaks are clearly observable the FTIR spectra of the MnSe-TGA QD system (Fig. 2.16 (a)). These are located at ~3447 cm^{-1}, 1634 cm^{-1}, 1383 cm^{-1} and ~644 cm^{-1}. Referring to Fig. 2.16 (a), the peak at ~3447 cm^{-1} is believed to be due to the hydroxyl (O-H) stretching mode of the TGA molecule, whereas, the peak at ~1634 cm^{-1} has arisen due to the asymmetric vibrational peak of -COO^- group of TGA molecules [27]. The peak corresponding to C=O stretching vibration is identified at ~1383 cm^{-1} [39]. In consistency with other reports, the peak witnessed at a relatively low wavenumber regime (~644 cm^{-1}) can be ascribed to the vibrational response due to Mn–OH stretching [40].

The FTIR spectrum of WZ MnSe-SDS QDs is shown in Fig. 2.16(b). The peak observed at ~2106 cm^{-1} is due to the symmetric -CH_2 stretching vibration $\nu_{sym}(-CH_2)$ of the SDS capping molecules [41]. This peak, infact, down shifted to a low wavenumber

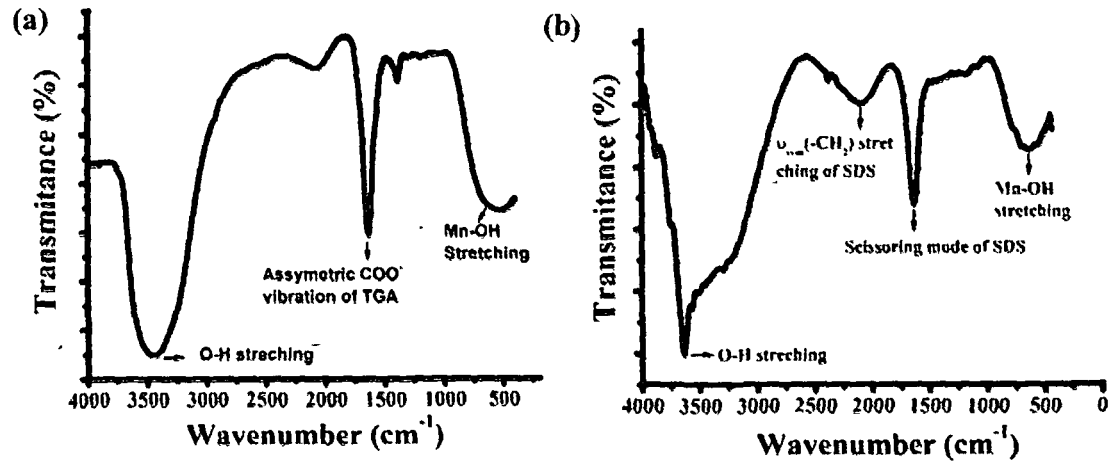

Figure 2.16: FTIR spectra of (a) MnSe-TGA (b) MnSe- SDS QDs

value as compared the symmetric -CH_2 stretching mode (~2860 cm^{-1}) of the pure SDS molecule [41]. The shifting of peak position, towards a lower wavenumber signifies the likelihood formation of a close packed crystallite surfactant layer at the surface of MnSe QD [37, 41]. The crystalline nature of the SDS molecules, on the QD surface can also be ensured from the well resolved diffraction peak noticeable in the diffractogram of MnSe-SDS QDs. (Fig. 2.10). Finally, the peak at a much lower wavenumber value (~644 cm^{-1}), is assigned to Mn–OH stretching [40].

2.3.5 Exploring optical phonons through Raman spectroscopy[‡‡]

Raman spectroscopy deals with the inelastic scattering of light from both molecular species and solid state objects. Raman scattering is a powerful technique to get information on different vibrational characteristics obtained from different vibrational states of a solid [42].

2.3.5 (a) Raman spectra of CdSe QDs

Figure 2.17 depicts the Raman spectra of the as synthesized CdSe QDs. In reference to Fig. 2.17(a), the characteristic Raman peak for CdSe-TGA QDs are observed at 203 cm^{-1}

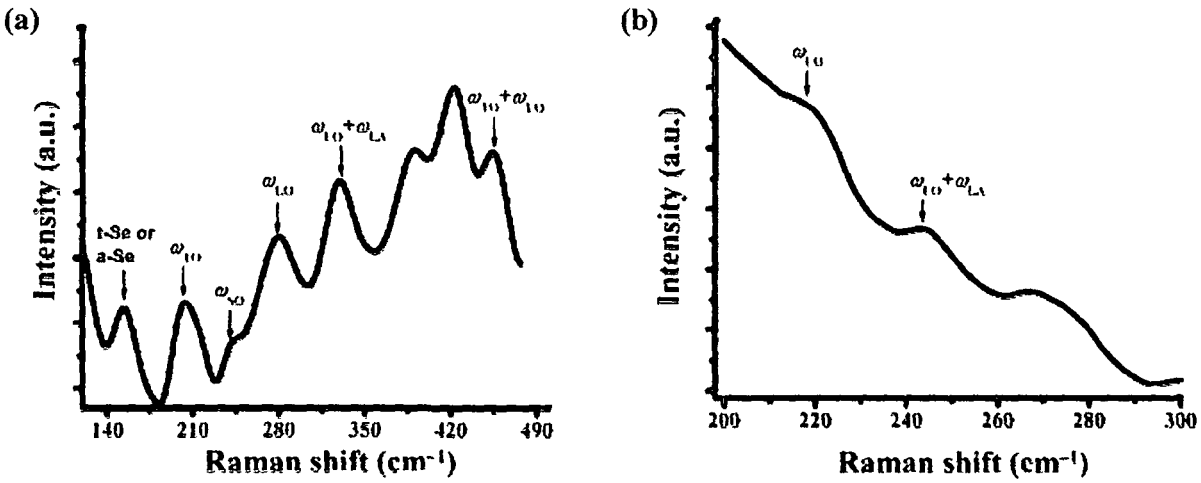

Figure 2.17: Raman spectra of (a) CdSe-TGA and (b) CdSe-SDS QDs

[‡‡] *Appendix-3*

and 279 cm^{-1}. The peaks can be identified as transverse optical (TO) and longitudinal optical (LO) phonon mode, which are blue shifted from the corresponding phonon modes of bulk CdSe (TO=170 cm^{-1}, LO=210 cm^{-1}) system [43]. For nanocrystallites, the confinement effect induces a broadening and downward shift of the Raman peaks [44]. The Raman shifting due to the phonon confinement effect can be described by the confinement model [45]. When the particle size decreases in the nanometer scale, a volume contraction occurs within the nanoparticle due to the size-induced radial pressure and this might lead to a substantial increment in the force constant value which in turn decreases interatomic distances. In vibrational transitions, the wavenumbers vary approximately in proportion to $k^{1/2}$, where k is the force constant. Consequently, an enhanced magnitude of the force constant would be characterized by a shifting of the Raman band towards a higher wavenumber side [46,47].

The respective LO and TO modes satisfy the well known Lydanne-Sachs- Teller (LST) expression given by [48]:

$$\epsilon_\infty / \epsilon_d = \omega_{TO}^2 / \omega_{LO}^2 \qquad (2.12)$$

Here, the high frequency dielectric constant (ϵ_∞) of CdSe system is 6 [49] and the static dielectric constant (ϵ_d) is 8.6. As the surface optic (SO) vibrational mode of the nanoscale systems normally exists in between LO and TO phonon frequencies, the Raman peak at ~238 cm^{-1} is attributed to SO phonon mode. The frequency of the SO modes depends on the dielectric environment (ϵ_s) of the QDs and can be expressed by Klein formulation [50]:

$$\omega_l^2 = [\omega_{TO}^2 \{(l+1)/l\} + \omega_{LO}^2(\epsilon_\infty / \epsilon_s)]/[\{(l+1)/l\} + \epsilon_\infty / \epsilon_s] \qquad (2.13)$$

where $l = 1, 2\ldots.$ and $\epsilon_s = 78.30$ for water. The theoretically obtained value of lowest SO mode ($l=1$) is (206 cm^{-1}) which is close to the experimentally observed value i.e, 238 cm^{-1}. Note that, since the Klein eqn. generally valid for non-functionalized nanoparticles, the effect of surface ligands on SO is ignored. In our case, we predict that the upsift of the SO mode from the theoretically calculated value may be because of effect of TGA coating layer around the QDs. The spectra also shows mixed modes such as, LO+LA (~329 cm^{-1}) and TO+LO (456 cm^{-1}). The peak at 155 cm^{-1} can be designated

to amorphous selenium (*a-Se*) which exhibits Raman shift (Δv) in the range of 140-150 cm^{-1} [51].

On the other hand, the QDs coated with SDS surfactant shows Raman modes at 217 cm^{-1} and 243 cm^{-1} and can be attributed to the LO mode and possibly a combined mode of LO+LA (Fig. 2.17(b)).

2.3.5 (b) Raman spectra of MnSe QDs

The Raman spectra of the MnSe QDs are shown in Fig. 2.18. The peaks at ~295 cm^{-1} and ~225 cm^{-1} are identified as LO and TO phonon modes of the MnSe system. The blue shifting of the LO and TO phonon modes from the ZB bulk MnSe values of 257 cm^{-1} and 219.5 cm^{-1} [52]; respectively suggest strong phonon confinement in the system [53,54]. Till date, we are unaware of corresponding LO and TO modes of WZ phase bulk MnSe system. Here, the observed values of LO and TO clearly satisfy the LST relation quoted in eqn. (2.12). The Raman peak at ~244 cm^{-1} is attributed to SO vibrational mode of phonons. Using eqn. (2.13), and including the value of high frequency dielectric constant (ϵ_∞ = 5.99 [55]) and dielectric constant of the surrounding medium (ϵ_s = 78.30) the lowest (l=1), SO mode of the QDs under study is positioned at 228 cm^{-1}, reassembling an experimentally observed value of ~244 cm^{-1}. The weak mode, observable at

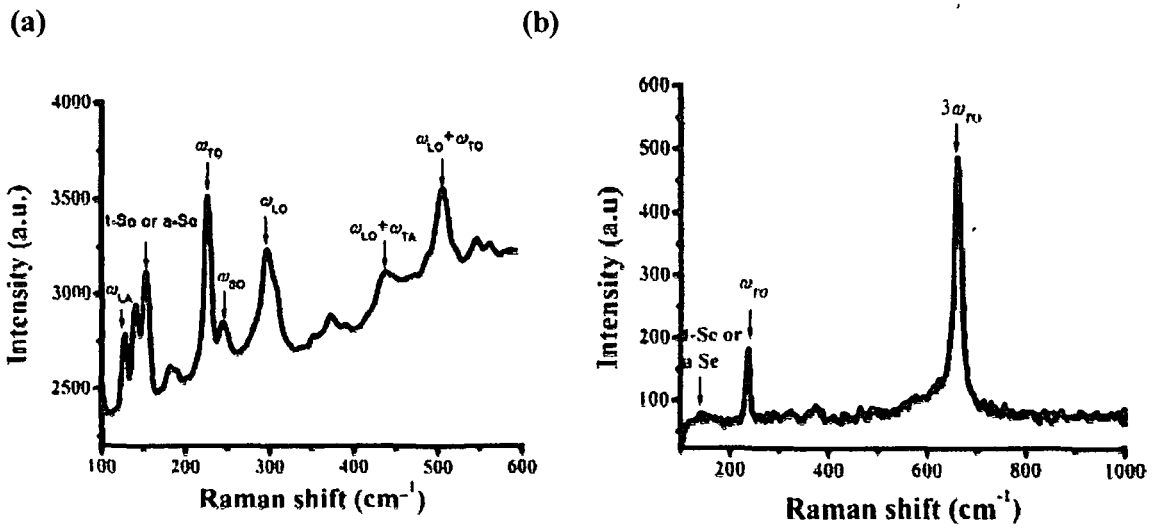

Figure 2.18: Raman spectra of (a) MnSe-TGA (b) MnSe-SDS QDs

~127 cm^{-1} might have arisen from the longitudinal acoustic (LA) phonons [56]. On the other hand, the peaks observed at ~506 cm^{-1} can be identified as a collective mode due to combination of LO+TO modes. The peak at ~140 cm^{-1} and 152 cm^{-1} are assigned to triogonal (*t*-Se), monoclinic (*mono*-Se) and amorphous selenium (*a-Se*) components.

The Raman spectrum of the MnSe-SDS QDs is shown in Fig. 2.18(b). Only two prominent Raman peaks have observed for this system. Here, the peak at ~225 cm^{-1} is identified as TO phonon mode of the MnSe system which is weakly blue shifted from the corresponding TO mode (219.5 cm^{-1}) of the ZB bulk MnSe [52] ensuring adequate phonon confinement in the system. A strong mode, observable at ~675 cm^{-1} is identified as the third harmonic of the TO (3TO) mode. Strong Frohlic interaction between exciton and phonons can account for such an event which is sensitive to size can account for such an event [55]. Resonant Raman scattering upto third order has been reported by previous workers [57]. The peak at ~150 cm^{-1} is assigned to trigonal (*t*-Se), monoclinic (*mono*-Se) and amorphous selenium (*a-Se*) phase(s).

2.4. Characterization of ternary $Cd_{1-x}Mn_xSe$ QDs

Herein, we discuss various properties of TGA coated compound semiconductor $Cd_{1-x}Mn_xSe$ QD systems.

2.4.1 Structural and morphological analyses of ternary QDs

The crystal structure and crystallographic orientation of the as-synthesized $Cd_{1-x}Mn_xSe$ QDs were assessed through XRD analysis. Figure 2.19 shows a series of diffractograms of the studied systems corresponding to different stoichiometric parameter, x. As can be found, for x=0 (CdSe) and x=1 (MnSe), the systems exhibite phase-pure hexagonal structure, but with non-similar diffraction peaks corresponding to different Bragg's angle (2θ). The diffractograms for these phase pure systems have already been discussed in (section #2.3.2(a) and (b)). On the other hand, a mixed phase of WZ MnSe, WZ CdSe and cubic CdMnSe is retrieved for ternary $Cd_{1-x}Mn_xSe$ QDs with stoichiometry values $x = 0.3$ and $x = 0.8$. As for $x = 0.3$. For $x = 0.3$, the diffraction peaks, due to the hexagonal WZ CdSe phase, are witnessed at 2θ~35.7° and 48.7° which corresponded to (102) and

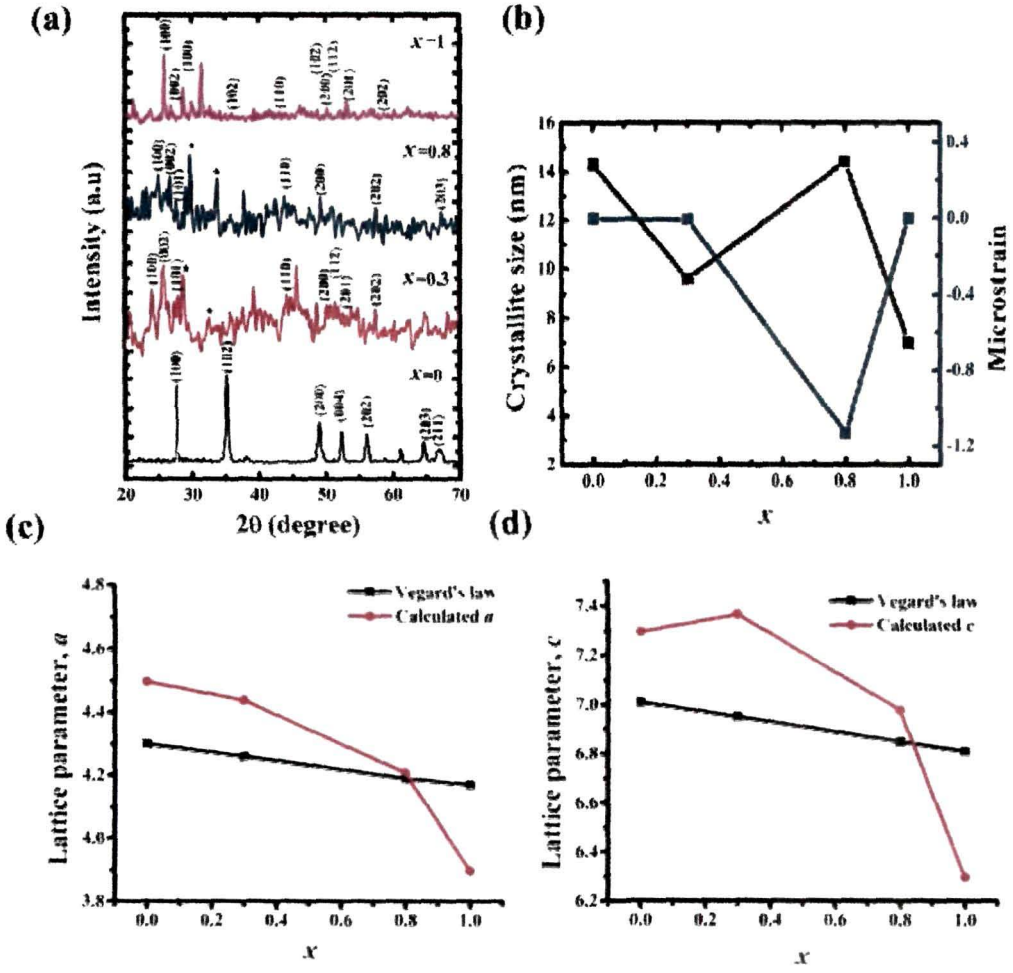

Figure 2.19: (a) XRD patterns of different $Cd_{1-x}Mn_xSe$ systems, (b) variation of average crystallite size and micro-strain with x. The sub-figures (c) and (d) depict variation of effective lattice parameters a and c with x considering general theory (red label) and Vegard' law (black label).

(200) crystallographic planes. In addition, the diffraction peaks observable at 24.0°, 25.8°, 28.02°, 43.9°, 50.1°, 51.4°, 53.0° and 57.4° are identified as (100), (002), (101), (110), (200), (112), (201) and (202) crystallographic planes of MnSe. Moreover, the cubic phase of CdMnSe is also detected in view of the existence of peaks located at 28.7° and 32.5^0 which characterize to (111) and (200) planes (represented by * marks) [58]. At a stoichiometry value of $x = 0.8$, the diffraction peaks at 24.9°, 26.7°, 27.8°, 43.9°, 49.0°, 57.4° and 67.0° represent (100), (002), (101), (110), (200), (202) and (203)

crystallographic planes of WZ MnSe-QDs. However, no diffraction peak due to independent CdSe phase is noticed in this case. Nevertheless, prominent (111) and (200) diffraction peaks due to cubic CdMnSe phase are identified at 2θ~29.6° and 33.6° (shown by * marks).

The average crystallite size has increased from a value of ~3.7 to 9.6 nm, when x is varied within 0 and 0.3; where as pure MnSe QDs (x=1) experience an average size of ~7 nm. While experiencing a maximum value corresponding to x=0.8, the magnitude of microstrain is found to vary in the range of 1.1- 8.3×10^{-3}. The negative values of the measured microstrains indicate presence of relaxed crystallites in the system under study [24]. The alloyed crystallites are much more relaxed as compared to those in either CdSe or MnSe system. The introduction of a stable cubic phase, with the inclusion of a small amount of Cd^{2+} ions, is likely to induce such an observable effect. With calculation of the lattice parameters a, and c, using eqn. (2.11) and (2.12), it is assumed a standard error of ±0.05%. It is observed that, with increasing x from 0 to 0.8, the c/a value vary between ~1.62 and 1.66. With x = 1, the pure MnSe QDs have experienced the least c/a value (1.61). We anticipate that, Mn^{2+} ions occupy the CdSe lattice mainly along the c-axis [59]. As for x=0.8 composition, all the Mn^{2+} ions are not necessarily fully embedded inside the CdSe core lattice, but can be available at the surfaces there by affecting the magnitude of lattice parameters by substantial amounts [59]. Table 2.9 depicts different parameters obtained through XRD analysis.

Table 2.9: Physical parameters obtained through XRD analysis of $Cd_{1-x}Mn_xSe$ NCs

Stoichiometry parameter, x	D_{cry} (nm)	ε ($x10^{-3}$)	Through XRD analyses (Å)	c/a (XRD)	Through Vegard's law (Å)	c/a (Vegard)
0	3.7	-3.0	$a=b=4.33$, $c=7.03$	1.62	$a=b=4.3$, $c=7.01$	1.62
0.3	9.6	-7.4	$a=b=4.44$, $c=7.37$	1.65	$a=b=4.26$, $c=6.95$	1.63
0.8	4.5	-8.3	$a=b=4.21$, $c=6.98$	1.66	$a=b=4.19$, $c=6.85$	1.63
1	7.0	-1.1	$a=b=4.15$, $c=6.78$	1.61	$a=b=4.17$, $c=6.81$	1.61

We also intended to verify if there is a possibility of formation of hetero-structure QDs while considering coexistence of CdSe and MnSe phases. The criterion is that, the lattice constant of an alloy can be expressed by a linear interpolation between its constituents. In this case, Vegard' law allows [60] us to predict the effective lattice parameter ($a_{eff} = b_{eff}$ and c_{eff}) given by:

$$a_{\text{eff}} = x\, a_{\text{MnSe}} + (1\text{-}x)\, a_{\text{CdSe}} \qquad (2.14\text{ (a)})$$

$$c_{\text{eff}} = x\, c_{\text{MnSe}} + (1\text{-}x)\, c_{\text{CdSe}} \qquad (2.14\text{ (b)})$$

The results are shown in Fig. 2.19(c) and 2.19(d) and compared with conventional theoretical results. As can be found, at a lower stoichiometry parameter x, the effective parameters calculated by the Vegard's relation, experience much lower values than the theoretical ones. However, at a higher x (with dominant Mn) value the magnitudes of a_{eff} and c_{eff} become close to the values approximated through eqns. 2.9 and 2.10. In other words, formation of CdSe/MnSe QD hetero-structure cannot be completed denied and possibly, occur near $x = 0.8$. It is worth mentioning here that, the conditions $x = 0$ and $x = 1$ basically represent independent CdSe and MnSe phases and the development of hetero-structure cannot arise in these case. Accordingly, we have not noticed deviation from the Vegard's law for both the cases.

Figure 2.20(a) depicts TEM images of the QD system corresponding to $x = 0.3$. As revealed from the low resolution micrograph, the synthesized QDs are nearly spherical and with an average size of ~9.5 nm. Since the size is close to the average

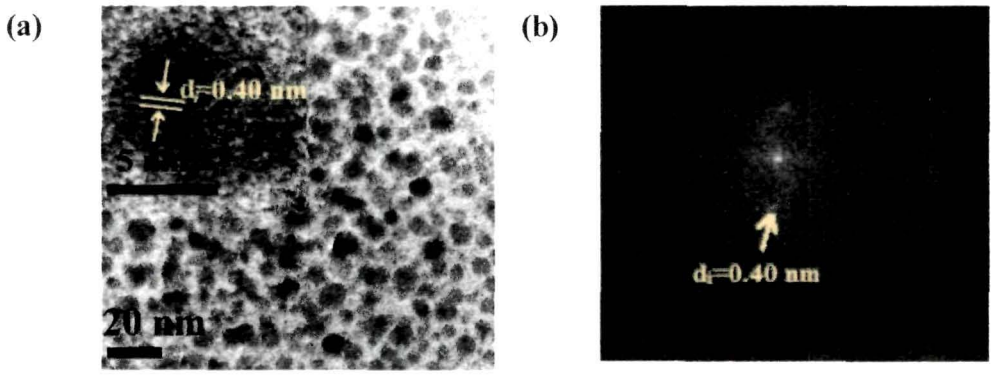

Figure 2.20: TEM images of $Cd_{1-x}Mn_xSe$ QDs with $x = 0.3$, (b) depicts the FFT pattern of inset of (a)

crystallite size predicted by XRD, the synthesized product characterize good amount of monocrystallinity. The inset, shown in the upper left corner of the micrograph, is basically a single QD. Apparently, a lattice fringe pattern with an interplanar spacing of ~0.40 nm is quite apparent from the inset. The FFT image of the figure inset shown in Fig. 2.20(b). This predicts the hexagonal structure of the system with an interplanar spacing of ~0.40 nm along (100) crystallographic orientation.

2.4.2 Optical characterizations through absorption and emission spectroscopy studies

The optical properties of $Cd_{1-x}Mn_xSe$ QDs, synthesized for different values of x, have been adequately analyzed through UV-Vis and PL spectroscopy and are discussed below.

2.4.2 (a) Effect of stoichiometry variation on the optical absorption spectra

Fig. 2.21 shows the optical absorption spectra of different $Cd_{1-x}Mn_xSe$ QDs of varying x. The response indicates adequate quantum confinement in the QDs, as evident from the blue-shifting of the onset of absorption, with increasing x. Since our QD systems are mostly compound types, we intended to evaluate the first order derivative plot of the absorption spectra so as to probe major changes in a particular spectrum. The direct optical band gap (E_g) can be predicted from the sharp peaks valid for different QD systems (Fig. 2.21(b) - (f)). Without inclusion of Mn, the absorption maximum of pure CdSe QDs is observed to be located at ~430 nm (2.8 eV) (Fig. 2.21(b)); which is strongly blue shifted from the bulk CdSe value (λ=714 nm, E_g=1.73 eV). The broad, subsidiary peak, observed at a relatively lower energy (2.4 eV) is expected to be due to the Urbach tailing [61] owing to association of carrier transitions between extended to localized states and vice-versa. As for x=0.3 (Fig. 2.21(c)), the optical gap is characterized by a sharp absorption peak positioned at ~481 nm (2.58 eV) along with a weak, subsidiary band at a lower energy. A further increase of Mn concentration (x = 0.6 and 1), has led to an enhancement of the optical gap with absorption maxima varying from 2.59 to 3.95 eV (Fig. 2.21(d)-(f)). Conversely, in these cases, the secondary broad peak is completely suppressed. We speculate that, beyond a certain Mn-level, the red shift of the absorption maxima followed by blue-shifting can be due to bowing effect Fig. 2.21(g)) [62]. Whereas, a significant blue shift is attributed to *sp–d* exchange interaction between electrons confined in the conduction, valence band electrons states and those located in the partially filled Mn^{2+} states [63-65]. This explanation [66] is also

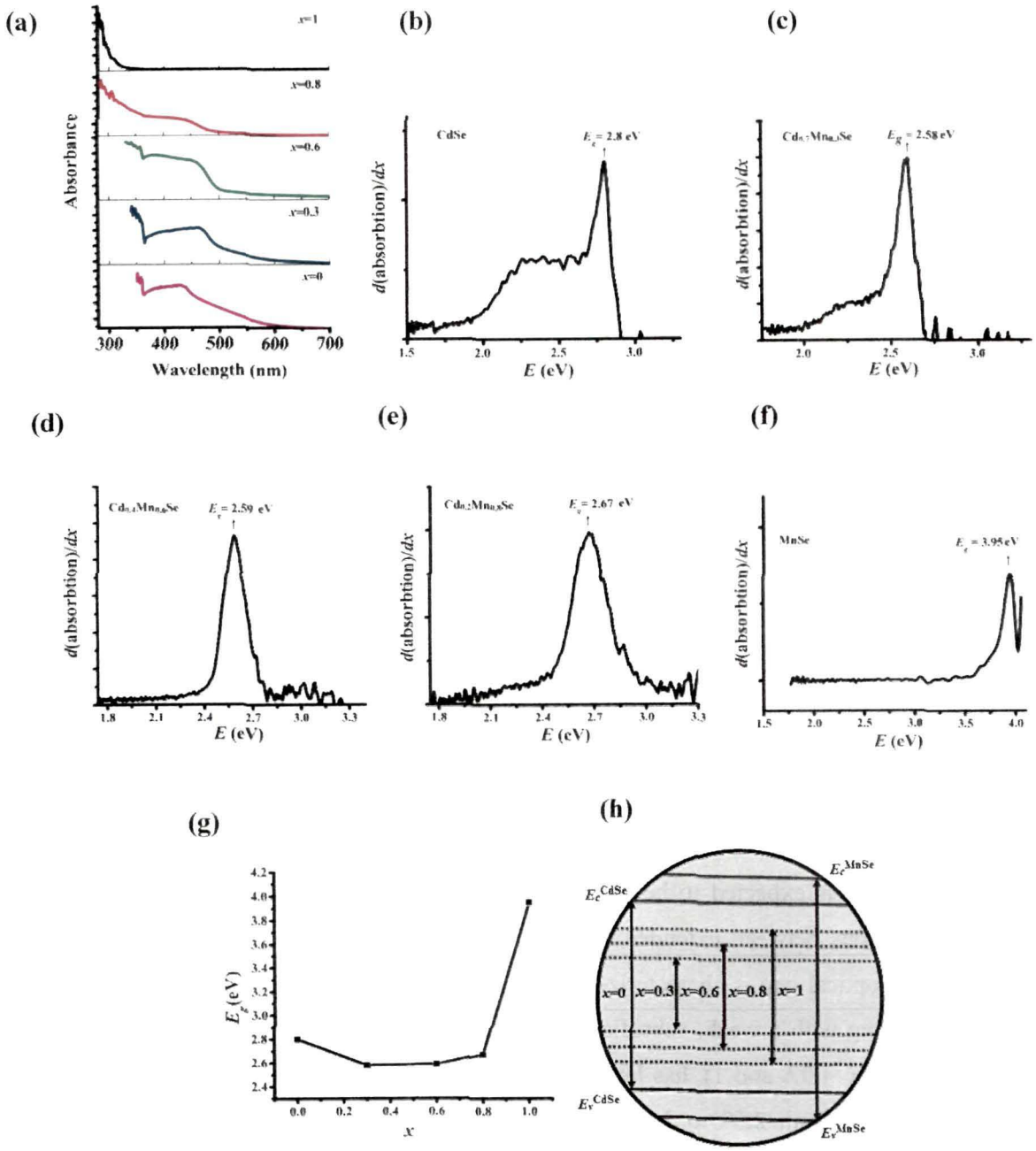

***Figure 2.21**: (a) Optical absorption spectra of $Cd_{1-x}Mn_xSe$ QDs. The first order derivative spectra of QD systems, with varying stoichiometric parameters are shown in (b)-(f). The variation of band gap with x and a schematic of band gap engineering are presented in (g) and (h); respectively.*

supported by the argument that, the replacement of Cd by Mn (in $Cd_{1-x}Mn_xSe$, $0.3 \leq x \leq 0.8$) would help varying the energy gap between 1.74 and 3.5 eV for the bulk CdSe (x = 0), and the WZ-MnSe (x=1) systems; respectively [23]. The bowing parameter, βw, for $Cd_{1-x}Mn_xSe$ system has been calculated by following equation,

$$E_g^{Cd_{1-x}Mn_xSe} = xE_g^{MnSe} + (1-x)E_g^{CdSe} - \beta_w x(1-x) \qquad (2.15)$$

E_g^{MnSe} and E_g^{CdSe} are band edge emission energy obtained from PL data. The values are found to be changed from -0.76 to 1.75 eV with changing x from 0.3 to 8. This is the reason why there is abrupt change in the band gap for this composition [15].

The optical band gaps, for different QDs of varying stoichiometric parameter x are presented in Table 2.9. A scheme illustrating band gap engineering in the concerned QD systems is depicted in Fig. 2.21(h).

2.4.2 (b) Effect of stoichiometry variation on the optical emission spectra

Figure 2.22(a) depicts the emission spectra of $Cd_{1-x}Mn_xSe$ QDs along with multi- peak deconvolution fits. Each of the spectra is characterized by a number of emission peaks. In case of CdSe QDs (x = 0), the first peak at ~590 nm is ascribed to the near band edge (NBE) emission [67]. The second peak, located at ~657 nm, is due to radiative emission mediated via trap states of the QDs [68]. With increasing value of x from 0 to 0.3, the NBE emission response of $Cd_{0.7}Mn_{0.3}Se$ system is blue-shifted to ~484 nm [63]. While the peak at ~510 nm ensure presence of shallow, virtual levels of the QDs [69], the appearance of a small peak at ~580 nm is believed to be owing to the pseudo-tetrahedral ($^4T_1 \rightarrow {}^6A_1$) transition of the Mn^{2+} ions introduced into the CdSe QDs [63]. The broad emission band, with a peak maximum at ~628 nm, could not be fitted by single Gaussian-component. This affirms the complexity of the ternary system and association of multiple emissions of different origin, yet providing comparable recombination probabilities. An enlarged view of the PL spectrum with deconvolution is depicted for QDs with x = 0.3 in Fig. 2.22(b). As predicted in earlier works, mostly deep defect levels are likely to occur in hexagonal wurtzite structure of CdSe, or $Cd_{1-x}Mn_xSe$ QDs [65, 70,71]. The deconvoluted peaks, located at ~640 and ~670 nm, can be due to the deep trap levels. Possibly, the origin of these defect levels is related to the V_{Cd}-V_{Se} divacancy centers[§§]

[§§] *Appendix-4*

associated to the absence of Cd^{2+} and Se^{2-} in the nanocrystalline elements [65, 72,73]. One di-vacancy is related to the orientation along *c*-axis; whereas the other one is believed to be oriented along the basal Cd–Se bond directions [74]. In earlier works, the size dependence of these trapping levels was confirmed for CdSe NCs [65]. Also one can explain independent emissions emanating from the QDs (labeled as, Em_1 and Em_2) as well as from the bulk-like NCs (labeled as, E_{b1}) that might occur in ternary $Cd_{1-x}Mn_xSe$ QD systems (Fig. 2.22(b)). Interestingly, the excitonic emission at ~484 nm of $Cd_{1-x}Mn_xSe$ QDs is almost suppressed by sufficiently large non-radiative channels via ~628 nm peak [69]. Further, the band edge emission response of $Cd_{1-x}Mn_xSe$ system, for x = 0.6 is further blue- shifted to ~480 nm. The emission due to shallow trap levels is observed at ~512 nm along with a weak orange emission band, appearing in the wavelength range of ~535-620 nm. The emission peak is centered at ~550 nm, is ascribed to the forbidden *d–d* transition $^4T_1(^4G)$–$^6A_1(^6S)$ of the Mn^{2+} ions [75]. With an increasing x from 0.3 to 0.6, the non-radiative emission via trap levels that originated from the V_{Cd}-V_{Se} di-vacancies, is completely disappeared. This indicates that, the replacement of V_{Cd}–V_{Se} vacancies by Mn^{2+} ions is more effective in the QDs with an increased Mn^{2+}concentration [69].

Referring to $Cd_{0.2}Mn_{0.8}Se$ QDs (of x = 0.8), the NBE emission is located at ~473 nm apart from the existence of a shallow level positioned at ~521 nm. No orange emission is inadvertently detected in this configuration. Moreover, as for MnSe QDs (x = 1), the NBE emission response is located at ~400 nm. The emission peak, observable at ~459 nm, is likely to be accompanied by defect states originated from the metastable WZ nanocrystal core [31]. Thus, the PL spectra of $Cd_{1-x}Mn_xSe$ QDs is extremely sensitive to parameter x. A perturbed lattice structure, in each composition, and with different x may have direct influence on the emission spectrum of definite origin. Moreover, the absence of Mn^{2+} emission, as for x = 0.8 case, signifies that Mn^{2+} ions, are incorporated into the CdSe cluster by surface adsorption rather than direct inclusion into the CdSe core [63]. This is expected especially at a higher concentration of Mn^{2+} concentration. An increasing Mn^{2+} ions with increasing x, reduces the average distance between the two Mn^{2+} ions thus favouring diffusion of these magnetic ions from the nanocrystal core to the nanocrystal surface [74]. The diffusion of the Mn^{2+} ions through

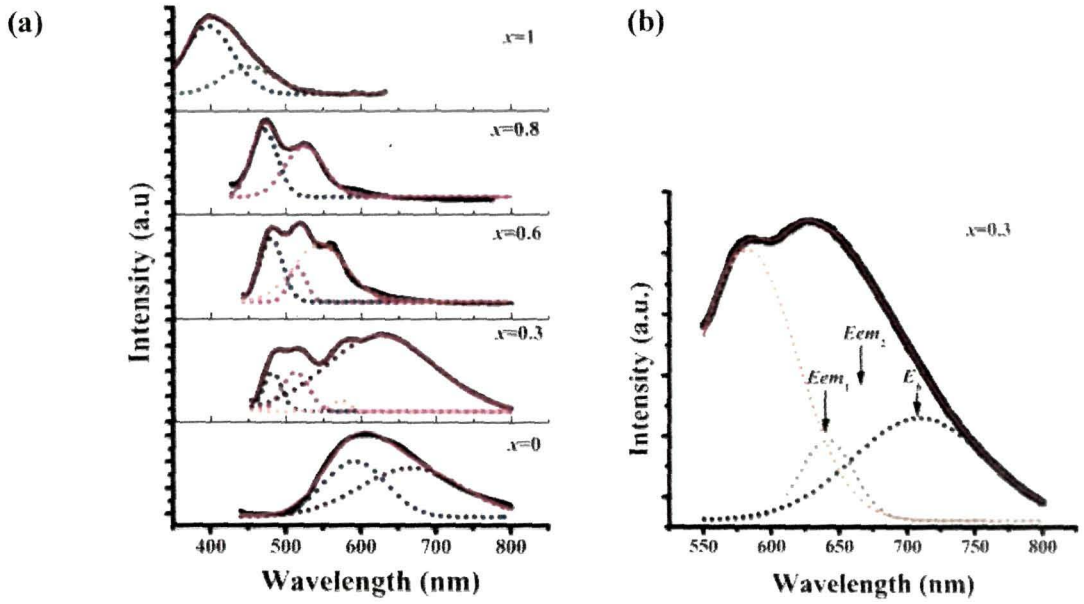

Figure 2.22: (a) Room temperature PL spectra of QDs with different stoichiometric parameters, $0 \leq x \leq 1$ (b) deconvoluted PL spectra of the QDs system corresponding to $x=0.3$.

the NCs is known as a 'self-purification' mechanism and is an intrinsic property of impurities/defects in semiconductor NCs [74]. As the ionic radius of Mn^{2+} (ionic radius ~82 pm) is smaller than the ionic radius of the Cd^{2+} (ionic radius ~95 pm) ion, it is quite apparent that, this diffusion is substantial in $Cd_{1-x}Mn_xSe$ NCs [74]. The existence of Mn^{2+} in CdSe core has also been predicted from the XRD analysis as discussed above.

Table 2.10: Optical energy gap and emission peaks observed for ternary $Cd_{1-x}Mn_xSe$ QD systems

x	**Band gap energy (E_g)**	**NBE emission peak (nm)**	**Defect emission peak (nm)**			
			Metastable WZ core	**Shallow trap emission**	**Mn^{2+} Orange emission**	**Deep trap emission (nm)**
0	2.8	590	-	-	-	657
0.3	2.58	484.3	-	510	580	628
0.6	2.59	480	-	512	550	-
0.8	2.67	473	-	521	-	-
1	3.95	400	459	-	-	-

The NBE emission peak maxima, along with defect related contributions, for different QDs are depicted in Table 2.10

2.4.2 (c) Electron- phonon coupling and analysis through Raman spectroscopy

In a semiconductor, the exciton–phonon interaction determines the shape of the absorption and emission spectra. In NPs, the electron–phonon or exciton–phonon coupling strength is determined by both quantum confinement and the surface characteristics [76]. The electron phonon coupling strength is described by Huang –Rhys parameter '*S*' according to Franck-Condon approximation*** [77]. The parameter '*S*' can be estimated from the Stokes shift [78]

$$\Delta_{Stokes} = 2S\hbar\omega_{LO} \qquad (2.15)$$

Here, ω_{LO} is the longitudinal optical phonon frequency of the QDs. The strength of interaction is expected to play a deterministic role on the optical and optoelectronic responses exhibited by a specimen under study. Accompanied by phonons, the interaction is likely to facilitate an enhanced absorption near the fundamental band edge along with broadening of the emission peak [79]. Consequently, with different values of $\hbar\omega_{LO}$ and Δ_{Stokes} for different QD systems, the parameter S may vary appreciably. As for CdSe, ω_{LO}= 210 cm^{-1} (0.03 eV) and for MnSe, ω_{LO}= 257 cm^{-1} (0.034 eV). For the compound system, we assumed ω_{LO}= 210 cm^{-1}, and predict that no significant change of ω_{LO} is likely to occur with alteration of x [59].

The S values are calculated using Fig. 2.21 and 2.22 and are highlighted in Table 2.11. A high coupling constant value in phase pure CdSe (x=0) and MnSe (x=1) cases, signify radiative recombination due to the many-body effects on the excitonic states of the NCs [66]. A larger S value displayed by the later could account for inherent participation of delocalized electrons of the Mn^{2+} states. However, the ternary QD system show a weak electron-phonon coupling characterized by S<1. Essentially, a similar range of Stokes' shift is witnessed in case of $Cd_{1-x}Mn_xS$ systems. Since the Huang–Rhys factor depends strongly on the distributions of the density of electron and hole charges [79], we

*** *Appendix-5*

speculate that the charge distribution has been significantly manifested in all the QDs with different stoichiometric values. The Stokes shift and coupling strengths as estimated for varying stoichiometry parameter x are highlighted in Table 2.11.

Table 2.11: Calculation of coupling strength for different QDs of varying stoichiometric parameter x

Value of x	Absorption peak (eV)	NBE Peak (eV)	Difference, Δ_{Stokes} (eV)	Coupling Strength (S)
0	2.8	2.10	0.70	11.6
0.3	2.58	2.56	0.02	0.33
0.6	2.59	2.58	0.01	0.16
0.8	2.67	2.62	0.05	0.83
1	3.95	3.1	0.85	14.16

We have also assessed Raman spectroscopy studies. The Raman spectra of the QDs, with x=0.3 is shown in Fig. 2.23. The $Cd_{0.7}Mn_{0.3}Se$ system has exhibited only one mode identified at ~202 cm^{-1} which is close to the LO phonon mode of CdSe QDs (ω_{LO}= 210 cm^{-1}). Apart from the distinct ω_{LO} peak, existence of broad feature in the high

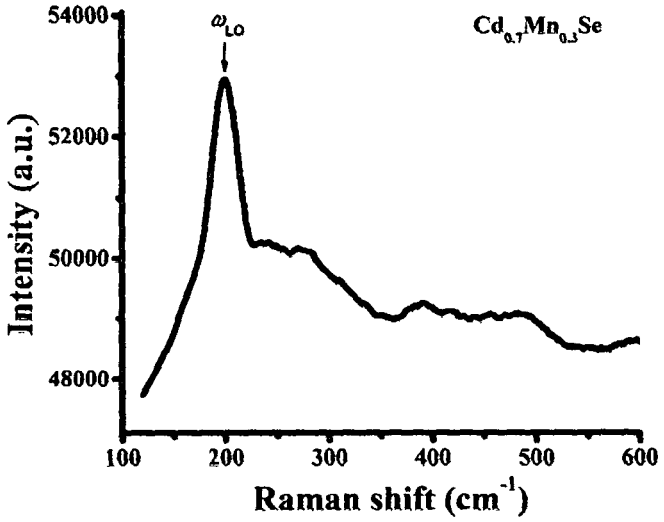

Figure 2.23: Raman spectra of $Cd_{1-x}Mn_xSe$ QDs for x=0.3

frequency regime may represent mixed modes originated from the superimposition of one or more low lying peaks. On the other hand, pure WZ CdSe and WZ MnSe system have showed Raman peaks at different mode as shown in Fig. 2.17 (a) 2.18(a).

Considering, ω_{LO}=202 cm^{-1}, for x=0.3 system we have calculated the Huang–Rhys factor *S*, by using eqn. 2.15. The corresponding S parameter is found to ~4 equivalent to the theoretically calculated value 0.33 (Table 2.11)

References

[1] Qi, L. & Gao, Emerging application of quantum dots for drug delivery and therapy, *Expert opin. Drug. Deliv.* **5**(3), 263--267, 2008.

[2] Jamieson, T., et al. Biological applications of quantum dots, *Biomaterials* **28**(31), 4717--4732, 2007.

[3] Alexson, D., et al. Semiconductor nanostructures in biological applications, *J Phys. Condens. Matter* **17**(26), R637--R656, 2005.

[4] Ma, X.-D., et al. Preparation and characterization of polyvinyl alcohol-capped CdSe nanoparticles at room temperature, *J. Coll. Interf. Sci.* **252**(1), 77--81, 2002.

[5] Zhou, X., et al. Preparation of silica encapsulated CdSe quantum dots in aqueous solution with the improved optical properties, *Appl. Surf. Sci.* **242**(3), 281--286, 2005.

[6] Gerion, D., et al. Synthesis and properties of biocompatible water-soluble silica-coated CdSe/ZnS semiconductor quantum dots, *J. Phys. Chem. B* **105**(37), 8861--8871, 2001.

[7] Rogach, A. L., et al. Synthesis and characterization of a size series of extremely small thiol-stabilized CdSe nanocrystals, *J. Phys. Chem. B* **103**(16), 3065--3069, 1999.

[8] Mansur, H. S., et al. Synthesis and characterization of CdS quantum dots with carboxylic-functionalized poly (vinyl alcohol) for bioconjugation, *Polymer* **52**(4), 1045--1054, 2011.

[9] Biju, V., et al. Photoinduced photoluminescence variations of CdSe quantum dots in polymer solutions, *J. Phys. Chem. C* **111**(22), 7924--7932, 2007.

[10] Mohanta, D., et al. Influence of ion bombardment on the photoluminescence response of embedded CdS nanoparticles, *Central Europ. J. Phys.* **4**(2), 187--195, 2006.

[11] Schärtl, W. & Schärtl, W. Current directions in core–shell nanoparticle design, *Nanoscale* **2**(6), 829--843, 2010.

[12]. Zhang, Y. & Clapp, A. Overview of stabilizing ligands for biocompatible quantum dot nanocrystals, *Sensors* **11**(12), 11036--11055, 2011.

[13] Karimi, A., et al. Fabrication and mechanical characterization of a polyvinyl alcohol sponge for tissue engineering applications, *Perfusion*, **29**(3), 231--237, 2014.

[14] Nuttelman, C. R., et al. Attachment of fibronectin to poly (vinyl alcohol) hydrogels promotes NIH3T3 cell adhesion, proliferation, and migration, *J. biomed. Mater. Res.* **57**(2), 217--223, 2001.

[15] Pereira, M. M., et al. Preparation of bioactive glass-polyvinyl alcohol hybrid foams by the sol-gel method, *J. Mater. Sci. Mater. Med.* **16**(11), 1045--1050, 2005.

[16] David, H. S., Ezio, R., & Paul, C., *Polymerization process and polymers produced thereby*, **US Patent No. 4581429 A**, April 8, 1986

[17] Byrne, S. J., et al. Optimisation of the synthesis and modification of CdTe quantum dots for enhanced live cell imaging, *J. Mater. Chem.* **16**(28), 2896--2902, 2006.

[18] Yu, Y., et al. Hydrothermal synthesis of GSH–TGA co-capped CdTe quantum dots and their application in labeling colorectal cancer cells, *Collo. Surf. B.* **95**, 247--253, 2012.

[19] Bhandari, S., et al. Charge transport and electrochromism in novel nanocomposite films of poly (3, 4-ethylenedioxythiophene)-Au nanoparticles– CdSe quantum dots, *J. Phys. Chem. C* **114**(34), 14606--14613, 2010.

[20] Maehashi, K., et al. Structural and optical properties of CdSe/ZnSe self-organized quantum dots, *J. Crystal Growth* **227–228**(0), 1116--1120, 2001.

[21] Yang, X., et al. Morphology-controlled synthesis of anisotropic wurtzite MnSe nanocrystals: optical and magnetic properties, *CrystEngComm* **14**(20), 6916--6920, 2012.

[22] Freeman, D., et al. The structure and Bijvoet ratios of cadmium selenide, *Acta Crystallogr. Sect. A* **33**(3), 355--359, 1977.

[23] Sines, I. T., et al. Colloidal synthesis of non-Equilibrium wurtzite-Type MnSe, *Angew. Chem. Int. Ed.* **49**(27), 4638--4640, 2010.

[24] Langford, J., et al. The breadth and shape of instrumental line profiles in high-resolution powder diffraction, *J. Appl. Crystallogr* **24**(5), 913--919, 1991.

[25] Bittencourt, D. X-Ray powder diffraction data for sodium octyl sulfate, sodium decyl sulfate and sodium dodecyl sulfate, *Powder Diffr.* **3**(04), 244--245, 1988.

[26] Gupta, P. & Ramrakhiani, M. Influence of the particle size on the optical properties of CdSe Nanoparticles, *Tano. J.* **3**, 15--19, 2009.

[27] Pradhan, N. & Peng, X. Efficient and color-tunable Mn-doped ZnSe nanocrystal emitters: control of optical performance via greener synthetic chemistry, *J. Am. Chem. Soc.* **129**(11), *3339--3347, 2007.*

[28] Furdyna, J. K. Diluted magnetic semiconductors, *J. Appl. Phys.* **64**(4), R29--R64, 1988.

[29] Heulings, H. I., et al. Mn-substituted inorganic-organic hybrid materials based on ZnSe: Nanostructures that may lead to magnetic semiconductors with a strong quantum confinement effect, *Nano lett.* **1**(10), 521--526, 2001.

[30] Lei, S., et al. Solvothermal synthesis of α-MnSe uniform nanospheres and nanorods, *Materials Lett.* **60**(13–14), 1625--1628, 2006.

[31] Zhu, K., et al. Manganese-doped MnSe/CdSe core/shell nanocrystals: Preparation, characterization, and study of growth mechanism, *J. Mater. Res.* **26**(18), 2400--2406, 2011.

[32] Deng, Z., et al., Water-based route to ligand-selective synthesis of ZnSe and Cd-doped ZnSe quantum dots with tunable ultraviolet A to blue photoluminescence *Langmuir* **25** (1), 434--442, 2009.

[33] Kubin, R. F. & Fletcher, A. N. Fluorescence quantum yields of some rhodamine dyes, *J. Lumin.* **27**(4), 455--462, 1983.

[34] Atabey, E., et al. Fluorescent electrospun polyvinyl alcohol/CdSe@ ZnS nanocomposite fibers, *J. Compos. Mater.* **47**(25), 3175--3185, 2013.

[35] Hamizi, N. A. & Johan, M. R. Optical and FTIR studies of CdSe quantum dots, *In. Nanoelectronics Conference (INEC), 3rd International,* Hhongkong, 3-8 Jan 2010.

[36] Sperline, R., et al. Temperature dependent structure of adsorbed sodium dodecyl sulfate at the Al_2O_3/water interface, *Langmuir* **13**(14), 3727--3732, 1997.

[37] Mehta, S. K., et al. Facile synthesis, growth mechanism, and optical properties of CdSe nanoparticles in self-assembled micellar media and their efficient conjugation with proteins, *J. Nanopart. Res.* **12**(5), 1697--1709, 2010.

[38] Scheuing, D. R. & Weers, J. G. A Fourier transform infrared spectroscopic study of dodecyltrimethylammonium chloride/sodium dodecyl sulfate surfactant mixtures, *Langmuir* **6**(3), 665--671, 1990.

[39] Zhao, B., et al. Preparation and characterization of quantum dots with polyacrylic acid modified method in water-Soluble core-shell structure, *Spectrosc. Spect. Anal.* **31**(12), 3362--3365, 2011.

[40] Dhanam, M., et al. Structural analysis of CBD γ-MnS thin films, *Chalcogenide Lett.* **6**(10), 541--547, 2009.

[41] Viana, R. B., et al. Infrared spectroscopy of anionic, cationic, and zwitterionic surfactants, *Adv. Phys. Chem.* **2012** (2012), 1--14, 2012.

[42] Nandakumar, P., et al. Raman spectra of CdS nanocrystals in Nafion: longitudinal optical and confined acoustic phonon modes, *Physica E* **11**(4), 377--383, 2001.

[43] Vasiliev, R., et al. IR-active vibrational modes of CdTe, CdSe, and CdTe/CdSe colloidal quantum dot ensembles, *J. Phys. Conf. Ser* **92**, 012054, 2007.

[44] Campbell, I. H. & Fauchet, P. M. The effects of microcrystal size and shape on the one phonon Raman spectra of crystalline semiconductors, *Solid State Commun.* **58**(10), 739--741, 1986.

[45] Arora, A. K., et al. Raman spectroscopy of optical phonon confinement in nanostructured materials, *J. Raman Spectrosc* **38**(6), 604--617, 2007.

[46] Pal, M., et al. Effects of crystallization and dopant concentration on the emission behavior of TiO_2: Eu nanophosphors, *Nanoscale Res. Lett.* **7**(1), 1--12, 2012.

[47] Choi, H. C., et al. Size effects in the Raman spectra of TiO_2 nanoparticles, *Vib. Spectrosc.* **37**(1), 33--38, 2005.

[48] Lyddane, R., et al. On the polar vibrations of alkali halides, *Phys. Rev.* **59**(8), 673, 1941.

[49] Mohr, M. & Thomsen, C. Phonons in bulk CdSe and CdSe nanowires, *Nanotechnology* **20**(11), 115707, 2009.

[50] Klein, M., et al. Size dependence of electron-phonon coupling in semiconductor nanospheres: The case of CdSe, *Phys. Rev. B* **42**(17), 11123, 1990.

[51] Lucovsky, G., et al. Identification of the fundamental vibrational modes of trigonal, α - monoclinic and amorphous selenium, *Solid State Commun.* **5**(2), 113--117, 1967.

[52] Lao, P. D., et al. Optical-phonon behavior in $Zn_{1-x}Mn_xSe$: Zinc-blende and wurtzite structures, *Phys. Rev. B: Conden. Matt.* **48**(16), 11701--11704, 1993.

[53] Dzhagan, V., et al. Phonon Raman spectra of colloidal CdTe nanocrystals: effect of size, non-stoichiometry and ligand exchange, *Nanoscale Res. Lett.* **6**(79), 1--10, 2011.

[54] Gouadec, G. & Colomban, P. Raman spectroscopy of nanomaterials: how spectra relate to disorder, particle size and mechanical properties, *Prog. Cryst. Growth Charact. Mater.* **53**(1), 1--56, 2007.

[55] Agarwal K C, et al. Carrier -density-dependent electron effective mass in $Zn_{1-x}Mn_x$ Se for $0 \leq x \leq 0.13$ *App. Phys. Lett.* **86** 181907, 2005

[56] Popović, Z. V., et al. Raman spectroscopy of polycrystalline α-MnSe, *Materials Science Forum*, **453,** 2004.

[57] Rodríguez-Suárez, R., Multiphonon resonant Raman scattering in nanocrystals, *Phys. Rev. B* **62**(16), 11006--11016, 2000.

[58] Wiedemeier, H. & Sigai, A. G. Phase equilibria in the solid region of the system manganese selenide-cadmium selenide, *J. Solid State Chem.* **2**(3), 404--409, 1970.

[59] Bhattacharyya, S., et al. One-Pot synthesis and characterization of Mn^{2+}-doped wurtzite CdSe nanocrystals encapsulated with carbon, *J. Phys. Chem. C* **112**(20), 7624--7630, 2008..

[60] Titantah, J. T., et al. Size effects and strain state of $Ga_{1-x}In_xAs$/GaAs multiple quantum wells: *Monte Carlo* study, *Phys. Rev. B* **78**(16), 165326, 2008.

[61] Boubaker, K. & Boubaker, K. A physical explanation to the controversial Urbach tailing universality, *Eur. Phys. J. Plus* **126**(1), 1--4, 2011.

[62] Guo, B., et al. Reverse micelles synthesis and optical characterization of manganese doped CdSe quantum dots, *AIP Conference Proceedings*. **772**(1), 605 2005.

[63] Yu, J. H., et al. Giant Zeeman splitting in nucleation-controlled doped CdSe: Mn^{2+} quantum nanoribbons, *Nature Mater.* **9**(1), 47--53, 2010.

[64] Neto, E. S. F., et al. Carrier dynamics in the luminescent states of $Cd_{1-x}Mn_xS$ nanoparticles: effects of temperature and x-concentration, *Phys. Chem. Chem. Phys.* **14**(4), 1493--1501, 2012.

[65] Neto, E. S. F., et al. Magneto-optical properties of $Cd_{1-x}Mn_xS$ nanoparticles: influences of magnetic doping, Mn^{2+} ions localization, and quantum confinement, *Phys. Chem. Chem. Phys.* **14**(9), 3248--3255, 2012.

[66] Dantas, N., et al. Evidence of $Cd_{1-x}Mn_xS$ nanocrystal growth in a glass matrix by the fusion method, *Appl. Phys. Lett.* **93**(19), 193115--193115--193113, 2008.

[67] Wolcott, A., et al. Silica-coated CdTe quantum dots functionalized with thiols for bioconjugation to IgG proteins, *J. Phys. Chem. B* **110**(11), 5779--5789, 2006.

[68] Schneider, R. & Balan, L. Hydrothermal routes for the synthesis of CdSe core Quantum Dots, in *Nanotechnology and Nanomaterials: State of the Art of Quantum Dot Systems Fabrications*, In Tech, Ahmadi, A. ed., France, 2012, 119-140.

[69] Dantas, N. O. & Neto, E. S. d. F. Carrier dynamics and magneto-optical properties of $Cd_{1-x}Mn_xS$ Nanoparticles, in *Nanocrystals - Synthesis, Characterization and Applications*, Neralla, S. eds., Intech, Croatia, 2012, 1--28.

[70] Jain, M. *Diluted magnetic semiconductors*, World Scientific, Singapore, 1991.

[71] Cheng, Y., et al. Shape control of monodisperse CdS nanocrystals: hexagon and pyramid, *J. Phys. Chem. B* 110(19), 9448-9451, 2006.

[72] Ernesto, S. F. N., et al. Control of luminescence emitted by $Cd_{1-x}Mn_xS$ nanocrystals in a glass matrix: x concentration and thermal annealing, *Nanotechnology* **22**(10), 105709, 2011.

[73] Babentsov, V., et al. Deep level defect luminescence in cadmium selenide nano-crystals films, *J. Crys. Growth* **280**(3), 502--508, 2005.

[74] Neto, E. S. d. F., et al. Control of luminescence emitted by $Cd_{1-x}Mn_xS$ nanocrystals in a glass matrix: x concentration and thermal annealing, *Nanotechnology* **22**(10), 105709, 2011.

[75] Sun, J., et al. Blue-white-orange color-tunable luminescence of Ce^{3+}/Mn^{2+}-codoped $NaCaBO_3$ via energy transfer: potential single-phase white-light-emitting phosphors, *RSC Advances* **3**(40), 18395--18405, 2013.

[76] Wei, C., et al. Size dependence of Eu^{2+} fluorescence in $ZnS:Eu^{2+}$ nanoparticles *J. Appl. Phys.* **89**(5), 2671--2675, 2001.

[77] Huang, K. & Rhys, A. Theory of light absorption and non-radiative transitions in F-centres, *Proc. R. Soc. A.* **204**(1078), 406--423, 1950.

[78] Huang, K. & Rhys, A. Theory of light absorption and non-radiative transitions in F-Centres, *Proc. R. Soc. A* **204**(1078), 406--423, 1950.

[79] Zhang, X., et al. Influence of electron-phonon interaction on the optical properties of III nitride semiconductors, *J. Phys. Condens. Matt.* **13**(32), 7053, 2001.

CHAPTER- 3: Optimization of Optical Stability of CdSe and MnSe QDs

CHAPTER 3

Optimization of Optical Stability of CdSe and MnSe QDs

For application of QDs in biosensing, biolabeling and bioimaging, it is extremely important to evaluate the controlling parameters that might influence optical properties drastically. In practice, cellular-biology and biophysical experiments are conducted in a complex biological environment which contains a mixture of amino acids, salts, glucose and vitamins. Undoubtly, behavior of QDs under these environments must be known for in *vitro* or in *vivo* studies. It is well-known that, bare nanoparticles (NPs) agglomerate immediately after they are added to the culture media [1]. In this regard, surface functionality along with the presence of some essential biological materials (such as, protein, serum, nutrients etc.) may help forming a stable dispersion of the QDs [1,2].

The optimization of optical stability accounts for controlled optical response through controlled inhomogenity and resistible clusterity. In this chapter, we study the assessment of CdSe-PVA QDs while varying concentration of cadmium precursors (Cd^{2+}/Se^{2-}), reaction time etc. Similarly, we optimize the stability of WZ phase MnSe-TGA QDs by standardizing different factors, i.e., concentration of capping agent (TGA) and QD precursor ratio (Mn^{2+}/Se^{2-}). In order to evaluate the QD dispersion in cell media, special emphasis is given to study the media dependent optical responses of CdSe-PVA and MnSe-TGA QDs while bovine serum albumin (BSA) protein was used as a dispersing agent. BSA was selectively chosen, knowing that serum albumin is the most abundant protein in blood plasma [3]. In addition, BSA has been widely used as a model protein for dispersing NPs in physiological fluids [4,5]. We assessed commonly used cell culture media: a) Dulbecco's Modified Eagle Media (DMEM) ®, b) Minimum Essential Medium (MEM) ® and c) Roswell Park Memorial Institute-1640 (RPMI) ® media. In addition, the optical stability of CdSe QDs is examined considering natural media: the first being rose water and the other was citric media (derived from lemon) for storing of the synthesized QDs naturally.

3.1 Effect of reaction parameters on the optical stability of PVA dispersed CdSe-QDs

The optical properties of CdSe-PVA QDs and their dependence on reactant concentration and reaction times are as detailed below.

3.1.1 Effect of reactant concentration

Fig 3.1(a) depicts the effect of Cd^{2+}/Se^{2-} precursor concentration on the UV-Vis spectra of CdSe QDs, dispersed in PVA solution. All the spectra were acquired using PVA as reference in the spectrophotometer. The samples of QDs of varying concentration ratios of Cd^{2+}/Se^{2-} i.e., 1:1, 2:1, 3:1, 4:1 were labeled as S_1, S_2, S_3, S_4; respectively. In all the cases, the onset of absorption is found to be blue shifted from the bulk value ($\lambda_{onset} \sim 714$ nm). This implies effective quantum confinement of the charge carriers in the QDs. The samples S_3 and S_4, (curves (iii) and (iv)) with a higher concentration of Cd^{2+} exhibit strong 1*s*-1*s* excitonic absorption, at $\lambda_{ex} = 310$ nm. Conversely, for a low concentration of Cd^{2+} the QDs exhibit featureless characteristics with long tailing, depicting adequate inhomogenity in the samples (S_1, S_2, curves (i) and (ii)). This ground state excitonic absorption value (~310 nm) resembles the reported value where mercapto-acetic acid was used as a capping agent [6]. Our results indicate the formation of smaller sized QDs for precursors that are rich in Cd^{2+}. This behavior was also witnessed by other groups [7-9]. It is possible that, a proportionally large concentration of Cd^{2+} ions (as compared to Se^{2-} ions) is capable of providing a sufficiently high number of nucleating sites for the growth of CdSe QDs. The nucleation sites at a given concentration of Se^{2-} precursor, facilitates growth of smaller sized QDs [7]. A large number of nucleation sites, around

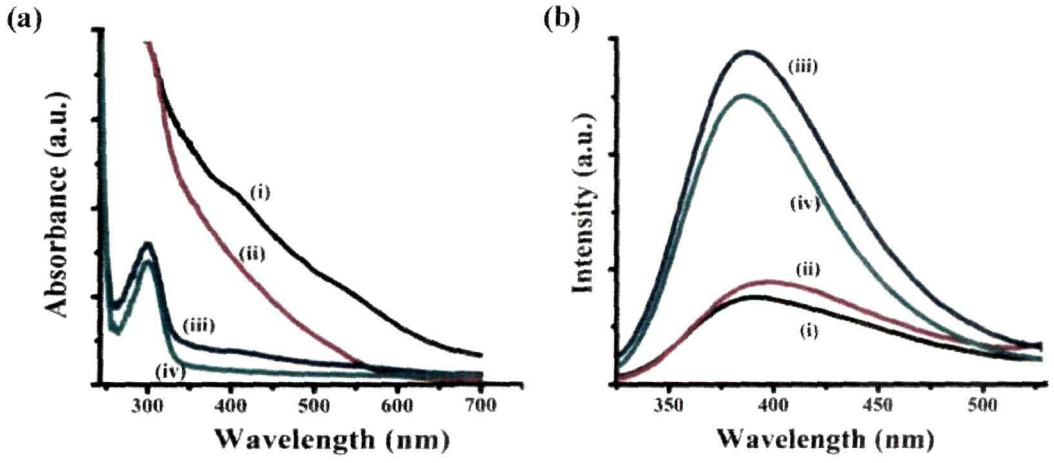

Figure 3.1: (a) UV-Vis and (b) PL spectra of CdSe QDs derived from a precursor of Cd^{2+}/Se^{2-} ratio (i) 1:1, (ii) 2:1, (iii) 3:1, and (iv) 4:1

the Cd^{2+} ions is because of smaller ionic radii of Cd^{2+} ions (~109 pm) as compared to the Se^{2-} ions (~184 pm). The optical band gap of the QDs can be calculated from the respective onsets of absorption. The band gap values can be used to estimate the average size of the QDs using the well known equation* proposed by Brus *et al* [10]. The calculated band gaps and QDs sizes are found to be in the range of ~2.5-3.7 eV and ~4.5-2.7 nm; respectively (Table 3.1).

Table 3.1: Energy gap and average size of the CdSe QD for different precursor ratio

Sl. No.	Cd^{2+}:Se^{2-} Ratio	Wavelength (nm)	Band gap (eV)	Blue shift energy (eV)	Average Size of QDs (nm)
1	1:1	495	2.50	0.76	4.5
2	2:1	497	2.49	0.75	4.4
3	3:1	328	3.78	2.04	2.7
4	4:1	330	3.75	2.01	2.8

The photoluminescence (PL) spectra of CdSe-PVA QDs of different Cd^{2+} concentration, under an excitation wavelength ~280 nm, are shown in Fig. 3.1 (b). The PL spectra of the QDs are chiefly comprised of two emission peaks: emission due to the band-edge emission (λ_{BE}) and the defect related emission (λ_{DE}). The λ_{BE} is found to be located at ~380 nm with a full width at half maxima (FWHM) ~65 nm. The λ_{DE} is in the range of 415-428 nm for QDs derived from precursors of varying Cd^{2+}/Se^{2-} ratios (1:1 to 4:1). For smaller values of Cd^{2+}/Se^{2-} ratio (S_1 and S_2 of curves (i) and (ii)), the emission response are seen weaker. But with the increase of Cd^{2+} concentration, the PL intensity (λ_{BE}) gets enhanced with sample S_3 (curve (iii)) exhibiting very strong feature (FWHM ~ 59 nm). The λ_{DE} peak however, remains significant for a varying Cd^{2+}/Se^{2-} ratio in S_1, S_2 samples. The ratio of band edge-to-defect emission intensities falls in the range 1.01-1.27 for different cases of Cd^{2+}/Se^{2-} (S_1 to S_4).

The observed defect related emission response is attributed to the radiative transitions mediated via surface trap states. The states are believed to be created by entrapped electrons inside a selenium vacancy with holes in the valence band [9]. As observed from the PL spectra, the dominant response of the defect related emission over

* *Appendix-6*

the band edge emission, in samples S_1 and S_2, signifies inadequate surface passivation of the QDs. Previously, a lowered of concentration of Cd^{2+} was found to be insufficient for an effective dispersion in PVA [6]. The intense band edge emissions, for S_3 and S_4, are ascribed to significant passivation of surface defect mediated through non-radiative centres. Whereas, a significantly higher Cd^{2+} concentration is likely to results inadequate surface capping by the PVA host [7]. This is why we observed a reduced intensity wrt band edge-to-defect related emission, for S_4 as compared to S_3. The sharp absorption features and symmetric luminescence behavior of S_3 and S_4 samples indicate a narrow size distribution of the synthesized CdSe QDs.

As the effect of reactant concentration provided the best quality specimen for $[Cd^{2+}]/ [Se^{2-}] = 3:1$ (S_3), we opted for studying the effect of reaction time and aging for this precursor along with consideration of different dispersing media.

3.1.2 Effect of reaction time

Fig. 3.2 (a) and (b) depict the dependence of absorption and emission responses of PVA dispersed QDs obtained for different reaction times but for a fixed Cd^{2+} concentration. The reaction time was counted right after the SeO_2 reactant was added into the Cd^{2+}/PVA precursor. Upto 30 min. of reaction, only featureless characteristics are observed

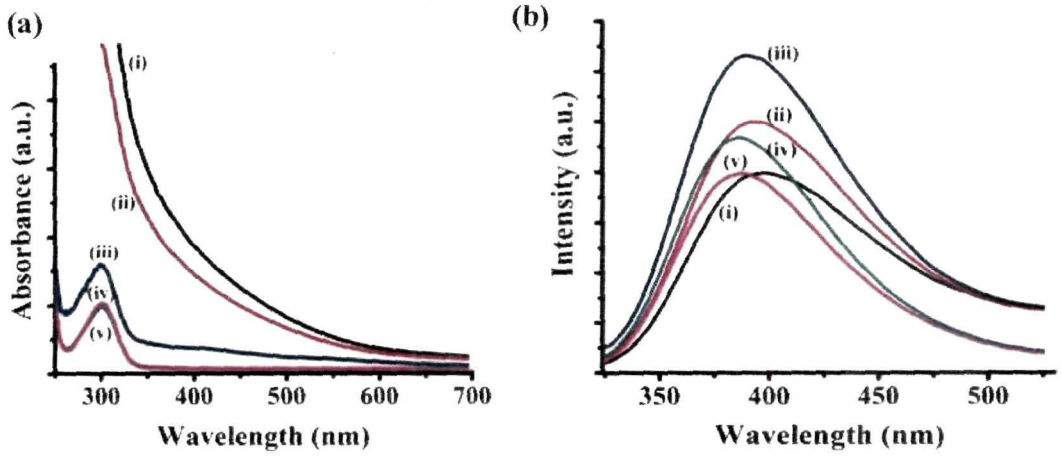

Figure 3.2: (a) UV-Vis and (b) PL spectra of CdSe QDs of reaction time (i)10, (ii) 30, (iii) 60, (iv) 90, and (v) 120 minutes

thereby no prominent excitonic absorption (curves (i) and (ii)). A sharp absorption response is observed at ~328 nm when the reaction was allowed for 60 min (curve (iii)) and beyond (curve (iv) and (v)). Since the position of the absorption maxima do not change with time the average size of the QDs is expected to be uniform. Previously, it was argued that PVA matrix can efficiently restrict the growth of the particles, while the growth process is homeostatic [7].

Table 3.2: Energy gap and average size of the CdSe QDs for different reaction time

Sl. No.	Reaction time (min)	Wavelength (nm)	Band gap (eV)	Blue shift energy (eV)	Average Size of QDs (nm)
1	10	-	-	-	-
2	30	-	-	-	-
3	60	328	3.78	2.04	2.7
4	90	328	3.78	2.04	2.7
5	190	328	3.78	2.04	2.7

Fig. 3.2(b) depicts the asymmetrically stretched photoluminescence spectra of the CdSe-QDs. Upon deconvolution (not shown), the λ_{BE} is found to be located at ~380 nm and λ_{DE} at ~417 nm, when the reaction time was varied in the range of 10-120 min. Although, defect related emission is prominent for samples prepared under less reaction time environment, the overall PL emission is found to be strongest for the sample prepared with a reaction time duration of 60 min (curve (iii)). A further increase of reaction time can lead to assimilation of nanocrystallites into clusters as a result of which a suppressed emission response is realized. Whereas, insufficient reaction time leads to unsaturated bonding between Cd^{2+} and Se^{2-} ions. After a series of studies, a 60 min. of reaction time is found to suitable that ensure a sharp exciton absorption and an intense emission response.

3.2 Effect of reaction parameters on the optical stability of WZ-MnSe QDs

In order to obtain water soluble WZ MnSe-TGA QDs of high quality, we have carefully examined different reaction conditions as discussed below.

The QD samples were processed by varying TGA concentrations of 1, 5, 10% and with molar concentrations (of Mn^{2+}/Se^{2-}) as 2:1, 3:1, 4:1. We labeled the respective samples with TGA concentration of 1, 5, 10% as T_1, T_2, T_3 and with Mn^{2+}/Se^{2-} molar ratios of 2:1, 3:1, 4:1 as P_1, P_2, P_3. Note that, P_1 is equivalent to sample T_3.

3.2.1. Effect of TGA concentration

Fig. 3.3(a) shows the effect of TGA concentration on the UV-Vis spectra of MnSe-TGA QDs. As can be found, the samples T_1 (curve (i)) and T_2 (curve (ii)) have exhibited relatively long tailing feature as compared to T_3 (curve (iii)) in which the prominent absorption peak is located at ~303 nm (E_g ~4.09 eV). This implies effective quantum confinement of the charge carriers in the QDs which is characterized by a blue-shift (~0.59 eV) from the bulk value (E_g~3.5 eV) of the WZ-MnSe system [11-14]. But the estimated value of E_g is ~1.6 fold larger as compared to the RS type MnSe (~2.5 eV) system [11]. A slight blue shifting of ~0.07 eV from the bulk value can be noticed for sample T_2. On the other hand, in case of sample T_1, we observe a blue shifting of ~0.73 eV wrt the RS type of bulk MnSe system. Note that, the observed blue shifts, for samples T_2 and T_3 are fairly small and are in the range of ~0.07-0.5 eV. This could be due to the highly localized nature of 3*d* electronic bands of Mn atoms [14]. Correspondingly, the

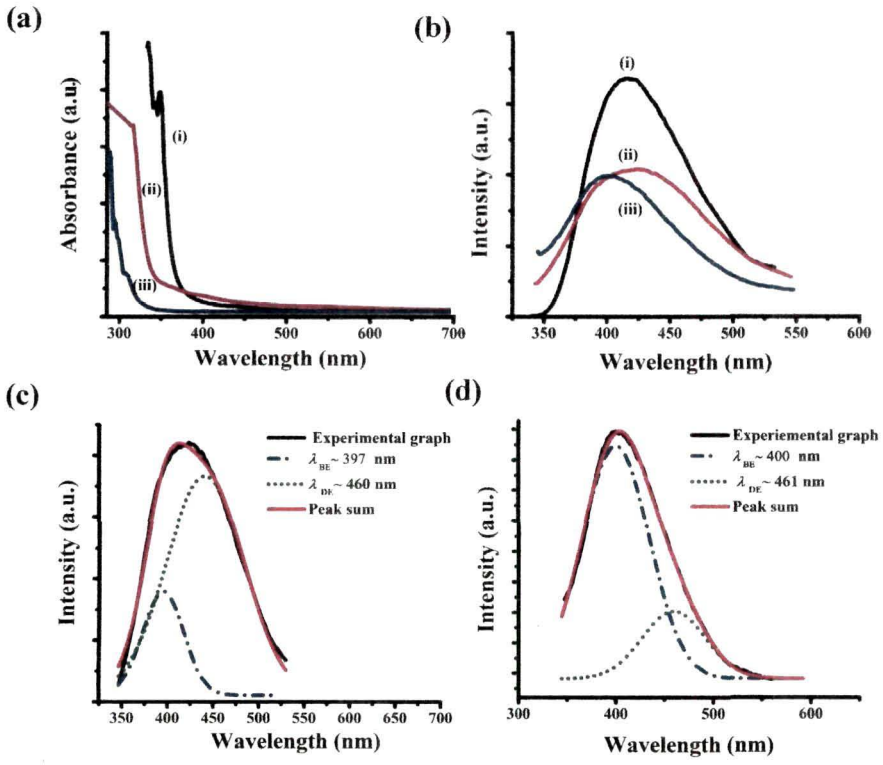

Figure 3.3: (a) UV-Vis and (b) PL spectra of MnSe-TGA QDs prepared with different TGA concentration of (i) 1% (T_1), (ii) 5%, and (T_2) (iii) 10 % (T_3), for a fixed Mn^{2+}/Se^{2-} = 2:1. In (c) and (d), the deconvoluted PL spectra of QDs of T_2 and T_3 specimens are shown with experimental and empirical traces.

quantum confinement induced by cordially bonded organic layers might lead to a much smaller change in these bands [14].

The corresponding photoluminescence (PL) spectra (λ_{ex}=300 nm) of the MnSe QD systems T_1, T_2, and T_3, are shown in Fig. 3.3(b). Each of the emission spectra was subjected to deconvolution so as to uncover different peak positions. As mentioned earlier, upon deconvoulution, each of the emission spectra is found to primarily comprise of two emission peaks. The narrow and symmetric one is ascribed to near band edge (NBE) emission (λ_{BE}), whereas the broad and asymmetric one is due to the defect related emission (λ_{DE}). The λ_{BE} of the samples T_2 and T_3, located at ~397 and ~400 nm are close to the near band-edge emission (~364 nm) of the ZB type MnSe system [15]. As for T_1, the λ_{BE} position is located at ~406 nm but λ_{DE} peak positioned at ~460 nm for all the samples. The defect related emission can be attributed to intrinsic defect states in the metastable WZ nanocrystal core [16]. The respective band edge-to-defect related emission intensity ratios are estimated as ~1.03, 0.58 and 2.37 for T_1, T_2 and T_3 systems. It is quite apparent that, the NBE response of 10% TGA coated MnSe QDs is over other cases and gives more prominent a FWHM of ~81 nm. A stronger defect related emission of T_2 over T_3 is predicted due to inadequate passivation of QDs by the linkers in the former case. On the other hand, the intense and symmetric NBE emission is evident due to significant passivation of the surface defects in the metastable WZ MnSe QDs (of

Table 3.3: Parameters obtained from optical spectra of MnSe QDs prepared by varying TGA concentration

TGA concentration	Excitonic wavelength, λ (nm)	Band gap energy E_g (eV)	Blue shifted energy, ΔE_g (eV)	λ_{BE} (nm)	λ_{DE} (nm)	I_{BE}/I_{DE}
1%	383	3.23	0.73 (blue shifted from RS MnSe)	406	460	1.03
5%	347	3.57	0.07 (blue shifted from WZ MnSe)	397	460	0.58
10%	303	4.09	0.59	400	460	2.37

sample T_3). As the QDs are characterized by a blue-shifted, sharp excitonic absorption feature along with an intense band edge emission response, we opted T_3 sample for subsequent experiments with different precursor concentrations. Table 3.3 highlights different parameters related to the optical spectra of the MnSe QDs coated with molecules with definite concentration.

3.2.2 Effect of precursor concentration

Figure 3.4(a) and (b) represent the dependence of absorption and emission behavior of MnSe QDs coated with 10% TGA and for different precursor concentrations of (Mn^{2+}/Se^{2-}). The sample P_1 (Fig. 3.4(a), curve (i)), exhibits a strong excitonic absorption feature at ~303 nm (E_g = 4.09 eV). Whereas, with an increasing value of the precursor ratio (P_2, curve (ii) and P_3, curve (iii)) a significant red shifting (ΔE ~1.03 eV) of the exciton peak is observed (λ = 408 nm, E_g = 3.03 eV). It may be noted that, the band gap of sample P_1 is slightly blue shifted (~0.59 eV) from the bulk value of WZ type MnSe (E_g = 3.5 eV). In contrast, the samples P_2 and P_3 derived with higher Mn^{2+} concentrations show an adequate blue shift (~0.5 eV) wrt the bulk RS type structure (E_g = 2.5 eV). This may suggest that, with the incorporation of an excess amount of Mn^{2+} concentration, there can be a partial phase transformation from WZ to RS one [17].

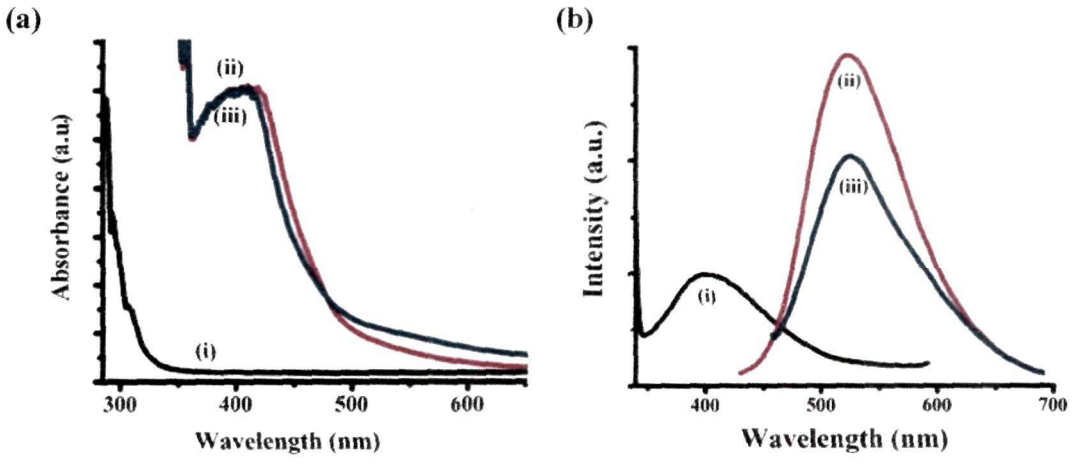

Figure 3.4: (a) UV-Vis and (b) PL spectra of MnSe-TGA (TGA: 10%) QDs with different Mn^{2+} /Se^{2-} ratio of (i) 2:1 (P_1), (ii) 3:1 (P_2), and (iii) 4:1 (P_3)

The PL responses of MnSe QDs with different Mn^{2+}/Se^{2-} precursor ratios are depicted in Fig. 3.4(b). The spectrum recorded for sample P_1 (curve (i)) exhibits near band edge emission (λ_{BE}) at ~400 nm [15] along with surface defect related emission (λ_{DE}) at ~459 nm [16]. Conversely, intense emission bands are observed at ~515 nm and ~517 nm as for samples P_2 (curve (ii)) and P_3 (curve (iii)); respectively. The PL emission intensity of the P_3 sample is adequately lowered as compared to the P_2 specimen. The deconvoluted PL spectra (not shown) have revealed other emission peaks located at ~554 nm and ~566 nm; for P_2 and P_3 samples; respectively. These emission bands are ascribed to the *3d electron transitions of* Mn^{2+} [14]. A lowered emission intensity value by a factor of ~1.18 in case of P_3, sample over the P_2 one, is probably due to the strong interaction of the neighboring Mn^{2+} ions at the nearest, the second nearest, and at the third nearest neighboring-sites owing to the availability of substantially concentration of Mn^{2+} [17].

The crystallographic planes and phase of the as-synthesized MnSe QDs derived for different precursor ratios have been identified through XRD analysis. Fig. 3.5(a) and (b) depict XRD patterns of MnSe QDs, prepared from different precursors of Mn^{2+}/Se^{2-} and for a definite concentration of TGA (10%). Referring to Fig. 3.5(a) (Mn^{2+}/Se^{2-} = 2:1) the diffraction peaks located at 25.8°, 26.8 °, 28.6 °, 36.1°, 43.9 °, 47.8 °, 50.2 °, 52.05 °, 53 and 58.7 ° correspond to (100), (002), (101), (102), (110), (103), (200), (112), (201)

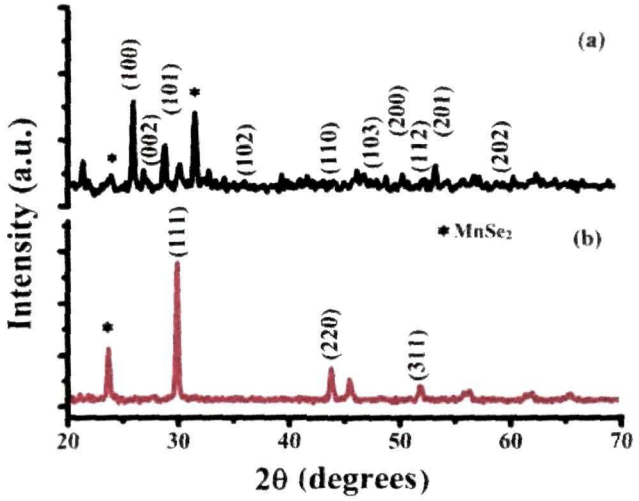

Figure 3.5: XRD patterns of MnSe QDs prepared with 10% TGA and of Mn^{2+}/Se^{2-} (a) 2:1 (b) 3:1

and (202) crystallographic planes of the hexagonal WZ MnSe crystal structure of MnSe and are consistent to available reports [11, 18]. Moreover, an impurity related $MnSe_2$ phase is also witnessed at a diffraction angle of ~23.8° (JCPDS-653336) and 31.4° [11] (shown with * mark). The XRD pattern of the sample P_2 (Mn^{2+} /Se^{2-} = 3:1) is shown in Fig. 3.5(b). The subsequent diffraction peaks at 29.8°, 43.8° and 51.1° correspond to (111), (220) and (311) crystallographic planes, which resemble the RS MnSe crystal structure of the system (JCPDS-270311). Moreover, trace amount of $MnSe_2$ phase can be seen in the diffractogram at a diffraction angle of ~23.7° (JCPDS-653336).

From the above discussion, it is now clear that, the QDs derived from a precursor of [Mn^{2+}]/ [Se^{2-}] = 2:1 and TGA concentration of 10%, are likely to display strong blue shifted excitonic absorption and prominent band edge emission features corresponding WZ MnSe system.

3.3 QD dispersion and optical stability in biological environment

The optical response and colloidal stability of the fluorescent QDs, in different culture media environment, are regarded as essential prerequisites for their relevance in bio-labeling and bio-sensing. It is expected that, different dispersing agents (like, FBS, BSA protein etc.) can have an influential role on the absorption and emission characteristics. The optical responses of the synthesized QDs, in cell culture media, are described below.

3.3.1 Dispersion of CdSe –PVA QDs in cell culture media

First, we have analyzed the dispersion stability of CdSe-PVA QDs in different cell culture media by using BSA as dispersing agent. Without addition of BSA agent, the excitonic absorption peak (~300 nm) is found to remain unaltered in phosphate buffer solution (PBS), DMEM and MEM media (Fig. 3.6(a)). But the peak is slightly red shifted to ~312 nm, in RPMI media. Interestingly, with the inclusion of dispersing agent BSA, the absorption peak is apparently blue shifted to ~283 nm in PBS, DMEM and MEM media. However, in RPMI media, the peak position is unchanged. Similarly, in presence of BSA protein, CdSe-PVA QDs in MEM media exhibit a stronger PL response over DMEM and RPMI media, thus signifying an effective conjugation of BSA molecules to QDs surfaces in the MEM media than other media (Fig. 3.6 (b)).

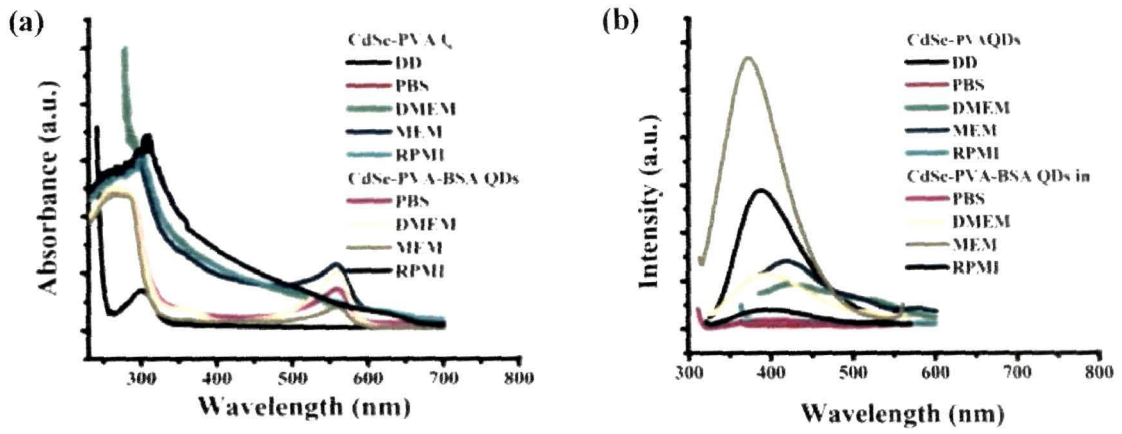

Figure 3.6 : (a) UV-Vis and (b) PL spectra of CdSe-PVA QDs in different dispersing media in presence and absence of BSA acting as dispersing agent.

3.3.2 Dispersion of MnSe –TGA QDs in cell culture media

We have also performed a comparative study on the nature of stability of MnSe QDs in different dispersion media and by considering both the presence and absence of the dispersing agent. Figure 3.7(a) demonstrates that, in the absence of BSA, the excitonic absorption peak (at ~303 nm) of the MnSe QDs in PBS, remains unchanged as we

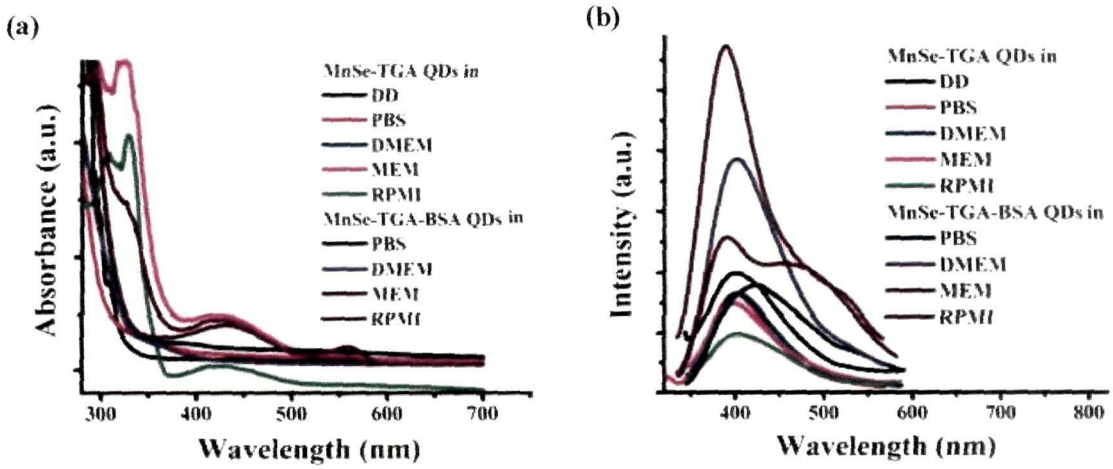

Figure 3.7 : (a) UV-Vis and (b) PL spectra of MnSe-TGA (TGA 10 %, Mn^{2+}/Se^{2-} = 2:1) QDs in different dispersing media in presence and absence of BSA acting as dispersing agent

observe in aqueous media. However, the position gets red shifted to ~313, ~321 and ~329 nm, when QDs were dispersed in DMEM, MEM and RPMI media; respectively. This indicates likely aggregation of QDs in these media. In contrast, a fairly stable dispersion of the MnSe-TGA QDs is observed upon addition of BSA into the respective media. The exciton absorption peak remains almost fixed (~303 nm) in both PBS as well as in DMEM media. In contrast, it is slightly (~308 nm) and significantly (~327 nm) red-shifted in MEM and RPMI media; respectively. We anticipate that the interaction of BSA with the constituents of the cell culture media has deterministic role on determining the colloidal stability of the QDs. Similarly, an enhanced overall emission response of the QDs, with BSA dispersion, signifies the improved stability of the QDs as compared to the QDs dispersed directly in the cell media without BSA inclusion (Fig. 3.7 (b)). Moreover, in presence of BSA protein, MnSe-TGA QDs in DMEM and MEM media exhibited stronger PL response wrt QDs in RPMI. This suggests significant surface passivation of the QDs by way of effective adsorption of BSA in former media than the latter one. Different physical parameters related to the optical spectra of CdSe-PVA and MnSe-TGA QDs and dispersed in cell culture media are highlighted in Table 3.4.

Table 3.4: Parameters related to the optical spectra of CdSe-PVA and MnSe-TGA QDs in cell culture media.

CdSe-PVA			**MnSe-TGA**		**Maximum PL intensity ratio (with BSA/without BSA)**		
Dispersing media	with out BSA inclusion	with BSA inclusion	without BSA inclusion	with BSA inclusion	CdSe		MnSe
	λ (nm)	λ (nm)	λ (nm)	λ (nm)	Dispersing media	Ratio	Ratio
DD	300	-	303	-	PBS	0.44	1.08
PBS	300	283	303	303	DMEM	2.12	2.61
DMEM	300	283	313	303	MEM	4.02	3.89
MEM	300	283	321	308	RPMI	1.24	2.33
RPMI	312	312	329	327			

Essentially, in cell culture media, a high ionic strength is responsible for dominant van-der Waal's attraction over electrostatic repulsive behavior and this is the reason why QDs tend to coalesce into larger sized particles, as observed for QDs [1]. But, a stable dispersion of the CdSe-PVA QDs, even in absence of dispersing agent has been observed.

3.3.3 Aging effect of CdSe- PVA QDs in cell culture media

Effect of aging in optical response is an important concept, which is likely to quench/shoot up absorption and emission characteristics.

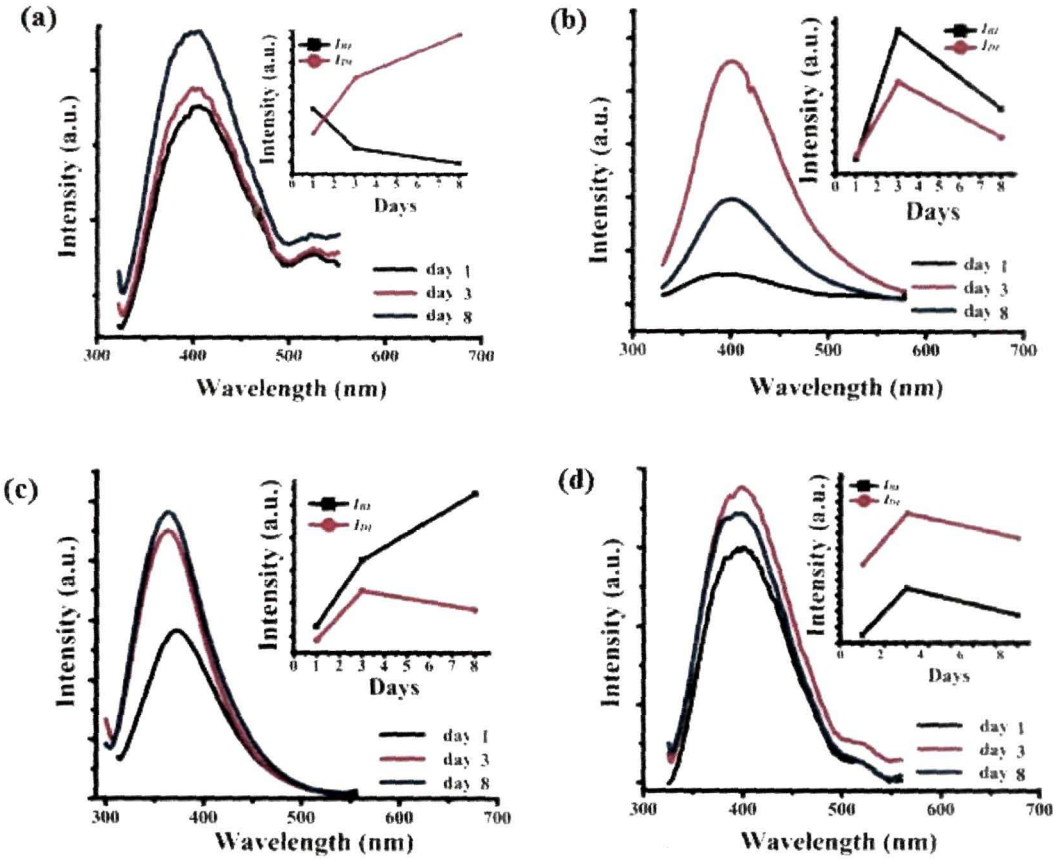

Figure 3.8 : PL spectra of CdSe-PVA QDs in different dispersing media (a) PBS, (b) DMEM, (c) MEM, and (d) RPMI with aging. The insets show the change of I_{BE} and I_{DE} with aging in the respective media in presence of dispersing agent BSA.

With aging, though the maximum intensity of the CdSe-PVA QDs increases, the near band edge emission intensity (I_{BE}) gets suppressed over defect related emission intensity (I_{DE}) when the QDs are dispersed in PBS media (Fig. 3.8(a)). The I_{BE} response which is about 1.2 times of I_{DE} on the day of synthesis is reduced by a factor of ~2.58 after 8 days of aging. Whereas, the emission intensity of CdSe-PVA QDs in DMEM media attains maximum value, after 3 days of aging (Fig. 3.8(b)). Essentially, the intensity is increased by a factor of ~7.3 wrt the day of synthesis. Note that, the I_{BE} in the DMEM media, is always dominant over I_{DE} in 3 and 8 days of aging. With a dominant response over I_{DE}, as for MEM, an increased band-edge emission response was revealed after 8 days of aging by a factor of ~2.17 wrt day of QD synthesis (Fig. 3.8(c)). Interestingly, in the RPMI cell culture media (Fig. 3.8(d)), with a dominant I_{DE} response over I_{BE} with aging, the QD emission follows a reverse trend in comparison to DMEM and MEM media. The aging dependent I_{BE} to I_{DE} relative strength of emission values are enlisted in Table 3.5 and represented by Fig. 3.8(e)

Table 3.5: Parameters obtained from aging study of CdSe-PVA QDs in different cell culture media

Dispersing media	**Aging (days)**	I_{BE}/I_{DE}
PBS	1	1.2
	3	0.614
	8	0.43
DMEM	1	0.8
	3	1.56
	8	1.8
MEM	1	1.15
	3	1.21
	8	1.94
RPMI	1	0.73
	3	0.76
	8	0.74

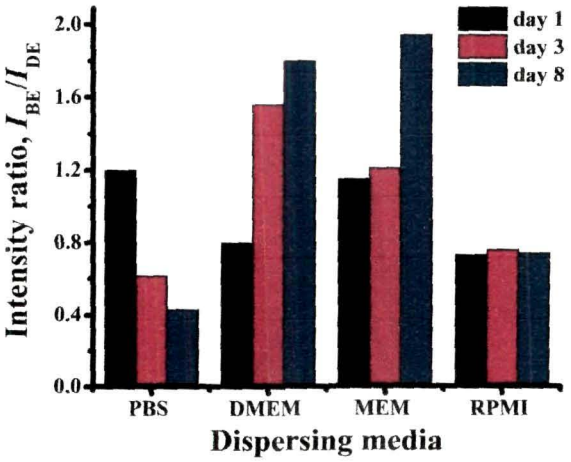

Figure 3.8 (e): Graphical représentation of intensity ratios of CdSe QDs in different dispersing media with aging

3.3.4 Aging effect of MnSe-TGA QDs in cell culture media

Figure 3.9(a-d) depict a number of PL spectra highlighting studies with regard to stability of the MnSe-TGA QDs in different dispersing media and also responses due to independent aging effect. In PBS media, the PL emission response wrt I_{BE} and I_{DE} experienced a steady rise up to 5 days of aging.

As shown in Fig. 3.9(b), the near band edge emission intensity (I_{BE}) of the QDs is improved by a factor of ~1.85 when the specimen was subjected to 3 days of aging in DMEM media. Nevertheless, excessive aging effect did not show any further improvement, but with as diminishing overall emission when aged for 5 days. In this

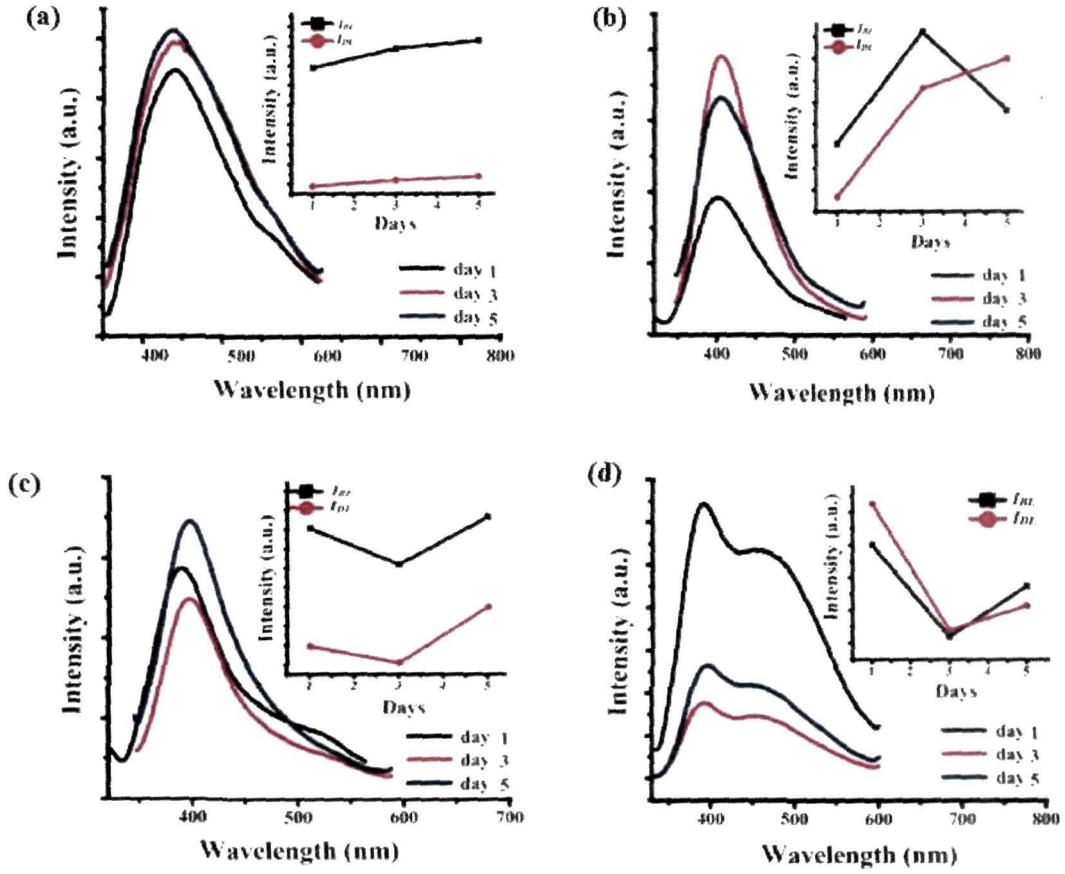

Figure 3.9: PL spectra of MnSe-TGA QDs (prepared with TGA:10% and Mn^{2+}/Se^{2-} =2:1) (when BSA is added as dispersing agent) in dispersing media (a) PBS, (b) DMEM, (c) MEM, and (d) RPMI with aging

case, the emission feature is characterized by an enhancement of only ~1.24 times wrt as prepared QD system. The defect related emission response is dominant by a factor of ~1.32 wrt NBE emission after 5 days of aging (inset of Fig 3.9(b)). On the other hand, in the MEM media (Fig. 3.9(c)), the QDs experience a slightly diminished emission after 3 days of aging (by a factor of ~1.18 wrt day of QD synthesis). Interestingly, the emission becomes more strong (by a factor 1.23) with extended aging up to 5 days. As can be seen from Fig. 3.9 (d), in RPMI media, the maximum emission intensity of MnSe-TGA QDs is drastically reduced but 3 days of aging but increase upon 5 days of aging. In this case, the band edge emission intensity gets reduced by a factor of ~3.3 and ~2.18 after 3 days and 5 days of aging; respectively wrt the response observed on the day of synthesis. It is to be noted, however that, in the RPMI media the defect related emission behavior is adequately intense after 1st and 3rd days of aging. The variation of I_{BE}/I_{DE} with aging of MnSe-TGA QDs, in different cell culture media can be found from Table 3.6 and represented by Fig. 3.9(e).

Table 3.6: Relative emission strength of MnSe-TGA QDs in cell culture media with aging

Dispersing media	**Aging (days)**	I_{BE}/I_{DE}
PBS	1	3.06
	3	3.09
	5	3.02
DMEM	1	1.65
	3	1.30
	5	0.76
MEM	1	2.02
	3	2
	5	1.58
RPMI	1	0.76
	3	0.85
	5	1.27

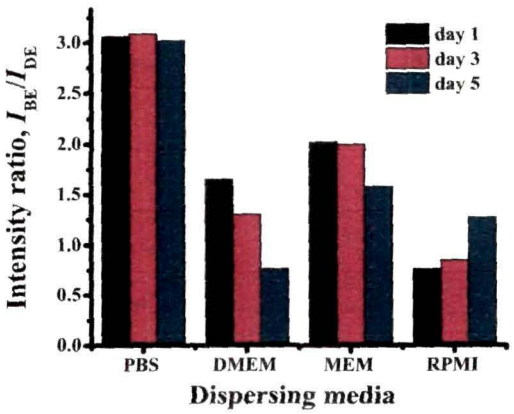

Figure 3.9 (e): Graphical représentation of intensity ratios of MnSe QDs in different dispersing media with aging

From section 3.3.3 and 3.3.4, we can invoke that, MnSe-TGA and CdSe- PVA QDs are more stable in DMEM (3 days of aging) and MEM media (5 days of aging) than RPMI cell culture media.

A greater stability of PVA coated superparamagnetic iron oxide nanoparticles (SPION) and BSA coated TiO_2 particles in DMEM media over RPMI media was also predicted in an earlier works [1, 19]. Note that, NPs in biological media are coated by a protein corona, which can significantly influence the colloidal stability of the NPs [20]. In DMEM and MEM media, the presence of a larger amount of divalent cations (Ca^{2+}, Mg^{2+}) can act as an effective bridge to bind negatively charged BSA protein molecules to negatively charged MnSe-TGA and CdSe-PVA QDs forming a stable protein corona [1]. In contrast, a relatively higher concentration of phosphate ions in RPMI media (as compared to the other media) is likely to compete with BSA molecules to adsorb in to the QDs surfaces. This results in adequate instability of QDs in RPMI media. It is worth mentioning here that, nearly 70% release of BSA from hydroxyapatite microspheres has been observed in the presence of 10 mM phosphate in half an hour has been as reported by Boonsongrit et al. [21].

3.4 Optical characteristics of QDs in natural media

Since the optical stability is critical in storing and subsequent use of QDs, we have also intended to examine the effect of natural media on the stability of QDs. In this context, we have chosen lemon water and rose water media extracted from lemon (scientific name: *Citrus* × *limon*, genus: *Citrus*, family: *Rutaceae*) and rose (scientific name: *Rosa Bucbi*; genus: *Rosa*, family: *Rosaceae*); respectively for our study. The lemon water media is chosen because of its natural acidic property containing citric acid, along with its various health benefits. Whereas, rose media is considered as naturally available base media which is used for many cosmetic products due to its refreshing fragrance and enhancing benefits to the skin and hairs.

3.4.1 Optical response of CdSe QDs

The typical absorption and emission behavior of CdSe-QD dispersed in different dispersive media are shown in Fig. 3.10 (a) and Fig. 3.10 (b); respectively. As can be

observed from the optical spectra, the excitonic absorption is found to be located at ~300 nm (~4.13 eV) for QDs in PVA as well as in lemon water media. The characteristic QD excitonic feature is relatively broad in citric acid (lemon water) media than the neutral PVA one. Possibly, a larger degree of inhomogenity (on QD size distribution) might have led to an observable broadening in citric media. The QD response in rose water media is however, characterized by an adequate red shift (~ 0.76 eV) of the exciton absorption along with a broad absorption feature.

Fig. 3.10(b) depicts the PL response of the QDs dispersed in the lemon water, PVA and aqueous rose media. As in other cases, an asymmetrically stretched spectrum corresponds to existence of at least two prime peaks, away from each other; band-to-band emission (λ_{BE}) and defect-related emission (λ_{DE}). While the first peak is located at ~380 nm for both PVA and citric media, the respective λ_{DE} peaks are positioned at ~430 nm and ~416 nm. Note that, the defect-related emission intensity is predominantly high in case of lemon water over other environment. The respective band edge-to-defect emission strengths are ~0.61 and 1.07; respectively for citric (pH = 3.42) and PVA media (pH = 7.02). Interestingly, the QDs in rose water medium exhibit suppressed emission response. In this case, the respective intensity of the band edge emission is reduced by a factor of ~1.81 and 1.47 as compared to the PVA and lemon water media. Because of the

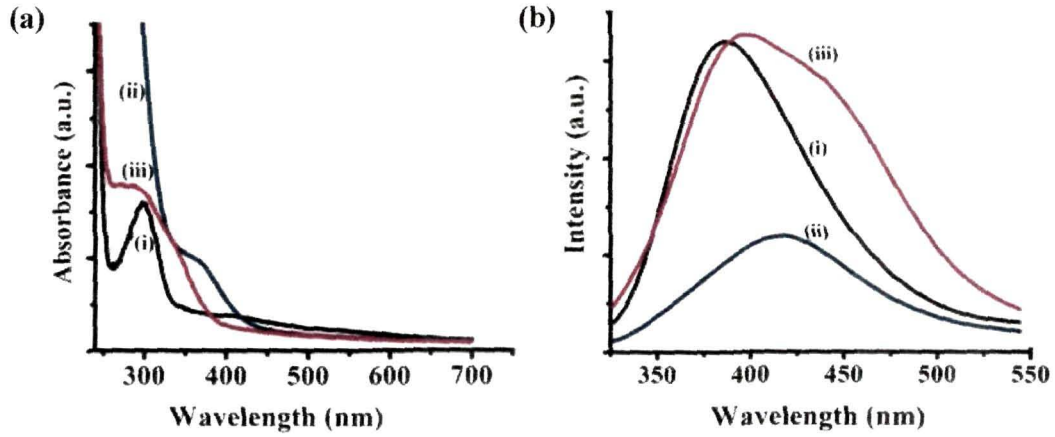

Figure 3.10: (a) UV-Vis and (b) PL spectra of CdSe QDs in (i) PVA, pH = 7.06, (ii) rose water, pH = 7.42, and in (iii) lemon water, pH = 3.42 media

improved defect related emission behavior in lemon water, the emission response of the QDs becomes more asymmetric in this media as compared to others.

Figure 3.11 depicts a set of spectra highlighting studies with regard to stability of the QDs due to independent aging effect in respective media. As shown in Fig. 3.11(a), the NBE gets improved by a factor of ~4 when the specimen was subjected to aging for 6 days in lemon water. However, exessive aging effect did not facilitate further improvement. As can be found, the maximum emission response is suppressed when the specimen was aged for 10 days. In this case, the emission feature is characterized by an enhancement of ~7 as compared to synthesized QDs. As a general trend, the peak due to the defect related emission of QDs in lemon water gets suppressed with aging. However, as can be seen from Fig. 3.11(b), the CdSe QDs in rose water exhibit a red shifting (from λ=416 to 475 nm; E=2.98 to 2.61 eV) of the emission peak (as well as absorption peak, Fig. 3.11 (c)) as a result of the aging effect. The red shifting may be ascribed to the particle growth size effect due to clustering of QDs. Interestingly, though a peak-shift was evident with aging, the overall emission intensity remained uniform for all the specimens. The probable reason for the higher stability of CdSe-PVA QDs in lemon water medium may be attributed to the fact that, the PVA is esterified to PVA-C in presence of the citric acid ($C_6H_8O_7$) contained in the lemon water [22].

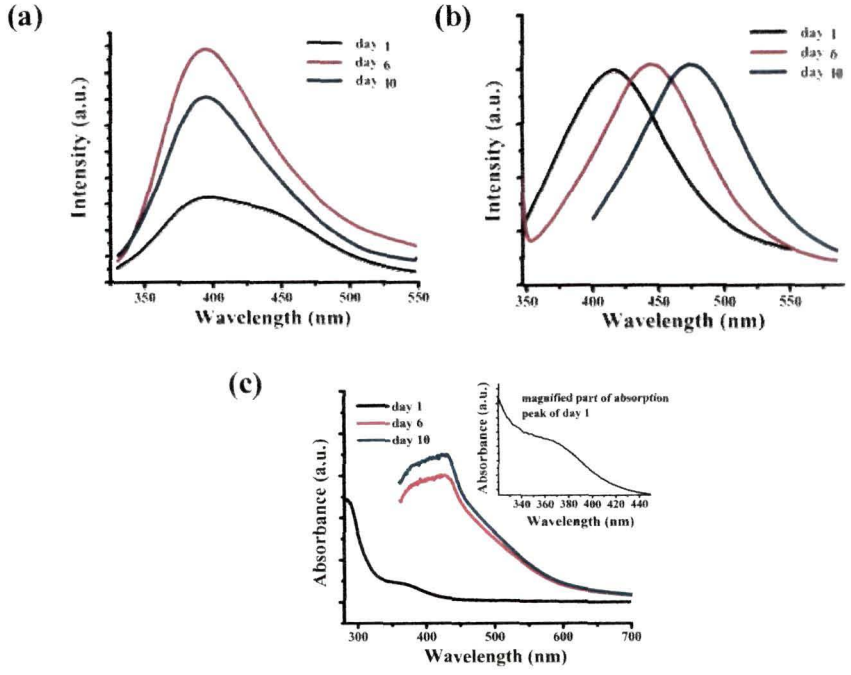

Figure 3.11: PL spectra of CdSe-PVA QDs with aging effect when they are dispersed in natural media (a) lemon water of pH = 3.42, and (b) rose water, pH = 7.42. Fig (c) shows the UV-Vis spectra of QDs in rose water with aging.

The schematic representation of esterification reaction of PVA with lemon water (citric acid) is given below.

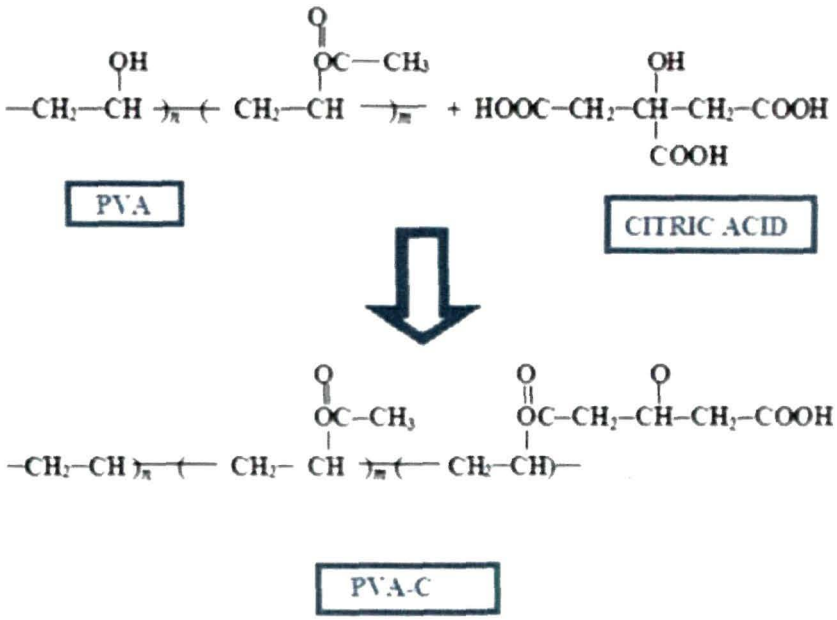

Figure 3.12: Schematic diagram of esterification of CdSe-PVA QDs to CdSe-PVA-C in lemon water media

As far as QD stability is concerned, the carboxyl-functionalized PVA host provides a better environment over the untreated PVA [22]. This is because of the availability of ample amount of free Cd^{2+} ions which are capable of imparting charge balancing with carboxylate (COO^-) ions. Consequently, it results in a more stable colloidal system. Moreover, after esterification of PVA with citric acid, it becomes moderately hydrophilic in nature as compared to the highly hydrophilic behavior of untreated PVA. This is the reason why PVA-C has a large affinity for cell attachment and spreading. This modified PVA is reasonably less cytotoxic and therefore attractive for cellular studies [23].

On the other hand, in rose water medium, because of the presence of geraniol in the rose oil the PVA-rose water mixure becomes superhydrophobic in nature [24]. This superhydrophobic oil -in -water system behaves as a miceller based microreactor system. Consequently, there is a high probability that the QDs would come closer to each other

and coalesce outside these microreactors. This leads to adequate red shift both in the absorption spectra (Fig. 3.10) as well as emission spectra (Fig. 3.11).

3.4.2 Optical response of MnSe QDs

Figure 3.13 depicts the absorption spectra of MnSe-TGA QDs dissolved in different natural media. It can be observed that, the excitonic absorption peak of the MnSe TGA QDs, in distilled water (~303 nm), is red shifted to ~323 nm and 372 nm when they are

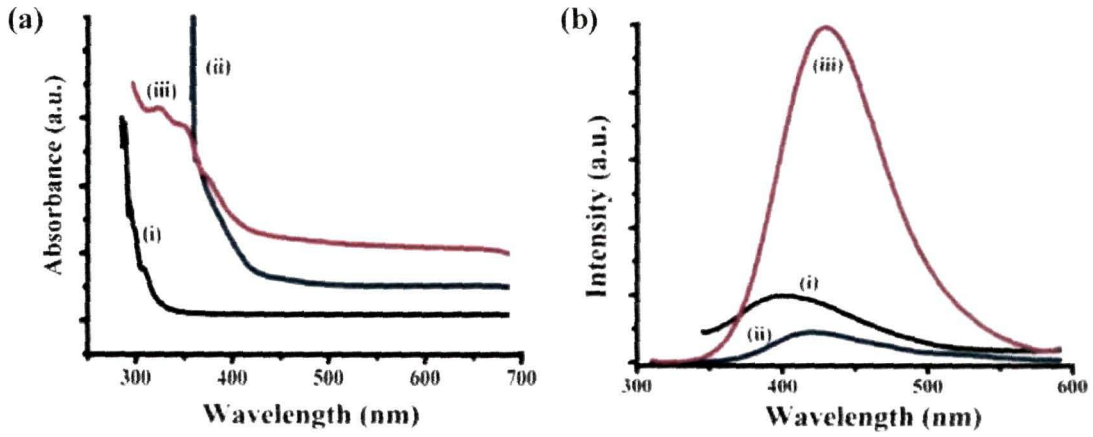

Figure 3.13: (a) UV-Vis and (b) PL spectra of MnSe-TGA QDs in (i) distilled water, (ii) rose water, and (iii) lemon water media

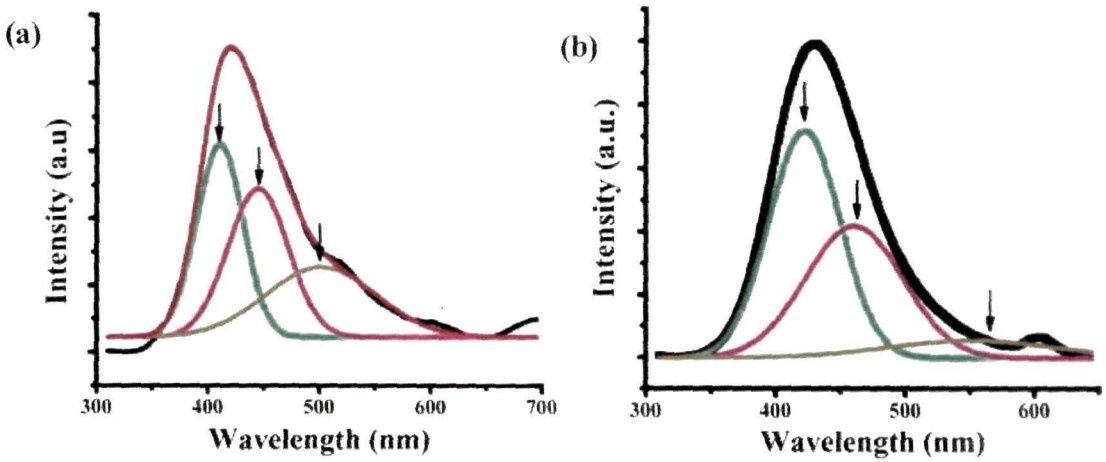

Figure 3.14: Deconvouluted emission spectra MnSe QDs in (a) rose water (b) lemon water

dispersed in lemon and rose water media; respectively. However, a significant enhancement of the emission intensity (by factor 5.08) of the QDs dispersed in lemon water compared to that of distilled water can be observed from the PL spectra (Fig. 3.13(b), *curve* (iii)). In contrast, the intensity reduces (by a factor ~2.12) as soon as they are dispersed in rose water (Fig. 3.13(b), *curve* (ii)). Upon deconvoultion of each of the emission spectra in rose (Fig. 3.14 (a)) and lemon water (Fig. 3.14(b)), we found that each spectrum is likely to comprise of three emission peaks. In rose water media, the first peak, is assigned to the band edge emission response (λ_{BE}), which is located at ~410 nm case. In contrast, in lemon water media, QDs a show band edge emission at ~422 nm. The defect related emission peak arising at ~445 and ~462 nm, for the respective media may have arisen from the defects in the metastable WZ nanocrystal core [16]. The peak at ~500 in rose water media is due to the shallow trap emission whereas, ~561 nm in lemon water media is attributed to *3d* electron transitions of Mn^{2+} ($_4T^1 \rightarrow {}_6A^1$). Note that, the emission response from *3d* electronic transition is missing for the QDs dispersed in distilled water media. However, band edge emission (~400 nm) and defect related emission (~462 nm) are observed (Fig. 3.13(b), *curve* (i)).

Fig. 3.15(a) and (b) depict a comprehensive assesment on optical stability

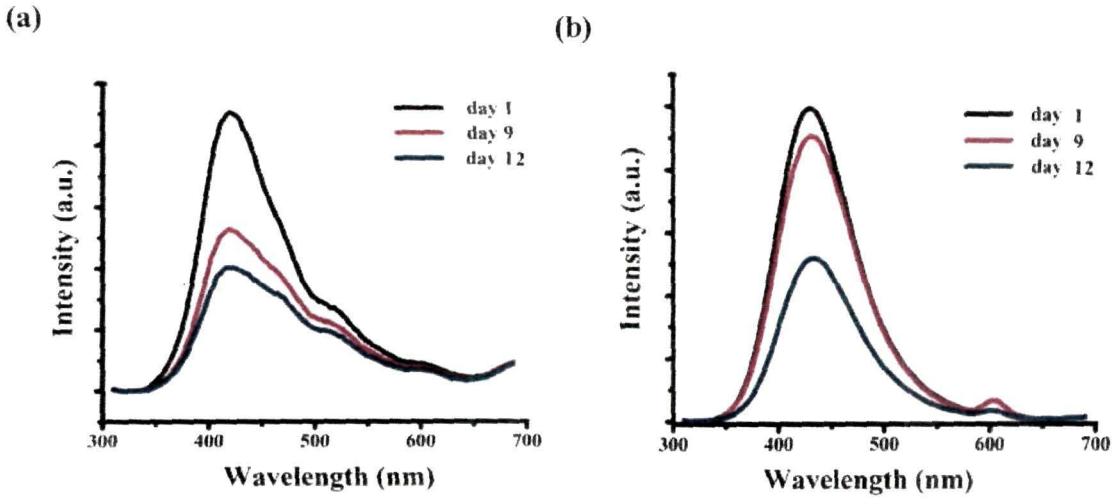

Figure 3.15: PL spectra of MnSe-TGA QDs (prepared with TGA:10% and Mn^{2+}/Se^{2-}=2:1) with aging effect when dispersed in (a) rose media (b) lemon water media

of MnSe-TGA QDs considering aging effect in different media. In rose water, the emission peak arising from different emission response remained at nearly same position with aging (Fig. 3.15(a)). Similar behaviour has been noticed in lemon water also (Fig. 3.15 (b)). However, there is siginificant variation of QDs emission intensity with aging in both the media. Note that, the maximum intesnity of the QDs in rose water media falls linearly with aging (3.15(b)). The intensity gets reduced by factor ~1.73 and ~2.25 than the synthesized day on 9^{th} and 12^{th} days of aging. In contrast, steady drop of maximum intensity of MnSe-TGA QDs has been observed with aging in lemon water media (Fig. 3.15(b)). The maximum intensity of the QDs does not change substantially upto 9 days. There is drastic reduction of maximum intensity for 12 days of aging.

The higher stability of MnSe QDs coated with TGA in lemon water is may be because of formation of di-carboxilic acid coating layer around the surface of the QDs through intermolecular hydrogen (H-) bonding. The interaction happen between carboxylic acid group of TGA molecule and carboxylic acid present in the citric media. The resultant intermolecular H- bonding provides larger water solubility of the QDs as well as making them more biocompatible.

References

[1] Ji, Z., et al. Dispersion and stability optimization of TiO_2 nanoparticles in cell culture media, *Environ. Sci. Technol.* **44**(19), 7309--7314, 2010.

[2] Jing, L., et al. Surface-biofunctionalized multicore/shell CdTe@SiO(2) composite particles for immunofluorescence assay, *Nanotechnology* **22**(50), 505104, 2011.

[3] Poderys, V., et al. Interaction of water-soluble CdTe quantum dots with bovine serum albumin, *Nanoscale Res. Lett.* **6**, 9, 2011.

[4] Bihari, P., et al. Optimized dispersion of nanoparticles for biological in vitro and in vivo studies, *Part. Fibre Toxicol.* **5**(1), 14, 2008.

[5] Elgrabli, D., et al. Effect of BSA on carbon nanotube dispersion for in vivo and in vitro studies, *Nanotoxicology* **1**(4), 266--278, 2007.

[6] Gupta, P. & Ramrakhiani, M. Influence of the particle size on the optical properties of CdSe nanoparticles, *Open Nanoscience Journal* **3**, 15--19, 2009.

[7] Shah, C. P., et al. Precursor concentration and temperature controlled formation of polyvinyl alcohol-capped CdSe-quantum dots, *Beilstein J. Nanotechnol.* **1**(1), 119--127, 2010.

[8] Sharma, H., et al. Effect of ratios of Cd: Se in CdSe nanoparticles on optical edge shifts and photoluminescence properties, *Physica E* **31**(2), 180--186, 2006.

[9] Šimurda, M., et al. Modification of carrier dynamics in CdSe nanocrystals by excess Cd in deposition bath. *Physica E* **36**(2), 205--210, 2007.

[10] Brus, L. E. A simple model for the ionization potential, electron affinity, and aqueous redox potentials of small semiconductor crystallites. *J. Chem. Phys.* **79**(11), 5566--5571, 1983.

[11] Sines, I. T., et al. Colloidal synthesis of non-equilibrium wurtzite-type MnSe, *Angew. Chem. Int. Ed.* **49**(27), 4638--4640, 2010.

[12] Pradhan, N. & Peng, X. Efficient and color-tunable Mn-doped ZnSe nanocrystal emitters: control of optical performance via greener synthetic chemistry, *J. Am. Chem. Soc.* **129**(11), 3339--3347, 2007.

[13] Furdyna, J. K. Diluted magnetic semiconductors, *J. Appl. Phys.* **64**(4), R29--R64, 1988.

[14] Heulings, H. I., et al. Mn-substituted inorganic-organic hybrid materials based on ZnSe: Nanostructures that may lead to magnetic semiconductors with a strong quantum confinement effect, *Nano Lett.* **1**(10), 521--526, 2001.

[15] Lei, S., et al. Solvothermal synthesis of α-MnSe uniform nanospheres and nanorods, *Mater. Lett.* **60**(13–14), 1625--1628, 2006.

[16] Zhu, K., et al. Manganese-doped MnSe/CdSe core/shell nanocrystals: preparation, characterization, and study of growth mechanism, *J. Mater. Res.* **26**(18), 2400--2406, 2011.

[17] Biswas, S., et al. Optical and magnetic properties of manganese-incorporated zinc sulfide nanorods synthesized by a solvothermal process, *J. Phys. Chem. B* **109**(37), 17526--17530, 2005.

[18] Yang, X., et al. Morphology-controlled synthesis of anisotropic wurtzite MnSe nanocrystals: optical and magnetic properties, *CrystEngComm* **14**(20), 6916--6920, 2012.

[19] Petri-Fink, A., et al. Effect of cell media on polymer coated superparamagnetic iron oxide nanoparticles (SPIONs): colloidal stability, cytotoxicity, and cellular uptake studies, *Eur. J. Pharm. Biopharm.* **68**(1), 129--137, 2008.

[20] Maiorano, G., et al. Effects of cell culture media on the dynamic formation of protein–nanoparticle complexes and influence on the cellular response, *ACS nano* **4**(12), 7481--7491, 2010.

[21] Boonsongrit, Y., et al. Controlled release of bovine serum albumin from hydroxyapatite microspheres for protein delivery system, *Mater. Sci. Eng. B* **148**(1), 162--165, 2008.

[22] Mansur, H. S., et al. Synthesis and characterization of CdS quantum dots with carboxylic-functionalized poly (vinyl alcohol) for bioconjugation, *Polymer* **52**(4), 1045--1054, 2011.

[23] Thomas, L. V., et al. A biodegradable and biocompatible PVA–citric acid polyester with potential applications as matrix for vascular tissue engineering, *J. Mater. Sci. Mater. Med.* **20**(1), 259--269, 2009.

[24] Feng, L., et al. Petal effect: a superhydrophobic state with high adhesive force, *Langmuir* **24**(8), 4114--4119, 2008.

CHAPTER- 4: Magnetic Properties of as Synthesized MnSe QDs

CHAPTER 4

Magnetic Properties of as synthesized MnSe QDs

Magnetic materials can be classified by their response to an externally applied magnetic field. The types of magnetism are described as: diamagnetism, paramagnetism, ferromagnetism, antiferromagnetism and ferrimagnetism, depending on the orientations, nature and magnitude of the magnetic moments. The origin of magnetism is normally attributed to the orbital and spin motion of electrons and how the electrons interact with one another as pertained to their spin. Diamagnetism is the fundamental properties of all materials which display weak repulsion to an applied magnetic field giving rise to negative susceptibility ($\chi < 0$). In terms of the electronic configuration of diamagnetic materials, they are composed of atoms with net magnetic moments equals to zero. All other types of magnetic behaviors are observed in materials in which the atomic shells are filled with unpaired electrons. In paramagnetic materials, magnetic domains are absent though an individual atom has a net magnetic moment due to unpaired electrons. When the paramagnetic material

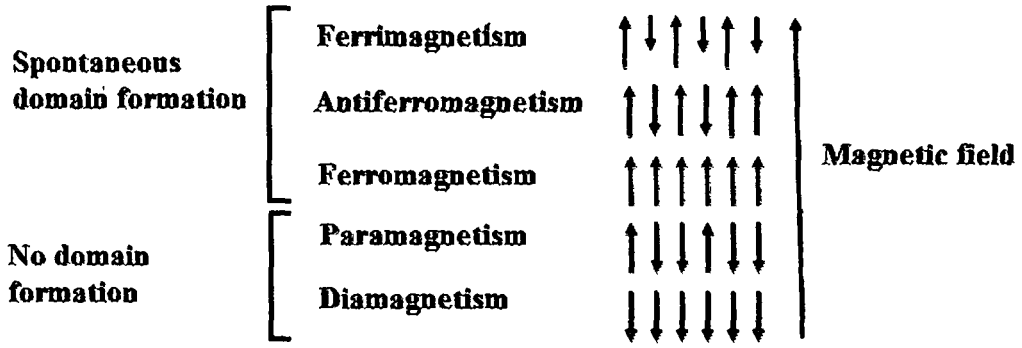

Figure 4.1: Schematic diagram of different types of magnetic behavior in presence of a magnetic field

is placed in a magnetic field, the magnetic moments of the atoms align along the direction of the applied magnetic field forming a weak net magnetic moment. These materials do not retain magnetic moment when the magnetic field is removed. Materials with ferromagnetism behavior, have aligned atomic magnetic moments of equal magnitude and their crystalline structure provides direct coupling interaction between the moments [1]. Accordingly, it results a spontaneous magnetization in the absence of an applied

magnetic field. Antiferromagnetic materials have magnetic moments that are equal in magnitude and opposite in direction which results in zero net magnetic moment. Similarly, ferrimagnetic materials are characterized by antiparallel magnetic moments, but the magnetic moments do not cancel out. This is because of different magnitudes of magnetic moments resulting in a net spontaneous magnetic moment. When placed in a magnetic field, antiferromagnetic and ferrimagnetic materials show a behavior similar to that of ferromagnetic ones. Figure 4.1 shows the schematic of different types of magnetic effects when a material is subjected to an external magnetic field.

Magnetic nanoparticles (MNPs) are those nanoparticles (NPs) that exhibit some noticeable response under an applied magnetic field. As the size of the particle decreases, the ratio of the surface area to the volume of the particle increases. For the NPs, this ratio becomes significantly large causing a large portion of the atoms to reside on the surface as compared to those in the core of the particles. Note that, large surface-to-volume ratio of the NPs is the basis of novel physical, chemical, and mechanical properties with regard to bulk material. The magnetic moment per atom and the magnetic anisotropy of the NPs as well as other magnetic properties, such as, the Curie (T_C) or Néel (T_N) temperatures, and the coercivity field (H_C) are different than those of a bulk specimen [1]. Two main features that dominate the magnetic properties of the NPs are: (a) finite-size effects (single-domain or multi-domain structures and quantum confinement of the electrons), (b) surface effects, which result from the symmetry breaking of the crystal structure at the surface of the particle, oxidation, dangling bonds, existence of surfactants, surface strain.

In this chapter, we study the magnetic properties of water soluble MnSe QDs coated with different surfactants; namely TGA and SDS. The presence of Mn $3d^5$ half filled shells in MnSe NPs and corresponding Mn^{2+}- Mn^{2+} exchange interaction results profound magnetic responses. It may be noted that thiols are regarded as excellent candidates for inducing magnetic properties, even in diamagnetic substances [2-5]. By capping with a thiol group, charge transfer between the SH^- group and surface atoms takes place, thereby inducing a net magnetization [6]. In this context, we have explored the effect of TGA concentration on the magnetic response of MnSe QDs. Moreover, we have exploited the magnetic characteristics of TGA coated $Cd_{1-x}Mn_xSe$ systems for a definite value of the stoichiometry parameter, x.

4.1 Magnetic response of TGA coated MnSe QDs

Figure 4.2 depicts temperature and field dependent magnetization responses of MnSe QDs derived from a fixed precursor ratio of Mn^{2+}/Se^{2-} (=2:1) and coated with 1 and 10% TGA concentrations. In case of zero field cooling (ZFC), the sample was first cooled down to a temperature of ~27 K under no field, and then, the magnetization data was acquired in the warming process when subjected to an applied field of 500 G. As can be seen from Fig. 4.2(a), 1% TGA coated QD system has a Neel temperature (T_N) is located at ~39 K. Whereas, the QDs prepared with a coating layer of 10% TGA concentration is characterized by a non-sharp T_N value of 59 K (Fig. 4.2(b)). Below T_N, the specimen is anti-ferromagnetic and above T_N it exhibited as a paramagnetic system owing to likely randomization of moments associated with the magnetic ordering process. Note the exhibition of steady fall in the magnetization feature in Fig. 4.2(b), suggests coexistence of anti-ferromagnetic and paramagnetic ordering, but to variable extents.

Figure 4.2(c) and (d) represent respective M~H hysteresis plots of the MnSe QDs (with 1 and 10% TGA concentrations) measured at 27 K. The hysteresis loop observed for 1% TGA functionalized QDs may be arisen because of mixure of ferrimagnetic and antiferromagnetic phase or canted-antiferromagnetic arrangements of spins [7,8]. Spin-canted antiferromagnetism is a special condition of noncollinear spin alignment with adequate deflection from the antiferromagnetic order, yielding a weak net magnetism. A coercivity (H_c) value of ~1520 G and remanence (M_r) of ~1.2 emu/g (Fig. 4.2(c)) has been observed for the system. Our T_N and H_c values are comparable with the values predicted for the WZ type MnS nanowires (T_N=30 K, H_c=1020 G) [9] and those of tetrapod-shaped MnSe nanocrystals [10]. In contrast, the respective T_N, H_c and M_r values were found to be ~59 K, ~56 G and ~0.0002 emu/g in case of 10% TGA coated QDs. The magnitude of T_N and H_c are close to the WZ type, spherical and water droplet-shaped MnSe nanoparticles [11]. Nevertheless, the MnSe QDs are likely to experience characteristic paramagnetic features, at room temperature, irrespective of TGA concentration level (Fig. 4.2(e) and (f)). As mentioned above, the surface- defects along with a layer of surfactants could influence the magnetic properties of the NPs to a great extent, especially when thermal agitation is lowered. With decreasing size of the NPs, surface contribution to the magnetization increases as compared to the core of the particles [12]. However, the total magnetization is expected to be contributed by both surface spins and the core of the

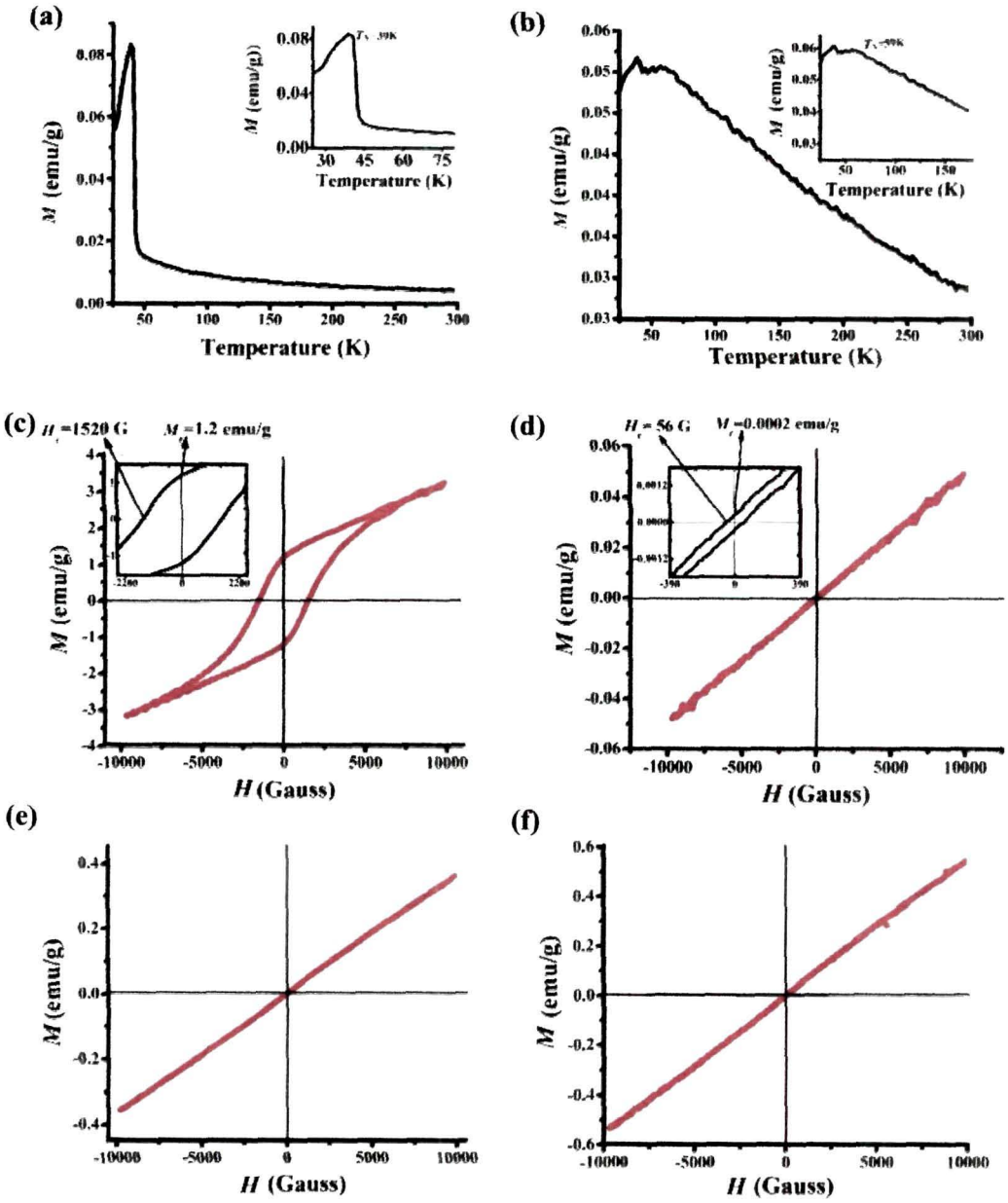

Figure 4.2: (a,b) ZFC curves of different MnSe QDs obtained for a low field of ~500 G applied at a temperature of 27 K. The figure-inset depicting magnetization-peak referring to Neel temperature. The sub-figures (c,d) and (e,f) highlight hysteresis loops of MnSe QDs measured at 27 K and 300 K; respectively. The insets of (c,d) depict the region around the zero field. The sub-figures (a,c,e) and (b,d,f) corresponded to TGA concentration of 1% and 10% and for a constant molar concentration of Mn^{2+}/Se^{2-}= 2:1; respectively.

particles. It is worth mentioning here that, the electronic structure of the whole system can be adequately controlled by the strength of interaction of capping molecules with NP surfaces. Earlier it was demonstrated that, the variation of electronic structure has a strong influence on the magnetic properties [2, 6]. In our case, a larger value of Neel temperature, exhibited by 10% TGA coated QDs suggests that, a relatively higher thermal energy is required to disrupt the magnetic ordering as expected in 1% TGA coated QDs having a smaller T_N. It is possible that, proportionately large no. of SH^- ions are available on the surfaces of the MnSe QDs of higher TGA concentration. This supports efficient charge transfer process between the TGA molecule and 3*d* orbitals of Mn^{2+} ions, and become responsible for strong magnetic signature. Moreover, a higher TGA concentration leads to a slower decrement of magnetic ordering with temperature, whereas a steep fall was witnessed for a lower TGA concentration (Fig. 4.2(a), (b)). Thus, a small magnitude of thermal energy (at low T_N) is sufficient enough to break the magnetic ordering in the later case. The surface dependent magnetic properties of MnSe nanoparticles have also been reported by other workers [8, 13]. Additionally, a lowered value of coercivity (by a factor of ~27.1) as regards 10% TGA coated MnSe QDs, and observed at a relatively low temperature, provides an advantage over the colloidal stability of the QDs. A lowered coercivity indicates quick disappearance of magnetism with the removal of the applied field. We anticipate that, the 10% TGA coated MnSe QDs is a better choice over its 1% counterpart for safe use in biological application, where QDs can be kept un-agglomerated upon removal of the field [10]. Different magnetic parameters, as predicted for the QDs of varying TGA concentrations, are highlighted in Table 4.1.

Table 4.1: Magnetic parameters of MnSe QDs (Mn^{2+}/Se^{2-} =2:1). The H_r and M_r values are measured at 27 K

Sl. No	TGA concentration	Neel temperature, T_N (K)	Coercivity, H_c (G)	Remanence, M_r (emu/g)
1	1%	39	1520	1.2
2	10%	59	56	0.0002

4.2 Magnetic features of binary and ternary $Cd_{1-x}Mn_xSe$ QDs

We have also evaluated the magnetic features of the TGA-coated $Cd_{1-x}Mn_xSe$ QDs. Figure 4.3 depicts temperature and field dependent magnetization responses of the $Cd_{1-x}Mn_xSe$ QD system. In zero field cooling (ZFC), the sample was first cooled down to a temperature of 27 K under no field, and then, the magnetization response is acquired in the warming process, when subjected to an applied field of 500 G. As can be seen from Fig. 4.3(a), no peak is clearly observed for x=0.3. This suggests that, the sample is paramagnetic in this case since at low Mn concentration, the individual Mn^{2+} spins exist in isolation from one another [14]. In a previous work, a similar behavior was also witnessed for $Zn_{1-x}Mn_xS$ nanoparticle system, with a lower value of Mn concentration [14]. On the other hand, the QD system exhibited a Neel temperature (T_N) value of ~59 K, corresponding to a stoichiometric parameter of x=1 (MnSe).

Figure 4.3(b) shows the M~H hysteresis plots of the NP system with x=0.3 and 1 measured at 27 K. The QDs systems essentially characterize paramagnetic behavior but to different degrees, as evident from the varying tilts of the M-H traces.

It may be noted that, a constant TGA concentration was used as a capping material while preparing the $Cd_{1-x}Mn_xSe$ system for different stoichiometric values. This condition offers an equal magnitude of field strength as contributed by the SH^- group of

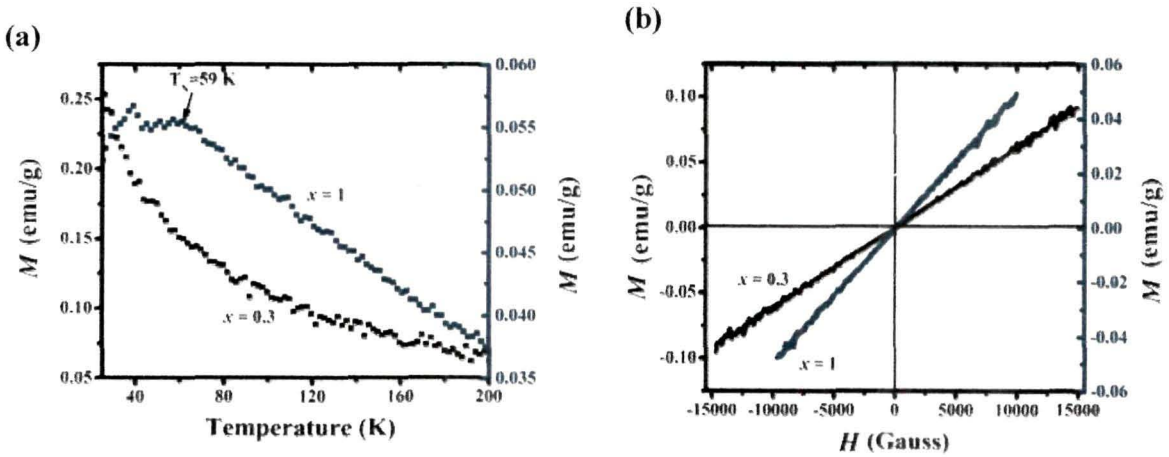

Figure 4.3: (a) ZFC and (b) hysteresis curves of $Cd_{1-x}Mn_xSe$ systems measured at 27 K, for x = 0.3 and x = 1

TGA the layer in all the cases. But, with increasing value of x, the Mn^{2+} concentration at the QD surface increases, thus exhibiting enhanced charge transfer events between the SH^- group and Mn^{2+} ions. This results in a definite value of Neel temperature, as compared to the case for a lower value of x, where a clear evidence of Neel temperature is absent. A larger value of Mn^{2+} ion concentration, for a higher value of x, is associated with a self diffusion mechanism as discussed in *Chapter 2*.

It is worth mentioning to here that, in II-VI semiconductor, the substituted paramagnetic Mn^{2+} ions exhibit spin 5/2, and clusters are formed by antiferromagnetic interaction among neighbouring and next-neighbouring Mn spins [15]. Increasing of Mn content, the cluster size increases by coupling of more and more spins in the cluster [16]. Consequently, the magnetization dynamics is dominated by Mn-Mn interactions in anti-ferromagnetic clusters.

4.3 Magnetic features of SDS coated MnSe QDs

We also intended to explore the magnetic properties of MnSe QDs coated with a long chain, anionic surfactant SDS. Figure 4.4 (a) depicts the temperature dependent magnetic

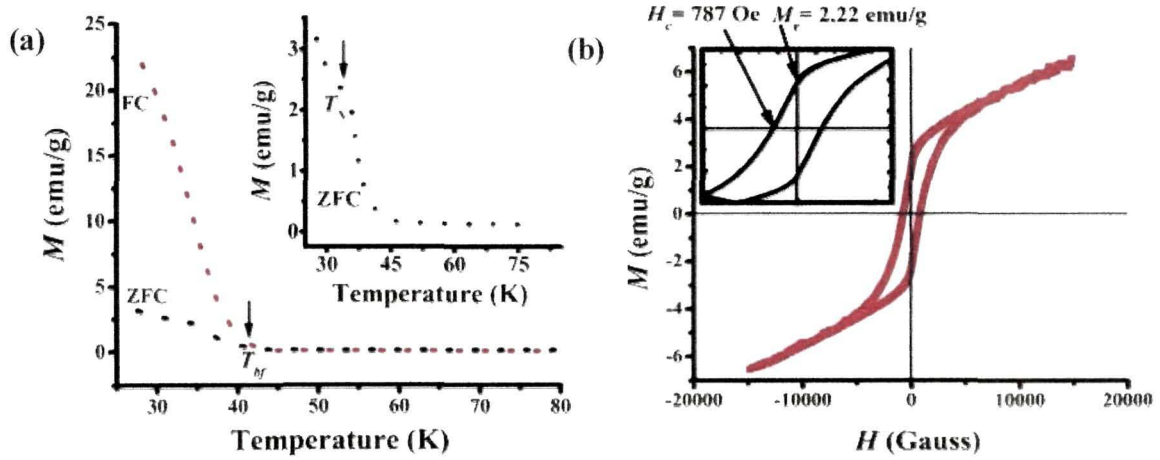

Figure 4.4: (a) ZFC and FC curves of MnSe-SDS QDs studied at a temperature 27 K and under a field of ~100 Oe applied. The figure-inset depicts the ZFC curve highlighting Neel temperature T_N. (b) hysteresis loops of MnSe-SDS QDs measured at 27 K. The inset depicts the region around the zero field.

responses of MnSe-SDS QDs (SDS concentration 10%) under an applied field of 100 Oe. In particular, M(T) was studied by ZFC and field-cooling (FC) modes between 27 K to 250 K. As for the ZFC curve, the sample was first cooled down to T = 27 K under zero applied field, followed by an acquisition of magnetization signal under an applied field of 100 Oe, during the warming process. In contrast, for FC measurement, the sample was cooled under a magnetic field, 100 Oe. The magnetization measurements shown in Fig. 4.4(a) affirm the coexistence of anti-ferromagnetic and paramagnetic mixed phases in the investigated samples. In comparison to the Neel temperature (T_N) 10% TGA coated QDs (average size, d=14 nm, obtained from *Chapter* 2) at ~59 K, the Neel temperature (T_N) of 10% SDS coated QDs (average size, d=10.9 nm, obtained from *Chapter* 2) is observed to be at ~35 K. (inset of Fig. 4.4(a)). This suggests that changing of surface coating layer the Neel temperature changes. Moreover, the value of T_N reduced with decreasing diameter. The size-dependent Neel temperature is attributed to a surface effect. The surface effect is strong enough to destroy the anti-ferromagnetic exchange coupling above the Neel temperature [8]. Size dependent phase-transition character has been witness by workers in ZB-MnSe films [17] and MnO [18] NCs. Note that , the observed Neel temperature resembled the value for oleic acid (organic surfactant, OA) capped tetrapod-shaped MnSe NCs (T_N=35 K) and close to the value of WZ MnS nanowires (T_N=30 K) [9].

As can be seen in the FC and ZFC magnetization plots, the SDS coated MnSe QDs display a characteristics splitting (bifurcation) feature below a critical temperature T_{bf} ~ 41 K. The irreversibility arises owing to the formation of magnetic domains and domain-wall movement [19], which leads to the reorientation of Mn^{2+} spins, in domain boundaries [20]. A similar bifurcation of the FC and ZFC can also be observed in case of different transition metal compounds and transition metal dopped compound [21,22]. The bifurcation temperature T_{bf}, depends on the magnetocrytalline anisotropy, applied magnetic field, coericivity etc [23].

The magnetic hysteresis curve of MnSe-SDS QDs (measured at 27 K) is presented in Fig. 4.4(b). The QDs exhibited a coercivity (H_c) of ~787 Oe and remanence (M_r) of ~2.22 emu/g.

Thus from the present discussion, the magnetic properties of the MnSe QDs can be efficiently controlled by different surface coating agents in the same way as observed

for iron oxide NPs [23]. This is because; surface effects have a strong influence on the magnetic properties of magnetic NPs, which can vary from coating agent to coating agent [24]. It is observed that using of same coating agents, TGA, the charge transfer behavior between SH^- and QDs of types MnSe and $Cd_{1-x}Mn_xSe$ varies substaially influencing their magnetic properties. Similarly, use of different coating agents TGA and SDS contribute different order of magnetic behavior in the MnSe QDs.

References

[1] Akbarzadeh, A., et al. Magnetic nanoparticles: preparation, physical properties, and applications in biomedicine, *Nanoscale Res. Lett.* **7**(1), 1--13, 2012.

[2] Garcia, M. A., et al. Magnetic properties of ZnO nanoparticles, *Nano Lett.* **7**(6), 1489--1494, 2007.

[3] Yamamoto, Y., et al. Direct evidence for ferromagnetic spin polarization in gold nanoparticles, *Phys. Rev. Lett.* **93**, 116801, 2004

[4] Guerrero, E., et al. Surface plasmon resonance and magnetism of thiol-capped gold nanoparticles, *Nanotechnology* **19**(17), 175701, 2008.

[5] Crespo, P., et al. Permanent magnetism in thiol capped nanoparticles, gold and ZnO, *Acta Phys. Pol. S. A* **113**(1), 515, 2008.

[6] Crespo, P., et al. Permanent magnetism, magnetic anisotropy, and hysteresis of thiol-capped gold nanoparticles, *Phys. Rev. Lett.* **93**(8), 087204, 2004.

[7] Lecren,L., et al. Slow Relaxation in a One-Dimensional Rational Assembly of Antiferromagnetically Coupled [Mn4] Single-Molecule Magnets, *J. Am. Chem. Soc.***127**, 17353, 2005.

[8] Yan, F. Tailoring surface phase transition and magnetic behaviors in $BiFeO_3$ via doping engineering, *Sci Rep.*,**5**, 9128, 2015

[9] Jun, Y.-W., et al. Architectural control of magnetic semiconductor nanocrystals, *J. Am. Chem. Soc.* **124**(4), 615--619, 2002.

[10] Yang, X., et al. Morphology-controlled synthesis of anisotropic wurtzite MnSe nanocrystals: optical and magnetic properties, *CrystEngComm* **14**(20), 6916--6920, 2012.

[11] Sines, I. T., et al. Colloidal synthesis of non-equilibrium wurtzite-type MnSe, *Angew. Chem. Int. Ed.* **49**(27), 4638--4640, 2010.

[12] Issa, B., et al. Magnetic nanoparticles: surface effects and properties related to biomedicine applications, *Int. J. Mol. Sci.* **14**(11), 21266--21305, 2013.

[13] Zhang, J., et al. Uniform wurtzite MnSe nanocrystals with surface-dependent magnetic behavior, *Nano Res.* 1--11, 2013.

[14] Wang, Z.-H., et al. Cluster spin-glasslike behavior in nanoparticles of diluted magnetic semiconductors ZnS: Mn, *J. Mater. Res.* **22**(09), 2376--2383, 2007

[15] Kneip, M. K., et al. Electric field control of magnetization dynamics in ZnMnSe/ZnBeSe diluted-magnetic-semiconductor heterostructures, *Appl. Phys. Lett.* **88**(21), 212105--3, 2006.

[16] Larson, B. E., et al Effects of internal exchange fields on magnetization steps in diluted magnetic semiconductors, *Phys. Rev. B* **33**(3), 1789--1796, 1986.

[17] Samarth, N., et al. Antiferromagnetism in ZnSe/MnSe strained-layer superlattices, *Phys. Rev. B* **44**(9), 4701--4704, 1991.

[18] Puglisi, A., et al. Monodisperse Octahedral α-MnS and MnO Nanoparticles by the Decomposition of Manganese Oleate in the Presence of Sulfur, *Chem. Mater.* **22**(9), 2804--2813, 2010.

[19] Chernova, N. A., et al. Solitary excitations and domain-wall movement in the two-dimensional canted antiferromagnet $(C_2N_2\ H_{10})V_2FePO_4(OH)$, *Phys. Rev. B* **70**(14), 144405, 2004.

[20] Midya, A., et al. Magnetocaloric effect in $HoMnO_3$ crystal, *Appl. Phys. Lett.* **96**(14), 142514 - 142514-3 , 2010.

[21] Kellerman, D. G., et al. Some aspects of antiferromagnetic ordering in $LiMnP_{0.85}V_{0.15}O_4$: Neutron diffraction and DC-magnetization studies, *J. Magn. Magn. Mater.* **324**(19), 3181--3188, 2012.

[22] Choudhury, B. & Choudhury, A. Oxygen vacancy and dopant concentration dependent magnetic properties of Mn doped TiO_2 nanoparticle, *Curr. Appl. Phys.* **13**(6), 1025--1031, 2013.

[23] Spada, F., et al. Hc enhancement in partially reduced γ-Fe_2O_3 via surface treatment with sodium polyphosphate (revisited), *J. Appl. Phys.* **69**(8), 4475--4477, 1991.

[24] Mahmed, N. "Development of multifunctional magnetic core nanoparticles,1-115." Diss.Italy, 2013. Print

CHAPTER-5: Biophysical Characterization of CdSe and MnSe QDs

CHAPTER 5

Biophysical Characterization of CdSe and MnSe QDs

The bioconjugated-nanoparticles (or, QDs) have emerged as an important concept in nanobio interface applications, such as, bioimaging, biolabeling, immunoassay etc. There has also been a growing interest in creating hybrid semiconductor–protein conjugates for use where the proteins provide biofunctionality while the fluorescent semiconducting nanoparticles (NPs) allow spatio-temporal tracking. Note that, serum albumin is the most abundant protein in blood plasma which plays a key role in the transport of a large number of metabolites, endogenous ligands, fatty acids, bilirubin, hormones, anesthetics and other commonly used drugs [1].

In this chapter, emphasis is given to a number of biophysical techniques of the synthesized QDs. Herein, we shall account for the interaction of SDS and TGA capped CdSe and MnSe QDs with the bovine serum albumin (BSA) proteins. Infact, bio-conjugation responses are evaluated by photoluminescence spectroscopy (PL), time resolved photoluminescence (TR-PL), and fluorescence resonance energy transfer (FRET) mechanism. For safe use of QDs in biological environments, a critical evaluation is made with regard to cytotoxicity aspect of the CdSe-TGA and MnSe-TGA QDs by using live cells of (human lymphocytes). Moreover, the cellular uptake of the QDs is elaborated through fluorescence imaging and confocal microscopy data.

5.1 Bio-conjugation of water soluble, CdSe and MnSe QDs with albumin proteins

As stated above, BSA (~69 kD*, Sigma-Aldrich & Co., 99.9% pure) was opted for studying the bio-conjugation capability of water soluble TGA and SDS coated CdSe and MnSe QDs. At first, lyophilized BSA is subjected to denaturing in 1 mM aqueous $NaBH_4$ at 70°C. The excess borohydride is removed by spontaneous decomposition by heating. For effective bio-conjugation, the denatured BSA was prepared with a concentration of 10 μg/ml and is treated with 7 ml CdSe-TGA (SDS) and MnSe-TGA(SDS) QDs dispersed in distilled water, independently. The test tubes containing CdSe-TGA-BSA (CdSe-SDS-BSA) and MnSe-TGA-BSA(MnSe-SDS-BSA) mixtures, upon well shaking, were made airtight with teflon seals. The samples were then incubated at room

* *1 kD = 10^3 daltons = 1.66×10^{-24} Kg*
Where, 1 dalton=1 66 × 10^{-27} Kg

temperature for 1 h followed by centrifugation at ~5,000 rpm, for 10 min. The final residues, as obtained through filtration steps, were thoroughly washed with distilled water several times. The relevant steps of centrifugation and filtration were repeated a number of times in order to remove away the free TGA and SDS after conjugation with BSA.

5.1.1 Bio-conjugation response of CdSe QDs

The bio-conjugation aspects of CdSe QDs, with BSA proteins are as discussed below.

5.1.1(a) Emission response of non-conjugated and BSA conjugated CdSe QDs

The effect of BSA conjugation on emission properties of CdSe QDs is being discussed here. Fig. 5.1(a) depicts that with BSA conjugation the maximum PL intensity of the CdSe QDs decreases by factor of ~1.28 when the QDs are capped by TGA. In contrast, in case of CdSe-SDS QDs, the intensity shoots up by a factor of ~1.31 (Fig. 5.1(b)). However, in both the systems (TGA as well SDS coated QDs) the band edge emission (λ_{BE}) and defect related emission (λ_{DE}) peak remain at same positions after BSA conjugation. The λ_{BE} and λ_{DE} of TGA coated CdSe QDs are observed at ~590 nm and ~657 nm; respectively in both BSA non-conjugated and conjugated case. Similarly, SDS

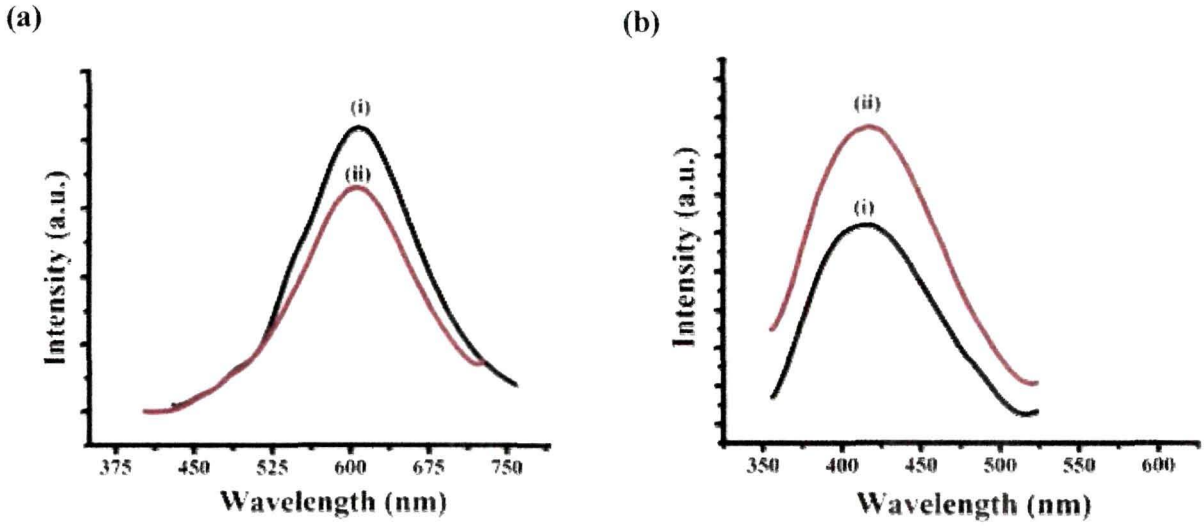

Figure 5.1: PL spectra of (i) non-conjugated and (ii) BSA conjugated (a) CdSe-TGA (b) CdSe-SDS QDs

coated CdSe QDs exhibit λ_{BE} at ~418 nm and λ_{DE} ~575 nm for both BSA non-conjugated and conjugated systems.

The reduction of maximum emission intensity of TGA coated QDs system with addition BSA may suggest effective energy transfer from the QDs to the BSA molecule by quenching its intensity. Whereas, BSA acts as surface passivator in case of BSA conjugated CdSe-SDS QDs with respect to the non-conjugated ones resulting enhancement of PL intensity.

5.1.1(b) TR-PL study of non-conjugated and BSA conjugated CdSe QDs[†]

The fluorescence decay profiles of TGA (or, SDS) coated colloidal CdSe QDs, and bio-conjugated are depicted in Fig. 5.2. All the spectra basically exhibit bi-exponential decay characteristics with decay parameters seen in different timescale. In case of non-conjugated CdSe-TGA QDs, the parameters are found to be τ_1~5.42 ns, τ_2~47.03 ns (Fig. 5.2(i)). As for SDS coated QDs, the respective decay constants are estimated as τ_1~0.53 ns, τ_2~1.6 ns (Fig. 5.2(ii)). Here, the shorter life time (τ_1) can be ascribed to the direct radiative transitions of the free excitons (core-state recombination) while the second, a relatively slower component (τ_2) is believed to be due to the radiative recombination via

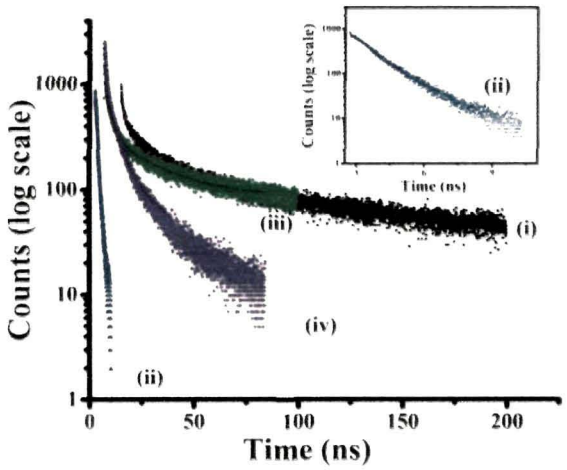

Figure 5.2: (a) TR-PL spectra of (i) CdSe-TGA (ii) CdSe-SDS (iii) CdSe-TGA-BSA (iv) CdSe-SDS-BSA QDs (λ_{ex}=375 nm, λ_{em}= 400 nm). Inset shows the clear plot of TR-PL spectra of CdSe-SDS QDs.

[†] *Appendix-7*

surface-trap sites [2]. One can use the following expression for calculating average lifetime of non-conjugated QDs with different surfactant coatings:

$$\tau_{average} = \frac{A_1\tau_1^2+A_2\tau_2^2}{A_1\tau_1+A_2\tau_2} \quad (5.1)$$

where A_1 and A_2 are the pre-exponential factors for the fast and slow processes; respectively. The average life time of the non-conjugated CdSe QDs capped by TGA and SDS layers are calculated to be ~35.1 ns and ~1.16 ns; respectively. It is observed that, τ_2 of CdSe-TGA QDs is ~29.5 times larger than the τ_2 of CdSe-SDS QDs. This may account for a amount of larger surface states available in the CdSe TGA QDs, which is likely to enhance the localization time of the trapped excitons as compared to the other QD counterpart. Nevertheless, the conjugation of CdSe-TGA QDs with BSA molecules yields time constants as, τ_1~2.81 ns and τ_2~23.12 ns, and with an average lifetime of τ_{av} ~19.24 ns (Fig. 5.2(iii)). As for SDS capped QDs, the respective time constants are predicted to be τ_1 ~1.54 ns and τ_2 ~7.75 ns (Fig. 5.2(iv)). With the attachment of BSA to CdSe-TGA QDs, the average lifetime reduces by a factor of ~1.82 as compared to the non-conjugated CdSe-TGA QDs system. On the other hand, an enhancement of average life time by a factor of ~1.82 has been realized for BSA conjugated CdSe-SDS QDs as compared to the BSA non-conjugated one.

The reduction of average lifetime of CdSe-TGA QDs over BSA conjugation can be assigned to adequate energy transfer mechanism from CdSe-TGA QDs to the BSA molecules [3,4]. The shortening of donor average lifetime in presence of acceptor one is one of the characteristic features of efficient energy transfer in the close donor-acceptor systems [5.6].

Table 5.1: Different decay parameters related to CdSe QD systems

Non-conjugated QDs						**BSA conjugated QDs**					
QDs	τ_1 (ns)	τ_2 (ns)	A_1	A_2	τ_{av} (ns)	QDs	τ_1 (ns)	τ_2 (ns)	A_1	A_2	τ_{av} (ns)
CdSe-TGA	5.42	47.03	0.12	0.03	35.1	CdSe-TGA	2.81	23.12	470.19	244.65	19.24
CdSe-SDS	0.53	1.60	0.02	0.01	1.16	CdSe-SDS	1.54	7.75	872.5	642.5	6.43

On the other hand, an enhanced of average lifetime is observed in CdSe-SDS QDs after BSA conjugation. We observe τ_{av} of CdSe-SDS-BSA QDs is ~1.82 times larger than τ_{av} of CdSe-SDS QDs. From the magnitude of A_1 and A_2, for CdSe-SDS-BSA QDs, the probability of recombination via. surface traps is drastically suppressed as compared to the probability of core-state recombination. In addition, with BSA conjugation, the probability of core-state recombination (intensity A_1) is drastically increased by factor 43625 (Table 5.1) over BSA conjugated CdSe-SDS QDs.

With BSA conjugation, the enhancement of maximum PL intensity of CdSe-SDS QDs along with increase of average lifetime (diminishing probability of recombination via. surface traps and increasing probability of core-state recombination), suggests that BSA acts as a efficient surface passivator for SDS coated CdSe QDs. Different time components predicted for various CdSe systems are shown in Table 5.1.

5.1.2 Bio-conjugation response of MnSe QDs

The optical response of BSA conjugated MnSe QD systems are explained as below.

5.1.2(a) Emission response of non-conjugated and BSA conjugated MnSe QDs

Quenching of emission intensity by factor of ~1.39 has been observed for MnSe-TGA QDs when they are conjugated with BSA protein (Fig. 5.3(a)). This quenching behavior is similar to the case as we have observed for CdSe-TGA QDs, and one can predict

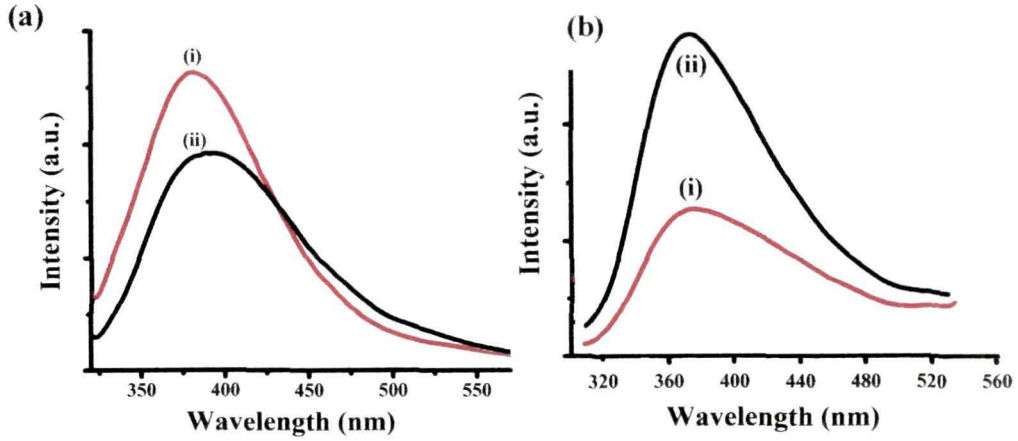

Figure 5.3: PL spectra of (i) non-conjugated and (ii) BSA conjugated (a) MnSe-TGA (b) MnSe-SDS QDs

occurring of energy transfer from MnSe-TGA to BSA protein. In contrast, enhancement of emission intensity in case of in MnSe-SDS QDs (by factor of ~2.13) with conjugation of BSA protein (Fig. 5.3(b)) signifies the surface passivation of the QDs by BSA protein.

5.1.2(b) TR-PL study of non-conjugated and BSA conjugated MnSe QDs

The TR-PL spectra of BSA conjugated and non-conjugated MnSe QDs are shown in log scale in Fig. 5.4. Each of the spectra exhibits exponential decay behavior but to varying degree. The non-cojugated MnSe-TGA QDs characterized by lifetime as, τ_1~0.60 ns, τ_2~2.61 ns and τ_3~3401.8 ns (Fig. 5.4(i)). The respective time constants for the SDS coated MnSe QDs are found to be τ_1~1.04 ns, τ_2~5.11 ns and τ_3~5.11 ns (Fig. 5.4(ii)). The time constant τ_1 is due to the direct exciton recombination, τ_2 is assigned to surface-trapped excitons, whereas, the third component, τ_3 is assigned to radiative and nonraditive response due to carriers trapped at the surface sites [7]. The τ_3 counterpart, infact suggest localization of carriers at the surface states with small overlapping between electron and hole wave-functions [8]. The average lifetime of different MnSe QDs systems can be calculated by using the extended version of eqn. (5.1), given by:

$$\tau_{average} = \frac{A_1\tau_1^2+A_2\tau_2^2+A_3\tau_3^2}{A_1\tau_1+A_2\tau_2+A_3\tau_3} \qquad (5.2)$$

Where, A_1 , A_2, A_3 are the pre-exponential factors involved in the fast and slow processes; respectively.

The average life time of the non-conjugated MnSe QDs (coated with TGA and SDS) are calculated to be ~3401.5 ns and 1.20 ns; respectively. With conjugation of BSA to MnSe-TGA QDs the life times are observed to be τ_1 ~0.55 ns, τ_2 ~2.36 ns, τ_3 ~7.24 ns and with an average lifetime of τ_{av} ~4.71 ns (Fig. 5.4(iii)). Whereas, for SDS capped MnSe-BSA QDs the respective time constants are found as τ_1 ~0.92 ns, τ_2 ~3.7 ns, τ_3 ~9.24 ns (Fig. 5.4(iv)). In this case, the average life time is calculated to be 4.79 ns. Note that, with the addition of BSA to MnSe-TGA QDs the average lifetime substantially reduced by a factor of ~722.1. In contrast, in case of MnSe-SDS QDs the average lifetime increases by a factor of ~3.92 with BSA conjugation as compared to the non-conjugated case. Moreover, the probability of core-state recombination (intensity A_1) increases by

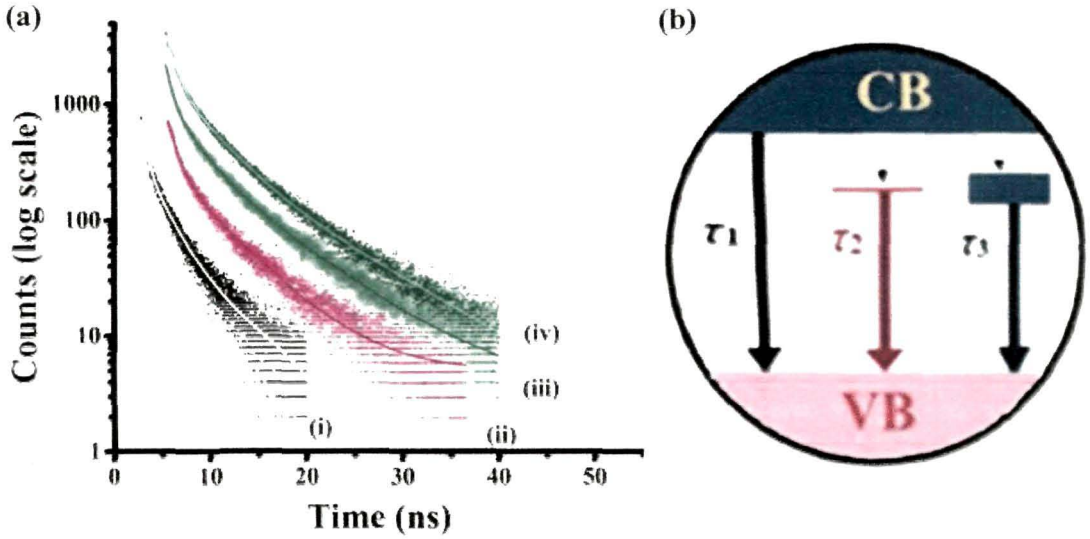

Figure 5.4: (a) TR-PL spectra of (i) MnSe-TGA (ii) MnSe-SDS (iii) MnSe-TGA-BSA (iv) MnSe-SDS-BSA QDs (λ_{ex}=375 nm, λ_{em}= 400 nm). The schematic shown in (b) depicts radiative /nonradiative pathways in the MnSe-QD systems.

Table 5.2: Different decay parameters related to MnSe QD systems

Non-conjugated QDs							**BSA conjugated QDs**						
QDs	τ_1 (ns)	τ_2 (ns)	τ_3 (ns)	A_1	A_2	A_3	QDs	τ_1 (ns)	τ_2 (ns)	τ_3 (ns)	A_1	A_2	A_3
MnSe-TGA	0.60	2.61	3401.9	347.04	282.41	3101.20	MnSe-TGA	0.55	2.36	7.24	1304.40	834.56	418.79
MnSe-SDS	1.04	5.11	5.11	92951.7	124.80	910.40	MnSe-SDS-	0.92	3.7	9.24	750763.78	5488.24	535.61

~8.07 times in case of MnSe-SDS-BSA QDs as compared to MnSe-SDS ones.

The reduction of average lifetime of MnSe-TGA QDs over BSA conjugation may predict the possibility of energy transfer mechanism from MnSe-TGA QDs to the BSA protein [3,4]. Different time constants, related to the MnSe system are shown in Table 5.2.

From the PL and TR-PL data, we expect that the CdSe-TGA–BSA and MnSe-TGA-BSA pairs are likely to display FRET mechanism. While, BSA acted as a surface passivator in case of BSA conjugated SDS coated CdSe and MnSe QDs.

5.1.3 FRET mechanism in BSA conjugated CdSe-TGA and MnSe-TGA QDs

The main criteria for an efficient FRET process is rely on significant overlapping between the absorption spectrum of the acceptor particle and the emision spectrum of the

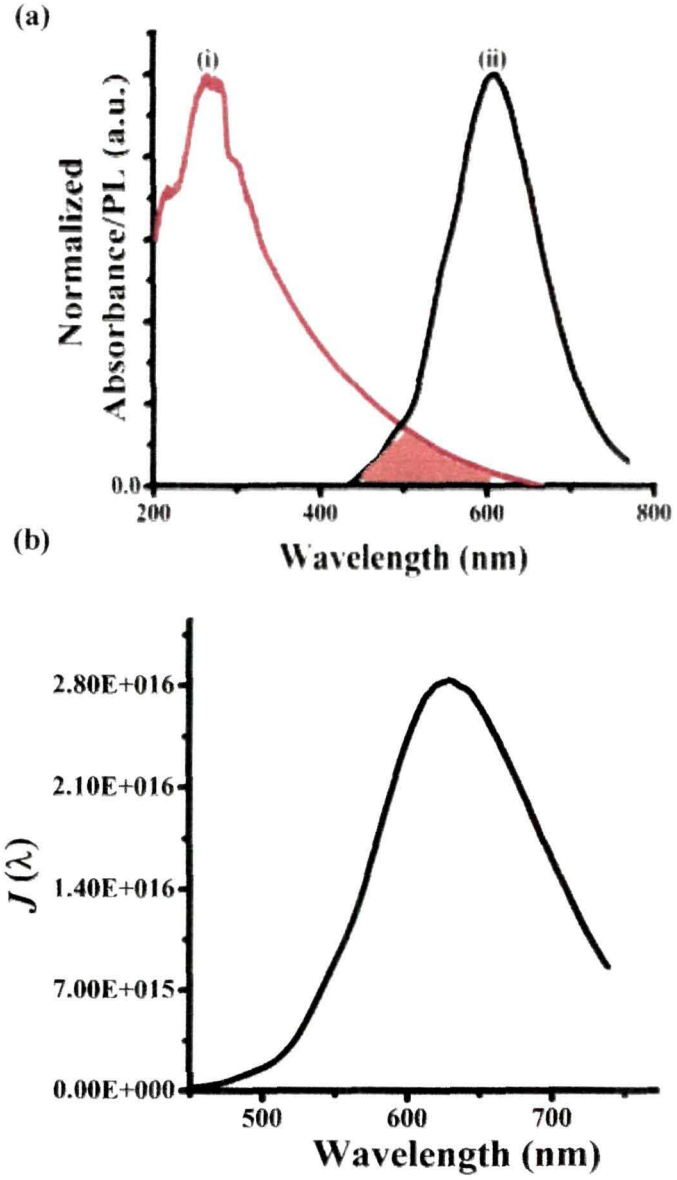

Figure 5.5: (a) Normalized (i) absorbance spectrum of BSA and (ii) PL spectrum of CdSe-TGA QDs (b) the overlapping integral spectrum ($J(\lambda)$) vs. λ between the two spectra, with $J(\lambda$ expressed in $M^{-1}cm^{-1}nm^{4}$.

excited donor particle [3,4]. In principle, FRET process reduces the emission intensity of the donor particle and enhances the intensity of the acceptor one. Moreover, for an effective FRET event, the flourescent lifetime of the donor should be substaintially larger than the acceptor molecule [3,4]. The FRET event between a donor and an acceptor results in shortening of the donor lifetime ($\tau_{DA}<\tau_D$). The conjugation of BSA proteins with the CdSe-TGA and MnSe-TGA QDs is characterized by the shortening of lifetime in comparison with the the non-conjugated QDs as discussed above (#section 5.1.1 and 5.1.2). Fig. 5.5(a) represents an overlapping feature of the normalized absorbance spectrum of acceptor (BSA) and PL spectrum of the donor (CdSe-TGA QDs). The resultant overlapping integral spectra is shown in Fig. 5.5(b). The overlapping integral is calculated by using the following equation [9]

$$J(\lambda) = \frac{\int_0^{\infty} F_D(\lambda)\varepsilon_A(\lambda)\lambda^4 d\lambda}{\int_0^{\infty} F_D(\lambda)d\lambda} \tag{5.3}$$

Here, F_D (λ) is the integrated fluorescence intensity of the donor, ε_A is the molar extinction coefficient of the acceptor. In this case, ε_A = 43824 Mol^{-1} cm^{-1} at 280 nm (for BSA protein) and λ is the wavelength in nanometers. The strength of overlapping integral (maxima) is of the order of ~2.8×10^{16}, which signifies efficient energy transfer from the CdSe-TGA QDs to the BSA molecules. The FRET efficiency can be measured experimentally and is commonly defined as [6]

$$E_F = 1\text{-}F_{DA}/F_D \tag{5.4}$$

where F_{DA} is the integrated fluorescence intensity of the donor (CdSe-TGA) in presence of the acceptor (BSA) and F_D is the integrated fluorescence intensity of the donor alone. In the present case, the energy transfer efficiency of the CdSe-TGA QDs to the BSA molecule is found to be nearly 71%. Another important parameter of the FRET process is the Förster radius, R_0[‡] [10]. It represents the donor–acceptor separation distance at which the FRET efficiency is ~50%.

$$R_0 = 0.211(k^2 J(\lambda)\, n^{-4}\, \Phi_Q)^{1/6} \tag{5.5}$$

[‡] *Appendix-8*

Here, k^2 is the dipole orientation factor and its value is 2/3 for randomly oriented dipoles [10], n (1.33) is the refractive index of solvent, Φ_Q is the quantum yield of donor. The quantum yield of our CdSe-TGA QDs is ~89% (as compared to the rhodamine 6G dye®, as discussed in *Chapter* 2). Considering above parameters, the R_0 value for CdSe-TGA-BSA (donor-acceptor) system is calculated to be ~8.2 nm. The donor-acceptor separation distance (r) can be calculated using following relation:

$$r = R_0 (1/E_F - 1)^{1/6} \tag{5.6}$$

The magnitude of r is found as ~6.9 nm.

The spectral overlapping behavior of the donor MnSe-TGA QDs and BSA acceptor is shown in Fig. 5.6(a) and (b). The QDs are characterized by an energy transfer efficiency of 61% with an overlapping integral maxima $J(\lambda)$ value of ~5.9×10^{15}. Following discussion meant for CdSe system, the values of R_0 and r for MnSe system are estimated to be ~6.7 and ~6.12 nm; respectively. Different parameters related to CdSe-TGA-BSA and MnSe-TGA-BSA systems are highlighted in Table 5.3.

On comparing FRET parameters of CdSe-TGA QDs and MnSe-TGA QDs, we could say that former system is more efficient than the later one. This can be due to a larger overlapping integral value of the CdSe based system over MnSe one.

Table 5.3: Different FRET parameters related to CdSe-TGA-BSA and MnSe-TGA-BSA systems

FRET Parameters	CdSe-TGA-BSA	MnSe-TGA-BSA
$J(\lambda)$ ($M^{-1}cm^{-1}nm^4$) (maxima)	2.8×10^{16}	5.89×10^{15}
R_0 (nm)	8.2	6.7
E_F	71%	61%
r (nm)	6.97	6.12

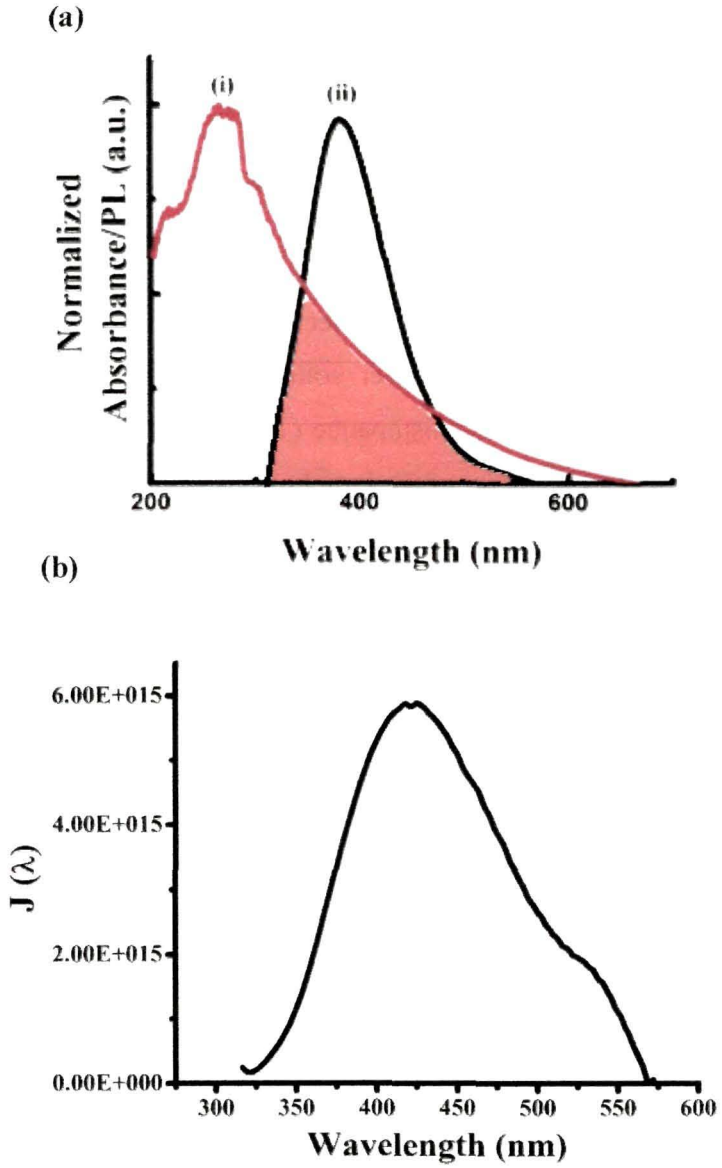

Figure 5.6: (a) Normalized (i) absorbance spectrum of BSA and (ii) PL spectrum of MnSe-TGA QDs, (b) the overlapping integral spectrum ($J(\lambda)$) vs. λ between the two spectra, which is expressed in $M^{-1}cm^{-1}nm^4$.

5.2 Cytotoxicity studies on CdSe-TGA and MnSe-TGA QDs

Undoubtly, the toxicity of QDs is the most complicated aspect today, in biomedical research which has not been resolved with absolute certainly. On one hand, the physical and chemical properties are different from one type of QDs to the other, the level of

toxicity is largely governed by their composition, structure, size, surface coating, charge, concentration etc.

5.2.1 Isolation, culture, and treatment of lymphocytes

The cytotoxicity effect of the CdSe-TGA and MnSe-TGA QDs were assessed by targeting isolated human lymphocytes, collected voluntarily. Anti-coagulated human blood was diluted with phosphate buffer solution (PBS) (v/v 1:1) followed by the formation of a 6 mL layer in 6 mL histopaque (1.07 g/mL). It was centrifuged at 400 g for 30 minutes, and prior collection of the lymphocytes from the buffy layer. The isolated lymphocytes were then washed with 2 mL PBS and 2 mL RPMI media following centrifugation steps separately, at 250 g for 10 minutes. The pelleted lymphocytes were then suspended in RPMI-1640, and the cell viability was checked by Trypan blue exclusion method using a hemocytometer. The lymphocytes with viability more than 90% were used for subsequent studies. Aliquots of 200 mL of isolated cells were cultured in RPMI supplemented with 10% heat-inactivated fetal bovine serum (FBS). Initially cells were incubated (at 37°C in 5% CO_2) for 4 h in RPMI-1640 without FBS. The cells were then treated as per requirements and then maintained with the inclusion of FBS for 8 h.

5.2.2 MTT [3-(4,5-dimethylthiazol-2-yl)-2,5-diphenyl tetrazolium bromide] Assay

Most of the recent evaluations of the toxicity of QDs are performed by using *in vitro* or *in vivo* assays. Among the most commonly used method *in vitro* studies is the MTT assay. This is a colorimetric technique which helps in evaluating the viability of live cells. The SDH (succinatedehydrogenase) from mitochondria of living cells is likely to reduce MTT to formazan, which is an insoluble purple precipitate that subsequently, redissolved in DMSO (dimethyl sufloxide) [11].

The cytotoxicity assay was performed by measuring the viability of cells according to the method described by Denizot and Lang [12]. Mitochondrial dehydrogenase of viable cells would cleave the tetrazolium ring of the yellowish MTT to insoluble purple formazan crystals. This is followed by dissolving the formazan crystals in a suitable solvent. 0.1% TGA was used as vehicle in which CdSe and MnSe-QDs were

suspended independently. The resulting purple solution was evaluated through spectrophotometrical means. An increase, or decrease in cell number resulted in a concomitant change in the amount of formazan formed, which would indicate the degree of cytotoxicity caused by the test material. Upon treatments, cells were treated with 1% of MTT for 2 h followed by dissolving the formazan crystals in solvent and measuring the absorbance of the solution at ~570 nm. The background absorbance was measured at ~690 nm and subtracted from the response at ~570 nm. The absorbance of control cells was set as 100% viability, whereas corresponding values of the treated cells were calculated as percentage of control.

5.2.3 Cytotoxicity assessment of synthesized QDs on lymphocytes

Since the lymphocytes are readily available without much difficulty, we intended to explore the influence of MnSe-TGA QDs on the cell viability. The study was carried out using different amounts of MnSe QDs. As can be noticed from Fig. 5.7(a), with the treatment of a 0.2 μM MnSe QDs (for 8 h), the lymphocyte cells sustain a maximal viability of 98.3%. Whereas, the cell viability, which was fairly uniform (~95%) upto a QD concentration of 0.5 μM, get drastically reduced with further increase of QD

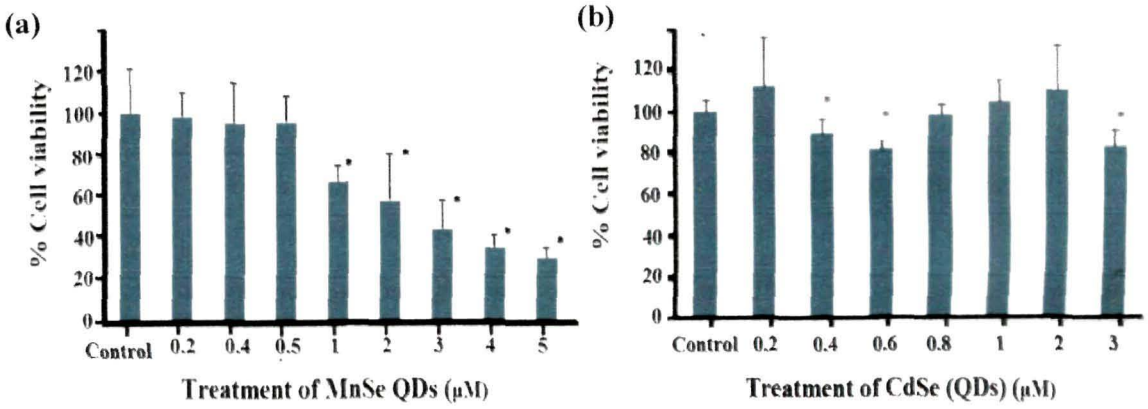

Figure 5.7: Effect of (a) MnSe-TGA QDs (b) CdSe-TGA QDs on lymphocyte cell viability assessed with the *MTT* assay (n_i=4). All the results were expressed as means±SD from four independent sets of experiments. Each of the columns reflect the cell viability. Results were statistically analyzed by student's *t*-test for significant difference between the group means using GraphPad software®. The significant difference between the experimental and the control group was set as *$p \leq 0.05$.

concentration. It may be noted that, the survival of maximum amount of cells is utmost necessary so as to explore cellular uptake mechanism and bioimaging response under select excitation. This calls for the use of MnSe QDs under a safe limit which could help minimizing the cytotoxicity and other environmental and health hazard issues. We speculate that, the safe limit in our case is below 0.5 μM. It is possible that, depending on the macromolecular structural organization of cells and the physiological state, the safe limit of using MnSe QDs might vary from one cell type to the other. For instance, healthy and disease affected cells including epithelial, epidermal, and epithermal cells etc. may necessarily not require similar concentration of QDs for exploiting safe cellular uptake process. Our MnSe QDs can have potential in cellular studies while using magnetic and emission responses collectively, unlike conventional systems where the use of simultaneous properties is quite limited [13].

Figure 5.7(b) depicts the cytotoxicity aspects of CdSe-TGA QDs when subjected to treatment on lymphocyte cells. It can be observed that, the cell viability vary randomly with QD concentration. Moreover, in some concentrations the cell viability goes above 100%. Unregulated growth and cell proliferation can cause such an abrupt behavior during adsorption of QDs through cytoskeleton region.

5.3 Fluorescence imaging study *in vitro*

At first Isolated lymphocytes were cultured in RPMI media and then supplemented with 10% FBS, in presence of different QDs. The cells were incubated at 37°C and in 5% CO_2 for 10 h. The lymphocytes were initially grown (without FBS) for 2 h, prior treatment with QDs. Imaging of different specimens was carried out independently under a fluorescence microscope.

Figure 5.8 shows a series of imaging snap-shots of lymphocyte cells treated with different types of QDs. All the bright-field and fluorescent images were highlighted through a number of panels, shown in Fig. 5.8 (a-h). Fig. 5.8(a) and (b) depict (CdSe-TGA) QD treated lymphocyte cells. The cellular uptake of CdSe-SDS QDs in the respective imaging modes can be found in Fig. 5.8(c) and (d).

Furthermore, we assessed the cellular uptake of the MnSe QDs. Fig. 5.8 (e) and (f) depict bright-field and fluorescent images of the cells treated with MnSe-TGA QDs.

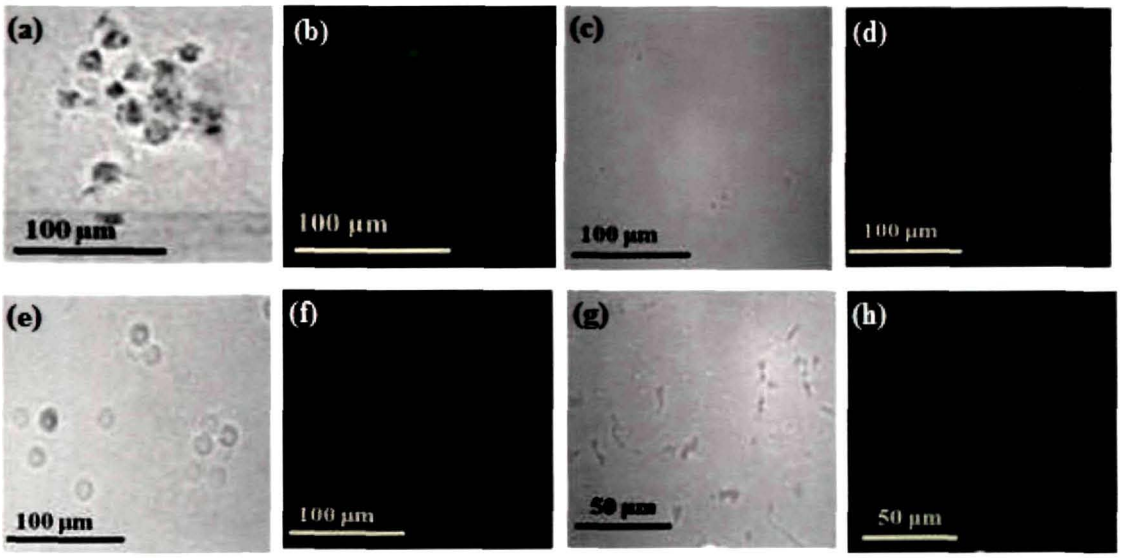

Figure 5.8: Bright-field imaging of lymphocyte cells with (a) CdSe-TGA (c) CdSe-SDS QDs. The fluorescent imaging mode (λ_{ex} = 300 nm) of the respective QDs in the cells is shown in (b) and (d). The bright-field and fluorescent (λ_{ex} = 300 nm) images of MnSe QDs coated by TGA ((e), (f)) and SDS ((g) (h)) are shown in lower panel.

The response of the MnSe-SDS QDs, in the respective modes are shown seen in the lower panel (Fig. 5.8 (g) and (h)). The photographs represent high biocompatibility and fluorescent behavior of QDs in the cellular environment. The bright-spots, in each of the fluorescent images, basically represent a number of QDs localized in the cellular membrane via. a site specific linkage. For instance, the head groups of the surfactant are highly accessible to the carboxyl functional groups of the membrane or membrane proteins of certain kind.

Using image J-1.46r[§] software® and following previous works reported elsewhere [14-16], one can make a quantitative assessment of the fluorescence count of the respective QDs (while present in the cellular environment). Figure 5.9 shows the selected area of interest and selected background area of fluorescent image of CdSe and MnSe QDs coated with TGA and SDS capping layers. The corrected total fluorescent (CTCF) intensity value was calculated for each case, using the relation given by,

[§] *Appendix-9*

CTCF= Integrated density – (Area × mean fluorescent of background setting) (5.6)

The integrated density of a fluorescent image is the sum of the values of the pixels in the selected regions of a definite photograph. As can be found in Fig. 5.9, different selected fluorescent areas are labeled as A, B, C, D.... etc. whereas the selected background regions (cell region without fluorescence) are represented as bk1, bk2, bk3.....etc. The average of mean gray value for the selected regions gives the value of mean fluorescence of background setting in the formula.

Figure 5.10 highlights the histograms of CTCF and integrated density (Int. Den.) of different QDs. It can be observed that with the fluorescence area, both the CTCF and Int. Den. vary to different degrees. In order to evaluate biocompatibility along and fluorescent behavior of the QDs, the average CTCF and average Int. Den. need to be compared (Fig. 5.11). As can be seen, TGA coated QDs posseses a stronger fluorescence response over SDS coated ones. The fluorescence efficiency gets quenched dramatically

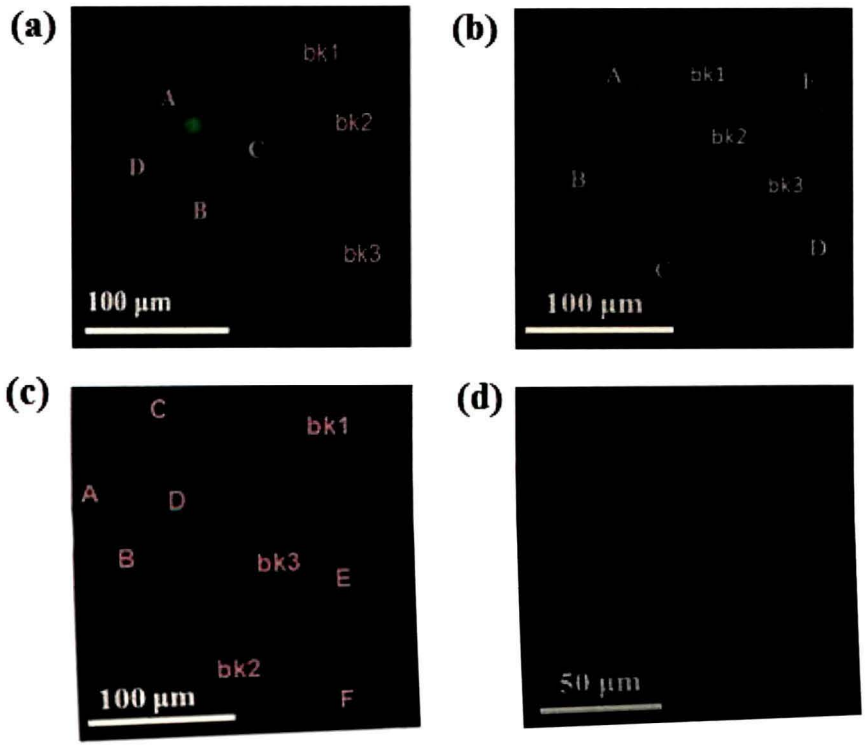

Figure 5.9: Selected fluorescent and background areas of fluorescent image of (a) CdSe-TGA (b) CdSe-SDS (c) MnSe-TGA (d) MnSe-SDS QDs while treated with the lymphocyte cells

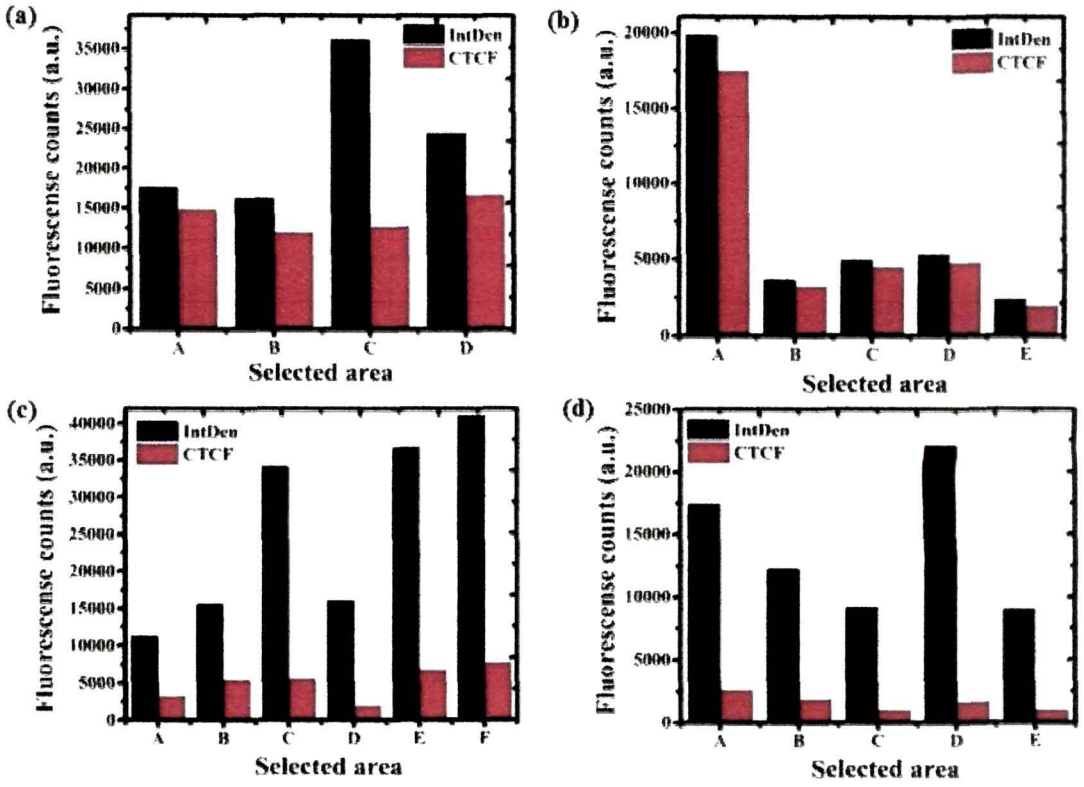

Figure 5.10: Histograms representing the fluorescence counts of (a) CdSe-TGA (b) CdSe-SDS (c) MnSe-TGA (d) MnSe-SDS QDs corresponding to different select fluorescent areas considering without (Int. Den.) and with (CTCF) background fluorescence.

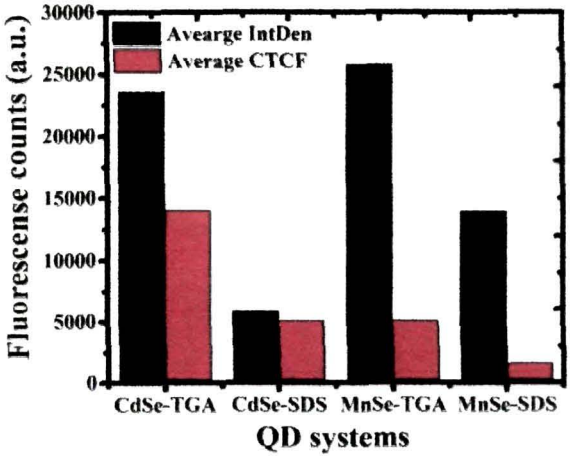

Figure 5.11: Histograms representing the average value of Int. Den. and CTCF of different types QD systems.

in case of SDS capping. To be specific, the fluorescent counts (CTCF) of TGA coated CdSe QDs is ~2.8 times larger than the SDS coated counterpart. Similarly, MnSe-TGA QDs are characterized by a stronger fluorescence capability (by factor of ~3.24) as compared to the MnSe-SDS QDs.

As already discussed in *Chapter* 3, a higher optical stability of MnSe QDs in cell culture media can be generated when BSA is added as a dispersing agent. The higher optical stability of the QDs in presence of BSA, is because of adsorption of protein into the QDs surfaces which is likely to dependent on the constituents of the cell culture

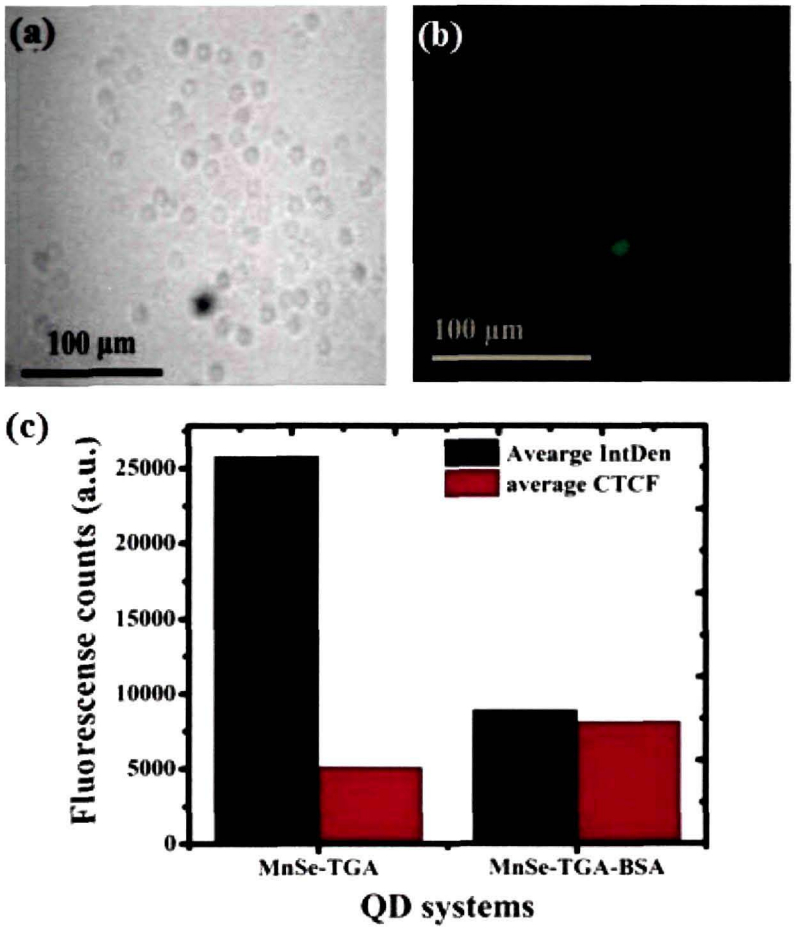

Figure 5.12: (a) Bright field and (b) fluorescent field (λ_{ex} = 300 nm) imaging of lymphocyte cells using MnSe TGA QDs while considering BSA as a dispersing agent. Whereas, (c) represents the histograms of average Int. Den. and CTCF corresponding to MnSe-TGA QDs in absence and presecnce of dispersing agent BSA.

media. As the albumin protein is the most abundant protein in the blood plasma, the knowledge of adsorption of albumin to QD surfaces is very much useful. We have explored the biocompatiblity and fluorescent imaging capability of MnSe-TGA QDs in lymphocyte cells using BSA as a dispersing agent. Fig. 5.12(a,b) shows the bright-field and fluorescent images of MnSe-TGA QDs while considering BSA as a dispersing agent. It is quite apparent that, BSA has a remarkable stand with regard to a better QD dispersity and fairly homogeneous cellular uptake in comparison to the case of non use of BSA (Fig. 5.8(f)). The effect of BSA could be clearly visualized by a superior QD fluorescence over the MnSe-TGA one (Fig. 5.12). The fluorescence capability of MnSe-TGA QDs gets enhanced by a factor of ~1.6 when BSA was used as a dispersing agent (Fig.5.12(c)). The adsorbed protein in the QD surfaces is likely to alter the cellular uptake capability. Thus, the cellular uptake and bioimaging aspects are significantly affected by the nature of surface functionalization and use of a dispersing agent. Note that, modification through surface capping would change the zeta potential of the QD systems which is also capable of altering the cellular uptake response [17]. Thus, it is possible to localize the NPs/QDs to specific intracellular targets (lysosomes, cytoplasm, mitochondria etc.) by modifying their surface (functional) property [17].

5.4 Imaging of MnSe QDs in live cells

The cellular uptake of QDs and the distribution arrangement of MnSe QDs within the cell bodies were also analyzed through confocal microscopy. By staining cells with QD labeling, one can visualize the cytoskeleton of the cells and can analyze the distribution of the QDs fluorescence intensity within the cell.

For confocal microscopy experiments the cell culture procedure and injection of QDs into cells are as described below.

5.4.1 Cell culture and QD treatment

NIH-3T3 cells were first cultured in M28 flasks with DMEM as media which is mixed with 10% v/v FBS in a 5% CO_2 in humidified atmosphere at 37° C. Since the cells experience very fast growth and degeneration, the media was supplemented by 100 μg/ml penicillin-streptomycin (Gibco). After careful microscopic inspection, the medium was

changed twice a week and new cell lines were accessed with an appropriate dilution of the main sample (ratio of 1:8). For cell detachment, 1 ml, 0.25% trypsin plus 1 mM ethylenediaminetetraacetic acid (EDTA) was added to the flask followed by incubation upto 10 min. The cells were recollected after centrifugation for 4-5 minutes. Pipetting was considered in fresh media. The cultured cells were then made ready in petri dishes.

A few circular Petri dishes with cover slip fixed at the bottom (VWR) were sterilized before sub culturing of cells. Then 0.1 g/ml collagen was spread over the inner cover slip region by using a micropipette. The dishes were exposed to UV light for 40 min. followed by washing with the phosphate buffer several times. About ~100 µl of cell line was gently placed into the collagenated region. The dishes containing cells were then incubated for 15 min. for cell adhesion. Then sufficient media was added to each of the dishes so as to make them healthy. The specimen were kept undisturbed in 95% air and 5% CO_2 atmosphere, for 24 h.

On the day of imaging study, the cell lines were taken out from the incubator and the excess media was removed with the help of a suction pump. Then the MnSe QDs solution (10^{-10} µg/µl) was injected into the central region of the disc containing cells. The cells were incubated for 30 min in 5% CO_2 atmosphere. The cells were taken out from the incubator and the excess QDs and the media were washed out with the help of phosphate buffer solution. Fresh media is now transferred to the disc containing cells followed by incubation for 15-20 min.

5.4.2 Live cell imaging after QD-treatment

Figure 5.13(a-c) shows the bright-field, fluorescent and phase contrast (bright + fluorescent) microscopic images of NIH-3T3 cells treated with MnSe-TGA QDs. From the figure it can be observed that a large no. of QDs exist in the perinuclear region i.e in the cytoplasm of the cell, while only a small number of QDs are found in the nuclear membrane region, or across the nuclear boundary. The fluorescent intensity histogram (Fig. 5.13(d)) gives a clear indication of presence of different number of fluorescent MnSe-TGA QDs inside the cell. As can be expected, the average CTCF of the QDs in the nuclear membrane is nearly half than the value at the cytoplasm. This could be due to the fact that the nuclear membrane thickness is almost double than the lipid bilayer

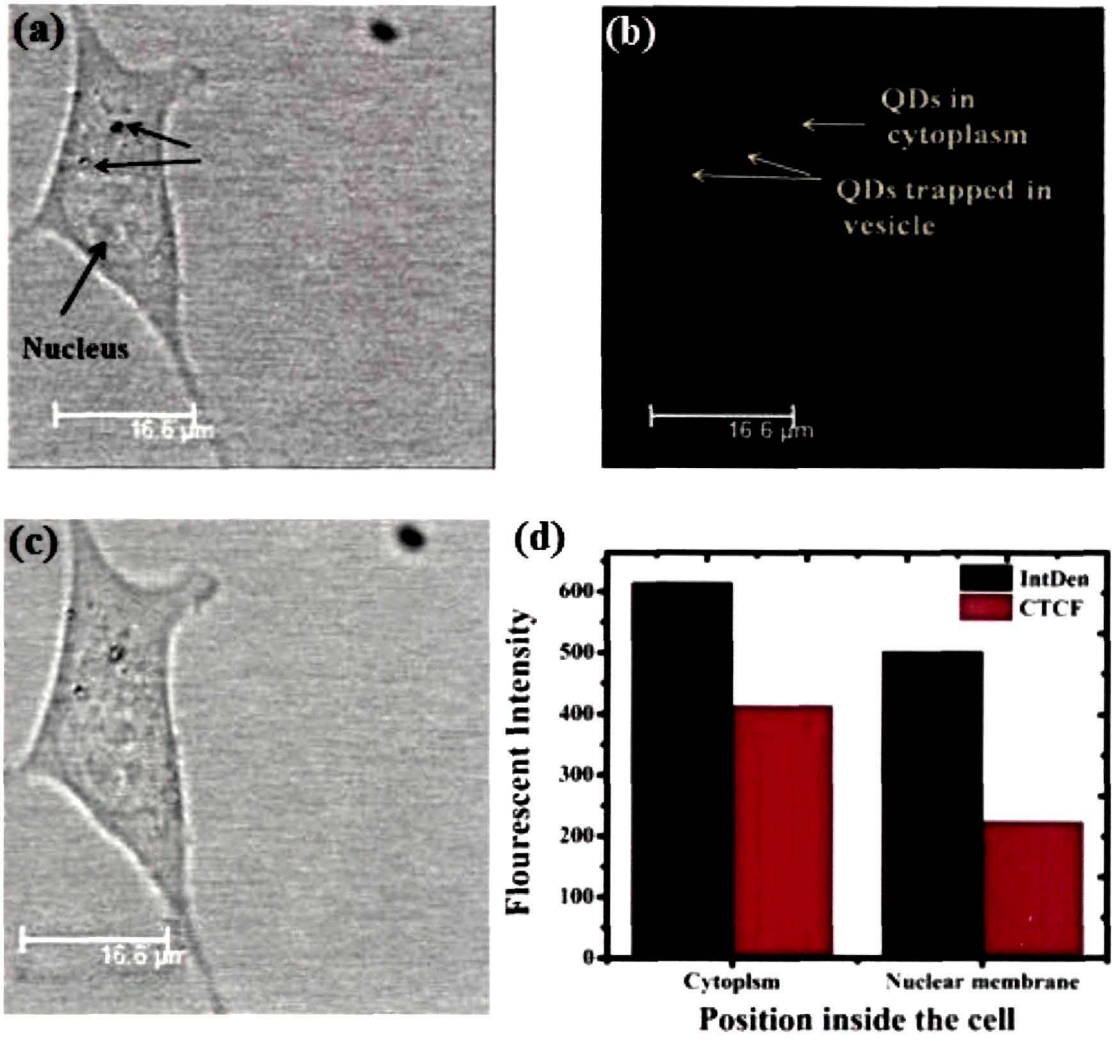

Figure 5.13: (a) Bright field (b) fluorescent Field (c) Composite field image of 3T3 cell treated by MnSe-TGA QDs (d) depicts the fluorescent counts of MnSe TGA QDs inside NIH 3T3 cell

membrane. A larger fluorescence contribution, by the QDs in the cytoplasm area over the nuclear region was also predicted by other researchers [18]. The minimal probability of getting QDs localized across the nuclear boundary region, is due to the movement of some vesicles to the nuclear membrane region inside which the QDs get trapped [19]. Note that, the uptake of NPs by cells can be viewed as a two-step process: first a binding step at the cell membrane and second as the internalization step [20]. The attachment of

the particles to the cell membrane, in first step seems to be mostly affected by the surface charge of the particles. When a negatively charge QD, like MnSe-TGA is attached to the cell, they are repelled by the negatively charged cellular membrane. As soon as they get repelled, the negatively charged NPs bind at some cationic sites of the cells in the form of clusters. This is followed by reduction of charge density of them and favors adsorption of more free NPs. Thus, the high cellular uptake of negatively charged NPs is related first to the non specific process of NPs adsorption on the cell membrane and second to the formation of NPs clusters [17, 20]. The two steps adsorption, of anionic superparamagnetic nanoparticles by HeLa cells, has been reported by Wilhelm et al [20].

The observed fluorescent intensity near the nuclear boundary region suggests that, our MnSe-TGA QDs are likely to mediate through macropinocytosis mechanism inside the 3T3 cells, after adsorption on the cell membrane. A Similar behavior has been observed for carboxylic acid coated QD uptake by breast epithelial cells [21].

Furthermore, we have observed also the change of intensity of QDs with time when they are trapped inside the vesicle like structures (selected regions: **ROI1, ROI2, ROI3) and in cytoplasm region (selected regions: ROI4, ROI5). Imaging was conducted for 15 sec. with an imaging speed of 13.7 frame/sec. It can be seen that the QDs intensity unit in cytoplasm (ROI4, ROI5) significantly remain higher with time (Fig. 5.14(c)) compared to when they are trapped inside vesicles like structures. Earlier, the reduction of fluorescence intensity of QDs after being entrapped inside the vesicle like structure has been reported [22,23]. Acidic environment along with protein adsorption, generating free radicals of the QDs inside these structures may lead to the quenching of fluorescence as compared to the QDs found in the cytoplasm [22]. Moreover, the variation of oxygen species may also contribute to this phenomenon [22].

** Region of interest: ROI

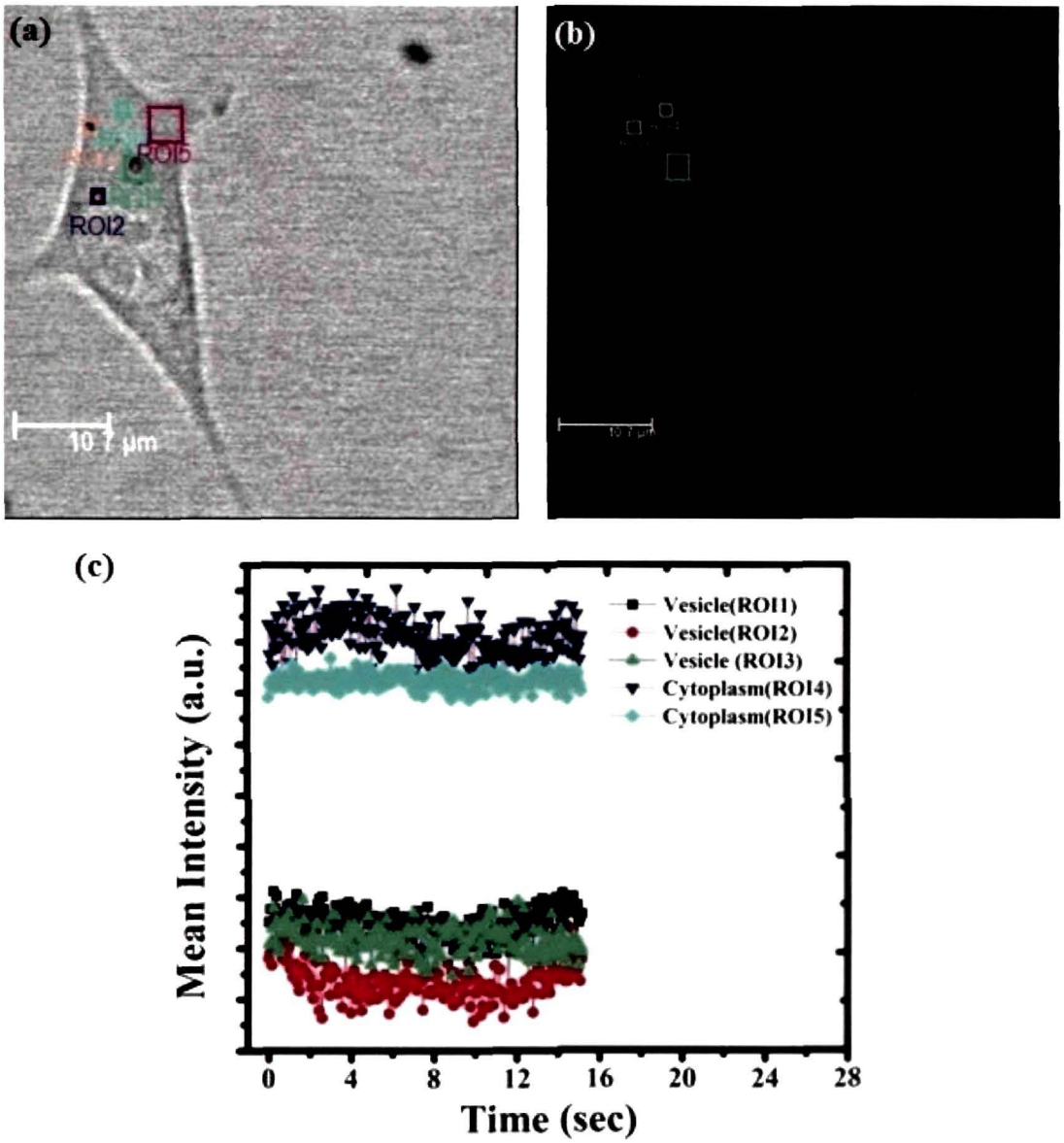

Figure 5.14: Selected regions in cytoplasm and vesicle structure of 3T3 cell occupied by MnSe-TGA QDs is shown in (a) bright field (b) fluorescent Field (c) depicts the variation of mean fluorescent intensity of the QDs when they are in the respective positions.

References

[1] Poderys, V., et al. Interaction of water-soluble CdTe quantum dots with bovine serum albumin, *Nanoscale Res. Lett.* **6**, 9, 2011.

[2] Mohanta, D., et al. Time-resolved photoluminescence decay characteristics of bovine serum albumin-conjugated semiconductor nanocrystallites, *J. Exp. Nanosc.* **4**(2), 177--191, 2009.

[3] Clapp, A. R., et al. Can luminescent quantum dots be efficient energy acceptors with organic dye donors?, *J. Am. Chem. Soc.* **127**(4), 1242--1250, 2005.

[4] Medintz, I. L. & Mattoussi, H. Quantum dot-based resonance energy transfer and its growing application in biology, *Phys. Chem. Chem. Phys.* **11**(1), 17--45, 2009.

[5] Shivkumar, M. A., et al. FRET from CdSe/ZnS core-shell quantum dots to fluorescein 27 dye, *Open J. Phys. Chem.* **3**(1), 40--48, 2013.

[6] Clapp, A. R., et al. Fluorescence resonance energy transfer between quantum dot donors and dye-labeled protein acceptors, *J. Am. Chem. Soc.* **126**(1), 301--310, 2004.

[7] Jones, M., et al. Quantitative modeling of the role of surface traps in CdSe/CdS/ZnS nanocrystal photoluminescence decay dynamics, *Proc. Natl. Acad. Sci.* **106**(9), 3011--3016, 2009.

[8] Lefebvre, P., et al. Dynamics of photoluminescence in medium-size CdSe quantum crystallites, *Semicond. Sci. Tech.* **12**(8), 958, 1997.

[9] Iqbal, A., et al. Orientation dependence in fluorescent energy transfer between Cy3 and Cy5 terminally attached to double-stranded nucleic acids, *Proc. Natl. Acad. Sci.* **105**(32), 11176--11181, 2008.

[10] Qi, Z.-D., et al. Biocompatible CdSe quantum dot-based photosensitizer under two-photon excitation for photodynamic therapy, *J. Mater. Chem.* **21**(8), 2455--2458, 2011.

[11] Qu, Y., et al., Preliminary biocompatible evaluation of nano-hydroxyapatite/polyamide 66 composite porous membrane, *Int. J. Nanomedicine*, **5**, 429--435, 2010

[12] Denizot, F. & Lang, R. Rapid colorimetric assay for cell growth and survival: modifications to the tetrazolium dye procedure giving improved sensitivity and reliability, *J. Immunol. Methods*, **89**(2), 271--277, 1986.

[13] Sarma, R., et al. Physical and biophysical assessment of highly fluorescent, magnetic quantum dots of a wurtzite-phase manganese selenide system, *Nanotechnology*, **25**(27), 275101, 2014.

[14] Burgess, A., et al. Loss of human Greatwall results in G2 arrest and multiple mitotic defects due to deregulation of the cyclin B-Cdc2/PP2A balance, *Proc. Natl. Acad. Sci.*,**107**(28), 12564--12569, 2010.

[15] Gavet, O. & Pines; J. Progressive Activation of CyclinB1-Cdk1 Coordinates Entry to Mitosis, *Dev. Cell* **18**(4), 533--543, 2010.

[16] Potapova, T. A., et al. Mitotic progression becomes irreversible in prometaphase and collapses when Wee1 and Cdc25 are inhibited, *Mol. Biol. cell* **22**(8), 1191--1206, 2011.

[17] Patil, S., et al. Protein adsorption and cellular uptake of cerium oxide nanoparticles as a function of zeta potential, *Biomaterials* **28**(31), 4600--4607, 2007.

[18] Danner, S., et al. Quantum dots do not alter the differentiation potential of pancreatic stem cells and are distributed randomly among daughter cells, *Int. J. Cell Biol.* **2013**, 918242, 2013.

[19] Sakhtianchi, R., et al. Exocytosis of nanoparticles from cells: Role in cellular retention and toxicity, *Adv. Coll. Inter. Sci.* **201–202**, 18--29, 2013.

[20] Wilhelm, C., et al. Intracellular uptake of anionic superparamagnetic nanoparticles as a function of their surface coating, *Biomaterials* **24**(6), 1001-1011, 2003.

[21] Xiao, Y., et al. Dynamics and mechanisms of quantum dot nanoparticle cellular uptake, *J. Nanobiotech.*, **8**, 13 2010.

[22] Generalov, R., et al. Entrapment in phospholipid vesicles quenches photoactivity of quantum dots, *Int. J. Nanomedicine* **6**, 1875--1888, 2011.

[23] Faklaris, O., et al. Photoluminescent diamond nanoparticles for cell labeling: study of the uptake mechanism in mammalian cells, *ACS nano* **3**(12), 3955--3962, 2009.

CHAPTER- 6: Application in Electrophysiology: Micropore formation, Lipid extraction and Ion channel Recording

CHAPTER 6

Application in Electrophysiology: Micropore formation, Lipid extraction and Ion channel Recording

Ion selectivity, ion conduction, and ion channel activation are generally characterized by electrophysiological experiments such as, patch clamp and planar chip technology [1-3]. However, the later technique (which is based on solid supported bilayer experiment) is found to be advantageous over traditional patch-clamp one owing to viable cost, preparatory conditions, simplicity of design, high reliability, versatility along with fast data acquisition [4,5]. The ion channel studies, in real cells, are generally based on patch-clamp techniques [3] whereas the practice of planar chip method is relatively new and is limited to artificial bilayers only [5,6]. The artificial bilayer membrane can be used as a model system to explore transient nanopore creation in presence of a field. On the other hand, in planar chip technique, the ion channel response, is largely dominated by thermal and electromagnetic noises along with the effective bilayer capacitance arising due to characteristic properties of the solid substrates. Thus, a stable bilayer (with a low effective bilayer capacitance) along with reduced thermal and electromagnetic noises (arising from the surrounding environment) is highly desirable for a superior ion channel experiment. Note that, a substrate having a good mechanical and thermal stability is only capable of supporting a stable bilayer. In addition, the substrate material should contribute only weakly to the effective bilayer capacitance. This is possible only if one works with a thick and low dielectric constant material. A small area of the electrolytic chamber can also offer an added advantage.

In this chapter, we touch upon appreciable conditions for ion channel measurement across a stable bilayer. Moreover, we highlight several useful techniques for obtaining micropores (apertures) of different desired diameters. An emphasis is also given to explore the possibility of reducing the effective bilayer capacitance and theoretical electromagnetic noise. A qualitative as well as quantitative analogy of several materials (e.g., Teflon (PTFE), Polypropylene (PP), Polystyrene (PS), Cellulose Acetate (CA), Polyethylene terephthalate (PET), Poly (methyl methacrylate) (PMMA), Quartz, Glass, Mica and Silicon) have been worked out on a comparative basis.

The micropore formation, lecithin extraction, lipid bilayer formation around the micropore are discussed along with the whole electrophysiology set up. Finally we

demonstrate CdSe QD induced ion channels across the soy-extracted lecithin bilayer. The experimental results are then analyzed in the light of simple theoretical models on nanopore creation by the aggregated QDs.

6.1 Dielectric noise and effective capacitance

The conductance fluctuation, across a solid-supported reconstituted phospholipid bilayer, provides the desired testimony in support of single ion channel events. As compared to the traditional patch clamp method, the planar chip technique has an improved experimental design, accessibility and precision control. However, the utility of planar bilayer method for studying single ion channel dynamics is limited primarily because of background current noise [7-9]. By suppressing rms noise, it is possible to resolve the small single-channel conductance states along with the fast gating dynamics. Moreover, by determining the individual sources of noise, it is now possible to create an environment for selective ion channel measurement. It may be noted that, in the planar chip technique, a bilayer is supported on the micropore located at the centre of the substrate material.

The nature of thermal energy dissipation results in thermal noise from the dielectric material and this type of noise is also known as dielectric noise. The power spectral density of dielectric noise, $S_D^2(f)$ and the rms dielectric noise, $I_D(f_c)$ can be expressed as [5]:

$$S_D^2(f) = 8\,\pi kTD_f C_D f \tag{6.1}$$

$$I_D(f_c) = 2\,(kTD_f C_D\,\pi c_1)^{1/2} f_c \tag{6.2}$$

where, k is the Boltzmann constant (1.38×10^{-23} J K^{-1}), D_f is the dissipation factor of the material, C_D is the capacitance of the dielectric, $c_1=1.3$ for a noise source with a power spectral density that grows linearly as a function of frequency f, and f_c is the cut-off frequency. Although the dissipation factor is frequency dependent, it has a constant value in the frequency range between 1 kHz and 100 kHz [5, 10]. The dissipation factor, D_f is contributed by the nature of the substrate, electrode holders etc. and they contribute unequally to the magnitude of C_D in eqn. 6.2. In the present work, we consider D_f as the dielectric loss of the substrate material (in which the pore is fabricated) which

significantly contributes to C_D. In the eqns. 6.1 and 6.2 therefore, it is reasonable to replace C_D with C_{se}, where C_{se} is the substrate capacitance. The capacitance of this substrate material is given by:

$$C_{se} = \frac{\varepsilon_r \varepsilon_0 A}{t_s} \tag{6.3}$$

where, A is the area of the substrate material; ε_r is the dielectric constant of the substrate material; ε_0 is the permittivity of free space ($\varepsilon_0 \approx 8.854 \times 10^{-12} F\ m^{-1}$); and t_s is the thickness of the substrate material.

In an electrophysiology experiment, the accuracy of temporal change of current flowing through the pore is determined by the signal bandwidth. To obtain a high bandwidth of the signal, the accessible parameter that could be adequately minimized is the total effective capacitance. The total capacitance can be expressed as [5]:

$$C_t = C_m + C_{se} + C_{el}, \tag{6.4}$$

where, C_{el} is the capacitance of the immersed electrode (~10 pF) [5] and membrane capacitance C_m can be written as:

Table 6.1: Physical properties of the substrate materials

Sl. No.	Substrate	Dielectric constant (ε_r)	Dissipation Factor (D_f)	Density (ρ) (g/cm^3)	Thermal Conductivity (K) (W/m/K)	Melting point (T_m) (°C)	Young's modulus (Y) (Gpa)
1	PTFE	2.1	8×10^{-4}	2.12	0.26	327	0.5
2	PP	2.2	3×10^{-4}	0.95	0.1-0.22	165	1.5-2
3	PS	2.5[11]	1×10^{-4}	1.06	0.14	240	3-3.5
4	CA	2.9	13×10^{-4}	1.28	0.16-0.36	159.02	2.4-4.1
5	PET	3.1	16×10^{-4}	0.98	0.24	260	2-2.7
6	PMMA	3.6	15×10^{-4}	1.17	0.20	140	3.4
7	Quartz	3.8	0.1×10^{-4}	2.21	1.36	1650	71.7
8	Borosilicate glass (Corning 7760)	4.5	0.0017	2.3	1.1	820	45
9	Mica	6.2	0.001	2.8	0.71	1340	60
10	Silicon	11.8[12]	0.032	2.32	150	1410	70

$$C_m = C_s \frac{\pi}{4} d_p^2 \tag{6.5}$$

Here, C_s and d_p signify specific capacitance of the bilayer and diameter of the pore; respectively. For the sake of simplicity, one can ignore the electrodes contribution in the electrophysiological recording experiment [10]. Some of the physical properties of the bilayer supporting solid materials are given in Table 6.1.

6.1.1 Effect of micro pore size on the bilayer membrane capacitance

An aperture located on the substrate, generally supports a reconstituted phospholipid bilayer. Beyond a critical diameter of the aperture, the lipid bilayer membrane is likely to rupture when subjected to a small mechanical and electrical disturbance. This is because of the ultra thin nature (~4 nm) of the phospholipid bilayer membrane [13]. The selection of a suitable micropore diameter would help not only in providing low membrane capacitance but also higher mechanical stability.

Fig. 6.1 represents a characteristic plot of membrane capacitance vs. pore diameter of the substrate material (eqn. 6.5). The membrane capacitance increases steadily with increase in pore diameter, while considering a constant specific capacitance (C_s) of 0.5 μF /cm^2 [4]. It can be seen that, for a pore diameter within a range of ~10-100 μm, the membrane is characterized by a very low capacitance in the range of ~0.4-40 pF. In reality, a pore size of ~10-40 μm could raise difficulty in safe handling with the

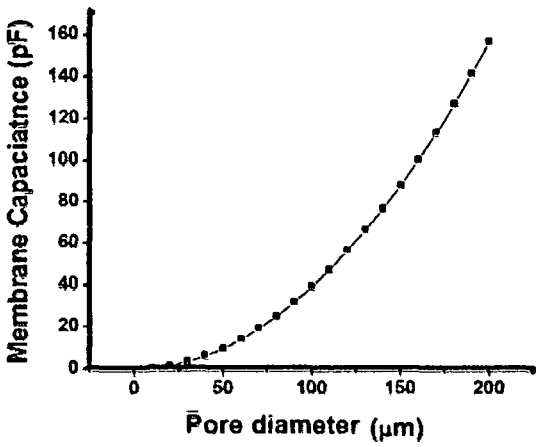

Figure 6.1: Membrane capacitance as a function of pore diameter

suspended bilayer. The bilayer, with pore diameter in the range of ~40-100 μm, however, gives moderate capacitance values (~7-40 pF). On the other hand, the membrane capacitance can be significantly large (~40-156 pF) as for considering pores of larger diameter (~100-200 μm).

For the sake of convenience, the pore diameter ~80-100 μm is generally recommended which accounts for fairly moderate values of capacitance (~25-40 pF). The significance of using planar chip technology within this range of diameter is also highlighted by various workers [10, 14]. Since, the overall idea is to suppress the effective capacitance, the contribution of the substrate capacitance should be smaller, or comparable to the bilayer capacitance value (~25-40 pF). The selection of a good substrate candidate, with a desired dimension, would certainly help in acquiring a low value of effective capacitance. The variation of substrate capacitance for different substrate candidates is discussed below.

6.1.2 Parameters which have direct influence on the substrate capacitance

As expected, the stability and the effective capacitance of the reconstituted lipid bilayer depend mainly on the area of the electrolytic chamber created, thickness and dielectric constant of the substrate material used in the electrophysiology study.

Fig. 6.2 represents the variation of substrate capacitance as a function of electrolytic area created on different substrate materials of finite thickness. In most of the electrophysiological experiments, the desired thickness of the substrate varies between ~150 to 300 μm [2, 5]. It can be observed from the Fig. 6.2 (a) that for a constant area of ~0.78 cm^2 (corresponding to an electrolytic chamber of dia ~1 cm), PTFE material has a very of low value capacitance (≤9 pF), when thickness is varied within 150-300 μm. However, working with such a small area is extremely difficult in real situations. An area of the order of ~1.76 cm^2 (dia ~1.5 cm) is also characterized by a low capacitance (~10-21 pF). But for a larger electrolytic area of ~ 4.8 cm^2 (dia ~2.47 cm), the capacitance is quite high (~29-60 pF). This clearly indicates that, PTFE could provide a capacitance value smaller than the bilayer capacitance value and for an effective area of ~1.76 cm^2 and substrate thickness ~150-300 μm. Moreover, materials such as PP, PS, also give smaller values of capacitances (~11-22 pF, ~12-26 pF, ~15-30 pF), as compared to the

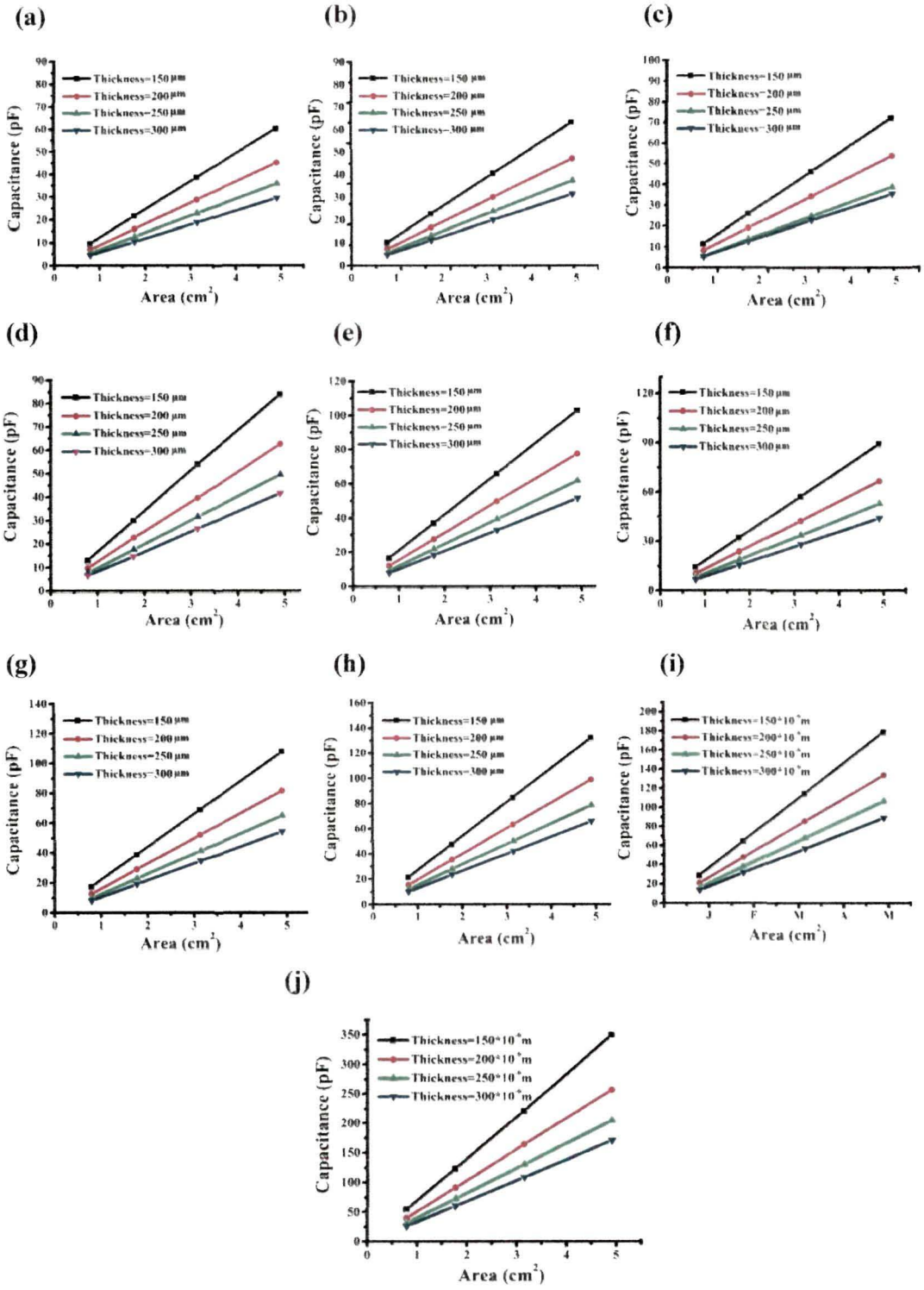

Figure 6.2: *C* vs. *A* for (a) Teflon (b) Polypropylene (PP) (c) Polystyrene (PS) (d) Cellulose acetate (CA) (e) Polyethylene terephthalate (PET) (f) Poly (methyl methacrylate) (PMMA) (g) quartz (h) glass (i) mica (j) silicon

bilayer capacitance for an electrolytic area of ~1.76 cm^2 (Fig. 6.2 (b)-(d)). In contrast, as shown in Fig. 6.2(e)-6.2(h), the respective capacitance response of the substrate materials such as, PET, PMMA, quartz and glass (for an area of ~1.76 cm^2 and substrate thickness ~150-300 μm) predict capacitance values in the range of ~16-31 pF, ~18-37 pF, ~19-38 pF, and ~23-46 pF. Note that the lower end capacitance values (150 μm thick substrate) are comparable to the bilayer capacitance (25-40 pF for an aperture of dia ~80-100 μm). However, as can be observed from the Fig. 6.2 (i) and (j), substrates like silicon and mica would show larger values of capacitances (~31-64 pF and ~62-123 pF) as compared to the corresponding bilayer capacitance.

It is now apparent that, with materials like polymers, glass and quartz one can obtain effective capacitance comparable to the bilayer capacitance while a proper choice is made on electrolytic area and substrate thickness. We anticipate that an electrolytic area of ~1.76 cm^2 (dia. ~1.5 cm) and substrate thickness of ~150 μm are suitable choices for achieving a reduced effective capacitance without losing the bilayer stability. The viable choice could provide a means for better physical handling of the electrophysiology set-up.

Shown in Fig. 6.3 is the variation of the substrate capacitance with the dielectric constant of the substrate candidates for a definite electrolytic area (~1.76 cm^2) and substrate thickness (~150 μm). As can be found that, PTFE has the lowest capacitance (~21 pF) value owing to its small dielectric constant. On the other hand, polymers (PP,

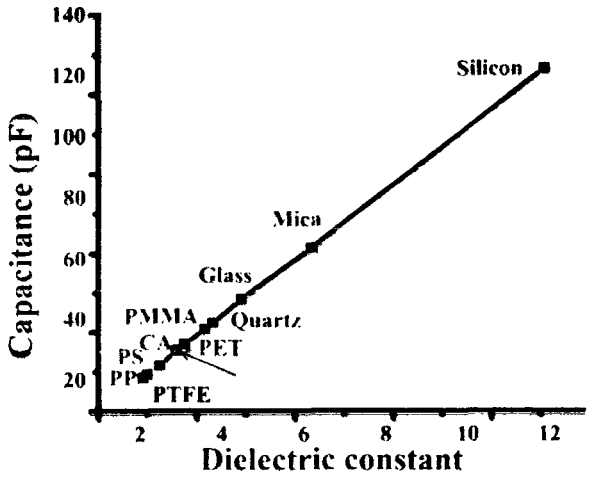

Figure 6.3: Capacitance vs. dielectric constant of the substrates

PS, CA, PET, and PMMA), show relatively low values of capacitances (~22-37 pF), while glass and quartz exhibited moderate values in the range ~39-47 pF. Materials with higher dielectric constant values, for instance, silicon (~63.9 pF) and mica (~122.5 pF) are associated with a very larger value of capacitance. Although substrate with a small dielectric constant can be opted, however, glass and quartz are generally considered owing to higher mechanical strength and thermal stability (see, Table 6.1).

6.1.3 Dielectric noise caused by the substrate materials

In a typical electrophysiology experiment, generally ion channel proteins are generally inserted across a reconstituted phospholipid bilayer. In order to record the current fluctuation due to insertion of ion channel proteins, it is desirable that the bilayer supporting substrate (planar chip) posses a good dielectric response with a minimal signal attenuation. Since the current fluctuation occurs in tens of pA level, rms noise should be much lower to help detecting and isolating actual current burst signals. In this context, low dissipation factor (D_f) of the substrate is highly desirable. This would facilitate the detection of single ion channel events while recording current bursts in the electrophysiology setup.

Fig. 6.4 (a) depicts the variation of rms dielectric noise with dissipation factor (dielectric loss) of the respective substrate materials for a constant cut-off frequency (f_c= 10 kHz) and constant substrate capacitance comparable to the bilayer capacitance (~20

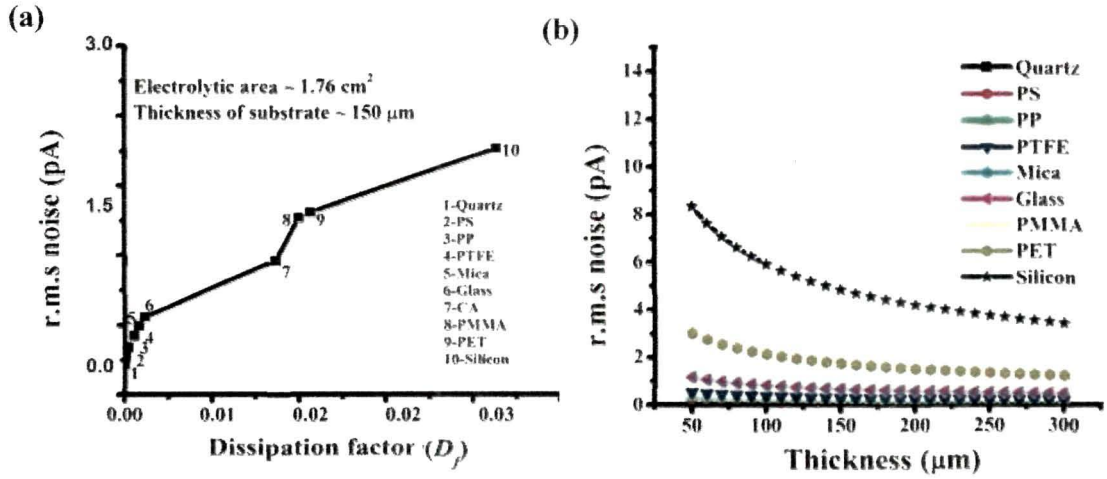

Figure 6.4: Dielectric noise vs. (a) dissipation factor and (b) thickness of the substrate materials

pF) (eqn. 6.2). For instance, ~150 μm thick PTFE exhibits this order of capacitance, for an electrolytic area ~1.76 cm^2. It can be observed that quartz possesses extremely low value of dissipation factor and thus, associated with a very low rms dielectric noise (~0.03 pA). Similarly, polymers (PS, PP, PTFE), mica, glass, CA are characterized by fairly small values of noise (~0.11-1 pA). On the other hand, it can be seen that polymers like PMMA and PET exhibit moderate values of rms noise (~1.4-1.45 pA). Conversely, silicon deals with a relatively higher rms dielectric noise compared to the above mentioned substrates (~2.05 pA). Moreover, it can be observed that the dielectric noise has an exponentially decreasing trend with the increasing thickness of the substrate materials (Fig. 6.4 (b)). The materials e.g., quartz, mica, glass and polymers (PTFE, PS, PP) are characterized by a very low dielectric noise (~0.04-0.48 pA) when the thickness varies between ~150 and 300 μm.

From the present discussion, one can say that in order to the support a mechanically stable lipid bilayer, appreciable range of diameter of the aperture can be ~80-100 μm (C_m ~25-40 pF), while working area and the thickness of the substrate are ~1.76 cm^2, and ~150-300 μm; respectively. Moreover, it is found that, materials having a low to moderate dielectric constant like polymers (PTFE, PP, PS, CA, PET, PMMA), quartz and glass were found to exhibit effective capacitances comparable to the bilayer capacitance (~25-40 pF). Though, glass and quartz provide higher capacitances compared to the polymers, the former is more advantageous owing to better mechanical strength and thermal stability. However, glass and quartz can be more attractive over other candidates owing to low values of dielectric noise. In addition, optical transparency in the visible to IR range would serve as an added advantage for simultaneous electrical and optical recordings. On the contrary, the use of silicon and mica is limited due to high dielectric constant (and hence, high capacitance values) even though they possess good mechanical strength.

6.2 Micropore formation on substrate material

The purpose of creating a micropore on the substrate is to use it in planar chip set-up, where two electrolytic chambers are isolated by an artificially reconstituted bilayer. There are a number of different techniques that can be employed to create micropores in

selectively chosen solid substrates. The techniques of making an aperture include, micro-drilling, spark assisted [15-17], laser ablation [18,19], *e*-beam [5, 20], and methods etc.

6.2.1 Spark assisted technique

The spark assisted (SA) method is generally employed owing to its cost-effectiveness and simplicity in design/assembly consideration. We made an attempt to create micropores on the ~150 μm thick chip (coverslip) made of borosilicate glass. The schematic of the set-up used for the SA method is shown in Fig. 6.5(a).

Materials used in the experiments are

(i) Induction coil (Model 25 M.M.SPARK, applied voltage 12 V) which was used to maintain a high voltage across the electrodes.

(ii) Electrically insulating coverage around the cover slip that separates two electrodes

(iii) Two needle shaped electrodes: one of graphite (tip diameter ~500 μm) and other of silver (tip diameter ~500 μm).

(iv) One screw gauge (least count: 0.01 mm, Mitutoyo Co.) for adjusting the air gap between the two electrodes.

(v) Suitable DC power supply (~12 V max.)

First, all the components were kept on a vibration free table. With the help of a screw gauge, an air gap of ~10 μm is established between the two electrodes along a vertical configuration. The surrounding area of the chip was made insulated with an insulating cover to minimize the scattering. The electrodes were subjected to a 12 V DC supply with the help of an induction coil that is capable of generate a high voltage spark across the tips of the electrodes, consequently an aperture of definite dimension is created on the substrate due to breakdown through electrically insulating region. This is equivalent to plasma arc discharge through the insulating media. We considered forming micropores with this arrangement, without and with thinning procedure. For thinning, 6N NaOH solution was used over 6 h in the cover slip followed by generation of spark across the thinned area make aperture.

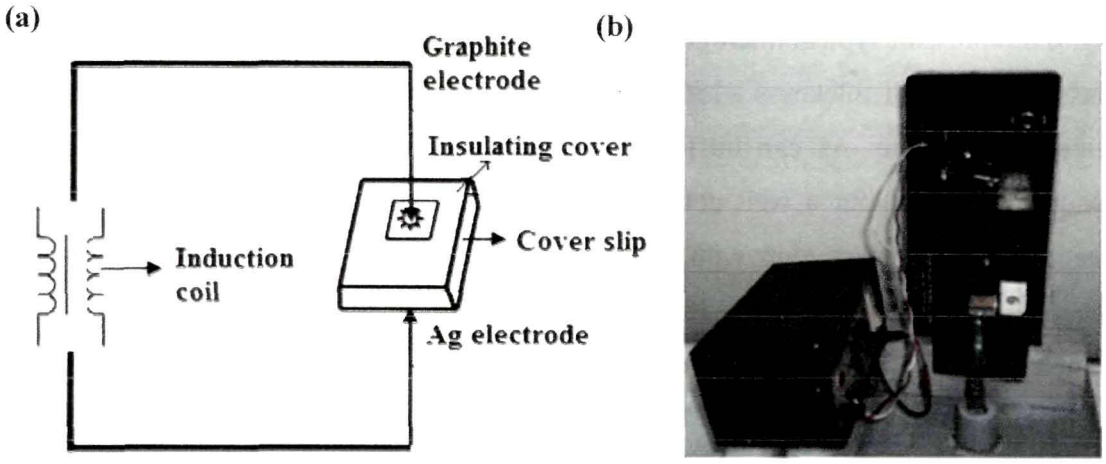

Figure 6.5: (a) Schematic of the spark assisted setup for creating micropore (not to scale) (b) actual set up used in our laboratory

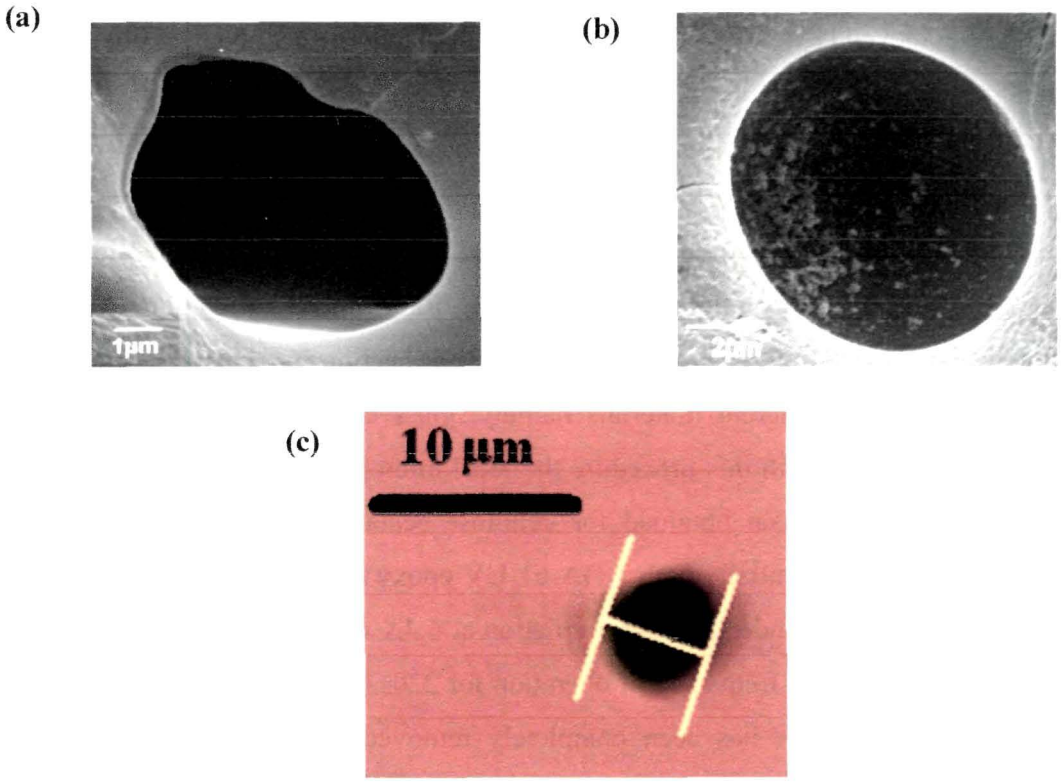

Figure 6.6: SEM image of a SA micropore formed (a) with pre thinning (b) without thinning the glass substrate (dia~10 μm) (c) Optical microscopic image of a micropore (dia~6.62 μm) in a glass substrate without thinning

Fig. 6.6 represents typical micrographs of the micropore formed on different borosilicate glass substrates of thickness ~150 μm, considering both pre-thinning and without pre-thinning procedure. As can be found, by adopting thinning procedure, micropore is generated but without a well defined circular shape (Fig. 6.6 (a)). Whereas, a direct treatment of the glass chip with the spark (without pre-thinning) results in a nearly spherical aperture of diameter ~10 μm dia. which can be revealed from the SEM image shown in Fig. 6.6(b). An aperture of dia. ~6.6 μm can be obtained with the application of a voltage of 10 V without pre-thinning, as observed from optical microscopy image shown in Fig. 6.6 (c). Unfortunately, micropores of these size could be efficiently used in animal cell studies [21] but not good enough to support planar lipid bilayers. Our experimental conditions did not provide pores of larger size, though it was demonstrated earlier that with the application of a very high voltage (~30 V), pores of diameter ~300 μm could be achieved [15]. Therefore, we looked for an alternate strategy to obtain pores of dia. 80-100 μm.

6.2.2 Laser drill method

The micropore formation by a laser assisted method was carried out at Laser Biomedical Applications & Instrumentation Division, Raja Ramanna Centre for Advanced Technology (RRCAT), Indore. Fluorine laser mask projection has been used to micro-machine the holes in different materials namely, glass cover slip, PMMA, cellulose acetate and polyimide. With this procedure the ideal micropore diameter useful for lipid bilayer experiment has been obtained for cellulose acetate substrate only*. Cellulose acetate sample is coated initially with NOA 61 UV epoxy on both sides and holes were ablated in the UV epoxy under 157 nm irradiation at 6.4X with 22 mJ pulse energy (455 mJ/cm^2 fluence) at 100 Hz frequency of operation for 220s (integrated power density 570 J/cm^2)) till the UV epoxy has been completely removed on both the sides, thereby exposing the sample with a circular pore. This has then been etched using 20% HF acid solution for 20 minutes thus creating a thorough hole of ~100 μm diameter in ~100 μm thick cellulose acetate substrate slip (Fig. 6.7).

---

* *Appendix-10*

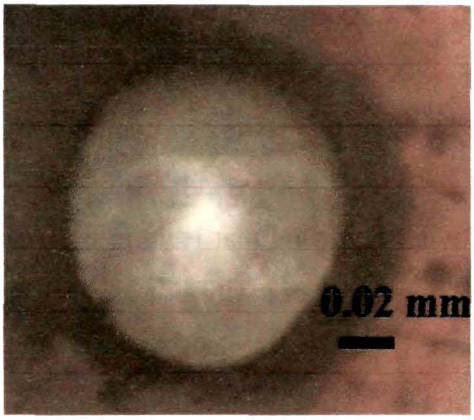

Figure 6.7: 100 μm hole in cellulose acetate substrate created by laser drill method

6.3 Extraction of lecithin from soya-bean seed

Lecithin is a yellow-brownish fatty substance, generally found in animals and plant tissues and comprise of phosphoric acids, choline, glycerol, phospholipids etc. It contains (21%) phosphatidylcholin (PC) and (20%) phosphatidylethanolamine (PE). A lecithin molecule consists of a hydrophobic tail and a hydrophilic head. When lipids are 'painted' in an aqueous solution across an aperture they self-assemble spontaneously where

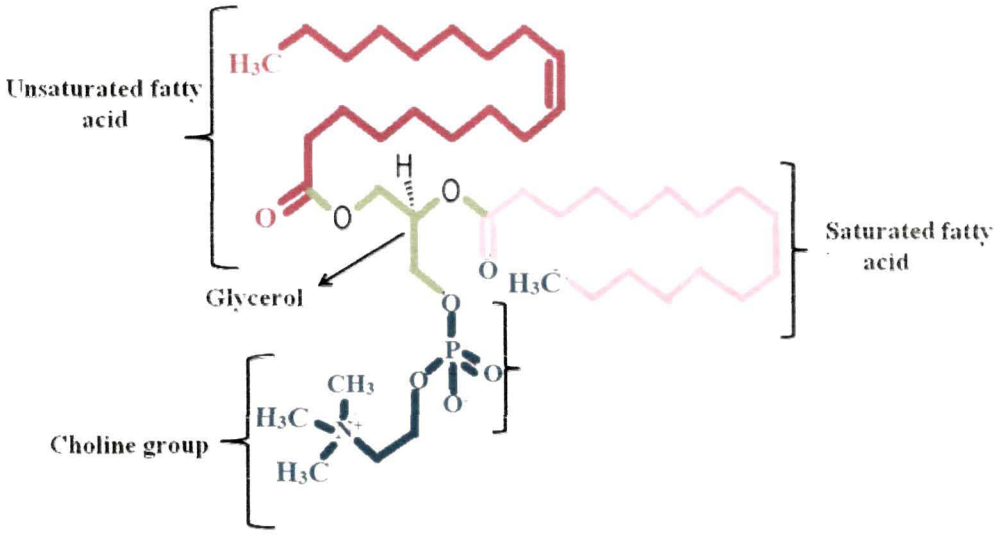

Figure 6.8: Schematic diagram of molecular structure of lecithin

hydrophobic and hydrophilic- ends align independently, thereby forming a stable bilayer [22]. The typical thickness of the lecithin bilayer is ~4 nm. Figure 6.8 shows the schematic diagram of a lecithin molecule. In real cells, phospholipids are the key elements of the bilayer membrane which regulate the flow of ions and other important molecules for cellular activity. Knowing that lecithin is a major source of phospholipids available in nature, we intended to work with bilayer derived from lecithin. The natural lecithin which was extracted from soya-been seed (model RKS-18) through solvent extraction process followed by water degumming process [23,24]. The step by step procedures are as described below.

6.3.1 Cleaning and crushing of soya-bean seed

At first, the collected soya-beans are cleaned, dried and de-hulled prior to oil extraction. The soya-bean hulls need to be removed as they absorb oil and give lower yield. The de-hulling is done by cracking the soya-beans and making a mechanical separation of the hulls and cracked soya-bean. The cracked soya-bean seeds are crushed with the help of a grinder prior oil extraction. The photographs shown in Fig. 6.9 are snapshots of soya-bean seeds (used for lecithin extraction) before and after grinding.

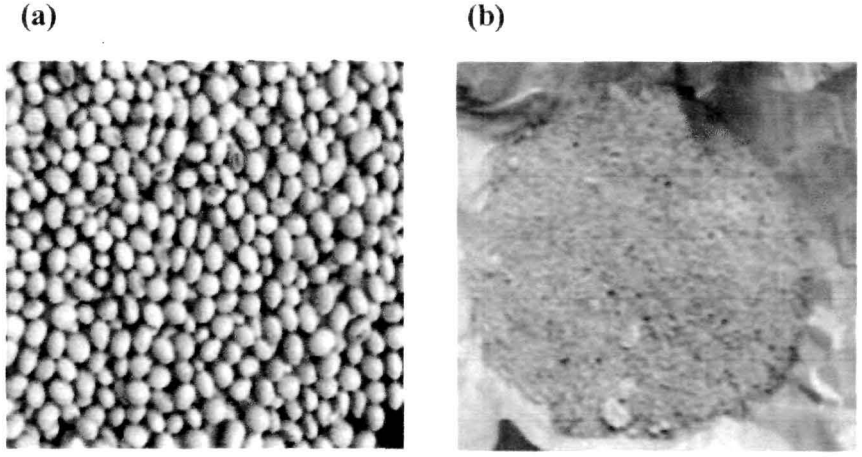

Figure 6.9: Soya-bean seed (model RKS-18) (a) before and (b) after grinding

6.3.2 Solvent extraction process

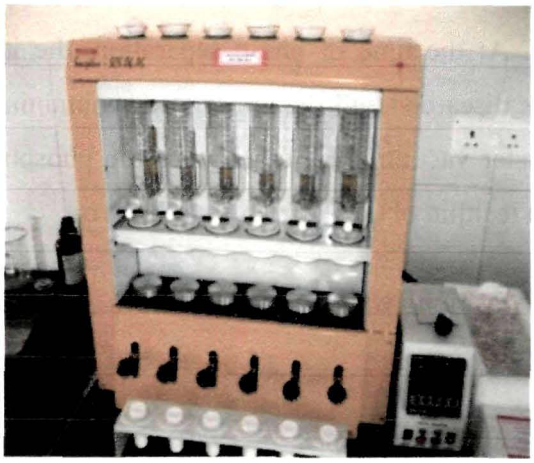

Figure 6.10: Typical solvent extraction system

The soya-bean flakes were placed into cellulose thimble in a solvent extraction system (Socs Plus) [25] and then combined with solvent hexane, which extracts the oil by dissolving it out of the flakes. Using heat a strong vacuum, the hexane is evaporated from the flakes, and recycled for further extraction processes. While the hexane free crude soybean oil is taken for further refining. Fig 6.10 shows a snap-shot of the solvent extraction under operation.

6.3.3 Degumming process

The crude soya-been oil obtained through solvent extraction method is likely to contain several impurities. The oil insoluble impurities were removed by filtration, whereas, the oil soluble impurities were removed by adopting following method:

Crude soya-bean oil (50 ml) was kept in a 500-mL round bottomed flask fitted with a stirring shaft and a paddle shape 7.5 cm long teflon impeller driven by a variable speed motor. The oil was purged with nitrogen through a sinter glass stick for 2 min and then brought to the desired temperature under a nitrogen blanket. Following by starting of the motor, desired amount of distilled water (5%) was added to it. When degumming was completed, the mixture was cooled down to 40° C and the gums were separated by centrifugation (at ~6000 rpm) for 15 min. The degummed oil was removed by decantation. Furthermore, in order to isolate lecithin partitioning the crude gums, equal

weight of crude gums along with an equal weight of hexane were stirred in a magnetic stirrer. With the magnetic stirring, absolute ethanol was then added until a distinct phase separation is occurred. At the time of phase separation, the lower layer, consisting of water and ethanol, was discarded and the upper layer containing lecithin was made free of solvent at 30° C under vacuum. Table 5.2 gives the phosphatide composition of the phosphatide fraction in lecithin obtained from soya-bean oil.

Table 6.2 Composition (wt%) of phosphatides of lecithin obtained from soya-bean oil

Phosphatides	**Soya-bean oil**
Phosphatidylcholine	32
Phosphatidylethanolamine	23
Phosphatidylinositol	21
Phosphatidic acid	8
Others	16

6.4. Bilayer formation and QD induced ion channel response using planar chip technology

Recognizing the importance of the lipid bilayer membrane in cell biology and biomedical applications, the use of size controlled QDs, in these 2-dimensional membrane structures, seems demanding and of significant interest in nanobio-interface applications. It may be noted that, nanopores and nanoporous artificial membranes were found extremely useful in the fields of bioengineering and environmental sciences, to name a few scope for DNA translocation [26], fuel cell studies [27], coulter counter device [28], and ultra-high water purification systems [29]. However, functional nanopore creation leading to passage of ions in live cells, has not been fully understood. In fact, the activity and longevity of cells are largely governed by the control uptake/release of ions and other molecular species through transient nanopores available in the bilayer membrane. To be specific, active and passive ion channels could determine the physiological state of the cells by way of

linking intracellular compartments with the extracellular matrix. Moreover, the unhealthy and disease-affected cells, both in animal and plant kingdoms, do not support normal ion transport process thereby causing abnormal intracellular activity. The ion channel studies, in real cells, are generally based on patch-clamp techniques [3], whereas, the practice of planar chip method is relatively new and is limited to artificial bilayers only [5,6]. The artificial bilayer membrane can be used as a model system to explore transient nanopore creation in presence of a field. In this context, the nanopore creation due to oligomeric aggregation of inorganic QDs will provide a closer account to understand ion transport mechanism in live cells and signaling activity including labeling with fluorescent QDs. Below we discuss steps involved in studying the electrophysiology experiment using QDs.

6.4.1 Building Faraday cage and electrophysiology system

As mentioned above, mechanical as well as electrical stability of the lipid bilayer is very much critical in every ion channel experiment. The current fluctuation across a bilayer is very sensitive even to the slightest mechanical and electromagnetic noise. Microscopic movement and vibration present in all buildings can be damped out by an appropriate vibration isolation table placed at a suitable location.

The complete ion channel experiment was performed using a patch-clamp amplifier (EPC10)[†] and patchmaster software (HEKA Elektronik, Germany)®. The main amplifier had an extension called the head-stage which was capable of interfacing amplifier and the planar chip components. Different components such as, patch clamp amplifier (main device), head stage (pre-amplifier) and lipid bilayer design were placed in a Faraday cage. The cage was connected to the building ground in order to reduce the electromagnetic noise to a minimum possible value. The side walls of the Faraday cage were draped by thick aluminum sheets. The electrophysiology setup along with patch master and fit master® data acquisition software was installed on a PC running on OS Windows 2007®. The following photograph shows the patch clamp set up along with Faraday cage, main amplifier and the computer interfacing. Fig. 6.11 shows the

[†] *Appendix-11*

specimens used in our laboratory for ion channel recordings. Note that, we preferred to use cellulose acetate as the bilayer supporting substrate as we could not obtain well defined pores on the coverslip (glass substrate). We have performed the lipid bilayer experiment using a ~100 μm thick cellulose acetate substrate that has a centrally located aperture of dia ~100 μm. The cellulose acetate system was chosen as it possesses good dielectric properties with a low dielectric constant, low dielectric loss and high values of elastic modulus that are comparable to the values observed for other polymeric materials

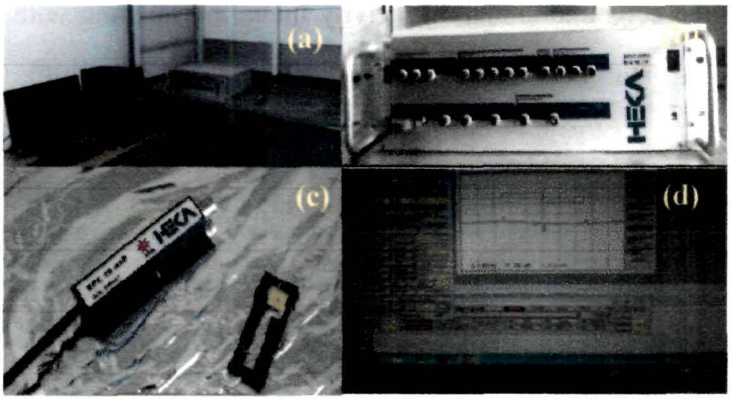

Figure 6.11: (a) Ion channel recording setup (b) main amplifier (c) head stage pre-amplifier that connects electrolytic chamber and the main amplifier (d) monitor of PC displaying use of patchmaster software® laboratory

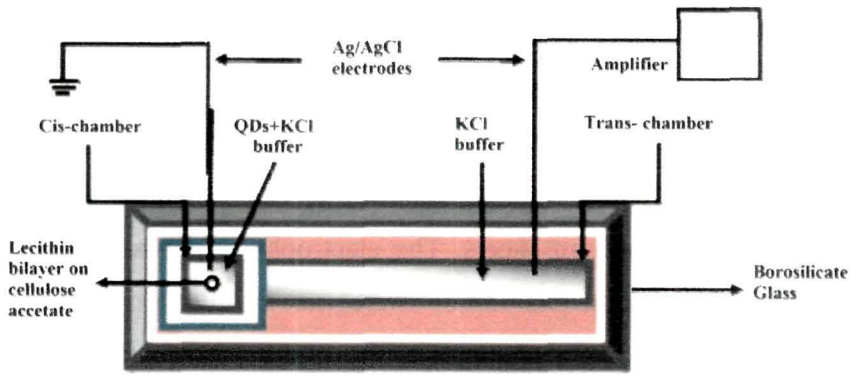

Figure 6.12: Schematic of ion channel measurement setup featuring different important components

(teflon, PP, PET). The cellulose acetate substrate with an aperture (of diameter d_a= 100 μm is shown in Fig. 6.7. A lecithin lipid bilayer membrane was formed around the aperture by a painting method [30-34] following an established procedure (Montal-Müeller technique)[‡] [22, 35-37]. The schematic of the set up used for ion channel experiment is illustrated in Fig. 6.12.

6.4.2 Formation of a stable lecithin bilayer around the aperture

Shown in Fig. 6.12, an experimental set-up is divided into two parts and they are connected via a small orifice (100 μm in diameter) located at centre of a cellulose acetate substrate that separates one chamber (cis) from the other (trans). Both the compartments are filled with electrolytic solution (1 mL of 1M KCl, 10 mM HEPES at pH= 7.5 at room temperature). The painting was done by using a thin brush and spreads a small amount of lipid/hexane solvent around the aperture on the trans side. This results in the formation of a monolayer of lipids on each side. The two lipid monolayers are then pulled naturally by van der Waals forces to a close proximity, in a process known as "thinning". Thick layer of lipid solution is thinned down by a pressure in the upper chamber. In the thinning process, primary contribution come from Platue-Gibbs border suction (PGB); which arise due to the surface tension of the curvature of the annulus (Plateau-Gibbs border) [38,39]. As the film approaches the thickness of a few hundred Angstroms, a second driving force, i.e. the van der Waals attraction between the aqueous phases on the either side of the thin bilayer become apparent. [39]. This is followed by simultaneous action of PGB suction and van der Waals attractive force, but in opposite direction to make the thinned bilayer stable.

The impermeable lecithin bilayer acts as a partition between the two compartments (cis and trans-chambers) containing electrolytic buffer. As mentioned above, the compartments were connected to the patch clamp amplifier via a pair of Ag/ AgCl electrodes prepared in 0.5 M KCl (Fig. 6.12). The resulting current fluctuations were filtered by a low-pass filter (with a four-pole Bessel filter at 1 kHz, with a sampling frequency of 10 kHz). In order to suppress electromagnetic noise, the whole setup was

[‡] *Appendix-12*

kept in a Faraday cage with ground connected to the building ground. The amplified current was recorded in a PC operating on OS windows 2007® using the patchmaster software®.

The bilayer capacitance is given by: $C_m = I/(dV/dt)$ [40]. Here, I is the measured current across the bilayer in response to an applied voltage ramp dV/dt. In the present case, 100 mV was applied for 20 ms, thus giving a ramp of $dV/dt = 5$ V/s. The membrane current was found to be ~209.5 pA (Fig. 6.13). Three traces were shown to ensure stability with lapse of time. The (lecithin) bilayer membrane capacitance was estimated to be ~42 pF. Theoretically, lecithin membrane capacitance is predicted as ~57 pF (for soya-lecithin bilayer C_s ~0.75 μF/cm^2 [41]) by using eqn. 6.5.

For obtaining a stable bilayer, the whole aperture was believed to be covered by the bilayer itself. In that case, the diameter of the aperture (d_a) is equal to the membrane carrying pore diameter (d_p). The relation between membrane capacitance (C_m) and the diameter (d_p) of the membrane carrying micro-pore can be expressed by:

$$C_m = \varepsilon_0 \varepsilon_m A / d_t \qquad (6.6)$$

Here, $A = \frac{\pi}{4} d_p^2$ is the area of the bilayer membrane, ε_0 is the permittivity of the free space ($\varepsilon_0 = 8.85 \times 10^{-12}$ F/m), ε_m is the dielectric constant of the membrane and d_t is the thickness of the lipid bilayer. Considering ε_m of lecithin equals to the dielectric constant

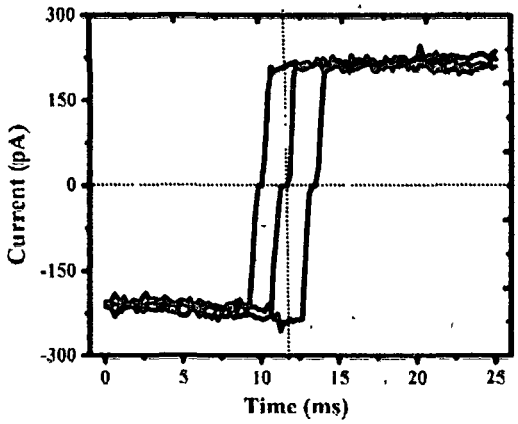

Figure 6.13: Variation of current with the application of a ramp voltage (100 mV/20 ms) across the lecithin bilayer, recorded at different times

of the supported lipid bilayer (ε_m= 3) in the aqueous solution [42], the lecithin bilayer thickness is calculated as ~4.96 nm. The bilayer under study was found to form a giga seal (~3-10 GΩ) around the micropore that is responsible for partitioning the two electrolytic chambers. The bilayer was fairly stable up to a time duration of ~390 s. The stability of the bilayer could be realized from a fairly uniform value of the membrane current (~209 pA), recorded at different intervals (Fig. 6.13).

6.4.3 QD induced ion channel response and induce nanopore formation

Biological membranes play an important role in the normal functioning of all biological cells. They maintain concentration gradients of ions inside and outside the cell by acting as a selective filter for ions and molecules of specific kind. The selective flow of ions across the membrane is governed by ion channels caused by special kind of proteins [43]. These proteins could form pores across the membrane which can open and close selectively. For basic understanding of the properties and functioning of biological membranes as well as ion channels, some model systems such as, artificial planar lipid bilayer membrane, artificial liposomes has been used by various groups. Our study on ion channel has value in the sense that, we used natural lipid extract derived from soya-seed. The bilayer formation around an aperture across a new substrate material, cellulose acetate is also a new addition to the study. The observed ion channel activity in our set-up is as detailed below.

After obtaining a stable bilayer around the aperture, 4.2 nmol/ml water soluble CdSe QDs (~20 nm size)**** were injected into the cis compartment of the electrolytic chamber with the help of a Hamilton® microsyringe. Note that, while trans- side of the chamber was connected to the head stage of the amplifier, the cis- compartment was held at virtual ground. The noise level of the whole setup was reduced to < 2 pA by grounding the Faraday cage with the ground of the building. About a minute later the QDs are added, current bursts were observed in response to an applied voltage across the lecithin bilayer membrane. Fig. 6.14 depicts the traces of current fluctuation when the bilayer was

---

**** *Appendix-13*

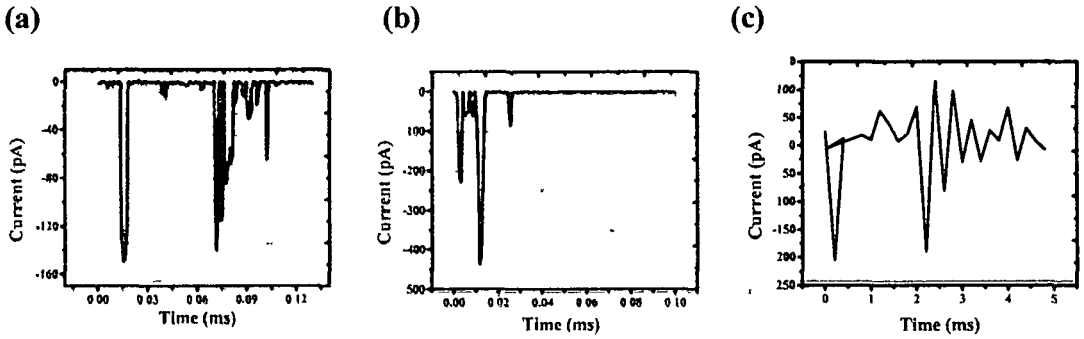

Figure 6.14: Current fluctuation measured across the lipid bilayer due to insertion of QDs at a biasing voltage of (a) -10 mV (b) -20 mV (c) -90 mV

subjected to different biasing voltages of -10 mV, -20 mV and -90 mV (Fig. 6.14). An apparently enhanced current magnitude was witnessed with an increasing biasing voltage from -10 to -20 mV. We anticipate instant oligomeric aggregation of QDs in the lecithin bilayer, allowing counter ions to pass through the nanopores under an external field. A higher voltage indeed facilitates a higher concentration of ions resulting in a higher magnitude of the current burst. But an extremely high voltage (-90 mV), since the leakage current was extremely large, we failed to record and extract the current bursts (due to QD aggregation) with absolute certainty. The leakage current, as a result of rupture of the bilayer, is generally noticed in the form of overall shift of the plot from the base line (Fig. 6.14(c)). The plots representing number of events vs. current histograms over a number of experiments are shown in Fig. 6.15. The main figure is a histogram to represents current vs. channel events corresponding to a biasing voltage. This has been replotted in terms of conductance (I/V) response to channel events (insets of Fig. 6.15). All these have been explored by using OriginPro-8.5 software. As can be found, there exist two dominant conductance states: a high-end level of ~14.3 nS and a low-end one as ~6.3 nS (inset of Fig. 6.15(a)), corresponding to a bias voltage of -10 mV. The respective conductance levels, corresponding to a higher bias voltage (-20 mV), are ~21.1 nS and ~11 nS (inset of Fig. 6.15(b)). Earlier, the prime conductance value of ~2.3 nS was observed by a group where ~12 nm CdSe QDs were inserted in an artificial phospholipid bilayer [37]. Moreover, the high-end value (~14.3 nS) is close to the conductance value ~15.8 nS, as predicted theoretically for ion channels created by 12 nm CdSe QDs and reported in an earlier work [44]. The dwell time, which signifies the duration of on/off condition of a particular

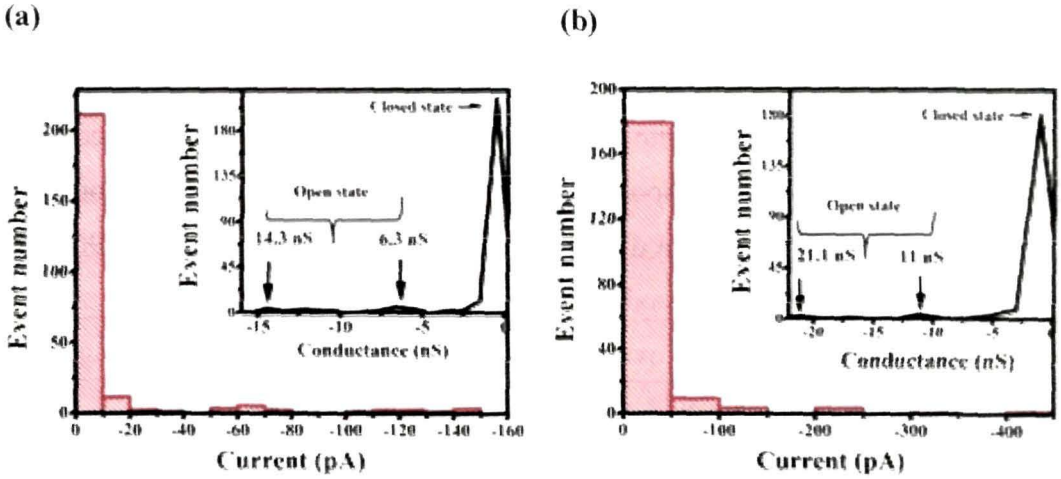

Figure 6.15: Event vs. current histograms of QD induced ion channels, corresponding to the bias voltages of (a) -10 mV (b) -20 mV. The figure-insets show the respective conductance-histograms for identifying individual open conductance states, away from the closed states

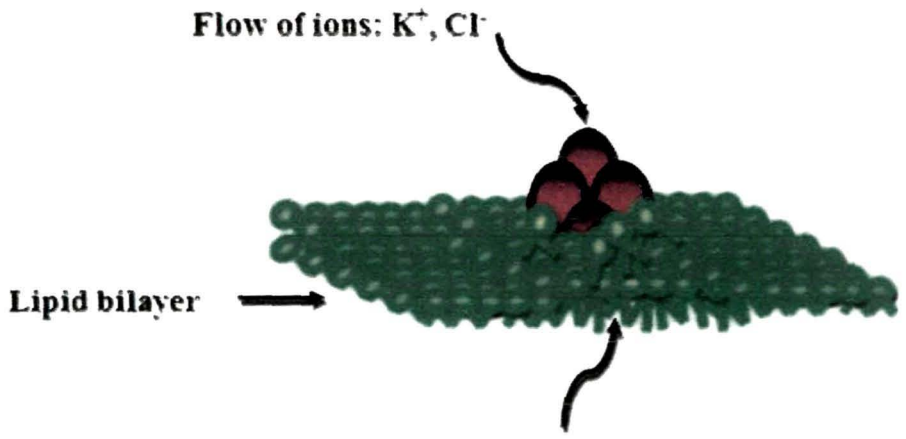

Figure 6.16: Schematic of flow of ions through nanopores created by aggregated QDs across a lecithin bilayer

conductance state, as a result of ion channel activity can be estimated by averaging over a number of events. In the present case, the magnitude of dwell times are predicted as ~384, 400 μs and 390, 411 μs, as for -10 mV and -20 mV biasing voltage cases; respectively.

Note that, each of the QDs has a permanent dipole moment that can be influenced by the application of an electric field producing a torque on the QD dipole. The torque produced, enforce QDs to insert into the bilayer. In this context, it is to be noted that the torque is the cross product of dipole moment $\vec{p}$ and the electric field vector $\vec{E_F}$. i.e. $\vec{\tau_F}=\vec{p}\times\vec{E_F}$. When the angle between dipole moment and electric field vector is 90° torque experienced by the QDs is maximum. In this situation, dipole-dipole attraction mechanism becomes dominant over Brownian movement, yielding an aggregated structure with a nanopore that could allow ions to pass through (Fig. 6.16).

6.4.4 Assessment of ion channel activity through simplified models

Know that, the conductance value is the intrinsic parameter of a definite ion channel and is largely dependent on the interface region of the nanopore created by QDs in aggregate form. As far as the interface region is concerned, there can be two possibilities of well-defined nanopore geometry: spherical and non-spherical nanopores. For mathematical simplicity, generally spherical nanopores are treated without considering curvature effect. Non-spherical nanopores involve complicated formula but better suited for large aggregation number. By assessing the behavior of ion passing mechanism through different shaped pores, one can control the ion channel activity in a more precise way. Presuming the ion mobility as uniform throughout the experimental chamber (ion mobility inside the pores is the same as in the bulk), here we discuss both the options to adjudge our experimental results.

Model 1: Ion channel activity due to spherical nanopores

This is an oversimplified version of the entrapped region created by spherical QDs. In this case, the conductance level G_s can be related to the spherical shaped nanopore of size d_{spore} as [37]:

$$G_s = \frac{\sigma\pi d_{spore}^2}{4d_{dot}} \tag{6.7}$$

Here, d_{dot} is the diameter of the QDs participating in the aggregated structure, σ is the conductivity of the electrolytic buffer. The conductivity of the 1 M KCl+10 mM HEPES buffer at 300 K is ~98 mS/cm, whereas size of the CdSe QDs used in the experiment is ~20 nm.

Model 2: Ion channel activity due to non-spherical nanopores

Pores of non-spherical geometry are mostly considered due to insertion of helical proteins in cell-membranes leading to ion channels. We can also use the relevant formula in the present case, owing to the curved surfaces of the QDs and knowing that, the aggregated system is far from static equilibrium. Since the pores are created by aggregation of QDs with curved surfaces, in reality, one cannot expect formation of spherically symmetric entrapped regions (spherical nanopores). In that case, ion channel conductance (G_{ns}) in a bilayer membrane can be related to the diameter of the QD-induced nonspherical pore as per following relation [45-47]:

$$G_{ns} = \frac{\sigma l \pi d_{nspore}^2}{4(l+(\pi d_{nspore})/4]} \tag{6.8}$$

Here, l is the length of the pore and σ being the conductivity of the buffer. In our case, l= 4.96 nm which is the thickness of the lecithin membrane; d_{nspore} is the diameter of the nonspherical pore formed as a result of QDs aggregation. Note that, the conductance values for *model*-1 and 2 are dimensionally differed by a length parameter "l". In the *model*-2 the resistance (R_{ns}) is defined as $R_{ns}=(l/G_{ns})$ [45-47].

Referring to *model*-1, and considering two conductance values of 6.3 nS and 14.3 nS (corresponding to a bias voltage -10 mV), we predict the size (d_{spore}) of the spherical nanopores as ~4 nm and ~6.09 nm. As for the case of the biasing voltage of -20 mV, the respective pore diameters of the spherical nanopores were calculated to be ~5.3 nm and ~7.5 nm which corresponded to the conductance levels of 11 nS and 21.1 nS; respectively. The corresponding pore diameters, as calculated using *model*-2 and applicable for the non-spherical nanopores (d_{nspore}), were estimated as ~0.95 nm and ~1.5 nm, for a bias voltage of -10 mV and ~1.22 nm and ~1.8 nm for a bias voltage of -20 mV. Apparently, $d_{nspore} \leq d_{spore}$. It may be noted that, consideration of non-spherical pore formation is a better approximation (over spherical ones) which could account for interfacial effects and

possible surface charge interactions among neighboring QDs. The consideration of non-spherical pores over spherical ones was also accommodated in a similar work [48]. Not surprisingly, the ion channels induced by the QDs can be dependent on the shape of the nanopores, which may be due to nonstatic nature of the aggregated QDs. Previously, nanopore shape- dependent ion conductance fluctuation was noticed for KasA potassium channels [48]. It was believed that, when the bilayer is subjected to a biasing field, the QDs permeate and aggregate owing to a net dipole moment of the dots [49]. However, the formation of nanopore is a transient process and can be affected by thermal effects and stress fluctuation. In presence of an external electric field, the QDs (with a dipole moment) would experience a torque enforcing their insertion into the membrane. The aggregation behavior of the QDs is believed to be due to the dominance of electrostatic interaction of the dots over Brownian agitation, resulting in a conformation of minimum surface energy.

As stated above, the variation of pore conductance strictly depends on the shape of the pore as well as on the diameter of specific nanopore. More precisely, the pores are created by the transient aggregation of QDs, creating current bursts of varied magnitudes. Now both the models can be used independently to compute the number of QDs (N_Q) involved in the creation of an aggregated structure, described by the following relation [49]:

$$d_{spore}, d_{nspore} = d_{dot}[1/\mathrm{Sin}\,(180/N_Q)\text{-}1] \qquad (6.9)$$

The spherical shaped nanopores, exhibiting high (14.3 nS) and low (6.3 nS) values of conductance states are as a result of aggregation of 3.6 and 3 nos. of QDs; respectively (Table 6.3). The corresponding N_Q values were ~2.6 and ~2.4, for non-spherical pores. It is worth mentioning here that, a coplanar assimilation of ~3 QDs would represent a close-packed network and ions are not necessarily allowed should the pores are filled with lipid molecules. It is very likely that, the migration of ions through the nanopores is highly stochastic in nature, but capable of forming most probable ion conductance states owing to activity of transient pores. This is because, an aggregation number with $N_Q < 3$ has no physical meaning, as far as the entrapped region is concerned. But, an aggregation of 3 QDs would represent a minimum energy configuration that might describe a small, open

conductance state when ions make their way for free passage, in response to a biasing voltage of -10 mV. In contrast, in a spherical nanopore approximation (*model*-1) an aggregation of ~3.6 QDs would indicate momentary involvement of an extra quantum dot in the aggregated state, giving rise to the formation of a larger nanopore, and consequently a higher conductance level. On the other hand, referring *model*-1, number of aggregated QDs corresponding to the conductance values of ~11 nS and 21.1 nS (gating voltage -20 mV) were found to be ~3.4 and ~3.9; respectively. In contrast, with reference to *model*-2 (non-spherical pores), the relevant conductance states are characterized by an aggregation no. (N_Q) of ~2.55 and ~2.7. The different parameters (pore diameter, no of aggregated QDs, conductance value) of ion channels created by the application of different bias voltage for both the models are highlighted in the Table 6.3.

Owing to the consideration of larger sized QDs in our experiment, the spherical pore size created by the QDs is found to be comparatively larger than the ones reported by other groups [37, 49]. Theoretically, an aggregation of 5, 6 QDs may be possible, but in reality, thermal agitation is likely to perturb such a configuration for a longer duration of time [44]. Consequently, it can flip either to 3 or, nearly 4 QD aggregation thereby exhibiting an assembly of minimum energy configuration that is thermodynamically favorable. The undulation of QD aggregation may also be responsible for this flipping action. It is highly likely that, the QDs which experience oligomeric aggregation depart from their exact positions with time. As a result, channel events may exhibit stochastic

Table 6.3: Different parameters related to QD induced ion channels considering different models

Bias voltage (mV)	**Conductance (nS)**	**Model 1**		**Model 2**	
		Spherical Nanopore diameter (nm)	**Aggregation no. of QDs (N_Q)**	**Non spherical nanopore dia (nm)**	**Aggregation no. of QDs (N_Q)**
-10	6.3 14.3	4.0 6.09	3.0 3.6	0.95 1.5	2.4 2.6
-20	11.0 21.1	5.3 7.5	3.4 3.9	1.22 1.8	2.55 2.7

trend due to dynamic nature of ion conducting pathways (nanopores). Nevertheless, the most probable states can be ascertained through histogram traces performed on a number of channel events and using available theory of nanopores. We also invoke that, the observation of two conductance states, for a given biasing voltage not necessarily represent independent states but may call for simultaneous opening of an independent state. In this regard, mixed states due to simultaneous opening of fundamental states need to be addressed, which is one of our future objectives. Note that, the ion channels could not be recorded at a higher biasing voltage owing to bilayer instability which caused large leakage current followed by abrupt.

References:

[1] Fertig, N., et al. Activity of single ion channel proteins detected with a planar microstructure, *Appl. Phys. Lett.* **81**(25), 4865--4867, 2002.

[2] Fertig, N., et al. Whole cell patch clamp recording performed on a planar glass chip, *Biophys. J.* **82**(6), 3056--3062, 2002.

[3] Levis, R. A. & Rae, J. L. Low-noise patch-clamp techniques, *Methods Enzymol.* **293**, 218--266, 1998.

[4] Fertig, N., et al. Microstructured apertures in planar glass substrates for ion channel research, *Receptors Channels* **9**(1), 29--40, 2003.

[5] Mayer, M., et al. Microfabricated teflon membranes for low-noise recordings of ion channels in planar lipid bilayers, *Biophys. J.* **85**(4), 2684--2695, 2003.

[6] Suzuki, H., et al. Electrophysiological recordings of single ion channels in planar lipid bilayers using a polymethyl methacrylate microfluidic chip, *Biosens. Bioelectron.* **22**(6), 1111--1115, 2007.

[7] Hall, L. T., et al. Monitoring ion-channel function in real time through quantum decoherence, *Proc. Natl Acad. Sci.* **107**(44), 18777--18782, 2010.

[8] Mak, D. & Webb, W. W. Conductivity noise in transmembrane ion channels due to ion concentration fluctuations via diffusion, *Biophys. J.* **72**(3), 1153--1164, 1997.

[9] Sigworth, F. J.& Klemic, K. G. Microchip technology in ion-channel research, *IEEE Trans Nanobioscience* **4**(1), 121--127, 2005.

[10] Sherman-Gold, R. *The Axon guide for electrophysiology & biophysics laboratory techniques,* Axon Instruments, Foster City, CA, 1993.

[11] Kim, Y. C., Kim, J.K., Yu, J., Park, O. and Park, J.H. *Device with a polymer insulating nanolayer having a dielectric constant of less than 3.0 between a cathode and a polymer emitting layer, increasing the injection of the electron,* **US Patent No. US7242142,** July 10 2007

[12] Liu, D., et al., *Advanced Millimeter-wave Technologies: Antennas, Packaging and Circuits.* Wiley-Blackwel, United Kingdom, 2009

[13] Pfeiffer, I., et al. Vesicle adsorption and phospholipid bilayer formation on topographically and chemically nanostructured surfaces, *J. Phys. Chem. B* **114**(13), 4623--4631, 2010.

[14] Suzuki, H. & Takeuchi, S. Microtechnologies for membrane protein studies, *Analyt. Bioanal. Chem.* **391**(8), 2695--2702, 2008.

[15] Wüthrich, R., et al. Spark assisted chemical engraving (SACE) in microfactory, *J. Micromech. Microeng.* **15**(10), S276--S280, 2005.

[16] Sandison, M. E., et al. Micromachined glass apertures for artificial lipid bilayer formation in a microfluidic system, *J. Micromech. Microeng.* **17**(7), S189--S 196, 2007.

[17] Wüthrich, R., et al. Physical principles and miniaturization of spark assisted Chemical Engraving (SACE), *J. Micromech. Microeng.* **15**, 268--275, 2005.

[18] O'Shaughnessy, T. J., et al. Laser ablation of micropores for formation of artificial planar lipid bilayers, *Biomed. Microdevices* **9**(6), 863--868, 2007.

[19] Khan Malek, C. Laser processing for bio-microfluidics applications (part I), *Analyt. Bioanalyt. Chem.* **385**(8), 1351--1361, 2006.

[20] Holmes, M. R., et al. Micropore and nanopore fabrication in hollow antiresonant reflecting optical waveguides, *J. Micro-Nanolith. MEM* **9**(2), 023004--023006, 2010.

[21] Ionescu-Zanetti, C., et al. Mammalian electrophysiology on a microfluidic platform, *Proc. Natl. Aca. Sci. U. S. A.* **102**(26), 9112--9117, 2005.

[22] Montal, M. & Mueller, P. Formation of bimolecular membranes from lipid monolayers and a study of their electrical properties, *Proc. Natl. Aca. Sci.* **69**(12), 3561--3566, 1972.

[23] Patil, V. V., et al. Extraction and purification of phosphatidylcholine from soyabean lecithin, *Sep. Purif. Technol.* **75**(2), 138--144, 2010.

[24] Ceci, L., et al. Oil recovery and lecithin production using water degumming sludge of crude soybean oils, *J. Sci. Food Agr.* **88**(14), 2460--2466, 2008.

[25] Pramparo, M., et al. Immersion vs. percolation in the extraction of oil from oleaginous seeds, *J. Am. Oil Chem. Soc.* **79**(10), 955--960, 2002.

[26] Panwar, A. S. & Muthukumar, M. Enzyme-modulated DNA translocation through a nanopore, *J. Am. Chem. Soc.* **131**(51), 18563--18570, 2009.

[27] Tominaka, S. & Osaka, T. Nanoporous PdCo catalyst for microfuel cells: Electrodeposition and dealloying, *Adv. Phys. Chem.* **2011**, 1--13, 2011.

[28] Ito, T., et al. Simultaneous determination of the size and surface charge of individual nanoparticles using a carbon nanotube-based coulter counter, *Anal. Chem.* **75**(10), 2399--2406, 2003.

[29] Menzl, G., et al. Phase transition and interpore correlations of water in nanopore membranes, *Phys. Rev. Lett.* **109**(2), 020602, 2012.

[30] Mueller, P., et al. Reconstitution of cell membrane structure in *vitro* and its transformation into an excitable system, N*ature* **194**, 979--980, 1962.

[31] Creasy, M. A., et al. Self-healing of bilayer lipid membranes formed over silicon substrates with a single pore, *Proc. SPIE* 6929, Behavior and Mechanics of Multifunctional and Composite Materials 2008, 69290P (April 02, 2008); doi:10.1117/12.776375

[32] Requena, J., et al. Van der Waals forces in oil-water systems from the study of thin lipid films. I. Measurement of the contact angle and the estimation of the van der Waals free energy of thinning of a film, *Proc. R. Soc. A.* **347**(1649), 141--159, 1975.

[33] Dhoke, M., et al. Porous membranes for reconstitution of ion channels, *Biochim. Biophys. Acta -Biomembranes* **1716**(2), 117--125, 2005.

[34] Oiki, S. Planar lipid bilayer method for studying channel molecules, in *Patch Clamp Techniques: from begineing to advanced protocols*, Yasunobu O, ed., Springer, Japan, 2012, 229--275, 2012.

[35] Batishchev, O. V., & Indenbom, A. V. Alkylated glass partition allows formation of solvent-free lipid bilayer by Montal–Mueller technique, *Bioelectrochem.* **74**(1), 22--25, 2008.

[36] Lakey, J. H., et al. The voltage-dependent activity of Escherichia coli porins in different planar bilayer reconstitutions, *Eur. J. Biochem.* **186**(1-2), 303--308, 1989.

[37] Klein, S. A., et al. Formation of nanopores in suspended lipid bilayers using quantum dots, *JPCS*, **109**, 012022, 2008.

[38] Fujiwara, H., et al. Dynamics of the spontaneous formation of a planar phospholipid bilayer: A new approach by simultaneous electrical and optical measurements, *J. Chem. Phys.* **119**(13), 6768--6775, 2003.

[39] White, S. H., The physical nature of planar bilayer membranes, *Ion channel reconstitution* **1**, 3--35, 1986.

[40] Robello, M. & Gliozzi, A. Conductance transition induced by an electric field in lipid bilayers, *Biochim. Biophys. acta* **982**(1), 173--176, 1989.

[41] Brzezinski, P., et al. Charge displacements in interfacial layers containing reaction centers. *J. Membr.Biology* **165**(3), 213--225, 1998.

[42] Gramse, G., et al. Nanoscale measurement of the dielectric constant of supported lipid bilayers in aqueous solutions with electrostatic force microscopy, *Biophys. J.* **104**(6), 1257--1262, 2013.

[43] Hodgkin, A. L. A quantitative description of membrane current and its application to conduction and excitation in nerve, *J. Physiol.* **117**(4), 500--544, 1952.

[44] Sarma, R. & Mohanta, D. A Comprehensive view on the brownian motion of quantum dots in electrolytic solution, lipid bilayer and their aggregated state in the lipid biomembrane, *J. Comput. Theor. Nanos.* **9**(8), 1070--1077, 2012.

[45] Noronha, F. S., et al. Macrophage damage by Leishmania amazonensis cytolysin: evidence of pore formation on cell membrane, *Infect.Iimmun.* **68**(8), 4578--4584, 2000.

[46] Chen, J., et al. Cationic nanoparticles induce nanoscale disruption in living cell plasma membranes, *J. Phys. Chem. B* **113**(32), 11179--11185, 2009.

[47] Eaton, D. C. Ionic channels of excitable membranes. Bertil Hille. Sunderland, Ma: Sinauer Associates, 1984, *J. Neurosci. Res.* **13**(4), 599--600, 1985.

[48] Kuyucak, S., et al. Models of permeation in ion channels, *Rep. Prog. Phys.* **64**(11), 1427--1472, 2001.

[49] Ramachandran, S., et al. Current bursts in lipid bilayers initiated by colloidal quantum dots, *Appl. Phys. Lett.* **86**(8), 083901--083903, 2005.

CHAPTER- 7: A Theoretical Approach on the Aggregation of Spherical QDs into Reconstituted Phospholipid Bilayer for Ion Channel Activity

CHAPTER 7

A Theoretical Approach on the Aggregation of Spherical QDs into Reconstituted Phospholipid Bilayer for Ion Channel Activity

Over the years, as an essential and promising component of nano-biotechnology, size selective QDs have gained accelerating research interest owing to their ability to act as carrier to translocate proteins, drug molecules and other useful materials into cells and biomembranes [1-4]. The potential biomedical application of QDs, in fact, requires a precise control over QD–cellular interaction, while ensuring a high degree of selectivity and bio-compatibility. Governed by thermo-diffusing property, the interaction can largely dependent on a particular QD geometry. The shape of the QDs also plays key role on the nature of interaction with the biomembrane and shape of the nanoparticles (NPs) has a direct influence on the cellular uptake process [5-8]. The geometry effect is likely to dictate their ability to select specific cell types and may alter the dwell time response inside the cell. It may be noted that, the penetrating capability of the NPs across a lipid bilayer, is determined by the contact area, the orientation between the particle and the lipid bilayer, apart from their hydrophilic and hydrophobic functionality at large [9-11].

For a particle undergoing Brownian motion, the mean square displacement (*MSD*) is defined as the square of the displacement of the particle at one time relative to the position of the particle at zero time, averaged over many particles [12]. In case of unobstructed (simple) diffusion which occurs partly due to thermal effect, the *MSD* of the diffusing particle is directly proportional to time. But in disordered systems such as in cell membrane, the *MSD* is proportional to a fractional power of time not equal to one besides the simple one. The non-typical, obstructed diffusion is recognized as anomalous diffusion [13].

The simple diffusion of a particle is possible only in homogeneous free solution. But while it moves through semi permeable membrane e.g., live cell, lipid bilayer membrane etc. their diffusion is hindered by different diffusible and immobile molecular crowding agents such as, lipid domains, proteins, immobile species and several cytoskeleton elements. In this case, the particle departs from simple Brownian mechanics and show several other modes of complex diffusion including confined, sub-diffusion, and heterogeneous diffusion [14].

Typically, a lipid bilayer is nothing but a thin polar membrane made of two lipid leaflets with hydrophilic 'head' groups on both the sides while hydrophobic 'tails' immersed in the core. Because of this 'hydrophilic–hydrophobic–hydrophilic' makeup, cell membranes present an obstruction to most polar molecules. In order a NP to permeate through the bilayer, there must be an interface between the NP and the lipid bilayer so that the NP could be delivered easily without affecting the bilayer stability [15,16]. In this regard, the surface morphology of the NPs, play a critical role while NPs find their way in the bilayer [17]. The NPs coated with a structured surface monolayer of hydrophobic and hydrophilic ligands are capable of penetrating the lipid bilayer via interaction between the NPs and the lipid. When surface of the NP is composed of a mixture of hydrophobic and hydrophilic ligands, they are capable of rearranging themselves in order to maximize their favorable interactions with the hydrophobic core [18]. When a hydrophilic NP comes in contact with the lipid bilayer, the hydrophilic heads of the bilayer get attracted by the NPs, while the hydrophobic tails are repelled and consequently, generating a hydrophilic hole around it inside the bilayer [19].

In this chapter, we have highlighted the movement of spherical QDs in different environments, namely electrolytic solution and lipid bilayer in their pre-aggregated state. Both qualitative as well as quantitative analogies on the behavior of the Brownian motion of spherical QDs are discussed in conjunction with the formation mechanism of aggregated states responsible for the evolution of various ion conducting pathways (ion channels). At first, a theoretical model is developed with respect to diffusion aspect of spherical QDs and later, a correlation is put forward between the aggregated states of the QDs and ion channel conductance states. In every case, the dependence of mean square displacement (*MSD*) [12] and relaxation time (τ) has been evaluated as a function of QD size (spherical QDs and that of the aggregated structure). The schematic shown in Fig 7.1 (a-d) depicts the nature of Brownian motion of spherical QDs with special consideration to complete insertion and partial insertion across the bilayer.

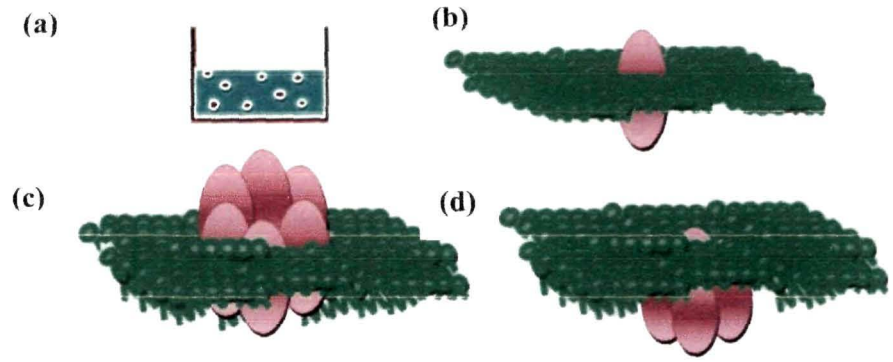

Figure 7.1: Schematics representing the behavior of QDs in (a) electrolytic solution and (b) lipid bilayer in pre-aggregated state. The QD aggregated state with full and partial insertions are depicted in (c) and (d); respectively

7.1 Brownian movement of spherical QDs in different media

7.1.1 In electrolytic solution

The *MSD* ($<r^2>$) of a spherical QD undergoing Brownian motion in free solution, in 2-dimension is given by [20],

$$<r^2>=4D_0t \tag{7.1}$$

Here, D_0 is the diffusion coefficient of the QD and t is the diffusion time [12].

According to the Stokes-Einstein relation, the diffusion coefficient (D_0) of a spherical QD of diameter d in free solution is given by [20,21]:

$$D_0=\frac{kT}{3\pi\eta_s d} \tag{7.2}$$

where, k is the Boltzmann constant, T is the absolute temperature, η_s is the viscosity of pure solvent.

The relaxation time (τ_r) i.e., time in which QDs undergo Brownian movement to a distance equal to the radius of the QDs and experience successive collisions in the electrolytic solution, can be expressed by:

$$\tau_r=\frac{\left(\frac{d}{2}\right)^2}{D_0}$$

Substituting D_0 from Eq. (7.2), we get

$$\tau_r = \frac{\left(\frac{d}{2}\right)^2}{\left(\frac{kT}{3\pi\eta_s d}\right)} \tag{7.3}$$

Essentially, a large particle size and a higher particle concentration may suppress the bilayer stability significantly by increasing their surface coverage in the bilayer [20]. In principle, the parameterization of QD size, depending on their concentration, is beneficial while considering tolerable insertion in the bilayer of interest. As shown earlier, in electrolytic solution, the concentration of the salt [i.e., NaCl (0-300 mM)] has a little effect on the diffusion behavior of the QDs (CdSe-ZnS) [20]. Nevertheless, concentration of the QDs is likely to affect the diffusion response of the individual QDs. The effective diffusion coefficient (D_{cl}) of a QD in an electrolytic solution is given as [22],

$$D_{cl}=D_0(1+k_dC) \tag{7.4}$$

Here, k_d is the interdot interaction parameter and C is the QD concentration in the solution. As in the present case we consider only neutral hydrophilic QDs, it is expected that the diffusion response is affected only by permanent dipole-dipole interactions among them. Whereas, other interaction phenomena such as, electrostatic, hydrodynamic interaction etc. will have the least effect. For dipolar interaction cases, the interaction parameter (dipole strength) can be defined by [23,24]

$$\lambda_i = \frac{U}{kT} \tag{7.5}$$

Here, $U = -\frac{e^2d^2}{4\pi\epsilon_0\epsilon_s L_i^3}$ represents attractive interaction energy [25] between the two dipoles (QDs) (diameter d) separated by a distance L_i in an electrolytic solution of dielectric constant ϵ_s (for water ϵ_s=78). kT signifies thermal energy associated with the system. Now substituting λ_i for k_d in eqn. (7.4), i.e., considering attractive dipole-dipole interaction, we have

$$D_{cl}=D_0(1+\lambda_i C)$$

Further, the concentration dependent MSD (MSD_c) of a QD in an electrolytic solution can be rewritten as

$$<r^2>=4[D_0\ (1+\ \lambda_i C)]t \tag{7.6}$$

and, the relaxation time as, $\tau_c = \frac{\left(\frac{d}{2}\right)^2}{D_{c1}} = \frac{\left(\frac{d}{2}\right)^2}{[D_0\ (1+\lambda_i C)]}$ (7.7)

7.1.2 In reconstituted phopholipid bilayer (pre-aggregate state)

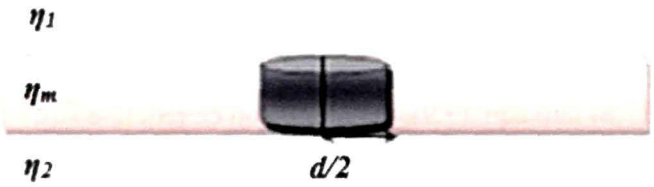

Figure 7.2: A scheme of membrane inclusion of size *d/2* in a lipid bilayer of surface viscosity η_m surrounded by viscous fluids of viscosities η_1 and η_2

Unlike the Brownian movement of a particle in a homogeneous medium, in the lipid bilayer environment, the particle movement is characterized by a well known *Saffman-Delbruck* (SD) approximation, which accounts for the diffusion coefficient and the particle size [26,27]. The SD model describes the hydrodynamic problem of translational and rotational diffusion of the membrane inclusions surrounded by the respective media with respective bulk viscosities η_1 and η_2, shown schematically in Fig. 7.2 [28].

As per the hydrodynamic model, the membrane inclusion of diameter d is characterized by a reduced size, $\varepsilon_h = d/l_h$, where $l_h = \frac{\eta_m}{\eta_1+\eta_2}$ can be defined as the hydrodynamic length scale or the Saffman-Delbruck (SD) length [29]. The translational and rotational diffusion of the particles in the membrane would change depending on the ratio of $\varepsilon_h = d/l_h$ and the model is valid especially for $d < \varepsilon_h$ [30]. Essentially, the diffusion of a particle of diameter d, in the lipid bilayer, can be described as [26,27, 31]:

$$D_L = \frac{kT}{4\pi\eta_m h}[\ln(\lambda_L)-\gamma] \tag{7.8}$$

Here, h is the lipid bilayer thickness and for a phospholipid bilayer h =4 nm, η_m is the surface viscosity of the membrane (for a homogenous membrane, $\eta_m=\mu h$ with μ as bulk viscosity) [28] and η is the viscosity of the membrane surrounding fluid. By and large,

the SD approximation is accurate for $\eta_m << \eta$ [32]. In addition, $\lambda_L = 2/\varepsilon_h = \frac{\eta_m}{\eta\left(\frac{d}{2}\right)}$, where $\eta_m = 4\times10^{-10}$ Pa.s.m [28, 32], and $\eta_{1,2} = 10^{-3}$ Pa.s (see Fig.7.2), and $\gamma = 0.577$ is the Euler's constant [30]. Therefore, eqn. (7.8) is valid only for the particles having radius $\frac{d}{2} < \frac{\eta_m}{2\eta}$.

For the free diffusion of spherical QDs in a lipid bilayer, the MSD_L ($<r^2>$) is given by [33]

$$<r^2> = 4D_L t \tag{7.9}$$

Substituting eqn. (7.8) into eqn. (7.9), the MSD_L can be redefined as,

$$<r^2> = 4\left\{\frac{kT}{4\pi\eta_m h}\left[ln\left(\lambda_L\right) - \gamma\right]\right\} t \tag{7.10}$$

The relaxation time, in this case, is given by

$$\tau_L = \frac{\left(\frac{d}{2}\right)^2}{D_L}$$

or,
$$\tau_L = \frac{\left(\frac{d}{2}\right)^2}{\left\{\frac{kT}{4\pi\eta_m h}\left[ln\left(\lambda_L\right) - \gamma\right]\right\}} \tag{7.11}$$

Owing to dipole-dipole interaction (with QD concentration C) in lipid bilayer, the expression for MSD_{LC} can be stated as,

$$<r^2> = 4D_{c2} t$$

where, $D_{c2} = D_L(1 + \lambda_i C)$.

or,
$$<r^2> = 4\left\{\frac{kT}{4\pi\eta_m h}\left[ln\left(\lambda_l\right) - \gamma\right](1 + \lambda_i C)\right\} t \tag{7.12}$$

Putting $\varepsilon_L = 2$, for lipid bilayer [34] in the expression $U = -\frac{e^2 d^2}{4\pi\varepsilon_0\varepsilon_L L_l^3}$.

In this case, relaxation time expression can be redefined as,

$$\tau_{LC} = \frac{\left(\frac{d}{2}\right)^2}{D_{c2}}$$

i.e., $$\tau_{LC} = \frac{\left(\frac{d}{2}\right)^2}{\left\{\frac{kT}{4\pi\eta_m h}[ln\,(\lambda_l)-\gamma](1+\lambda_l C)\right\}} \quad (7.13)$$

7.1.3 In reconstituted phopholipid bilayer (aggregated state or, ion conducting state)

As reported earlier [35], after insertion into the bilayer, QDs aggregate and form ion conducting pores. The diameter of the pore (d_{pore}) formed as a result of aggregation of N_Q number of QDs, is given by [35]:

$$d_{pore} = d_{dot}(1/(\mathrm{Sin}\pi)/N_Q)\text{-}1) \quad (7.14)$$

Here, d_{dot} is the diameter of the participating QDs (assuming negligible inhomogenity) that results in the formation of a nanopore. Using this relation, for a uniform size of QDs, the diameter of the pores corresponding to an aggregation of a certain no. of QDs can be predicted.

The conductance state (G), and the diameter of QDs forming pores can be expressed as per the following equation [36],

$$G = \frac{\sigma\,\pi\,d_{pore}^{\,2}}{4d_{dot}}$$

Therefore, $$d_{pore} = \left(\frac{4G}{\sigma\,\pi}\right)^{\frac{1}{2}} \quad (7.15)$$

Here, σ is the conductivity of the bulk solution (98 mSie/cm of 1M KCl+20 mM HEPES buffer at pH 7.5) [36]: used in the lipid bilayer experiment. We can evaluate the translational Brownian motion (MSD_{LA} and τ_{LA}) of the aggregated structure, representing the conductance state G by substituting d_{dot} (diameter of QD) by d_{pore} (diameter of QD forming pore) in eqn.(7.10) and eqn.(7.11); respectively.

The MSD_{LA} of the aggregated structure formed by spherical QDs during current burst can be expressed as,

$$<r^2> = 4\left\{\frac{kT}{4\pi\eta_m h}\left[\ln\left(\lambda_l''\right) - \gamma\right]\right\}t \quad (7.16)$$

Here, $$\lambda_l'' = \frac{\eta_m h}{\eta\left(\frac{d_{dot}G}{\pi\sigma}\right)^{\frac{1}{2}}}$$

Accordingly, the relaxation time, in this case, can be formulated as

$$\tau_{LA} = \frac{\left(\frac{d_{pore}}{2}\right)^2}{D_{LA}} \tag{7.17}$$

Here, $D_{LA}=\left\{\frac{kT}{4\pi\eta_m h}\left[\ln\left(\lambda_i''\right)-\gamma\right]\right\}$ is the diffusion coefficient of the conductive QD ion channel across the lipid bilayer.

7.2 Assumptions made in the theoretical treatment

An associated problem with the QDs for tracking molecules in live cells is their scope of nonspecific adsorption. Of technological interest, we considered here spherical QDs of dimension in the range of d = 2-20 nm. Note that, in the respective range of dimensions, the reduced size of both the QD types i.e., ε_{sp} have values << 1. In other words, the length scale falls within the scope of the SD approximation (eqn. (7.8)). Moreover, the reduced size of the aggregated structures, formed as a result of assimilation of spherical QDs (ε_{LA}) is expected to be <<1 for a given value of d.

The exclusive use of the SD equation (eqn. (7.8)) is considered for exploiting diffusion dynamics of the QDs in their aggregated state. In the present work, the QDs are presumed to be hydrophilic, so that an easy permeation through the bilayer can be ensured while dictated the mechanism is by simple diffusion dynamics.

Applying a theoretical treatment on the suitably chosen range of spherical QDs, we obtained several characteristic plots that meaningfully describe the nature of diffusion dynamics of the pre-aggregate and aggregated states. We have studied free diffusion considering a typical diffusion time as 0.1 sec, for the calculation of *MSD*. The viscosity of the solvent and temperature of the solution are considered as 0.862 cP and 298 K (room temperature); respectively. Whereas, for lipid bilayer the temperature is assumed to be 298 K, equal to the electrolytic solution.

7.3 Movement of QDs in different media

7.3.1 In electrolytic solution

In an electrolytic solution, the free diffusion of a QD can be affected by its size, QD concentration and viscosity of the solvent. First we consider that there is no any interaction between the QDs. As can be observed from Fig. 7.3 that *MSD* falls rapidly and then slowly with the increasing the size of the QDs (eqn. (7.1)). Conversely, the relaxation time, τ_r shows a reverse trend (eqn. (7.3)). The ~2 nm QD sized has a characteristic *MSD* magnitude of ~10.12 μm^2. However, the 20 nm dots exhibited a much lowered *MSD* as ~1.01 μm^2. The respective τ_r values are estimated as ~0.03 and ~39.52

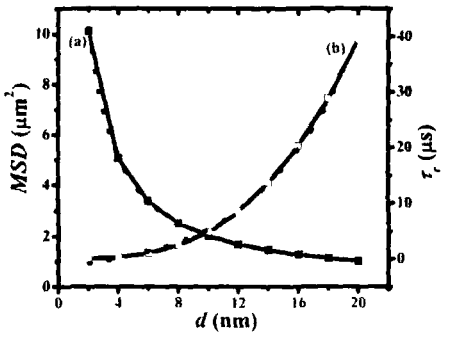

Figure 7.3: *MSD* and τ_r vs. size of spherical QDs in electrolytic solution

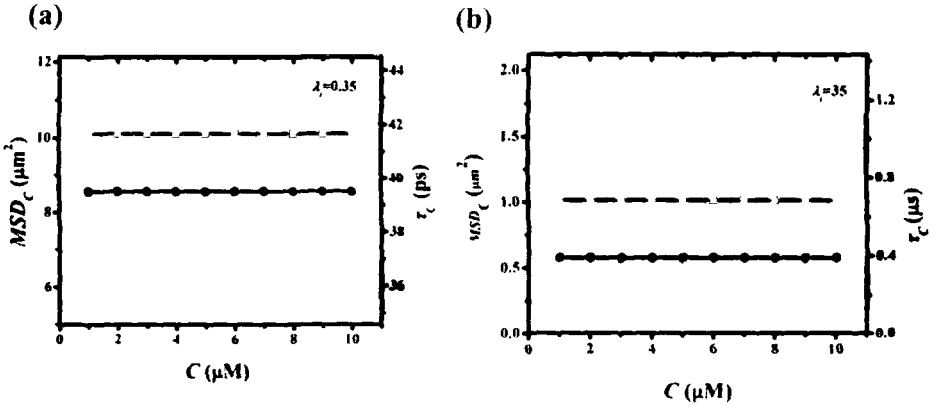

Figure 7.4: MSD_C and τ_C vs. concentration of QDs of dia. (a) 2 nm (b) 20 nm in the electrolytic solution

μs; respectively. Thus, the smaller QDs experience a larger magnitude of *MSD* but a reduced value of relaxation time. The red-dotted line curve (a) depicts a close fit of *MSD* dependency on diameter, *d*. The fitted curve, in fact, signifies bi-exponential decay behavior: $y = A_1 \, exp \, (-x/d_1) + A_2 \, exp \, (-x/d_2) + y_0$, with $y_0 = 0.760$, $A_1 = 6.064$, $d_1 = 6.376$, $A_2 = 22.785$, $d_2 = 1.306$. Thus, one can easily predict the *MSD* of a spherical QD for a known value of *d*, as per formulation. This gives $MSD = 6.064 \, exp \, (-d/6.376) + 22.785 \, exp \, (-d/1.306) + 0.760$. On the other hand, the variation of relaxation time τ_r, with *d*, exhibited a bi-exponential growth trend (green dotted curve, curve (b)) following $y = A_1 \, exp \, (x/d_1) + y_0$ where $y_0 = -3.313$, $A_1 = 1.812$, $d_1 = 6.3$. Similarly, the value of τ_r, corresponding to any value of *d* can be calculated by using $\tau_r = 1.812 \, exp \, (d/6.300) - 3.313$.

The effective dipole-dipole interaction between QDs is considered assuming interdot separation as 2 nm (eqn. (7.6) & (7.7)). Knowing the dipole interaction parameter, λ_i is a function of QD diameter, *d*, the following plots can be obtained for both the small (2 nm), and large (20 nm) sized QDs. As can be evident from Fig. 7.4(a) and 7.4(b), MSD_C and τ_C are not affected with the increase of QD concentration from 1-10 μM for both the QD sizes with respective interaction parameters as $\lambda_i = 0.35$ and 35.

7.3.2 In lipid bilayer, in the pre-aggregated state of QDs

In a bilayer, the diffusion response of the spherical QDs, can be affected by QD size and concentration. While temperature of the lipid bilayer is considered same as the electrolytic solution, one can address the diffusion behavior of QDs in pre-aggregate state, as described below.

Figure 7.5 display a size dependent, weak exponential decay and raising behavior of the MSD_L (curve a, with fitted graph $y = y_0 + A_1 \, exp \, (-(x-x_0)/d_1)$, $y_0 = 0.227$, $x_0 = 1.826$, $A_1 = 0.807$, $d_1 = 7.451$) and the relaxation time, τ_L (curve b with fitted curve $y = A_1 \, exp \, (x/d_1) + y_0$, $y_0 = -3.117$, $A_1 = 2.876$, $d_1 = 11.108$) while QDs undergoing diffusion in the bilayer (eqn. (7.10) and (7.11)). The 2 nm QDs posses an MSD_L is ~1.03 μm^2, whereas, 20 nm QDs as, ~0.28 μm^2. It predicts, MSD_L are nearly ~10 times smaller than those found in the electrolytic media and consistent to the value predicted experimentally [37]. The reduction of MSD_L is attributed to the components such as, higher viscosity of

the bilayer than the electrolytic counterpart. In contrast, the relaxation time (τ_L) of ~2 nm sized QDs in lipid bilayer is found to be ~9.7 times relaxation times in the electrolytic solution. On the other hand, for ~20 nm QDs in the electrolytic solution, exhibit ~2.7 times the relaxation time in lipid bilayer. This indicates greater localization of smaller sized QDs across the bilayer over that of the larger ones (QDs).

It is also important to assess the diffusion response for a varying QD concentration. Figures 7.6(a) and (b) show MSD_{LC} (and τ_{LC}) versus concentration of QDs in lipid bilayer and in presence of dipole-dipole interactions between the QDs (for QD dia. = 2 nm and 20 nm) separated by a distance of ~2 nm (using eqn. (7.12) and (7.13)).

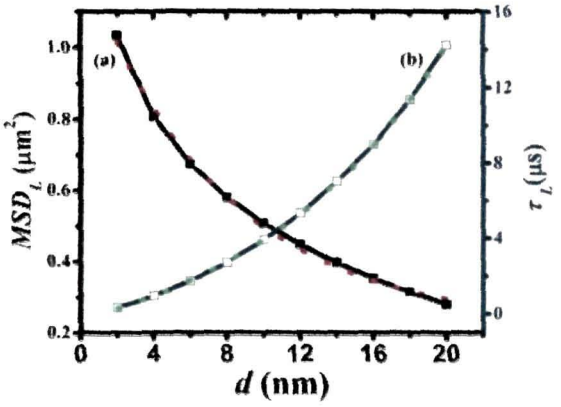

Figure 7.5: MSD_L and τ_L vs. size of spherical QDs in lipid bilayer

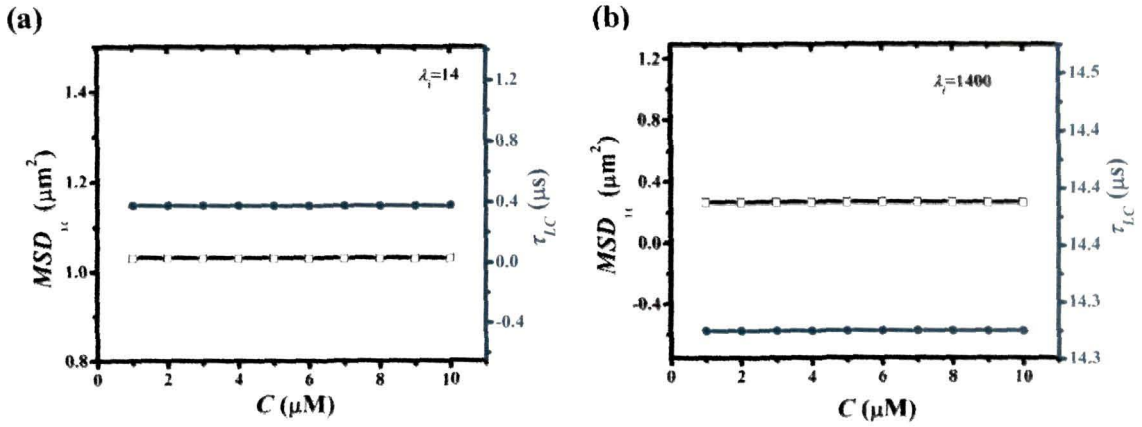

Figure 7.6: MSD_{LC} and τ_{LC} vs. concentration of QDs of dia. (a) 2 and (b) 20 nm in lipid bilayer

Here, the MSD_{LC} and the τ_{LC} are found to exhibit nearly analogous behavior as obtained in case of electrolytic solution, for both the sizes. But it may be noted that the dipole interaction response is stronger in lipid bilayer than the electrolytic media with dipole interaction parameter λ_i =14 and 1400 for 2 and 20 nm QDs; respectively.

7.3.3 In lipid bilayer, in the aggregated state of QDs

Earlier, it was demonstrated that after insertion of QDs into the lipid bilayer, in presence of an electric field, the QDs aggregate and form ion conducting pores. In the lipid bilayer, the pore formation is established as a result of aggregation of a minimum number (3 nos.) of QDs [35].

During current bursts, owing to different conductance states of the QD induced ion channels, the addition and subtraction of QDs may occur in an aggregated state similar to the case of alamethicin ion channel [38]. The diffusion behavior of aggregated QDs (representing different conductance states) is useful in the study of QD ion induced channels on the assumption that, pre-aggregate states do not correspond to appreciable conductance fluctuations. Using eqn. (7.14) we obtained a set of plots on the size of pores formed by the QD aggregation undergoing diffusion across the reconstituted lipid bilayer (Fig. 7.7). As can be seen, the pore dia. tends to increase with the aggregation number as well as with the size of the QDs. For an aggregated structure of 3 QDs (each of dia. 12

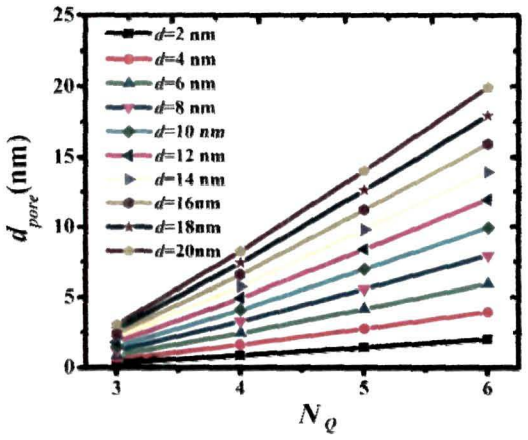

Figure 7.7: Size of the nanopore (d_{pore}) formed by aggregated QDs vs. no. of aggregated QDs of various size

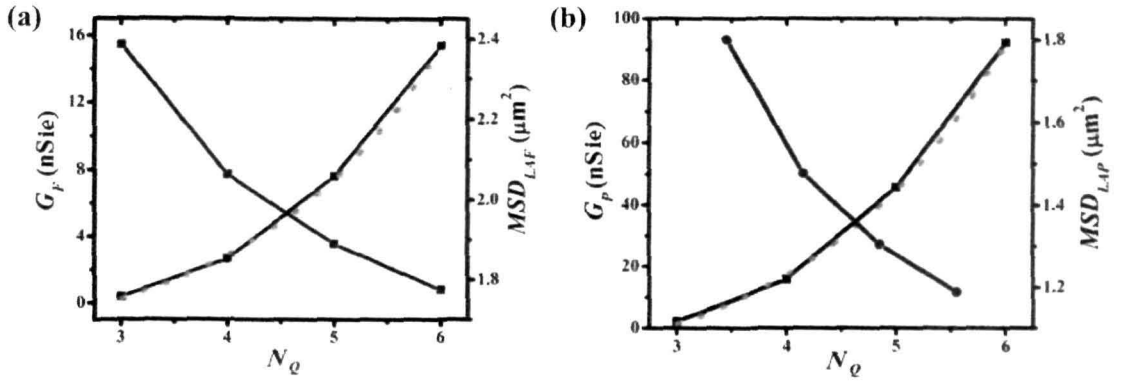

Figure 7.8: Conductance state and *MSD* value vs. no. of aggregated spherical QDs, with (a) full insertion (G_F, MSD_{LAF}) (b) partial insertion (G_P, MSD_{LAP}) cases shown independently

nm), the size of the pore is estimated to be ~1.85 nm, and is consistent to an earlier report [36]. Note that, with $N_Q = 6$, the pore formed by the QDs becomes nearly equal to their finite size. Therefore, any structure formed with this value of N_Q corresponds to a conductance state between 3-6 QD aggregates with high-end conductance state for $N_Q = 6$ and low-end state for $N_Q = 3$. This is because, for any aggregation with $N_Q > 6$ would result in a situation where the pores can accommodate additional QDs that lead to intermediate (sub-) conductance states.

It is also important to encounter the nature of QD insertion for definite ion channel activity. In the present case, we have considered two extreme cases of QD size: the first, ~2 nm QDs- a case of complete insertion into the ~4 nm thick bilayer (Fig.7.1(c)). Second, ~12 nm QDs- a case of partial insertion (Fig. 7.1(d)). Fig. 7.8 depicts variation of conductance and the MSD_{LA} values with the no. of aggregated QDs while considering the response under full (MSD_{LAF}) and partial insertion (MSD_{LAP}) cases (Fig. 7.8 (a) and (b)). Each of the conductance state corresponds to the current burst across the bilayer and thus depicting an abrupt ion transduction pathway. As a general trend, it can be observed that in both the cases, the MSD_{LA} follows an exponentially growing behavior with the aggregation number of the QDs (N_Q). From the fitted curve (green dotted line), one can easily determine the movement of an aggregated structure depending on N_Q and insertion behavior. As for full and partial insertion cases, the

respective simplified relations of the MSD_{LAF} and MSD_{LAP} can be stated as MSD_{LAF} = -3.272+0.666 *exp* (0.555N_Q) and MSD_{LAP} = 1.045+3.890 *exp* (-0.547N_Q).

For N_Q = 3 (each of QD dia. ~2 nm), the conductance (G_F) associated with the current burst (ion channel) is estimated to be ~0.368 nanoSiemens (nSie), whereas MSD_{LAF} is ~2.38 μm^2. Similarly, for N_Q = 4, the G_F and the MSD_{LAF} are ~2.64 nSie and ~2.06 μm^2; respectively. In contrast, aggregated structure formed by N_Q = 6, has corresponding values as ~15.39 nSie and ~1.77 μm^2.

In the same way, the conductance states can arise due to the aggregation of larger sized QDs (each of dia.12 nm) which predict that the minimum conductance value (G_P) for a current burst is ~2.2 nS. This value is in close agreement with the experimentally observed conductance state [36]. The corresponding MSD_{LAP} is ~1.79 μm^2. Moreover, the conductance state (G_P ~15.8 nSie) described for N_Q = 4 is accompanied by an MSD_{LAP} value of ~1.47 μm^2. Similarly, a high value of conductance level (G_P ~92.3 nSie), with N_Q= 6 is characterized by a reduced MSD_{LAP} value of ~1.18 μm^2.

The intersection point of conductance and MSD_{LA} responses for both the size dependent situations turn out a common aggregation number of ~4.6. The corresponding parameters for 2 and 12 nm QDs are ~5.73 nSie, ~1.95 μm^2 and ~35 nSie, ~1.36 μm^2; respectively. Since the MSD_{LA} is ~1.4 times smaller in case of larger sized QDs (MSD_{LAP}<1.4MSD_{LAF}), it is likely that the QD aggregates are associated with slow undulatory motion and thus establishing stable ion conducting pathways. Also a larger sized QD aggregation is characterized by a ~6 fold increment in conductance corresponding to the smaller sized ones (MSD_{LAP}>6MSD_{LAF}).

As expected, the aggregation state of ~2 nm sized QDs shows a weak undulation behavior with accompanying current burst, than the movement of a single ~2 nm sized QDs (MSD_{LAF}<MSD) in the electrolytic solution (Fig. 7.3). But, these aggregated structures (N_Q = 3, 4, 5, 6) characterize higher diffusive response in comparison with a bare 2 nm QD (MSD_{LAF}>MSD_L) in the pre-aggregate state in the bilayer (MSD_L ~1.03 μm^2) (Fig. 7.5). On the other hand, the MSD_{LAP} of the conductance state, due to the aggregation of only 3 nos. of 12 nm sized QDs exhibits a nearly equal value (~1.7 μm^2) to that of a bare, 12 nm sized QD (MSD_{LAP}≈MSD for N_Q = 3) in the electrolytic solution (~1.68 μm^2) (Fig. 7.3). A higher conductance states, as described by 4, 5 and 6 QDs

aggregation, the corresponding MSD_{LAP} value gradually reduces, giving MSD_{LAP}<1.14MSD (for N_Q = 4), MSD_{LAP}<1.3MSD (for N_Q = 5) and MSD_{LAP}<1.42 MSD (for N_Q = 6). In contrast, for these conductive states, the resulting aggregated structures exhibit higher undulation behavior than the pre-aggregated bare 12 nm QDs (MSD_L ~0.44 μm^2, Fig. 7.5, MSD_{LAP}>MSD_L). Consequently, we get MSD_{LAP}>4MSD_L (for N_Q = 3), MSD_{LAP}>3.28MSD_L (for N_Q = 4), MSD_{LAP}>2.9MSD_L (for N_Q = 5) and MSD_{LAP}>2.63MSD_L (for N_Q = 6).

Thus, it is now apparent that the complex lipid bilayer environment has a control on the diffusion behavior of the aggregated structures created by complete insertion of smaller sized (~2 nm) QDs. In this case, their thermal motion is restricted within the viscous lipid bilayer surrounding. Consequently, there is a significant reduction of their mobility in the medium as compared to the electrolytic environment. Alternatively, the aggregated structure formed as a result of the partial insertion of larger sized (~12 nm) QDs is not substantially affected. This is due to the fact that, the aggregated structure may come in contact with a substantial volume of the electrolytic environment. Note that, in both (complete insertion as well as partial insertion) the cases, the high viscous nature of the bilayer would bind the bare QDs more tightly in the pre-aggregate state than the aggregated state. Thus, the thermal movement of the pre-aggregate QDs is largely obstructed relative to the aggregated ones.

It can be found from Fig. 7.9, the relaxation time increases by nearly ~56 and ~64 folds for N_Q=6 and corresponding 2 and 12 nm QDs; respectively. As for ~2 nm sized QDs the relaxation times for associated conductance states are obtained as, 0.004 μs (N_Q = 3), and 0.033 μs (N_Q = 4), 0.225 μs (N_Q = 6). Similarly, 12 nm QDs forming aggregated structure exhibit 0.191, 1.67, 12.11 μs for N_Q = 3, 4, 5, 6; respectively. This signifies that the relaxation time is higher for a larger value of N_Q (exhibiting higher conductance level) and larger size QD (d). In other words, a larger aggregated structure as well as larger sized QDs respond slowly to the thermal agitation even though, while representing definite ion transport pathways. With adequate curve fitting, relevant expressions that account for relaxation time with aggregated number (in both full and partial insertion cases) can be obtained and stated as τ_{LAF} = 0.247 exp (N_Q/1.489) -1.760 and τ_{LAF} = 0.00583 exp (N_Q/1.575)-0.036

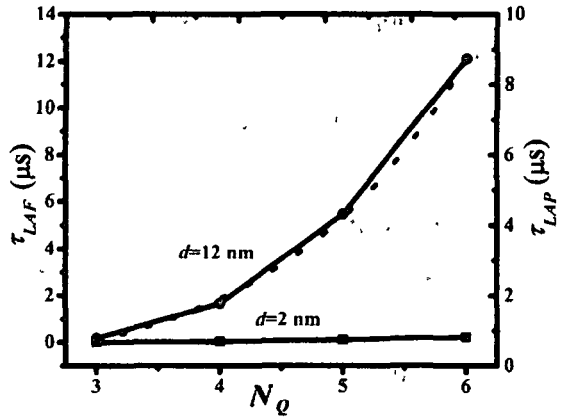

Figure 7.9: Relaxation time vs. no. of aggregated spherical QDs, for (a) full insertion (τ_{LAF}, (b) partial insertion (τ_{LAP})

The τ_{LAF} of the aggregated structure formed by 3 QDs (each of dia. 2 nm) in the bilayer is ~ 9 times lower than the bare 2 nm QDs ($\tau_{LAF} < \tau_r$ for $N_Q = 3$) in the electrolytic solution (~0.04 μs). Whereas, the aggregated state created by 4 QDs exhibits nearly same order (~0.034 μs) ($\tau_{LAF} \approx \tau_r$ for $N_Q = 4$). The other aggregated states with $N_Q = 5$, 6 are characterized by higher values of relaxation times that a single ~2 nm sized QD experience ($\tau_{LAF} > 3.05\ \tau_r$ for $N_Q = 5$, and $\tau_{LAF} > 6.6\tau_r$ for $N_Q = 6$) in the electrolytic environment (Fig. 7.3). In fact, all the aggregated states exhibit lower values of relaxation time that a bare QDs ($\tau_{LAF} < \tau_L$) exhibits in the pre-aggregate form (~0.38 μs) (Fig. 7.5). Conversely, ~12 nm sized QDs forming aggregated structure with N_Q = 3, 4 and 5 are associated with the lower values of relaxation times ($\tau_{LAP}<\tau_r$) corresponding to the bare QD in the electrolytic solution (τ_L ~8.53 μs). Accordingly, we observe $\tau_{LAP}<44.6\tau_r$ (N_Q = 3), $\tau_{LAP}<5.2\tau_r$ ($N_Q = 4$), $\tau_{LAP}<1.66\tau_r$ ($N_Q = 5$) (Fig. 7.3). Interestingly, we get ($\tau_{LAP}>1.4\tau_r$ for $N_Q = 6$.

The aggregated states (N_Q = 3, 4) formed by 12 nm sized QDs, exhibit smaller relaxation times ($\tau_{LAP}<28.21\tau_L$, $\tau_{LAP}<3.20\tau_L$ for $N_Q = 3$, 4), than a bare 12 nm QD in pre-aggregate state in lipid bilayer (τ_L ~5.36 μs) (Fig. 7.5). The aggregated state with $N_Q = 5$ exhibit $\tau_{LAP} \approx \tau_L$, while $N_Q = 6$ state is characterized by $\tau_{LAP}>2.25\tau_L$. Hence, it signifies that, the response time of an aggregated structure with $N_Q = 4$ of 2 nm QDs aggregating into a bilayer is close to that of the response of individual QDs in the electrolytic solution, and the response time of an aggregated structure formed by assimilation of 5

number QDs aggregation (each of QD 12 nm dia.) is similar to the response of each QD in the pre-aggregated state. This suggests that as the size of the QDs increases, they tend to respond in nearly equal time in comparison to a pre-aggregated structure while undergoing diffusion. Further, it is also clear that an aggregated structure with more no. of QDs move slowly with respect to their equilibrium position.

Moreover, it is found that, an aggregated structure formed by the later kind (d = 12 nm) of QDs exhibits a six fold increase in the conductance value compared to the former one (d = 2 nm). Consequently, the response time of the conductance states of the ion channel formed by the larger sized QDs is ~50 times greater than the states created by smaller sized QDs.

From the present discussion, one can say that in absence of interdot interaction, the translational *MSD* (and relaxation time) of QDs in electrolytic solution as well as in lipid bilayer in the pre-aggregate state, would decrease (and increase) with the QD size. Moreover, the translational *MSD* (and relaxation time) of an aggregated structure, inside the reconstituted lipid bilayer also decreases (and increases) with the no. of QD aggregates (N_Q) and with the size of the individual QDs (d) in the structure. In presence of interdot (dipole-dipole) interaction, however, with the increase of concentration, the diffusion behavior of QDs remains unaffected both in the electrolytic solution and in the lipid bilayer in pre-aggregated state. Based on these analysis we argue that, QD concentration within range ~1-10 μM can be desirable for ion channel and electrophysiological studies. Also, the larger aggregated structures of the QDs representing higher conductance states of ion channels are thermally stable with higher orders of relaxation times. Furthermore, the *MSD* of partially inserted QD aggregates has a lower magnitude than the fully inserted ones. Also, as the *MSD* of an aggregated structure is higher than the pre-aggregate counter part, the diffusion response is slower in the later case. This fact was also substantiated in case of higher diffusion response of the QDs in intracellular environment of live cells [30].

Our model is based on the independent opening and closing of individual ion channels. In this regard, the diffusive response of QDs either in isolated form or in aggregated form was discussed with special reference to size of QDs and surrounding environment. For simultaneous opening and closing purpose one need to include further

References

[1] Patlolla, R. R., et al. Translocation of cell penetrating peptide engrafted nanoparticles across skin layers, *Biomaterials* **31**(21), 5598--5607, 2010.

[2] Qi, L. & Gao, X. Emerging application of quantum dots for drug delivery and therapy, *Expert Opin. Drug Deliv.* **5** (3), 263--267, 2008.

[3] Alivisatos, A. P., et al. Quantum dots as cellular probes, *Annu. Rev. Biomed. Eng.* **7**, 55--76, 2005.

[4] Baba, K. & Nishida, K. Single-molecule tracking in living cells using single quantum dot applications, *Theranostics* **2**(7), 655, 2012.

[5] Qiu, Y., et al. Surface chemistry and aspect ratio mediated cellular uptake of Au nanorods, *Biomaterials* **31**(30), 7606--7619, 2010.

[6] Gratton, S. E., et al. The effect of particle design on cellular internalization pathways, *Proc. Natl. Acad. Sci.* **105**(33), 11613--11618, 2008.

[7] Zhang, K., et al. Shape effects of nanoparticles conjugated with cell-penetrating peptides (HIV Tat PTD) on CHO cell uptake, *Bioconjugate Chem.* **19**(9), 1880--1887, 2008.

[8] Chithrani, B. D., et al. Determining the size and shape dependence of gold nanoparticle uptake into mammalian cells, *Nano Lett.* **6**(4), 662--668, 2006.

[9] Ding, H.-M. & Ma, Y.-Q. Interactions between janus particles and membranes, *Nanoscale* **4**(4), 1116--1122, 2012.

[10] Yang, K. & Ma, Y.-Q. Computer simulation of the translocation of nanoparticles with different shapes across a lipid bilayer, *Nature Nanotech.* **5**(8), 579--583, 2010.

[11] Li, Y., et al. Computational investigation of interaction between nanoparticles and membranes: hydrophobic/hydrophilic effect, *J. Phys. Chem. B* **112**(51), 16647--16653, 2008.

[12] Dix, J. A. & Verkman, A. Crowding effects on diffusion in solutions and cells, *Annu. Rev. Biophys.* **37**, 247--263, 2008.

[13] Saxton, M. J. Anomalous diffusion due to obstacles: a *Monte Carlo* study, *Biophys. J.* **66**(2), 394--401, 1994.

[14] Jin, S. & Verkman, A. Single particle tracking of complex diffusion in membranes: simulation and detection of barrier, raft, and interaction phenomena, *J. Phys. Chem. B* **111**(14), 3625--3632, 2007.

[15] Almquist, B. D., et al. Nanoscale patterning controls inorganic–membrane interface structure, *Nanoscale* **3**(2), 391--400, 2011.

[16] Chipot, C. & Tarek, M. Interaction of a peptide nanotube with a water–membrane interface, *Phys. Biology* **3**(1), S20, 2006.

[17] Verma, A., et al. Surface-structure-regulated cell-membrane penetration by monolayer-protected nanoparticles, *Nature Mater.* **7**(7), 588--595, 2008.

[18] Van Lehn, R. C. & Alexander-Katz, A. Penetration of lipid bilayers by nanoparticles with environmentally-responsive surfaces: simulations and theory, *Soft Matter* **7**(24), 11392--11404, 2011.

[19] Liu, F., et al. Analysis of nanoprobe penetration through a lipid bilayer, *Biochim. Biophys. Acta* **1828**(8), 1667--1673, 2013.

[20] Chen, C., et al. Diffusion behaviors of water-soluble CdSe/ZnS Core/Shell quantum dots investigated by single-particle tracking, *J. Phys. Chem. C* **112**(48), 18904--18910, 2008.

[21] Li, Q., et al. Tracking single quantum dot and its spectrum in free solution with controllable thermal diffusion suppression, *Anal. Biochem.* **377**(2), 176--181, 2008.

[22] Pons, T., et al. Hydrodynamic dimensions, electrophoretic mobility, and stability of hydrophilic quantum dots, *J. Phys. Chem. B* **110**(41), 20308--20316, 2006.

[23] Abrahamson, J. & Marshall, J. Permanent electric dipoles on gas-suspended particles and the production of filamentary aggregates, *J. Electrostat.* **55**(1), 43--63, 2002.

[24] Promislow, J. H. E., et al. Aggregation kinetics of paramagnetic colloidal particles, *J. Chem. Phys.* **102**(13), 5492--5498, 1995.

[25] Gea-Banacloche, J., et al. Optical switching in arrays of quantum dots with dipole-dipole interactions, *Phys. Rev. B* **74**(16), 165330, 2006.

[26] Saffman, P. & Delbrück, M. Brownian motion in biological membranes, *Proc. Natl. Acad. Sci.* **72**(8), 3111--3113, 1975.

[27] Saffman, P. G. Brownian motion in thin sheets of viscous fluid, *J. Fluid Mech.* **73**(04), 593--602, 1976.

[28] Petrov, E. P. & Schwille, P. Translational diffusion in lipid membranes beyond the Saffman-Delbrück approximation, *Biophys. J.* **94**(5), L41--L43, 2008.

[29] Hughes, B. D., et al. The translational and rotational drag on a cylinder moving in a membrane, *J. Fluid Mech.* **110**, 349--372, 1981.

[30] Petrov, E. P., et al. Translational and rotational diffusion of micrometer-sized solid domains in lipid membranes, *Soft Matter* **8**(29), 7552--7555, 2012.

[31] Bussell, S. J., et al. Effect of hydrodynamic interactions on the diffusion of integral membrane proteins: tracer diffusion in organelle and reconstituted membranes, *Biophys J.* **68**(5), 1828--1835, 1995.

[32] Peters, R. & Cherry, R. J. Lateral and rotational diffusion of bacteriorhodopsin in lipid bilayers: experimental test of the Saffman-Delbrück equations, *Proc. Natl. Acad. Sci.* **79**(14), 4317--4321, 1982.

[33] Cicuta, P., et al. Diffusion of liquid domains in lipid bilayer membranes, *J. Phys. Chem. B* **111**(13), 3328--3331, 2007.

[34] Hanke, W. & Schulue, W. *Planar lipid bilayers: methods and applications*, Academic Press, CA, 1993.

[35] Ramachandran, S., et al. Current bursts in lipid bilayers initiated by colloidal quantum dots, *Appl. Phys. Lett.* **86**(8), 083901--083903, 2005.

[36] Klein, S. A., et al. Formation of nanopores in suspended lipid bilayers using quantum dots, *J. Phys. Conf. Ser.* **109**, 0120122. 2008.

[37] Chen, X., et al. A cell nanoinjector based on carbon nanotubes, *Proc. Natl. Acad. Sci.* **104**(20), 8218--8222, 2007.

[38] Hall, J. E., et al. Alamethicin. A rich model for channel behavior, *Biophys. J.* **45**(1), 233--247, 1984.

CHAPTER- 8: Conclusion and Future Directions

CHAPTER 8

Conclusion and Future Directions

With the progressive development of biocompatible QDs, their usefulness could be immediately realized in biomedical and nano-biotechnology fields [1]. Highly fluorescent, non-toxic, water soluble QDs of various kinds are already in use as far as bio-labeling/sensing is concerned [2]. The quest for magneto-fluorescent materials is still on. The present work exploits the possibility of using a wurtzite phase, MnSe QD system in biophysical environment owing to their excellent fluorescent and magnetic responses [3]. Both CdSe, MnSe quantum dots have been studied with regard to colloidal stability, surface functionalization, cytotoxicity and bioimaging features. The optical stability was evaluated for of all the synthesized QDs with regard to varying reactant concentration, pH and aging prior biophysical characterizations.

First water soluble CdSe QDs were fabricated using PVA as the host matrix. The optical characteristics were compared in citric and rose-water environment. Next, CdSe and MnSe QDs were synthesized independently with TGA and SDS as capping agents. To make a stoichiometry dependent study, the water soluble, ternary QDs of $Cd_{1-x}Mn_xSe$ (x = 0 to 1) systems were also investigated considering TGA as capping agent. All the synthesized QDs were characterized by standard characterization techniques such as, TEM, XRD, UV-Vis, PL spectroscopy, Raman spectroscopy, FTIR spectroscopy etc.

The optical absorption and photoluminescence behavior of $Cd_{1-x}Mn_xSe$ QDs are found to be largely affected by the Mn^{2+}concentration. From the absorption spectra, the observed blue-shift of the absorption peak with increasing stoichiometry x, can be attributed to *sp–d* exchange interactions between electrons confined in the conduction, valence band electrons states and those located in the partially filled Mn^{2+} states. The PL spectra signify the occurrence of characteristic orange emission due to participation of Mn^{2+} ions only, with the incorporation of magnetic impurities in the NC core. As for larger values of x ($\geq$0.6), we observed a suppression/disappearance of the $^4T_1$–$^6A_1$ transition assisted via Mn^{2+} ions. Besides, the dominant character of the transitions from the trap levels as well as the internal Mn^{2+} transitions relative to the recombination of electron–hole pairs can be witnessed in the PL spectra. The deep defects occurring in $Cd_{1-x}Mn_xSe$ QDs were attributed to the presence of V_{Cd}–V_{Se} divacancies in the hexagonal wurtzite structure.

The optical absorption as well as PL emission of the synthesized CdSe QDs are strongly modulated and found to be dependent on varying Cd^{2+}/Se^{2-} concentration, reaction time, dispersing medium and on aging effect. The QDs prepared from larger Cd^{2+}/Se^{2-} ratio (3:1) of the precursor are expected to be monodisperse, of smaller diameter which showed intense emission characteristics. Moreover, the average size of the QDs is expected to be uniform beyond a reaction time of 60 min. Similarly, the optical properties of the MnSe QDs are found to be strongly manifested depending on the capping agent and reaction environment. The crystal structure of the MnSe QDs are optimized to wurtzite (WZ) type for a TGA concentration of 10% and Mn^{2+}/Se^{2-} ratio of 2:1. The synthesized WZ phase, MnSe QDs exhibited enhanced optical response with a quantum yield as high as ~75% as compared to the Rhodamine 6G®.

In addition, we have studied the optical stability of CdSe-PVA and MnSe-TGA QDs, using BSA as dispersing agent in different cell culture media. In cell culture media, a high ionic strength results in dominant van-der Waal attraction over electrostatic repulsive behavior, yielding agglomerated particles. The CdSe QDs dispersed in PVA are generally stable in cell culture media, even in the absence of any dispersing agent. In contrast, the MnSe-TGA QDs experienced spontaneous aggregation when they are directly transferred to the cell culture media. Moreover, the addition of BSA as dispersing agent has significantly improved the QD dispersity in DMEM and MEM media over RPMI-1640 one. The variation of QD stability, in different cell culture media, is likely to be dependent on the degree of protein interaction mechanism in the respective media. Furthermore, the CdSe-PVA QDs, in lemon water,indicated a better optical response than in rose water media. The carboxyl (-COOH) functional group available in the PVA dispersed CdSe QDs is esterified to PVA-C in the citric acid media, ensuing an improved stability [4]. Whereas, in case of MnSe-TGA QDs the higher stability in lemon water media is attributed to the formation of di-carboxylic acid layer around the surface of the QDs through intermolecular hydrogen (H^-) bonding.

The magnetic characterization of the MnSe-TGA QDs has revealed surface dependent magnetic property for varying TGA concentration.The higher value of Neel temperature (T_N = 59 K) exhibited by 10% TGA coated MnSe QDs is attributed to the adequate charge transfer between the SH^- group and Mn^{2+} ions. In contrast, for lower

concentration of TGA (1%), charge transfer mechanism is low thereby providing a lower magnetic ordering (T_N =39K) in the QDs. The Neel temperature was different for different TGA concentration, the QDs being antiferromagnetic below Neel temperature and above it paramagneticin nature. From the hysteresis plots it can be observed that, 10% TGA coated QDs possess a lower value of coercivity as compared to the 1% TGA coated one at low temperature. Thus, as for biological relevance, 10% TGA QDs is a suitable choice, where the QDs are expected not to agglomerate on removal of the magnetic field. Also, magnetic characteristics are found to bedependent on the stoichiometry parameter x, in ternary $Cd_{1-x}Mn_xSe$ QD systems. The self-diffusion behavior of the Mn^{2+} ions, for a larger value x could provide a higher value of Neel temperature (x =1). With increasing x, the diffusion of Mn^{2+} ions from the core to the surface would facilitate the charge transfer between Mn^{2+} ions and the capping agent TGA. At a lower x, however, most of the Mn atoms are likely to concentrate in very small clusters providing thereby isolated Mn^{2+} spins. Accordingly, the QD system is characterized by a paramagnetic feature. From the magnetic behavior of SDS capped MnSe QDs, a bifurcation between the ZFC and the FC is witnessed which may be due to theformation of magnetic domains and domain-wall movement [5,6]. In this QD system, the Neel temperature and bifurcation temperature are found as, 35K and 41K; respectively.

The BSA conjugation aspects of CdSe and MnSe QDs, suggest that the TGA coated QDs can efficiently participate in FRET energy transfer process. This was ascertained from the PL, TR-PL and overlapping behavior of acceptor (BSA) absorption spectra and donor (QDs) emission spectra. The energy transfer efficiency is found to be ~71% and 65% for CdSe-TGA and MnSe-TGA QDs; respectively. Whereas, for SDS capped QDs, BSA would act as a surface passivator, thus facilitating enhanced radiative emission response of the conjugated QDs. The cytotoxicity study has revealed a lowered toxicity level of the MnSe QDs as compared to the CdSe QDs. This may be because of lower photo-bleaching behavior of the Mn^{2+} precursor as compared to Cd^{2+}one under UV environment. Note that, former is a hard Lewis acid while the latter is a soft one. From the fluorescence microscopy data, it can be seen that, all the synthesized QDs are highly biocompatible with a high fluorescent contrast in cellular (lymphocyte) environment. The

fluorescent imaging capability (CTCFs) of the QDs is found to vary with capping agent and system types. Furthermore, the cellular uptake of the MnSe QDs, as evident from a clear bioimaging response, is demonstrated to be more advantageous in case of use of BSA as a dispersing agent in the cell culture media. Most importantly, the confirmation of intracellular localization of the MnSe QDs is also affirmed throughconfocal microscopy experiments, while targeting on live NIH-3T3 cells.

As an important application in electrophysiology, the CdSe QDs are employed for studying current bursts (ion channel) in an artificial bilayer membrane (soy-extracted lecithin bilayer). The CdSe QDs exhibited voltage dependent current fluctuation with well-defined conductance states. With the application of different biasing voltage, the concentration of ions passing through the pores created by QD aggregation is believed to have changed. The number of QDs participating in the formation of nanopores generally vary and also, that the specific conductance state is largely dependent on the shape of the nanopores. We discussed our results based on 'spherical' and 'non-spherical' models [7,8]. While formation of spherical pores raise over simplification approach, the non-spherical nanopores are believed to be more practical so as to explainthe flow of ions and interrelating with a finite conductance state [9]. A conductance state of ~14.3 nS, created by an aggregation of ~3.6 QDs, resulted in a spherical nanopore of diameter ~6.09 nm. This was corresponded to a biasing voltage of -10 mV. Whereas, a lower conductance state of ~6.3 nS is observed corresponding to an aggregation of 3 QDs. On the other hand, similar conductance states might have been created by non-spherical nanopores of a relatively smaller diameter of ~1.5 nm (with $N_Q = 2.6$) and ~0.95 nm (with $N_Q = 2.4$). With an increase of biasing voltage to -20 mV, the conductance values are increased to ~11 nS and 21.1 nS which corresponded to a spherical nanopore diameter of ~5.3 and 7.5 nm; respectively. In contrast, the sizes of the non-spherical nanopores, for the respective conductance states, are estimated as ~1.22 nm and ~1.8 nm. A large magnitude of the conductance state at a higher biasing voltage (as compared to the lower one), is because of the flow of higher concentration of ions through wider nanopores which includes interfacial curvature effects.

In the light of a theoretical framework, the Brownian movement of QDs was explored for different situations [10]. In the pre-aggregate state, owing to a higher

relaxation time experienced by smaller QDs (~2 nm) they tend to get localized more tightly in the bilayer as compared to the larger sized QDs (~20 nm). Moreover, an aggregated structure is found to be more diffusive than a bare QD, in the pre-aggregate state. The relaxation time shoot up by a factor of ~56 and ~64 folds for highest (6 QDs aggregation) conductance state with respect to the lowest one (3 QDs aggregation) for ion channels created by fully (each QD size ~2 nm) and partially inserted (each QD size~12 nm) aggregated structures; respectively. Consequently, the response time of the conductance states of the ion channel formed by the larger sized, partially inserted QDs is about 50 times greater than the states created by smaller sized, fully inserted counterparts. It also provided the highest conductance value (~92.31 nS)and an *MSD* of ~1.18 μm^2.
The important findings of the present thesis can be summarized into following points:

(a) Processing of non-iron based, highly fluorescent, magnetic QDs of WZ phase MnSe system
(b) Improved biocompatibility and efficient bioimaging of MnSe QDs in live cells (NIH-3T3)
(c) Recording of ion channels across a lecithin (soy-extracted) bilayer due to insertion of CdSe QDs
(d) Efficient FRET mechanism between TGA coated CdSe and MnSe QDs with BSA proteins
(e) Optimal conditions for obtaining CdSe and MnSe QDs as luminescent probes

The prospective studies that can be planned in near future can be as highlighted below.

(a) The water soluble, nontoxic, non-iron based, MnSe QDs can work as an alternative candidate to conventional iron based non fluorescent nanoparticles in different areas of biophysical and biomedical research. More control studies e.g., size dependent correlation on fluorescence and magnetic characteristics are needed prior relevance in cellular imaging *in vivo*, targeted drug delivery including examination of intracellular processes and deep penetration into tissues.
(b) As an important concept for specific biophysical application, highly fluorescent CdSe and MnSe QDs, in lemon water environment, could provide an improved

optical stability against environmental degeneration. Size dependent aspect may also be considered to evaluate their efficiency.

(c) The ion channel activity displayed by the CdSe QDs, in a natural phospholipid bilayer, will provide a closer account to understand ion transport mechanism in live cells. The magneto-gated/light-gated ion channels could also be explored when subjected to static magnetic field/light illumination.

(d) Permeation of non-spherical QDs into bilayers and correlation with current bursts will provide a completely new approach on obtaining a definite conductance state of interest. This may find immense value in screening suitable QDs meant for precise control of ion channel activity.

Finally, as nanotechnology is an emerging field with plentiful promise in health and energy sectors, however, the industrial and commercial use of nanomaterials is still under scrutiny owing to several environmental issues. Toxicity, waste management, and other health hazard issues are required to be fixed at an early stage so that living organisms and the ecosystem can be protected at large.

References

[1] Alexson, D., et al. Semiconductor nanostructures in biological applications, *J. Phys. Condens. Matt.* **17**(26) R637--R656, 2005.

[2] Menon, J. U., et al. Nanomaterials for photo-based diagnostic and therapeutic applications, *Theranostics* **3**(3), 152--166, 2013.

[3] Sarma, R., et al. Physical and biophysical assessment of highly fluorescent, magnetic quantum dots of a wurtzite-phase manganese selenide system, *Nanotechnology* **25**(27), 275101, 2014.

[4] Mansur, H. S., et al. Synthesis and characterization of CdS quantum dots with carboxylic-functionalized poly (vinyl alcohol) for bioconjugation, *Polymer* **52**(4), 1045--1054, 2011.

[5] Chernova, N. A., et al. Solitary excitations and domain-wall movement in the two-dimensional canted antiferromagnet $(C_2N_2\ H_{10})_{1/\ 2}FePO_4(OH)$, *Phys. Rev. B* **70**(14), 144405, 2004.

[6] Midya, A., et al. Magnetocaloric effect in $HoMnO_3$ crystal, *Appl. Phys. Lett.* **96**(14), 142514 - 142514-3, 2010.

[7] Noronha, F. S., et al. Macrophage damage by Leishmania amazonensis cytolysin: evidence of pore formation on cell membrane, *Infect.Iimmun.* **68**(8), 4578--4584, 2000.

[8] Ramachandran, S., et al. Current bursts in lipid bilayers initiated by colloidal quantum dots, *Appl. Phys. Lett.* **86**(8), 083901--083903, 2005.

[9] Sarma, R. & Mohanta, D. Recording ion channels across soy-extracted lecithin bilayer generated by water-soluble quantum dots, *Philos. Mag.* 94(4), 345-357, 2014.

[10] Sarma, R. & Mohanta, D. A Comprehensive view on the brownian motion of quantum dots in electrolytic solution, lipid bilayer and their aggregated state in the lipid biomembrane, *J. Comput. Theor. Nanos.* **9**(8), 1070--1077, 2012.

***

Appendix

Appendix-1

Analytical techniques employed

QD size and morphological features were revealed through high resolution transmission electron microscopy (HRTEM, JEOL, JEM-2100) working at an accelerating voltage of 200 kV. Whereas, the structural phase of the samples under study was characterized by an X-ray diffractometer (XRD, MiniFlex, Rigaku) equipped for CuK_{α} radiation (λ=1.543 Å). The characteristic optical absorption features were recorded through UV–Visible optical absorption spectroscopy (UV 2450, Shimadzu Corporation), whereas photoluminescence (PL) spectra were obtained by using a PerkinElmer LS 55 spectrophotometer. In the latter case, the PL data was acquired through a computer controlled standard monochromator based photodetection system. The IR-active vibrational features were assessed through Fourier transform infrared (FTIR) (Nicolet model Impact-410) studies. As for FTIR study of the as-synthesized QD systems, solid powder was employed to make pellets in KBr. Furthermore, vibrational features were explored by Raman spectroscopy using a micro- Raman spectrometer (Renishaw, UK) at room temperature. On the other hand, magnetic characterization and carrier lifetime measurement of the QDs were performed by a vibrating sample magnetometer (VSM, LakeShore's 7400 series) and a time resolved photoluminescence system (TR-PL, LifeSpec II, Edinburg Instruments, UK); respectively. Finally, bright field as well as fluorescence imaging of the lymphocytes (treated with QDs) was adopted using a Leica DM 3000 fluorescence microscope under uniform light exposure and using a 40X objective/NA=1.25. The confocal microscopy experiment was carried out by using Leica DM (TCS SP 5) confocal microscope using a 60X objective/NA=1.25.

Appendix-2

X-Ray diffraction technique (XRD)

XRD is a versatile technique exploited to recognize the crystal structure and composition of a material. In this method, an X-ray beam is allowed to strike a target material and the beam is diffracted according to well known Bragg"s law. The characteristic of the target material is identified from the received diffraction pattern. Physical properties such as amount of crystallinity, stress, strain, and defects are investigated with this technique. Moreover, XRD is also used in indentifying size distribution of the particles by measuring full width at half maxima (FWHM) of various peaks. Crystallite size (D_{cry}) can be estimated using popular Williamson–Hall (W-H) equation:

$$\beta Cos\theta = 4\varepsilon_s Sin\theta + k\lambda / D_{cry}$$

Here, λ is the wavelength of the CuK_α line (1.543 Å), β is the full width at half maxima, θ is the Bragg's diffraction angle and κ is the shape factor (~0.9). By plotting the values of $\beta\ cos\theta$ against $4\ sin\ \theta$, micro strain (ε_s) of the nano-crystallites could be obtained from the slope, and the average crystallite size from the intercept on the vertical axis.

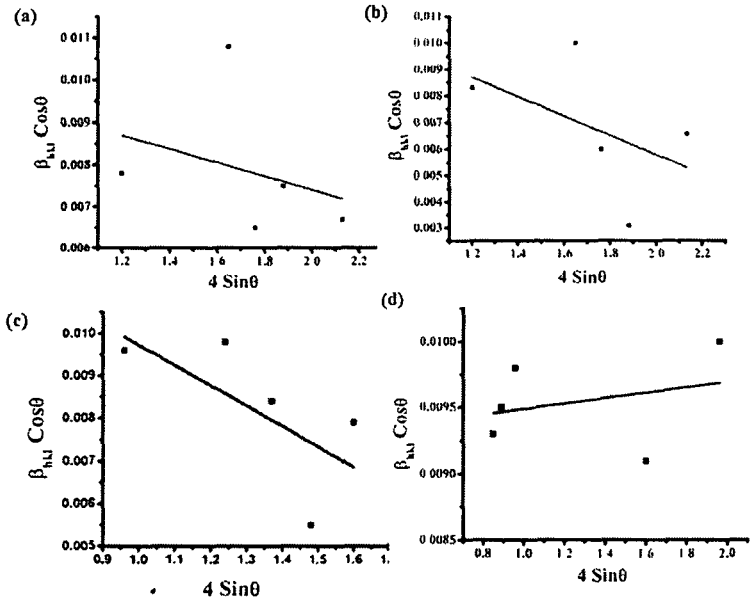

Figure 1: W- H plot of (a) CdSe-TGA (b) CdSe-SDS (c) MnSe-TGA (d) MnSe-SDS system

Appendix-3

Raman spectroscopy

Collective vibrations of atoms or molecules occur in crystals are defined by quasi-particles, phonons. For a three-dimensional (3D) solid containing N unit cells with p atoms each, ($3pN$-6) different phonons can propagate and their wavevectors (k) exists in a volume of the reciprocal space called the Brillouin Zone (BZ). The phonon having in and out phase oscillations of neighboring atoms are termed as acoustic and optical phonons; respectively. Both acoustic and optical phonons can be obtained as longitudinal or transversal, depending on whether the atoms move parallel or perpendicular to the direction of wave propagation given by k. Consequently, we can have longitudinal (LA) and transverse (TA) acoustic phonons and longitudinal (LO) and transverse (TO) optical phonons/vibrations. In addition to the ordinary lattice vibrations in a bulk solid (phonons), there exist surface optic (SO) phonon, which is the quantum of a lattice vibration mode associated with a solid surface. Surface vibrations are however, distinct from the bulk vibrations, as they arise from the abrupt termination of a crystal structure at the surface of a solid

When light incident into solid state molecules, some part of the light is elastically scattered from the phonons. This is called Rayleigh scattering. In contrast, the Raman scattering defines the inelastic scattering of light with a different frequency from the phonons. In principle, Raman effect, can be explained by the deformation of molecules with molecular polarizability α in presence of electric field E. E is originated from an oscillating electromagnetic wave sourced from an incident laser light with photon of frequency υ_0. Upon interaction of E with the sample, molecule deforms due to the induced electric dipole moment $P=\alpha E$ and start vibrating with characteristic frequency υ_m. The resulting frequency of scattered light is reduced to υ_0-υ_m. This Raman frequency is called Stokes frequency.

Raman spectroscopy can evaluate dual properties of an investigated material; electrical as well as mechanical. And, two kinds of parameters influence the Raman spectra: 1.parameters acting on the "mechanics" (atomic mass, bond geometry), and 2. parameters acting on the "charge transfer" (iono-covalency, band structure) [1].

Appendix-4

Origin of deep trap level

In an ideal crystal lattice of a semiconductor, if there is deviation of atomic positions from their designated positions defects are arises. In a semiconductor, if an atom is removed from its regular lattice site, the created empty lattice site is termed as vacancy defect. A divacancy defect will occur when two vacancies come together with the removal of two neighboring atoms form a stable complex. Divacancies in semiconductor can be created by particle irradiation either as primary defect or as a secondary defect by pairing of single vacancies. These defects may introduce electronic energy states into the semiconductor band-gap such as shallow level defects and deep level defects. Shallow lavels are located near their related band edge and they are thermally ionize at room temperature. In contrast, deep-level traps are "deep" in the sense that the energy required to remove an electron or hole from the trap to the valence or conduction band is much larger than the characteristic thermal energy kT, where k is the Boltzmann constant and T is temperature. In CdSe WZ bulk system two broad deep level emissions are observed at energy of 1.30 and 1.05 eV [1]. The origin of these luminescence centres can be explained by V_{Cd}–V_{Se} divacancy centre model as proposed by Schneider et al [2]. According to this model V_{cd} and V_{se} are monovalent acceptor and donor pair and there is a strong tendency for their association either with foreign impurities or by forming nearest neighbor cation–anion divacancies (V_{Cd}–V_{Se},).This divacancies have much higher activation energy for diffusion, as compared to the monovacancies. Consequently, cation–anion divacancies become dominant stoichiometric lattice defect in as-grown CdSe, and other II_B–VI compounds [2]. In WZ CdSe, two different types of V_{Cd}–V_{Se} associates create the observed two deep trap level emission responses orienting along two directions. One divacancy is oriented along the hexagonal c axis and the other is oriented along the basal Cd–Se bond directions. These two different types of divacancy become energetically different after trapping electron and hole pair. In QDs, the radiative or nonradiative relaxation of excitation via these deep level states competes with the recombination in the intrinsic excitonic states and reduces the intensity of excitonic emission [1].

Appendix-5

The Franck-Condon approximation

Classically, Franck–Condon principle is based on the approximation that an electronic transition is most likely to occur without changing the position of the neuclei in a molecular structure. The transition occurs is a vertical transition with momentum conservation. Quantum mechanically this principle defines that, the intensity of a vibronic transition is proportional to the square of the overlap integral between the vibrational wavefuntions and the two states involved in the transition [3]. After an electronic transition, the nuclei respond by moving to a new equilibrium position which results change of the molecule to the excited state configuration. The configuration change is called as lattice relaxation and the energy involved in the process is called relaxation energy [4]. The emission follows the same path in reverse direction. The relaxation of the nuclei position can be defined as Stokes shift, which is the difference between the absorption and emission maxima. Within the Franck condon approximation the electron phonon coupling strength is defined by Huang Rhys parameter *S*.

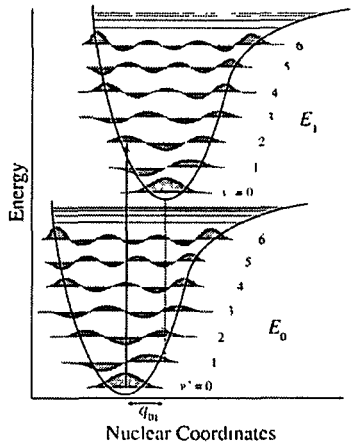

Figure: Franck-Condon principle energy diagram. Since electronic transitions are very fast compared to nuclear motions, vibrational levels are favored when they correspond to a minimal change in the nuclear cordiantes. The potential wells are shown favoring transitions between v=1 and 2

Appendix-6

Brus model

Brus has developed a popular effective mass model relating particle size and band gap energy of a semiconductor which can be expressed as follows:

$$E_g = E_g(0) + \frac{\hbar^2}{8d^2}\left[\frac{1}{m_e^*} + \frac{1}{m_h^*}\right]$$

Here, $E_g$is the bandgap of nanoparticle, $E_g(0)$ is the bulk band gap, m_e^* is the effective mass of electron, m_h^* is the effective mass of hole and d is size of QDs. For CdSe QDs m_e^* and m_h^* are $0.13m_0$ and $0.45m_0$; respectively. $E_g(0)$=1.74 for CdSe QDs. Putting these values in the above equation the size of CdSe QDs can be calculated by using the following equation [5]

$$E_g = 1.7 + 3.7/d^2$$

Appendix-7

TR-PL spectroscopy

Spectral and temporal evolution of the emission of a sample can be determined by TR-PL spectroscopy when the sample is illuminated by a short pulse of light. In a semiconductor, the characteristic charge carrier lifetime decay, from excited to ground state, is classified as radiative and non-radiative.

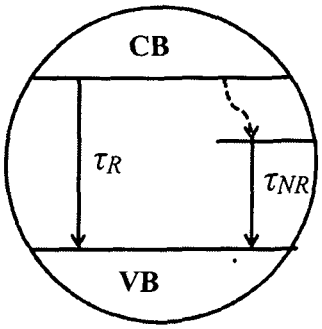

Figure: Schematic depicts radiative and non-radiative decay parameters in a semiconductor system

The photoluminescence decay rate of a can be expressed as sum of the radiative (k_R) and non-radiative (k_{NR}) decay rates [6]:

$$k_{PL}=k_R+k_{NR}$$

Knowing that decay rates and decay time constants are inversely related [7], we have

$$\tau_{PL}^{-1}=\tau_R^{-1}+\tau_{NR}^{-1}$$

$$\tau_{PL}=(\tau_R+\tau_{NR})/\tau_R\tau_{NR}$$

Where τ_{PL}, τ_R, and τ_{NR} are the time constants of PL, radiative decays and non radiative decays.

The decay parameters are highly dependent on the nature and dimensions of the materials. Furthermore, surface effects, dopants, impurities can introduce significant variations in this parameter. Thus, interaction of semiconductor with the surrounding environment is reflected in TRPL spectra. Hence, the TRPL is highly suited for the analysis of the phenomena that determine fast charge carrier dynamics in a semiconductor.

Appendix-8

Förster radius, R_0.

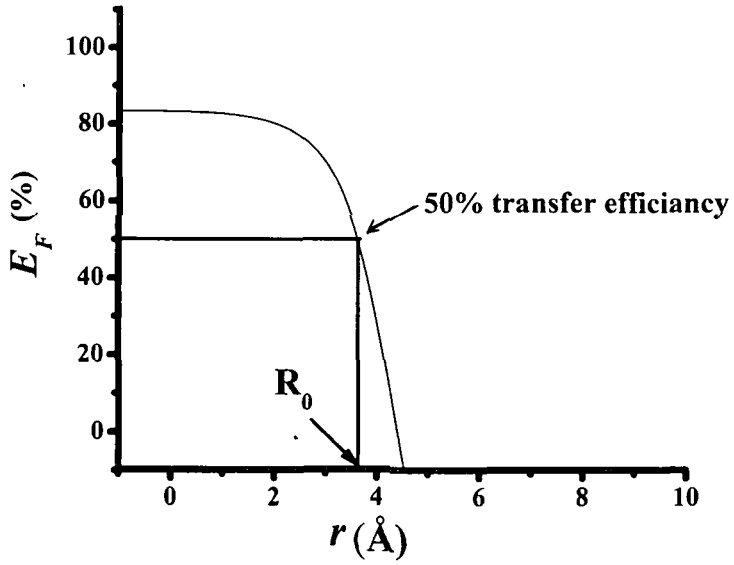

Figure: Variation of energy transfer efficiency (E_F) in percentage with donor and acceptor separation distance r. The Förster radius (R_0) is shown by arrow mark where FRET pair shows 50% energy transfer efficiency.

Appendix-9

Calculation of CTCF using ImageJ (J-1.46r) software

Image analysis techniques are applied to count the total fluorescence in a QD treated cell using software ImageJ(J-1.46r). It is a basically a public domain Java image processing program that was developed at the National Institute of Health, USA [8,9]. The basic steps involved in counting of fluorescent cells are listed below:

1. The fluorescent image to be analyzed is imported into the software.
2. The basic measurements to analyze the cell such as area, mean gray value and Integrated Density are then adjusted using the software menu bar.
3. A specified area for the fluorescent stained cell for analysis is selected using free hand selection. This helps to quantify a specific region of the imported cell for fluorescence.
4. Background (the non – fluorescent part of the image) is selected to minimize the maximum errors in the fluorescent counting of a cell. For the background selected region area, mean gray value and integrated density are calculated.
5. From the results, the total fluorescence per cell is then analyzed using Excel sheet.
6. Repetition of above steps for different fluorescent and background selected regions to obtain results with minimum error.
7. The corrected total fluorescent (CTCF) intensity value is calculated for each case, using the relation given by, CTCF= Integrated density – (Area × mean fluorescent of background setting) and average is calculated

Appendix-10

Laser drill method used for micropore formation

Using laser ablation method Glass cover slip was ablated under 157 nm irradiation at 6.4X with 22 mJ pulse energy (455 mJ/cm^2 fluence) at 50Hz for 25 s (integrated power density 570 J/cm^2)) to create a thorough hole of ~160 μm diameter in ~150 μm thick cover slip (Fig. 6.7(a)).The 1 mm thick PMMA sample was ablated under 157 nm mask projection with same pulse energy for 250s at 100 Hz so as to create a micropore of diameter ~80 μm (Fig. 6.7(b)). In contrast, the ~60 μm thick polymide sample took 50 s (100 Hz) to form a 110 μm sized hole, as shown in Fig.6(c)

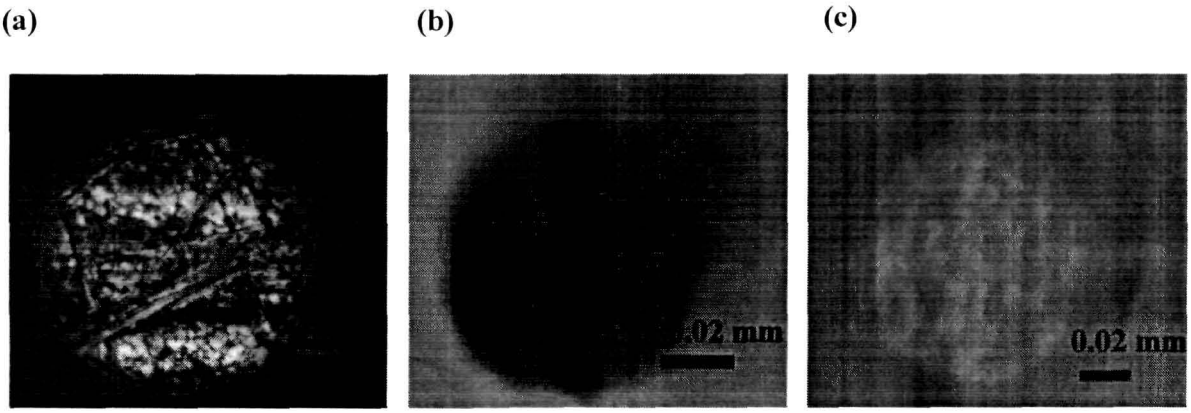

Figure: (a) 160 μm hole in borosilicate glass cover slip, b) 80 μm hole in PMMA, c) 110 μm hole in polyimide

Appendix-11

EPC 10 Patch-clamp amplifier

The complete ion channel experiment was performed using a Patch Clamp Amplifier (EPC10) and patchmaster software (HEKA Elektronik, Germany) ®. The patch clamp technique permits high-resolution recording of the ionic currents flowing through a cell's plasma membrane. With different configurations, patch clamp amplifier allow to record and manipulate the currents that flow through single ion channels or multiple ion channels i.e across the whole plasma membrane. EPC 10 Patch clamp amplifier is a complete data acquisition system acquainted with Patchmaster software. Patchmaster software includes a digital storage oscilloscope, a variable analog filter, a sophisticated pulse generator and a fully featured data acquisition analysis system. The detail regarding the mentioned amplifier can be obtain by following web-link

www.heka.com

Appendix-12

Montal-Müeller technique (Painting method)

The painting method was first described by Mueller and colleagues [10, 11]. It is the simplest one for obtaining fast forming bilayer on solid substrates or across apertures. In the technique, an experimental chamber is divided into two parts and they are connected via a small micron size aperture (80–100 μm in diameter) located on the center of a suitable hydrophobic substrate material. Both the compartments are filled with aqueous solutions followed by painting a lipids-solvent (hexane) mixture on both sides of the aperture using thin brush. This results in formation of bilayer in presence of different forces.

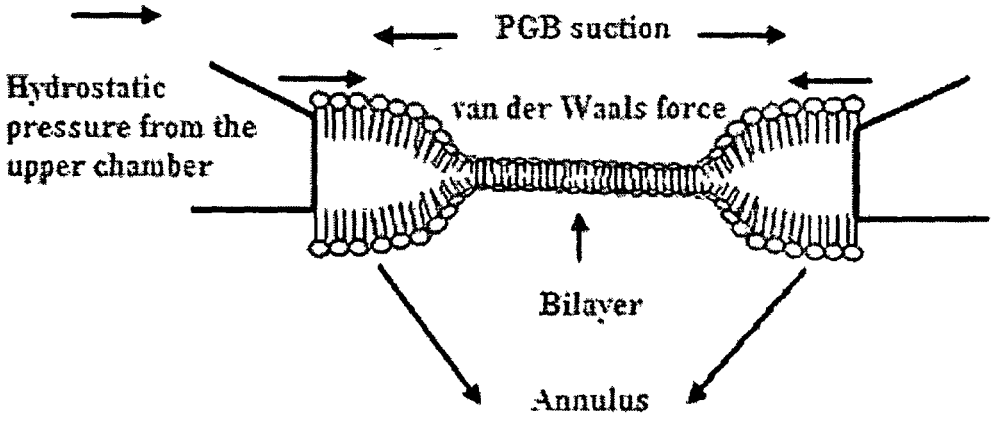

Figure: Schematic of a bilayer forming in an aperture in presence of different forces

Although it incorporates hydrocarbon molecules from the organic solvent that affects lipid thickness, it is widely used even today [12].

Appendix-13

Optical characterization of water soluble CdSe QDs used in ion channel experiment

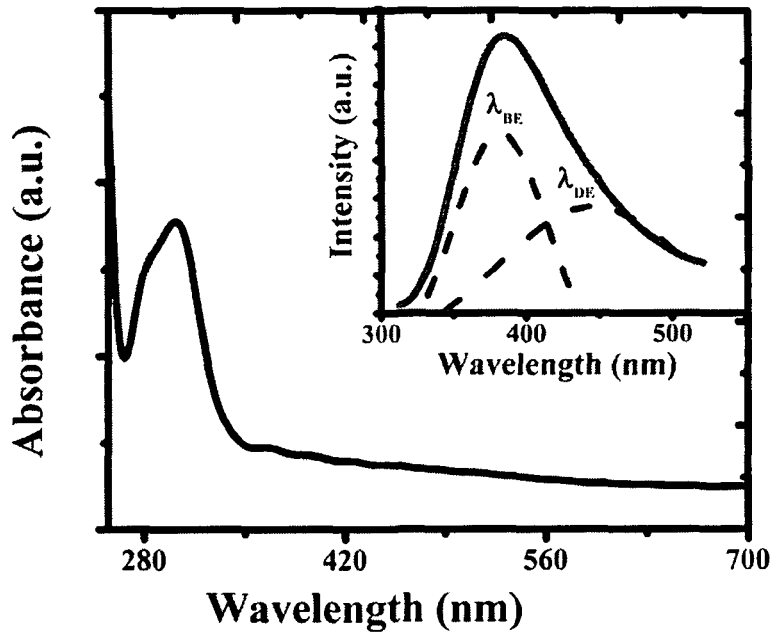

Figure: Optical absorption and de-convoluted photoluminescence spectra of CdSe QDs

References

[1] Babentsov, V. & Sizov, F. Defects in quantum dots of IIB–VI semiconductors,*Opto-Electronics Rev.***16**(3), 208--225, 2008.

[2] Babentsov, V., et al. Deep level defect luminescence in cadmium selenide nano-crystals films,*J. Crys. Growth* **280**(3–4), 502--508, 2005.

[3] Naler, S., *Optical studies of ordering phenomena in manganese oxides*, Cuvillier Verlag, Hamburg Univ, 2005.

[4] Holt, J. M. & Utah, T. U."Ultrafast Optical Measurements of Charge Generation and Transfer Mechanisms of Pi-conjugated Polymers for Solar Cell Applications,1720-1902." Diss.The University of Utah, 2009.

[5] Shah, C. P., et al. Precursor concentration and temperature controlled formation of polyvinyl alcohol-capped CdSe-quantum dots, *Beilstein J. Nanotech.***1**(1), 119--127, 2010.

[6] Schlegel, G., et al. Fluorescence decay time of single semiconductor nanocrystals,*Phys. Rev. Lett.* **88**(13), 137401, 2002.

[7] Li, C. P., et al. Photoluminescence and time-resolved photoluminescence of star-shaped ZnO nanostructures,*Solid State Commun.* **139**(7), 355--359, 2006.

[8] http://amrita.vlab.co.in/index.php?sub=3&brch=278&sim=1474&cnt=1

[9] http://sciencetechblog.com/2011/05/24/measuring-cell-fluorescence-using-imagej/

[10] Mueller, P., et al. Reconstitution of cell membrane structure in vitro and its transformation into an excitable system, N*ature* **194**, 979--980, 1962.

[11] Mueller, P. and Rudin, D. O.Bimolecular Lipid Membranes: Techniques of Formation, Study of Electrical Properties, and Induction of Ionic Gating Phenomena, in *Laboratory Techniques in Membrane Biophysics*, H. Passow et al., eds. Springer, Berlin, Heidelberg. 1969, 141-156.

[12] Kongsuphol, P., et al. Lipid bilayer technologies in ion channel recordings and their potential in drug screening assay,*Sensors and Actuators B: Chemical,* **185**, 530--542, 2013.

Addenda

IOP Publishing Nanotechnology
Nanotechnology 25 (2014) 275101 (15pp) doi 10 1088/0957 4484/25/27/275101

Physical and biophysical assessment of highly fluorescent, magnetic quantum dots of a wurtzite-phase manganese selenide system

Runjun Sarma[1], Queen Das[1], Anowar Hussain[2], Anand Ramteke[2,3], Amarjyoti Choudhury[1] and Dambarudhar Mohanta[1,3]

[1] Emerging Nanoscience and Soft Matter Laboratory, Department of Physics, Tezpur University, PO Napaam, Assam-784 028, India
[2] Cancer Genetics and Chemoprevention Research Group, Department of Molecular Biology and Biotechnology, Tezpur University, PO Napaam, Assam-784 028, India

E-mail aramteke@gmail com (A Ramteke) and best@tezu ernet in (D Mohanta)

Received 22 January 2014, revised 19 March 2014
Accepted for publication 31 March 2014
Published 24 June 2014

Abstract

Combining fluorescence and magnetic features in a non-iron based, select type of quantum dots (QDs) can have immense value in cellular imaging, tagging and other nano–bio interface applications, including targeted drug delivery Herein, we report on the colloidal synthesis and physical and biophysical assessment of wurtzite-type manganese selenide (MnSe) QDs in cell culture media Aiming to provide a suitable colloidal system of biological relevance, different concentrations of reactants and ligands (e g , thioglycolic acid, TGA) have been considered The average size of the QDs is ~7 nm, which exhibited a quantum yield of ~75% as compared to rhodamine 6 G dye® As revealed from time-resolved photoluminescence (TR-PL) response, the near band edge emission followed a bi-exponential decay feature with characteristic times of ~0 64 ns and 3 04 ns At room temperature, the QDs were found to exhibit paramagnetic features with coercivity and remanence impelled by TGA concentrations With BSA as a dispersing agent, the QDs showed an improved optical stability in Dulbecco's Modified Eagle Media® (DMEM) and Minimum Essential Media® (MEM), as compared to the Roswell Park Memorial Institute® (RPMI-1640) media Finally, the cell viability of lymphocytes was found to be strongly influenced by the concentration of MnSe QDs, and had a safe limit upto 0 5 μM With BSA inclusion in cell media, the cellular uptake of MnSe QDs was observed to be more prominent, as revealed from fluorescence imaging The fabrication of water soluble, nontoxic MnSe QDs would open up an alternative strategy in nanobiotechnology, while preserving their luminescent and magnetic properties intact

Keywords quantum dot, semiconductor, emission, cell culture, bioimaging

(Some figures may appear in colour only in the online journal)

1. Introduction

Semiconductor quantum dots (QDs) find widespread application mostly due to their bright fluorescence property Manganese selenide (MnSe) is a classic example in the family of chalcogenides and binary-semiconductor systems MnSe QDs, in particular, have attractive magneto-optic responses owing to the availability of a large number of unpaired electrons in Mn^{2+} high-spin state, along with size-dependent optical gaps that could vary over a broad range of the

[3] Authors to whom any correspondence should be addressed

electromagnetic spectrum (from ultraviolet (UV) to visible wavelengths) [1, 3] Essentially, MnSe comes in two polymorphic forms α-MnSe with a cubic modification that gives a rock salt structure (RS), and with a hexagonal modification of zinc blende (ZB, β-MnSe) and wurtzite structures (WZ, γ-MnSe) [4, 5] The octahedrally coordinated RS structure of MnSe offers a stable cubic phase, while the system is metastable in the hexagonal configuration [5, 6] Although ZB and WZ types of *MnSe* are quite unstable and are extremely rare, they are of significant interest because of their structural compatibility with other II–VI semiconductor systems which are not only fluorescent but are also highly photostable [7] Moreover, the cooperative effect of fluorescence response and magnetic ordering could offer a new window for tuning bright-fluorescence imaging in response to an externally applied magnetic field

To date, amongst highly fluorescent semiconductor systems, Cd-based ones (e g , CdSe, CdTe, CdS and CdSe/ZnS core shell QDs) have received maximum attention in biophysical research, particularly as tagging, labeling and imaging agents Nevertheless, the biocompatible nature of these QDs, in a cellular environment and under UV illumination, remained questionable owing to high toxicity level of free Cd, thereby limiting applications in nano-biotechnology and bioengineering fields [8, 9] Since the energy of the UV radiation is close to the chemical bond energy, the semiconductor particles are likely to experience photolytic dissolution, releasing toxic heavy metal ions of Cd^{2+} Replacing Cd with Mn (for instance, choosing MnS and MnSe instead of CdS and CdSe), would help reduce the toxicity level by avoiding the photobleaching of Mn^{2+} [10–13] The Mn^{2+} precursor is a hard Lewis acid [11, 14] while the Cd^{2+} precursor is relatively softer one, so the former is less reactive to the surroundings, thereby experiencing a much lowered photobleaching compared to the latter [11] While employing QDs in nanobio-interface research, everyone is concerned about critical issues such as water solubility, bio-functionality and bio-specificity In this regard, MnSe QDs are likely to be more environment-friendly and biocompatible, with reduced cellular toxicity [15] By adopting a suitable approach, the surface-modified QDs could not only provide water solubility but also bioconjugation capability through the use of effective linkers, such as silica, polymers, thiol-ligands, phospholipid micelles and surfactant molecules [16, 17] Cellular biology experiments are generally conducted in a complex biological environment which contains a mixture of amino acids, salts, glucose, vitamins and other nutrients Undoubtedly, it is extremely important to evaluate QD behavior in such environments both *in vitro* and *in vivo* studies It was known that bare nanoparticles tend to agglomerate immediately after they are added to the culture media In this regard, surface functionality, along with the presence of some essential biological materials (such as protein, serum and nutrients), could largely help in obtaining a stable dispersion of the desired QDs [18, 19]

In this work, we demonstrate a convenient colloidal route for synthesizing water-soluble MnSe QDs, using thioglycolic acid (TGA) as the capping agent/ligand Although pure glycolic acid is water soluble, TGA is somewhat not when present in an excess amount, but due to its capability of providing efficient coating and extra-photostability to the fluorescent QDs, there has been a rapid growth in the development of TGA-capped QDs for biological applications [20, 21] We optimize the synthesis of water soluble WZ-structure MnSe-TGA QDs by standardizing different factors, *viz* , the concentration of the capping agent (TGA) and the QD precursor ratio (Mn^{2+}/Se^{2-}) As mentioned above, in order to evaluate the QD-dispersion ability in cell media, special emphasis was given to decipher the media-dependent optical response of MnSe-TGA QDs while bovine serum albumin (BSA) was used as a dispersing agent Note that BSA is the most abundant protein in blood plasma [22], and it has been widely used as a model protein for dispersing nanoparticles in physiological fluids [23, 24] In this work, apart from physical characterizations, we assessed the response of TGA capped MnSe QDs in commonly used cell culture media a) Dulbecco's Modified Eagle Media (DMEM)®, b) Minimum Essential Medium (MEM)® and c) Roswell Park Memorial Institute (RPMI-1640)® media In addition, a critical evaluation with respect to the cytotoxicity aspect of the MnSe-TGA QDs is discussed and the cellular uptake of the QDs by lymphocyte cells (obtained from human blood) is highlighted through fluorescence imaging data

2. Experimental details

2 1 Materials and reagents

The chemicals used in this work include manganese chloride-tetra hydrate ($MnCl_2\,4H_2O$), fetal bovine serum (FBS), histopaque and cell culture media, all purchased from Himedia Pvt Ltd The selenium dioxide (SeO_2) and TGA were obtained from Merck Specialities Pvt Ltd, whereas the sodium hydroxide (NaOH) was purchased from Qualigens Fine Chemicals Ltd Sodium borohydride ($NaBH_4$) and BSA were purchased from Sigma-Aldrich, Mumbai

2 2 Synthesis of TGA coated MnSe QDs

In a typical synthesis procedure, 0 62 g of $MnCl_2\,4H_2O$ and 0 11 g of SeO_2 were dissolved in 22 mL deionized (Millipore) water, followed by the addition of 0 1 g of $NaBH_4$ as a reductant The pH of the solution was then adjusted to 11 by adding aqueous NaOH in a drop-wise manner Next, 2 mL TGA was mixed under vigorous stirring (~350 rpm, 5 mins) while the temperature was set at 60 °C Finally, the solution was transferred to a 50 mL teflon-lined stainless steel autoclave, and after sealing properly it was subjected to oven-heating (~180 °C) for 6 h On completion of the reaction in the solution phase, the autoclave was allowed to cool down to room temperature The precursor extract was then subjected to centrifugation (~5000 rpm) followed by filtration using a Whatman® filter paper In order to remove the excess amount of TGA from the QD surfaces, the precipitate (residue) was

washed several times with DI water following a procedure reported by other workers [25]

Since TGA can be toxic, the purification of TGA-capped QDs is extremely important prior to biological application One useful strategy for purifying magnetic nanoparticles is the use of an external magnetic field [26] A permanent magnet can be used to magnetize the particles so that they become attached to each other and subsequently particles can be separated from the unbound TGA The excess unbound TGA needs to be poured away, while the nanoparticles are required to be washed repeatedly Using this procedure, the trace amount of TGA could be efficiently controlled in the final product of the WZ MnSe quantum dots

The QD samples were processed by varying TGA concentrations of 1, 5 and 10% and molar concentrations of Mn^{2+}/Se^{2-} as 2 1, 3 1 and 4 1 We labeled the respective samples with TGA concentration of 1, 5 and 10% as T_1, T_2 and T_3 and with Mn^{2+}/Se^{2-} molar ratios of 2 1, 3 1 and 4 1 as S_1, S_2 and S_3 The subsequent chemical reactions resulting in the MnSe QDs are as given below

$$\textit{Dissociation} \quad MnCl_2 \rightarrow Mn^{2+} + 2\,Cl^-$$

$$\textit{Initial Reduction} \quad SeO_2 \rightarrow Se^0 + 1/2\,O^{2-}$$

$$\textit{Subsequent Reduction} \quad Se^0 \rightarrow Se^{2-}$$

$$\textit{Complete Redox Reaction} \quad Mn^{2+} + Se^{2-} \xRightarrow{180^\circ C} MnSe\,(QDs)$$

2 3 Optical response of MnSe-TGA QDs in culture media environment

In order to examine photostability of the QDs in culture media, a series of experimental steps was employed following an earlier report [23] At first, a suitable amount (~20 $\mu M\,\mu L^{-1}$) of MnSe-TGA QDs was sonicated in DI water followed by the addition of $30\,\mu g\,mL^{-1}$ BSA protein and, finally, different cell culture media in separate petri-dishes The specimen samples were incubated at ~37 °C for about 6 h

2 4 Cytotoxicity studies with MnSe-TGA QDs

2 4 1 Isolation, culture, and treatment of lymphocytes The cytotoxicity effect of the MnSe-TGA QDs was assessed by using isolated human lymphocytes, collected voluntarily Anti-coagulated human blood was diluted with a phosphate buffer solution (PBS) (v/v 1 1) followed by the formation of a 6 mL layer in 6 mL histopaque ($1\,07\,g\,mL^{-1}$) Subsequently, it was centrifuged at 400 g for 30 min and lymphocytes were collected from the buffy layer The isolated lymphocytes were then washed with 2 mL PBS and 2 mL RPMI-1640 media through centrifugation steps separately for 10 min at 250 g [27] The pelleted lymphocytes were then suspended in RPMI-1640, and viability was checked by the Trypan blue exclusion method using a hemocytometer [28] Lymphocytes with a viability of more than 90% were used for subsequent study Aliquots of 200 mL of isolated cells were cultured in RPMI-1640 supplemented with 10% heat-inactivated FBS Initially, cells were incubated (at 37 °C in 5% CO_2) for 4 h in RPMI-1640 without FBS The cells were then treated as per experimental requirement and maintained with the inclusion of FBS for 8 h

2 4 2 MTT assay The cytotoxicity assay was performed by measuring the viability of cells according to the method described by Denizot and Lang [29] The key component [3-(4, 5-dimethylthiazol-2-yl)-2,5-diphenyl tetrazolium bromide] (MTT) is yellowish in color and the mitochondrial dehydrogenase of viable cells cleave the tetrazolium ring, yielding purple insoluble formazan crystals, which were dissolved in a suitable solvent [30] In this report, 0 1% TGA was used as the vehicle in which MnSe-QDs were suspended The resulting purple solution was evaluated through spectrophotometrical means An increase or decrease in cell number resulted in a concomitant change in the amount of formazan formed and would indicate the degree of cytotoxicity caused by the test material Briefly, after treatments, cells were treated with 1% of MTT for 2 h, then the formazan crystals were dissolved in solvent and the absorbance of the solution was measured at 570 nm The background absorbance was measured at 690 nm and was subtracted from 570 nm The absorbance of the control cells was set at 100% viability and the values of the treated cells were calculated as a percentage of the control

2 5 Fluorescence imaging study in vitro

Isolated lymphocytes were cultured in RPMI-1640 media supplemented with 10% FBS in the presence of MnSe-TGA (or MnSe-TGA-BSA) systems and maintained for 10 h at 37 °C in 5% CO_2 in an incubator Before treatment with MnSe-TGA (or MnSe-TGA-BSA), the lymphocytes were grown without FBS for 2 h Imaging of different specimens was carried out independently under a fluorescence microscope

2 6 Analytical tools and techniques

The characteristic optical absorption features were recorded through UV–visible optical absorption spectroscopy (UV 2450, Shimadzu Corporation), whereas photoluminescence (PL) spectra were obtained by using a PerkinElmer LS 55 spectrophotometer In the latter case, the PL data was acquired through a computer controlled standard monochromator-based photodetection system The structural phase of the samples under study was characterized by an x-ray diffractometer (XRD, MiniFlex, Rigaku) equipped for CuK_α radiation ($\lambda = 1\,543$ Å), whereas the MnSe QD size and morphological features were revealed through high resolution transmission electron microscopy (HRTEM, JEOL, JEM-2100) working at an accelerating voltage of 200 kV The vibrational features were explored by Raman spectroscopy using a micro-Raman spectrometer (Renishaw, UK) at room temperature Furthermore, IR-active vibrational features were assessed through Fourier transform infrared (FT-IR) (Nicolet model Impact-410) studies As for the FTIR study of as-

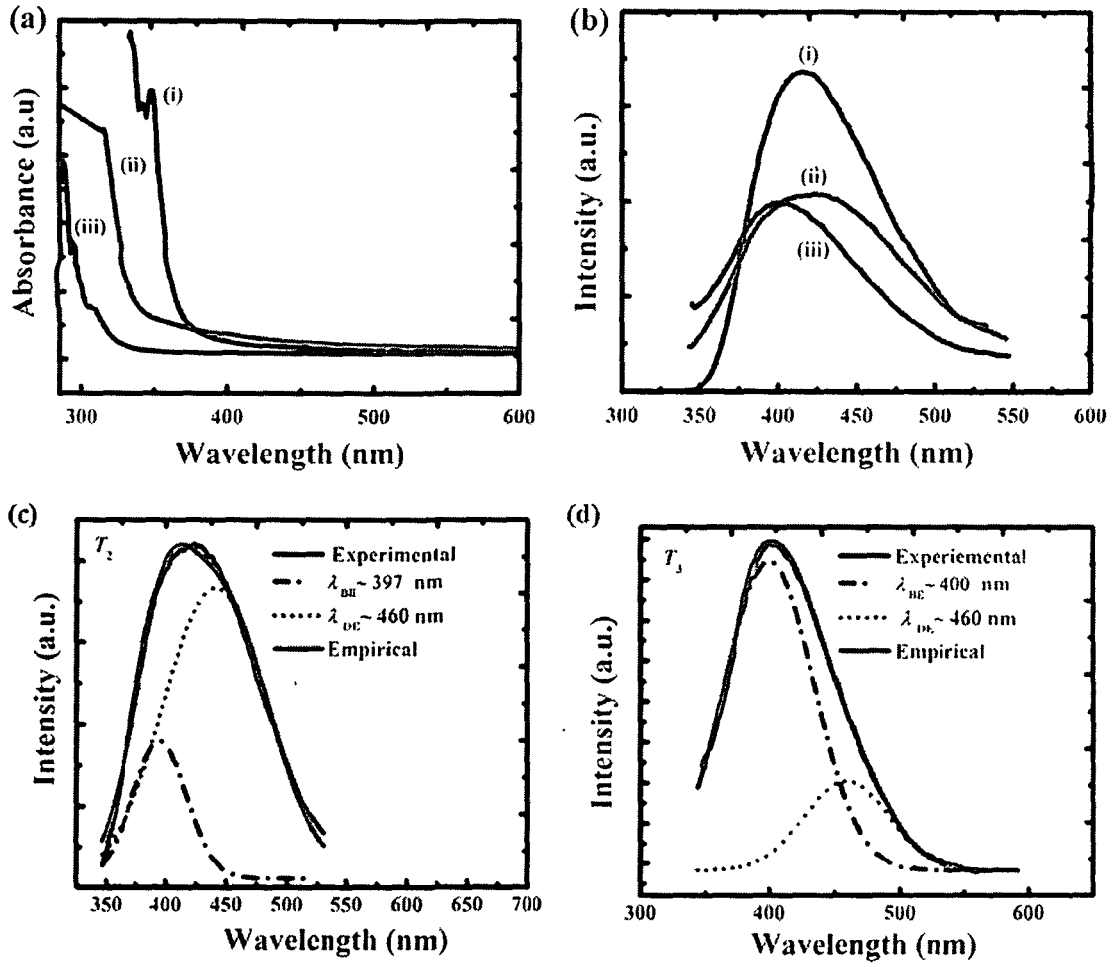

Figure 1. (a) Optical absorption and (b) photoluminescence spectra of MnSe-TGA QDs prepared with different TGA concentrations of (i) 1% (T_1), (ii) 5% (T_2) and (iii) 10% (T_3) for a fixed $Mn^{2+}/Se^{2-} = 2{:}1$. In (c) and (d), the deconvoluted PL spectra of QDs of T_2 and T_3 specimens are shown with experimental and empirical traces.

synthesized MnSe-TGA QD system, solid powder was employed to make pellets in KBr.

On the other hand, the carrier lifetime measurement and magnetic characterization of the QDs were performed by a time resolved photoluminescence system (TR-PL, LifeSpec II, Edinburg Instruments, UK) and a vibrating sample magnetometer (VSM, LakeShore's 7400 series), respectively. Finally, bright field as well as fluorescence imaging of the lymphocytes (treated with MnSe QDs) was adopted using a Leica DM 3000 fluorescence microscope under uniform light exposure and using a 40X objective/NA = 1.25.

3. Results and discussion

3.1. Optimization of control parameters through optical spectroscopy studies

In order to achieve quality water soluble WZ MnSe-TGA QDs, we have carefully examined different reaction conditions, which are as discussed below.

3.1.1. Effect of TGA concentration. Figure 1(a) depicts the effect of the TGA concentration on the UV—visible spectra of MnSe-TGA QDs. As can be seen in the figure, the samples T_1 (curve i) and T_2 (curve ii) show relatively longer tailing than T_3 (curve iii), in which the prominent absorption edge was located at ~303 nm ($E_g \sim 4.09$ eV). This implies effective quantum confinement of the charge carriers in the QDs, and that characterize a blue shift (~0.5 eV) from the bulk value ($E_g \sim 3.5$ eV) of the WZ-MnSe system [1, 3, 15, 31]. But the estimated value of E_g is ~1.6 fold larger than the RS type MnSe (~2.5 eV) system [1]. A slight blue shifting of ~0.07 eV with respect to the (WZMnSe) bulk value was noticed for the QDs of sample T_2. On the other hand, in the case of sample T_3, we observed a blue shifting (~0.73 eV) with respect to the bulk RS type MnSe. Note that the observed blue shifts for samples T_2 and T_3 are very small, and are in the range of ~0.07–0.5 eV. This could be due to the highly localized nature of 3*d* electronic bands of Mn atoms. Correspondingly, the quantum confinement induced by cordially bonded organic layers might lead to a much smaller change in these bands [31].

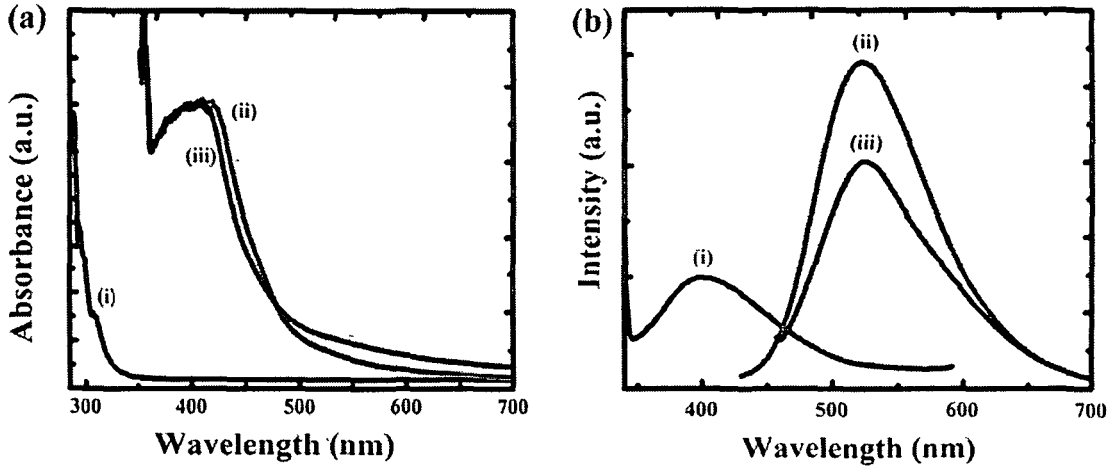

Figure 2. (a) Absorption and (b) photoluminescence spectra of MnSe (TGA: 10%) QDs with different Mn^{2+}/Se^{2-} ratios of (i) 2:1 (S_1), (ii) 3:1 (S_2) and (iii) 4:1(S_3).

The corresponding photoluminescence (PL) spectra ($\lambda_{ex} = 300$ nm) of the MnSe QD systems T_1, T_2 and T_3 are shown in figure 1(b). Each of these emission spectra was subjected to deconvolution to uncover different peak positions. Upon deconvolution (shown for T_2 and T_3 samples in figures 1(c) and (d)), each of the emission spectra was found to comprise of two emission peaks: the narrow and symmetric one is ascribed to near band edge (NBE) emission (λ_{BE}), whereas the broad and asymmetric one is due to the defect related emission (λ_{DE}). The λ_{BE} of the samples T_2 and T_3, located at ~397 nm and ~400 nm, were close to the near band-edge emission (~364 nm) of the ZB type MnSe system [32]. As for T_1, the λ_{BE} position was located at ~406 nm, but the λ_{DE} peak was positioned at ~460 nm for all the specimens. The defect-related emission may have arisen from the defect states in the metastable WZ nanocrystal core [33]. The respective band-edge-to-defect related emission intensity ratios were estimated as ~1.03, 0.58 and 2.37 as for T_1, T_2 and T_3 systems. It is quite apparent that the NBE response of 10% TGA coated MnSe QDs is much more prominent with a full width at half maximum of ~81 nm. A stronger defect-related emission of T_2 over T_3 was predicted due to the inadequate passivation of QDs by the linkers in the former case. On the other hand, the intense and symmetric NBE emission was evident due to significant passivation of the surface defects in the metastable WZ MnSe QDs of sample T_3, where a higher percentage of the capping agent TGA was considered. As these QDs are characterized by a blue-shifted, sharp excitonic absorption feature along with intense and symmetric band edge emission response, we opted for sample T_3 for further exploration of the effect of precursor concentration.

3.1.2. Effect of precursor concentration. Figures 2(a) and (b) depict the dependence of the absorption and emission behavior of MnSe QDs coated with 10% TGA and prepared at a definite precursor concentration ratio (Mn^{2+}/Se^{2-}). The sample S_1 (figure 2(a), curve i), exhibits a strong excitonic absorption feature at ~303 nm ($E_g = 4.09$ eV), whereas, with an increasing value of the precursor ratio (S_2, curve ii and S_3, curve iii), a significant red shifting ($\Delta E \sim 1.03$ eV) of the exciton peak was observed, which corresponds to $\lambda = 408$ nm ($E_g = 3.03$ eV). It may be noted that the band gap of the sample S_1 is slightly blue shifted (~0.59 eV) from the bulk value of the WZ type MnSe ($E_g = 3.5$ eV). In contrast, the samples S_2 and S_3 derived with higher Mn^{2+} concentrations showed an adequate blue shift (~0.5 eV) with respect to the bulk RS type structure ($E_g = 2.5$ eV). This may suggest that, with the incorporation of an excess amount of Mn^{2+} concentration, there could be a partial phase transformation of the WZ phase to an RS one [34].

The PL responses of MnSe QDs with different Mn^{2+}/Se^{2-} precursor ratios are depicted in figure 2(b). The spectrum recorded for sample S_1 (curve i) exhibits NBE emission (λ_{BE}) at ~400 nm [32] along with surface defect related emission (λ_{DE}) located at ~459 nm [33] (the deconvolution is not shown). Conversely, intense emission bands were observed at ~515 nm and ~517 nm as for samples S_2 (curve ii) and S_3 (curve iii), respectively. The PL emission intensity of the S_3 sample is adequately lowered as compared to the S_2 specimen. The deconvoluted PL spectra (not shown) have revealed other emission peaks located at ~554 nm and ~566 nm, for S_2 and S_3 samples, respectively. These emission bands are ascribed to the $3d$ electron transitions of Mn^{2+} [31]. An emission intensity lowered by a factor of ~1.18 in the case of the S_3 sample over the S_2 one is probably due to the strong interaction of the neighboring Mn^{2+} ions at the nearest, the second nearest and at the third nearest neighboring sites owing to an increased concentration of Mn^{2+} [34]. From the above discussion, it is now apparent that the QDs as derived from $[Mn^{2+}]/[Se^{2-}] = 2:1$ and a TGA concentration of 10% (with $S_1 \equiv T_3$) are likely to display strong, blue shifted excitonic absorption and prominent band edge emission features.

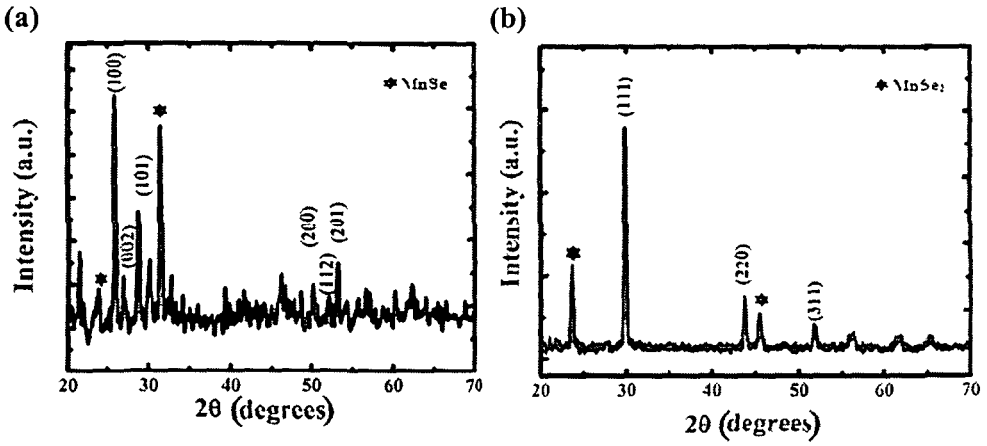

Figure 3. X-ray diffractograms of MnSe QDs prepared with 10% TGA and Mn^{2+}/Se^{2-} (a) 2 1 and (b) 3 1

The quantum yield of the MnSe-TGA QDs can be evaluated using the relation [35]

$$Q = Q_{ref}\left(\eta/\eta_{ref}\right)^2\left(I/I_{ref}\right)\left(A_{ref}/A\right) \quad (1)$$

where Q and Q_{ref} represent the respective yields of the QDs and reference specimens, I (QDs) and I_{ref} (reference) are the integrated emission intensities, A (QDs) and A_{ref} (reference) are the absorption intensities, and n (sample) and n_{ref} (reference) are the refractive indices of the solvents Considering rhodamine 6 G® as the reference, the quantum yield of the MnSe QDs was calculated to be ~75%

3 2 Crystallographic and morphological features of MnSe QDs

The crystallographic planes and phase of the as-synthesized MnSe QDs can be identified through XRD analyses The analysis was required to ascertain the desired WZ phase of the synthesized MnSe product, as predicted through optical behavior (sections 3 1 1 and 3 1 2) Figures 3(a) and (b) depict XRD patterns of the MnSe QD products, as prepared from different precursors of Mn^{2+}/Se^{2-} = 2 1 (S_1) and 3 1 (S_2), for a fixed concentration of TGA (10%) Referring to figure 3(a), the diffraction peaks located at 25 8°, 26 8°, 28 6°, 50 2°, 52 05° and 53° correspond to the (100), (002), (101), (200), (112) and (201) crystallographic planes of the hexagonal WZ MnSe crystal structure and are consistent with available reports [1, 7] Moreover, the $MnSe_2$ phase is also observed in the form of an impurity at a diffraction angle of ~23 8° and 31 4° [1] The lattice parameters ($a = b$ and c) can be estimated using the following relation applicable for a hexagonal system

$$1/\left(d_{hkl}^2\right) = 4/3\left\{\left(h^2 + k^2 + l^2\right)/a^2\right\} + l^2/c^2 \quad (2)$$

and

$$c/a = \left(8/3\right)^{1/2} \quad (3)$$

Here, a = 3 9 Å and c = 6 34 Å, nearly consistent with an earlier report [1] Furthermore, by using the Williamson–Hall equation [36], we estimated the average crystallite size (d) as ~7 nm and a negative microstrain magnitude of the order $\sim 10^{-3}$ A small, negative slope was believed to have arisen due to a nominal strain broadening effect and indicates the presence of more relaxed crystallites [37]

The XRD pattern of the sample S_2 is shown in figure 3(b) The subsequent diffraction peaks at 29 8°, 43 8° and 51 1° corresponding to the (111), (220) and (311) crystallographic planes depict an RS type MnSe crystal structure (JCPDS-270311) [38] The peaks at ~23 7° and 46° could be due to the coexistence of the $MnSe_2$ phase with MnSe The RS type structure was also predicted for the S_2 sample, as described in Section 3 1 2

The visible evidence of the MnSe QD system (S_1) is depicted in the TEM micrograph (figure 4) Isolated, spherical QDs with an average size ~7 nm can be found with a particle size distribution highlighted in the figure inset (figure 4(a)) A magnified view of the QDs is shown in figure 4(b), where lattice fringes of each of the QDs are clearly visible However, the individual planes were more distinct in the enlarged view of a single QD, incorporated as the inset in figure 4(b) The interplanar spacing is estimated as ~0 25 nm, which is in close agreement with an earlier report on the WZ-type MnSe system [7] In addition, a few point defects (vacancies) and edge-dislocations were identified in the corresponding image, which are highlighted by red and pink arrows, respectively

3 3 Exploring optical phonons and molecular vibrations in TGA coated MnSe QDs

Raman spectroscopy deals with the inelastic scattering of light from both molecular species and solid-state objects It is possible to predict different vibrational modes through Raman spectroscopy studies The Raman spectrum of the WZ-type MnSe QDs (of S_1 specimen) is shown in figure 5(a) The respective Raman peaks at 225 and 295 cm^{-1} were identified as transverse optical (TO) and longitudinal optical (LO) phonon modes of the MnSe system The blue shifting of the TO and LO phonon modes from the ZB bulk MnSe values of 219 5 and 257 cm^{-1} [39], respectively, may suggest strong

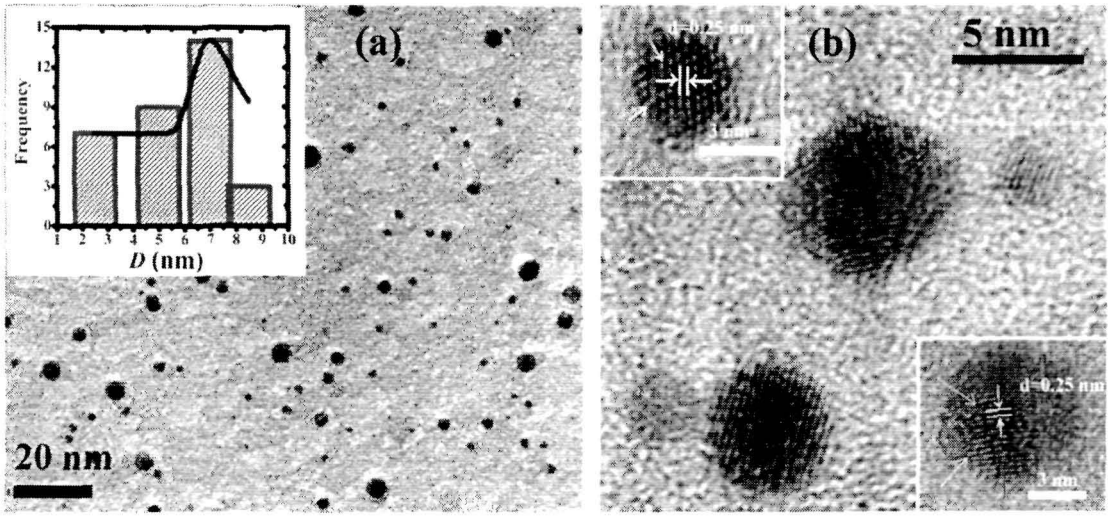

Figure 4. HRTEM images of MnSe QDs (TGA = 10%, $Mn^{2+}/Se^{2-} = 2:1$) at (a) low and (b) high magnifications. The histogram shown as the figure inset (a) depicts the particle-size distribution. The enlarged, isolated QDs are shown in (b), and with crystal lattice fringes in the two inset figures (upper ~3 nm, lower ~7 nm QD).

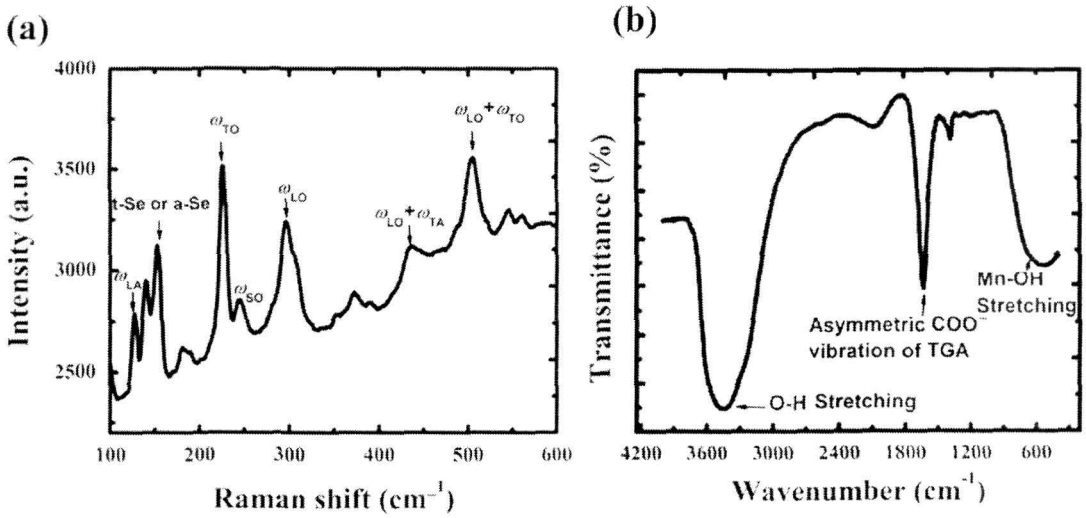

Figure 5. (a) Raman and (b) FTIR spectra of MnSe-TGA QDs (TGA = 10%, $Mn^{2+}/Se^{2-} = 2:1$).

phonon confinement in the system under study [40, 41]. When the particle size decreases in the nanometer scale, a volume contraction occurs within the nanoparticle due to the size-induced radial pressure, and this might lead to a substantial increase in the force constant value as a result of the decrease in the interatomic distances. In vibrational transitions, the wavenumbers vary approximately in proportion to $k^{1/2}$, where k is the force constant. Consequently, an enhanced magnitude of the force constant would be characterized by a shifting of the Raman band towards a higher wavenumber side [42, 43].

As the surface optic (SO) vibrational mode of the nanoparticles generally exists in-between LO and TO phonon frequencies, the Raman peak at ~244 cm^{-1} is attributed to SO phonons. The frequency of the SO modes is dependent on the dielectric environment of the QDs as proposed by Klein *et al* and expressed as [44]:

$$\omega_l^2 = \left[\omega_{TO}^2\left\{(l+1)/l\right\} + \omega_{LO}^2(\varepsilon_\infty/\varepsilon_d)\right] \Big/ \left[\left\{(l+1)/l\right\} + \varepsilon_\infty/\varepsilon_d\right], \quad (4)$$

where $l = 1, 2, 3.....$ The high frequency dielectric constant (ε_∞) of the MnSe system is 5.99 [45] and the constant of the surrounding medium (ε_d) is 78.30 for water [46]. The estimated value of the SO mode (~228 cm^{-1}) corresponding to the lowest ($l = 1$) state is very close to the experimentally observed value (~244 cm^{-1}).

The weak mode observable at ~127 cm^{-1} might have arisen from the longitudinal acoustic (LA) phonons [47], whereas no Raman peak corresponding to the transverse acoustic phonon (TA) mode was duly witnessed. On the other hand, the peak observable at ~506 cm^{-1} can be identified as

the collective feature due to the combination of LO and TO modes. The peaks at ~140 cm^{-1} and 152 cm^{-1} can be assigned to trigonal (*t*-Se), monoclinic (*m*-Se) and amorphous selenium (a_m-Se), which would exhibit Raman shifts ($\Delta\nu$) in the range of 140–150 cm^{-1}. The assigned Raman peaks of the MnSe QDs are highlighted in table 1.

The Raman shifting due to the phonon confinement effect can be described by the confinement model. The size-dependent Raman shift can be represented by [48]:

$$\Delta\omega = \omega(D) - \omega_0 = -A\left(a/d_{clus}\right)^{\gamma}. \quad (5)$$

Here, $\omega(D)$ is the frequency of the phonon in a nanocrystal of size D, ω_0 is the frequency of the bulk MnSe, $\Delta\omega$ is the Raman frequency shift, a is the lattice parameter ($a = 0.432$ nm) of MnSe, d_{clus} is the nanocluster size, and A and γ are the parameters related to nanocrystal geometry. The parameter A has a value of 52.3 cm^{-1} in the Richter model, and the value of the *Grüneisen parameter* (γ) is 1.1 and is relevant for LO mode of the bulk II-VI semiconductor systems [49]. Putting these values into equation (4), the size of the QDs is estimated as ~8.5 nm. This value resembles closely the crystallite size and average particle size obtained through XRD and TEM analyses.

The FTIR spectrum of MnSe-TGA QDs is depicted in figure 5(b). Four prominent IR- sensitive vibrational peaks were clearly distinguishable in each of the FTIR spectra of the MnSe-TGA QD system. These are located at ~3447 cm^{-1}, 1634 cm^{-1}, 1383 cm^{-1} and ~644 cm^{-1}. The peak at ~3447 cm^{-1} was believed to be due to the hydroxyl O–H stretching mode of the TGA molecule. The peak at ~1634 cm^{-1} may have arisen due to the asymmetric vibrational peak of the -COO^- group of TGA molecules [15], whereas, the peak corresponding to the C=O stretching vibration is identified at ~1383 cm^{-1} [50]. Consistent with other reports, the peak witnessed in a relatively low wavenumber regime (~644 cm^{-1}) can be ascribed to the vibrational response due to Mn–OH stretching [51].

3.4. Carrier lifetime measurements of TGA coated MnSe QDs

The life-time aspect associated with the carrier recombination events can be revealed by TR-PL measurements. In general, the PL decay curve of colloidal NCs has a bi-exponential form, given by [52]:

$$A = A_1 e^{-t/\tau_1} + A_2 e^{-t/\tau_2}. \quad (6)$$

Here, τ_1 and τ_2 are the decay time constants of the rapid and slow processes, and A_1 and A_2 are the corresponding emission intensities. We intended to explore the time-resolved characteristics around the main, NBE emission peak, observable at 400 nm. The TR-PL spectra of TGA-coated MnSe QDs, measured for two close emission wavelength values (λ_{em} = 400 and 420 nm), are depicted in figure 6. It is quite apparent that the emission kinetics have a stretched-exponential trend with a dependence on the radiative emission line. Interestingly, the TR-PL data exhibited bi- and tri-exponential fits for emission wavelengths of ~400 and 420 nm, respectively. For the aforesaid cases, the reduction of PL intensity with time is

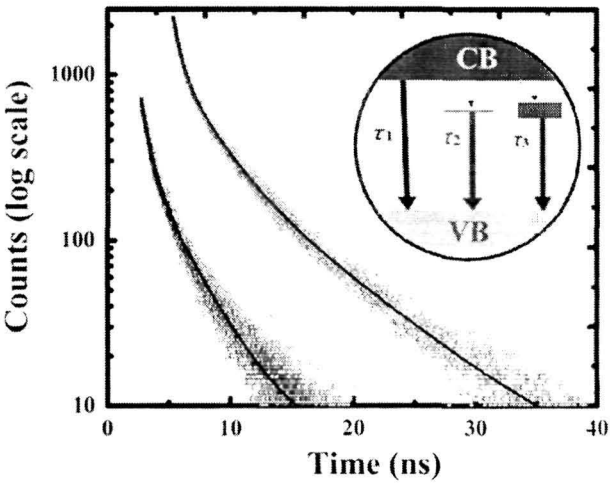

Figure 6. TR-PL spectra of MnSe–TGA QDs (TGA = 10%, Mn^{2+}/Se^{2-} = 2:1). Blue and red experimental traces basically represent the nature of PL decays corresponding to λ_{em} = 400 nm and 420 nm, respectively. The inset shows the scheme of radiative /nonradiative pathways in the MnSe-QD system.

Table 1. Assignment of Raman peaks of the MnSe QD system.

Sl. No	Assigned mode	Reported/ predicted* values (cm^{-1})	Measured values (cm^{-1})
1	ω_{LA}	127	127
2	ω_{TO}	219.5	225
3	ω_{SO} (ω_l, $l = 1$)	228*	244
4	ω_{LO}	257	295
5	$\omega_{LO} + \omega_{TO}$	520*	506
6	Mixed-phase/defect arisen peaks (trigonal (*t*-Se), monoclinic (*m*-Se) and amorphous (a_m-Se) selenium)	140–150	140, 152

accompanied by two independent mechanisms and with different decay parameters. The time constants, associated with the TR-PL spectrum of 400 nm emission, are $\tau_1 \sim 0.64$ ns and $\tau_2 \sim 3.04$ ns with the corresponding intensities found to be $A_1 = 31\,814.4$ and $A_2 = 682.4$ in arbitrary units. Here, the shorter life-time can be ascribed to the direct radiative transitions of the free excitons (core-state recombination), while the second, a relatively slower component, is believed to be due to the radiative recombination via surface-trap sites [53]. A nearly ~4.7 fold increment in the core-state recombination response over the surface-trap ones was anticipated in this case. On the other hand, the PL decay is mediated via three independent processes corresponding to an emission wavelength ~420 nm. The decay parameters, as predicted from most suitable (tri-exponential) fitting, are $\tau_1 \sim 0.56$ ns, $\tau_2 \sim 2.42$ ns and $\tau_3 = 7.45$ ns, with respective intensities of $A_1 = 1412.27$, $A_2 = 859.03$ and $A_3 = 401.87$. Here, we assign τ_1 to the core-state recombination, τ_2 to the surface-trapped

excitons and τ_3 to the radiative and nonradiative responses due to carriers trapped at the surface sites [54] On comparing the TR-PL spectra of 400 nm emission with that of the 420 nm one, it is quite clear that both the fast (τ_1) and slow (τ_2) components become faster by ~1 2 times in the latter case, and along with the evolution of a third component τ_3 The possible radiative pathways with various decay components are schematically shown as inset of figure 6 Note from the magnitudes of A_1 and A_2 that the probability of core-state recombination is drastically suppressed as compared to the probability of recombination via surface traps Moreover, PL decay via surface trapped excitons and carrier trapping at surface sites becomes competitive in this case We anticipate that the long exponential behavior with time constant τ_3 would suggest the localization of carriers on the surface states with a small overlap between electron and hole wavefunctions [55] A stronger localization event is likely to exhibit more prominent exponential stretching and, hence, a longer decay parameter

3 5 Magnetic properties of TGA-coated MnSe QDs

We have also evaluated the magnetic features of the TGA-coated MnSe QDs In this regard, the effect of TGA concentration on the magnetic response of the QDs has been explored Figure 7 depicts temperature and field dependent magnetization responses of MnSe QDs prepared with 1 and 10% TGA concentrations, and at a fixed precursor ratio ($Mn^{2+}/Se^{2-} = 2$ 1) In zero field cooling (ZFC) conditions, the sample was first cooled down to a temperature of 27 K under no field, and then the magnetization signal was recorded in the warming process when subjected to an applied field of 500 G As can be seen from figure 7(a), the 1% TGA-coated QD system has a Neel temperature (T_N) located at ~39 K In contrast, the QDs prepared with a coating of 10% TGA are characterized by a non-sharp T_N value of 59 K (figure 7(b)) Below T_N, the specimen is anti-ferromagnetic in nature and above T_N it would behave as a paramagnetic system owing to the likely randomization of moments associated with the magnetic ordering process Note the exhibition of a steady fall in the magnetization in figure 7(b), which could represent the coexistence of anti-ferromagnetic and paramagnetic ordering, but to different degrees Figures 7(c) and (d) represent respective $M \sim H$ hysteresis plots of the MnSe QDs (with 1 and 10% TGA concentrations) measured at 20 K It was revealed that 1% TGA functionalized QDs have an anti-ferromagnetic hysteresis with a coercivity (H_c) of ~1520 G and a remanence (M_r) of ~1 2 emu g^{-1} (figure 7(c)) Our T_N and H_c values are comparable with the values predicted for the WZ type MnS nanowires ($T_N = 30$ K, $H_c = 1020$ G) [55] and those of tetrapod-shaped MnSe nanocrystals [7] In contrast, the T_N, H_c and M_r values were found to be ~59 K, ~56 G and ~0 0002 emu g^{-1} in case of 10% TGA coated QDs The T_N and H_c values are close to the WZ type, spherical shaped and water droplet-shaped MnSe nanoparticles [1] Nevertheless, the MnSe QDs experience characteristic paramagnetic features at room temperature (figures 7(e) and (f)), irrespective of the TGA concentration level

The surface defects along with a layer of surfactants could influence the magnetic properties of the nanoparticles drastically, especially when thermal agitation is lowered With the decreasing size of the NPs, surface contribution to the magnetization increases as compared to the core of the particles [56] However, total magnetization is expected to be contributed to by both surface spins and the core of particles It is worth mentioning here that the electronic structure of the whole system can be adequately controlled by the strength of interaction of capping molecules with NP surfaces Earlier, it was demonstrated that the variation of the electronic structure has a strong influence on the magnetic properties [57, 58] Moreover, thiols are regarded as excellent candidates for inducing magnetic properties, even in diamagnetic substances [58–61] By capping with a thiol group, charge transfer between the SH group and surface atoms takes place, thereby inducing a net magnetization [57] In our case, a larger value of Neel temperature exhibited by 10% TGA-coated QDs suggests that a relatively higher thermal energy is required to disrupt the magnetic ordering as expected in 1% TGA-coated QDs with a smaller T_N It is possible that a proportionately large no of Mn^{2+} ions are available on the surfaces of MnSe QDs of higher TGA concentration, which might undergo an efficient charge transfer process between the TGA molecule and the 3*d* orbitals of Mn^{2+} ions and become responsible for displaying a strong magnetic response Moreover, while a higher TGA concentration leads to a gradual decrement of the magnetic moment with temperature, a steep fall was realized for a lower TGA concentration (figures 7(a), (b)) Thus a small magnitude of thermal energy (at low T_N) is sufficient to break the ordering of magnetic moments in the latter case The surface-dependent magnetic properties of MnSe nanoparticles have also been reported by other workers [7, 62] Additionally, a lowered value coercivity of 10% TGA-coated MnSe QDs at a low temperature provides an advantage over the colloidal stability of QDs A lowered coercivity indicates the quick disappearance of magnetism with the removal of the applied field Considering the fact that QDs would not agglomerate upon the removal of the field [56], the MnSe QDs with 10% TGA could be the preferred choice over its 1% counterpart for safe biological application Different magnetic parameters, as predicted for MnSe QDs of varying TGA concentrations, are highlighted in table 2

3 6 Biophysical evaluation of TGA-coated MnSe QDs

3 6 1 Dispersion and stability of MnSe-TGA QDs in cell culture media The optical response and colloidal stability of the fluorescent QDs, in different chemical environments, are regarded as essential prerequisites for use in biolabeling and biosensing applications It is known that different dispersing agents, such as FBS and BSA proteins, have an influential role on the stability of the QDs in a biological environment In this regard, we performed a comparative study of the MnSe QDs (of S_1 specimen) in different dispersion media and by considering both the presence and absence of the dispersing agent (BSA protein) Figure 8(a) demonstrates that, in the absence of dispersing agent (BSA), the excitonic absorption

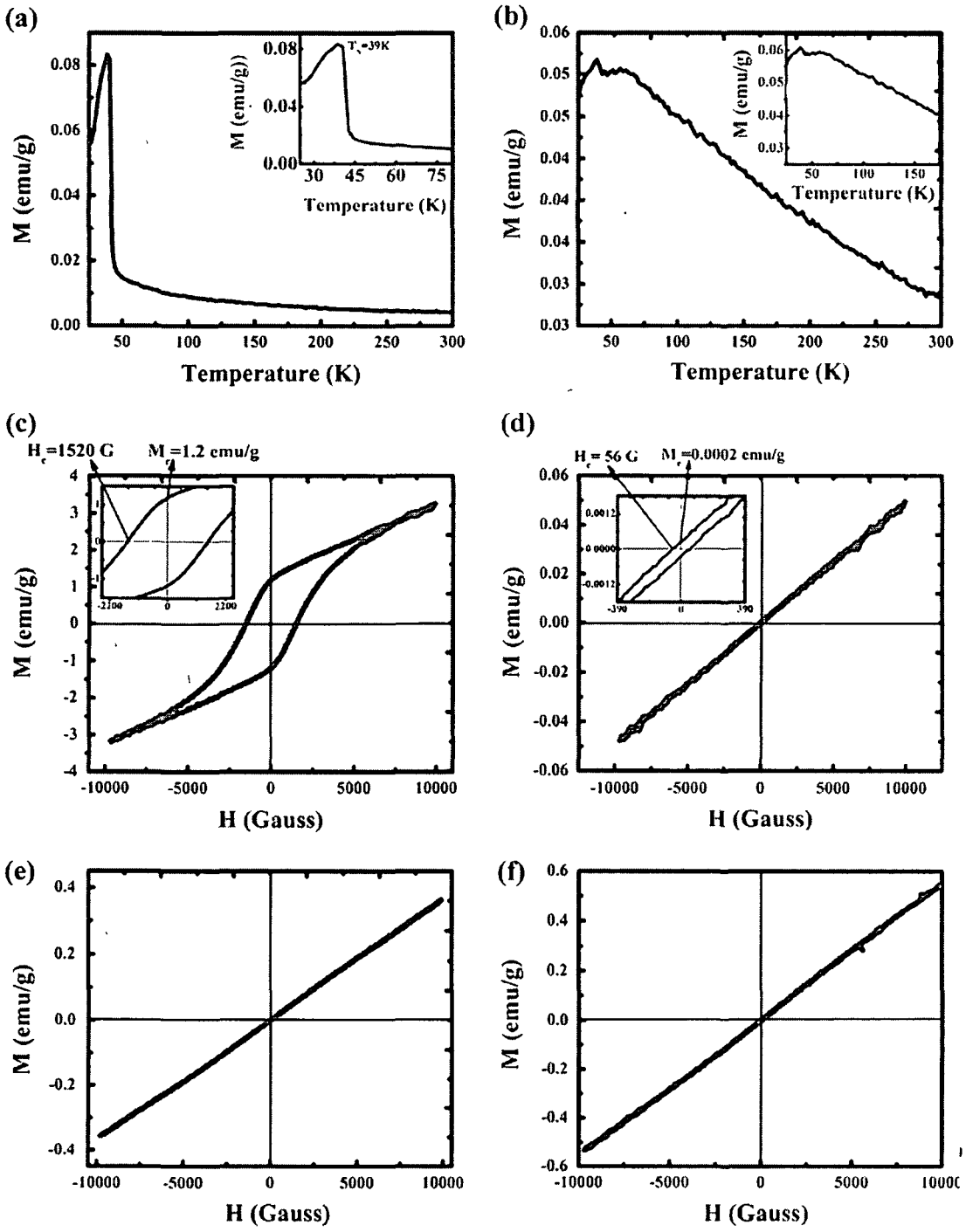

Figure 7. (a), (b) ZFC curves of different MnSe QDs obtained for a low field of ~500 G and applied at a temperature of 26 K. The figure inset, depicting the magnetization peak, represents the Neel temperature. The sub-figures (c), (d) and (e), (f) highlight the hysteresis loops of MnSe QDs measured at 26 K and 300 K, respectively. The insets of (c), (d) depict the region around the zero field. The respective subfigures (a), (c), (e) and (b), (d), (f) correspond to TGA concentrations of 1% and 10% for a constant molar concentration of $Mn^{2+}/Se^{2-} = 2:1$.

Table 2. Magnetic parameters of MnSe QDs ($Mn^{2+}/Se^{2-} = 2:1$). The H_c and M_r values were measured at 26 K.

Sl. No	TGA concentration	Neel temperature, T_N (K)	Coercivity, H_c (G)	Remanence, M_r (emu g^{-1})
1	1%	39 (sharp)	1520	1.2
2	10%	59 (non-sharp)	56	0.0002

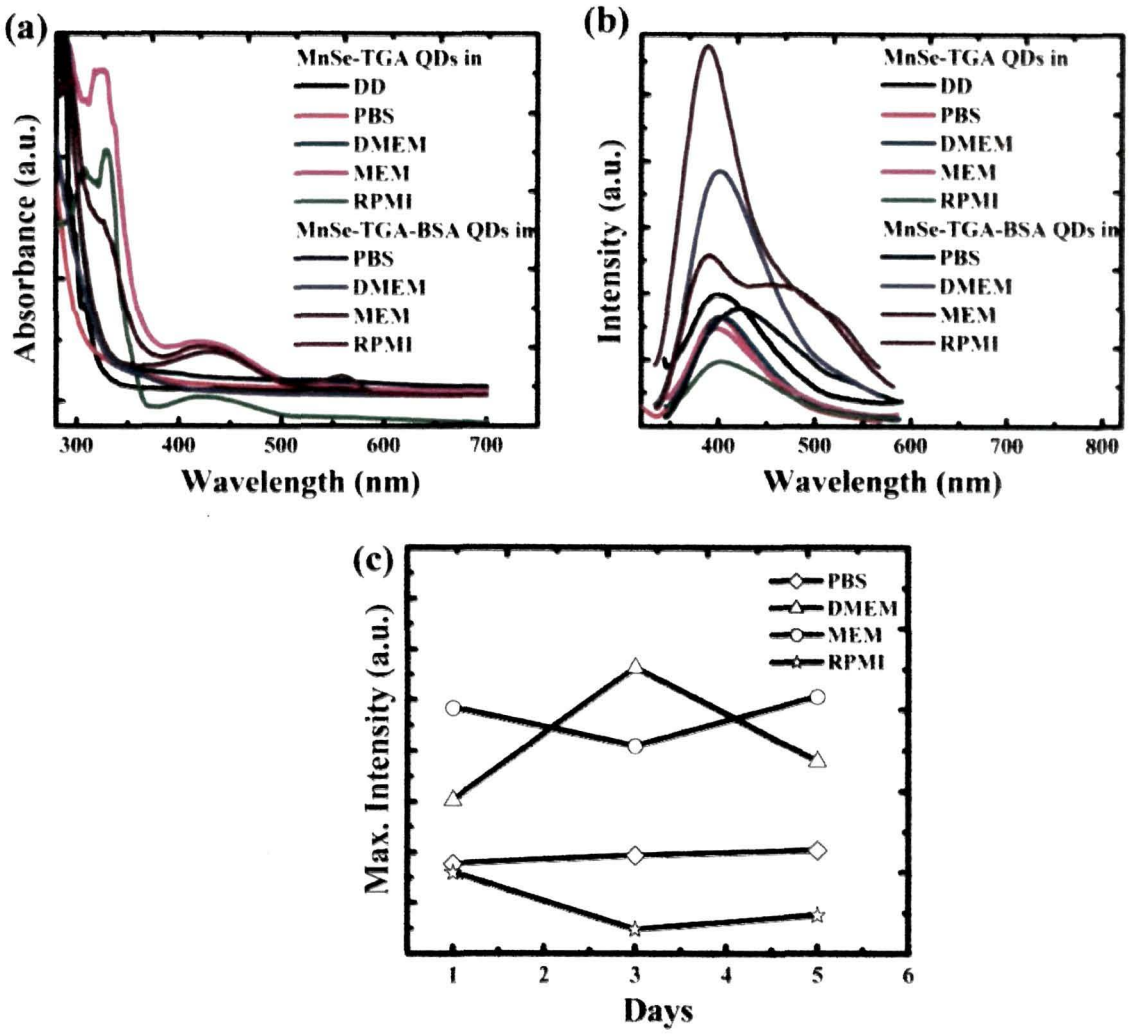

Figure 8. (a) Absorption and (b) photoluminescence spectra of MnSe QDs (TGA = 10%, $Mn^{2+}/Se^{2-} = 2:1$) in different dispersing media in the presence and absence of the dispersing agent BSA. (c) Depicts maximum PL intensity of MnSe-TGA QDs with aging effect when BSA was added as a dispersing agent.

peak at ~303 nm of the MnSe QDs in PBS remains unaffected as observed in the aqueous media. Conversely, the absorption peak is red-shifted to ~313, ~321 and ~329 nm, when QDs were dispersed in DMEM, MEM and RPMI-1640 media, respectively. This indicates the likely aggregation of the QDs in these media. Essentially, in cell culture media, a high ionic strength is responsible for the dominant van-der Waal's attraction over electrostatic repulsive behavior, and this is the reason why QDs might coalesce into larger sized ones [18]. In contrast, a fairly stable dispersion of the MnSe-TGA QDs was observed upon the addition of BSA into the respective media. The exciton absorption peak (~303 nm) seems unaltered in PBS and DMEM media, whereas it was slightly (~308 nm) and significantly (~327 nm) red-shifted in MEM and RPMI-1640 media, respectively. Thus, we can predict that the interaction of the BSA dispersing agent with the constituents of the cell culture media has strong influence on determining the colloidal stability of MnSe QDs. Similarly, the enhanced emission response of the QDs with BSA dispersion signifies an improved QD stability as compared to the case of nonuse of the dispersing agent (figure 8(b)). Moreover, in presence of the BSA protein, MnSe-TGA QDs in DMEM and MEM media exhibited stronger PL responses over the RPMI-1640 one. This may suggest considerable surface passivation of the QDs in the former media with effective absorption of BSA compared to the latter one.

Figure 8(c) depicts a series of maximum intensity profiles, highlighting responses upon BSA inclusion in different cell culture media. The nature of radiative emission with aging can also be evaluated. As compared to the RPMI-1640 cell culture media, the MnSe-TGA QDs are likely to experience stable emission features in DMEM (3 days of aging) and MEM media (5 days of aging). An enhanced stability of PVA-coated SPION and BSA-coated TiO_2 particles in DMEM media, over RPMI-1640 media, was predicted in earlier works [18, 63]. Not surprisingly, in DMEM and MEM media, owing to the presence of a larger

concentration of divalent cations (e g Ca^{2+}, Mg^{2+}), they are likely to act as an effective bridge to bind negatively charged BSA protein molecules on one side with the negatively charged TGA-coated QDs on the other side [18] In contrast, a relatively higher concentration of phosphate ions in RPMI-1640 media, would compete with BSA molecules to adsorb into the QD surfaces resulting in instability Earlier an almost 70% release of BSA from hydroxyapatite microspheres was realized in half an hour in the presence of 10 mM phosphate, as reported by Boonsongrit and coworkers [64]

3 6 2 Cytotxicity assessment and bioimaging of lymphocytes using MnSe QDs First, we intended to explore the influence of MnSe QDs (of S_1 specimen) on lymphocyte cell viability The study was carried out using different amounts of MnSe QDs synthesized from the precursor of 10% TGA and $Mn^{2+}/Se^{2-} = 2\ 1$ As shown in figure 9(A) with the treatment of a 1 μM MnSe QD for 8 h, the lymphocyte cells were believed to sustain with a maximal viability of 98 3%, whereas the cell viability which was fairly uniform (~95%) up to a QD concentration of 0 5 μM, gets drastically reduced with the further increase of QD concentration It may be noted that the survival of the maximum amount of cells is of utmost necessity to unravel the cellular uptake mechanism and bioimaging response under select excitation This calls for the use of MnSe QDs under a safe limit, which could help minimize the cytotoxicity and other environmental and health hazard issues We speculate that the safe limit in our case is below 0 5 μM It is possible that, depending on the macromolecular structural organization of the cells and their physiological state, the safe limit of using MnSe QDs might vary from one cell type to another For instance, healthy and disease affected cells, including epithelial, epidermal and epithermal cells may necessarily not require a similar concentration of QDs for exploiting the safe cellular uptake process Our MnSe QDs could have immense potential in cellular study while using magnetic and emission responses collectively unlike conventional systems where the use of simultaneous properties is quite limited

Figures 9(B) (a–f) depict cell imaging responses with regard to the treatment of MnSe QDs to the lymphocytes Figures 9(B) (a) and (d) are basically bright and fluores cence image snapshots of the untreated lymphocyte cells (without the addition of QDs) Figures 9(B) (b) and (e) depict the uptake of the MnSe QDs by cultured lymphocyte cells (without considering a dispersing agent) in bright and fluorescence imaging modes, respectively The photographs depict the high biocompatibility and fluorescent behavior of the QDs in a cellular environment Furthermore, we assessed the cellular uptake of the QDs while considering BSA as a dispersing agent in the culture media Figures 9(B) (c) and (f) depict bright and fluorescence images demonstrating the cellular uptake response in the presence of BSA in the culture media It was confirmed that BSA has a remarkable stand with regard to a better QD dispersion and a fairly homogeneous cellular uptake The one-to one correspondence as evident from the bright field view and bright, isolated spots of the fluorescent image is quite apparent in this case The effect of BSA could be clearly visualized by a superior QD fluorescence response over the other discussed ones The cellular uptake and bioimaging responses are believed to be significantly affected by the nature of surface functionalization and the use of BSA as a dispersing agent

4. Concluding remarks

We have demonstrated the synthesis and physical and biophysical characteristics of TGA-coated, WZ-phase MnSe QDs of average size ~7 nm Apart from identifying various Raman and IR active modes in the system we observed multi-exponential PL decay around the NBE emission The QDs exhibited paramagnetic behavior at room temperature and a mixed anti-ferromagnetic and paramagnetic ordering at low temperature The optical and colloidal stability of the MnSe QDs, in different cell culture media were found to improve with the inclusion of BSA as a dispersing agent From the cytotoxicity measurements on lymphocytes, we predict that the safe limit of using MnSe QDs in biophysical applications is below 0 5 μM In addition, we have noticed an improvement on the lymphocyte cell imaging capability of the QDs when BSA was used as a dispersing agent in the RPMI-1640 media

Though we are aware of earlier works on Mn-doped systems [65–67], the present work is unique in the sense that the studied system is both a semiconductor and a magnetic one, which can be made stable even in the WZ phase and finally can be efficiently employed in cellular imaging These water-soluble WZ–MnSe QDs can be regarded as an alternative candidate in biophysical and biomedical research, where both fluorescence and magnetic responses are desired simultaneously Recently, we explored conductance fluctuations across lecithin bilayers due to the creation of nanopores as a result of the insertion of CdSe quantum dots [68] We also demonstrated a magneto-gated ion channel response due to the insertion of magnetite nanoparticles in artificial bilayers [69] In this context, the investigated MnSe QDs can be advantageous with regard to the simultaneous recording of optical and electrical data when subjected to static magnetic fields or light illumination The optical stability of QDs in different cell culture media along with minimal toxicity level will certainly provide a valuable platform in biophysical, biomedical and nanobiotechnology research In addition, suitable deployment of these QDs would find potential in frontier applications, including targeted drug delivery enabling the direct visualization of nanocarriers' transport at subcellular resolution Both from diagnostic and therapeutic points of view the examination of intracellular processes and deep penetration into tissues can find a remarkable advantage with the use of such QDs

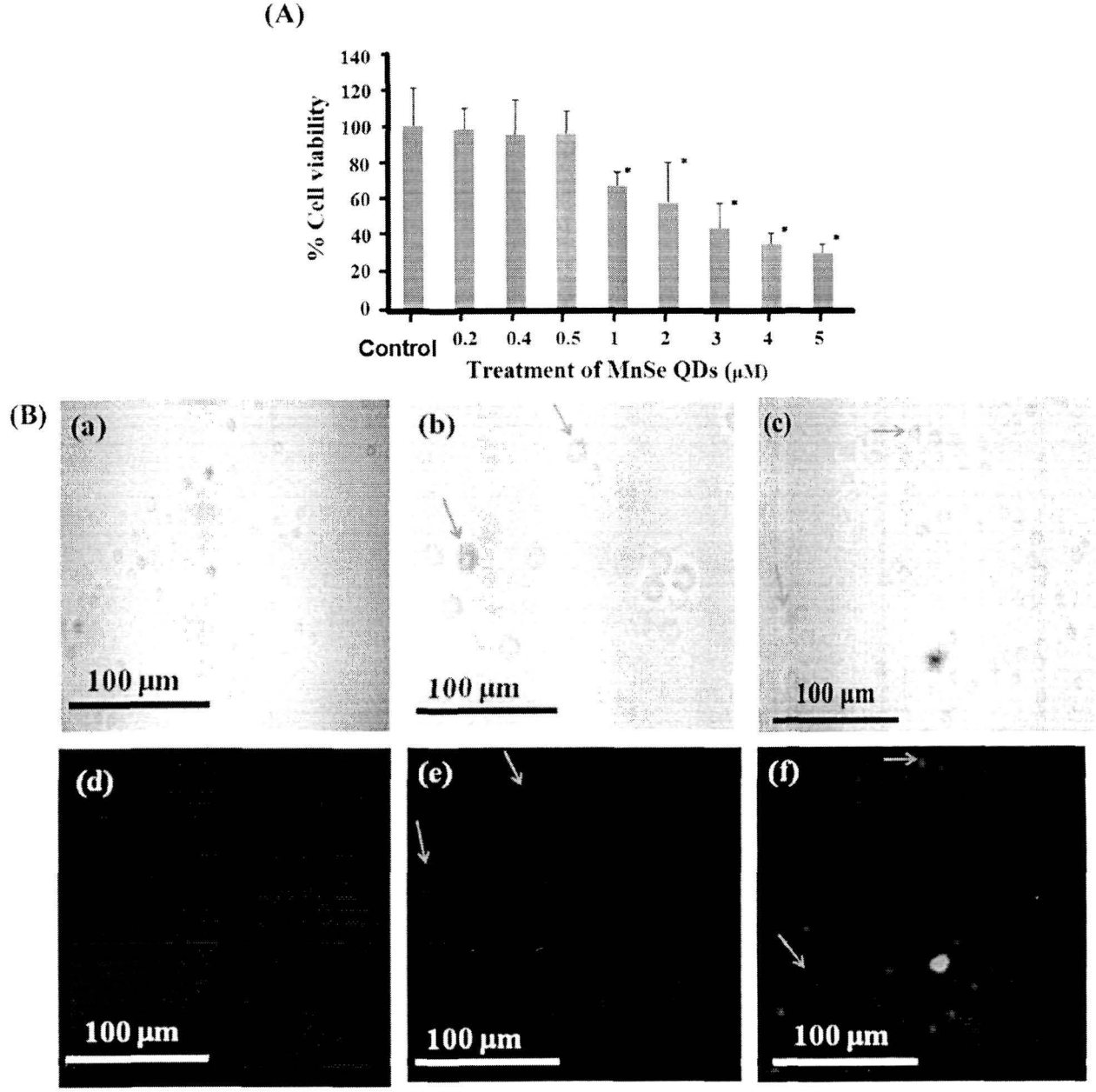

Figure 9. (A) Effect of MnSe–TGA QDs on lymphocyte cell viability assessed with the MTT assay ($n = 4$). All the results were expressed as mean ± SD from four independent sets of experiments. Each of the columns reflects the cell viability. The results were statistically analyzed by Student's *t*-test for the significant difference between the group means using GraphPad software®. The significant difference between the experimental and the control group was set as $*p \leqslant 0.05$. (B) Bright field imaging of lymphocyte cells (a) without QDs, (b) with QDs and (c) with QDs with BSA in the culture media. The respective fluorescence imaging ($\lambda_{ex} = 300$ nm) can be seen in (d), (e) and (f). Note the cellular uptake of QDs in (e) and (f) and their correspondence with bright field views (b) and (c).

Acknowledgments

The authors (RS and DM) thank DST, New Delhi, for financial support (project no. SR/FTP/PS07/2008) and colleagues for valuable discussions. The manuscript was initiated while one of the authors (DM) was visiting Harvard University through the Indo-US research program of IUSSTF, New Delhi. The authors gratefully acknowledge Dr A Saha of UGC-DAE-CSR, Kolkata for extending the Raman spectroscopy facility. As for TEM measurements, the help and support received from Dr Jungwon Park at SEAS, Harvard University, is gratefully acknowledged. The authors thank Dr A Srinivasan and Dr S Sarma of Department of Physics, IIT-G, for magnetic characterizations, and CIF, IIT-G, for extending TR-PL measurements. The author AH would like to acknowledge DST for INSPIRE SRF.

References

[1] Sines I T Misra R Schiffer P and Schaak R E 2010 Colloidal synthesis of non-equilibrium wurtzite-type MnSe *Angew Chem Int Ed* **49** 4638–40

[2] Wu M, Xiong Y, Jiang N, Ning M and Chen Q 2004 Hydrothermal preparation of α-MnSe and $MnSe_2$ nanorods *J Crystal Growth* **262** 567–71

[3] Furdyna J K 1982 Diluted magnetic semiconductors an interface of semiconductor physics and magnetism *J Appl Phys* **53** 7637–43

[4] Bouroushian M 2010 *Electrochemistry of Metal Chalcogenides* (Berlin Springer)

[5] Lindsay R 1951 Magnetic susceptibility of manganese selenide *Phys Rev* **84** 569–71

[6] Schlesinger M E 1998 The Mn–Se manganese–selenium system *J Phase Equil* **19** 588–90

[7] Yang X, Wang Y, Sui Y, Huang X, Cui T, Wang C, Liu B Zou G and Zou B 2012 Morphology-controlled synthesis of anisotropic wurtzite MnSe nanocrystals optical and magnetic properties *Cryst Eng Comm* **14** 6916–20

[8] Xing Y and Rao J 2008 Quantum dot bioconjugates for *in vitro* diagnostics and *in vivo* imaging *Cancer Biomarkers Section A Disease Markers* **4** 307–19

[9] Derfus A M, Chan W C W and Bhatia S N 2003 Probing the cytotoxicity of semiconductor quantum dots *Nano Lett* **4** 11–8

[10] Battaglia D M, Liu Y and Peng X 2007 Efficient, stable, small and water-soluble doped ZnSe nanocrystal emitters as non-cadmium biomedical labels *Nano Lett* **7** 312–7

[11] Pradhan N, Goorskey D Thessing J and Peng X 2005 An alternative of CdSe nanocrystal emitters pure and tunable impurity emissions in ZnSe nanocrystals *J Am Chem Soc* **127** 17586–7

[12] Wang C Gao X Ma Q and Su X 2009 Aqueous synthesis of mercaptopropionic acid capped Mn^{2+}-doped ZnSe quantum dots *J Mater Chem* **19** 7016–22

[13] Zhu D, Jiang X, Zhao C, Sun X, Zhang J and Zhu J-J 2010 Green synthesis and potential application of low-toxic Mn ZnSe/ZnS core/shell luminescent nanocrystals *Chem Commun* **46** 5226–8

[14] Pearson R 1963 Hard and soft acids and bases *J Am Chem Soc* **85** 3533–9

[15] Pradhan N and Peng X 2007 Efficient and color tunable Mn-doped ZnSe nanocrystal emitters control of optical performance via greener synthetic chemistry *J Am Chem Soc* **129** 3339–47

[16] Gerion D, Pinaud F, Williams S C, Parak W J, Zanchet D, Weiss S and Alivisatos A P 2001 Synthesis and properties of biocompatible water-soluble silica-coated CdSe/ZnS semiconductor quantum dots *J Phys Chem* B **105** 8861–71

[17] Zhang Y and Clapp A 2011 Overview of stabilizing ligands for biocompatible quantum dot nanocrystals *Sensors* **11** 11036–55

[18] Ji Z, Jin X George S, Xia T, Meng H, Wang X Suarez E, Zhang H, Hoek E M and Godwin H 2010 Dispersion and stability optimization of TiO_2 nanoparticles in cell culture media *Env Sci Technol* **44** 7309–14

[19] Jing L, Li Y, Ding K, Qiao R, Rogach A L and Gao M 2011 Surface-biofunctionalized multicore/shell CdTe@SiO_2 composite particles for immunofluorescence assay *Nanotechnology* **22** 505104

[20] Byrne S J Corr S A, Rakovich Y P, Donegan J F, Mitchell S and Volkov Y 2006 Optimisation of the synthesis and modification of CdTe quantum dots for enhanced live cell imaging *J Mater Chem* **16** 2896–902

[21] Yu Y, Xu L, Chen J, Gao H, Wang S, Fang J and Xu S 2012 Hydrothermal synthesis of GSH–TGA co-capped CdTe quantum dots and their application in labeling colorectal cancer cells *Colloids Surf* B **95** 247–53

[22] Poderys V, Matulionyte M, Selskis A and Rotomskis R 2011 Interaction of water-soluble CdTe quantum dots with bovine serum albumin *Nanoscale Res Lett* **6** 9

[23] Bihari P, Vippola M, Schultes S, Praetner M, Khandoga A G Reichel C A, Coester C, Tuomi T, Rehberg M and Krombach F 2008 Optimized dispersion of nanoparticles for biological *in vitro* and *in vivo* studies *Particle Fibre Toxicol* **5** 14

[24] Elgrabli D, Abella-Gallart S, Aguerre-Chariol O, Robidel F, Rogerieux F, Boczkowski J and Lacroix G 2007 Effect of BSA on carbon nanotube dispersion for *in vivo* and *in vitro* studies *Nanotoxicology* **1** 266–78

[25] Hu H Y Dou X R Jiang Z L Tang J H, Xie L and Xie H 2012 Cytotoxicity and cellular imaging of quantum dots protected by polyelectrolyte *J Pharmaceut Anal* **2** 293–7

[26] Sun P, Zhang H, Liu C, Fang J, Wang M, Chen J, Zhang J, Mao C and Xu S 2010 Preparation and characterization of Fe3O4/CdTe magnetic/fluorescent nanocomposites and their applications in immuno-labeling and fluorescent imaging of cancer cells *Langmuir ACS J Surf Colloids* **26** 1278–84

[27] Winchester R, Winfield J, Siegal F, Wernet P, Bentwich Z and Kunkel H 1974 Analyses of lymphocytes from patients with rheumatoid arthritis and systemic lupus erythematosus occurrence of interfering cold-reactive antilymphocyte antibodies *J Clin Invest* **54** 1082–92

[28] Gomez-Lechon M Iborra F Azorin I, Guerri C and Renau-Piqueras J 1992 Cryopreservation of rat astrocytes from primary cultures *J Tissue Culture Methods* **14** 73–7

[29] Denizot F and Lang R 1986 Rapid colorimetric assay for cell growth and survival modifications to the tetrazolium dye procedure giving improved sensitivity and reliability *J Immunol Methods* **89** 271–7

[30] Talorete T P, Bouaziz M Sayadi S and Isoda H 2006 Influence of medium type and serum on MTT reduction by flavonoids in the absence of cells *Cytotechnology* **52** 189–98

[31] Heulings H R, Xiaoying H and Li J 2001 Mn-substituted inorganic–organic hybrid materials based on ZnSe nanostructures that may lead to magnetic semiconductors with a strong quantum confinement effect *Nano Lett* **1** 521–6

[32] Lei S, Tang K and Zheng H 2006 Solvothermal synthesis of α-MnSe uniform nanospheres and nanorods *Mater Lett* **60** 1625–8

[33] Zhu K, Zhang X, Wang L, Zhang H, Wei J, Wang L, Zhou M and Feng B 2011 Manganese-doped MnSe/CdSe core/shell nanocrystals preparation characterization and study of growth mechanism *J Mater Res* **26** 2400–6

[34] Biswas S Kar S and Chaudhuri S 2005 Optical and magnetic properties of manganese-incorporated zinc sulfide nanorods synthesized by a solvothermal process *J Phys Chem* B **109** 17526–30

[35] Deng Z, Lie F L, Shen S, Ghosh I, Mansuripur M and Muscat A J 2009 Water-based route to ligand-selective synthesis of ZnSe and Cd-doped ZnSe quantum dots with tunable ultraviolet A to blue photoluminescence *Langmuir* **25** 434–42

[36] Williamson G K and Hall W H 1953 X-ray line broadening from filed aluminium and wolfram *Acta Metal* **1** 22–31

[37] Cernik R J and Louer D 1991 The breadth and shape of instrumental line profiles in high-resolution powder diffraction *J Appl Cryst* **24** 913–9

[38] Murray R M, Forbes B C and Heyding R D 1972 The preparation and paramagnetic susceptibility of β-MnSe *Can J Chem* **50** 4059–61

[39] Lao P D Guo Y, Siu G G and Shen S C 1993 Optical-phonon behavior in $Zn_{1-x}Mn_xSe$ zinc-blende and wurtzite structures *Phys Rev* B **48** 11701–4

[40] Dzhagan V, Lokteva I, Himcinschi C, Jin X, Kolny-Olesiak J and Zahn D R 2011 Phonon Raman spectra of colloidal CdTe nanocrystals effect of size, non-stoichiometry and ligand exchange *Nanoscale Res Lett* **6** 79

[41] Gwénael G and Philippe C 2007 Raman spectroscopy of nanomaterials how spectra relate to disorder, particle size and mechanical properties *Prog Cryst Growth Charact Mater* **53** 1–56

[42] Pal M, Pal U, Jimenez J and Perez-Rodriguez F 2012 Effects of crystallization and dopant concentration on the emission behavior of TiO_2 Eu nanophosphors *Nanoscale Res Lett* **7** 1–12

[43] Choi H, Jung Y and Kim S 2005 Size effects in the Raman spectra of TiO_2 nanoparticles *Vib Spectrosc* **37** 33–8

[44] Klein M C, Hache F, Ricard D and Flytzanis C 1990 Size dependence of electron–phonon coupling in semiconductor nanospheres The case of CdSe *Phys Rev* B **42** 11123–32

[45] Agarwal K C, Daniel B, Grun M, Feinaugle P, Klingshirn C and Hetterich M 2005 Carrier-density-dependent electron effective mass in $Zn_{1-x}Mn_xSe$ for $0 \leq x \leq 0.13$ *Appl Phys Lett* **86** 181907

[46] Malmberg C G and Maryott A A 1956 Dielectric constant of water from 0° to 1000 °C *J Res Nat Bur Stand* **56** 369131–8

[47] Milutinovi A, Popovi Z V, Tomi N and Devi S 2004 Raman spectroscopy of polycrystalline α-MnSe *Mater Sci Forum* **453** 299–304

[48] Faraci G Gibilisco S, Russo P, Pennisi A R and La Rosa S 2006 Modified Raman confinement model for Si nanocrystals *Phys Rev* B **73** 0333071–3

[49] Alivisatos A P, Harris T D, Brus L E and Jayaraman A 1988 Resonance Raman scattering and optical absorption studies of CdSe microclusters at high pressure *J Chem Phys* **89** 5979–82

[50] Zhao B, Zhao S Q, Cai Y F, Peng W, Zhang K and Liu D 2011 Preparation and characterization of quantum dots with polyacrylic acid modified method in water-soluble core–shell structure *Spectrosc Spect Anal* **31** 3362–5

[51] Dhanam M, Kavitha B and Shanmugapriya M 2009 Structural analysis of CBD γ-MnS thin films *Chalcogenide Lett* **6** 541–7

[52] Li C, Guo L, Wu Z, Ren L, Ai X, Zhang J, Lv Y, Xu H and Yu D 2006 Photoluminescence and time-resolved photoluminescence of star-shaped ZnO nanostructures *Solid State Commun* **139** 355–9

[53] Mohanta D, Narayanan S, Pal S and Raychaudhuri A 2009 Time-resolved photoluminescence decay characteristics of bovine serum albumin-conjugated semiconductor nanocrystallites *J Exp Nanosci* **4** 177–91

[54] Lefebvre P, Mathieu H, Allegre J, Richard T, Combettes-Roos A, Pauthe M and Granier W 1997 Dynamics of photoluminescence in medium-size CdSe quantum crystallites *Semicond Sci Technol* **12** 958

[55] Jun Y, Jung Y and Cheon J 2002 Architectural control of magnetic semiconductor nanocrystals *J Am Chem Soc* **124** 615–9

[56] Issa B, Obaidat I M, Albiss B A and Haik Y 2013 Magnetic nanoparticles surface effects and properties related to biomedicine applications *Int J Mol Sci* **14** 21266–305

[57] Crespo P, Litrán R, Rojas T, Multigner M, De la Fuente J, Sánchez-López J, Garcia M, Hernando A, Penadés S and Fernández A 2004 Permanent magnetism, magnetic anisotropy, and hysteresis of thiol-capped gold nanoparticles *Phys Rev Lett* **93** 087204

[58] Garcia M A *et al* 2007 Magnetic properties of ZnO nanoparticles *Nano Lett* **7** 1489–94

[59] Yamamoto Y, Miura T, Teranishi T, Miyake M, Hori H, Suzuki M, Kawamura N, Miyagawa H, Nakamura T and Kobayashi K 2004 Direct evidence for ferromagnetic spin polarization in gold nanoparticles (arXiv cond mat/04)

[60] Guerrero E, Mũnoz-Marquez M A, García M, Crespo P, Fernandez-Pinel E, Hernando A and Fernandez A 2008 Surface plasmon resonance and magnetism of thiol-capped gold nanoparticles *Nanotechnology* **19** 175701

[61] Hernando A, Sampedro B, Litran R, Rojas T C, Sánchez-López J C and Fernandez A 2006 Room temparature permanent magnetism in thiol-capped Pd-rich nanoparticles *Nanotechnology* **17** 1449–53

[62] Zhang J *et al* 2013 Uniform wurtzite MnSe nanocrystals with surface-dependent magnetic behavior *Nano Res* **6** 275–85

[63] Petri-Fink A, Steitz B, Finka A, Salaklang J and Hofmann H 2007 Effect of cell media on polymer coated superparamagnetic iron oxide nanoparticles (SPIONs) colloidal stability, cytotoxicity, and cellular uptake studies *Eur J Pharm Biopharm* **68** 129–37

[64] Boonsongrit Y, Abe H, Sato K, Naito M, Yoshimura M, Ichikawa H and Fukumori Y 2008 Controlled release of bovine serum albumin from hydroxyapatite microspheres for protein delivery system *Mater Sci Eng* B **148** 162–5

[65] Zeng R *et al* 2010 Synthesis of highly emissive Mn-doped ZnSe nanocrystals without pyrophoric reagents *Chem Mater* **22** 2107–13

[66] Sharma V, Guzelturk B, Erdem T, Kelestemur Y and Demir H 2014 Tunable white-light-emitting Mn-doped ZnSe nanocrystals *ACS Appl Mater Interfaces* **6** 3654–60

[67] Sonawane K G, Ch R, Temgire M and Mahamuni S 2011 A case study Te in ZnSe and Mn-doped ZnSe quantum dots *Nanotechnology* **22** 305702

[68] Sarma R and Mohanta D 2014 Recording ion channels across soy-extracted lecithin bilayer generated by water-soluble quantum dots *Phil Mag* **94** 345–57

[69] Mohanta D, Stava E, Yu M and Blick R H 2014 Creation and regulation of ion channels across reconstituted phospholipid bilayers generated by streptavidin-linked magnetite nanoparticles *Phys Rev* E **89** 012707

IOP Publishing Nanotechnology
Nanotechnology 25 (2014) 359601 (1pp) doi:10 1088/0957-4484/25/35/359601

Erratum: Physical and biophysical assessment of highly fluorescent, magnetic quantum dots of a wurtzite-phase manganese selenide system (2014 *Nanotechnology* 25 275101)

Runjun Sarma[1], Queen Das[1], Anowar Hussain[2], Anand Ramteke[2], Amarjyoti Choudhury[1] and Dambarudhar Mohanta[1]

[1] Nanoscience and Soft Matter Laboratory, Department of Physics, Tezpur University, PO: Napaam, Assam-784 028, India
[2] Cancer Genetics and Chemoprevention Research Group, Department of Molecular Biology and Biotechnology, Tezpur University, PO: Napaam, Assam-784 028, India

E-mail: aramteke02@gmail.com (A Ramteke) and best@tezu.ernet.in (D Mohanta)

Received 14 July 2014
Accepted for publication 14 July 2014
Published 13 August 2014

There is a misprint in equation (2) in the published version of this article. Equation (2) should read as:

$$1/\left(d^2{}_{hkl}\right) = 4/3\left\{\left(h^2 + hk + k^2\right)/a^2\right\} + l^2/c^2. \qquad (2)$$

Philosophical Magazine, 2014
Vol. 94, No. 4, 345–357, http://dx.doi.org/10.1080/14786435.2013.853140

Taylor & Francis
Taylor & Francis Group

Recording ion channels across soy-extracted lecithin bilayer generated by water-soluble quantum dots

Runjun Sarma and Dambarudhar Mohanta*

Nanoscience and Soft Matter Laboratory, Department of Physics, Tezpur University, PO: Napaam, Tezpur 784028, Assam, India

(*Received 5 June 2013; accepted 4 October 2013*)

We report on the quantum dot (QD)-induced ion channels across a soya-derived lecithin bilayer supported on a laser drilled of ~100 μm aperture of cellulose acetate substrate that separates two electrolytic chambers. Adequate current bursts were observed when the bilayer was subjected to a gating voltage. The voltage-dependent current fluctuation, across the bilayer, was attributed to the insertion of ~20 nm sized water-soluble CdSe QDs, forming nanopores due to their spontaneous aggregation. Apart from a closed state, the first observable conductance levels were found as 6.3 and 11 nS, as for the respective biasing voltages of −10 and −20 mV. The highest observable conductance states, at corresponding voltages were ~14.3 and 21.1 nS. Considering two simplified models, we predict that the non-spherical pores (d_{nspore}) can be a better approximation over spherical nanopores (d_{spore}) for exhibiting a definite conductance level. At times, even $d_{\text{nspore}} \leq 4d_{\text{spore}}$ and that the non-spherical nanopores were associated with a smaller No. of QDs than the case for spherical nanopores, for a definite conductance state. It seems like the current events are partly stochastic, possibly due to thermal effects on the aggregated QDs that would form nanopores. The dwell time of the states was predicted in the range of 384–411 μs. The ion channel mechanism in natural phospholipid bilayers over artificial ones will provide a closer account to understand ion transport mechanism in live cells and signaling activity including labelling with fluorescent QDs.

Keywords: quantum dot; absorption; emission; bilayer; ion channel

1. Introduction

Semiconductor quantum dots (QDs) are now recognized as efficient luminescent probes in biophysical research owing to their unique optoelectronic properties such as, size-dependent colour tunability, broad absorption but narrow emission line-width, resistance to photobleaching and multiplex capabilities [1–3]. Recognizing the importance of the lipid bilayer membrane in cell biology and molecular biology, the use of size-controlled QDs, in these 2-dimensional membrane structures, is highly demanding and of significant interest as far as nanobio-interface application is concerned. It may be noted that, nanopores and nanoporous artificial membranes were proven to be useful in the fields of bioengineering and environmental sciences, to name a few, scope for DNA

*Corresponding author. Email: best@tezu.ernet.in

translocation [4], fuel cell studies [5], Coulter counter device [6] and ultra-high water purification systems [7]. However, functional nanopore creation leading to passage of ions in live cells, has not been fully understood. In fact, the activity and longevity of cells are largely governed by the control uptake/release of ions and other molecular species through transient nanopores available in the bilayer membrane. To be specific, active and passive ion channels could determine the physiological state of the cells by way of linking intracellular compartments with the extracellular matrix. Moreover, the unhealthy and disease-affected cells, both in animal and plant kingdoms, do not support normal ion transport process thereby causing abnormal intracellular activity. The ion channel studies, in real cells, are generally based on patch-clamp techniques [8], whereas the practice of planar chip method is relatively new and is limited to artificial bilayers only [9,10]. The artificial bilayer membrane can be used as a model system to explore transient nanopore creation in presence of a field.

Lecithin, is a yellow-brownish fatty substance, generally found in animals and plant tissues which comprise of phosphoric acids, choline, glycerol, phospholipids etc. It contains (21%) phosphatidylcholin (PC) and (20%) phosphatidylethanolamine (PE). A lecithin molecule consists of a hydrophobic tail and a hydrophilic head. When lipids are 'painted' in an aqueous solution across an aperture they self-assemble spontaneously where hydrophobic and hydrophilic ends align independently, thus forming a stable bilayer [11]. The typical thickness of the lecithin bilayer is ~4 nm.

In this work, we demonstrate the possible electrophysiological application of highly fluorescent CdSe QDs. First, a stable lecithin bilayer is formed across an aperture of a cellulose acetate substrate that separates two electrolytic chambers. Then, current fluctuation was assessed in response to an applied voltage. Moreover, we correlate the ion conduction phenomena of voltage-gated ion channels [12] with the resulting nanopore created as a result of oligomeric aggregation of CdSe QDs. Furthermore, the experimental results are discussed in the light of simple theoretical models on nanopore creation.

2. Experimental details

This section describes synthesis and characterization of colloidal QDs including set-up for measuring ion channel activity.

2.1. *Synthesis of colloidal CdSe QDs*

First, 0.62 g of cadmium nitrate-tetra hydrate [$Cd(NO_3)_2.4H_2O$, 99% pure, Merck] was dissolved in 100 mL of water followed by stirring for 20 min at 60°C temperature. The pH of the solution was adjusted to 11 by adding aqueous sodium hydroxide (NaOH) in a dropwise manner. A few minutes later, 0.111 g of selenium di-oxide (SeO_2, 99.5% pure, Merck) was put into the above sol followed by addition of 0.1 g of sodium borohydride ($NaBH_4$) as a reductant. Finally, the mixture was subjected to vigorous stirring (~250 rpm) for 1 h and at a temperature of 100°C. The final product was obtained through repeated centrifugation and filtration. The involved chemical reaction for obtaining QDs is as follows:

$$Cd^{2+}(aq.) + Se^{2-}(aq.) \longrightarrow CdSe\ (QDs)$$

2.2. *Optical and microscopic characterizations*

Optical absorption response was revealed by UV–Visible absorption spectroscopy (UV 2450 Shimadzu), whereas photoluminescence (PL) spectrum was obtained from a LS 55 PerkinElmer spectrophotometer, with a Xe lamp as the excitation source (λ_{ex} = 280 nm). The data acquisition was processed through a computer-controlled standard monochromator-based photodetection system. The morphological characterization of the CdSe QDs was performed by a high-resolution transmission electron microscope (HRTEM, JEOL, JEM-2100) working at an accelerating voltage of 200 kV.

2.3. *Bilayer formation and measurement of ion channel activity*

The lipid bilayer experiment was performed using a cellulose acetate substrate. The cellulose acetate system is chosen as it possesses good electrical properties (low dielectric constant, low dielectric loss), good thermal properties along with high value of elastic modulus that are comparable to the values observed for other polymeric materials (Teflon, PP, PET) generally used for this type of application. A substrate, having a good mechanical and thermal stability, is capable of supporting a very stable bilayer. In addition, the substrate material with low dielectric constant and dielectric loss can contribute only weakly to the effective capacitance and thus may help even in the detection of single ion channel events. The physical parameters related to cellulose acetate substrate are shown in Table 1. In a typical ion channel experiment, the preferred diameter of the aperture is in the range of ~80–100 μm [13]. Shown in Figure 1, is an aperture (of diameter d_a = 100 μm) located at the centre of the cellulose acetate substrate, which was developed by using a femto-second KrF excimer laser available at RRCAT, Indore. In order to obtain a lecithin bilayer, we have extracted soy lecithin from soya-bean seed (model RKS-18) through solvent extraction process followed by water degumming process [14,15].

The complete ion channel experiment was performed using a patch-clamp amplifier (EPC10) and patchmaster software (HEKA Elektronik, Germany)®. The main amplifier had an extension called the head-stage which was capable of interfacing amplifier and the planar chip device. The head-stage was connected to Ag/AgCl electrodes for the data acquisition of single ion channels across the lipid bilayer (Figure 2). A lecithin lipid bilayer membrane was formed around the aperture by a painting method following an established procedure (Montal-Mueller technique) [11]. The impermeable bilayer would act as a partition between the two compartments (cis and trans chamber) containing electrolytic buffer (1 mL of 1 M KCl, 10 mM HEPES at pH = 7.5 at room temperature). As mentioned above, the compartments were connected to the patch clamp amplifier via a pair of Ag/AgCl electrodes prepared in 0.5 M KCl (Figure 2). The resulting currents were filtered by a low-pass filter (with a four-pole Bessel filter at

Table 1. Physical properties of the cellulose acetate substrate.

Substrate	Dielectric constant (ε_r)	Density (ρ) gm/cm^3	Thermal conductivity (K) W/m/K	Melting point (T_M) °C	Young modulus (Y) Gpa
Cellulose acetate	2.9	1.28	0.16–0.36	159.02	2.4–4.1

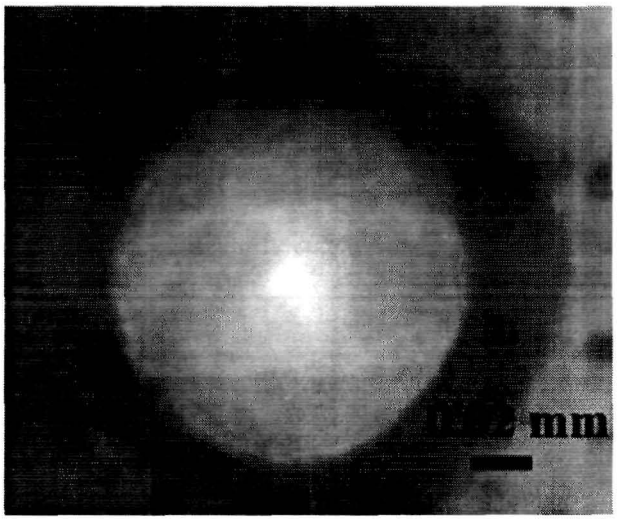

Figure 1. (colour online) A cellulose acetate specimen (with 100 μm aperture) used to support lecithin bilayer.

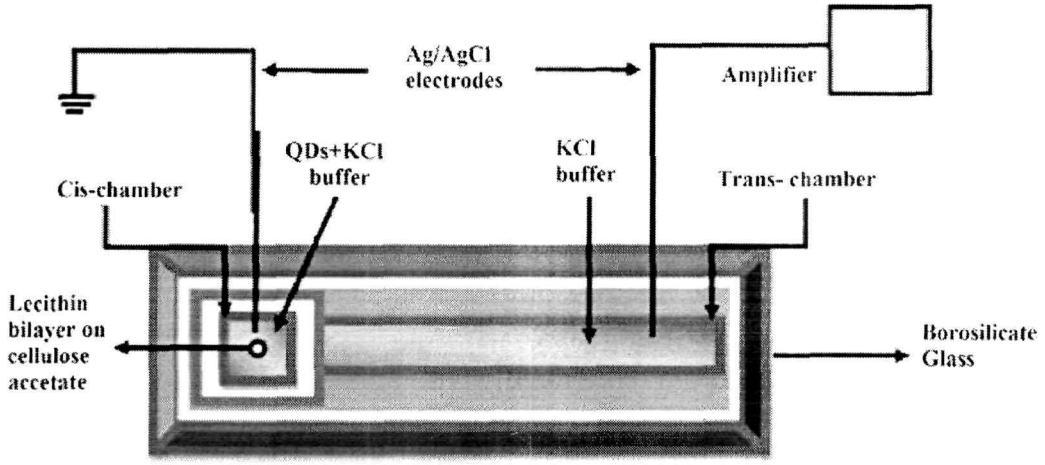

Figure 2. (colour online) Schematic of a typical ion channel measurement setup showing different components.

1 kHz, with a sampling frequency of 10 kHz by a computer with an analog-to-digital converter). In order to suppress electromagnetic noise, the whole set-up was kept in a Faraday cage with ground connected to the building ground. The amplified current was recorded in PC which works on OS windows 2007® using the patchmaster software®.

3. Results and discussion

The optical characterization, formation of a stable lecithin bilayer and ion channel response as a result of QD insertion, are as discussed below.

3.1. *Optical studies of water-soluble CdSe QDs*

The optical absorption and emission characteristics of water-soluble CdSe QDs are presented in Figure 3. The UV–vis optical spectrum is characterized by a strong 1*s*–1*s*

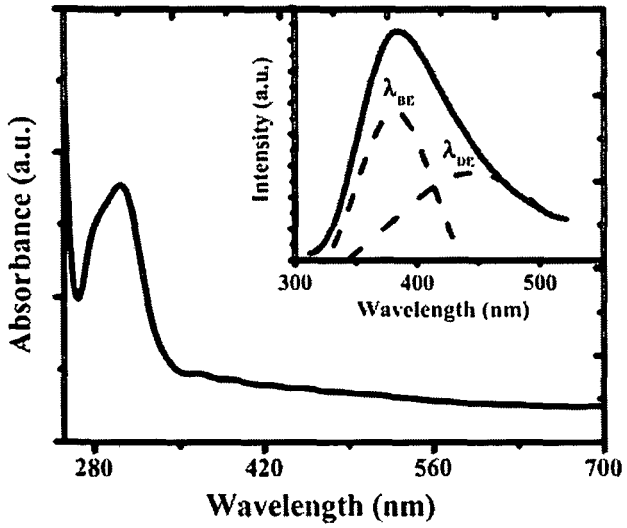

Figure 3. (colour online) Optical absorption and de-convoluted photoluminescence spectra of CdSe QDs.

excitonic absorption at ~303 nm ($E_g = 4.09$ eV). The quantum confinement of the charge carriers in the QDs has led to significant blue shift of the onset of absorption with respect to the corresponding bulk value ($\lambda_{onset} \sim 716$ nm). The ground state excitonic wavelength value is comparable with that of the value (~310 nm) predicted in an earlier work where polyvinyl alcohol (PVA) was used as a dispersing medium [16]. The photoluminescence spectrum of the CdSe QDs (under an excitation wavelength of 280 nm), is shown as an inset. The PL response of the QDs is mainly contributed by band-edge (λ_{BE}) and defect (λ_{DE}) related emissions. The respective positions of λ_{BE} and λ_{DE} are located at λ_{BE} at ~380 and ~443 nm. In fact, the asymmetrically stretched PL curve is due to significant contribution of λ_{DE} emission which is attributed to the radiative transitions mediated via trap states. The trap states can be produced by structural defects, such as atomic vacancies, local lattice mismatches, dangling bonds, or adsorbates at the surface [17,18]. The difference between the absorption and emission maxima, which is also called the Stokes shift, is given by [19]

$$\Delta_{stokes} = 2S\hbar\omega_{LO} \tag{1}$$

Here, S is defined as Huang–Rhys parameter which represents the electron phonon coupling strength of the QDs and ω_{LO} is the longitudinal optical phonon frequency (=210 cm^{-1}) of the CdSe QDs. The value of $\hbar\omega_{LO}$ of CdSe QDs is approximately 30 meV [20]. Considering $\hbar\omega_{LO}$ value in Equation (1) and measuring the absorption and emission peak from Figure 3, the Huang–Rhys parameter (S) is calculated to be ~13.3. A high coupling constant value, as a measure of strong electron phonon interaction, may signify discretization of optical modes due to phonon confinement effect [21].

3.2. *Evidence of formation of a stable lecithin bilayer around the aperture*

The bilayer capacitance is given by: $C_m = I/(dV/dt)$ [22]. Here, I is the measured current across the bilayer in response to an applied voltage ramp dV/dt. In the present case,

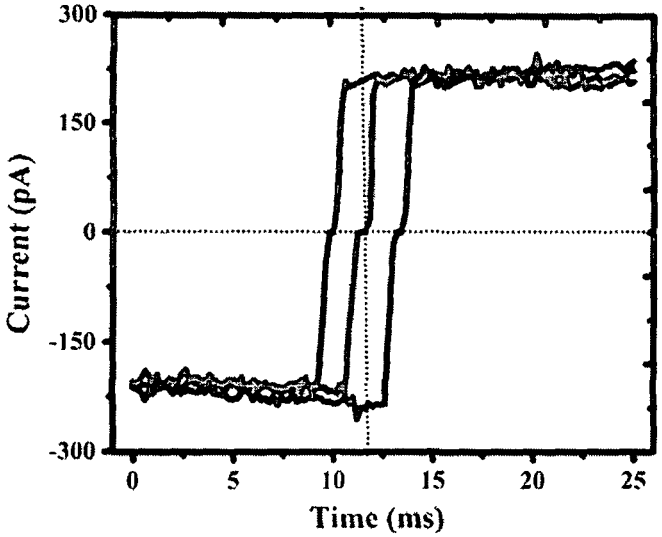

Figure 4. (colour online) Variation of current with the application of ramp voltage in the lecithin bilayer, recorded at different times.

100 mV was applied for 20 ms giving out a ramp of dV/dt = 5 V/s. The membrane current was found to be ~209.5 pA (Figure 4). Three traces were shown to ensure stability with lapse of time. The estimated (lecithin) bilayer membrane capacitance is found to be ~42 pF. Theoretically, lecithin membrane capacitance was predicted as ~57 pF by using the following relation [9]:

$$C_m = C_s \frac{\pi}{4} d_p^2, \tag{2}$$

where, C_s is the specific capacitance of the soya-lecithin bilayer (~0.75 μF/cm^2) [23]. For obtaining a stable bilayer, the whole aperture is believed to be covered by the bilayer itself. In that case, the diameter of the aperture (d_a) is equal to the membrane diameter (d_p). Again, in planar lipid bilayer experiment, the membrane capacitance (C_m) and the diameter (d_p) of the membrane carrying micropore are related as,

$$C_m = \frac{\varepsilon_0 \varepsilon_r A}{d}. \tag{3}$$

Here, $A = \frac{\pi}{4} d_p^2$ is the area of the membrane, ε_0 is the permittivity of the free space ($\varepsilon_0 = 8.85 \times 10^{-12}$ F/m), ε_r is the dielectric constant of the membrane and d is the thickness of the lipid bilayer. Considering ε_r of lecithin equal to the dielectric constant of the supported lipid bilayer in the aqueous solution (ε_r = 3) [24], the lecithin bilayer thickness is calculated as ~4.96 nm. The bilayer under study was found to form a giga seal (~3–10 GΩ) and the bilayer was fairly stable up to a time duration of 390 s. The stability of the bilayer can be assessed from a fairly constant value of membrane current (~209 pA), recorded at different time (Figure 4).

3.3. *QD induced ion channel response, nanopore formation and theoretical assessment*

After obtaining a stable bilayer around the aperture, 4.2 nmol/ml water-soluble CdSe QDs (~20 nm size as revealed from HRTEM micrograph, Figure 5) were injected into

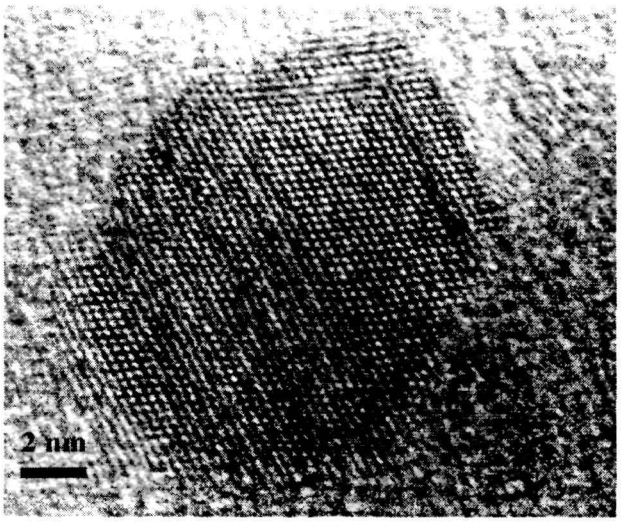

Figure 5. HRTEM image of a CdSe QD, showing lattice fringe pattern.

the cis compartment of the electrolytic chamber with the help of a Hamilton® microsyringe. Note that, while trans-side of the chamber was connected to the head stage of the amplifier, the cis-compartment was held at virtual ground. The noise level of the whole set-up was reduced to <2 pA by grounding the Faraday cage with the ground of the building. About a minute later the QDs were added, current bursts were observed in response to an applied voltage across the lecithin bilayer membrane. Figure 6 depicts the traces of current fluctuation when the bilayer was subjected to two different biasing voltages of −10 mV (Figure 6(a)) and −20 mV (Figure 6(b)). An apparently enhanced current magnitude was witnessed with an increasing biasing voltage. We anticipate instant oligomeric aggregation of QDs in the lecithin bilayer, allowing counter ions to pass through the nanopores under an external field. A higher voltage indeed facilitates a higher concentration of ions resulting in a higher magnitude of the current burst. The

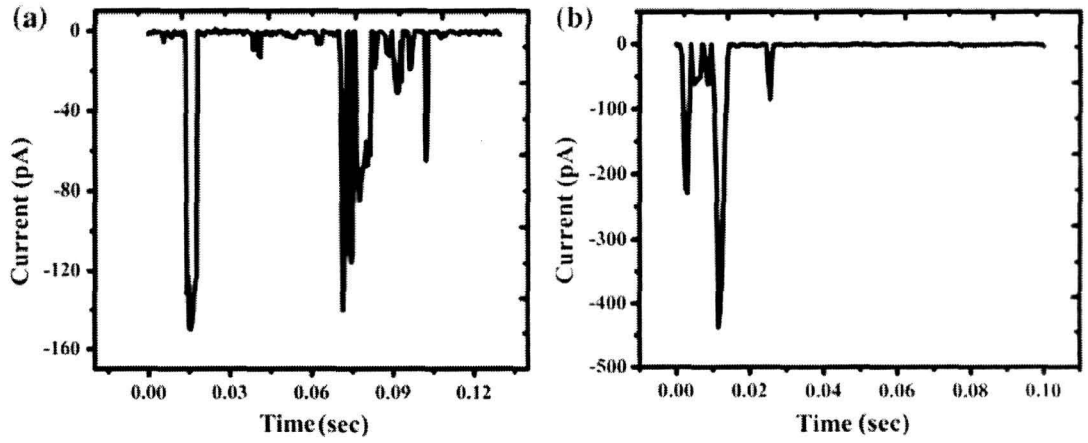

Figure 6. Current fluctuation measured across the lipid bilayer due to insertion of QDs at a biasing voltage of (a) −10 mV (b) −20 mV.

plots representing number of events vs. current histograms over a number of experiments are shown in Figure 7. As can be found, there exist two dominant conductance states: a high-end level of 14.3 nS and a low-end one of 6.3 nS (inset of Figure 7(a)), corresponding to the bias voltage of −10 mV. The respective conductance levels, corresponding to a higher bias voltage (−20 mV), are 21.1 and 11 nS (inset of Figure 7(b)). Earlier, the prime conductance value of ~2.3 nS was observed by an earlier group where 12 nm CdSe QDs were inserted in an artificial phospholipid bilayer [25]. Moreover, the high-end value (~14.3 nS) is close to the conductance value ~15.8 nS, as predicted theoretically for ion channels created by 12 nm CdSe QDs and reported in an earlier work [26]. The dwell time, which signifies the duration of on/off condition of a particular conductance state, as a result of ion channel activity can be estimated by averaging over a number of events. In the present case, the magnitude of dwell times are estimated to be 384, 400 μs and 390, 411 μs, as for −10 and −20 mV bias-voltage cases, respectively.

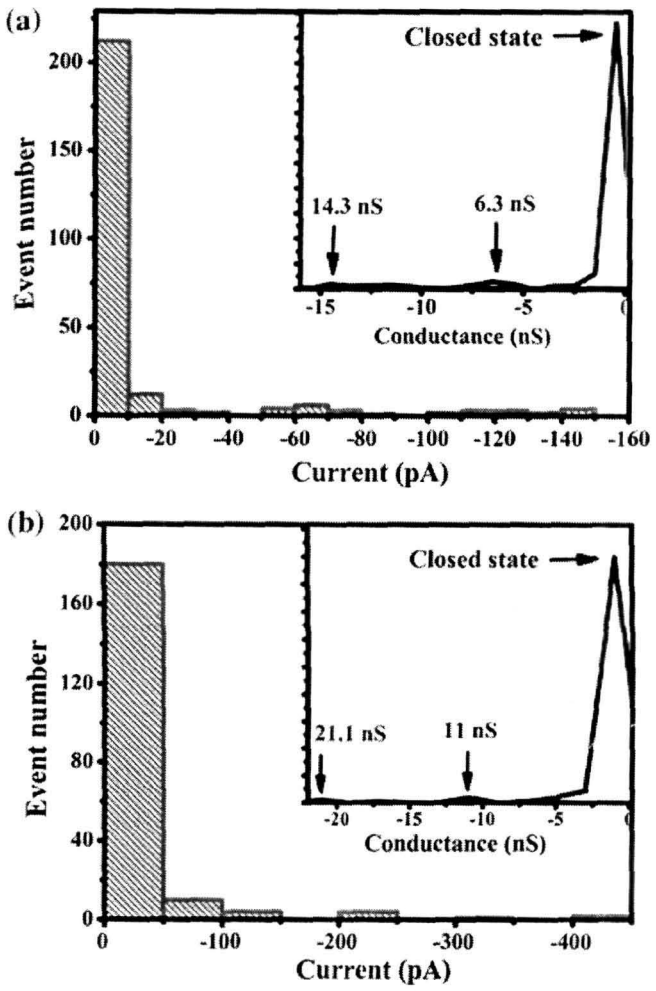

Figure 7. (colour online) Event vs. current histograms of QD induced ion channels, corresponding to the bias voltages (a) −10 mV (b) −20 mV. The figure-insets showing the respective conductance histograms for identifying individual open conductance states, away from the closed states.

Know that, the conductance value is the intrinsic parameter of a definite ion channel and is solely dependent on the interface region of the nanopore created by QDs in aggregate form. As far as the interface region is concerned, there can be two possibilities of well-defined nanopore geometry: formation of spherical and non-spherical nanopores. For mathematical simplicity, generally spherical nanopores are treated without curvature effect. Non-spherical nanopores involve complicated formula but better suited for large aggregation number. Presuming ion mobility uniform throughout the experimental chamber, here we discuss both the approximations to adjudge our experimental results.

Model 1: Ion channel activity due to spherical nanopores
This is an oversimplified version of the entrapped region created by spherical QDs. In this case, the conductance level G_s can be related to the spherical-shaped nanopore of size d_{spore} as [25]:

$$G_s = \sigma \frac{\pi d_{\text{spore}}^2}{4D}. \tag{4}$$

Here, D is the diameter of the QDs forming the aggregated structure and σ is the conductivity of the electrolytic buffer. The conductivity of the 1 M KCl + 10 mM HEPES buffer at 300 K is ~98 mS/cm, whereas size of the CdSe QDs used in the experiment is ~20 nm.

Model 2: Ion channel activity due to non-spherical nanopores
Pores of non-spherical geometry are mostly considered due to insertion of helical proteins in cell membranes leading to ion channels. We can also use the relevant formula in the present case, owing to the curved surfaces of the QDs and knowing that, the aggregated system is far from equilibrium. Since the pores are created by aggregation of QDs with curved surfaces, in reality, one cannot expect formation of spherically symmetric entrapped regions (spherical nanopores). In that case, ion channel conductance (G_{ns}) in a bilayer membrane can be related to the diameter of QD-induced non-spherical pore as per following relation [27–29]

$$G_{\text{ns}} = \frac{\sigma l \pi d_{\text{nspore}}^2}{[4(l + \pi d_{\text{nspore}}/4)]} \tag{5}$$

Here, l is the length of the pore and σ being the conductivity of the buffer. In our case, l = 4.96 nm which is the thickness of the lecithin membrane; d_{nspore} is the diameter of the nonspherical pore formed by the QDs.

Referring to model 1, and considering two conductance values of 6.3 and 14.3 nS (corresponding to a bias voltage −10 mV), we predict the size (d_{spore}) of the spherical nanopores as ~4 and ~6.09 nm. The corresponding pore diameters, as calculated using model 2 and applicable for the non-spherical nanopores (d_{nspore}) were estimated to be ~0.95 and ~1.5 nm. Apparently, $d_{\text{nspore}} \leq d_{\text{spore}}$. As for the case of the biasing voltage of −20 mV, the respective pore diameters of the spherical nanopores were observed to be ~5.3 and ~7.5 nm that corresponded to the conductance levels of 11 and 21.1 nS, respectively. The non-spherical pores are, however, characterized by a smaller dimension of ~1.22 and ~1.8 nm in this case.

It is likely that non-spherical pore formation is a better approximation which could account for interfacial effects and possible surface charge interactions among neighbouring QDs. The consideration of non-spherical pores over spherical ones was also realized in a similar work [30]. Not surprisingly, the ion channels induced by the QDs can be dependent on the shape of the nanopores, which may be due to the non-static nature of the aggregated QDs. Previously, nanopore shape-dependent ion conductance response was noticed for KasA potassium channels [30]. It was believed that, when the bilayer is subjected to a biasing field, QDs permeate and aggregate owing to a net dipole moment of the dots [31]. However, the formation of nanopore is a transient process and may be affected by thermal effect and a stress fluctuation. In presence of an external electric field, the QD with a dipole moment experiences a torque thus enforcing its insertion into the membrane. The aggregation behaviour of QDs is believed to be due to the dominance of electrostatic interaction of dots over Brownian agitation resulting in a conformation of minimum surface energy.

As stated above, the variance of pore conductance strictly depends on the shape of the pore as well as on the diameter of specific nanopore. More precisely, the pores are created by the transient aggregation of QDs, creating current bursts of varied magnitudes. Now both the models can be used independently to compute the number of QDs (N) involved in the creation of an aggregated structure, described by the following relation [31]:

$$d_{\text{sporc}}, d_{\text{nsporc}} = D_{\text{dot}}[1/\sin(180/N) - 1] \tag{6}$$

The spherical shaped nanopores, exhibiting high (14.3 nS) and low (6.3 nS) values of conductance states are as a result of aggregation of 3.6 and 3 Nos. of QDs, respectively (Table 2). The corresponding N values were 2.6 and 2.4, for non-spherical pores. It is worth mentioning here that a coplanar assimilation of ~3 QDs would represent the most close-packed network, and ions will not be necessarily allowed should the pores be filled with lipid molecules. It is very likely that the migration of ions through nanopores is highly stochastic in nature, but capable of forming most probable ion conductance states owing to activity of transient pores. This is because an aggregation number $N < 3$ has no physical meaning, as far as the entrapped region is concerned. But an aggregation of 3 QDs would represent a minimum energy configuration that might describe a small, open conductance state when ions make their way for free passage, in response to a biasing voltage of −10 mV. In contrast, in a spherical nanopore approximation (model 1) an aggregation of ~3.6 QDs would indicate momentary involvement

Table 2. Different parameters related to QD induced ion channels considering different models.

		Model 1		Model 2	
Bias voltage (mV)	Conductance (nS)	Spherical nanopore diameter (nm)	Aggregation No. of QDs (N)	Non-spherical nanopore diameter (nm)	Aggregation No. of QDs (N)
−10	6.3	4.0	3.0	0.95	2.4
	14.3	6.09	3.6	1.5	2.6
−20	11.0	5.3	3.4	1.22	2.55
	21.1	7.5	3.9	1.8	2.7

of an extra QD in the aggregated state, giving rise to the formation of a larger nanopore and consequently a higher conductance level. On the other hand, number of aggregated QDs corresponding to the conductance values of 11 and 21.1 nS (corresponding to a gating voltage −20 mV) are found to be 3.4 and 3.9, respectively. In contrast, with reference to model 2 (non-spherical pores), the relevant conductance states are characterized by an aggregation No. of 2.55 and 2.7. The different parameters (pore diameter, no of aggregated QDs and conductance value) of ion channels created by the application of different bias voltage are depicted in the Table 2.

Owing to consideration of larger sized QDs, we observed that the spherical pore diameter created by the QDs are comparatively larger than those reported by other groups [25]. Theoretically, an aggregation of five, six QDs may be possible, but in reality, thermal agitation is likely to perturb such a configuration for a longer duration of time [26]. As a consequence, it can flip either to three or, nearly four QD aggregation exhibiting a minimum energy configuration that is thermodynamically favourable. The undulation of QD aggregation may also be responsible for this flipping action. It is highly likely that QDs which experience oligomeric aggregation depart from their exact positions with time. As a result, channel events may exhibit stochastic trend due to dynamic nature of ion conducting pathways (nanopores). But the most probable states can be ascertained through histogram plots on a number of channel events and using theory of nanopores. We also invoke that, the observation of two conductance states, for a given biasing voltage may not represent independent ones but may call for simultaneous opening of an independent state. In this regard, mixed states due to simultaneous opening of fundamental states need to be addressed, which is in progress. It may be noted that, the ion channels could not be recorded at a higher biasing voltage owing to bilayer instability causing large leakage current.

4. Conclusions

Monodisperse, water-soluble CdSe QDs of average size of ~20 nm have been synthesized and characterized. The synthesized QDs exhibited voltage-dependent current fluctuations across the reconstituted soy-extracted lecithin bilayer supported on a cellulose acetate substrate. A higher biasing voltage could facilitate the migration of a higher concentration of ions, thereby exhibiting a higher current fluctuation. The ion channels were believed to be caused by the passage of ions through entrapped regions of the QD aggregates (nanopores). The number of QDs, responsible for creating a conductance state was found to vary with the model type and characterized by different nanopore size. As a general trend, non-spherical nanopores with a smaller diameter, would exhibit similar ion conductance pathways as the case for spherical nanopores with a larger diameter. Referring to spherical nanopore formation, a conductance state of ~14.3 nS was believed to be created by an aggregation of ~3.6 QDs and with a pore diameter of ~6.09 nm (under a biasing voltage of −10 mV); a lower conductance state (~6.3 nS) was realized corresponding to an aggregation No. 3 and with a spherical nanopore size of 4 nm. In contrast, in the model which is based on creation of non-spherical pores, the respective conductance states were believed to be created by a relatively smaller pore diameter of ~1.5 nm (QD aggregation of N = 2.6) and ~0.95 nm (QD aggregation of N = 2.4). By increasing the biasing voltage to −20 mV, the conductance values were increased to 11 and 21.1 nS which corresponded to 5.3 and 7.5 nm of the

spherical pores, and 1.22 and 1.8 nm as for diameters of the non-spherical pores. Being the aggregation number $N \leq 3$ is physically unrealistic in view of nanopore formation, the migration of ions could be stochastic due to non-static feature of the aggregated QDs owing to thermal effects. While the models, to a large extent, describe the QD induced nanopores and consequently, ion channel activity, more work in this direction is required to incorporate the effects due to QD size and shape distribution. Once this is worked out, one can really get access to control the ion conducting pathways in a more precise way.

The voltage-gated ion channel activity generated by highly fluorescent CdSe QDs in naturally extracted lecithin bilayer supported on a new substrate material would find ample scope in biochemical detection, DNA sequencing, cellular drug delivery and other electrophysiological applications.

Acknowledgements

The authors thank DST, New Delhi for extending financial support (Project No. SR/FTP/PS07/2008). The authors gratefully acknowledge Dr. P.K. Gupta of Raja Ramanna Centre for Advanced Technology (RRCAT), Indore for making micropores in the desired substrate used in this study. We also extend our sincere thanks to SAIF-NEHU, Shillong for providing HRTEM facility. One of the authors (RS) is thankful to Mr. R. Arondhara and to the Department of Food Engineering and Technology, TU for extending help in the extraction of lecithin from soybean seeds.

References

[1] L. Qi and X. Gao, Expert Opin. Drug Delivery 5 (2008) p.263.
[2] A. Dimitri, C. Hongfeng, C. Michael, D. Mitra, L. Yang, S. Peng, R. Amit, R. Dinakar, P. Shaunak, A.S. Michael and V. Milana, J. Phys.: Condens. Matter 17 (2005) p.R637.
[3] T. Jamieson, R. Bakhshi, D. Petrova, R. Pocock, M. Imani and A.M. Seifalian, Biomaterials 28 (2007) p.4717.
[4] A.S. Panwar and M. Muthukumar, J. Am. Chem. Soc. 131 (2009) p.18563.
[5] J.C. Biffinger, R. Ray, B. Little and B.R. Ringeisen, Environ. Sci. Technol. 41 (2007) p.1444.
[6] T. Ito, L. Sun and R.M. Crooks, Anal. Chem. 75 (2003) p.2399.
[7] G. Menzl, J. Köfinger and C. Dellago, Phys. Rev. Lett. 109 (2012) p.020602.
[8] R.A. Levis and J.L. Rae, *Low-noise patch-clamp techniques*, in *Methods in Enzymology*, P.M. Conn, ed., Academic Press, 1998, p. 218, Vol. 293.
[9] M. Mayer, J.K. Kriebel, M.T. Tosteson and G.M. Whitesides, Biophys. J. 85 (2003) p.2684.
[10] H. Suzuki, K.V. Tabata, H. Noji and S. Takeuchi, Biosens. Bioelectron. 22 (2007) p.1111.
[11] M. Montal and P. Mueller, Proc. Nat. Acad. Sci. 69 (1972) p.3561.
[12] W.A. Catterall, S. Cestèle, V. Yarov-Yarovoy, F.H. Yu, K. Konoki and T. Scheuer, Toxicon 49 (2007) p.124.
[13] H. Suzuki and S. Takeuchi, Anal. Bioanal. Chem. 391 (2008) p.2695.
[14] V.V. Patil, R.V. Galge and B.N. Thorat, Sep. Purif. Technol. 75 (2010) p.138.
[15] L. Ceci, D. Constenla and G. Crapiste, J. Sci. Food Agric. 88 (2008) p.2460.
[16] R. Sarma, A. Chetry and D. Mohanta, Nanosci. Nanotechnol. Lett. 4 (2012) p.775.
[17] M. Šimurda, P. Němec, F. Trojánek, K. Neudert, T. Miyoshi, K. Kasatani and P. Malý, Physica E 36 (2007) p.205.
[18] M. Frasco and N. Chaniotakis, Sensors 9 (2009) p.7266.
[19] K. Huang and A. Rhys, Proc. R. Soc. A 204 (1950) p.406.

[20] P. Guyot-Sionnest, B. Wehrenberg and D. Yu, J. Chem. Phys. 123 (2005) p.074709.
[21] J. Devreese, V. Fomin, E. Pokatilov, V. Gladilin and S. Klimin, Phys. Status Solidi C 0 (2003) p.1189.
[22] M. Robello and A. Gliozzi, Biochim. Biophys. Acta 982 (1989) p.173.
[23] P. Brzezinski, A. Messinger, Y. Blatt, A. Gopher and D. Kleinfeld, J. Membr. Biol. 165 (1998) p.213.
[24] G. Gramse, A. Dols-Perez, M.A. Edwards, L. Fumagalli and G. Gomila, Biophys. J. 104 (2013) p.1257.
[25] S.A. Klein, S.J. Wilk, T.J. Thornton and J.D. Posner, J. Phys: Conf. Ser. 109 (2008) p.012022.
[26] R. Sarma and D. Mohanta, J. Comput. Theor. Nanosci. 9 (2012) p.1070.
[27] F.S. Noronha, J.S. Cruz, P.S. Beirão and M.F. Horta, Infect. Immun. 68 (2000) p.4578.
[28] J. Chen, J.A. Hessler, K. Putchakayala, B.K. Panama, D.P. Khan, S. Hong, D.G. Mullen, S.C. DiMaggio, A. Som and G.N. Tew, J. Phys. Chem. B 113 (2009) p.11179.
[29] D.C. Eaton, J. Neurosci. Res. 13 (1984) p.599.
[30] S. Kuyucak, O.S. Andersen and S.-H. Chung, Rep. Prog. Phys. 64 (2001) p.1427.
[31] S. Ramachandran, G.L. Kumar, R.H. Blick and D.W. van der Weide, Appl. Phys. Lett. 86 (2005) p.083901.

Nanoscience and
Nanotechnology Letters
Vol 4 1–8 2012

Synthesis, Stabilization of CdSe Quantum Dots and the Role of Rose Water and Citric Environment

Runjun Sarma, Arati Chetry, and Dambarudhar Mohanta*

Nanoscience and Soft Matter Laboratory Department of Physics Tezpur University, PO Napaam Assam 784028 India

In this report, we present the colloidal synthesis and environmental stability of CdSe QDs using PVA (polyvinyl alcohol) as a dispersing media Aiming to provide a stable colloidal system for biological study, different ambient conditions, such as different Cd^{2+} concentration, reaction time and pH values Moreover, the aging effect has been studied by solubilizing the QDs using natural media lemon (citric acid) and rose water The optical properties investigated by different spectroscopic tools have revealed that CdSe QDs are more stable in citric environment due to esterification of PVA to PVA-C (functionalization with carboxyl group) Highly fluorescent CdSe-QDs in citric environment would find scope in biophysical applications including imaging and labeling molecules

Keywords: Quantum Dot, CdSe, Polyvinyl Alcohol, Absorption, Emission

1. INTRODUCTION

In recent years, semiconductor nanocrystals, or quantum dots (QDs) are regarded as efficient luminescent probes and labels for numerous biological applications This is because they display unique optical and optoelectronic properties, such as, size dependent tunable color, narrow emission line-width, resistance to photobleaching and multiplex capabilities [1–3] Despite the potential use of QDs as fluorescent probes in biological environment several issues are need to be addressed which include environmental stability, size selectivity, bio-specificity etc [2] As a first strategy, the QDs were synthesized via various methods in hydrophobic media e g , using organic solvents like *tri-octylphosphine* and *tri-n octylphosphine oxide* (TOP/TOPO) at high temperatures [4] The solvents were used both for bare and core–shell type of QDs These QDs are soluble only in nonpolar hydrophobic solvent such as chloroform They are mostly toxic to biological materials To overcome these difficulty, several attempts have been made for synthesizing water soluble QDs [5–8] Unfortunately, these synthesis processes were found to be complicated which use expensive precursors In this regard, QD synthesis in polymers (e g , polyvinyl alcohol (PVA), polyvinyl pyrrolidone (PVP) can be an interesting approach due to their commercial availability, water solubility and bio-compatibility [9] Moreover, these polymeric hosts are not only capable of improving the surface passivation of the QDs but also enhance the exci tonic emission These polymers have been widely used for encapsulating semiconductor nanocrystals [10–13]

In recent decades, a great deal of research work on QDs (of II–VI compound semiconductor system) have been carried out worldwide Of particular interest cadmium selenide (CdSe) which is regarded as a suitable optoelectronic candidate due to an advantage of large band gap tunability and bright emission response It was predicted that CdSe QDs are about ~20 times brighter and 100 times more stable than single rhodamine 6G dye molecules [14] Moreover, it was reported that the toxicity level of Cd^{2+} ion reduces in nanometer reason when it form CdTe or CdSe compound than the elemental Cd [15] In addition, cytotoxicity in the cellular level study is mainly contributed from the capping material rather than core metalloid complex itself [16] Consequently, there exist plentiful scope for safe using of nanoscale CdSe in biological systems

To use the QDs in biological application such as biosensing, biolabeling, bioimaging, it is very much important to understand the parameters that influence their optical properties significantly In this work, we report the preparation of high-quality CdSe QDs and their stabilization considering different factors such as varying concentration of cadmium precursor, reaction time and aging etc In addition, a special emphasis was given on the study of dispersing media dependent stability of CdSe QDs by considering natural media the first being rose water and the other one is citric media (derived from lemon)

*Author to whom correspondence should be addressed

2. EXPERIMENTAL DETAILS

The protocol used for the synthesizing and characterizing QDs are as detailed below

2 1. Synthesis of CdSe QDs

At first, 10% PVA solution was prepared by dissolving 10 g of PVA in 100 mL distilled water followed by stirring for 3 h Then 0 62 g of cadmium nitrate-tetra hydrate [$Cd(NO_3)_2$ $4H_2O$] was dissolved in 100 mL of water followed by stirring for 20 min at 60 °C temperature 20 mL of 10% PVA was added to Cd^{2+} solution during stirring The pH of the solution was adjusted to 11 by adding sodium hydroxide (NaOH) in a drop-wise manner Then, 0 11 g of selenium di-oxide (SeO_2) was added after sometime and then followed by addition of 0 1 g sodium borohydride ($NaBH_4$) The purpose of adding reductant $NaBH_4$ was to reduce SeO_2 Finally, the mixture was subjected to stirring for 1 h at 100 °C temperature In order to examine the photostability of PVA dispersed CdSe QDs in natural media, the QDs were dispersed in freshly prepared lemon water and in rose water The pH of the undispersed CdSe–PVA was found to be drastically changed from a value of pH = 7 02 to 3 42 and 7 42 in lemon and rose water media, respectively

The following chemical reactions are favoured in the formation of CdSe QDs

$$\text{Dissociation} \quad Cd(NO_3)_2 \longrightarrow Cd^{2+} + 2NO_3^- \quad (1)$$

$$\text{Hydrolysis} \quad SeO_2 + H_2O \longrightarrow H_2SeO_3 \quad (2)$$

$$\text{Reduction} \quad H_2SeO_3 \longrightarrow NaHSe \longrightarrow Se \quad (3)$$

$$\text{Subsequent Reduction} \quad Se \longrightarrow Se^{2-}(aq) \quad (4)$$

Complete Redox Reaction

$$Cd^{2+}(aq) + Se^{2-}(aq) \longrightarrow CdSe(QDs) \quad (5)$$

2.2. Characterization Techniques

The structural characterization of the CdSe QDs was performed by a high resolution transmission electron microscopy (HRTEM), (Model JEM-2100, at NEHU) working at an accelerating voltage of 200 kV The optical absorption study was performed by the UV-Visible absorption spectroscopy (UV 2450, Shimadzu Corporation) The size distribution aspect of the QDs was also studied by dynamic light scattering (DLS) (nano ZS90, Malvern instruments, UK) technique The room temperature photoluminescence (PL) spectra were revealed by using a Perkin Elmer LS 55 spectrophotometer, having Xe lamp as the excitation source ($\lambda_{ex} = 280$ nm) The data were collected by a computer controlled standard monochromator based photodetection system

3. RESULTS AND DISCUSSION

For meaningful application in biological systems, the QDs need to pass through a series of stability and compatibility tests It is essential to study the factors that have significant influence on their dimension, optical absorption and emission characteristics We have investigated the dependence of PVA dispersed CdSe QDs on the reactant concentration, reaction time and on aging The samples of QDs of varying concentration ratio of Cd^{2+}/Se^{2-} i e , 1 1, 2 1, 3 1, 4 1 are labeled as S_1, S_2, S_3, S_4, respectively

3.1. Bare and Hydrodynamic Size of QDs

Microscopy experiment was performed on QD-sample S_3 The TEM micrographs of the as-synthesized CdSe QDs are shown in Figure 1(a) The average size of the QDs is found to be ~20 nm with large-sized ones, more spherically symmetric as compared to the smaller ones The large size could be due to QD-coalesce as there was an unavoidable time gap of 6 days from the synthesis to TEM experiment The impression of aggregated structures (at a low magnification) could also be due to QD image contrast of subsequent planes But, isolated and non aggregated QDs can be clearly witnessed at a higher magnification, shown in the inset of Figure 1(a) Further, the evidence of clear lattice fringes has ensured good crystallinity of the sample (Fig 1(b)) The perfect periodicity of the lattice atoms was mostly witnessed in the core, while missing atoms and planes were observable close to the surface The typical interplanar spacing (d) was estimated to be ~0 33 nm which is close to the value predicted in an earlier work [17] As can be found at the upper right side portion of the figure, the orientation of atomic planes has altered with respect to the lower part We speculate the existence of some edge dislocation in the QD-material [18] This edge-dislocation could occur as a result of undeveloped lattice planes at the QD surface/boundary

The DLS study is based on the principle of light scattering that is used to probe particles undergoing Brownian motion in a given medium Therefore, instead of predicting core-size it is capable of providing information with regard to hydrodynamic diameter Typical Gaussian fitted size distribution plots of the QDs, as obtained from DLS measurement, are shown in Figure 2 The average sizes of the QDs, in different media are presented in Table I The hydrodynamic size of the QDs in PVA only media is ~ 15 nm The size becomes 14 5 and 19 nm when they were dispersed in lemon water, and rose water media, respectively Further, the FWHM value has substantially dropped from a value of ~6 8 in PVA only media to ~4 7 in lemon water media thus indicating a narrow size distribution in citric environment Whereas, the FWHM in rose media has increased to ~7 8 signifying thereby enhanced polydispersity in the system

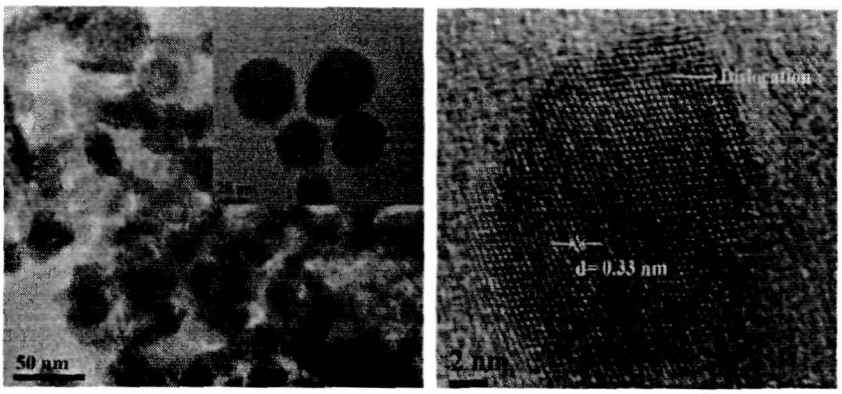

Fig. 1. (a) TEM image of CdSe QDs. (b) The enlarged view with lattice fringes.

3.2. Effect of Reactant Concentration

Figure 3(A) depicts the effect of Cd^{2+}/Se^{2-} precursor concentration on the UV-Vis spectra of CdSe QDs, dispersed in PVA solution. In all the cases, the onset of absorption was found to be blue shifted from the bulk value ($\lambda_{onset} \sim$ 716 nm). This implies effective quantum confinement of the charge carriers in the QDs. The samples (S_3, S_4) with higher Cd^{2+} concentration exhibit strong $1s$–$1s$ excitonic absorption at $\lambda_{ex} = 310$ nm. A low concentration of Cd^{2+} leads to the featureless characteristics with long tailing depicting inhomogeneity in the samples (S_1, S_2). The position of the ground state excitonic absorption was also observed previously where mercapto-acetic acid was used as a capping agent.[19] Our results indicate the formation of smaller sized QDs for precursors that are rich in Cd^{2+}. This behavior has also been witnessed in other works.[20–22] It may be due to the fact that proportionately larger concentration of Cd^{2+} ions (compared to Se^{2-} ions) provides suitable nuclear sites for the growth of CdSe QDs. Consequently, an adequate number of nucleation sites at a given concentration of Se^{2-} precursor would lead to the formation of smaller sized QDs.[20] A large no. of nucleation sites around the Cd^{2+} ions is because of smaller ionic radii of Cd^{2+} ions ($\sim$ 109 pm) compared to the Se^{2-} ions ($\sim$ 184 pm). The optical band gap of the QDs can be calculated from the respective onsets of absorption. The calculated band gap values can be used to estimate the average size of the QDs as per eqn. given by Brus et al.[23] The estimated band gap and QDs sizes are found to be in the range of $\sim$ 2.5–3.7 eV and $\sim$ 4.5–2.7 nm; respectively (Table II).

The PL spectra of CdSe–PVA QDs of different Cd^{2+} concentration, under an excitation wavelength 280 nm, are shown in Figure 3(B). The PL spectra of QDs are chiefly comprise of two emission peaks: emission due to the band-edge emission (λ_{BE}) and the defect related emission (λ_{DE}). The λ_{BE} was found to be located at $\sim$ 380 nm with a FWHM $\sim$ 65 nm. The λ_{DE} was in the range of 415–428 nm for QDs derived from varying Cd^{2+}/Se^{2-} ratios (1:1 to 4:1). For lower values of Cd^{2+}/Se^{2-} ratios (S_1, S_2), the emission response is weaker. But with the increase of Cd^{2+} concentration, the PL intensity (λ_{BE}) gets enhanced with sample S_3 exhibiting strongest response (FWHM $\sim$ 59 nm). The λ_{DE} peak, however remains significant for varying Cd^{2+}/Se^{2-} ratio (S_1, S_2) samples. The ratio of band edge-to-defect emission intensity varies between 1.01 and 1.27 for different Cd^{2+}/Se^{2-} ratios (S_1 to S_4).

The observed defect related emission response is attributed to the radiative transitions mediated via surface trap states. The states are created by entrapped electrons inside a selenium vacancy with holes in the valence band.[22, 24] As observed from the PL spectra, the dominant feature of defect related emission over the band edge emission, in samples S_1 and S_2, signifies inadequate surface passivation of the QDs. Previously, a lower Cd^{2+} concentration was considered to be insufficient for effective dispersion in PVA.[19] In our case, the intense band edge emissions, for S_3 and S_4, are due to significant passivation of the surface defects. Note that, a higher Cd^{2+} concentration would experience insufficient PVA host for effective capping[20] and that is why we observed reduced band edge-to-defect related emission for S_4 as compared to S_3. The sharp absorption features along with symmetric luminescence behavior of S_3 and S_4 samples indicate narrow size distribution of synthesized QDs.

As the effect of reactant concentration provided the best quality sample for $[Cd^{2+}]/[Se^{2-}] = 3{:}1$ (S_3), we opted this precursor for studying the effect of reaction time, aging as well as the role of two different natural media.

3.3. Effect of Reaction Time

Figures 4(A) and (B) show the dependence of absorption and emission properties of PVA dispersed QDs with reaction time for a fixed Cd^{2+} concentration. The reaction time was counted right after the SeO_2 reactant was added into

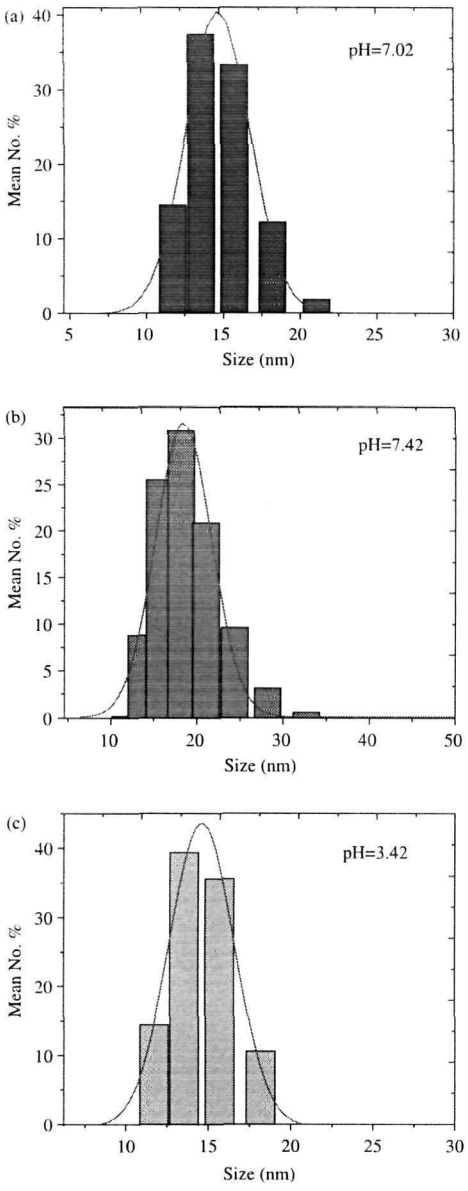

Fig. 2. DLS study along with Gaussian fitted histograms of the size distribution of the QDs in different pH media (a) PVA (b) rose water (c) lemon water.

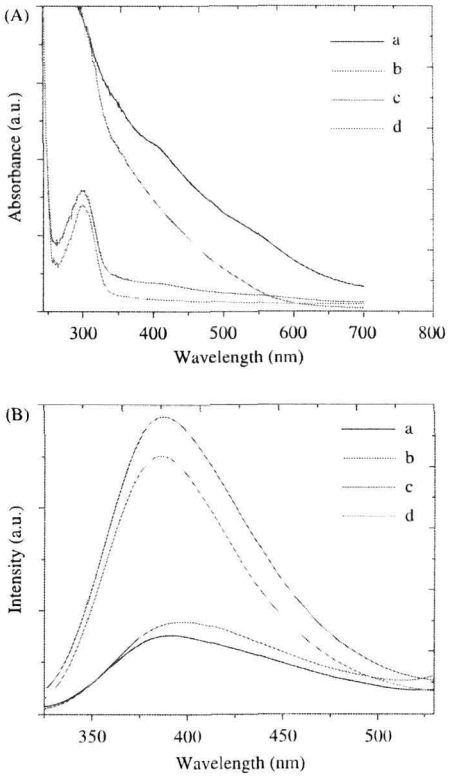

Fig. 3. (A) Absorption spectra of CdSe QDs of Cd^{2+}:Se^{2-} ratio (a) 1:1 (b) 2:1 (c) 3:1 (d) 4:1. (B) Photoluminescence spectra of CdSe QDs of Cd^{2+}:Se^{2-} ratio (a) 1:1 (b) 2:1 (c) 3:1 (d) 4:1.

the Cd^{2+}/PVA precursor. Upto 30 min of reaction, only featureless characteristics were observed revealing thereby no excitonic absorption. A sharp absorption response was observed at ~ 328 nm when the reaction was allowed for 60 min and beyond. Since the position of the absorption maxima did not change with time the average size of the QDs are expected to be uniform. Previously, it was argued that PVA matrix would restrict the growth of the particles and therefore, the growth process becomes homostatic.[20]

The PL response of the CdSe-QDs depicts asymmetrically stretched spectra as shown in Figure 4(B). Upon deconvolution (not shown), the λ_{BE} was found to be located at ~ 380 nm while λ_{DE} is positioned at ~ 417 nm, when the reaction time was varied in the range of

Table I. Hydrodynamic size of CdSe QDs predicted by DLS technique.

Sl. no.	Medium	pH	Mean size of CdSe QDs (nm)
1	PVA	7.02	15
2	Rose water	7.42	19
3	Lemon water	3.42	14.5

Table II. Energy gap and the average size of the CdSe QDs.

Sl. no.	Cd^{2+}:Se^{2-}	λ_{onset}	Band gap (eV)	Blue-shift energy (eV)	Average size (d) (nm)
1	1:1	495	2.50	0.76	4.5
2	2:1	497	2.49	0.75	4.4
3	3:1	328	3.78	2.04	2.7
4	4:1	330	3.75	2.01	2.8

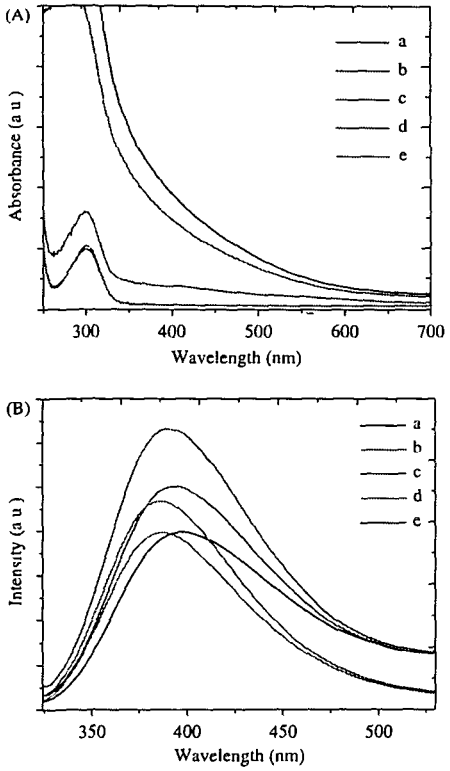

Fig 4 (A) Absorption spectra of CdSe QDs prepared with a reaction time of (a) 10 (b) 30 (c) 60 (d) 90 (e) 120 min (B) Photoluminescence spectra of CdSe QDs prepared with a of reaction time of (a) 10 (b) 30 (c) 60 (d) 90 (e) 120 min

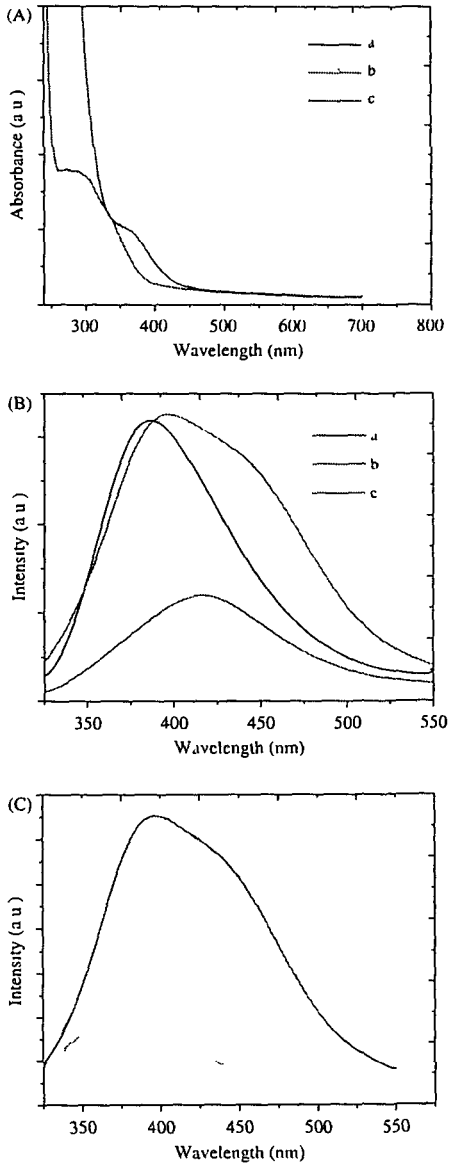

Fig 5 (A) Absorption spectra and (B) photoluminescence spectra of CdSe QDs in (a) PVA pH = 7 06 (b) rose water pH = 7 42 and in (c) lemon water pH = 3 42 media The deconvoulated emission response of QDs in lemon water medium is depicted in (C)

10–120 min Although, defect related emission was prominent for samples prepared with short reaction time environment, the overall PL emission was found to be strongest for the sample prepared under 60 min of duration Further increase of reaction time leads to the possibility of collective assimilation of nanocrystallites leading to suppressed emission response Whereas, insufficient reaction time would lead to unsaturated bonding between Cd^{2+} and Se^{2-} ions It is quite apparent that 60 min of reaction duration is good enough to ensure a sharp exciton absorption and intense emission response

3.4. Role of Dispersive Media and Aging

The typical absorption and emission behavior of CdSe-QDs dispersed in different dispersive media are shown in Figures 5(A) and (B), respectively One can notice from the absorption spectra that the excitonic absorption is located at ~300 nm (~4 13 eV) for neutral PVA as well as lemon water media The characteristic excitonic feature is relatively stronger and broader for citric media than the PVA only media The response of rose water media is characterized by a significant red shift (~0 76 eV) of the exciton absorption along with broadened absorption behavior

Figure 5(B) signifies the PL response of QDs dispersed in the lemon water, PVA and rose water media Each of the PL spectra is comprised of two emission bands, band-to-band emission (λ_{BE}) and defect-related emission (λ_{DE}) both in case of lemon water and PVA media While the first peak is located at ~380 nm for both the cases, the

λ_{DE} maxima are positioned at ~430 nm and ~416 nm in lemon water and PVA media, respectively Note that, the defect-related emission intensity is predominantly high in case of lemon water than the other environment The ratio of the band edge-to-defect emission intensity was found to be ~0 61 and 1 07, respectively for lemon water (pH = 3 42) and PVA media (pH = 7 02) The deconvoluted response of the PL curve is shown by dotted lines in Figure 5(C) Interestingly, the QDs in rose water media exhibit suppressed emission response The respective intensity of the band edge emission is reduced by a factor of ~ 1 8 and 1 5 as compared to the PVA and lemon water media Because of the improved defect related emission behavior in lemon water, the emission response of the QDs becomes more asymmetric in this media as compared to others

Figure 6 depicts a set of spectra highlighting studies with regard to the stability of the QDs due to independent aging effect in respective media As shown in Figure 6(A), the near band edge emission (NBE) gets improved by factor of ~4 when the specimen was subjected to aging for 6 days in lemon water However, exessive aging effect did not show further improvement The emission response is suppressed when the specimen was aged for 10 days In this case, the emission feature is characterized by an enhancement of ~2 7 w r t as-synthesized QD sample As a general trend, the peak due to the defect related emission of QDs in lemon water gets suppressed with aging However, it is evident from Figure 6(B) that CdSe-QDs in rose water exhibit red shifting (from $\lambda = 416$ to 475 nm, $E = 2\ 98$ to 2 61 eV) of the emission peak with the aging effect The red shifting can be ascribed to the size effect owing to the clusturing of QDs Surprisingly, though a peak-shift was evident with aging, the overall emission intensity remained unaltered for all the specimens Figure 6(C) accounts for comprehensive QD stability of the aging effect while referring to different media In rose water, the NBE intensity remained constant with aging while in PVA medium, the NBE intensity did not vary substantially upto 6 days But there is a drastic reduction of NBE for 10 days of aging Contrary to these observations, the emission intensity is significantly enhanced in lemon water for 6 days of aging beyond which only a slow decay was realized Compared to the case of PVA, the NBE for lemon water is found to be ~3 5 and ~7 2 times more intense for an aging duration of 6 days and 10 days, respectively In contrast, in rose water, the NBE is about ~1 6 and 1 8 times less intense in reference to PVA only media Therefore, among all these media, the citric media is most effective and ensure adequate stability

We have compared the optical properties of CdSe QDs dispersed in natural medium (lemon and rose water separately) with the laboratory prepared dispersing solution at fixed pH For pH control in CdSe–PVA solution, few drops of dil HCl and NaOH were added to make pH = 3 42 and 7 42, respectively We depict below the characteristic

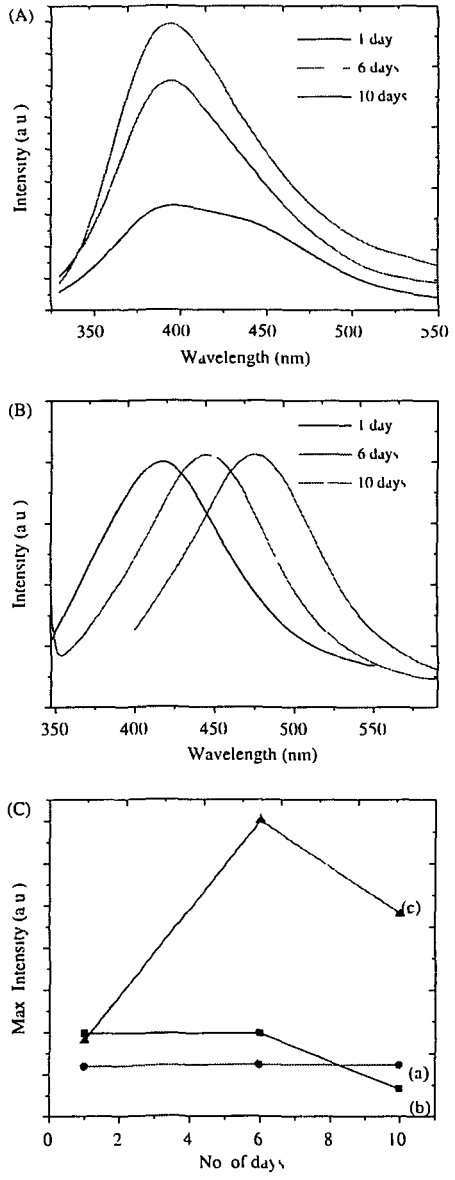

Fig 6 (A) Photoluminescence spectra of CdSe QDs in lemon water of pH 3 42 (B) Photoluminescence spectra of CdSe QDs in rose water of pH 7 42 (C) Maximum intensity versus no of days of CdSe QDs in (a) PVA pH = 7 02 (b) rose water pH = 7 42 and in (c) lemon water pH = 3 42 medium

photoluminescence response of CdSe–PVA QDs in lemon water and HCl media at same pH of 3 42 (Fig 7(A)), as well as in rose water and NaOH media of same pH = 7 42 (Fig 7(B)) It can be seen that in HCl media, the PL intensity is dropped by a factor of ~4 2 as compared to lemon water case Also, defect related emission response is not prominent in HCl media Note that in NaOH media,

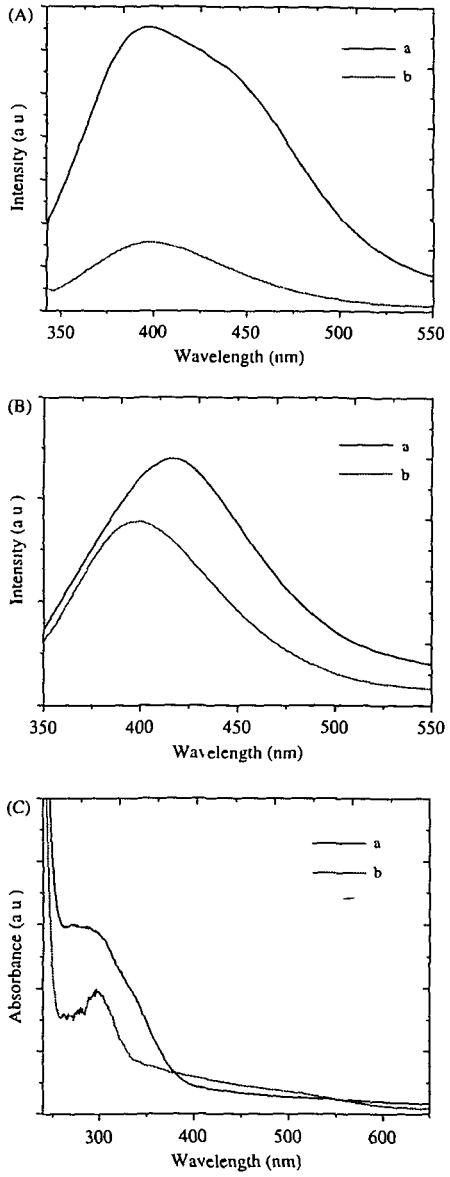

Fig 7 (A) Photoluminescence spectra of CdSe QDs in (a) lemon water (b) HCl media of same pH 3 42 (B) Photoluminescence spectra and (C) absorption spectra of CdSe QDs in (a) rose water and (b) NaOH media of same pH 7 42

the QDs show slightly intense emission response than in rose water but with shifting of the band-edge emission peak The absorption response of the rose water and NaOH media is shown in Figure 7(C)

The probable reason for the higher stability of QDs in lemon water media may be attributed to the fact that the PVA is esterified to PVA-C in presence of citric acid ($C_6H_8O_7$) contained in the lemon water [25] The schematic representation of esterification reaction of PVA with lemon water (citric acid) is as given below

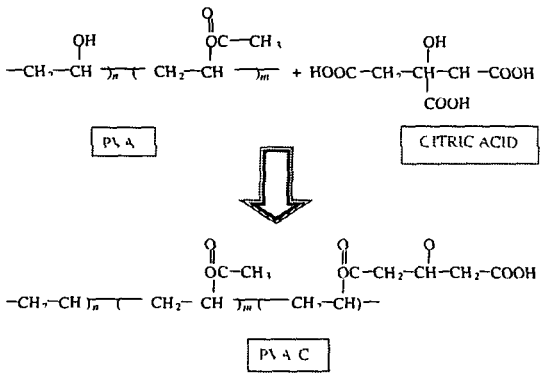

As far as QD stability is concerned, the carboxyl-functionalized PVA host provides better environment over untreated PVA [23] This is because of larger availability of free Cd^{2+} ions which are capable of imparting charge balancing with carboxylate ($-COO^-$) ions Consequently, it results in a more stable colloidal system Moreover, after esterification of PVA with citric acid it becomes moderately hydrophilic in nature compared to the highly hydrophilic behavior of untreated PVA and that is why PVA-C has a large affinity for cell attachment and spreading This modified PVA is reasonably less cytotoxic and therefore attractive for cellular studies [24]

On the other hand, in rose water media, because of the presence of geraniol in the rose oil the PVA-rose water mixure becomes superhydrophobic in nature [25] This superhydrophobic oil-in-water system behaves as a miceller based microreactor system Consequently, there is a high probability that QDs would come close to each other and coalesce outside these microreactors This could lead to a red shifting both in the emission spectra as well as absorption spectra (Figs 2 and 3)

4. CONCLUSIONS

In this work, we demonstrated the evolution of optical response of CdSe QDs in natural media citric and rose water environment The optical absorption as well as emissive behavior of the synthesized QDs were strongly modulated and found to be dependent on varying Cd^{2+}/Se^{2-} concentration, reaction time, dispersing medium and on aging effect The QDs prepared from larger Cd^{2+}/Se^{2-} ratio (3 1) of the precursor are expected to be monodisperse, of smaller diameter and show intense emission characteristics Moreover, the average size of the QDs is expected to be uniform beyond a reaction time duration of 60 min Further, in terms of stability, the QDs in lemon water has a better optical response than rose water media The injection of carboxyl (–COOH) functional group with

the PVA is provided by the esterification of PVA to PVA-C in the citric acid media [21] It was also apparent that, though pH has some role in determining optical properties of the QDs but they are chiefly governed by the constituents of lemon water and rose water

Essentially, highly fluorescent CdSe QDs in citric media would provide an important system for specific biophysical applications owing to higher stability against environmental degeneration The media can preserve QDs for a longer duration of time ensuring stability and reliability

Acknowledgments: The authors thank DST, New Delhi for financial support (project no *SR/FTP/PS07/* 2008) and colleagues for valuable discussion

References and Notes

1. L Qi and X Gao, *Expert Opin Drug Deliv* 5, 263 **(2008)**
2. D Alexson, H Chen, M Cho, M Dutta, Y Li, P Shi, A Raichura, D Ramadurai, S Parikh, M A Stroscio, and M Vasudev, *J Phys Condens Matter* 17, R637 **(2005)**
3. T Jamieson, R Bakhshi, D Petrova, R Pocock, M Imani, and A M Seifalian, *Biomaterials* 28, 4717 **(2007)**
4. X Ma, X Qian J Yin, H Xi, and Z Zhu, *J Colloid Interf Sci* 252, 77 **(2002)**
5. X Zhou, Y Kobayashi, V Romanyuk, N Ochuchi, M Takeda, S Tsunekawa, and A Kasuya, *Appl Surf Sci* 242, 281 **(2005)**
6. A L Rogach, L Katsikas, A Kornowski, S Dangsheng, and A Eychmuller, *Ber Bunsenges Phys Chem* 1778, 1772 **(1996)**
7. D Gerion, F Pinaud, S C Williams, W J Parak, D Zanchet, S Weiss and A Alivisatos, *J Phys Chem B* 105, 8861 **(2001)**
8. A L Rogach, A Kornowski, M Gao, A Eychmuller, and H Weller, *J Phys Chem B* 103, 3065 **(1999)**
9. H S Mansur, A A P Mansur and J C Gonzalez, *Polymer* 52 1045 **(2011)**
10. B Vasudevanpillai, R Kanemoto, M Yuusuke, I Sayaka, S Nakanishi, I Tamitake, B Yoshinobu, and I Mitsuru, *J Phys Chem C* 111, 7924 **(2007)**
11. D Mohanta, F Singh, D K Avasthi and A Choudhury, *Cent Eur J Phys* 4, 187 **(2006)**
12. N Singh, R M Mehra, A Kapoor, and T Soga, *J Renewable Sustainable Energy* 4, 013110 **(2012)**
13. L Saravanan, S Diwakar, R Mohankumar, A Pandurangan, and R Jayave, *Nanomater Nanotech* 1, 42 **(2011)**
14. W C Chan, D J Maxwell, X Gao, R E Bailey, M Han, and S Nie, *Curr Opin Biotechnol 13, 40 (2002)*
15. J Zayed and S Phillipe, *Int J Toxicol* 28 259 **(2009)**
16. R Hardman, *Environ Health Perspect* 114, 165 **(2006)**
17. S Bhandari, M Deepa, S N Sharma A G Joshi, A K Srivastava, and R Kant *J Phys Chem C* 114, 14606 **(2010)**
18. K Maehashi et al , *J Cryst Growth* 227, 1160 **(2001)**
19. P Gupta and M Ramrakhiani, *The Open Nanoscience Journal* 3, 15 **(2009)**
20. C P Shah, M Rath, M Kumar, and P N Bajaj, *Beilstein J Nanotechnol* 1, 119 **(2010)**
21. H Sharma, S N Sharma, G Singh and S M Shivaprasad, *Physica E* 31, 180 **(2006)**
22. M Simurda, P Nemec F Trojanek, K Neudert, T Miyoshi, K Kasatani, and P Maly, *Physica E* 36 205 **(2007)**
23. H S Mansur and A A P Mansur, *Mater Chem Phys* 125, 709 **(2011)**
24. L V Thomas, U Arun S Remya, and P D Nair, *J Mater Sci — Mater Med* 20, 259 **(2009)**
25. L Feng, Y Zhang, J Xi, Y Zhu, N Wang, F Xia, and L Jiang, *Langmuir* 24, 4114 **(2008)**

Received xx Xxxx Xxxx, Accepted xx Xxxx Xxxx

Journal of
Computational and Theoretical Nanoscience
Vol. 9, 1–8, 2012

A Comprehensive View on the Brownian Motion of Quantum Dots in Electrolytic Solution, Lipid Bilayer and Their Aggregated State in the Lipid Biomembrane

Runjun Sarma and Dambarudhar Mohanta*

Nanoscience and Soft Matter Research Laboratory, Department of Physics, Tezpur University, P.O. Napaam, Assam 784028, India

The present work highlights size-dependent diffusion response of quantum dots (QDs) in electrolytic solution and reconstituted phospholipids. While accounting for the Brownian motion across the biomembrane, we considered both nonaggregate and aggregated form of QDs to represent ion channel response correlating a definite conductance state with a select nos. of QD aggregation. The mean square displacement (MSD) of partially inserted QDs (each of 12 nm) is found to be suppressed by a factor of 1.4 compared to those of fully inserted QDs (each of 2 nm) ensuring that former is more stable against thermal agitation with the response time (τ_{12}) nearly 50 times than the later case (τ_2). Further, an aggregated structure with larger sized QDs tending to show nearly competitive diffusion behavior compared with that of the electrolytic solution. Also, for both partial and fully inserted conditions τ increases substantially (nearly ~56 and ~64 folds; respectively) for highest (6 QDs aggregation) compared the lowest one (3 QDs aggregation). A comparative study of the Brownian motion of QDs will largely help in assessing nature of QD migration in biomembrane and shall provide deep insight to understand QD-induced ion channels and signal transduction in biological systems for nanobiotechnology applications.

Keywords: Quantum Dot, Brownian Motion, Relaxation Time, Bilayer, Ion Channel.

RESEARCH ARTICLE

1. INTRODUCTION

Inorganic semiconductor nanocrystals, also called colloidal quantum dots (QDs), are regarded as useful fluorescent labels for staining cells. The use of semiconductor nanocrystals/QDs, in biological systems, has emerged as an important aspect in fundamental biophysical areas of research as well as in nanobiotechnology applications. Owing to their novel optical properties such as size dependent tunable color, narrow emission line-width, resistance to photobleaching, they have potential biomedical applications ranging from intracellular tagging of biological molecules to applications such as tracking devices for neuronal receptors and as interfaces between nerve cells.[1–3] As many of the applications of QDs in cell biology involve interaction with lipid bilayer membranes, the behavior of QDs on these structures is of significant interest to the scientific communities. It is already reported that like alamethicin (ion channel forming protein), QDs aggregate and form ion conducting pores across reconstituted lipid bilayer.[4,5]

For a particle undergoing Brownian motion, the mean square displacement (MSD) is defined as the square of the displacement of the particle at one time relative to the position of the particle at zero time, averaged over many particles.[6] In case of un-obstructed (simple) diffusion, the MSD of the diffusing particle is directly proportional to time. But in disordered systems such as in cell membrane, the MSD is proportional to a fractional power of time not equal to one besides the simple one. These types of obstructed diffusion are called anomalous diffusion.[7]

Simple diffusion of a particle is possible only in homogeneous free solution. But while it moves through semi permeable membrane e.g., live cells, lipid bilayer membrane etc. their diffusion is hindered by different diffusible and immobile molecular crowding agents such as lipid domains, binding sites in various immobile species and several cytoskeleton elements. In this case, they deviate from simple Brownian mechanics and show several other modes of complex diffusion (confined and sub-diffusion), as like as heterogeneous diffusion.[8]

*Author to whom correspondence should be addressed.

In particular, in lipid bilayer QDs satisfy confined diffusion and directed diffusion along with the simple diffusion phenomena.[9] In this report, a special emphasis is given to simple diffusion of QDs (neutral) in pre-aggregate and aggregated (nano pore forming) state in lipid bilayer besides their behavior in electrolytic solution, as reference. In every case, the dependence of MSD on their size (QDs and that of the aggregated structure) and concentration are studied. Moreover, the Brownian responses of the aggregated structure in different conductance states of QD ion channel are studied. Here, we consider highly fluorescent CdSe–ZnS[10] hydrophobic QDs for our study, which is very much useful in QD induced ion channel technology. Because many of the applications of QDs in cell biology involve interaction with lipid bilayer membranes, the dynamic behavior of QDs on these structures is of significant interest. A qualitative as well as quantitative analogy on the behavior of the Brownian motion of QDs are highlighted in the present work.

2. BROWNIAN MOTION OF QDs IN DIFFERENT MEDIA

The motion of an ultra small condensed matter system in air is different from its motion in other media. In this context, ion channel formation across phospholipid bilayer as a result of QD aggregation requires critical analysis of QD movement as it passes through different media. The schematic shown in Figures 1(a)–(d) depicts nature of the Brownian motion of QDs in different environment with special consideration to complete insertion and partial insertion across the bilayer.

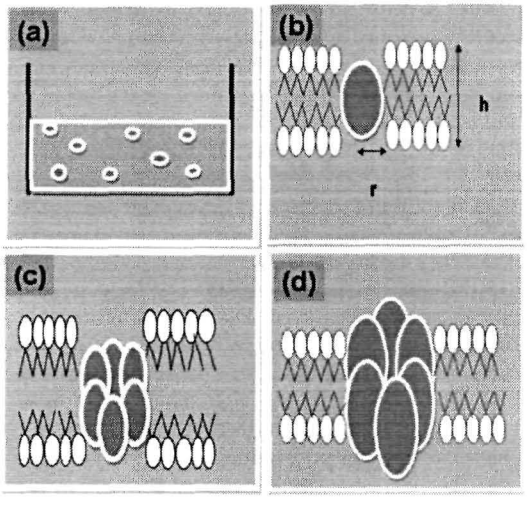

Fig. 1. Schematics representing the behavior of QDs in (a) electrolytic solution and (b) lipid bilayer in non-aggregated state. The QD aggregated state with full insertion and partial insertion are depicted in (c) and (d); respectively.

2.1. Electrolytic Solution

The $MSD(\langle r^2 \rangle)$ of a QD undergoing Brownian motion in free solution in 2-dimensions is given by[11]

$$\langle r^2 \rangle = 4D_0 t \tag{1}$$

Here, D_0 is the diffusion coefficient of the QD and t is the diffusion time.[6]

According to the Stokes-Einstein relation, the diffusion coefficient (D_0) of a spherical QD of diameter d in free solution is given by:[11, 12]

$$D_0 = \frac{kT}{3\pi\eta_s d} \tag{2}$$

where, k is the Boltzmann constant, T is the absolute temperature, η_s is the pure solvent viscosity.

The relaxation time (τ) i.e., time in which QDs undergo Brownian motion to a distance equal to the radius of the QD and experience successive collisions in the electrolytic solution can be expressed by:

$$\tau = \frac{(d/2)^2}{D_0}$$

Substituting D_0 from Eq. (2),

$$\tau = \frac{(d/2)^2}{(kT/3\pi\eta_s d)} \tag{3}$$

In electrolytic solution, the concentration of the salt [i.e., NaCl (0–300 mM)] has a little effect on the diffusion behavior of QDs (CdSe–ZnS).[11] Nevertheless, concentration of the QDs would affect the diffusion response of the individual QDs. The effective diffusion coefficient (D_{e1}) of a QD in an electrolytic solution is given by[13]

$$D_{e1} = D_0(1 + k_d C) \tag{4}$$

Here, k_d is the interdot interaction parameter and C is the concentration of QD in the solution. As in the present case we consider only neutral hydrophobic QDs, it is expected that the diffusion response will be affected only by permanent dipole–dipole interaction among them. Other interaction phenomena such as electrostatic, hydrodynamic interaction etc. will have least effect. For dipolar interaction cases, the interaction parameter (dipole strength) can be defined by[14, 15]

$$\lambda = \frac{U}{kT} \tag{5}$$

where, $U = -(e^2 d^2/4\pi\varepsilon_0\varepsilon_r L^3)$ represents attractive interaction energy[16] between the two dipoles (QDs) (each of diameter d) separated by a distance L in an electrolytic solution of dielectric constant ε_r (for water, $\varepsilon_r = 80$). kT signifies thermal energy associated with the system.

Substituting λ for k_d in Eq (4), i e , considering attractive dipole–dipole interaction, we have

$$D_{c1} = D_0(1 + \lambda C)$$

Now the MSD of a quantum dot in an electrolytic solution can be rewritten as

$$\langle r^2 \rangle = 4[D_0(1 + \lambda C)]t \quad (6)$$

and, the relaxation time will be

$$\tau = \frac{(d/2)^2}{D_{c1}} = \frac{(d/2)^2}{[D_0(1 + \lambda C)]} \quad (7)$$

2.2. Reconstituted Phopholipid Bilayer (Pre-Aggregate State)

In lipid bilayer, the water soluble QDs are attracted to the bilayer by electrostatic interaction existing between the net negative charges of QDs and the cationic headgroups of the lipid bilayer [5 17] Moreover, due to presence of the permanent dipole moment in QDs they are influenced by electric field (~10 kV/cm) In lipid bilayer, application of an electric field produces a torque on the QD dipole and force them to insert into the bilayer These QDs undergo very complex diffusions along with simple diffusion, the way other membrane bound molecules do which have already been reported by various workers [6 18–20] The diffusion coefficient of a quantum dot in lipid bilayer cannot be described by Eq (2), but can be demonstrated by the Saffman–Delbruck theory [21 22]

$$D_L = \frac{kT}{4\pi\eta_m h}[\ln(\lambda_l) - \gamma] \quad (8)$$

Here h is the lipid bilayer thickness, for phospholipid bilayer $h = 4$ nm,[23] η_m and η are viscosities of the membrane (1 poise)[24] and membrane surrounding fluid (0 01 poise),[5] respectively, $\lambda_l = \eta_m h/\eta(d/2)$, and $\gamma = 0\ 57$ is the Euler s constant The Eq (8) is valid only for the QD having radius $d/2 < h\eta_m/2\eta$ [21 22] The typical value of $\eta_m h/2\eta$ is ~200 nm

For the free diffusion of QDs in a lipid bilayer, the MSD ($\langle r^2 \rangle$) is given by[26]

$$\langle r^2 \rangle = 4D_l t \quad (9)$$

Substituting Eq (8) into Eq (9), the MSD can be redefined as

$$\langle r^2 \rangle = 4\left\{\frac{kT}{4\pi\eta_m h}[\ln(\lambda_l) - \gamma]\right\}t \quad (10)$$

The relaxation time in this case is given by

$$\tau = \frac{(d/2)^2}{D_L}$$

or,

$$\tau = \frac{(d/2)^2}{\{(kT/4\pi\eta_m h)[\ln(\lambda_l) - \gamma]\}} \quad (11)$$

Owing to dipole–dipole interaction (with QD concentration C) in lipid bilayer, the expression for MSD can be stated as

$$\langle r^2 \rangle = 4D_{c2}t$$

Where $D_{c2} = D_l(1 + \lambda C)$
i e ,

$$\langle r^2 \rangle = 4\left\{\frac{kT}{4\pi\eta_m h}[\ln(\lambda_l) - \gamma](1 + \lambda C)\right\}t \quad (12)$$

for $\varepsilon_r = 2$ (for lipid bilayer)[27] in the expression $U = -(e^2d^2/4\pi\varepsilon_0\varepsilon_r R^3)$

In this case, the relaxation time expression can be redefined as

$$\tau = \frac{(d/2)^2}{D_{c2}}$$

i e ,

$$\tau = \frac{(d/2)^2}{\{(kT/4\pi\eta_m h)[\ln(\lambda_l) - \gamma](1 + \lambda C)\}} \quad (13)$$

2.3. Reconstituted Lipid Bilayer (Aggregated State or, Conducting State)

As reported earlier, after insertion into the lipid bilayer, QDs aggregate and form ion conducting pores The diameter of the pore (d_{pore}) formed as a result of aggregation of N number of QDs is given by[4]

$$d_{pore} = d_{dot}\left(\frac{1}{\sin\pi/N} - 1\right) \quad (14)$$

Here, d_{dot} is the diameter of an individual QD participating in the formation of nanopore Using this relation, for a fixed size QDs, the diameter of pores corresponding to a definite no of QD aggregation can be predicted

Again the conductance state (G) and the diameter of QDs forming pore related by the following equation [5]

$$G = \frac{\sigma\pi d_{pore}^2}{4d_{dot}}$$

Therefore,

$$d_{pore} = \left(\frac{4d_{dot}G}{\sigma\pi}\right)^{1/2} \quad (15)$$

Here, σ is the conductivity of the bulk solution (98 mS/cm of 1 M KCl + 20 mM HEPES buffer at pH 7 5)[5] used in lipid bilayer experiment So, we can study the translational Brownian motion (MSD and τ) of the aggregated structure in conductance state G by substituting d_{dot} (diameter of QD) by d_{pore} (diameter of QD forming pore) in Eqs (10) and (11), respectively

The MSD of the aggregated structure during current burst can be expressed as

$$\langle r^2 \rangle = 4\left\{\frac{kT}{4\pi\eta_m h}[\ln(\lambda_l'') - \gamma]\right\}t \quad (16)$$

RESEARCH ARTICLE

Here

$$\lambda_l = \frac{\eta_m h}{\eta(d_{\text{dot}} G/\pi\sigma)^{1/2}}$$

Consequently, the relaxation time i e in this case the time for moving a distance equal to the radius of the pore will be

$$\tau = \frac{(d_{\text{pore}}/2)}{D_{\text{LA}}} \quad (17)$$

Here $D_{\text{LA}} = (kT/4\pi\eta_n h)[\ln(\lambda_l) - \gamma]$ is the diffusion coefficient of the conductive QD ion channel in the lipid bilayer

3. RESULTS AND DISCUSSION

Applying theoretical treatment on a given range of QDs (dia 2–20 nm) we obtained a no of characteristic plots that describe the nature of the Brownian motion in different environments In every case we are considering a constant diffusion time 0 1 sec for calculation of MSD We also encounter QD induced ion channels where a specific conductance is characterized by a definite aggregation of certain no of QDs

In an electrolytic solution the free diffusion of a QD can be affected by its size QD concentration and viscosity of the solvent We have studied the free diffusion considering viscosity of the solvent and temperature of the solution as 0 862 cP and 298 K (room temperature) respectively In electrolytic solution it is assumed that there is no interaction between QDs In this condition it can be observed from Figure 2 that MSD decreases rapidly and then slowly with the increase of size of the QDs (Eqs (1) and (2)) Conversely relaxation time τ (in moving the respective dia) shows the reverse behavior (Eq (3)) Again, it can be observed that for ~2 nm QDs the characteristics value of MSD is ~10 12 μm^2 Moreover, for ~20 nm dots the MSD is obtained as 1 01 μm^2 The respective values for the τ are 0 03 and 39 52 μs respectively Thus smaller QDs experience larger MSD while possessing lower magnitude with regard to relaxation time

Taking into account interdot separation as 2 nm we considered the effective dipole–dipole interaction between

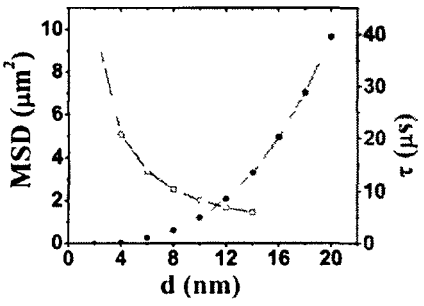

Fig 2 MSD and τ versus size of the QDs in electrolytic solution

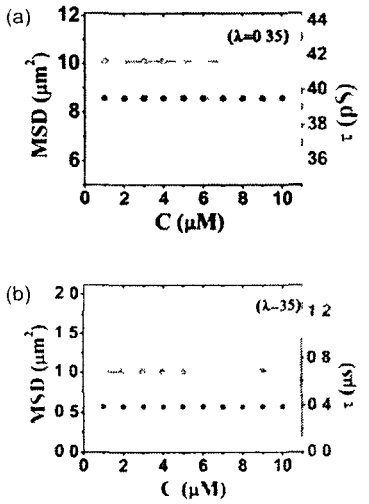

Fig 3 MSD versus concentration of QDs of dia (a) 2 nm (b) 20 nm in the electrolytic solution

QDs while undergoing diffusion (Eqs (6) and (7)) Knowing the dipole interaction parameter λ as a function of QD diameter d (Eq (5)) the following plots can be obtained for smallest (2 nm) and largest (20 nm) sized QDs As can be evident from Figures 3(a) and (b), the MSD and τ are not affected with the increase of QD concentration within 1–10 μM for both the cases of QD size with respective interaction parameters $\lambda = 0\ 35$ and 35

Like the case of an electrolytic solution the diffusion response of spherical QDs embedded in a lipid bilayer can be affected by its size and concentration Assuming temperature of the lipid bilayer same as the electrolytic solution one can address the diffusion behavior of QDs in pre-aggregate state as described below

Figure 4 displays a weak exponential decay and raising behavior of MSD and relaxation time (τ) of the QDs with their size (Eqs (10) and (11)) in lipid bilayer while undergoing diffusion There is a significant change in the nature of the plot in this case than the case as discussed before Moreover it is found that for 2 nm particles, the MSD is ~1 03 μm^2 The corresponding value for

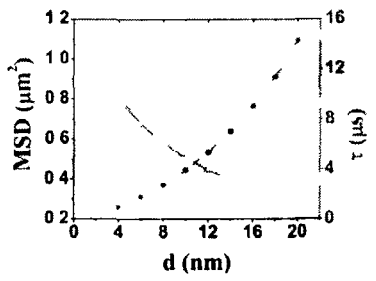

Fig 4 MSD and τ versus size of the QDs in lipid bilayer

~20 nm QDs is obtained as 0 28 μm^2 These values of MSD are near about 10 times smaller than that was found in case of electrolytic media and is consistent with the value predicted experimentally [28] The reduction of MSD is attributed to the components such as higher viscosity of bilayer than the electrolytic solution In contrast compared with the electrolytic solution, the relaxation time has substantially increased for 2 nm QDs and by a factor of ~9 7 On the other hand, the 20 nm sized QDs exhibit lower value of relaxation time (by a factor of ~2 7) compared with the electrolytic solution Thus it signifies that smaller sized QDs become more localized across the bilayer compared to the larger ones It is also important to assess the diffusion response for varying QD concentration Figures 5(a) and (b) show MSD versus concentration of QDs in lipid bilayer and in presence of dipole–dipole interactions between the QDs (for QD dia = 2 nm and 20 nm) separated by a distance of 2 nm (using Eq (12) and (13)) Here the MSD and the τ are found to exhibit nearly analogous behavior as obtained in case of electrolytic solution for both the sizes But it may be noted that the dipole interaction response is stronger in lipid bilayer than the electrolytic media with values of $\lambda \sim 14$ and ~1400 for 2 nm and 20 nm sized QDs respectively

Earlier it was reported that[4] after insertion inside the lipid bilayer in presence of electric field the QDs aggregate and form ion conducting pores In the lipid bilayer the pore formation is established as a result of aggregation of a minimum (3 nos) of QDs [4] During current bursts owing to different conductance states of QD ion channels the addition and substraction of QDs may occur in an aggregated state similar to the case of alamethicin ion channel [29] In this context, the diffusion behavior of aggregated QD structures (representing different conductance states) will be useful in the study of QD induced ion channels assuming that pre-aggregate states do not correspond to appreciable conductance fluctuations

Using Eq (14), we obtained a set of plots on the size of pores formed by the QD aggregation while undergoing diffusion across a reconstituted lipid bilayer (Fig 6) As can be seen the pore dia is found to be increased with the no of aggregated QDs as well as with the size of the QDs For an aggregated structure of 3 QDs each of dia 12 nm, the size of the pore was estimated to be ~1 85 nm, which is consistent with an earlier report [5] Note that, with 6 nos of QD-aggregation the pore formed by the QDs becomes nearly equal to their finite size Therefore any structure formed as a result of aggregation of more than 6 QDs would corresponds to a conductance state between 3–6 QD aggregates with highest conductance state for 6 QDs and lowest one for 3 QDs Any aggregation larger than 6 nos of QDs would result in a situation where the pores are capable of accommodating additional QDs leading to intermediate (sub-) conductance states Figure 7 displays a series of plots representing a weak exponential decay behavior of MSD versus the no of QD aggregates (Eq (16)) The MSD is decreased or increased depending on the increase of no of QD aggregation and on the size of the individual QDs Similarly Figure 8 represents the variation of relaxation time (the time taken by the aggregated QDs to move a distance equal to the dia of the pore) with the no of aggregated QDs for different sizes of QDs (Eq (17)) The relaxation time increases exponentially with the no of QDs and size of the individual QDs

Using Eq (16), we obtained a set of representative curves that describe the variation of conductance and the MSD with the no of aggregated QDs (each QD of dia 2 nm and 12 nm respectively) (Eq (16)) while considering the response under current burst Each of the conductance state corresponds to the current burst across the bilayer and thus depicting an abrupt ion transduction pathway As a general trend it can be observed that when the conductance of the QD ion channel increases with the no of aggregated QDs the MSD drops in a sub-linear way For a

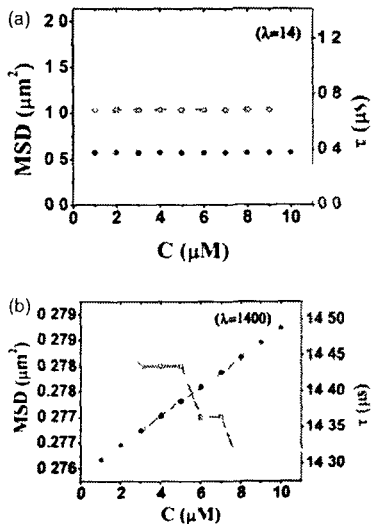

Fig 5 MSD versus concentration of QDs of dia (a) 2 nm (b) 20 nm in lipid bilayer

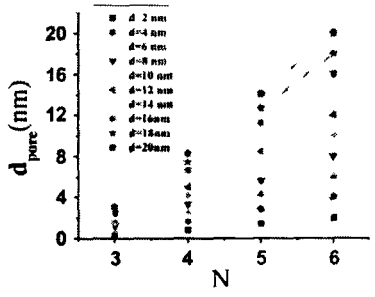

Fig 6 Size of the nanopore formed by QDs versus no of aggregated QDs of various size

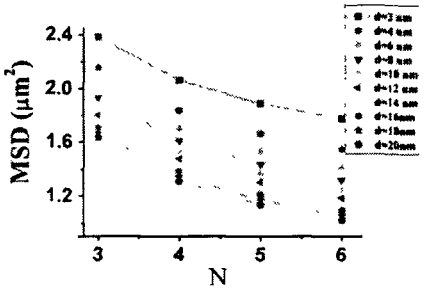

Fig. 7. MSD versus nos. of aggregated QDs of various size.

3 nos. of QD aggregation (each of QD dia. 2 nm), the conductance of the ion channel is estimated to be ~0.368 nS and the corresponding MSD is ~2.38 μm^2. Similarly, for a 4 nos. of QD aggregation, the conductance and the MSD are found to be ~2.64 nS and ~2 06 μm^2; respectively. For a conductance state created by 6 nos. of QD aggregation, the corresponding values are ~15.39 nS and ~1.77 μm^2. In the same way, conductance states can arise due to the aggregation of larger sized QDs (each of dia. 12 nm) which predict that the minimum conductance value for a current burst is ~2.2 nS and this value agrees reasonably well with the experimentally observed conductance state.[5] The corresponding MSD is ~1.79 μm^2. Moreover, the conductance state (~15.8 nS) described by a 4 nos. of QD is accompanied by a MSD value of ~1.47 μm^2. Similarly, the highest conductance state (~92.31 nS), as a result of 6 nos. of QD aggregation is characterized by a reduced MSD value of ~1.18 μm^2. As can be found from Figures 9(b) and 10(b) (Eq. (17)), the relaxation time increases by nearly ~56 and ~64 folds for highest (6 QDs aggregation) conductance state compared with the lowest one (3 QD aggregation) for ion channels formed by the aggregation of 2 and 12 nm QDs; respectively. For 2 nm QD case, the respective values of the relaxation times for associated conductance states are obtained as 0.004 μs (3 QD aggregation), 0.033 μs (4 QD aggregation), 0.225 μs (6 QD aggregation). In the same way, for ion

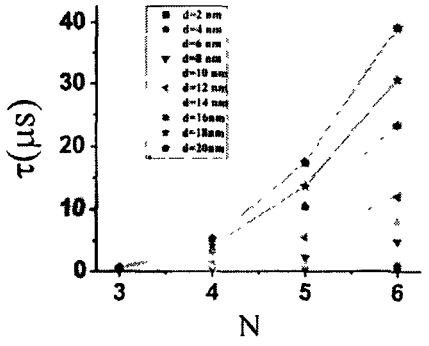

Fig. 8. Relaxation time versus no of aggregated QDs of various size

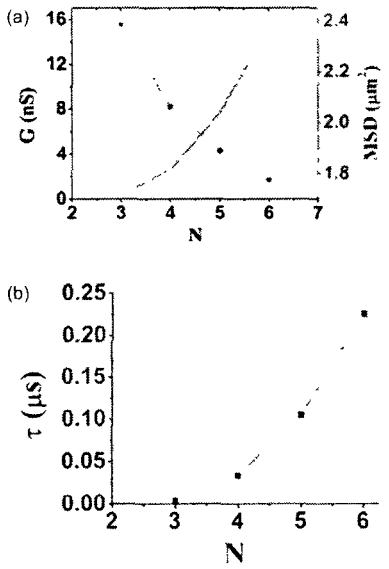

Fig. 9. (a) Conductance state and MSD, (b) relaxation time versus no of aggregated QDs (each of dia 2 nm)

channels with ~12 nm sized QDs, the respective time constants are characterized by 0.191, 1 67, 12.11 μs. This signifies that the relaxation time is higher both for more nos. of QD aggregation (exhibiting higher conductance level) and for the larger size of each of the QDs. In other words, a larger aggregated structure as well as larger sized QDs respond slowly to the thermal agitation even though, while representing definite ion transport pathways.

It is also important to encounter the nature of QD insertion and definite ion conduction mechanism through the reconstituted bilayer. In the present case, we have considered two extreme cases of QD size: the first, ~2 nm QDs—a case of complete insertion into the ~4 nm thick bilayer (Fig. 1(c)). Second, ~12 nm QDs—a case of partial insertion (Fig. 1(d)). Note that, an aggregated structure formed by the later kind of QDs exhibits a six fold increase in the conductance value compared to the former one. Consequently, the response time of the conductance states of the ion channel formed by the larger sized QDs is ~50 times higher than the states created by smaller sized QDs.

The intersection point of conductance and MSD responses for both the size dependent situations turns out a common aggregation no. of 4.6. The corresponding values for 2 and 12 nm QDs are (~5.73 nS, ~1.95 μm^2) and (~35 nS, ~1.36 μm^2); respectively. Since the MSD is ~1.4 times smaller in case of larger sized QDs, it is likely that the QD aggregates are associated with slow undulatory motion thus establishing stable ion conducting pathways. Also the larger sized QD aggregation is characterized by a ~6 fold increment corresponding to the smaller sized ones.

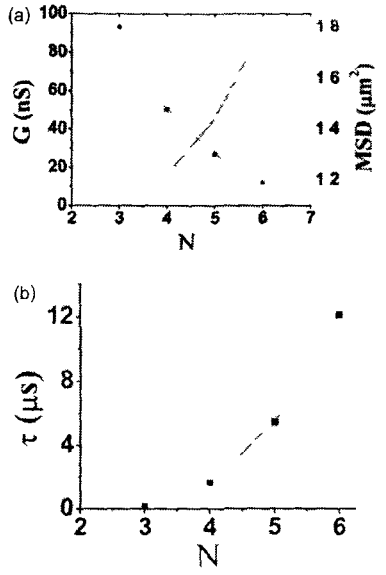

Fig 10 (a) Conductance state and MSD (b) relaxation time versus no of aggregated QDs (each of dia 12 nm)

As expected, the aggregation state of 2 nm QDs shows less undulation behavior (during current burst) than a bare 2 nm QD in electrolytic solution (Fig 2) For conductance states with 3, 4, 5, and 6 aggregations of QDs these values are reduced by the factors of ~4 28, ~4 91, ~5 35 and ~5 71 respectively But, these aggregated structures show higher diffusive response (by factors of ~2 31, ~2, ~1 83 ~1 71) in comparison with a bare 2 nm QD in pre aggregate state across the bilayer (~1 03 μm^2) (Fig 4) On the other hand, the MSD of the conductance state due to the aggregation of 3 nos of 12 nm QDs exhibits nearly equal value (~1 7 μm^2) to that of a bare 12 nm QD in electrolytic solution (~1 68 μm^2) (Fig 2) But as it goes to the higher conductance states e g , with 4 5 and 6 aggregations, the corresponding MSD values gradually decrease by a factor of ~1 14, ~1 3 ~1 42 compared to the electrolytic environment For these conductive states, the MSD which is a measure of the strength of undulation is higher (by a factor of ~4, ~3 28, ~2 9, ~ 2 63) compared with the pre-aggregate bare 12 nm QDs (MSD ~0 44 μm^2, Fig 4) Thus it is apparent that the complex lipid bilayer environment has a control on the diffusion behavior of the aggregated structures created by complete insertion of smaller sized (~2 nm) QDs into the bilayer In this case their thermal motion is restricted within the viscous lipid bilayer surrounding Consequently there is a significant reduction of their mobility in the medium compared to the electrolytic solution environment Alternatively the aggregated structure formed by the partial insertion of larger sized (~12 nm) QDs is not largely affected This is due to the fact that the aggregated structure may come in contact with a substantial volume of electrolytic environment

Note that in both (complete insertion as well as partial insertion) the cases the high viscous nature of the bilayer would bind the bare QDs tightly in the pre-aggregate state as compared with the aggregated state Thus the thermal movement of the pre-aggregate QDs is largely obstructed relative to the aggregated ones

Note that, the relaxation time of an aggregated structure is higher or lower than the electrolytic solution and lipid bilayer in certain conductance states Let us denote the relaxation time the aggregated structure formed by 2 nm and 12 nm as τ_2 and τ_{12}, respectively The τ_2 of the aggregated structure formed by 3 QDs (each of 2 nm) in the bilayer is ~ 9 times lower than the bare QDs in the electrolytic solution (~0 04 μs), whereas the aggregated state created by 4 QDs exhibits nearly same order (~0 034 μs) The other aggregated states (with 5 and 6 nos of QD aggregations) are characterized by higher values of relaxation times (by factors of ~3 05 ~6 6, respectively) than a single 2 nm QD experiences in the electrolytic environment (Fig 2) In fact all the aggregated states exhibit lower values of relaxation time than the bare QDs in the pre-aggregate form (~0 38 μs) (Fig 4) In contrast the aggregated structures of 3, 4 and 5 nos of 12 nm QDs are associated with the lower values of relaxation times (τ_{12}) (by a factor of ~44 6, ~5 2, ~1 6) corresponding to a bare QD in the electrolytic solution (~8 53 μs) (Fig 2) Interestingly the response time of the largest aggregated state (6 QDs) in the bilayer is ~1 4 times higher than the bare QD in the electrolytic solution Similarly, the aggregated states (with 3 nos of QD aggregation and 4 nos of QDs aggregation) exhibit smaller relaxation times (by factor ~28 21 ~3 20) than the pre-aggregate QDs in lipid bilayer (~5 36 μs) (Fig 4) The aggregated state (corresponding to a conductance state created by 5 nos of QDs) exhibit nearly equal relaxation value (~5 46 μs) while a state represented by 6 nos QD has a comparatively higher value (with a factor of ~2 25) Hence, it signifies that the response time of an aggregated structure with 4 nos of 2 nm QDs aggregation in a bilayer is close to that of the response of individual QD in electrolytic solution and the response time of 5 nos of QDs aggregation (each of QD 12 nm dia) is similar to the response of each QD in the pre-aggregated state This proves that as the size of the QDs increases they tend to respond in nearly equal time in comparison to a pre-aggregate structure while undergoing diffusion Further, it is also clear that an aggregated structure with more no of QDs move slowly with respect to their equilibrium position

From the present discussion one can say that in absence of interdot interaction the translational MSD (and relaxation time) of QDs in electrolytic solution as well as in lipid bilayer in pre-aggregate state would decrease (and increase) with QDs size Moreover, the translational MSD (and relaxation time) of an aggregated structure inside a reconstituted lipid bilayer also decreases (and increases)

RESEARCH ARTICLE

with the no of QDs aggregates and with the size of the individual QDs in the structure In presence of interdot (dipole–dipole) interaction however, with the increase of concentration the diffusion behavior of QDs remains unaffected both in the electrolytic solution and the lipid bilayer in the pre aggregate state Based on these analysis we argue that QD concentration within range ~1–10 μM will be most suitable for ion channel and electrophysiological studies Also the larger aggregated structures of QDs representing higher conductance states of ion channels are thermally more stable with higher orders of relaxation times Furthermore, the MSD of partially inserted QD aggregates has a lower magnitude than the fully inserted ones Finally, as the MSD of an aggregated structure is higher than the pre-aggregate counter part the diffusion response is slower in the later case This fact was also substantiated in case of higher diffusion response of QDs in intracellular environment [30]

Our model is based on the independent opening and closing of individual ion channels In this regard, the diffusive response of QDs either in isolated form or in aggregate form was discussed with special reference to size of QDs and surrounding environment For simultaneous opening and closing purpose one need to consider further the interaction between individual ion channels which is in progress

RESEARCH ARTICLE

4. CONCLUSIONS

To conclude in the pre-aggregate state owing to higher relaxation time experienced by smaller QDs (~2 nm) they tend to be localized across the bilayer more tightly compared to the larger sized QDs (~20 nm) Moreover an aggregated structure is found to be more diffusive than a bare QD in the pre-aggregate state The relaxation time gets increased by a factor of ~56 and ~64 folds for highest (6 QDs aggregation) conductance state compared with the lowest one (3 QDs aggregation) for ion channels created by an aggregation of 2 and 12 nm sized QDs, respectively Consequently the response time of the conductance states of the ion channel formed by the larger sized QDs ($\tau_{1>}$) is ~50 times higher than the states created by smaller sized QDs ($\tau_<$) It has also provided with a highest conductance and MSD of ~92 31 μS and ~1 18 μm^2, respectively In addition the relaxation time of the aggregated structure aroused due to the 4 nos QDs aggregation (each of QD size 2 nm) and due to 5 nos of QD aggregation (each of QD size 12 nm) were found to be nearly equal to those of the electrolytic solution and the pre-aggregate state in the lipid bilayer respectively Understanding dynamics of QDs while making their ways through the semi permeable biomembrane would find scope when specific ion channel regulation and targeted drug delivery is desired

Acknowledgments: The authors thank DST, New Delhi for financial support (project no SR/FTP/PS-07/2008) and colleagues for valuable discussion

References

1 L Qi and X Gao *Expert Opin Drug Deliv* 5 263 **(2008)**
2 D Alexson et al *J Phys Condens Matter* 17 R637 **(2005)**
3 T Jamieson R Bakhshi D Petrova R Pocock M Imani and A M Seifalian *Biomaterials* 28 4717 **(2007)**
4 S Ramachandran G L Kumar R H Blick W van der and W Daniel *Appl Phys Lett* 86 083901 **(2005)**
5 S A Klein S J Wilk T J Thornton and J D Posner *J Phys Conf Series* 109 012022 **(2008)**
6 J A Dix and A S Verkman *Annu Rev Biophys* 37 247 **(2008)**
7 M J Saxton *Biophys J* 66 394 **(1994)**
8 S Jin and A S Verkman *J Phys Chem B* 111 3625 **(2007)**
9 H Chen I Titushkin M Stroscio and M Cho *Biophys J* 92 1399 **(2007)**
10 F Chen and D Gerion *Nano Lett* 4 1827 **(2004)**
11 C Chen S Liu R Cui B Huang Z Tian P Jiang D Pang and Z Zhang *J Phys Chem C* 112 18904 **(2008)**
12 Q Li R Han X Meng H Gai and E S Yeung *Analyt Biochem* 377 176 **(2008)**
13 T Pons H T Uyeda I L Medintz and H Mattoussi *J Phys Chem B* 110 20308 **(2006)**
14 J Abrahamson and J Marshall *J Electrostat* 55 43 **(2002)**
15 J H E Promislow A P Gast and M Fermigier *J Chem Phys* 102 5492 **(1995)**
16 J Gea Banacloche M Mumba and M Xiao *Phys Rev B* 74 165330 **(2006)**
17 T A Spurlin and A A Gewirth *Nano Lett* 7 531 **(2007)**
18 D S Banks and C Fradin *Biophys J* 89 2960 **(2005)**
19 Q Tang and M Edidin *Biophys J* 84 400 **(2003)**
20 G Guigas C Kalla and M Weiss *FEBS Lett* 581 5094 **(2007)**
21 S J Bussell D L Koch and D A Hammer *Biophys J* 68 1828 **(1995)**
22 A Naji A J Levine and P A Pincus *Biophys J* 93 L49 **(2007)**
23 I Pfeiffer S Petronis I Koper B Kasemo and M Zach *J Phys Chem B* 114 4623 **(2010)**
24 D B Kell and C M Harris *Eur Biophys J* 12 181 **(1985)**
25 B A Camley C Esposito T Baumgart and F L H Brown *Biophys J* 99 L44 **(2010)**
26 P Cicuta S L Keller and S L Veatch *J Phys Chem B* 111 3328 **(2007)**
27 W Hanke and W R Schulz Biological Techniques Planar Lipid Bilayers Methods and Applications Academic Press London New York **(1993)**
28 X Chen A Kis A Zettl and C R Bertozzi *PNAS* 104 8218 **(2007)**
29 J E Hall I Vodyanoy T M Balasubramanian and G R Marshall *Biophys J* 45 233 **(1984)**
30 I Y Wong B D Almquist and N A Melosh *Mater Today* 13 14 **(2010)**

Received 15 July 2011 Accepted 16 August 2011

International Journal of Advanced Materials Science
ISSN 2231-1211 Volume 3, Number 2 (2012), pp. 87-96

http://www.ripublication.com/ijams.htm

Role of the Supporting Substrates for Implementing Planar Chip Technology in Ion Channel Experiments

Runjun Sarma and Dambarudhar Mohanta*

Nanoscience Laboratory, Department of Physics,
Tezpur University, Assam-784028, India
**Corresponding Author E-mail: best@tezu.ernet.in;*

Abstract

We report here the suitable environment and material characteristics for employing planar chip technology meant for ion channel/electrophysiology experiments. The ion channel response, to a great extent, is influenced by thermal and electromagnetic noise and the effective bilayer capacitance arising due to the nature of substrate material. Ideally, the quality of a substrate (planer chip) is characterized by good mechanical strength, thermal stability and low dielectric constant. Since the ion channel dynamics across a reconstituted membrane is a stochastic phenomena, selection of a suitable substrate along with desired dimension are important aspects apart from surrounding electromagnetic noise. In the present study, we make a critical survey of various substrate materials (Teflon, Polystyrene, Polypropylene, PET, PMMA, Quartz, Glass, Mica and Silicon) of different dielectric constant, thickness and cross sectional area. We also encounter for the ideal environment for carrying out ion channel experiments. We suggest that for effective electrophysiology recording, working area of the electrolytic chamber and thickness of the substrate material can be of the order of ~1.76 cm^2 (dia. ~1.5cm) ~150 μm; respectively. Reduced dissipation factor, low effective capacitance combined with high mechanical stability, makes glass and quartz as the most suitable candidate for planar chip architecture.

Keywords: Planar chip; bilayer; electrophysiology; ion channel

PACS Nos.: 87.14.Cc; 87.16 D-; 87.16.Vy; 87.85.dh; 87.80.Jg

Introduction

Most of the biological activities including cellular functions, in living organisms are regulated by ion transport mechanism [1]. The electrophysiological events in the cells

that include both prokaryotic and eukaryotic types generally involve ion channel (Na^+, K^+, Ca^{2+}) processes [2-4]. In this context, both patch-clamp and planar lipid bilayer experiments allow studies with regard to the function of single ion channels [5-7]. In recent years, solid supported bilayer experiments are shown to be better methods over patch-clamp ones owing to several advantages including viable cost, preparatory conditions, simplicity of designing, reliable and fast data acquisition [8,9]. Moreover, the signal-to-noise ratio can be improved, to a great extent, in planar chip technology. In a typical planar chip method, a thin phospholipid bilayer (~4nm) is painted around a small aperture on a solid substrate which separates the two electrolytic chambers. The conductance fluctuation, as a result of ion migration, can be studied in relation with the application of biasing voltage across the bilayer [10, 11]. For a good ion channel experiment, it is desired that the bilayer be stable and the effective capacitance suppressed. It was known that a substrate having a good mechanical and thermal stability is capable of supporting a stable bilayer. In addition, the substrate material should contribute only weakly to the effective capacitance. In other words, one needs to work with thick and low dielectric constant materials. Small effective area of the electrolytic chambers will also be an additional advantage.

In the present work, considering several technologically important materials, we elaborate upon conditions that are attractive for obtaining stable bilayers which could help performing meaningful ion channel experiments. A special emphasis is given to explore the possibility of suppressing effective bilayer capacitance and theoretical noise. Here we present a qualitative as well as quantitative analogy of several materials (e.g., Teflon (PTFE), Polypropylene (PP), Polystyrene (PS), Polyethylene terephthalate (PET), Poly (methyl methacrylate) (PMMA), Quartz, Glass, Mica and Silicon) that can help in predicting their suitability to act as bilayer supporting substrate in planar chip technology.

Theory on dielectric noise and effective capacitance

The conductance fluctuation, across a solid-supported reconstituted artificial phospholipid bilayer, provides a unique approach for studying single ion channels. Compared to standard patch clamp method, the planar chip technique has an improved experimental design and precision control. However, the utility of planar bilayer method for studying single ion channel dynamics may be limited primarily by the background current noise. By suppressing rms noise it is possible to resolve the small single-channel conductance states along with the fast gating dynamics. By determining the individual sources of noise, it is possible to create an environment for suitable ion channel measurements. Note that, for ion channel experiment based on planar chip technology, a bilayer has to be supported on the micropore located at the centre of the substrate material. The nature of thermal energy dissipation results in thermal noise from this dielectric material and this type of noise is also known as dielectric noise. The power spectral density of dielectric noise, $S_D^2(f)$ and the rms dielectric noise, $I_D(f_c)$ can be expressed as [12]:

$$S_D^2(f) = 8\,\pi kTDC_D f, \tag{1}$$

$$I_D(f_c) = 2\,(KTDC_D\,\pi c_1)^{1/2} f_c\,; \tag{2}$$

where, D is the dissipation factor of the material(s), C_D is the capacitance of the dielectric(s), $c_1=1.3$ for a noise source with a power spectral density that grows linearly as a function of f, and f_c is the cut-off frequency. Although the dissipation factor is frequency dependent, it is usually approximated as a constant in the frequency range between 1 kHz and 100 kHz [8, 13]. The dissipation factor, D is contributed by the nature of the substrate, electrode holders etc. and they contribute unequally to the magnitude of C_D in Eqn.2. In the present work, we consider D as the dielectric loss of the substrate materials in which the pore is fabricated, which significantly contribute to C_D. In the eqns. (1) and (2) it is therefore, reasonable to replace C_D with C_{se}, where C_{se} is the substrate capacitance. The capacitance of this substrate material is given by:

$$C_{se}=\varepsilon_r \varepsilon_0 \frac{A}{d} \tag{3}$$

where, C_{se} is the substrate capacitance; A is the area of the substrate material; ε_r is the dielectric constant of the substrate material; ε_0 is the permittivity in free space ($\varepsilon_0 \approx 8.854\times10^{-12} F\, m^{-1}$); and d is the thickness of the substrate material.

In the electrophysiology experiment, the accuracy of temporal change of current flowing through the pore is determined by the signal bandwidth. To obtain high bandwidth of the signal, the most accessible experimental parameter that has to be minimized is the total effective capacitance. The total capacitance is given by [8]

$$C_t=C_m + C_{se} + C_{el}. \tag{4}$$

where, C_{el} is the capacitance of the immersed electrode (~10pF) [8] and $C_m= Cs\ \frac{\pi}{4} d_p^2$, the membrane capacitance. Here, C_s and d_p are specific capacitance and diameter of the pore; respectively. As noise generated by the substrate material takes major rule than the electrode generated noise, for the sake of simplicity we ignore the later's contribution in the electrophysiological recording experiment [13]. Some of the physical properties of the bilayer supporting solid materials are given in Table 1.

Table 1: Physical properties of the substrates materials

Sl. No.	Substrate	Dielectric constant (k)	Dissipation Factor (D)	Density (ρ) in gm/cm^3	Thermal Conductivity (K) in W/m/K	Melting point (T_m) in °C	Young's modulus (Y) in Gpa
1	PTFE	2.1	0.0008	2.12	0.26	327	0.5
2	PP	2.2	0.0003	0.95	0.1-0.22	165	1.5-2
3	PS	2.5	0.0001	1.06	0.14	240	3-3.5
4	PET	3.1	0.016	0.98	0.24	260	2-2.7
5	PMMA	3.6	0.015	1.17	0.20	140	3.4
6	Quartz	3.8	0.00001	2.21	1.36	1650	71.7
7	Borosilicate glass (Corning 7760)	4.5	0.0017	2.3	1.1	820	45
8	Mica	6.2	0.0012	2.8	0.71	1340	60
9	Silicon	11.8	0.032	2.32	150	1410	70

Results and discussion

By applying theoretical treatments on various materials, for different electrolytic area and thicknesses, we obtained characteristic plots necessary to assess the quality of the substrates.

Effect of pore diameter on the membrane capacitance

An aperture on the substrate generally supports a reconstituted phospholipid bilayer. With an aperture of larger diameter, the lipid bilayer membrane become mechanically fragile and can be easily broken by small mechanical and electrical disturbance. This is because of the ultra thin nature (~4 nm) of the phospholipid bilayer membrane. Selection of a suitable diameter of the pore would help in providing not only low membrane capacitance but also higher mechanical stability.

Fig.1 represents a characteristic plot of membrane capacitance vs. pore diameter of the substrate material. It is clear that membrane capacitance increases with the diameter of the pore for a constant specific capacitance (C_s) of 0.5 μF /cm^2 [9]. It is seen that for a pore diameter ~10-100 μm, the membrane is characterized by a very small low capacitance in the range of ~0.4-40 pF. But for practical purpose, a pore with ~10-40 μm diameters is difficult in terms of visualization and handling with the suspended bilayer. The bilayer with pore diameter in the range ~40-100 μm will give moderate capacitance values (~7-40 pF). On the other hand, for the pores having larger values of diameter (~100-200 μm), the membrane capacitance would increase to the range of ~40-156 pF.

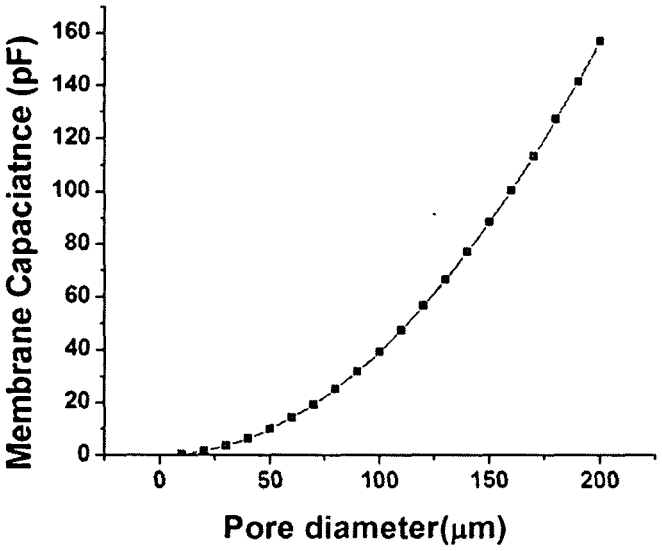

Figure 1: Membrane capacitance as a function of pore diameter

For the sake of convenience, the pore diameter ~80-100 μm is suggested which accounts for the moderate values of capacitance (corresponding capacitance ~25-40

pF). Thus the suitable range of pore diameter that can be efficiently used in the planar chip technology is (~80-100 μm). The importance of using planar chip technology within this range of diameter is also reported by various workers [13, 14]. Alternatively, the stability of a bilayer in the electrophysiology experiment is governed by the dimension as well as the dielectric properties of the substrate material. The overall idea is to suppress the effective capacitance. The contribution of substrate capacitance should be such that it is comparable or smaller than the value of the bilayer capacitance (~25-40 pF). The selection of a good substrate candidate with a desired dimension would help in obtaining low effective capacitance. The variation of substrate capacitance for different possible substrate candidates is discussed below.

Parameters which have direct influence on the substrate capacitance

The stability and the effective capacitance of the reconstituted lipid bilayer depend mainly on the area of the electrolytic chamber created on the substrate material, thickness and dielectric constant of the substrate material.

Fig.2 represents the variation of substrate capacitance as a function of electrolytic area created on different substrate materials of given thickness. In most of the electrophysiological experiments, the thickness of the substrate varies between ~150-300μm [6, 8]. It can be observed from the Fig.2 (a) that for a constant area 0.78 cm^2 (corresponding to electrolytic chamber of dia~1cm), PTFE exhibits very low capacitance (≤9 pF) when thickness is varied within 150-300 μm. However, mechanical handling of such a small area is difficult in real situations. Similarly, the area of the order of ~1.76 cm^2 (dia~1.5 cm) also characterized by a low capacitance (~10-21 pF). But for a larger area of ~ 4.8 cm^2 (dia~2.47 cm), the capacitance becomes quite high (~29-60 pF). So this clearly indicates that PTFE is characterized by a capacitance less than the value of bilayer capacitance for an effective area of ~1.76 cm^2 and thickness~150-300 μm. Similarly, materials such as PP, PS (Fig. 2(b), 2(c)) also give lower values of capacitance (~11-22 pF, ~12-26 pF), compared to the bilayer capacitance for an electrolytic area of ~1.76 cm^2.

In contrast, as shown in Fig. 2(d)-2(g), the capacitance response of the substrate materials such as PET, PMMA, quartz and glass (for an area of ~1.76 cm^2 and thickness ~150-300 μm) predicts values ~16-31 pF, ~18-37 pF, ~19-38 pF, ~23-46 pF; respectively. Note that the lower end values (150 μm thick substrate) are comparable with the capacitance of the bilayer (25-40 pF for an aperture ~80-100 μm). On the other hand, it can be observed from the Fig. 2(h) and 2 (i) that silicon and mica show very large values of capacitances (~31-64 pF and ~62-123 pF) than the corresponding bilayer capacitance.

Therefore, it is now apparent that with materials like polymers, glass and quartz one can obtain effective capacitance comparable to the bilayer capacitance by proper choice of adequate electrolytic area and substrate thickness. We expect that an electrolytic area of ~1.76 cm^2 (dia~1.5) and thickness of ~150-300 μm will be convenient for establishing reduced effective capacitance and also provides a means for better physical handling of the electrophysiology experiment.

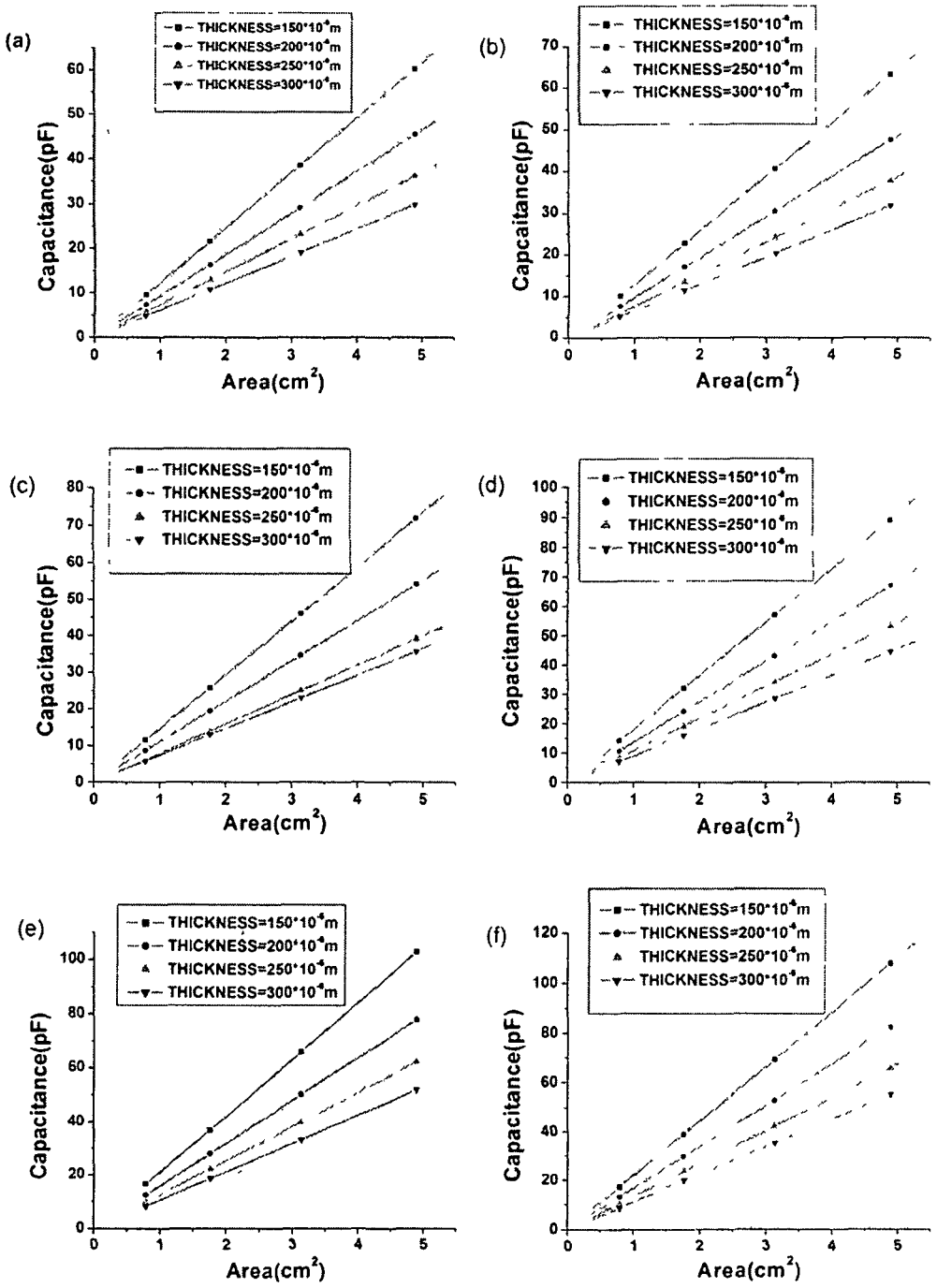
(a)
THICKNESS=150*10⁻⁴m
THICKNESS=200*10⁻⁴m
THICKNESS=250*10⁻⁴m
THICKNESS=300*10⁻⁴m
Capacitance(pF)
Area(cm²)
(b)
THICKNESS=150*10⁻⁴m
THICKNESS=200*10⁻⁴m
THICKNESS=250*10⁻⁴m
THICKNESS=300*10⁻⁴m
Capcaitance(pF)
Area(cm²)
(c)
THICKNESS=150*10⁻⁴m
THICKNESS=200*10⁻⁴m
THICKNESS=250*10⁻⁴m
THICKNESS=300*10⁻⁴m
Capacitance(pF)
Area(cm²)
(d)
THICKNESS=150*10⁻⁴m
THICKNESS=200*10⁻⁴m
THICKNESS=250*10⁻⁴m
THICKNESS=300*10⁻⁴m
Capacitance(pF)
Area(cm²)
(e)
THICKNESS=150*10⁻⁴m
THICKNESS=200*10⁻⁴m
THICKNESS=250*10⁻⁴m
THICKNESS=300*10⁻⁴m
Capacitance(pF)
Area(cm²)
(f)
THICKNESS=150*10⁻⁴m
THICKNESS=200*10⁻⁴m
THICKNESS=250*10⁻⁴m
THICKNESS=300*10⁻⁴m
Capacitance(pF)
Area(cm²)

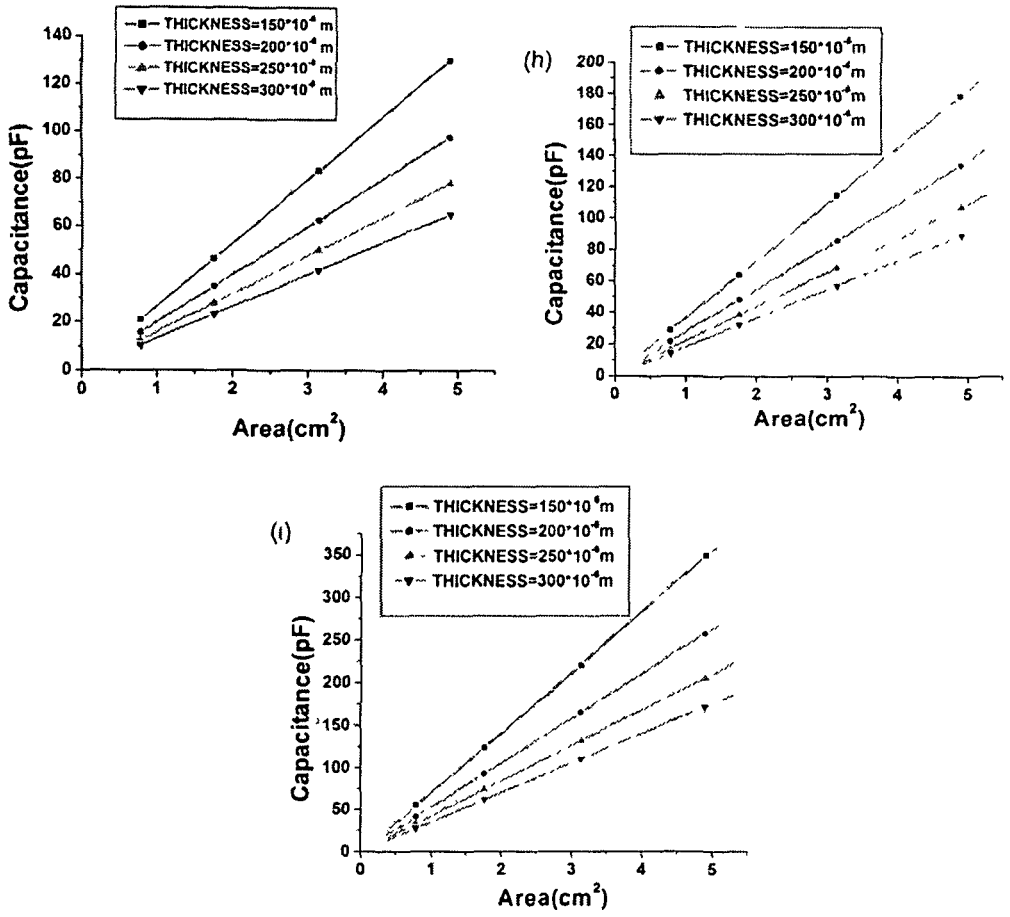

Figure 2: Capacitance vs. area of the substrate (a) PTFE, (b) PP, (c) PS, (d) PET, (e) PMMA, (f) Quartz, (g) Glass, (h) Mica, and (i) Silicon

Fig.3 represents the variation of the substrate capacitance with the dielectric constant of the respective materials considering the desired electrolytic area and thickness to be ~1.76 cm^2, ~150 μm; respectively. It can be observed from the Fig.3 that PTFE, bearing least dielectric constant value and hence lowest capacitance (~21 pF). Similarly, materials such as polymers (PP, PS, PET, and PMMA), show low values of capacitance (~22-37 pF) while glass and quartz exhibit moderate values of capacitance (~39-47 pF). But, materials having higher dielectric constant such as silicon (~63.86 pF) and mica (~122.5 pF) are characterized by larger values of capacitance. Thus it is clear that candidates with lower dielectric constant (PTFE, PP, PS, PET, PMMA, glass, quartz) can be potential candidates in the planar chip technology. However, glass and quartz are generally considered owing to better mechanical strength and thermal stability (see Table 1).

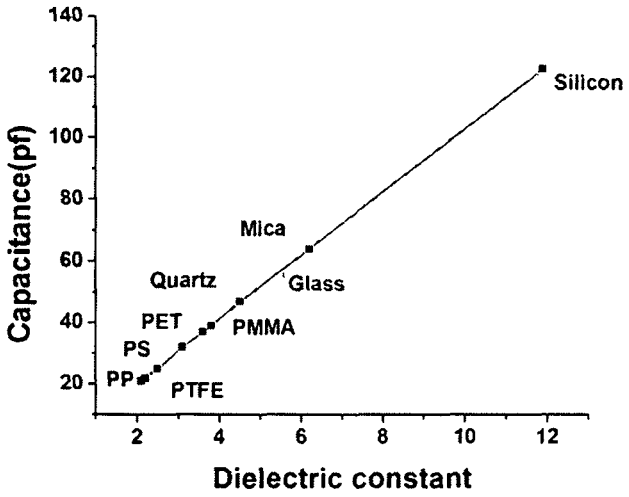

Figure 3: Capacitance vs. Dielectric constant of the substrates

Dielectric noise generated by the substrate materials

In a typical electrophysiology experiment generally ion channel proteins are inserted across a reconstituted phospholipid bilayer. In order to record the current burst due to insertion of ion channel proteins, it is desirable that the dielectric response of the bilayer supporting substrate (planar chip) be good with minimal signal attenuation. Since the current fluctuation would occur in tens of pA level, rms noise should be low enough for isolating and detecting the actual signals. In this context, low dissipation factor (D) of the substrate is desired. This would facilitate in the detection of single ion channel events while recording current bursts in the electrophysiology experiment.

Fig. 4(a) represents the variation of rms dielectric noise with dissipation factor (dielectric loss) of the respective substrate materials (PTFE, PP, quartz [15], PS [16], PET [12], glass [13], PMMA [17], mica [18], silicon [19] for a constant cut-off frequency (f_c) of 10 kHz and constant substrate capacitance comparable to the bilayer capacitance (~20 pF). For instance, PTFE exhibits this order of capacitance for an electrolytic area ~1.76 cm^2 and thickness~150 μm. It can be observed that quartz is characterized by lowest value of dissipation factor and hence exhibits lowest rms dielectric noise (~0.03 pA). Similarly, polymers (PS, PP, PTFE), Mica and glass are characterized by small values of noise (~0.11-0.47 pA). On the other hand, it is seen that polymers like PMMA and PET exhibit moderate values of rms noise (~1.4-1.45 pA). Conversely, candidate such as silicon higher rms dielectric noise compared to the above materials (~2.05 pA). Moreover, the dielectric noise has an exponentially decreasing trend with the increasing thickness of the substrate materials (Fig.4 (b)). The materials e.g., quartz, mica, glass and polymers (PTFE, PS, PP) are characterized by very low dielectric noise (~0.04-0.48 pA) when the thickness varies between ~150 and 300 μm.

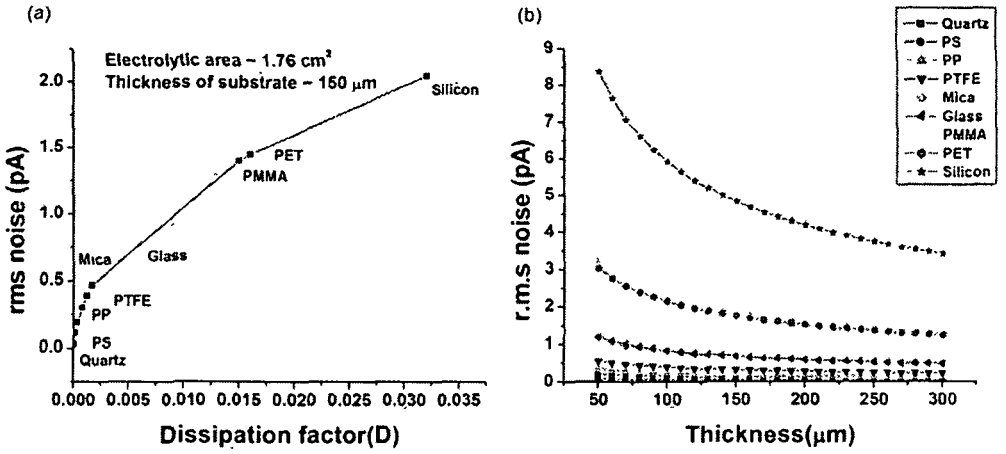

Figure 4: Dielectric noise vs. (a) Dissipation factor (b) Thickness of the substrate materials

From the present discussion, one can say that the diameter of the aperture of the respective substrates should be in the range of ~80-100 µm (C_m ~25-40 pF) to obtain a mechanically stable lipid bilayer. Again, for convenience, the working electrolytic area and the thickness of the substrate can be of the order of ~1.76 cm^2, ~150-300 µm; respectively. It is worth mentioning here that though a substrate material of thickness ~300 µm provides comparatively lower capacitance than that of ~ 150 µm, the latter is preferred owing to ease in making an aperture. Moreover, it is found that materials having low to moderate dielectric constant like polymers (PTFE, PP, PS,PET ,PMMA), quartz and glass were found to exhibit effective capacitance comparable to the bilayer capacitance (~25-40 pF). Though glass and quartz provide higher capacitance compared to the polymers, the former is a better option owing to better mechanical strength and thermal stability. On the other hand, glass and quartz exhibit desired low values of dielectric noise and can be attractive ion channel experiment. In addition, optical transparency in the visible to IR range would be added advantage for simultaneous electrical and optical recording. Conversely, the use of silicon and mica is limited by high dielectric constant (and hence, high capacitance values) even though they possess good mechanical strength.

Conclusions

To summarize, in order to establish an ideal environment for the planar chip technology following pre-requisites need to be satisfied.

1. The working area of the electrolytic chamber and thickness of the substrate can be ~1.76 cm^2 and 150 µm; respectively.
2. The bilayer supporting substrate bearing good dielectric properties (low dielectric constant and low dissipation factor) are desirable.

3. Glass and quartz are believed to be most preferred candidates for the electrophysiology experiment. Neither polymers, nor silicon / mica satisfy all the properties required for a substrate material.

Acknowledgements

The authors thank DST, New Delhi for financial support (project no. SR/FTP/PS-07/2008) and colleagues for valuable discussion.

References

[1] Z. Xie, T. Cai, Molecular interventions, 3 (2003) 157-168.
[2] R.D. Hinrichsen, J.E. Schultz, Trends Neurosci., 11 (1988) 27–32
[3] F. Visser , J. Lytton, Physiology, 22 (2007) 185-192
[4] A. Meir, R. Rahamimoff, J. Neurophysiol., 75 (1993) 1858-1870
[5] N. Fertig, M. George, R.H. Blick, J. C. Behrends, Applied **Physics** Letters, 81 (2002) 4865-4867
[6] N. Fertig, R.H. Blick, J.C. Behrends, Biophys. J., 82 (2002) 3056–3062.
[7] R.A. Levis, J.L. Rae, Methods Enzymol. 293 (1998) 218–266
[8] M. Mayer, J.K. Kriebel, M.T. Tosteson, G.M. Whitesides, Biophys. J., 85 (2003) 2684-2695
[9] N. Fertig M. George, M. Klau, C. Meyer, A. Tilke, C. Sobbotta, R.H. Blick, J.C. Behrends, Research, Receptors and Channels, 9 (2003) 29-40
[10] R. Pantoja, D. Sigg, R. Blunck, F. Bezanilla, J. R. Heath, Biophys.J., 81 (2001) 2389–2394
[11] S. Ramachandran, N.E. Merrill, R. H. Blick, D. W. Weide, Biosensors and Bioelectronics, 20 (2005) 2173–2176
[12] J.D. Uram, K. Ke, M. Mayer, ACS NANO, 2 (2008) 857-872
[13] S.R. Gold R. The Axon Guide; Axon Instruments, Inc., 1993
[14] H.Suzuki , S.Takeuchi, Anal Bioanal Chem., 391 (2008) 2695–2702
[15] R. A. Levis, J. L. Rae, Biophys. J., 65 (1993) 1666–1667
[16] http://a-toppolymers.com/wp-content/uploads/Engineering-Properties-of-Marlex-Resins.pdf
[17] http://books.google.co.in/books?id=RJWiilJLdxYC&pg=PA43&lpg=PA43&dq
[18] http://www.cde.com/catalogs/Radial-appGuide.pdf
[19] Dielectric constant and loss data, Laboratory for Insulation Research, Massachusetts Institute of Technology, Cambridge, MA. (http://www.dtic.mil/cgi-bin/GetTRDoc?Location=U2&doc=GetTRDoc.pdf&AD=ADA046172)

Materials Research Bulletin 62 (2015) 71–79

Contents lists available at ScienceDirect

Materials Research Bulletin

journal homepage: www.elsevier.com/locate/matresbu

Manifested luminescence and magnetic responses of stoichiometry dependent $Cd_{1-x}Mn_xSe$ quantum dots

Runjun Sarma, Geetamoni Deka, Dambarudhar Mohanta *

Nanoscience and Soft Matter Laboratory, Department of Physics, Tezpur University, Napaam, Assam 784028, India

ARTICLE INFO

Article history:
Received 5 June 2014
Received in revised form 2 November 2014
Accepted 3 November 2014
Available online 6 November 2014

Pacs No.:
78.67.Bf
61.82.Fk
81.05.Dz
63.20.-e
75.50. Pp

Keywords:
A. Chalcogenides
A. Nanostructures
A. Semiconductors
B. Chemical synthesis
C. Raman spectroscopy
C. X-ray diffraction
D. Crystal structure
D. Luminescence
D. Magnetic properties

ABSTRACT

We report on stoichiometry dependent manifested physical properties of thioglycolic acid (TGA) coated $Cd_{1-x}Mn_xSe$ QDs. While possessing a wurtzite phase, with increasing x, the QDs exhibited a notable blue-shifting of the onset of absorption. Attributed to V_{Cd}–V_{Se} di-vacancies, the QDs describe an intense deep-defect related emission response at smaller values of x (=0 to 0.3). Due to the facilitation of magnetic Mn^{2+} ion migration from the core to the QD surfaces, $^4T_1$–$^6A_1$ transition based Mn^{2+} orange emission get suppressed at a higher x (=0.6 to 1). While the FT-IR spectra of the alloyed QDs display characteristic Mn–OH stretching mode at ~644 cm^{-1}, the peak located at ~703 cm^{-1} is assigned to Cd-Se bending. Furthermore, the QDs with a low x (=0.3), exhibit paramagnetic characteristics owing to the presence of uncorrelated, isolated Mn^{2+} spins. The collective luminescence and magnetic features would find immense scope in bio-labeling and imaging applications, apart from solid state luminescent components.

1. Introduction

Semiconductor nanocrystals are known for their bright emission response with size dependent color tunability between the ultra violet (UV) and near infra-red (NIR) region of the electromagnetic spectrum. Of particular interest, the magnetic impurity doped systems (magnetic semiconductor nanocrystals/quantum dots, *ms*-NCs/QDs), such as, nanoscale $Cd_{1-x}Mn_xSe$ systems, have received growing interest owing to their immense potential in magneto-optics, nonlinear optics, nano-photonics and nano-biotechnology. This is because, these QDs exhibit special properties, like localization of magnetic ions that result in free electron and hole carriers [1,2], size-dependent sp-d exchange interaction [3,4] along with introduction of new energy levels within the forbidden gap. The strong sp-d exchange interaction may result in enhanced spin relaxation [5], giant Zeeman splitting of the electron and hole states when subjected to a magnetic field [6], along with the formation of excitonic magnetic polarons [3,7]. These interesting characteristics occurring in *ms*-NCs ensure their potential applicability in various fields including spintronics [8], tunable lasers [9], solar cells [10], magneto-optic elements [11], quantum computing etc.

Over the years, magnetic semiconductor systems of the form $A^{II}{}_{1-x}M_xB^{VI}$, (with cations $A^{II}=Cd^{2+}$, $M=Mn^{2+}$, anion $B^{VI}=Se^{2-}$) have drawn significant research interest owing to the strong dependence of sp–d exchange interaction on the amount of doping (mole fraction, x). Moreover, highly fluorescent II–VI semiconductor systems, mostly Cd-based ones (e.g., CdSe, CdTe, CdS, CdSe/ZnS core shell QDs etc.), have been investigated in great detail including their extensive deployment in biolabeling and bioimaging studies [12]. In this work, we demonstrate a simple, user-friendly approach for synthesizing $Cd_{1-x}Mn_xSe$ QDs, using thioglycolic acid (TGA) as the capping agent. Although TGA in excess amount is somewhat toxic, but due to its ability to provide effective surface functionalization and extra-photostability to the fluorescent QDs, the TGA capped QDs are found to be extremely

* Corresponding author. Tel.: +91 3712 275558; fax: +91 3712 267005.
E-mail addresses: best@tezu.ernet.in, dmohanta1973@gmail.com (D. Mohanta).

http://dx.doi.org/10.1016/j.materresbull.2014.11.011
0025-5408/

useful in practical situations [13,14]. Here, we discuss and compare structural, optical, vibrational and magnetic responses of the synthesized QDs in conjunction with stoichiometry variation.

2. Experimental: materials and methods

2.1 Production of $Cd_{1-x}Mn_xSe$ quantum dots

The step-by-step synthesis protocols, for obtaining various QD systems with varying stoichiometric parameter x, are as detailed below.

2.1.1 QD synthesis for x = 0

The procedure of synthesizing CdSe QDs ($x = 0$) can be found elsewhere [14]. Here, we employ a modified method along with inclusion of an anionic surfactant as coating element. At first, 0.93 g of cadmium nitrate-tetra hydrate [$Cd(NO_3)_2\ 4H_2O$] was dissolved in 100 mL of deionized (DI) water followed by stirring (~250 rpm) at a temperature of 60 °C, for 20 min. Then, 0.5 ml of TGA was added to the Cd^{2+} solution under stirring. The pH of the solution was adjusted to ~11 by adding aqueous sodium hydroxide (NaOH) in a drop-wise manner. Then, 0.22 g of SeO_2 was taken along with the 0.2 g sodium borohydride ($NaBH_4$), added as a reductant. Finally, the mixture was kept under stirring for 1 h and at a temperature of 80 °C. The precursor extract was then subjected to centrifugation (~5000 rpm) followed by adequate filtration using a Whatman filter[16]. The precipitate was washed with DI water several times and finally, cleansed with ethanol.

2.1.2 QD synthesis for x = 1

In a typical procedure, 0.62 g of manganese chloride-tetra hydrate [$MnCl_2\ 4H_2O$] and 0.11 g SeO_2 were dissolved in 22 ml DI water followed by the addition of 0.1 g $NaBH_4$. The pH of the solution was adjusted to ~11 by adding aq. NaOH. The stirring (~250 rpm) was maintained at 60 °C, for 5 min. Following the addition of 10% TGA, the whole mixture was transferred to a teflon-lined stainless steel autoclave of 50 ml capacity. The autoclave was sealed properly and kept under oven at 180 °C, for 6 h. On completion of the reaction, the autoclave was cooled down to room temperature naturally. The extract was subjected to centrifugation (~5,000 rpm) and subsequently, filtration. The residual content was washed away with DI water repeatedly and finally, with ethanol. The whole process was believed to facilitate homogeneous growth of the MnSe QDs [15].

2.1.3 QD synthesis for x = 0.3 to 0.8

A suitable stoichiometric variation was considered in order to make a comparative account on manifested properties of the synthesized QDs. The ternary QDs of $Cd_{1-x}Mn_xSe$, with $x = 0.3, 0.6, 0.8$ were prepared following the aforesaid procedure but with a little alteration. Here, considering a fixed amount of SeO_2, and $NaBH_4$ as reductant, the Cd^{2+} to Mn^{2+} molar concentration was

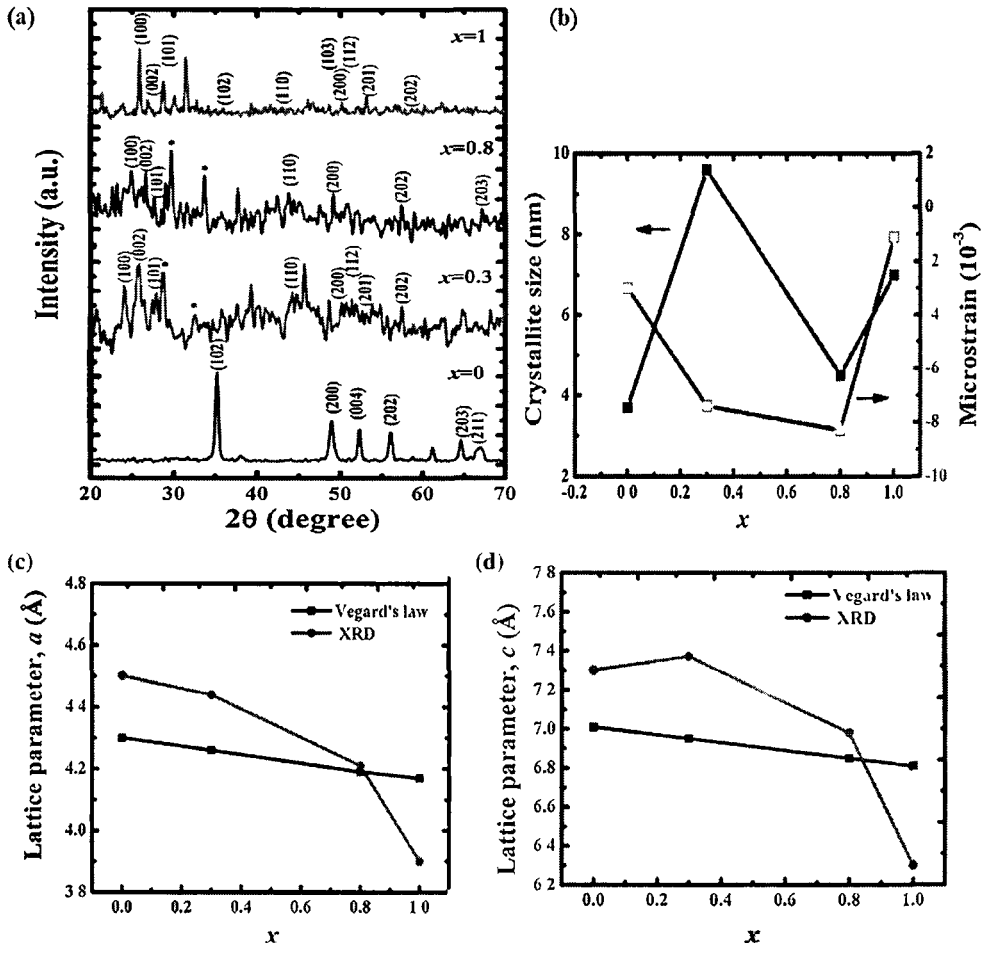

Fig 1 (a) XRD patterns of different $Cd_{1-x}Mn_xSe$ systems (b) variation of average crystallite size and microstrain with x. The sub figures (c) and (d) depict variation of effective lattice parameters a and c with x considering XRD analysis (red label) and Vegard's law (black label). (For interpretation of the references to colour in this figure legend, the reader is referred to the web version of this article.)

varied such that, $x = 0.3$, 0.6, 0.8. The reaction temperature, duration of reaction and TGA concentration were kept unaltered as mentioned in the aforesaid discussion.

2.2 Analytical techniques

The structural characterizations of the as-synthesized samples were performed by powder diffraction technique using an X-ray diffractometer (XRD, MiniFlex, Rigaku) equipped for CuKα radiation ($\lambda = 1.543$ Å). High resolution transmission electron microscopy (HRTEM, JEOL, JEM-2100) working at an accelerating voltage of 200 kV was employed to confirm the formation of QDs of definite size and shape. The characteristic optical absorption features were recorded by a UV–vis spectrophotometer (UV 2450, Shimadzu Corporation), whereas photoluminescence (PL) spectra were obtained by a Perkin Elmer LS 55 spectrophotometer with a Xe lamp as the excitation source ($\lambda = 350$ nm). The data acquisition was made through a computer controlled standard monochromator based photodetection system. Raman measurements were undertaken by using micro-Raman spectrometer (Renishaw, UK) at room temperature. As for fourier transform infrared (FT-IR, Nicolet Impact-410) studies, solid powder was employed to make pellets in KBr. Finally, both low and room temperature magnetic measurements on select samples were conducted with the help of a vibrating sample magnetometer (VSM, Lake Shore, 7400 series).

3. Results and discussion

Below we discuss various physical properties of the as-synthesized QDs of varying x.

3.1 Structural and morphological analysis of binary and ternary QDs

The crystal structure and crystallographic orientation of the as-synthesized $Cd_{1-x}Mn_xSe$ QDs were identified through XRD analyses. Fig. 1(a) depicts a series of XRD patterns of $Cd_{1-x}Mn_xSe$ QDs prepared with different stoichiometric parameter, x. As can be found, for $x = 0$ (CdSe) and $x = 1$ (MnSe), the systems show phase-pure hexagonal crystal structure but with dissimilar peaks corresponding to different diffraction angles (2θ). For $x = 0$, the diffraction peaks, located at ~35.1, 48.9, 52.2, 56.0, 64.5 and 67°, corresponded to (102), (200), (004), (202), (203) and (211) crystallographic planes of the CdSe- QDs that crystallize into a hexagonal wurtzite (WZ) phase [16]. In contrast, MnSe- QDs (for $x = 1$), characterize diffraction peaks positioned at ~25.8, 26.8, 28.6, 36.1, 43.9, 47.8, 50.2, 52.05, 53 and 58.7° which corresponded to (100), (002), (101), (102), (110), (103), (200), (112), (201) and (202) crystallographic planes of the hexagonal WZ MnSe structure and are consistent to earlier works [17,18]. The $MnSe_2$ phase, as evident from the peaks at ~23.8 and 31.4°, is likely to exist in the form of trace amount of byproduct [17]. On the other hand, a mixed phase of WZ MnSe, WZ CdSe and cubic CdMnSe can be retrieved for $Cd_{1-x}Mn_xSe$ QDs, and for $x = 0.3$ and 0.8. As for $x = 0.3$, the diffraction peaks that highlight WZ hexagonal phase of CdSe can be observed at $2\theta \sim 35.7$ and 48.7° which correspond to (102) and (200) planes; respectively. In addition, the diffraction peaks noticeable at ~24.0, 25.8, 28.02, 43.9, 50.1, 51.4, 53.0 and 57.4° are identified as (100), (002), (101), (110), (200), (112), (201) and (202) crystallographic planes of MnSe. Moreover, the cubic phase of CdMnSe can be identified owing to the existence of the respective diffraction peaks located at ~28.7, 32.5° and are assigned to (111) and (200) planes (represented by * marks) [19]. At a stoichiometry value of $x = 0.8$, the diffraction peaks located at ~24.9, 26.7, 27.8, 43.9, 49.0, 57.4, 67.0 represent (100), (002), (101), (110), (200), (202) (203) crystallographic planes of the WZ phase MnSe- QDs. In this case however, no diffraction peak due to independent CdSe phase could be witnessed. Nevertheless, the prominent (111) and (200) diffraction peaks due to the cubic phase CdMnSe are identified at $2\theta \sim 29.6$ and 33.6° (shown by * marks). Moreover a shifting of the peak position toward a higher diffraction angle is realized in this case as compared to the case for $x = 0.3$. One can estimate average crystallite size by using popular Williamson–Hall equation, given by [20]:

$$w\cos\theta = 4\varepsilon\sin\theta + \frac{k\lambda}{D_{cry}} \quad (1)$$

Here, λ is the wavelength of the CuKα line (1.543 Å), w is the full width at half maxima (FWHM), θ is the Bragg's diffraction angle and κ is the shape factor (~0.9). By plotting $w\cos\theta$ against $4\sin\theta$, the microstrain (ε) of the crystallites can easily be estimated from the slope, and average crystallite size (D_{cry}) from the intercept on the vertical axis. It can be noticed that, the QDs with a larger crystallite size, have a lower values of microstrain and vice versa (Fig. 1(b)). The average crystallite size has increased from a value of ~3.7–9.6 nm, when x is varied within 0 and 0.3, whereas pure MnSe QDs ($x = 1$) experienced an average size of ~7 nm. While experiencing a minimal value corresponding to $x = 0.8$, the magnitude of microstrain was found to vary in the range of $1.1–8.3 \times 10^{-3}$ and with a negative sign. The negative values of the measured microstrains indicate presence of relaxed crystallites in the system under study [21]. Essentially, the alloyed crystallites are much more relaxed as regards those of pure CdSe and MnSe systems. The lattice parameters, $a(=b)$ and c can be calculated by using the relations normally valid for a hexagonal system

$$\frac{1}{d_{hkl}^2} = \frac{4}{3}\left(\frac{h^2 + hk + k^2}{a^2}\right) + \frac{l^2}{c^2} \quad (2a)$$

$$\frac{c}{a} = \left(\frac{8}{3}\right)^{1/2} \quad \text{and (2b)}$$

Here, d_{hkl} is the inter-planar separation between the successive planes with index, hkl. The calculated values of a and c are depicted in Table 1 and assuming a standard error of ±0.05%. With an increasing x value from 0 to 0.8 the c/a value was found to vary between 1.62 and 1.66. Whereas the pure MnSe QDs showed a lowered c/a value of 1.61. We anticipate that the Mn^{2+} ions are likely to occupy the CdSe lattice mainly along the c-axis. As for

Table 1
Physical parameters obtained for $Cd_{1-x}Mn_xSe$ QD systems.

Stoichiometry parameter x	D_{cry} (nm)	$\varepsilon(\times 10^{-3})$	Through XRD analyses (Å)	c/a (XRD)	Through Vegard's law (Å)	c/a (Vegard)
0	3.7	−3.0	$a=b=4.5$ $c=7.3$	1.62	$a=b=4.3$ $c=7.01$	1.63
0.3	9.6	−7.4	$a=b=4.44$ $c=7.37$	1.65	$a=b=4.26$ $c=6.95$	1.63
0.8	4.5	−8.3	$a=b=4.21$ $c=6.98$	1.66	$a=b=4.19$ $c=6.85$	1.63
1	7.0	−1.1	$a=b=3.9$ $c=6.3$	1.61	$a=b=4.17$ $c=6.81$	1.63

$x = 0.8$ composition, all the Mn^{2+} ions are not necessarily fully embedded inside the CdSe core lattice, but can be available at the surfaces thereby affecting the magnitude of lattice parameters by substantial amounts [22].

We also intended to verify if the formation of QD heterostructure is feasible or not, especially when considering the coexistence of CdSe and MnSe phases. The criterion is that, the lattice constant of an alloy can be expressed through a linear interpolation between its constituents. In this case, Vegard's empirical law allows us to predict the effective lattice parameter ($a = b$) given by:

$$a_{eff} = (1 - x)a_{CdSe} + xa_{MnSe} \quad (3)$$

A similar formulation can also be employed for estimating the effective parameter, c_{eff}. The results are shown in Fig. 1(c–d) and can be compared with the results obtained from XRD measurements and using Eq. (2). As can be found, at a lower stoichiometry parameter x, the effective parameters calculated through the Vegard's relation have experienced much lower values than those measured through the XRD analyses. However, at a higher x value (with dominant Mn^{2+} content), the a_{eff} and c_{eff} as predicted through Vegard's law tend to approach the calculated values revealed through XRD analyses (Fig. 1(c–d)). In other words, the formation of CdSe/MnSe QD heterostructure cannot be completely denied and possibly occur near $x = 0.8$. Knowing that, the conditions $x = 0$ and $x = 1$ represent the independent existence of CdSe and MnSe systems, the development of QD heterostructure in these cases cannot arise. Apparently, we noticed significant departure of the parameters calculated by XRD with those predicted through Vegard's law (Fig. 1(c and d), Table 1).

Fig. 2(a and b) represent typical TEM images of the QDs corresponding to $x = 0.3$ and $x = 1$. As revealed from the low resolution micrographs, the respective QDs are nearly spherical and with an average size of D ~ 9.6 nm and 7.0 nm. The average QD size has been estimated from the frequency vs. particle size histograms presented at the right hand side of upper and lower panels. Since the values are close to the average crystallite size predicted by XRD, the synthesized products characterize good amount of mono-crystallinity. The insets, shown in the upper left and lower right corners of each of the micrographs, are basically isolated views of single QD structures along with fast fourier transform (FFT) imaging. The lattice fringe patterns of $Cd_{0.7}Mn_{0.3}Se$ and MnSe QDs have showed respective inter-planar spacings of ~0.40 nm and 0.23 nm. A close look on the FFT imaging has revealed a number of diffracted spots that ensure a hexagonal pattern around the zeroth order.

3.2. Analysis through optical absorption and emission spectroscopy studies

The optical properties of $Cd_{1-x}Mn_xSe$ QDs, synthesized for different values of x, have been adequately analyzed through UV–vis and PL spectroscopy techniques and are discussed below.

3.2.1. Effect of stoichiometry variation on the optical absorption response

Fig. 3(a) shows the optical absorption spectra of different $Cd_{1-x}Mn_xSe$ QDs of varying x. The spectra indicate adequate quantum confinement in the QDs systems, as significant blue-shifting was witnessed with increasing x. Since the investigated QDs are mostly alloyed types, we intended to evaluate the first order derivative plot of the absorption spectra to help evaluating major changes caused in a definite QD system. The direct optical band gap (E_g) of the QDs under study can be predicted from the sharp peaks in the spectra (Fig. 3(b–d), see also supplement). The absorption maximum of pure CdSe QDs is found to be located at ~430 nm (2.8 eV) (Fig. 3(b)); which is strongly blue-shifted from its

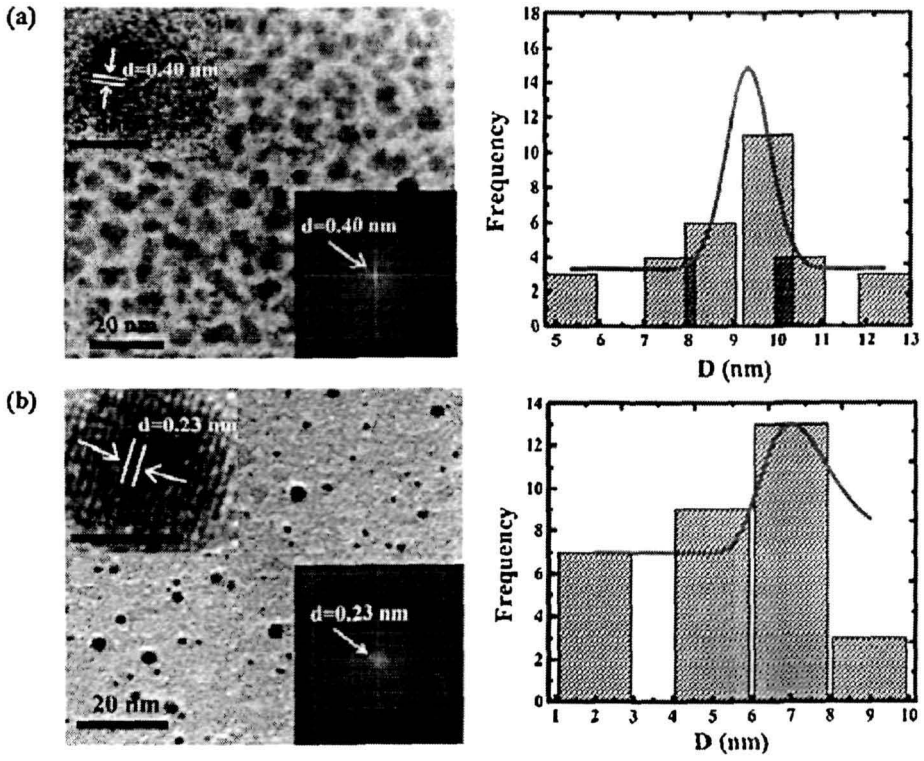

Fig. 2. TEM, FFT images and particle size histograms of $Cd_{1-x}Mn_xSe$ QDs (a) $x = 0.3$ and (b) $x = 1$.

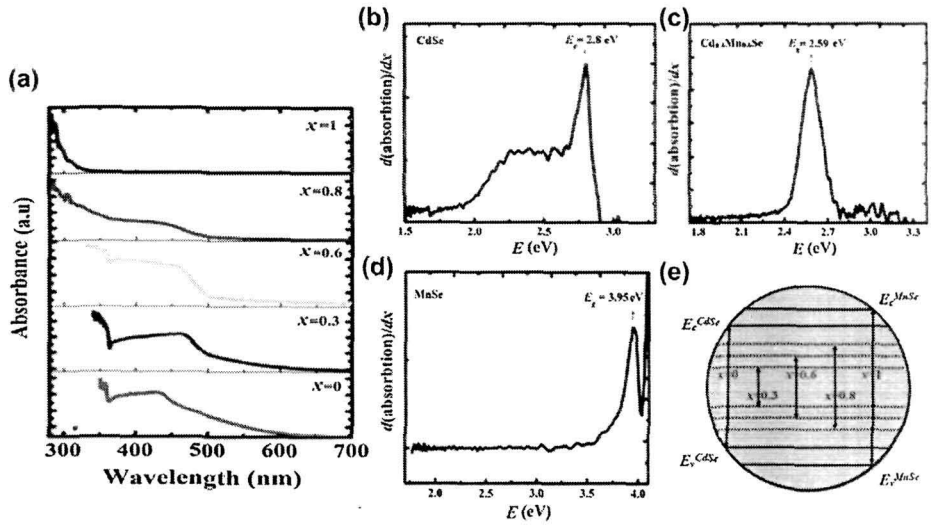

Fig. 3. (a) Optical absorption spectra of $Cd_{1-x}Mn_xSe$ QDs. The first order derivative spectra of the QDs with varying stoichiometric parameters are shown in (*b–d*). A scheme on band gap engineering is presented in (e). (see also supplement for detailed plots).

corresponding bulk CdSe value ($\lambda = 714$ nm) [23]. The comparatively broad, subsidiary peak, observed at a relatively lower energy (2.4 eV) is believed to have arisen owing to the Urbach tailing as a result of carrier transition between the extended and the localized states. As for $x = 0.3$ (Supplement of Fig. 3), the optical gap is characterized by a sharp absorption peak positioned at ~481 nm (2.58 eV) along with a weak subsidiary band at a lower energy. A further increasing of Mn content ($x = 0.6$ and 1), has led to a band gap enhancement with the absorption maxima varying in the range 2.59–3.95 eV (Fig. 3(c and d)). Conversely, in these cases, the secondary broad peak is completely suppressed. We speculate that, beyond a certain Mn-level, the band tailing as characterized by the Urbach states is minimal, as a result of which most of the transitions are likely to be accompanied via only extended states. As predicted earlier [24], with increasing Mn^{2+} concentration, the red shift of the absorption maxima followed by blue-shifting can be attributed to bowing effect (Supplement of Fig. 3). Whereas, a significant blue shift is ascribed to the sp–d exchange interactions between electrons confined in the conduction and valence band electron states and those located in the partially filled Mn^{2+} states [8,24–26]. This explanation [27] is also substantiated by the fact that, the replacement of Cd by Mn (in $Cd_{1-x}Mn_xSe$, $0.3 < x < 0.8$) would vary the energy gap between 1.74 and 3.5 eV, as for the bulk CdSe ($x = 0$), and the WZ-MnSe ($x = 1$) systems; respectively [17]. The optical band gap of the QDs with varying stoichiometric parameter *x*, are highlighted in Table 2. A scheme illustrating band gap engineering in the concerned QD systems can be found in Fig. 3(e).

3.2.2. Luminescence response of QDs of varying stoichiometry

Fig. 4(a) depicts the emission spectra of $Cd_{1-x}Mn_xSe$ QDs along with multi- peak de-convolution shown in dotted lines. Here, each of the spectra is characterized by a number of emission peaks. In case of CdSe QDs ($x = 0$), the first peak at ~590 nm is ascribed to the near band edge (NBE) emission [28]. The second peak, located at ~657 nm, is due to radiative emission mediated via trap states of the QDs [29]. With increasing value of *x* from 0 to 0.3, the NBE emission response of $Cd_{0.7}Mn_{0.3}Se$ system is blue-shifted to ~484 nm [8]. While the peak at ~510 nm corresponds to the shallow, virtual levels of the QDs [30], the appearance of a small peak at ~580 nm is believed to be owing to the pseudo-tetrahedral transitions ($^4T_1 \rightarrow {}^6A_1$) of the Mn^{2+} ions introduced into the CdSe QDs [8]. The broad emission band, with peak maxima at ~628 nm, could not be fitted by single Gaussian-fit, thus signifying complexity of the ternary systems. The association of multiple emissions, with comparable probabilities, can be attributed to recombination events of different origins. Shown in Fig. 4(b), is an enlarged view of the PL spectrum with de-convolution relevant for QDs with $x = 0.3$.

It may be worth mentioning here that, deep defect levels mostly appear in hexagonal wurtzite structures of CdSe, or $Cd_{1-x}Mn_xSe$ QDs [26,31,32]. The de-convoluted peaks, located at ~640 and ~670 nm, can be assigned to deep trap levels in the present case. Possibly, the origin of these defect levels is mediated via $V_{Cd} - V_{Se}$ divacancy centers available in the nanocrystalline specimens [26,33,34]. One di-vacancy is related to the orientation along *c*-axis, whereas the other one is believed to be oriented along the basal Cd—Se bond directions [26,35]. In earlier works, the size dependence of these trapping levels was affirmed for CdSe NCs [26]. Also one can explain independent emissions emanating from the QDs (labeled as, E_{m1} and E_{m2}) as well as from the bulk-like NCs (labeled as, E_{b1}) that might occur in ternary $Cd_{1-x}Mn_xSe$ QDs (Fig. 4(b)). Interestingly, the excitonic emission at ~484 nm of $Cd_{1-x}Mn_xSe$ QDs is nearly suppressed by sufficiently large non-radiative channels via ~628 nm peak [30]. The band edge emission response of $Cd_{1-x}Mn_xSe$ system, as for $x = 0.6$, is further blue-shifted to ~480 nm. The emission due to shallow trap levels, is observed at ~512 nm along with a weak orange emission band, appearing in the wavelength range of ~535– 620 nm. Moreover, the emission peak centered at ~550 nm, is ascribed to the forbidden *d–d* transitions ($^4T_1(^4G)$–$^6A_1(^6S)$) of the Mn^{2+}ions [36]. Note that, with increasing *x* from 0.3 to 0.6, the non-radiative emission via trap levels that originated through $V_{Cd} - V_{Se}$ di-vacancies, is completely disappeared. This indicates that, the

Table 2
Calculation of Stokes' shift and coupling strengths of the synthesized QDs.

x	Intense absorption (eV)	NBE peak (eV)	Stoke's shift, Δ_{Stokes} (eV)	Coupling strength (*S*)
0	2.8	2.10	0.7	11.6
0.3	2.58	2.56	0.02	0.33
0.6	2.59	2.58	0.01	0.16
0.8	2.67	2.62	0.05	0.83
1	3.95	3.1	0.85	14.16

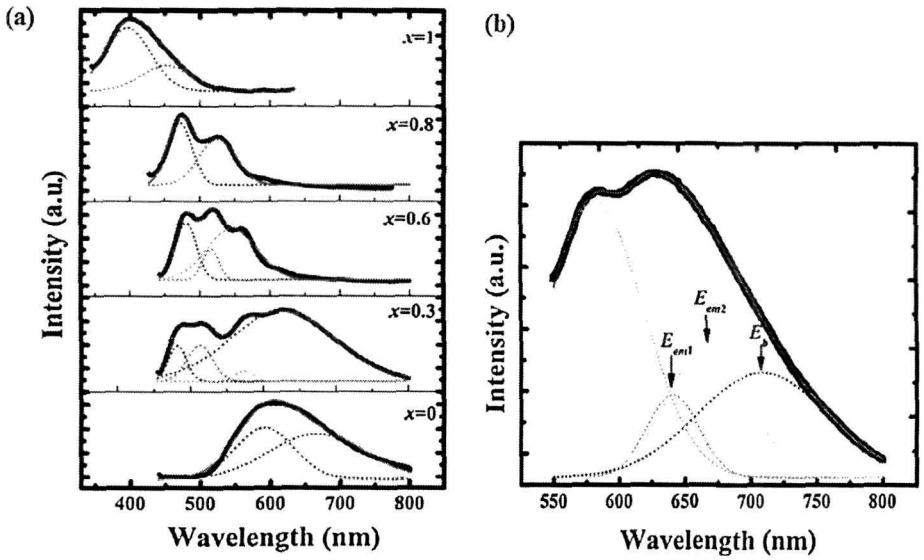

Fig. 4. (a) Room temperature PL spectra of QDs with different stoichiometric parameters, (b) deconvoluted PL spectra of the QDs corresponding to $x = 0.3$.

replacement of $V_{Cd} - V_{Se}$ vacancies by Mn^{2+}ions is much more effective in the QDs with increased Mn^{2+}content [30].

Referring to $x = 0.8$, the NBE emission of $Cd_{0.2}Mn_{0.8}Se$ QDs is found to be positioned at 473 nm, apart from a shallow level apparently located at ~521 nm. No orange emission can be inadvertently detected in this configuration. Moreover, as for MnSe QDs ($x = 1$), the NBE emission response is positioned at ~400 nm, in contrast to the response of the ZB type MnSe system with the peak maxima located at ~364 nm [37]. The emission peak, as observable at ~459 nm, is accompanied by numerous defect states originated from the metastable WZ nanocrystal core [38]. Thus, the PL spectra of the $Cd_{1-x}Mn_xSe$ QDs is extremely sensitive to parameter x. A perturbed lattice structure, in each composition, and with different x can have direct influence on the emission spectrum of definite origin. Besides, the absence of Mn^{2+} emission, as for $x = 0.8$ case, signifies that Mn^{2+} ions are incorporated into the CdSe cluster through surface adsorption rather than direct inclusion into the CdSe core [8]. This is expected especially at a higher concentration of Mn^{2+}. An increased amount of Mn^{2+} ions effectively reduces the average distance between the two Mn^{2+} ions thus favoring diffusion of these magnetic ions from the nanocrystal core to the nanocrystal surfaces [35]. The diffusion of the Mn^{2+} ions through these NCs is known as, 'self-purification' mechanism and is an intrinsic property of impurities/defects in semiconductor NCs. As the ionic radius of the Mn^{2+} is smaller than the ionic radius of the Cd^{2+} ions, it is quite apparent that this diffusion would occur in $Cd_{1-x}Mn_xSe$ NCs [35]. The existence of Mn^{2+} in the CdSe has also been predicted from the XRD analysis discussed above.

3.3. Electron- phonon coupling and analysis through Raman spectroscopy

The difference between the absorption and emission band edge maxima, which is also known as Stokes shift, can be expressed by [39]

$$\Delta_{Stokes} = 2Sh\omega_{LO} \quad (4)$$

In the Franck–Condon approximation, ω_{LO} is the longitudinal optical (LO) phonon frequency of the QDs while S is the Huang–Rhys parameter representing electron–phonon coupling strength of the QDs. The strength of interaction, is expected to play a deterministic role on the optical and optoelectronic responses exhibited by a specimen of interest. Accompanied by phonons, the interaction is likely to facilitate an enhanced absorption near the fundamental band edge along with the broadening of the emission peak [40]. Considering different values of ω_{LO} and Δ_{Stokes} for QDs of diverse kinds, there can be noticeable variation in parameter S. As for CdSe, $\omega_{LO} = 210\,cm^{-1}$ (0.03 eV) [41] and for MnSe, $\omega_{LO} = 257$

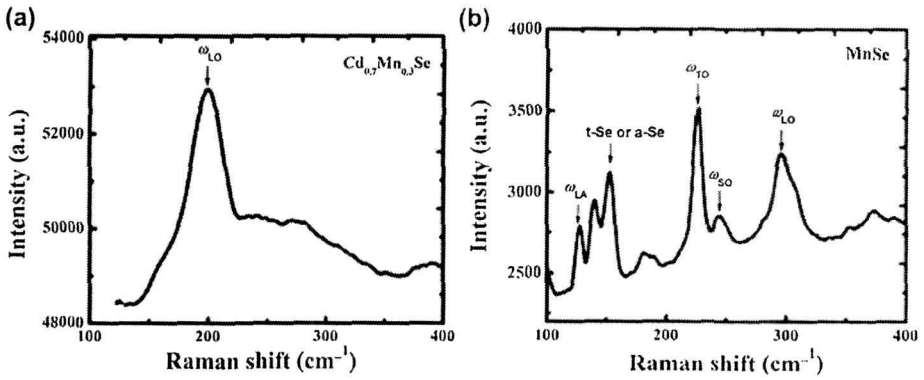

Fig. 5. Raman spectra of $Cd_{1-x}Mn_xSe$ QDs with (a) $x = 0.3$ and (b) $x = 1$.

cm^{-1} (0.034 eV) [42]. For the alloyed system, we considered $\omega_{LO} = 210\ cm^{-1}$, presuming that no significant change of ω_{LO} would occur with alteration of x [22]. The S values were calculated by using Fig. 3 and 4 and are highlighted in Table 2. A high coupling constant value in pure CdSe ($x = 0$) and MnSe ($x = 1$) cases, would signify radiative recombination due to many-body effects on the excitonic states of the NCs [27]. A larger value of S displayed by the later may account for inherent participation of delocalized electrons of the Mn^{2+} states. Nevertheless, the ternary QDs are characterized by $S < 1$ and represent a relatively weak electron-phonon coupling. A similar range of Stokes' shift was witnessed in case of $Cd_{1-x}Mn_xS$ QD systems [27]. Moreover, since the Huang-Rhys factor depends strongly on the distribution of the density of electron and hole charges [40], we speculate that the charge distribution is significantly manifested in the QDs of varying stoichiometry. The Stokes' shift and coupling strengths, as estimated for varying x, are highlighted in Table 2.

We have also assessed a few samples through Raman spectroscopy studies. The Raman active vibrational features could be adequately probed through this technique. The Raman spectra of the QDs ($x = 0.3$ and $x = 1$), are shown in Fig. 5(a, b). The $Cd_{0.7}Mn_{0.3}Se$ QDs exhibited only one mode, identifiable at ~202 cm^{-1} and is close to the LO phonon mode of the CdSe QDs. On the other hand, the pure WZ MnSe QD system showed Raman peaks at ~295 cm^{-1} and 225 cm^{-1} which can be identified as LO and transverse optical (TO) phonon modes of the concerned QD system (Fig. 5(b)). Knowing that, high frequency (ε_∞) and static (ε_0) dielectric permittivity of MnSe as 5.9 and 10, the anticipated modes are in agreement with the popular Lydanne–Sachs–Teller expression, given by

$$\frac{\epsilon_\infty}{\epsilon_0} = \frac{\omega_{TO}^2}{\omega_{LO}^2} \tag{5}$$

The blue-shifting of the LO and TO phonon modes, from the respective modes of the bulk zinc blend ZB MnSe of 257 cm^{-1} and 219.5 cm^{-1} suggests strong phonon confinement in the system [42,43]. Moreover, as the surface optic (SO) vibrational mode of the nanocrystals normally exist in between LO and TO phonon frequencies, the Raman peak at ~244 cm^{-1} is attributed to the SO phonons. The weak mode, observable at ~127 cm^{-1}, may have arisen due to the excitation of longitudinal acoustic (LA) phonons [44]. The peak at ~140 cm^{-1} and 152 cm^{-1} are assigned to trigonal (*t*-Se), monoclinic (mono-Se) and amorphous selenium (*a*-Se) which characterize Raman shifts in the range of 140–150 cm^{-1}. However, no such peaks could be noticed in case of QDs with $x = 0.3$. Apart from the distinct ω_{LO} peak, the existence of broad feature in the high frequency regime, basically characterize mixed modes that are originated as a result of the superimposition of one or more low lying Raman peaks.

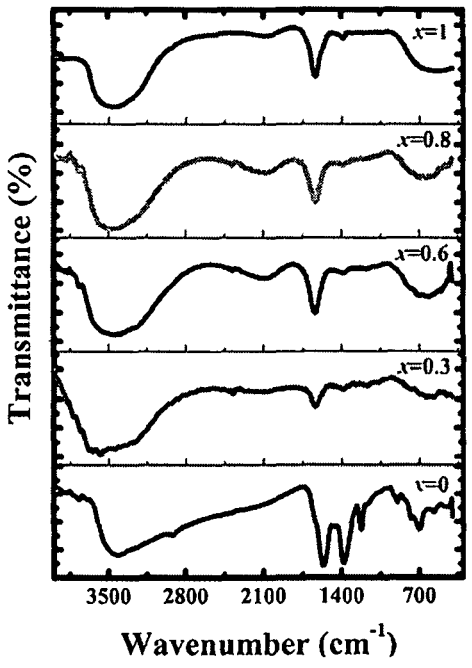

Fig. 6. FTIR spectra of $Cd_{1-x}Mn_xSe$ QDs with different values of x.

3.4 Molecular vibrational analysis through FT-IR spectroscopy

Fig. 6 depicts stoichiometry dependent FT-IR spectra of $Cd_{1-x}Mn_xSe$ QDs. The most prominent O-H stretching mode is found to be common for all the specimens, which typically exist in the range of 3435–3465 cm^{-1}. As for $x = 0$ the TGA coated QDs showed characteristic carboxyl (—COOH) and C=O stretching peaks found at ~1566 cm^{-1} and 1380 cm^{-1}, respectively. The peak observed at ~703 cm^{-1} is assigned to an effaceable bending of Cd-Se itself [45]. With increasing x value from 0 to 0.3, though the strength of the carboxyl (—COOH) and C=O peaks get considerably reduced, the positions remained unaltered. Note the Cd-Se bending peak, which is adequately suppressed in this case. On the other hand, a low intense peak has been observed at ~603 cm^{-1}, which is close to the position of Mn—OH stretching peak noticeable at ~644 cm^{-1} [46]. A new, evolutionary peak is arisen at ~2109 cm^{-1}, when x was varied from 0.6 to 1. This peak can be ascribed to the alkyl stretching (—C≡C—) which may occur due to vibrational twisting of the TGA molecules coated over the QD surfaces. As one moves from $x = 0.6$ to 0.8 and finally to 1, a prominent vibrational peak, located at ~644 cm^{-1} can be witnessed due to characteristic Mn—OH stretching. The inorganic elements and compounds being relatively heavy always correspond to low lying frequencies in the FT-IR spectra. Additionally, CdSe (~5.8 g/cc) being relatively denser than MnSe (~5.5 g/cc), the former could accommodate independent modes that are observable in the form of oscillatory peaks in the low wave number regime. In contrast the occurrence of close-spaced modes would exhibit superimposed feature, which is evident in the form of a broad peak in the spectrum of MnSe system.

3.5 Magnetic characterization of synthesized QDs

We have also evaluated the magnetic responses of the TGA coated $Cd_{1-x}Mn_xSe$ QD systems. Fig. 7 depicts temperature and field dependent magnetization responses of $Cd_{1-x}Mn_xSe$ QDs for $x = 1$ and $x = 0.3$. In zero field cooling (ZFC) condition, the sample was first cooled down to a temperature of 27 K under no field and then the magnetization signal was recorded in the warming process when subjected to an applied field of 500 G. As can be seen from Fig. 7(a) that, no peak is apparently observed for $x = 0.3$. This suggests that, the sample remains paramagnetic and owing to the fact that, at a lower Mn concentration, most of the Mn atoms in $Cd_{1-x}Mn_xSe$ system are concentrated in very small clusters. In this situation, the Mn^{2+} spins have independent existence, largely isolated from one another. A similar behavior was observed for $Zn_{1-x}Mn_xS$ nanoparticle system with a lower value of Mn concentration, as reported in an earlier work [47]. On the other hand, the QD system with $x = 1$ has a Neel temperature (T_N) located at ~59 K [15]. Below T_N, the specimen is anti-ferromagnetic in nature and above T_N it would behave as a paramagnetic system owing to randomization of moments associated with the magnetic ordering process. Note that, the exhibition of steady fall in the

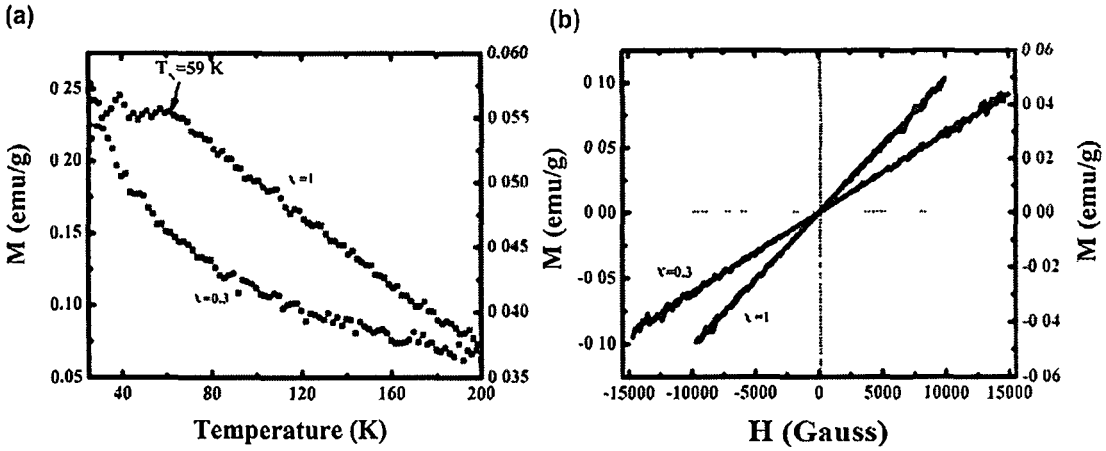

Fig. 7 (a) ZFC curves (b) M–H hysteresis traces of $Cd_{1-x}Mn_xSe$ QDs measured at 26 K and for $x = 0.3$ and $x = 1$

magnetization response (for $x = 1$ case) would characterize the mixed phase of anti-ferromagnetic and paramagnetic ordering Fig 7(b) depicts a set of $M \sim H$ hysteresis plots of the nanoparticle systems with $x = 0.3$ and 1, measured at 20 K Essentially, the QDs are paramagnetic in nature Nevertheless, the T_N value in our case (for $x = 1$) is close to the reported WZ type spherical shaped and water droplet-shaped MnSe nanoparticles [15 17]

The surface- defects along with a layer of surfactants could influence the magnetic properties of the nanoparticles drastically, especially when thermal agitation is lowered With decreasing size of the NPs, surface contribution to the magnetization increases as compared to the core of the particles [48] The total magnetization is believed to be contributed by both surface spins as well as contribution from the core of the particles It is worth mentioning here that, the electronic structure as well as the magnetic property of the whole system can be adequately controlled by the strength of interaction of capping molecules with the NP surfaces Thiols (–SH) are regarded as an excellent candidate for inducing magnetic properties, even in diamagnetic substances [49–51] By capping with a thiol group, an effective charge transfer between the SH^- group and the surface atoms would take place, inducing there by a net magnetization in the system [52] In our case, since the $Cd_{1-x}Mn_xSe$ QDs of different stoichiometric values are prepared with a fixed TGA concentration, magnetic response of the TGA coating layer can be fairly uniform Nevertheless, with increasing x the Mn^{2+} ion concentration on the surface is on the rise, which in turn, increases the charge transfer mechanism between the SH^- group and Mn^{2+}ions This is the reason why a finite value of Neel temperature is ascertained in this case as compared to the case of lower stoichiometry where a clear evidence of Neel temperature is not ensured

4. Conclusions

We have demonstrated structural, optical emission and magnetic responses of TGA coated $Cd_{1-x}Mn_xSe$ QDs The optical absorption, photoluminescence, and magnetic measurements have shown the dependence of the QDs on the concentration of Mn^{2+} ions in the system From the absorption spectra, the blue-shift of the absorption peak with increasing stoichiometry (x) is attributed to the sp–d exchange interactions between electrons confined in the conduction, valence band electrons states and those located in the partially filled Mn^{2+} states The PL spectra signify characteristic orange emission feature owing to the incorporation of magnetic impurity Mn^{2+} ions in the core of the QDs However, QDs with a larger value of x (≥ 0.6), have exhibited suppression/disappearance of the $^4T_1$–$^6A_1$ transitions assisted via Mn^{2+} ions The deep defects occurring in $Cd_{1-x}Mn_xSe$ QDs are attributed to the presence of V_{Cd}–V_{Se} di-vacancies in the hexagonal WZ structure Referring to FT-IR analysis, a prominent vibrational peak at $\sim 644\ cm^{-1}$ can be witnessed due to Mn–OH stretching at higher values of x, apart from various stretching vibrations due to carboxyl and ketonic groups Furthermore, the diffusion behavior of Mn^{2+} ions from the core to the QD surfaces is characterized by a higher value of Neel temperature for MnSe QDs ($x = 1$) At a lower x, however, most of the Mn atoms are likely to concentrate in very small clusters providing isolated Mn^{2+} spins Accordingly the QDs exhibited paramagnetic feature

The collective use of magnetic and fluorescent property of the QDs is a challenging issue in nano-bio interface applications considering its tremendous impact in bioengineering and bio-medical research In this regard, a non-iron based water soluble system like $Cd_{1-x}Mn_xSe$ can find immense value and serve as an alternative candidate for the desired cause

Acknowledgments

The authors thank DST, New Delhi for supporting the work through Fast Track scheme (SR/FTP/PS07/2008) As for magnetic measurements, the help and support received from IIT-G is gratefully acknowledged We acknowledge Dr A Saha, UGC-DAE CSR, Kolkata and Prof A Choudhury TU for extending Raman measurements

Appendix A. Supplementary data

Supplementary data associated with this article can be found in the online version, at http //dx doi org/10 1016/j materresbull 2014 11 011

References

[1] PI Archer SA Santangelo DR Gamelin Nano Letters 7 4, (2007) 1037
[2] R Beaulac PI Archer ST Ochsenbein DR Gamelin Adv Funct Mater 18 (24) (2008) 3873
[3] EA Chekhovich AS Brichkin AV Chernenko VD Kulakovskii IV Sedova S V Sorokin SV Ivanov Phys Rev B 76 (16) (2007) 165305
[4] P Kacman Semicon Sci Tech 16 (4) (2001) R25

[5] S Rana P Sen PK Sen J Phys Conf Series 365 (2012) 012036
[6] Y H Zhu J B Xia Phys Rev B 24 (2006) 245 321
[7] A A Maksimov G Bacher A McDonald V D Kulakovskii A Forchel C R Becker G Landwehr L W Molenkamp Phys Rev B 62 (12) (2000) R7767
[8] J H Yu X Liu K E Kweon J Joo J Park K T Ko D W Lee S Shen K Tivakornsasithorn J S Son J H Park Y W Kim G S Hwang M Dobrowolski J K Furdyna T Hyeon Nature Mat 9 (1) (2010) 47
[9] D J Norris A L Efros S C Erwin Science 319 (5871) (2008) 1776
[10] S C Erwin L Zu M I Haftel A L Efros T A Kennedy D J Norris Nature 436 (7047) (2005) 91
[11] A I Behan J R Neal R M Ibrahim A Mokhtari M Zieve H J Blythe A M Fox G A Gehring J Magn Magn Mater 310 (2007) 2158
[12] D R Larson W R Zipfel R M Williams Stephen W Clark Marcel P Bruchez Frank W Wise Watt W Webb Science 00 (5624) (2003) 1434–1436
[13] S J Byrne S A Corr T Y Rakovich Y K Gun'ko Y P Rakovich J F Donegan S Mitchell Y Volkov J Mater Chem 16 (28) (2006) 2896
[14] R Sarma A Chetry D Mohanta Nanosci Nanotech Lett 3 (2013) 775
[15] R Sarma Q Das A Hussain A Ramteke A Choudhury D Mohanta Nanotechnology 25 (2014) 275101–359601
[16] D Freeman S Mair Z Barnea Acta Crystallogr 33 (3) (1977) 355 Sect A
[17] I T Sines R Misra P Schiffer R E Schaak Angew Chem Int Ed 49 (27) (2010) 4638
[18] X Yang Y Wang Y Sun X Huang T Cui C Wang B Liu G Zou B Zou Cryst Eng Comm 14 (20) (2012) 6916
[19] H Wiedemeier A G Sigai J Solid State Chem 2 (3) (1970) 404
[20] G Williamson W Hall Acta Metall 1 (1) (1953) 22
[21] J Langford R Cernik D Louër J Appl Crystall 24 (5) (1991) 913
[22] S Bhattacharyya D Zitoun A Gedanken J Phys Chem C 112 (20) (2008) 7624
[23] J T Seo C Pompey Q Yang S Creekmore J Anderson J Mangana D Temple X Peng J L Qu W Yu A Wang A Mott M Namkung CLEO (2003)
[24] B C Guo Q Pang C L Yang W K Ge S H Yang J N Wang AIP Conf Proc 772 2005) 605
[25] F S F Neto N O Dantas S A Lourenço Phys Chem Chem Phys 14 (4) (2012) 1493
[26] F S F Neto N O Dantas S A Lourenço M D Teodoro G F Marques Phys Chem Chem Phys 14 (9) (2012) 3248
[27] N O Dantas F S F Neto R S Silva D R Jesus F Pelegrini Appl Phys Lett 93 (19) (2008) 193115
[28] A Wolcott D Gerion M Visconte J Sun A Schwartzberg S Chen J Z Zhang J Phys Chem B 110 (11) (2006) 5779
[29] R Schneider L Balan Nanotechnol Nanomater 119 (2012)
[30] N O Dantas E S D F Neto Nanotechnology and Nanomaterials Nanocrystals Synthesis Characterization and Applications InTech Croatia 2012 pp 953–976 ISBN 978 953 51 0714 9
[31] M Jain Diluted Magnetic Semiconductors World Scientific Singapore 1991
[32] Y Cheng Y Wang F Bai D Chen J Phys Chem B 110 (19) (2006) 9449
[33] S F N Ernesto O D Noelio M B N Newton C Ildi C Felipe Nanotechnology 22 (10) (2011) 105 709
[34] V Babentsov J Riegler J Schneider O Fhlcit T Nam M Fiederle J Cryst Growth 280 (3) (2005) 502
[35] L S F Neto N O Dantas N M B Neto I Guedes F Chen Nanotechnology 22 (10) (2011) 709
[36] J Sun Z Lian G Shen D Shen RSC Adv 3 (40) (2013) 18395
[37] S Lei K Tang H Zheng Mater Lett 60 (13–14) (2006) 1625
[38] K Zhu X Zhang L Wang H Zhang J Wei L Wang M Zhou B Feng J Mater Res 26 (18) (2011) 2400
[39] K Huang A Rhys Proc R Soc London Ser A 204 (1078) (1950) 406
[40] X Zhang T Taliercio S Kolliakos P Lefebvre J Phys Condens Matt 13 (32) (2001) 7053
[41] P Guyot Sionnest B Wehrenberg D Yu J Chem Phys 123 (7) (2005) 74 709
[42] P D Lao Y Guo G G Siu S C Shen Phys Rev B 48 (16) (1993) 711 701
[43] G Gwenael C Philippe Prog Cryst Growth Charact Mater 53 (1) (2007) 56
[44] A Milutinovic Z V Popovic N Tomic S Devic Mater Sci Forum 453 (2004) 299
[45] N A Hamizi M R Johan Optical and FTIR studies of CdSe quantum dots 3rd International Nanoelectronics Conference (INEC) Hongkong 3–9 Jan 2010
[46] M Dhanam B Navitha M Shanmugapriya Chalcogenide Lett 6 (10) (2009) 541
[47] Z H Wang D Y Geng D Li Z D Zhang J Mater Res 22 (09) (2007) 2376
[48] B Issa I M Obaidat B A Albiss Y Haik Int J Mol Sci 14 (11) (2013) 21 266
[49] M A Garcia J M Merino E Fernandez Pinel A Quesada J de la Venta M L Ruiz Gonzalez G R Castro P Crespo J Llopis J M González Calbet A Hernando Nano Lett 7 (6) (2007) 1489
[50] L Guerrero M A Munoz Marquez P Garcia E Fernandez Pinel A Hernando A Fernandez Nanotechnology 19 (17) (2008) 175 701
[51] P Crespo M A Garcia F Fernande Pinel I De la Venta J M Merino A Quesada A Hernando A Fernandez S Penades Acta Phys Pol Ser A 113 (1) (2008) 515
[52] P Crespo R Litrán T C Rojas M Multigner J de la Fuente J C Sanchez Lopez M A Garcia A Hernando S Penades A Fernandez Phys Rev Lett 93 (8) (2004) 087204

Journal of Luminescence 161 (2015) 395–402

Contents lists available at ScienceDirect

Journal of Luminescence

journal homepage: www.elsevier.com/locate/jlumin

Luminescence and bio-imaging response of thio-glycolic acid (TGA) and sodium dodecyl sulfate (SDS)-coated fluorescent cadmium selenide quantum dots

Runjun Sarma, Dambarudhar Mohanta *

Nanoscience and Soft Matter Laboratory, Department of Physics, Tezpur University, PO: Napaam, Assam 784028, India

ARTICLE INFO

Article history:
Received 30 September 2014
Received in revised form
26 December 2014
Accepted 27 December 2014
Available online 30 January 2015

Keywords:
Surfactant
Quantum dot
Life time
Emission
Bio-imaging

ABSTRACT

We demonstrate the usefulness of surfactant coated CdSe quantum dots in bio-imaging applications after evaluating their steady state and time resolved emission responses. The surfactant coated QDs, with the respective sizes of ~14 nm and 10 nm are synthesized considering two different types of coating agents, namely, thio-glycolic acid (TGA) and sodium dodecyl sulfate (SDS). The steady state luminescence response is characterized by both near band edge (NBE) and defect-related emissions, but with a strong dependency on the nature of surfactant coating. Time resolved photoluminescence (TR-PL) studies have revealed bi-exponential characteristics with CdSe–TGA QDs exhibiting longer life time decay parameters than those of CdSe–SDS QDs. To be specific, the fast (τ_1) and the slow (τ_2) components are characterized by ~10 and 30 times larger values in the former than the latter case. In the FT-IR spectra, several stretching and bending vibrations are observed to be adequately influenced by the nature of surfactant coating. The availability of plentiful Na^+ counter ions around SDS coated QDs, as evident from the FT-IR spectroscopy studies, can also be responsible for obtaining reduced size of the QDs. In contrast, Raman active modes are apparently distinguishable in TGA coated QDs, with LO and TO mode positions significantly blue-shifted from the bulk values. While attributing to the intense defect mediated emission of TGA coated QDs, the effect of TGA coating presented a stronger fluorescence imaging capability over the SDS coated ones. A detailed assessment of fluorescent counts, as a basis of bio-imaging response, is being discussed on a comparative basis.

1. Introduction

Of typical size 1–10 nm, the three dimensionally confined nano-scale structures, or semiconductor quantum dots (QDs), are recognized for displaying substantially enhanced energy gaps and atom-like discrete energy levels [1,2]. In recent decades, the importance of QDs has been extended to interdisciplinary arena of research with prime interest involving biophysical and nanobio-interface processes. For instance, the QDs could act as efficient luminescent probe in diagnostics [3], therapeutics [4], surgical implants [5], and novel drug delivery systems [6,7]. This is because of their size dependent tunable color, superior photostability, and better physico–chemical responses with improved surface reactivity. In chalcogenide families of CdX (X=S, Se, and Te) and ZnX (X=O, S, Se, and Te), cadmium selenide (CdSe) has a special place owing to the matchless advantage of large band gap tunability (over a broad energy spectrum) and brilliant emission response. Earlier, it was predicted that, CdSe QDs can be ~20 times brighter and nearly 100 times more photo-stable as compared to single rhodamine 6G dye molecules [8].

Essentially, the success of any biophysical application largely depends on water solubility, environmental stability, bio-conjugation capability, and biocompatibility response of the QDs over a prolonged period of time. Since the uncoated QDs, owing to lack of surface passivation, suffer from adequate fluorescence quenching, an enhanced efficacy is normally realized through adequate surface modification and functionalization with antibodies, peptides and other small molecules of biophysical relevance. The stable QDs, which exist in un-clustered form can be achieved by attaching organic ligands at the surface of the nano-crystals that include even QDs of core/shell types [9]. These organic coating ligands are nonpolar in nature and are mostly insoluble in aqueous solutions [4]. In order to avoid the problem of solubility and stability several strategies have been adopted, for instance, by using different stabilizing agents, QDs can be made practically water soluble [10]. The ligands used during synthesis provide ultimate surface coating anchor which need not require an additional exchange step. The ligand molecules carry functional groups that have high affinity

* Corresponding author. Tel.: +91 3712 275558; fax: +91 3712 267005.
E-mail address: best@tezu.ernet.in (D. Mohanta).

http://dx.doi.org/10.1016/j.jlumin.2014.12.060
0022-2313/

towards the nano-crystal surfaces at one end, and hydrophilic groups on the other end, thereby ensuring water solubility. In this regard, synthesis of thiol-coated CdSe QDs in aqueous solution was an appreciable effort [11,12]. The use of amphiphilic ligands can also be employed where the native non-polar molecules of the amphiphiles work as binding intermediates. Sodium dodecyl sulfate (SDS), through its hydrophilic tail, can help transferring a variety of hydrophobic QDs into the aqueous media [13].

As far as cellular imaging is concerned, while organic dyes possess relatively narrow absorption window and suffer adversely from photo-bleaching effect, the QDs are believed to be more sophisticated light emitting matter owing to their narrow and symmetric emission behavior [14]. The unique properties of the QDs are well suited for dynamic imaging of live and fixed cells and for multiplexed biomedical diagnostics with ultrahigh sensitivity [15]. However, imaging of nucleus-free cells, e.g., erythrocytes and lymphocytes by the fluorescent QDs is least studied especially while considering the influence of different surfactant types into account. In this report, we describe a simple colloidal route of biocompatible CdSe QDs using TGA and SDS as coating agents. Moreover, we highlight the optical emission and carrier life time aspects along with vibrational features of the QDs on a comparative basis. Finally, the fluorescent imaging response of the synthesized QDs is exploited on human lymphocyte cells.

2. Experimental details

2.1. Fabrication of TGA and SDS coated CdSe QDs

At first, 0.93 g of cadmium nitrate-tetra hydrate [$Cd(NO_3)_2 \cdot 4H_2O$, Merck] is dissolved in 100 mL of deionized Millipore® water followed by stirring (~250 rpm, ~40 C) for 20 min. Then, 0.046 g/L of thioglycolic acid (TGA, Merck) and of 0.16 g/L of SDS (Sigma-Aldrich, Mumbai) are added to two different solutions of Cd^{2+} during stirring. The pH of the solution was adjusted to 11 by adding aqueous sodium hydroxide (NaOH, Merck) in a dropwise manner. Next, 0.11 g of SeO_2 is added to the reaction mixture, followed by the inclusion of 0.1 g of solid $NaBH_4$. The mixture was then subjected to stirring for 1 h while temperature was set at 80 °C. Finally, the precursor extract was subjected to centrifugation (~5000 rpm) followed by filtration using a Whatman® filter. In a subsequent step, the precipitate (residue) was rinsed with distilled water several times. The whole process was repeated several times prior final washing with the AR-grade ethanol.

2.2. QD treatment of lymphocyte cells

The fluorescence imaging capability of the QDs was assessed by targeting isolated human lymphocytes, collected voluntarily. At first, anti-coagulated human blood was diluted in a phosphate buffer solution (PBS, Sigma-Aldrich) (v/v 1:1) and then, a layer (of volume 6 mL) was formed using 6 mL histopaque (HiSep, Himedia) (1.07 g/mL). Subsequently, lymphocytes were collected from the buffy layer formed as a result of centrifugation (at 400g) (Refrigerated Centrifuge, Model: 5430 R), for 30 min. The isolated lymphocytes were then washed with 2 mL PBS and 2 mL of a special media (RPMI-1640, Himedia) through independent centrifugation steps, each for 10 min at 250 g. The isolated lymphocytes were cultured in RPMI-1640 media and then supplemented with 10% Fetal Bovine Serum (FBS, Himedia), in the presence of QDs of similar concentration (~0.2 μM) and for two different types of surfactant coatings. The cells were then incubated at 37 °C and in an environment of 5% CO_2, nearly for 10 h. Imaging of normal and QD-treated cells was carried out independently with the help of a fluorescence microscope in ambient environment.

2.3. Analytical characterization techniques

The QD size and morphological features were revealed through high resolution transmission electron microscopy (HRTEM) (JEOL, JEM-2100) working at an accelerating voltage of 200 kV. The steady state luminescence response was studied by a PerkinElmer LS 55 spectrophotometer. On the other hand, carrier lifetime decay measurements of the fluorescent QDs were carried out by a time resolved photoluminescence system (TR-PL, LifeSpec II, Edinburg Instruments, UK). While a laser of excitation wavelength λ_{ex}= 375 nm was employed in the setup, the luminescence decay response was recorded independently (for two QD types) keeping the emission line fixed at λ_{em}=400 nm. The IR-active vibrational features were explored through Fourier transform infrared (FT-IR) (Nicolet model Impact-410) spectroscopy studies. Furthermore, a micro-Raman spectrometer (Renishaw, UK) equipped with He–Ne laser (λ=632 nm) was employed to exploit vibrational characteristics of phonons in TGA and SDS coated QDs. Finally, bright field as well as fluorescence imaging response of the lymphocytes (treated with QDs) are examined using a Leica DM 3000 fluorescence microscope under uniform light exposure (UV lamp, excitation wavelength, and λ_{ex}=300 nm) and using a 40X objective/NA=1.25. All the analytical instruments were operated at room temperature.

3. Results and discussion

Below we discuss TGA and SDS coated CdSe QDs characterized by different techniques.

3.1. Morphological analysis through transmission electron microscopy studies

The TEM images of the as-synthesized TGA and SDS coated CdSe QDs are shown in Fig. 1A and B; respectively. The QDs are observed to be fairly spherical in shape and exist in un-clustered form, in isolation from each other (Fig. 1A(a) and B(a)). The average size (d) of the CdSe–TGA and CdSe–SDS QDs, as assessed from the histogram traces, are predicted as ~14.3 nm and ~10.9 nm; respectively (insets of Fig. 1A(a) and B(a)). The fast Fourier transform (FFT) of an isolated CdSe–TGA QD is depicted in Fig. 1A(b). The hexagonal wurtzite crystal structure of the QD can be evident from the equispaced bright spots witnessed in the FFT image, indicating growth of the lattice planes along (101) and (102) directions. As for TGA coated QDs, the respective inter-planar spacings (d_i) corresponding to the lattice planes (101) and (102), are estimated to be ~0.35 nm, and ~0.22 nm. The inverse FFT pattern, shown in Fig. 1A(c), illustrates a section of well- resolved lattice planes of a single CdSe–TGA QD. In case of an isolated CdSe–SDS QD, the distinct diffraction spots corresponding to (101) plane could only be witnessed in the FFT image, as shown in Fig. 1B(b). Correspondingly, the bright spots around the zone center indicate prominent diffraction from the successive (101) planes having an inter-planar spacing (d_i) of ~0.35 nm. However, the spots corresponding to the (102) plane could not be resolved in this case. The inverse FFT pattern of an isolated CdSe–SDS QD has been depicted in Fig. 1B(c).

3.2. Analysis of steady state and time resolved photoluminescence responses

The steady state, PL spectra of the CdSe QDs prepared with different coating agents are depicted in Fig. 2A. The excitation wavelengths (λ_{ex}) are chosen from the strong absorption signature revealed in the optical absorption spectra (not shown) and accordingly, λ_{ex}=350 nm and 300 nm were considered for recording the

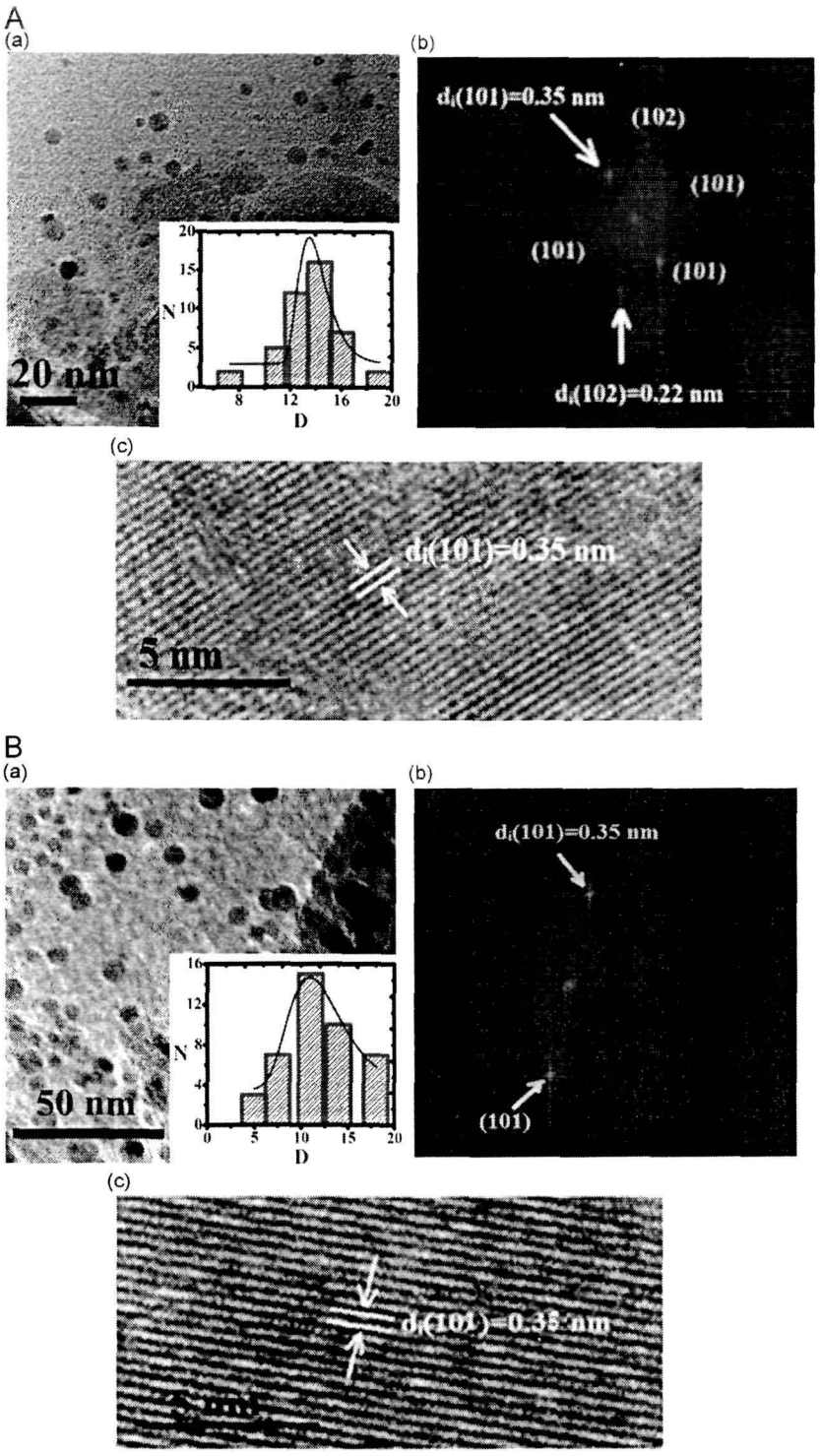

Fig. 1. A: (a) HRTEM image of CdSe–TGA QDs. Inset shows the particle-size distribution as histogram trace, FFT image of an isolated QD is shown in (b) along with spots indicating Miller indices, and (c) shows the inverse FFT pattern highlighting well- resolved lattice planes. B: (a) HRTEM image of CdSe–SDS QDs. Inset shows the particle-size distribution as histogram plot, FFT image of an isolated QD is shown in (b) along with spots indicating Miller indices, and (c) shows the inverse FFT pattern highlighting well-resolved lattice planes.

respective emission responses of CdSe–TGA and CdSe–SDS QDs. As can be noticed, each of the emission spectra has two characteristic peaks: the first one is near band edge emission (λ_{BE}, NBE) which appears via direct radiative recombination, while the second one is attributed to the defect mediated emission (λ_{DE}, DE). As for CdSe–TGA QDs, the NBE is located at ~475 nm and with a full width at half-maxima (FWHM) of ~53 nm (Fig. 2A(a)). Whereas, a broad, much intense DE peak can be found at ~605 nm and with a FWHM of ~134 nm. On the other hand, the SDS coated CdSe QDs exhibited λ_{BE} and λ_{DE} peaks that are located at ~418 nm and 575 nm; respectively (Fig. 2A(b)). The

appearance of both the QD samples, under UV light illumination, are also shown in Fig. 2A.

One can make out two important observations that, in case of TGA coated QDs the NBE is immensely weak but with a strong defect related emission signature. Nevertheless, the SDS coated QDs characterize strong NBE features along with a relatively weak defect emission peak away from each other. The NBE peak is broad in case of SDS coating (FWHM ~93 nm) as compared to the TGA case (FWHM ~53 nm). The nature of coating, as well as slight variation of the size of the QDs may account for manifested DE emission feature at large. A broad DE response could have originated from vacancies, interstitials and charged point defects which normally occur at different locations. The ratio of the band edge-to-defect emission intensities (I_{BE}/I_{DE}) are 0.08 and 1.71 for CdSe–TGA and CdSe–SDS QDs; respectively (Table 1). Accordingly it signifies a higher surface passivation of the CdSe QDs by SDS molecules as compared to the other coating agent.

The fluorescence life time decay profiles of TGA and SDS coated colloidal CdSe QDs, are depicted in Fig. 2B. The characteristic TR-PL spectra exhibited bi-exponential decay responses realized in different ranges of timescale. Here, the shorter life time (τ_1) can be ascribed to the direct radiative transitions of the free excitons (core-state recombination) while the second, a relatively slower component (τ_2) is believed to have arisen from the radiative recombination via surface-trap sites [16]. These surface sites are not necessarily deep trap states (positioned at higher wavelengths) but could exist close to the valence band/conduction band edge states. In case of CdSe–TGA QDs, the decay parameters are estimated as, τ_1 ~5.42 ns and τ_2 ~47.03 ns (Fig. 2B(a)). In contrast, the SDS coated QDs, have experienced much reduced decay constants e.g., τ_1 ~0.53 ns and τ_2 ~1.6 ns (Fig. 2B(b)). One can also use the following expression for calculating the average lifetime of the investigated QDs of different surfactant coatings:

$$\tau_{avg} = \frac{A_1\tau_1^2 + A_2\tau_2^2}{A_1\tau_1 + A_2\tau_2}, \quad (1)$$

where A_1 and A_2 are the pre-exponential factors for the fast and slow processes; respectively. The average life times of the CdSe QDs coated with TGA and SDS layers are calculated to be ~35.1 ns and ~1.16 ns; respectively. As can be noticed, the magnitude of τ_2 for CdSe–TGA QDs is nearly 30 times larger than the value for CdSe–SDS QDs. This may account for substantial amount of the available surface states in the CdSe–TGA QDs, which could help enhancing the localization time of the trapped carriers as compared to the other QD counterpart. The lifetime decay parameters associated with the TGA and SDS coated CdSe QDs are presented in Table 2.

3.3. Analysis of FT-IR and Raman spectra

Through FT-IR spectroscopy one can exploit information wrt molecular stretching, bending and bonding vibrations in a system under study. Whereas, Raman spectroscopy deals with the inelastic scattering of light from both molecular species and solid state objects. Apparently, phononic features including longitudinal and

Table 1
Parameters estimated from the PL spectra of different CdSe QDs.

QD system	λ_{BE} (nm)	$FWHM_{BE}$	λ_{DE} (nm)	$FWHM_{DE}$	I_{BE}/I_{DE}
CdSe–TGA	475	53	605	134	0.08
CdSe–SDS	418	93	575	42	1.71

Table 2
Different decay parameters associated with the fluorescent CdSe QDs.

QDs	τ_1 (ns)	τ_2 (ns)	A_1	A_2	τ_{av} (ns)
CdSe–TGA	5.42	47.03	0.12	0.03	35.1
CdSe–SDS	0.53	1.60	0.02	0.01	1.16

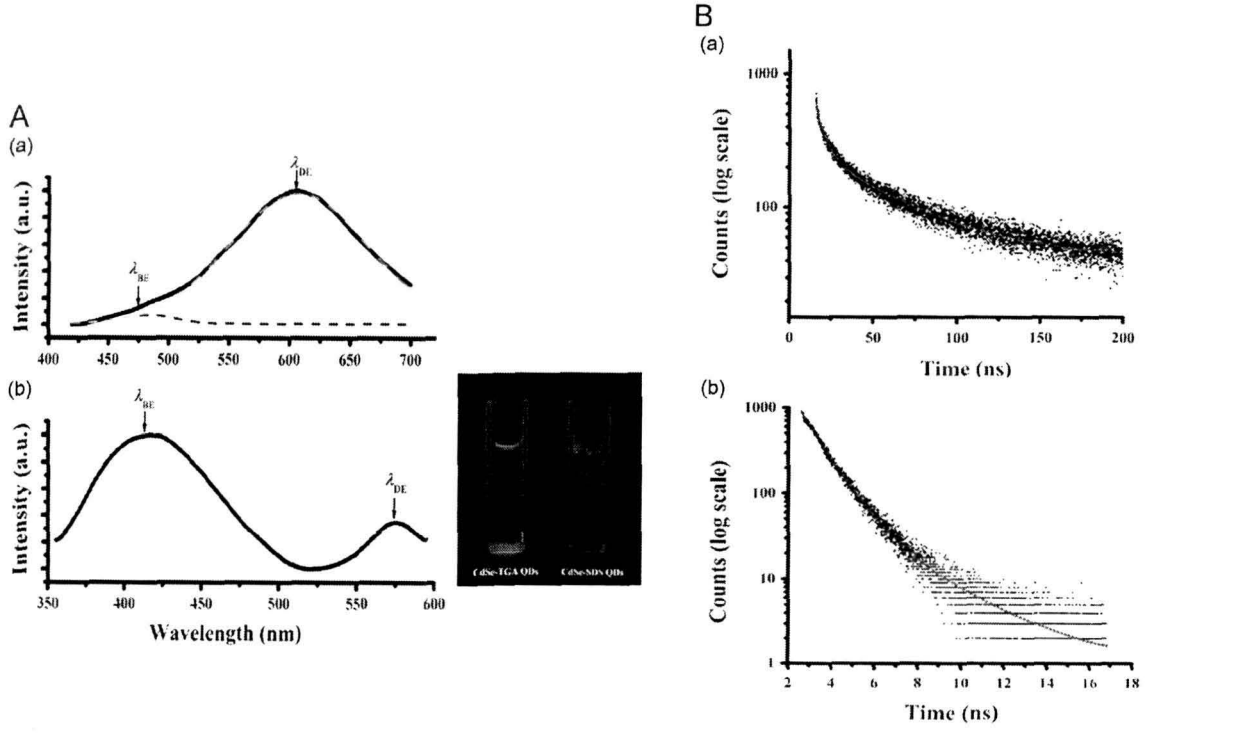

Fig. 2. A: (Left) PL spectra of (a) TGA and (b) SDS coated CdSe QDs with the respective excitation wavelengths as, λ_{ex} ~350 nm and 300 nm. (Right) A digital photograph illustrating the appearance of colloidal QDs under UV illumination. B: TR-PL spectra of (a) CdSe–TGA (b) CdSe–SDS QDs. The emission is fixed at 400 nm.

transverse modes of the vibrational states can be probed with great accuracy [17].

Fig. 3(a) depicts the FT-IR spectrum of the TGA coated CdSe QDs. The dip at $\sim 3418\ cm^{-1}$ arises from the hydroxyl O–H stretching mode of the water molecules present in the ambient environment. The appearance of the bands at $\sim 678\ cm^{-1}$, and at $1646\ cm^{-1}$ are attributed to C–S stretching and asymmetric $\nu_{as}(COO^-)$ vibration of the TGA coated QDs. Moreover, as mentioned earlier, the feature at $\sim 748\ cm^{-1}$ could be assigned to the Cd–Se bending mode [18]. The FT-IR spectrum of the SDS coated CdSe QDs is shown in Fig. 3(b). Though the band at $\sim 3434\ cm^{-1}$ can be attributed to the O–H stretching mode, the feature due to the asymmetric $-CH_2$ stretching ($\nu_{asym}(-CH_2)$) of the SDS surfactant is clearly witnessed at $\sim 2916\ cm^{-1}$ [19]. However, the dip at $\sim 1579\ cm^{-1}$ is assigned to the scissoring mode of the SDS surfactant; which is upshifted slightly to a higher wavenumber ($\sim 1620\ cm^{-1}$) value wrt $\sim 1559\ cm^{-1}$ position of pure SDS molecules [20]. It may be noted that, the spectral region located in the range of $1300–1400\ cm^{-1}$ accommodates the characteristic wagging modes of the $-CH_2$ in the SDS molecule [20]. This region contains features that are related to gauche conformations. Therefore, the $\sim 1381\ cm^{-1}$ position can be assigned to the $-CH_2$ wagging mode realized in the CdSe–SDS QDs. In contrast, the peak corresponding to $\nu_{sym}(-SO_3^-)$ stretching mode of the SO_3^{2-} group is located at $\sim 1272\ cm^{-1}$ [20]. An observable upshifting of the $\nu_{sym}(-SO_3^-)$ mode from a designated value of $1084\ cm^{-1}$(for pure SDS) to a value of $\sim 1272\ cm^{-1}$ (for CdSe–SDS QDs), is owing to an improved interaction of the head-groups with plentiful Na^+ counter-ions [20,21]. An effaceable bending of the inorganic Cd–Se itself can be visualized in the form of a dip at a relatively low wavenumber position of $\sim 713\ cm^{-1}$. We anticipate that, an enhanced interaction of the head-groups, as observed in case of SDS capped QDs would create a stable dispersion of the QDs in the aqueous media and thus resulting in the formation of smaller sized QDs with well surface passivation.

Fig. 4 depicts Raman spectra of the CdSe QDs taken over a wide range of Raman shifts $100–3000\ cm^{-1}$. It can be seen that, in the high frequency region, Raman modes of the CdSe–SDS QDs are drastically suppressed (Fig. 4(a)). Nevertheless, distinct envelops are observable in low as well as in high Raman shift regimes in case of the TGA coated QDs. In order to explore various Raman active modes in the low frequency range, we analyzed the Raman spectrum of the CdSe–TGA system only. Theoretically, longitudinal optical (LO) and transverse optical TO modes can satisfy the well known Lydanne–Sachs–Teller (LST) expression given by [22]

$$\frac{\varepsilon_\infty}{\varepsilon_0} = \frac{\omega_{TO}^2}{\omega_{LO}^2} \tag{2}$$

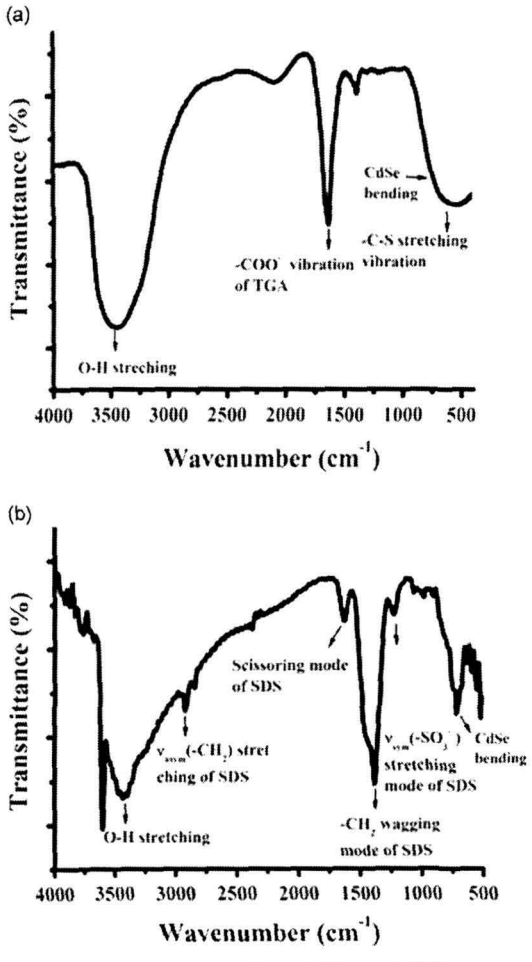

Fig. 3. FTIR spectra of CdSe QDs coated with (a) TGA and (b) SDS coating agents.

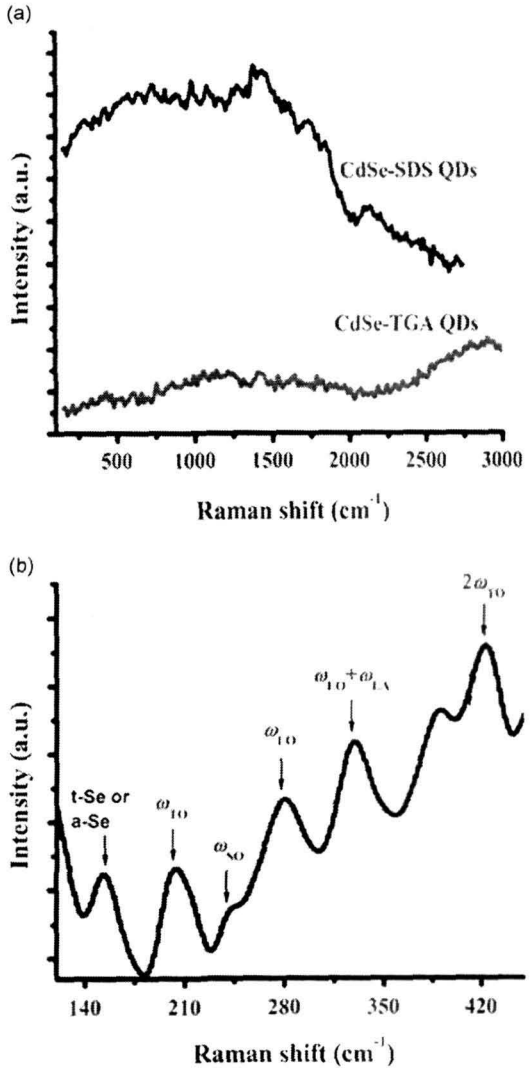

Fig. 4. Raman spectra of (a) different QDs in a broad range of wavenumbers. Referring to the CdSe–TGA QDs, (b) depicts the smoothened, close view of the spectrum in the low wavenumber regime.

Here, the high frequency (ε_∞) and static (ε_0) dielectric constants of the CdSe system are 6 and 9.5; respectively [23]. In reference to Fig. 4(b), the characteristic Raman peaks for the CdSe–TGA QDs are observed at ~222 cm^{-1} and 280 cm^{-1}. The peaks are identified as TO and LO phonon modes, which are believed to be blue-shifted from the corresponding phonon modes of the bulk CdSe system (TO=170 cm^{-1}, LO=210 cm^{-1}) [24]. In nano-scale crystallites, the confinement effect induces a broadening and downward shift of the Raman peaks [25]. Earlier Raman shifting due to the phonon confinement effect was described through the confinement model [26]. When the particle size decreases in the nanometer scale, volume contraction occurs within the nanoparticle due to the size-induced radial pressure. This could result in a significantly enhanced force constant value (k), which in turn decreases the interatomic distances. Since the wavenumber is approximately proportional to $k^{1/2}$, an enhanced force constant value would be characterized by a shifting of the Raman band towards a higher wavenumber side [27].

Since the surface optic (SO) vibrational mode of the nano-scale systems normally exists in between LO and TO phonon frequencies, the Raman peak at ~238 cm^{-1} is attributed to the SO phonon mode. The vibrational states associated with the SO mode largely depends on the dielectric environment (ε_d) of the QDs and one can determine SO frequencies using Klein's formulation [28]

$$\omega_{SO}^2 = \frac{\omega_{TO}^2 (1+1/l) + \omega_{LO}^2 (\varepsilon_\infty/\varepsilon_d)}{(1+1/l) + (\varepsilon_\infty/\varepsilon_d)} \tag{3}$$

where l= 1, 2.... and ε_d=78.30 for water. Here l=1 corresponds to the lower most excited state of the SO mode (225 cm^{-1}) which is close to the experimentally observed value (~238 cm^{-1}). Note that, since the Klein equation is generally valid for non-functionalized nanoparticles, the effect of surface ligands on SO is not considered in the formula. In our case, we speculate that the upshift of the SO mode from the theoretically calculated value is owing to the influence of TGA coating layer around the QDs. The spectrum also characterized mixed modes such as, LO+3LA at ~330 cm^{-1} (LA for CdSe bulk is 18 cm^{-1}). Moreover, second harmonic mode of the TO mode (2TO) has been observed at ~422 cm^{-1}. The peak at 155 cm^{-1} is assigned to the trace amount of amorphous selenium (a-Se) which generally presents Raman shift ($\Delta\nu$) in the range of 140–150 cm^{-1} [29].

3.4. Bio-imaging applications of TGA and SDS coated CdSe QDs

Fig. 5 shows a series of imaging snap-shots of lymphocyte cells treated with different QDs. Fig. 5(a) and (b) depict bright and fluorescence images of the lymphocyte cells without QD treatment. The CdSe–TGA and CdSe–SDS QD treated cells, in fluorescent imaging modes, are shown in Fig. 5(c) and (d); respectively. Essentially, the snapshots signify high biocompatibility and fluorescent behavior of the QDs in the cellular environment. The bright-spots, in each of the fluorescent images, basically represent several QDs localized in the cellular membrane via. site specific linkages. For instance, the head groups of the surfactant are highly accessible to the carboxyl functional groups of the membrane, or, membrane proteins of certain kind (e.g., IgG) [30,31].

Using a versatile *Image J-1.46r Software*® [32] and following previous works reported elsewhere [33–35], a quantitative analysis of the fluorescence counts could be done while QDs are present in the cellular environment and presuming complete localization of the QDs internally. Fig. 6A highlights the areas of interest and select background area of fluorescent images, marked with encircled regions. The corrected total counts of fluorescence (CTCF) intensity value are calculated for each case and using the relation given by

$$CTCF = Integrated\ density - (Area \times mean\ fluorescent\ of\ background\ setting) \tag{4}$$

The integrated density of a fluorescent image is the sum of the values of the pixels in the selected regions of a definite fluorescent image. As can be found in Fig. 6A(a) and (b), different selected fluorescent areas are labeled as A, B, C, D... etc. whereas the selected background regions (cell region without fluorescence) are represented as, bk1, bk2, bk3... etc. The average of mean gray value for the selected regions actually gives the value of the mean fluorescence of the background setting in the formula. A comparative view of representative histograms of the CTCF and the integrated density (Int. Den.) predicted for different cases can be found in Fig. 6B(a) and (b). With the fluorescent area, both the CTCF and Int. Den. were found to vary but to different extents. In order to adjudge the biocompatibility and fluorescent response of the QDs on a comparative basis, the average CTCF and average Int. Den. are compared and presented in Fig. 6B(c). Not surprisingly, the TGA coated QDs displayed a stronger fluorescence response over the SDS coated QDs. The fluorescence efficiency is dramatically quenched for the SDS coating case along with the lowering of CTCF magnitude by nearly 4.4 times as compared to its TGA counterpart. The cellular uptake and bio-imaging capabilities are believed to be significantly affected by the nature of surface functionalization of the QDs. The short TGA molecule, with its carboxyl part, is likely to preserve the fluorescent characteristics of the internalized region through prolonged defect mediated radiative emission of the QDs. The intense DE emission is mainly responsible for illuminating the cellular compartments. Conversely, the relatively long chain SDS molecule, in the absence of carboxyl components, would not protect the QD fluorescence in an efficient way. We also speculate that, the free end of SDS while interacting with membrane macromolecules, form complex overlayers as a result of which the QD fluorescence is drastically suppressed. Moreover, the modification through effective surface

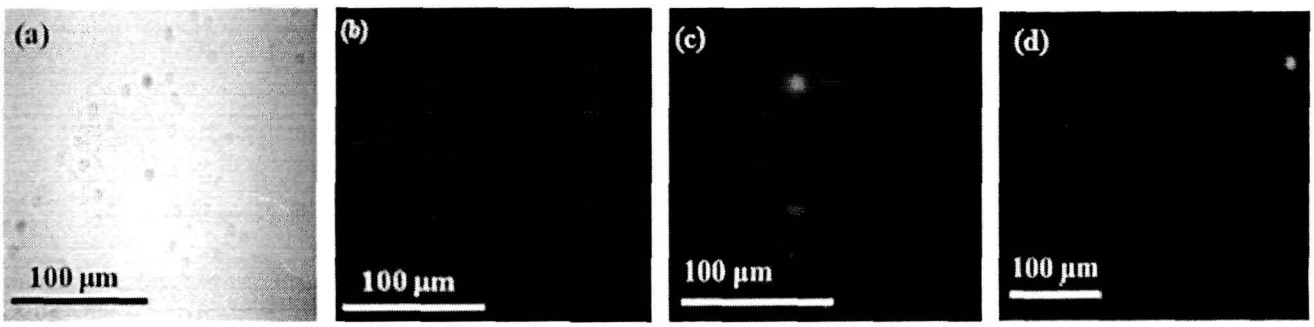

Fig. 5. Bright-field imaging of lymphocyte cells (a) without QDs. Fluorescent image of the lymphocyte cells (b) without QDs and with treatment of (c) CdSe–TGA and (d) CdSe–SDS QDs.

coating may alter the Zeta potential of the QDs, which is largely responsible for manifesting the cellular uptake processes [36,37]. The localization of the nano-scale particles to specific intracellular targets viz., lysosomes, cytoplasm, mitochondria etc. has been achieved by modifying their surface functional property [36]. It is now apparent that, not only the fluorescent property of the material system but also an efficient coating layer is essential for effective cellular imaging while obtaining one-to-one correspondence of the interior parts. The fluorescent QDs could find immense value including tagging of membrane proteins and mechano-sensitive ion channels in artificial and live cells. These ion channels, which form the basis of cellular activity can be

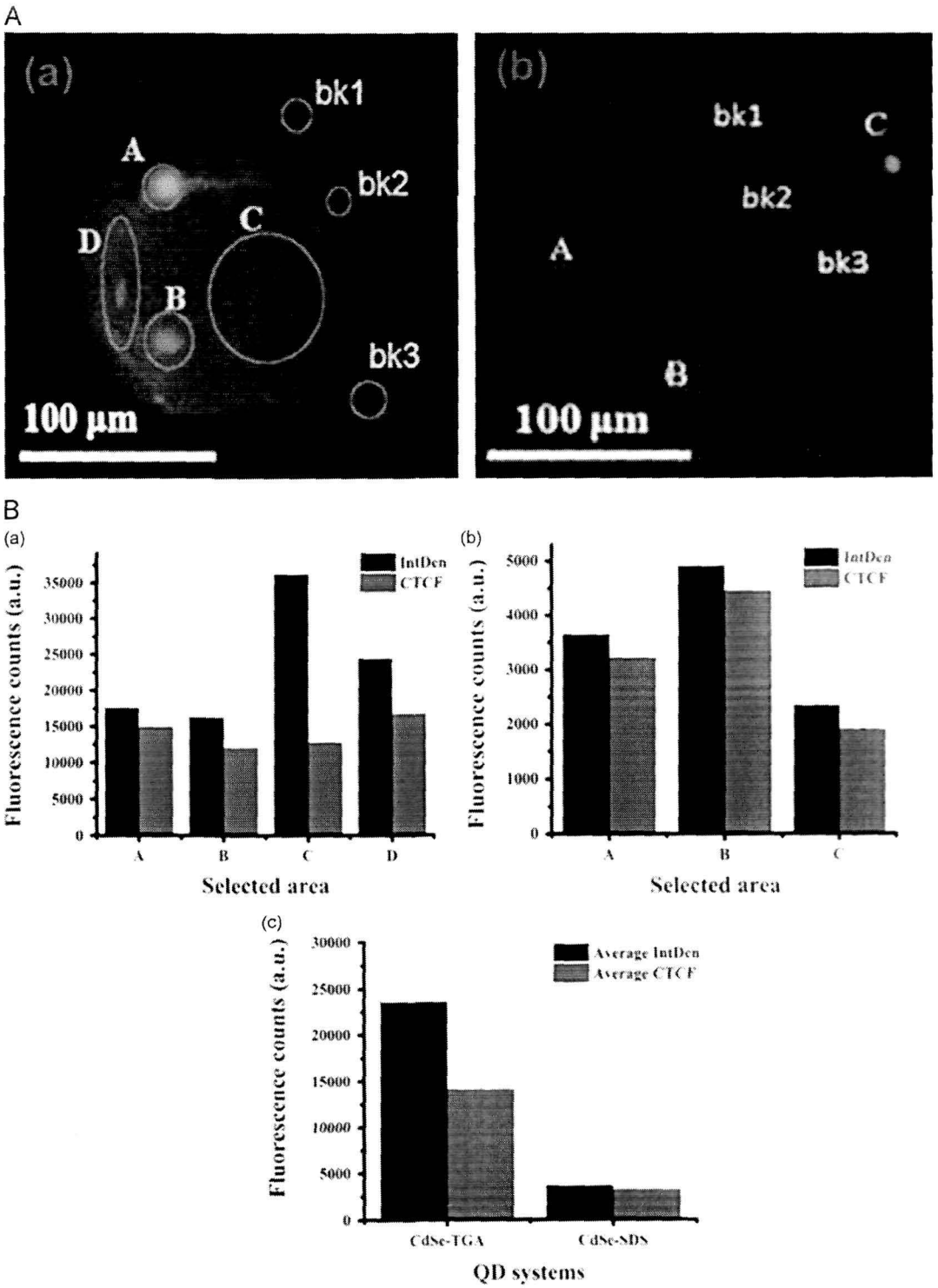

Fig. 6. *A: Selected fluorescent and background areas of the fluorescent image of (a) CdSe–TGA and (b) CdSe–SDS QDs upon treatment with the lymphocyte cells. B:* Histograms representing the fluorescent counts of (a) CdSe–TGA and (b) CdSe–SDS corresponding to select fluorescent areas considering without (Int. Den.) and with (CTCF) background fluorescence. The average value of Int. Den. and CTCF of different QD types is highlighted in (c).

directly controlled by moderate strength static magnetic fields [38,39]. More work wrt consideration of varying QD size and shape will bring in new insights in bio-imaging and bio-labeling applications.

4. Conclusions

The CdSe QDs have been characterized with special emphasis on the influence of surfactant coating and bio-imaging response. While exhibiting only weak band edge emission response, the TGA coated QDs are observed to be highly fluorescent mostly due to the defect mediated emission characteristics. In contrast, the SDS coated QDs exhibit a weak defect related emission, owing to adequate surface passivation as compared to the TGA coated ones. The lifetime measurements (conducted by fixing emission at 400 nm) have revealed that, the TGA coated QDs would experience longer decay parameters than the case for the SDS coated ones. Moreover, the TGA coated QDs, have featured Raman active modes both in the low and high wavenumber regimes. The existence of SO mode was evident within TO (222 cm^{-1}) and LO (280 cm^{-1}) modes which were blue-shifted from their corresponding bulk values. As revealed from the fluorescence microscopy imaging data, the synthesized QDs are highly biocompatible with a high fluorescent contrast in cellular (lymphocyte) environment. Furthermore, the fluorescent imaging capability (CTCFs) of the QDs was shown to vary with the nature of coating agent. Attributed to intense defect emission, the TGA coated QDs remained more fluorescent in the cellular environment as compared to the SDS coated ones. The bioimaging response of fluorescent and magneto-fluorescent QDs will advance the scope of understanding as regards the nature of cell proliferation, cell division and other random functions in disease affected live cells.

Acknowledgments

The authors gratefully acknowledge Dr. A. Saha of UGC-DAE-CSR, Kolkata for extending Raman spectroscopy facility. As for TEM measurements, the help and support received from Mr. J. P. Nongkynrih of SAIF, NEHU, Shillong is acknowledged. The authors thank Dr. A. Ramteke and Mr. Monoj Kumar Das of department of MBBT, TU for extending help in imaging of lymphocyte cells. The authors also acknowledge CIF, IIT-G for extending TR-PL measurements and department of Chemical Sciences, TU for FT-IR measurements.

References

[1] L.E. Brus, J. Phys. Chem. 90 (12) (1986) 2555.
[2] L.E. Brus, J. Chem. Phys. 80 (9) (1984) 4403.
[3] J.U. Menon, P. Jadeja, P. Tambe, K. Vu, B. Yuan, K.T. Nguyen, Theranostics 3 (3) (2013) 152.
[4] X. Xue, F. Wang, X. Liu, J. Mater. Chem. 21 (35) (2011) 13107.
[5] S. Sivolella, E. Stellini, G. Brunello, C. Gardin, L. Ferroni, F. Bressan, B. Zavan, J.Nanomater. 2012 (2012) 15.
[6] A. Zarrabi, M. Adeli, M. Vossoughi, M.A. Shokrgozar, Macromol. Biosci. 11 (3) (2011) 383.
[7] P. Gupta, M. Ramrakhiani, Open Nanosci. J. 3 (2009) 15.
[8] W.C. Chan, D.J. Maxwell, X. Gao, R.E. Bailey, M. Han, S. Nie, Curr. Opin. Biotech. 13 (1) (2002) 40.
[9] S.J. Rosenthal, J.C. Chang, O. Kovtun, J.R. McBride, I.D. Tomlinson, Chem. Biol. 18 (1) (2011) 10.
[10] B. Qin, Z. Zhao, R. Song, S. Shanbhag, Z. Tang, Angew. Chem. Int. Ed. 47 (2008) 9875.
[11] T. Rajh, O.I. Micic, A.J. Nozik, J. Phys. Chem. 97 (46) (1993) 11999.
[12] X. Liu, Y. Gao, X. Wang, S. Wu, Z. Tang, J. Nanosci. Nanotechnol. 11 (2011) 9941.
[13] W.J. Parak, T. Pellegrino, C. Plank, Nanotechnology 16 (2) (2005) R9.
[14] Y. Zhang, A. Clapp, Sensors 11 (12) (2011) 11036.
[15] T. Jamieson, R. Bakhshi, D. Petrova, R. Pocock, M. Imani, A.M. Seifalian, Biomaterials 28 (31) (2007) 4717.
[16] D. Mohanta, S.S. Narayanan, S.K. Pal, A.K. Raychaudhuri, I. Exp. Nanosci 4 (2) (2009) 177.
[17] P. Nandakumar, C. Vijayan, M. Rajalakshmi, A.K. Arora, V.V.G.S. Murti, Phys. E 11 (4) (2001) 377.
[18] N.A. Hamizi, M.R. Johan, in: Proceedings of the 3rd International Nanoelectronics Conference (INEC) (2010).
[19] R.P. Sperline, Y. Song, H. Freiser, Langmuir 13 (14) (1997) 3727.
[20] S.K. Mehta, S. Chaudhary, S. Kumar, S. Singh, J. Nanopart. Res. 12 (5) (2010) 1697.
[21] D.R. Scheuing, J.G. Weers, Langmuir 6 (3) (1990) 665.
[22] R. Lyddane, R.G. Sachs, E. Teller, Phys. Rev 59 (8) (1941) 673.
[23] M. Mohr, C. Thomsen, Nanotechnology 20 (11) (2009) 115707.
[24] R. Vasiliev, V.S. Vinogradov, S.G. Dorofeev, S.P. Kozyrev, I.V. Kucherenko, N.N. Novikova, Phys. Solid State 49 (3) (2007) 547.
[25] I.H. Campbell, P.M. Fauchet, Solid State Commun. 58 (10) (1986) 739.
[26] A.K. Arora, M. Rajalakshmi, T.R. Ravindran, V. Sivasubramanian, J. Raman Spectrosc. 38 (6) (2007) 604.
[27] M. Pal, U. Pal, J.M.G.Y. Jiménez, F. Pérez-Rodríguez, Nanoscale Res Lett 7 (1) (2012) 1.
[28] M.C. Klein, F. Hache, D. Ricard, C. Flytzanis, Phys. Rev. B 42 (17) (1990) 11123.
[29] G. Lucovsky, A. Mooradian, W. Taylor, G.B. Wright, R.C. Keezer, Solid State Commun. 5 (2) (1967) 113.
[30] K. Heckmann, G. Manecke, B. Pfannenmuller, K. Ring, H. Ringsdorf, Google Patents, US4758342 A (1988).
[31] L. Mi, A.D. White, Q. Shao, P. Setlow, Y. Li, S. Jiang, Chem. Sci. 5 (2014) 3320.
[32] (http://imagej.nih.gov/ij/).
[33] A. Burgess, S. Vigneron, E. Brioudes, J.C. Labbé, T. Lorca, A. Castro, Proc. Natl. Acad. Sci.USA 107 (28) (2010) 12564.
[34] O. Gavet, J. Pines, Dev. Cell 18 (4) (2010) 533.
[35] T.A. Potapova, S. Sivakumar, J.N. Flynn, R. Li, G.J. Gorbsky, Mol. Biol. Cell 22 (8) (2011) 1191.
[36] S. Patil, A. Sandberg, E. Heckert, W. Self, S. Seal, Biomaterials 28 (31) (2007) 4600.
[37] R. Sarma, Q. Das, A. Hussain, A. Ramteke, A. Choudhury, D. Mohanta, Nanotechnology 25 (2014) 275101.
[38] S. Hughes, A.J. El Haj, J. Dobson, B. Martinac, Eur. Biophys. J. 34 (2005) 461.
[39] D. Mohanta, E. Srava, M. Yu, R.H. Blick, Phys. Rev. E 89 (2014) 012707.

List of publications

1. Sarma, R., Das, Q., Hussain, A., Ramteke, A., Choudhury, A., and Mohanta, D., Physical and biophysical assessment of highly fluorescent, magnetic quantum dots of a wurtzite-phase manganese selenide system, *Nanotechnology*, **25**(27), 275101, (2014).
2. Sarma, R., and Mohanta, D., Recording ion channels across soy-extracted lecithin bilayer generated by water- soluble quantum dots, *Philos. Mag.*, **94**(4), 345-357, 2014.
3. Sarma, R., Chetry, A., and Mohanta, D., Synthesis, stabilization of CdSe quantum dots and role of rose water and citric environment, *Nanosci. & Nanotech. Lett.*, **4**(8), 775-782, 2013.
4. Sarma, R., and Mohanta, D., A comprehensive view on the Brownian motion of quantum dots in electrolytic solution, lipid Bilayer and their aggregated state in the lipid biomembrane, *J. Comput. Theor. Nanos.*, **9**(8), 1070-1077, 2012.
5. Sarma, R., and Mohanta, D., Role of the supporting substrates for implementing planar chip technology in ion channel experiments, *Int. J. Adv. Mater Sci.*, **3**(2), 87-96, 2012.
6. Sarma, R., Deka, G., and Mohanta, D., Manifested luminescence and magnetic responses of stoichiometry dependent $Cd_{1-x}Mn_xSe$ quantum dot systems, *Mater. Res. Bull.* **62**, 71-79, 2015.
7. Sarma, R., and Mohanta, D., Luminescence and bioimaging response of thioglycolic acid (TGA) and sodium dodecyl sulfate (SDS)- coated fluorescent cadmium selenide quantum dots, *J. Luim.***161**,395-402,2015.

Conference Attended

1. "Advanced spectroscopic characterizations of CdSe quantum dots with soy-extracted lecithin", 2014, National Magnetic Resonance Society Symposium (NMRS), Tezpur University, Assam, India.
2. "Water soluble SDS capped manganese selenide quantum dots and their bioconjugation response with bovin serum albumin protein", 2013, International Conference on Advanced Nanomaterials and Nanotechnology (ICANN), IIT-Guwahati, Assam, India.
3. "Interaction of CdSe quantum dots with soy-extracted lecithin", National Symposium on Nanobiotechnology, 2012, IIT-Mandi, Himachal Pradesh, India.
4. "A comprehensive study of Brownian motion of quantum dots in electrolytic solution, lipid bilayer and their aggregated state in lipid biomembrane", 2011, National Conference on Smart Nanostructures (NCSN), Tezpur University, Assam, India.
5. "Role of substrate supports for implementing planar chip technology in ion channel experiments", Condensed Matter Days (CMDAYS), 2010, Kalyani University, Kolkata, India.